Probing the Environment of Accreting Compact Objects

Untersuchung der Umgebung von akkretierenden kompakten Objekten

Der Naturwissenschaftlichen Fakultät
der Friedrich-Alexander-Universität
Erlangen-Nürnberg

zur

Erlangung des Doktorgrades
Dr. rer. nat.

vorgelegt von

Manfred Hanke

aus Wasserburg am Inn

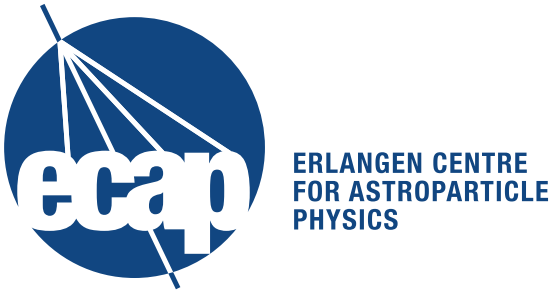

Als Dissertation genehmigt
von der Naturwissenschaftlichen Fakultät
der Friedrich-Alexander Universität Erlangen-Nürnberg

Tag der mündlichen Prüfung:	21. April 2011
Vorsitzender der Promotionskommission:	Prof. Dr. Rainer Fink
Erstberichterstatter:	Prof. Dr. Jörn Wilms, FAU Erlangen-Nürnberg
Zweitberichterstatterin:	Prof. Dr. Julia C. Lee, Harvard University
Drittberichterstatter:	Prof. Dr. Ulrich Heber, FAU Erlangen-Nürnberg

für Alexandra

Contents

Preface **i**
List of Figures . . . iii
List of Tables . . . iv
Zusammenfassung . . . v
Abstract . . . vii

1 Introduction **1**
1.1 Preliminaries from Stellar Astrophysics . . . 2
1.1.1 Roche Lobes . . . 2
1.1.2 Stellar Winds . . . 6
1.1.3 Remnants from Stellar Evolution . . . 11
1.2 Radiation Processes in X-ray Binaries . . . 14
1.2.1 Accreting Compact Objects . . . 14
1.2.2 Compton Scattering, Hard X-ray Spectra, and Spectral States . . . 16
1.2.3 Absorption by Neutral and/or Ionized Matter . . . 21
1.3 X-ray Observatories and their Instruments . . . 29
1.3.1 The *Rossi X-ray timing Explorer* (*RXTE*) . . . 29
1.3.2 The *Chandra* X-ray Observatory . . . 32
1.3.3 The *X-ray Multi-Mirror Mission (XMM) Newton* . . . 34
1.3.4 X-ray Data Analysis . . . 35

2 Analysis of Cygnus X-1 **41**
2.1 The System . . . 41
2.1.1 Parameters of HDE 226868 / Cyg X-1 . . . 42
2.1.2 Modelling the Wind Density Field . . . 45
2.2 Data from X-ray All-Sky Monitors . . . 51
2.2.1 Long Term Evolution and Spectral States . . . 51
2.2.2 Orbital Modulation of the *RXTE* ASM Flux Distribution . . . 55
2.3 Pointed Observations with *RXTE* (PCA) . . . 62
2.3.1 Spectral Modelling in Hard and Soft States . . . 63
2.3.2 Broken Power-Law Fits to all Data from 14.5 Years . . . 74
2.3.3 Orbital Modulation of N_{H} . . . 80
2.3.4 Variabilty of N_{H} on Short Time Scales . . . 84
2.4 *Chandra* Observations . . . 90
2.4.1 Overview . . . 90
2.4.2 The Photoionized Wind in the Hard State . . . 99
2.4.3 Absorption Dips . . . 108
2.5 *XMM-Newton* Observations . . . 116
2.5.1 Overview . . . 116
2.5.2 A Calibration Observation . . . 123
2.5.3 Spectral Changes during Absorption Dips . . . 126
2.6 The Multi-Satellite Campaign . . . 130

3 Investigation of LMC X-1 **135**

4 Summary and Outlook **141**
4.1 Conclusions . . . 141
4.2 Future work . . . 144

Appendix **147**
A A special polar coordinate system for the line of sight in binaries 147
B Bulky tables from the *RXTE* analysis of Cyg X-1 149
C *Chandra* HETGS observations of Cyg X-1 162
D Dynamically known high-mass X-ray binaries 169

Bibliography 171
Acknowledgments 179

List of Figures

A picture is worth a thousand words.

1.1 1d Roche potential (q=0.1) along x-axis . . . 3
1.2 2d Roche potential in the x-y and x-z planes . . . 4
1.3 3d Roche lobe and 90 vol-% equipotential surface (q=0.567) . . . 5
1.4 An integration volume to derive the density structure of a radial wind . . . 9
1.5 Radius of the marginally stable orbit around a black hole as a function of a . . . 13

1.6 Spectrum of an accretion disk with a $T \propto r^{-3/4}$ temperature profile . . . 15
1.7 Polarization and angle dependency of Thomson scattering. . . . 17
1.8 Klein-Nishina cross section for Compton scattering . . . 18
1.9 Sketch of possible X-ray emission geometries for Cyg X-1 . . . 19
1.10 Spectral evolution of transient black hole X-ray binaries along an outburst . . . 20
1.11 Feynman diagrams for photoabsorption and Compton scattering . . . 21
1.12 Position of ground state transitions of astrophysically relevant K-shell ions . . . 23
1.13 Position of K- and L-shell ionization thresholds of ions and neutral atoms . . . 23
1.14 Comparison of models for neutral absorption and Compton scattering . . . 24
1.15 Ioinization balance for different elements . . . 27
1.16 Absorption by neutral and photoionized matter . . . 28

1.17 Spectral coverage and sensitivity of current X-ray detectors . . . 30
1.18 Buffer overflow in binned modes of *RXTE* PCA . . . 31
1.19 A true scale model of *Chandra*'s High Energy Transmission Gratings . . . 34
1.20 Comparison of results from `aglc` before and after version 1.4 . . . 39

2.1 Focused wind model of Friend & Castor (1982) for HDE 226868 . . . 44
2.2 Coordinate systems for the line of sight in binary systems . . . 46
2.3 Lines of sight in a binary system with azimuthal symmetry . . . 47
2.4 Comparison of velocity laws with different β index . . . 47
2.5 Projected velocity onto the line of sight toward the black hole . . . 48
2.6 Velocity and density field of the focused wind (Gies & Bolton, 1986a) . . . 49
2.7 Density along the line of sight for three different models of the velocity field . . . 50

2.8 *RXTE* ASM / MAXI / *CGRO* BATSE & *Swift* BAT light curves of Cyg X-1 . . . 52
2.9 Correlation of *Swift* BAT fluxes and *RXTE*-ASM count rates of Cyg X-1 . . . 53
2.10 *RXTE*-ASM hardness-intensity diagrams of Cyg X-1 . . . 54
2.11 MAXI hardness-intensity diagrams of Cyg X-1 . . . 54
2.12 Joint distribution of *RXTE* ASM count rates of Cyg X-1 . . . 55
2.13 Distribution of the *RXTE* ASM A (1.5–3 keV) band count rate and its uncertainty 56
2.14 Orbital-phase resolved flux distribution of the *RXTE* ASM A rate of Cyg X-1 . . . 56
2.15 Distribution of the *RXTE* ASM (1.5–3 keV) count rate of Cyg X-1 . . . 57
2.16 Fit results for orbital-phase resolved *RXTE* ASM-A flux-distributions of Cyg X-1 59
2.17 Correlation between parameters of the orbital phase resolved flux distribution . 61

2.18 *RXTE* observations of Cyg X-1 and their orbital coverage . . . 62
2.19 Distribution of Cyg X-1 exposure times of the *RXTE* PCA data segments . . . 64
2.20 Number of PCUs that were active during the *RXTE* observations of Cyg X-1 . . . 64
2.21 *RXTE* PCA spectra of Cyg X-1 from all Xenon layers or the top layer only . . . 64
2.22 Confidence maps for the '`bknpower`' model for a hard state spectrum . . . 67
2.23 Confidence maps for the '`bknpower+diskbb`' model for a hard spectrum, '`ign 1-3`' 68
2.24 Confidence maps for the '`bknpower+diskbb`' model for a hard spectrum, '`ign 1-4`' 69
2.25 Flux models for a hard-state spectrum with and without disk component . . . 70

2.26 *RXTE* PCA spectra of Cyg X-1 in the soft state . . . 71
2.27 Confidence maps for the 'bknpower+diskbb' model for a soft spectrum, 'ign 1-3' . 72
2.28 Confidence maps for the 'bknpower+diskbb' model for a soft spectrum, 'ign 1-4' . 73
2.29 Flux models for a soft-state spectrum with disk component . . . 74
2.30 Effect of the background normalization factor c_{back} . . . 76
2.31 Goodness of fits with the bknpower (+ diskbb) model as function of Γ_1 . . . 76
2.32 Systematic difference in Γ_1 and N_{H} between 'bknpower' and 'bknpower+diskbb' 77
2.33 Systematic difference in Γ_1 and N_{H} between 'ign 1-3' and 'ign 1-4' . . . 77
2.34 Correlation between the photon indices Γ_1 and Γ_2 . . . 78
2.35 Orbital phase dependence of the deviation from the linear Γ_1-Γ_2 correlation . . . 78
2.36 Hardness intensity diagrams from spectral fits to *RXTE* PCA segments . . . 79
2.37 Spectral evolution of Cyg X-1 from 1996 to 2010 . . . 79
2.38 $N_{\mathrm{H}}(\phi_{\mathrm{orb}})$ from spectral fits with 'ign 1-3', 'syst 0' . . . 81
2.39 $N_{\mathrm{H}}(\phi_{\mathrm{orb}})$ from spectral fits with 'ign 1-3', 'syst 1 (0.5) %' only for # 4 (5) . . . 83
2.40 Variability of N_{H} on 128 s time scales in *RXTE* PCA observation R_1 . . . 85
2.41 Variability of N_{H} on 128 s time scales in *RXTE* PCA observation R_2 . . . 85
2.42 Close-up view on the strongest dip in R_1 . . . 88
2.43 Isolated strong absorption dip at ϕ_{orb}=0.756, lasting ∼34 s . . . 88

2.44 Orbital phase coverage of previous *Chandra* observations of Cyg X-1 . . . 90
2.45 Light curves and softness ratios of all *Chandra* observations of Cyg X-1 . . . 92
2.46 Light curves from ObsID 107, using the alternating exposure mode . . . 93
2.47 Light curve and fractional exposure during ObsID 3407 . . . 94
2.48 Light curve of the *Chandra* observation 2741 . . . 95
2.49 Light curve and fractional exposure during ObsID 3815 . . . 96
2.50 Pileup in the dispersed spectra of ObsID 12313 . . . 98
2.51 Energy-colored sky images from ObsIDs 11044 and 13219 . . . 98
2.52 Light curves from the joint *RXTE-Chandra* observation on 2003 April 19/20 . . . 99
2.53 *Chandra* light curve and softness ratio from ObsID 3814 . . . 100
2.54 Nondip MEG−1 spectrum from ObsID 3814 . . . 100
2.55 Nondip *Chandra* HETGS spectrum from ObsID 3814 . . . 101
2.56 Warm absorber model for the nondip spectrum from ObsID 3814 . . . 102
2.57 *Chandra* light curve and softness ratio from ObsIDs 8525 and 9847 . . . 103
2.58 Nondip *Chandra* HETGS spectrum from ObsID 8525 . . . 104
2.59 *Chandra* HETGS spectrum from ObsID 11044 . . . 106
2.60 Neutral absorption edges in the *Chandra* HETGS spectrum from ObsID 11044 . . . 106
2.61 Comparison of Ly α line profiles from ObsIDs 3814 and 11044 . . . 107
2.62 Sketch of a possible interpretation of the wind structure . . . 108
2.63 Color-color diagrams from ObsIDs 3814, 8525, and 9847 with strong dipping . . . 109
2.64 Effect of partial absorption with increasing N_{H} at constant covering factor . . . 109
2.65 Fit to the spectra from ObsID 8525 at different stages of dipping . . . 111
2.66 Evolution of the 5.9–7.5 Å spectrum from ObsID 8525 with dipping . . . 113
2.67 Evolution of the 5.9–7.5 Å spectrum from ObsID 9847 with dipping . . . 114
2.68 Evolution of the 4.6–5.5 Å spectrum from ObsID 8525 with dipping . . . 114
2.69 Deep dip spectrum from ObsID 8525 . . . 115

2.70 Orbital coverage of the *XMM* observations of Cyg X-1 . . . 117
2.71 *RXTE* ASM (1.5–12 keV) 1-day average count rate of Cyg X-1 in 2004 . . . 118
2.72 *XMM*-pn light curves of ObsIDs 020240 01 01, 020240 05 01, and 020240 06 01 . . . 118
2.73 *XMM*-pn light curves of ObsIDs 020240 11 01 and 020240 12 01 . . . 118
2.74 *XMM*-pn hardness-intensity diagram during absorption dips and soft state flares 118
2.75 *XMM*-pn light curves and HIDs of the modified timing mode observations . . . 120

2.76 *XMM* RGS light curves of the observations of Cyg X-1 in autumn 2004. 120
2.77 Design of the RGS readout sequence for *XMM* ObsID 050088 02 01 121
2.78 RGS CCD frame times of *XMM* ObsID 050088 02 01 121
2.79 EPIC-pn spectrum from *XMM* ObsID 061000 04 01 123
2.80 Confidence contours for the photon index and the disk temperature 124
2.81 RGS spectra from *XMM* ObsID 061000 04 01 125
2.82 EPIC-pn light curve of *XMM* ObsID 050088 02 01 126
2.83 EPIC-pn spectra at eight different levels of dipping 127
2.84 RGS spectra at eight different levels of dipping 129

2.85 Light curves from the multi-satellite observation on 2008 April 18/19 130
2.86 Hard X-ray light curves showing a minimum during the deepest dip 131
2.87 *Suzaku* XIS color-color diagram and ratios between dip and nondip spectra . . . 132
2.88 Time evolution of the absorption during dips, measured with *XMM* EPIC-pn . . 134

3.1 21 cm H I spectrum of LMC X-1 from the LAB survey 136
3.2 Flux-corrected spectra of LMC X-1 138
3.3 Correlation between the column density and the photon index 138
3.4 N_{H} as a function of orbital phase 140

A.1 Polar coordinates that are locally Euclidean on the line of sight 148

C.1 Images of the *Chandra* observation 107 162
C.2 Images of the *Chandra* observation 2741 163
C.3 Images of the *Chandra* observation 2742 163
C.4 Images of the *Chandra* observation 2743 163
C.5 Images of the *Chandra* observation 3814 164
C.6 Images of the *Chandra* observation 8525 164
C.7 Images of the *Chandra* observation 9847 164
C.8 Images of the *Chandra* observation 11044 165
C.9 Images of the *Chandra* observation 12313 165
C.10 Images of the *Chandra* observation 13219 165

C.11 *RXTE* PCA light curve during the *Chandra* observation 107 166
C.12 *RXTE* PCA light curve before the *Chandra* observation 1511 166
C.13 *RXTE* PCA light curve during the *Chandra* observation 2415 166
C.14 *RXTE* PCA light curve during the *Chandra* observation 3407 166
C.15 *RXTE* PCA light curve during the *Chandra* observation 3724 167
C.16 *RXTE* PCA light curve during the *Chandra* observation 3815 167
C.17 *RXTE* PCA light curve during the *Chandra* observation 3814 167
C.18 *RXTE* PCA light curve during the *Chandra* observations 8525 and 9847 167
C.19 *RXTE* PCA light curve during the *Chandra* observation 11044 168
C.20 *RXTE* PCA light curve during the *Chandra* observations 12313 and 12314 168
C.21 *RXTE* PCA light curve during the *Chandra* observation 12472 168
C.22 *RXTE* PCA light curve during the *Chandra* observation 13219 168

List of Tables

1.1 Parameters of equi-Roche-potential surfaces and their enclosed volumes 5

1.2 Galactic abundances defined by XSPEC, XSTAR, and LMC abundances 25

2.1 *RXTE* PCA modes used in the Cyg X-1 monitoring campaign 62

2.2 Parameters of the '`bknpower`' model for a hard state spectrum 66
2.3 Parameters of the '`bknpower+diskbb`' model for a hard state spectrum 66
2.4 Parameters of the '`bknpower+diskbb`' model for a soft state spectrum 71
2.5 Number of good / acceptable fits from 2247 *RXTE* PCA spectra of Cyg X-1 . . . 76
2.6 Orbital modulation of $N_{\rm H}$ from *RXTE* PCA segments 82
2.7 *RXTE* observations used to analyze $N_{\rm H}$ variations on a 128 s time scale 86
2.8 Parameters of the joint '`bknpower`' continuum for R_1 and R_2 86

2.9 *Chandra* HETGS observations of Cyg X-1 91
2.10 Column densities from H- and He-like ions' line series (ObsID 3814, nondip) . . 102
2.11 Parameters of warm absorber models fitted to hard nondip spectra of Cyg X-1 . 103
2.12 Parameters of P Cygni line profiles in the spectrum from ObsID 11044 107
2.13 Parameters for the partial covering model fit to the spectra from ObsID 8525 . . 111
2.14 Parameters of silicon $1\,{\rm s} \rightarrow 2\,{\rm p}$ absorption lines in ObsID 8525 113

2.15 *XMM-Newton* observations of Cyg X-1 117
2.16 Parameters of a joint fit to *XMM* spectra at eight levels of dipping 128

3.1 Elemental abundances in the LMC 136
3.2 Observations of LMC X-1 with *Chandra* HETGS, *XMM*, *Swift* XRT, or *Suzaku* XIS 137
3.3 Column density in units of $10^{22}\,{\rm cm}^{-2}$ for the six observations and the sine fit . . 138

B.1 Fit results for orbital-phase resolved ASM flux-distributions 150
B.2 Continuous segments from *RXTE* PCA observations of Cyg X-1 in 14.5 years . . 154

D.1 Orbital periods of high-mass X-ray binaries (Liu et al., 2005, 2006) 169

Zusammenfassung

Diese Arbeit beschäftigt sich mit Röngtendoppelsternen, bestehend aus einem kompakten Objekt – also einem schwarzen Loch oder einem Neutronenstern – und einem gewöhnlichen Stern, der Materie an das kompakte Objekt verliert. Die bei diesem Prozess der Massenakkretion freigesetzte Gravitationsenergie wird zum größten Teil in Röntgenstrahlung umgewandelt. Diese wird in der vorliegenden Arbeit genutzt, um die Umgebung des kompakten Objekts zu durchleuchten. Das Hauptaugenmerk richtet sich im Fall eines massereichen Begleitsterns auf dessen Wind, der nicht homogen ist, sondern Strukturen in Form von Temperatur- und Dichteschwankungen aufweisen kann. Da Sternwinden in der Astrophysik in mehrfacher Hinsicht große Bedeutung zukommt, besteht im Allgemeinen großes Interesse daran, diese Strukturen besser zu verstehen. Speziell für Röntgendoppelsterne, deren kompaktes Objekt Materie aus dem Wind des Begleitsterns bezieht, kann der Zustand des Windes einen entscheidenden Einfluss auf die Massenakkretion und die damit verbundenen Strahlungsprozesse haben. In Kapitel 1 wird eine detailierte Einführung in die Grundlagen von Sternwinden, kompakten Objekten, der Akkretion und Strahlungsprozessen in Röntgendoppelsternen sowie in die verwendeten Messinstrumente und Analysemethoden gegeben.

Der Schwerpunkt dieser Untersuchung liegt auf Cygnus X-1, einem Doppelsternsystem mit einem schwarzen Loch und einem blauen Überriesen, die aufgrund der Akkretion aus dem Sternwind eine beständig sehr helle Röntgenquelle bilden. Es ist seit langem bekannt, dass diese Quelle – wenn das schwarze Loch durch den dichten Sternwind gesehen wird – häufig abrupte Absorptionsereignisse zeigt, deren Ursache in Klumpen im Wind vermutet wird. Genauere physikalische Eigenschaften dieser Klumpen und des Winds im Allgemeinen werden in dieser Arbeit erforscht. Es wurden sowohl eigens für diese Studie eingeworbene Beobachtungen als auch Archivdaten von verschiedenen Satellitenobservatorien auf Signaturen des Winds und dessen Feinstrukturen untersucht. Diese Ergebnisse werden in Kapitel 2 dargestellt.

In einem ersten Teil der Analyse wurde die statistische Verteilung der Helligkeit von Cyg X-1, die mit dem Instrument zur Himmelsüberwachung des *RXTE* Satelliten seit 1996 gemessen wurde, in Zusammenhang mit der Bahnphase des Doppelsternsystems untersucht. Der Sternwind macht sich dabei durch Absorption der weichen Röntgenstrahlung bemerkbar. Dadurch konnte nicht nur gezeigt werden, dass die mittlere Säulendichte im Wind für Blickrichtungen nahe am Stern vorbei – wie bereits bekannt – größer ist, sondern dass der Wind dort auch stärker geklumpt ist. Zu dem gleichen Ergebnis kommt die Auswertung von über 2 000 Spektren des Proportionalzählers von *RXTE*, die innerhalb von 14,5 Jahren zum Großteil im Rahmen einer Messkampagne aufgenommen worden sind. Im Vergleich zu früheren Studien konnte durch eine sorgfältige Untersuchung der Qualität des Niederenergiespektrums die Genauigkeit der Messwerte erhöht werden, was nötig war, um deren Streuung aufgrund der Klumpigkeit zu erfassen.

Im nächsten Teil wurden mehrere hochaufgelöste Röntgenspektren ausgewertet, die mit dem Gitterspektrographen des stark nachgefragten *Chandra* Satelliten aufgenommen worden sind. Die Modulation der Absorption konnte damit zum ersten Mal auf den sehr stark ionisierten Wind zurückgeführt werden, was aufgrund der reduzierten Wirkungsquerschnitte im Vergleich zur neutralen Absorption Konsequenzen für deren quantitative Interpretation mit sich bringt. Zudem konnte die Beschleunigung des Windes mit zunehmendem Abstand vom Stern nachgewiesen werden, was einen wichtigen Beobachtungsbefund in Bezug auf die Windstruktur darstellt. Eine 2008 veröffentlichte Vermutung, dass sich in der ionisierten Umgebung der Röntgenquelle kein Wind ausbilden könne, ist damit widerlegt. Weiterhin wurde durch die Spektroskopie von starken Absorptionsereignissen zum ersten Mal eindeutig belegt, dass

diese auf eine Verschiebung des Ionisationsgleichgewichtes aufgrund der erhöhten Dichte der Klumpen zu weniger stark ionisiertem Gas zurückzuführen sind. Die Zunahme der Säulendichte niedrigerer Ionisationsstufen wird auch von der spektroskopischen Analyse der gleichzeitigen Beobachtung mit dem *XMM-Newton* Satelliten bestätigt.

Da diese simultanen Messungen im Rahmen der größten bisherigen Beobachtungskampagne von allen verfügbaren Röntgensatelliten begleitet wurden, konnte ebenfalls der Einfluss der Absorptionsereignisse auf die harte Röntgenstrahlung untersucht werden. In Lichtkurven bei hohen Energien, die nicht von der Absorption beeinflusst werden, wurde eine Reduktion des Flusses festgestellt, die zeitlich mit dem stärksten Absorptionsereignis zusammenfällt. Dieser Effekt konnte durch die zeitaufgelöste Spektroskopie der *XMM* Daten bestätigt und als Streuung an einer vollständig ionisierten Wolke interpretiert werden. Der Verlauf der Lichtkurve stellt daher eine Tomographie dieser Wolke dar, und enthüllt weitere Struktur im Sternwind. Das starke Absorptionsereignis wird vom Kern der Wolke verursacht, der so dicht ist, dass sich in ihm das Ionisationsgleichgewicht verschoben hat.

In Kapitel 3 werden kurz die Ergebnisse der Analyse einer weiteren Quelle präsentiert. Für das Röntgendoppelsternsystem LMC X-1 in der großen Magellanschen Wolke wurden sechs Spektren auf ihre Absorption untersucht. Dabei hat sich ein Zusammenhang mit der Bahnphase angedeutet, der auf Absorption durch Material innerhalb des Systems selbst hinweist.

Zum Abschluß dieser Arbeit werden die detaillierten Ergebnisse in Kapitel 4 zusammenfassend diskutiert, und es wird ein Ausblick auf weiterführende Forschungsmöglichkeiten gegeben.

Abstract

X-ray binaries are the topic of this thesis. They consist of a compact object – a black hole or a neutron star – and an ordinary star, which loses matter to the compact object. The gravitational energy released through this process of mass accretion is largely converted into X-rays. The latter are used in the present work to screen the environment of the compact object. The main focus in the case of a massive star is on its wind, which is not homogeneous, but may display structures in form of temperature and density variations. Since great importance is, in multiple respects, attached to stellar winds in astrophysics, there is large interest in general to understand these structures more thoroughly. In particular for X-ray binaries, whose compact object obtains matter from the wind of its companion star, the state of the wind can decisively influence mass accretion and its related radiation processes. A detailed introduction to the fundamentals of stellar winds, compact objects, accretion and radiation processes in X-ray binaries, as well as to the employed instruments and analysis methods, is given in chapter 1.

The focus of this investigation is on Cygnus X-1, a binary system with a black hole and a blue supergiant, which form a persistently very bright X-ray source because of accretion from the stellar wind. It had been known for a long time that this source – when the black hole is seen through the dense stellar wind – often displays abrupt absorption events whose origin is suspected to be in clumps in the wind. More detailed physical properties of these clumps and of the wind in general are explored in this work. Observations that were specifically acquired for this study, as well as archival data from different satellite observatories, are analyzed in view of signatures of the wind and its fine structures. These results are presented in chapter 2.

In a first part of the analysis, the statistical distribution of the brightness of Cyg X-1, as measured since 1996 with the *RXTE* satellite's all-sky monitor, is investigated in the context of the binary system's orbital phase. The stellar wind is here noticed via absorption of the soft X-radiation. This analysis has not only shown that the mean column density in the wind is – as already known – larger along lines of sight passing close by the star, but also that the wind is more clumpy there. The evaluation of more than 2 000 spectra from *RXTE*'s proportional counter, taken within 14.5 years and mostly in the framework of a monitoring campaign, has lead to the same result. Compared to previous studies, the accuracy of the measurements could be improved by a careful investigation of the quality of the low-energy spectrum, which was required to register the scatter due to the clumpiness.

In the next part, several high-resolution X-ray sepectra were analyzed, which were recorded with the gratings spectrometer of the highly requested *Chandra* satellite. The modulation of the absorption could, for the first time, be ascribed to the highly ionized wind, which has consequences for its quantitative interpretation due to the reduced cross sections compared to neutral absorption. Moreover, the acceleration of the wind with increasing distance from the star could be demonstrated, which constitutes an important observational evidence in terms of the wind structure. A conjecture published in 2008, according to which no wind might develop in the ionized environment of the X-ray source, is therewith disproved. By means of spectroscopy of strong absorption events, it was for the first time unequivocally demonstrated that these can be ascribed to a shift of the ionization balance to less strongly ionized gas, due to the enhanced density of the clumps. The increase of the column density of lower ionization stages is also confirmed by the spectroscopic analysis of the contemporaneous observation with the *XMM-Newton* satellite.

Since these simultaneous observations were, in the framework of the largest observational campaign to date, accompanied by all available X-ray satellites, the effect of the absorption events on hard X-rays could be investigated as well. A flux reduction was detected in light

curves at high energies, not affected by absorption, which coincides with the time of the strongest absorption event. This effect could be confirmed by time resolved spectroscopy of the *XMM* data, and be interpreted as due to scattering on a fully ionized cloud. The evolution of the light curve constitutes therefore a tomography of this cloud, and reveals further structure in the stellar wind. the strong absorption event is caused by the cloud's core, which is sufficiently dense that its ionization balance is shifted.

Results from the analysis of another source are briefly presented in chapter 3. For the X-ray binary system LMC X-1 in the Large Magellanic Cloud, six spectra have been analyzed in view of their absorption. A connection with the orbital phase was suggested, which indicates absorption by material within the system itself.

Concluding this thesis, the detailed results are summarized and discussed in chapter 4, and an outlook on future research possibilities is given.

Chapter I

Introduction

Among nature's four basic forces – the strong, weak, electromagnetic and gravitational interaction – electromagnetism seems at first sight to be the one which most phenomena of our daily life can be traced back to. This does not only hold for modern information technologies which obviously rely on electric circuits and magnetic effects. The diversity and properties of matter on atomic, micro-, meso-, and macroscopic scales is largely due to its electronic configuration. Light – which is still almost[1] the only information astronomers get from their objects of interest, unless they investigate the Solar system – is of electromagnetic nature, too. One could list many further examples. However, thinking about energy, one finds that – although all chemical or biological processes are, again, basically applied electromagnetism – the true origin of energy for living beings on Earth is the Sun, which releases its energy from nuclear fusion and thus due to the strong and weak interactions.[2] *Is the fourth force, gravity, only relevant for tidal power stations and planetary motions, but otherwise nothing but annoying when things keep on falling down?*

On astronomical scales, gravity *is* of course important. Unlike the other forces, it does not know signed 'charges', i.e., masses always attract each other. Gravity may therefore at some point dominate everything else. This is a fascinating idea, and there are indeed stars that are finally forced to collapse into *compact objects* because they are so massive that ordinary atomic matter cannot balance gravity any more. The class of compact objects comprises neutron stars, which still consist of nuclear matter, and black holes, which are thought to be infinitely dense singularities of spacetime that refuse their direct observation. Unlike neutron stars, black holes exist on very different scales. This thesis, however, is about compact objects of stellar mass in X-ray binary systems, although these share many properties and phenomena with 'intermediate mass' black holes and 'supermassive' black holes in Active Galactic Nuclei. The unity among black holes is due to the fact that many length and time scales are just proportional to the black hole mass. Matter accreted by a compact object, which basically simply *falls down* in the deep gravitational potential, releases large amounts of energy; accretion onto compact objects is in fact the most efficient way of converting mass into energy. Black holes are therefore not, as often commonly assumed, only destructive monsters wolfing everything that fatefully comes too close, but their interaction with matter produces also an important feedback to their environment: accretion usually produces ionizing radiation and is often linked with energetic outflows of matter. As both effects may be important for the formation of structure in the Universe, there is general interest in the physics of black holes and accretion onto compact objects, which emerges also from the key questions for European astronomy in the next 20 years noted by the ASTRONET consortium in their Science Vision (de Zeeuw & Molster, 2007):

A) Do we understand the extremes of the Universe?
B) How do galaxies form and evolve?
C) What is the origin and evolution of stars and planets?
D) How do we (and the Solar System) fit in?

Many details of these questions are directly related to black holes, in particular:

[1] The IceCube detector, for example, which might significantly contribute to a new age of neutrino astronomy, has just been completed on 2010-12-18.

[2] For the last decades, humans have been trying to use the same source themselves, in nuclear power plants and atomic bombs.

A.3) Can we observe strong gravity in action?
A.5) How do black hole accretion, jets and outflows operate?
B.2) What are the dominant sources for re-ionization of the Universe: Star light, black hole powered active galactic nuclei, or even decaying supersymmetric particles? How long did the process take?

This thesis is about X-ray observations of accreting compact objects in binary systems, probing their immediate environment from which matter is captured, i.e., the companion's stellar wind in the case of a high-mass X-ray binary with a massive donor star. The whole accretion process may therefore directly depend on properties of this wind, which partly still lack a thorough theoretical understanding. The present work provides observational constraints that will help to complete the pictures of clumping in the wind of massive stars and accretion flows in X-ray binary systems. It furthermore cautions that the stellar wind needs to be well understood and its absorption properly accounted for when modelling the soft X-ray spectrum of high-mass X-ray binary systems.

Outline of the Thesis. The first chapter introduces the general broad background of this work: general astrophysical actualities like binary systems, stellar winds, stellar evolution and their end products; X-ray binaries and the physical processes relevant to explain their observations; and finally the observing instruments and how X-ray data analysis is performed. The second chapter is wholly dedicated to the famous black hole X-ray binary Cygnus X-1, which provides the unique opportunity for this kind of study due to its large observational data set and high quality spectra. After a review of the system parameters, a statistical and spectral analysis of the *RXTE* ASM measurements, respectively the long-term PCA monitoring campaign, is performed in view of an orbital modulation by the environment of the donor star. The investigation of the wind structure is complemented by the subsequent analysis of *Chandra* and *XMM* observations, as well as our dedicated multi-satellite campaign. The third chapter briefly summarizes results obtained for another X-ray binary, LMC X-1. A summary of this work and an outlook is finally given in the last chapter.

1.1 Preliminaries from Stellar Astrophysics

Before introducing X-ray binaries, some general facts from stellar astrophysics are mentioned, as they will become relevant during the further course of this thesis. Section 1.1.1 briefly presents the theory of Roche lobes, which determines the shape of close binaries. An overview on stellar winds, and in particular line-driven winds from early-type stars, is given in Sect. 1.1.2. Finally, Sect. 1.1.3 is a short summary of how compact objects are produced as remnants from the evolution of massive stars.

1.1.1 Roche Lobes

The shape of a star in a binary system, whose rotation is synchronized with its orbit, is determined by the effective potential in the co-rotating system – the so-called *Roche potential* (named after the French astronomer Édouard Albert Roche, 1820–1883). It consists not only of the gravity of the two bodies (at $\vec{r}_1$ and $\vec{r}_2$, and with masses M_1 and M_2, respectively), but also takes the centrifugal potential of the rotation with angular velocity $\vec{\omega}$ around the barycenter at $\vec{r}_{\rm BC} = (M_1\vec{r}_1 + M_2\vec{r}_2)/(M_1+M_2)$ into account:

$$\Phi(\vec{r}) \;=\; -\frac{GM_1}{|\vec{r}-\vec{r}_1|} - \frac{GM_2}{|\vec{r}-\vec{r}_2|} - \frac{1}{2}\left[\vec{\omega}\times(\vec{r}-\vec{r}_{\rm BC})\right]^2 \qquad (1.1)$$

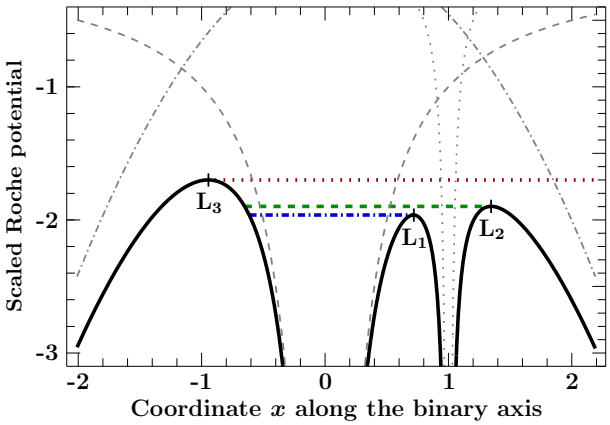

Figure 1.1: Roche potential of Eq. (1.3) for q=0.1 along the binary axis, together with its components (gray): potential of M_1 (dashed), potential of M_2 (dotted), and centrifugal potential (dash-dotted). The dash-dotted (blue), dashed (green), and dotted (red) horizontal lines show the limiting potentials of the L_1, L_2, and L_3 saddle points, respectively.

As ω is not an independent parameter, but given by Kepler's third law,[3]

$$\omega^2 \;=\; \frac{G(M_1+M_2)}{a^3} \tag{1.2}$$

where $a = |\vec{r}_2 - \vec{r}_1|$ is the binary separation, the shape of the Roche potential depends only on the mass ratio $q := M_2/M_1$. Without loss of generality, one can choose the coordinate system such that $\vec{r}_1$ is the origin, $\vec{r}_2 - \vec{r}_1$ is on the positive x-axis, and $\vec{\omega}$ points in the positive z-direction. The scaled Roche potential[4] then reads in dimensionless coordinates $\vec{r}/a = (x, y, z)$:

$$\frac{a}{GM_1}\,\Phi(\vec{r}) \;=\; \frac{-1}{\sqrt{x^2+y^2+z^2}} - \frac{q}{\sqrt{(x-1)^2+y^2+z^2}} - \frac{1+q}{2}\left[\left(x-\frac{q}{1+q}\right)^2 + y^2\right] \tag{1.3}$$

This potential has five critical points where $\vec{\nabla}\Phi = 0$, which are called *Lagrangian points* L_1–L_5 (after the Italian mathematician and astronomer Joseph-Louis Lagrange, 1736–1813). As $\partial\Phi/\partial z = z \cdot f(x, y, z)$ with $f(x, y, z) > 0$, all of them are found in the x-y plane. Figure 1.1 shows the Roche potential along the binary (x-) axis, where the three saddle points L_1–L_3 are located. Figure 1.2 visualizes $\Phi(\vec{r})$ in the x-y and x-z planes for different mass-ratios q=0.1 and 0.567, the latter corresponding to the HDE 226868/Cyg X-1 system. The upper plots show the *triangular Lagrange points* L_4 and L_5 at $(x, y) = (1, \pm\sqrt{3})/2$ to be the global maxima of the potential.

The *Roche lobes* are those equipotential surfaces around M_1 and M_2 which connect at L_1. Inside each Roche lobe, matter (that is corotating with the binary system) is bound to the corresponding mass. The shape of a synchronized star itself is an equipotential surface of the Roche potential, which will notably deviate from a sphere if the star fills a significant fraction of the Roche lobe volume. Table 1.1 lists geometrical parameters of a selection of such equipotential surfaces and Fig. 1.3 shows projections of a 3-dimensional Roche lobe and an equipotential surface that encloses 90 % of the Roche lobe volume, which is the estimated filling factor for HDE 226868.

The size of the Roche lobe around M_1 is often parameterized in terms of the effective radius $r_{\mathrm{Roche},1}$ of a sphere with the same volume. (The size of the lobe around M_2 is $r_{\mathrm{Roche},2}(q) = r_{\mathrm{Roche},1}(q^{-1})$.) A general approximation, accurate to <1 %, was found by Eggleton (1983, eq. 2):

$$r_{\mathrm{Roche},1/2}(q) \;\approx\; \frac{0.49}{0.6 + q^{\pm 2/3}\log\left(1+q^{\mp 1/3}\right)} \tag{1.4}$$

[3] „Sed res eſt certiſſima exactiſſimaque, quod proportio quae eſt inter binorum quorumcunque Planetarum tempora periodica, ſit praeciſe ſeſquialtera proportionis mediarum diſtantiarum, id eſt Orbium ipſorum.“ (Kepler, 1619)

[4] The definition of a reduced Roche potential is not unique. Another common choice, $\propto \Phi(\vec{r})/\omega^2$, is more symmetric in the two masses. For shape considerations, however, absolute values do not matter anyway.

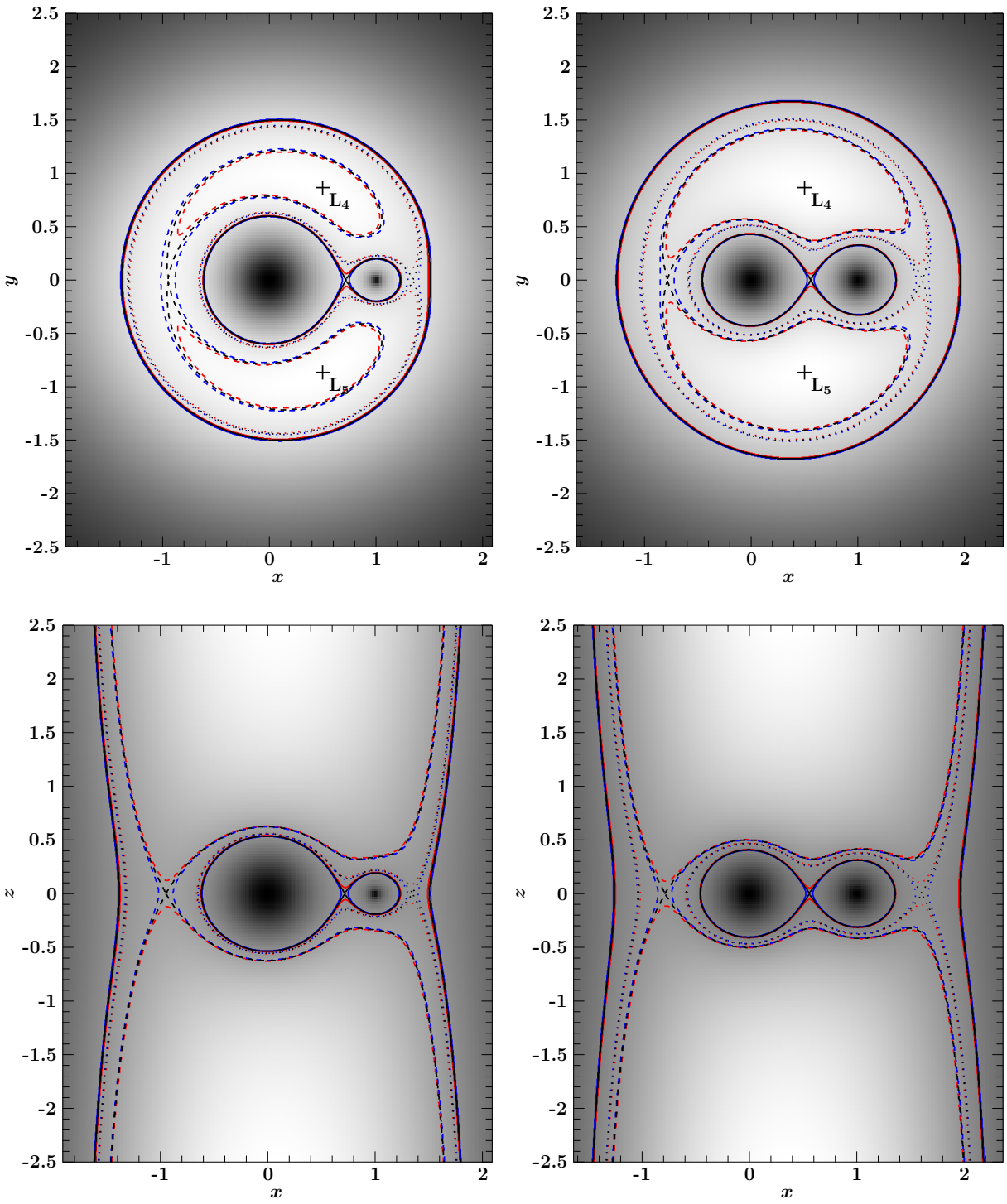

Figure 1.2: Roche potential in the x-y plane at z=0 (top) and in the x-z plane at y=0 (bottom) for $q = 0.1$ (left) and $q = 0.567$ (right), respectively. Brighter colors mean higher potentials. The black solid line shows the Roche lobes – the equipotential surfaces through the L_1 point. The black dotted and dashed lines show the equipotential surfaces through the L_2 and L_3 points, respectively. The blue (red) lines show the corresponding equipotential surfaces at 0.5 % lower (higher) potential. The triangular Lagrange points L_4 and L_5, which are the global maxima of the Roche potential, are indicated by labeled crosses.

Table 1.1: Parameters of equi-Roche-potential surfaces around M_1 and their enclosed volumes, calculated by numerical integration of Eq. (1.3).

q	$\phi_{\rm rel}$	x_+	x_-	y_0	z_0	$r_{\rm eff}$	ρ	V	$v_{\rm rel}$
0.1	1.00000	0.71751	0.61414	0.59601	0.53450	0.58029	1.00	0.81851	1.00
	1.01230	0.65951	0.60191	0.58530	0.52776	0.57045	0.98	0.77758	0.95
	1.02577	0.63268	0.58933	0.57416	0.52056	0.56026	0.97	0.73666	0.90
	1.05670	0.59049	0.56315	0.55064	0.50475	0.53869	0.93	0.65481	0.80
	1.09423	0.55335	0.53539	0.52525	0.48680	0.51524	0.89	0.57295	0.70
	1.14075	0.51739	0.50558	0.49757	0.46623	0.48943	0.84	0.49110	0.60
	1.20018	0.48062	0.47306	0.46693	0.44233	0.46058	0.79	0.40925	0.50
	1.47174	0.37213	0.37037	0.36804	0.35826	0.36556	0.63	0.20463	0.25
	1.95755	0.27108	0.27076	0.27007	0.26718	0.26935	0.46	0.08185	0.10
0.567	1.00000	0.55808	0.45637	0.42775	0.40376	0.43061	1.00	0.33446	1.00
	1.01111	0.50658	0.44750	0.42095	0.39837	0.42331	0.98	0.31773	0.95
	1.02330	0.48360	0.43829	0.41377	0.39261	0.41575	0.97	0.30101	0.90
	1.05121	0.44836	0.41897	0.39834	0.38002	0.39974	0.93	0.26757	0.80
	1.08486	0.41812	0.39836	0.38135	0.36583	0.38234	0.89	0.23412	0.70
	1.12626	0.38942	0.37617	0.36251	0.34973	0.36319	0.84	0.20067	0.60
	1.17879	0.36055	0.35191	0.34133	0.33119	0.34177	0.79	0.16723	0.50
	1.41557	0.27738	0.27527	0.27115	0.26702	0.27127	0.63	0.08361	0.25
	1.83364	0.20148	0.20108	0.19985	0.19862	0.19988	0.46	0.03345	0.10

Notes. $x_\pm$, y_0, and z_0 describe the dimensioning of the equipotential surface (around the primary star only) with a Roche potential $\phi_{\rm rel}$ relative to the critical potential $\Phi_{\rm Roche\,lobe}$, i.e.:
$\Phi(x_+, 0, 0) = \Phi(-x_-, 0, 0) = \Phi(0, \pm y_0, 0) = \Phi(0, 0, \pm z_0) = \phi_{\rm rel} \cdot \Phi_{\rm Roche\,lobe}$
$r_{\rm eff} = \rho \cdot r_{\rm eff,\,Roche}$ is the effective radius of a sphere with the same volume $V = v_{\rm rel} \cdot V_{\rm Roche}$ as enclosed by this equipotential surface, i.e., ρ and $v_{\rm rel} = \rho^3$ are the linear and volume filling factors of the Roche lobe. As these decrease, the equipotential surfaces become more spherical:

$$x_+ \;\rightarrow\; x_- \;\rightarrow\; r_{\rm eff} = [3V/(4\pi)]^{1/3} \;\leftarrow\; y_0 \;\leftarrow\; z_0$$

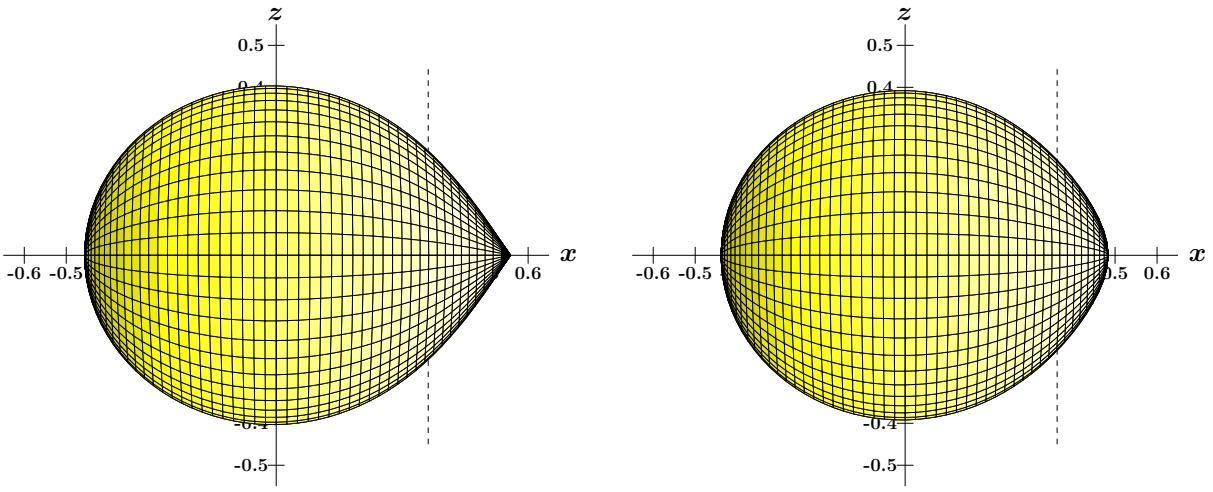

Figure 1.3: Roche equipotential surfaces for q=0.567 with 100 % (left) and 90 % (right) Roche lobe volume filling factors. The objects are seen in a parallel projection along the y-direction. The surface elements are colored according to the hypothetical illumination by an (unseen) secondary at $(x, y, z) = (1, 0, 0)$. The dashed line is the binary system's rotation axis.

1.1.2 Stellar Winds

During most of their 'life', stars are largely in hydrostatic equilibrium, where the pressure due to the energy release in the core balances the gravitational self-contraction. When a central fusion process is exhausted, the star may undergo a vast restructuring, sometimes involving the ejection of its outer layers (e.g., red giants, planetary nebula) or even its total disruption in a supernova explosion, which will be the subject of Sect. 1.1.3. But already during the steady phases, most stars lose constantly mass from their outer atmosphere through stellar winds.

Theoretical Framework

Because of their hydrodynamic nature, their coupling to the star's radiative transport, and sometimes even magnetic fields, stellar winds are a highly complex phenomenon. There are distinct theories for several types of stars, which are dominated by different physical effects such that correspondingly other approximations can be applied. This section will only present a brief overview. An early review is given by Cassinelli (1979), and more recent details can be found in the textbook by Lamers & Cassinelli (1999).

The Navier-Stokes equation (named after the French engineer and physicist Claude-Louis Navier, 1785–1836, and the Irish mathematician and physicist Sir George Gabriel Stokes, 1819–1903), which basically expresses Newton's second law[5] $m \cdot \mathrm{d}\vec{v}/\mathrm{d}t = \vec{F}$ and thus describes the conservation of momentum, reads for an incompressible flow:

$$\rho \left(\frac{\partial \vec{v}}{\partial t} \; + \; \vec{v} \cdot \vec{\nabla} \vec{v} \right) \;\; = \;\; -\vec{\nabla} p \; + \; \mu \, \nabla^2 \vec{v} \; + \; \vec{f} \tag{1.5}$$

Here, ρ is the mass density, $\vec{v}$ is the velocity field, p is the pressure, μ is the dynamic viscosity, and $\vec{f}$ is the external force density. In a simplified description, stellar winds can be considered as such flows that are also steady ($\partial v/\partial t \to 0$), radial ($\vec{\nabla} \to \mathrm{d}/\mathrm{d}r \, \hat{e}_r$), and inviscid ($\mu \to 0$). As the relevant external forces are due to gravity and radiative interactions with matter, the momentum equation for stellar wind usually[6] reads:

$$v \, \frac{\mathrm{d}v}{\mathrm{d}r} \;\; = \;\; -\frac{1}{\rho} \frac{\mathrm{d}p}{\mathrm{d}r} \; - \; \frac{GM}{r^2} \; + \; g_\mathrm{R} \tag{1.6}$$

The radiative acceleration g_R is a linear function of the stellar flux $F_\nu = \mathrm{d}E/(\mathrm{d}t \, \mathrm{d}A \, \mathrm{d}\nu)$ and the opacity $\kappa_\nu = (\mathrm{d}F_\nu/\mathrm{d}x)/(F_\nu \, \rho)$, which can be decomposed in continuum and line opacity:

$$g_\mathrm{R} \;\; = \;\; \frac{1}{c} \int_0^\infty \mathrm{d}\nu \; \left(\kappa_\nu^{(\mathrm{cont})} + \sum \kappa_\nu^{(\mathrm{line})} \right) \, F_\nu \;\; = \;\; g_\mathrm{R}^{(\mathrm{cont})} \; + \; \sum g_\mathrm{R}^{(\mathrm{line})} \tag{1.7}$$

Eddington luminosity. In Eq. (1.7), a lower limit for the (continuum) opacity of a highly ionized plasma is given by the Thomson cross section σ_Th for scattering off electrons (Sect. 1.2.2):

$$\kappa_\nu \;\; \geq \;\; \kappa_\nu^{(\mathrm{cont})} \;\; \geq \;\; \sigma_\mathrm{T} \, \frac{\mathrm{d}N_\mathrm{el}}{\mathrm{d}m} \tag{1.8}$$

Here, $\mathrm{d}N_\mathrm{el}/\mathrm{d}m$ is the number of electrons per unit mass:

$$\frac{\mathrm{d}N_\mathrm{el}}{\mathrm{d}m} \;\; = \;\; \frac{\sum_Z \sum_{N_\mathrm{el}=0}^{Z-1} A(Z;\, N_\mathrm{el}) \cdot (Z - N_\mathrm{el})}{\sum_Z A(Z) \cdot m_Z} \tag{1.9}$$

[5] „Mutationem motus proportionalem esse vi motrici impressae, et fieri secundum lineam rectam qua vis illa imprimitur". (Newton, 1687)
[6] Cassinelli (1979) uses an inconsistent sign convention for g_R.

where $A(Z) = \sum_{N_{\rm el}=0}^{Z} A(Z;\, N_{\rm el})$ is the abundance (by particle number) of the element with atomic number Z, $A(Z;\, N_{\rm el})$ is the abundance of those atoms/ions with $N_{\rm el}$ bound electrons, and m_Z is the atomic mass of this element. According to Table 1.2 on page 25, the abundance of metals with $Z{>}2$ is small, and $A(2) \approx 10\,\% \cdot A(1)$, such that $\mathrm{d}N_{\rm el}/\mathrm{d}m$ is close to $1/m_{\rm H}$ in an environment where hydrogen is (almost) fully ionized, i.e., where $A(1) \approx A(1;\, 0)$.

Using Eq. (1.8) and neglecting pressure forces in Eq. (1.6), the requirement $\mathrm{d}v/\mathrm{d}t \le 0$ for inward acceleration leads to the *Eddington limit* (named after the British astrophysicist Sir Arthur Stanley Eddington, 1882–1944) for the luminosity $L = 4\pi r^2 \int \mathrm{d}\nu\, F_\nu$ of a star or an accreting system under the assumption of isotropy and homogeneity:

$$L \;\le\; \frac{4\pi\, c\, G}{\sigma_{\rm T}\,(\mathrm{d}N_{\rm el}/\mathrm{d}m)} \cdot M \;=\; 1.258\times10^{38}\,\frac{\rm erg}{\rm s} \cdot \frac{\mathrm{d}m/\mathrm{d}N_{\rm el}}{m_{\rm H}} \cdot \frac{M}{M_\odot} \;=:\; L_{\rm Edd} \qquad (1.10)$$

The most luminous stars, 'luminous blue variables', radiate indeed close to the Eddington limit and therefore lose a substantial fraction of their mass through strong winds and especially during super-Eddington eruptions. (More details are given by, e.g., Owocki & van Marle, 2008.)

Wind driving mechanisms. Apart from the electron-scattering opacity of Eq. (1.8), the other components in Eqs. (1.6) and (1.7) may also become important under certain circumstances and thereby enable certain stars to lose mass from their atmosphere, even at $L < L_{\rm Edd}$:

- The pressure gradient $\mathrm{d}p/\mathrm{d}r$ (partly) drives the hydrodynamic expansion of the outer atmosphere of stars with strong coronal heating like the Sun (as originally proposed by Parker, 1958, 1960). Furthermore, pressure can be generated by sound or magnetic waves. The fast solar wind is largely due to the latter Alfvén waves (Lamers, 1998).

- The continuum absorption coefficient $\kappa_\nu^{(\rm cont)}$ due to dust absorption, which can only occur in very late-type stars, i.e., red giants and super giants with temperatures low enough to allow for grain condensation, launches dust-driven winds with mass loss rates up to $10^{-4}\,M_\odot\,\mathrm{yr}^{-1}$ and low terminal velocities $v_\infty \lesssim 40\,\mathrm{km\,s}^{-1}$ (Sedlmayr & Dominik, 1995; Woitke, 2006).

- The line opacity $\sum \kappa_\nu^{(\rm line)}$ causes the winds of early-type stars. Only those provide enough flux in the UV, where a large number of subordinate absorption lines reside (Lucy & Solomon, 1970; Castor et al., 1975; Abbott, 1982; Friend & Abbott, 1986).

Line-driven winds of early-type stars

Even though $\kappa_\nu^{(\rm line)}$ is strongly peaked, the Doppler shift will bring a stellar photon with frequency $\nu > \nu_0$ in resonance with an absorption line at ν_0 – provided that the velocity

$$v \;=\; \frac{\nu-\nu_0}{\nu_0}\cdot c \qquad (1.11)$$

is reached in the accelerating flow – and provided that this photon has not been absorbed before in another resonance transition. If the distribution of absorption lines is sufficiently dense, the wind may be optically thick for the whole spectrum, and nearly the entire momentum of the stellar radiation, L/c, may be transfered to the wind with terminal velocity v_∞ and mass loss rate $\dot{M} \lesssim (L/c)/v_\infty$. Cassinelli (1979) notes that this estimation gives $\dot{M}_{\rm max} = 7{\times}10^{-6}\,M_\odot/\mathrm{yr}$ for $L = 10^6\,L_\odot$ and $v_\infty = 3\,000\,\mathrm{km/s}$, which is *"just about the mass loss rate observed from the most luminous Of and Wolf-Rayet stars and OB supergiants"*. The kinetic

power of this wind, $\dot{M}\, v_\infty^2 \,/\, 2 = v_\infty / (2c) \cdot L$, is, however, only a small fraction ($\sim 0.5\,\%$) of the stellar luminosity L. The photons are thus not permanently destroyed, but will reappear in the redshifted emission component of P Cygni line profiles.

Castor, Abbott, & Klein (CAK; 1975) develop a theory of radiation-driven winds in O stars, taking the large number of subordinate absorption lines (connecting different excited states) into account. These authors find that those lines dominate the radiative force compared to the resonance lines (from the ground state), which were solely considered in earlier theories (e.g., Lucy & Solomon, 1970). The CAK model for the wind structure predicts the following velocity law (Castor et al., 1975, eq. 47):

$$v(r) \;=\; v_\infty \cdot \left(1 - \frac{R_\star}{r}\right)^{1/2} \tag{1.12}$$

Further refinements of this theory lead to a generalized semi-empirical velocity law

$$v(r) \;\simeq\; v_\infty \cdot \left(1 - \frac{R_\star}{r}\right)^{\beta} \tag{1.13}$$

with $\beta \approx 1$ (Friend & Castor, 1983, eq. 79), or $\beta \approx 0.8$ (Pauldrach et al., 1986, eq. 33; Friend & Abbott, 1986, eq. 11) – in good agreement with the observation of $\beta = 0.68 \pm 0.15$ by Groenewegen & Lamers (1989, sect. 5). The initial velocity at the photosphere, $v_0 = v(R_\star)$, often linked to the isothermal speed of sound (e.g. Puls et al., 2008), is usually introduced as:

$$v(r) \;\simeq\; v_0 \;+\; (v_\infty - v_0) \cdot \left(1 - \frac{R_\star}{r}\right)^{\beta} \tag{1.14}$$

or, similarly (e.g., Lamers & Cassinelli, 1999, eqs. 2.2 or 2.3–2.4, respectively):

$$v(r) \;\simeq\; v_\infty \cdot \left(1 - \frac{r_0}{r}\right)^{\beta} \qquad \text{with} \qquad r_0 \;:=\; R_\star \cdot \left\{1 - \left(\frac{v_0}{v_\infty}\right)^{1/\beta}\right\} \tag{1.15}$$

Lucy & Solomon (1970) infer $v(R_\star)$ from the continuity equation

$$\rho(r)\, v(r) \;=\; \frac{\dot{M}}{4\pi\, r^2} \tag{1.16}$$

by calculating the surface density $\rho(R_\star)$ under the assumption of pure hydrogen from the electron temperature T_e and electron pressure p_e, which they model as $T_\mathrm{e} = 0.7\, T_\mathrm{eff}$ and $\log p_\mathrm{e} = \log g - 0.5$ (Lucy & Solomon, 1970).

Density structure

The conservation of mass as stated in Eq. (1.16) allows to infer the density structure $\rho(r)$ of any stationary spherical flow from its velocity field $v(r)$ at given mass loss rate $\dot{M}$. This simple formula can easily be generalized. The generic vectorial mass flux $\vec{F}_\mathrm{mass}$ is then $\rho(\vec{r})\ \vec{v}(\vec{r})$. The continuity equation states the obvious, namely that there is no mass flow (balancing signed in- and outflows) through a closed surface ∂V unless there is a source $s := \mathrm{div}\, \vec{F}_\mathrm{mass} \neq 0$ inside the volume V:

$$\begin{aligned} \oiint_{\partial V} \mathrm{d}\vec{S} \cdot \vec{F}_\mathrm{mass}(\vec{r}) \;&=\; \iiint_V \mathrm{d}V\; s(\vec{r}) \\ &=\; 0, \quad \text{if there is no source in } V \end{aligned} \tag{1.17}$$

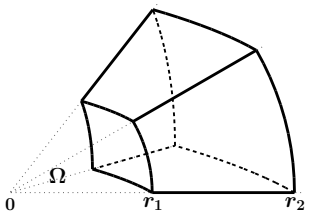

Figure 1.4: A volume whose lateral surfaces are always parallel to the radial direction, while the top and bottom surfaces are always perpendicular to the radial direction, i.e., each of them lies on a sphere and is defined by the same solid angle Ω and the radius r_1 or r_2, respectively.

If the star at $\vec{0}$ is the only source of mass and the velocity field is radial, i.e., $\vec{v}(\vec{r}) = v(\vec{r})\ \vec{r}/r$, the contribution of the lateral surfaces of a volume V ($\not\ni \vec{0}$) like the one sketched in Fig. 1.4 vanishes, and Eq. (1.17) gives the following result for the (unsigned) mass outflow:

$$r_1^2 \iint_\Omega \mathrm{d}\Omega\ \rho(\vec{r})\, v(\vec{r}) \;=\; r_2^2 \iint_\Omega \mathrm{d}\Omega\ \rho(\vec{r})\, v(\vec{r}) \;=\; \iint_\Omega \mathrm{d}\Omega\ \frac{\mathrm{d}\dot{M}}{\mathrm{d}\Omega}(\theta,\phi) \tag{1.18}$$

$\mathrm{d}\dot{M}/\mathrm{d}\Omega$ is here the mass loss rate in a given direction (θ,ϕ). The mass density profile, which is often also expressed in terms of the number density n_H of H-atoms, follows from Eq. (1.18) for an infinitesimal solid angle Ω:

$$\rho(\vec{r}) \;=\; \frac{\mathrm{d}\dot{M}/\mathrm{d}\Omega(\theta,\phi)}{r^2\, v(\vec{r})} \;=\; \mu\, m_\mathrm{H}\, n_\mathrm{H}(\vec{r}) \tag{1.19}$$

μ is the mean molecular weight per H-atom, which follows from the abundances as in Eq. (1.9):

$$\mu \;=\; \sum_Z \frac{A(Z)}{A(1)} \cdot \frac{m_Z}{m_\mathrm{H}} \;\approx\; 1 \,+\, 0.1 \cdot 4 \tag{1.20}$$

Using $\mu = 1.4$ gives the following numbers for a spherical mass loss rate $\mathrm{d}\dot{M}/\mathrm{d}\Omega = \dot{M}/(4\pi)$ and spherical velocity field $v(\vec{r}) = v(r)$:

$$n_\mathrm{H}(r) \;=\; \frac{\dot{M}/(\mu\, m_\mathrm{H})}{4\pi r^2\, v(r)} \;=\; 2.14\times10^{10}\,\mathrm{cm}^{-3} \;\cdot\; \frac{\dot{M}/[10^{-6}\,M_\odot\,\mathrm{yr}^{-1}]}{(r/[10^{12}\,\mathrm{cm}])^2 \;\cdot\; v(r)/[1\,000\,\mathrm{km\,s}^{-1}]} \tag{1.21}$$

Strictly speaking, these considerations hold for the *average* wind density. However, there is evidence that winds of early-type stars are *not homogeneous*.

Clumpy winds

Further analyses of line-driven winds have revealed that the stationary solution is quite unstable; small perturbations grow quickly and result in strong shocks (Owocki & Rybicki, 1984). Non-stationary hydrodynamic simulations show that dense cool shells of gas form already in deep wind regions close to the photosphere (Feldmeier et al., 1997; Dessart & Owocki, 2003). Large density, velocity, and temperature variations due to the de-shadowing instability (Owocki, 2004, sect. 6) further compress the gas in these shells and fragment them into "clumps". It is therefore expected that O star winds are formed out of two disjunctive structural components, namely these clumps and the remaining tenuous hot gas. An excellent review on inhomogeneous winds is given by Puls et al. (2008, sect. 6) and in the proceedings of the workshop on 'Clumping in hot-star winds' (Hamann et al., 2008).

Observational evidence from single O-type supergiants. Stochastic variable structures in the He II lines of the O I star ζ Puppis were revealed by Eversberg et al. (1998), and explained as an excess emission from the wind clumps. Markova et al. (2005) conclude that the line

profile variability observed in a large sample of O-type supergiants can be interpreted with a wind model consisting of coherent or broken shells. Oskinova et al. (2006) find clumpy winds to explain the X-ray emission line profiles observed in the *Chandra* spectra of O-type stars. Lépine & Moffat (2008) find variable subpeaks on top of the emission lines of He II $\lambda = 4686\,\text{Å}$ and He II/Hβ $\lambda = 4860\,\text{Å}$. Their movement in velocity space within hours is in good agreement with the acceleration of the wind itself.

The theory of clumping due to the line-driven instability mentioned above predicts the formation of clumps in the wind acceleration zone such that the outer wind should be more strongly clumped than the inner wind. Cantiello et al. (2009) have recently suggested that sub-surface convection zones in hot massive stars could induce density fluctuations at the stellar surface if the amplitude of velocity waves reaches the speed of sound. Such a mechanism could produce strong wind clumping already at the base of the wind. And indeed, in their detailed broad band analysis of nineteen O stars, Puls et al. (2006) were able to measure relative clumping factors in different regions of the wind, and find for dense winds that the innermost region is more strongly clumped than the outer wind. Thinner winds, on the other hand, have similar clumping properties across all regions.

Clumping and filling factors. The general *clumping factor* is defined by the temporal average of the wind density ρ and its square (Owocki et al., 1988):

$$f_{\rm cl}(\vec{r}) \;=\; \frac{\langle\, \rho(\vec{r})^2 \,\rangle}{\langle\, \rho(\vec{r}) \,\rangle^2} \;\geq\; 1 \tag{1.22}$$

For a wind consisting of a dense component with density $\rho^+ = D\,\langle\rho\rangle$ and *volume filling factor* $0 \leq f_{\rm V} \leq 1$, embedded in a tenous interclump gas of density ρ^-, the density is in general

$$\rho \;=\; f_{\rm V}\cdot\rho^+ \;+\; (1-f_{\rm V})\cdot\rho^- \tag{1.23}$$

If *all* matter is contained in clumps, i.e., the interclump medium is void ($\rho^- \to 0$), and in the ergodic limit, allowing to identify $\langle\ldots\rangle$ with the spatial mean, the clumping factor $f_{\rm cl}$ is just the inverse of the volume filling factor $f_{\rm V}$, which in turn is the inverse density contrast D:

$$f_{\rm cl} \;=\; \frac{f_{\rm V}\cdot(\rho^+)^2}{(f_{\rm V}\cdot\rho^+)^2} \;=\; \frac{1}{f_{\rm V}} \;=\; D \tag{1.24}$$

As the clumps are accelerated to the wind velocity $v(r)$, and individual clumps are considered to be conserved, the *number* density of clumps, $n_{\rm cl} = L^{-3}$ (with the average clump separation L), follows its own continuity equation (Oskinova et al., 2007, eqs. 11, 14):

$$n_{\rm cl}(r) \;=\; \frac{1}{L^3} \;\propto\; r^{-2}\cdot v(r)^{-1} \tag{1.25}$$

Ducci et al. (2009) assume that the density contrast D is constant, as $\rho^+(r)/\rho^-(r) \approx 200$ is required to maintain pressure equilibrium between the clumps and the interclump gas. The conservation of an individual clump's mass $V_{\rm cl}\cdot\rho^+ = V_{\rm cl}\cdot D\rho$ requires an expansion

$$V_{\rm cl}(r) \;\propto\; \rho(r)^{-1} \;\propto\; r^2\cdot v(r) \qquad\Rightarrow\qquad R_{\rm cl}(r) \;\propto\; r^{2/3}\cdot v(r)^{1/3} \tag{1.26}$$

of the clump volume $V_{\rm cl} \propto R_{\rm cl}^3$.

* * *

Stellar winds are in general of high interest for the astrophysical community. First, because they provide a feedback of processed material to the interstellar medium and therefore

contribute to the galactochemic evolution, and second, because they alter the stellar evolution (e.g., Hirschi et al., 2010). Understanding clumped winds is therefore particularly crucial, as the mass-loss rates inferred from ρ^2 diagnostics have to be reduced by a factor $f_{\rm cl}$ – and even more if individual clumps become optically thick (Oskinova et al., 2007). The present work presents the possibility to 'X-ray' winds of hot stars in binary systems with accreting compact objects, which will be introduced in the next section.

1.1.3 Remnants from Stellar Evolution

The evolution of stars is treated by most textbooks on astronomy (e.g. Unsöld & Baschek, 2001; Karttunen et al., 2007), and a very extensive discussion is given by Clayton (1983). This section shall only briefly recall how compact objects are formed as end products from massive stars.

As long as a star is able to maintain its fusion reactions, their pressure may counteract gravity and keep the star in hydrostatic equilibrium. After hydrogen is depleted in the core, the star starts H shell burning in outer layers, increasing its luminosity, such that the star expands and moves onto the red giant branch. A stars that is initially less massive than $\sim 8\,M_\odot$ may ignite at most He burning, which finally becomes unstable and leads to the ejection of the star's outer layers as a so-called planetary nebula. The remaining core is left with a mass below the *Chandrasekhar (1931) limit* of $\sim 1.44\,M_\odot$ and can therefore become a white dwarf, stabilized by the degeneracy pressure of atomic electrons.

Due to higher temperatures in the core of more massive stars, their fusion processes are more effective and hence their evolution proceeds much faster. At the end of its evolution, a massive star will first ignite higher fusion reactions up to iron. When the corresponding elements are depleted, no more energy can be released.[7] Ultimately, electrons are captured by atomic nuclei and the iron core of the star has to collapse to a compact object. The high flux of escaping neutrinos produced during the neutronization of the core may contribute to an accompanied ejection of the outer layers in a supernova explosion,[8] whose detailed mechanisms are still being investigated (e.g., Woosley & Janka, 2005; Janka et al., 2007). Stars initially more massive than $\sim 40\,M_\odot$ may collapse without supernova explosion (Fryer, 1999).

If the mass of the core finally does not exceed the Tolman (1939), Oppenheimer & Volkoff (1939) limit, a *neutron star* can form, which is balanced by the degeneracy pressure of neutrons and repulsive neutron-neutron interactions. However, neither these nor any other known forces can support a compact object with more than 2–3 $M_\odot$ (the uncertainty being due to the lack of knowledge on the equation of state for nuclear matter) against its own gravity. Such one must therefore continue to collapse into a *black hole*. These exotic objects had been predicted by General Relativity long before astrophysicists believed that they are inevitable end products of the evolution of massive stars. A short introduction to their theory will be given after the evolution of stars in a binary system is considered.

Binary evolution

The evolution of binary systems differs from the evolution of isolated stars as various kinds of mass transfer between the two components may occur (e.g., Iben, 1991; Verbunt, 1993): In a first step, the initially more massive star fills its Roche lobe, e.g., because of the expansion

[7] Fewell (1995) points out that ^{62}Ni is the nuclid with the highest specific binding energy, and not, as widely believed, ^{56}Fe, though the latter is the most abundant one of the iron group as produced by stellar nucleosynthesis.

[8] Amazingly, Baade & Zwicky (1934) have already suggested that "*the super-nova process represents the transition of an ordinary star into a neutron star*" – only 2 years after the neutron has been discovered (Chadwick, 1932).

during final stages of its evolution, or because of orbital shrinkage due to loss of angular momentum. Matter of the primary can then flow over the inner Lagrangian point L_1 to the less evolved secondary. When both stars fill their Roche lobes at the same time, a common envelope forms of matter spilling beyond both lobes. The torque exerted by frictional forces on the embedded stellar cores causes them to spiral in and the envelope to be expelled.

During and after the mass transfer, the stars continue with their evolution, and form the usual remnants: white dwarfs, neutron stars and black holes. However, there are three possibilities for the fate of the binary system itself: First, the system may be disrupted by a supernova explosion, possibly creating runaway stars with high velocities (Blaauw, 1961). Second, the system may stay bound and form a stable binary containing a – or later possibly even two – compact object(s). Third, the components of the system may merge into a single object, which subsequently evolves according to its mass.

Theory of Black Holes

From a historical point of view, black holes have been discovered as solutions to the Einstein field equations of General Relativity (1916).

Non-rotating black holes. Schwarzschild (1916) found the first static and spherical solution:

$$\mathrm{d}s^2 \;=\; \frac{\mathrm{d}r^2}{1-2R_\mathrm{g}/r} + r^2\,\left(\mathrm{d}\theta^2+\sin^2\theta\,\mathrm{d}\varphi^2\right) - c^2\left(1-\frac{2R_\mathrm{g}}{r}\right)\mathrm{d}t^2 \tag{1.27}$$

The gravitational radius of a mass M is $R_\mathrm{g} = G\,M/c^2$. In Eq. (1.27), the Schwarzschild radius

$$R_\mathrm{S} \;:=\; 2\,R_\mathrm{g} \;=\; \frac{2\,G\,M}{c^2} \;\approx\; 3\,\mathrm{km}\cdot\frac{M}{M_\odot} \tag{1.28}$$

appears to be a singularity for the chosen frame of reference. This is because R_S defines the non-rotating black hole's event horizon; i.e., there is no trajectory (not even for light) that leads from $r{<}R_\mathrm{S}$ to $r{>}R_\mathrm{S}$. According to a distant observer, objects falling into a black hole from $r{>}R_\mathrm{S}$ suffer from increasing redshifts and time-dilatations when approaching the horizon, yielding infinities at $r{=}R_\mathrm{S}$. This observer will thus never see the objects cross the horizon, but only fading away while slowing down. These objects themselves, however, can be described in, e.g., comoving Kruskal (1960) coordinates, which show that no singularity is encountered at $r{=}R_\mathrm{S}$. Hence, the only true singularity of the Schwarzschild metric in Eq. (1.27) is at $r{=}0$, which is where General Relativity (alone) indeed fails to describe the Universe and quantum effects may become important.

Rotating black holes. According to the so-called "no hair theorem" (Carter, 1971), the only properties of a black hole are its mass, spin, and electric charge. The most general 'metric of a rotating, charged mass' has been found by Newman et al. (1965), but it is usually not considered for astrophysical objects, as these – if charged – tend to quickly neutralize by attracting conjugately charged particles. In this sense, the complete spectrum of astrophysical black holes is described by the Kerr (1963) solution for the 'gravitational field of a spinning mass' with angular momentum J, which is usually expressed by the dimensionless Kerr-parameter $a = Jc/(GM^2)$, or the corresponding length scale $R_a = a\cdot R_\mathrm{g} = J/(Mc)$. In Boyer & Lindquist (1967) coordinates, where $\Delta := r^2 - 2R_\mathrm{g}\,r + R_a^2$ and $\Sigma := r^2 + R_a^2\,\cos^2\theta$, the following general metric contains the Schwarzschild solution of Eq. (1.27) for $a = 0$:

$$\mathrm{d}s^2 \;=\; \frac{\Sigma}{\Delta}\,\mathrm{d}r^2 + \Sigma\,\mathrm{d}\theta^2 + \left(r^2+R_a^2\right)\,\sin^2\theta\,\mathrm{d}\phi^2 - c^2\mathrm{d}t^2 + \frac{2\,R_\mathrm{g}\,r}{\Sigma}\left(c\mathrm{d}t - R_a\,\sin^2\theta\,\mathrm{d}\phi\right)^2 \tag{1.29}$$

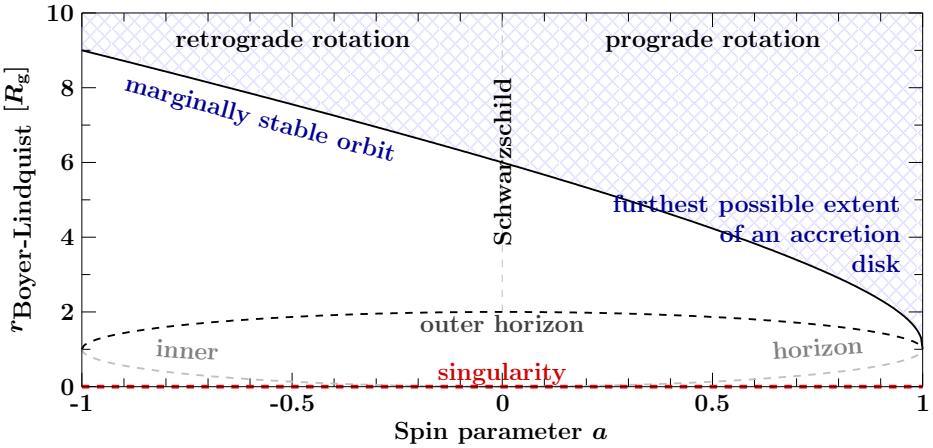

Figure 1.5: Radius of the marginally stable orbit as a function of the black hole's spin parameter a, for prograde ($a \geq 0$) and for retrograde ($a \leq 0$) rotation.

The zeros of Δ at $r_{\mathrm{H}^\pm} = \left(1 \pm \sqrt{1-a^2}\right) \cdot R_\mathrm{g}$ are again only pseudo-singularities corresponding to the outer (r_{H^+}) and inner (r_{H^-}) horizon of a Kerr black hole, while its sole true singularity is located where Σ vanishes, viz., at $r{=}0$ and $\theta{=}\pi/2$. Due to the non-Cartesian nature of Boyer & Lindquist (1967, eq. 2.6) coordinates for $a{\neq}0$, the horizons are actually oblate ellipsoids, and the singularity is an equatorial ring of radius R_a.[9]

The spin parameter a is not *directly* observable, but as the metric of space-time around a rotating black hole strongly differs from the non-rotating case, there are effects like frame-dragging that may finally allow to measure a, mostly related to orbits around black holes.

'Kepler' orbits. Bardeen et al. (1972) find the following angular velocity for circular orbits in the Kerr metric, which is asymptotically equivalent to Kepler's third law of Eq. (1.2):

$$\omega_\pm(r) \;=\; \frac{\mathrm{d}\phi}{\mathrm{d}t} \;=\; \frac{\pm c/R_\mathrm{g}}{\left(r/R_\mathrm{g}\right)^{3/2} \pm a} \;=\; \frac{2.03{\times}10^5\,\mathrm{Hz}}{(M/M_\odot)\cdot\left[\left(r/R_\mathrm{g}\right)^{3/2} \pm a\right]} \tag{1.30}$$

ω_+ holds for particles on prograde orbits, i.e., corotating with the black hole – and ω_- for retrograde, i.e., counter-rotating orbits.

The radius of the 'innermost stable circular orbit' (ISCO) – or more correctly termed: the radius of *marginal stability*, r_ms – is given by (Bardeen et al., 1972, eq. 2.21):

$$r_\mathrm{ms}(a) \;=\; \left(3 + Z_2 - \mathrm{sgn}(a)\,\sqrt{(3-Z_1)(3+Z_1+2Z_2)}\right) \cdot R_\mathrm{g} \tag{1.31}$$

where $Z_1 = 1 + (1{-}a^2)^{1/3}\cdot\left[(1{+}a)^{1/3} + (1{-}a)^{1/3}\right]$ and $Z_2 = \sqrt{3a^2+Z_1^2}$ for $-1{\leq}a{\leq}1$. Following Dauser et al. (2010), who call rotating black holes with counter-rotating accretion disks *negatively spinning* black holes, $a{<}0$ indicates retrograde orbits. A stable accretion disk (discussed in Sect. 1.2.1) around a Schwarzschild black hole can extend down to $r_\mathrm{ms}(a{=}0) = 6\,R_\mathrm{g}$. The frame dragging effect of a Kerr black hole allows a corotating disk to extend until $r_\mathrm{ms}(a{=}1) = 1\,R_\mathrm{g}$, while a counter-rotating one can only persist down to $r_\mathrm{ms}(a{=}{-}1) = 9\,R_\mathrm{g}$, see also Fig. 1.5. Equations (1.27)–(1.31) show that all relevant sizes simply scale with R_g, i.e., with the black hole mass M (assuming a fixed a), and so do times, according to Eq. (1.30). For this reason, supermassive black holes and stellar mass black holes behave very similarly, even if their masses differ by more than six orders of magnitude (Wilms, 2006).

[9] Some authors confuse Boyer & Lindquist (1967) coordinates with Cartesian coordinates and erroneously conclude from $r_{\mathrm{H}^-} \leq R_a \leq r_{\mathrm{H}^+}$ that the ring singularity is hidden *between* the two horizons (e.g. Müller, 2004, fig. 2.6).

1.2 Radiation Processes in X-ray Binaries

Due to their small size of $\mathcal{O}(20\,\mathrm{km})$, the thermal emission[10] of isolated neutron stars is very dim. Classical[11] black holes cannot directly emit radiation at all. *Accreting* compact objects in binary systems, however, are able to release vast amounts of energy – largely in form of X-rays. The 2–20 keV luminosity of these so-called X-ray binaries is typically $10^{36-38}\,\mathrm{erg/s}$ and thus much larger than the (bolometric electromagnetic) solar luminosity $L_\odot = 3.839\times10^{33}\,\mathrm{erg/s}$.

1.2.1 Accreting Compact Objects

When a mass m is accreted from large distance onto another mass M with radius $R > R_\mathrm{g}$ (where $R_\mathrm{g} = GM/c^2$ is again the gravitational radius of M), the gravitational potential energy

$$\Delta E_\mathrm{grav} \;=\; \frac{GMm}{R} \;=\; \frac{mc^2}{R/R_\mathrm{g}} \tag{1.32}$$

is released, which amounts to a large fraction of the rest-mass energy mc^2 if m is accreted onto a compact object with small R/M. A luminosity $L = \eta\,\dot{m}\,c^2 = 10^{37}\,\mathrm{erg/s}$, where $\eta = \mathcal{O}(0.1)$ is the total energy conversion efficiency, requires an accretion rate of $\dot{m} = 1.77\times10^{-10}\,M_\odot/\mathrm{yr}\,/\,\eta$. The Eddington luminosity of Eq. (1.10), however, limits the rate of spherical mass accretion.

X-ray binaries. Compact objects in binary systems may regularly accrete mass from their companion star. Different ways of mass transfer are possible, depending on the type of the donor, which is therefore often used to classify the X-ray binary system (e.g., White, 1989):

- In *high-mass X-ray binaries* (HMXBs), the donor is an early-type (O/B) star with a strong stellar wind. The compact object accretes constantly from this wind according to the model of Hoyle & Lyttleton (1939), Bondi & Hoyle (1944), and Bondi (1952) – see also the review by Edgar (2004). If the supergiant is already close to filling its Roche lobe, the wind can be particularly focused along the binary axis (Friend & Castor, 1982).
- In *Be binaries*, the donor is a fast rotating Be star (with *e*mission line spectrum), which indicates an equatorial circumstellar gas disk (Porter & Rivinius, 2003). Whenever the compact object, which moves on an eccentric orbit, passes close enough that accretion starts, an X-ray outburst happens. As (part of) the Be star's disk may be removed by such an encounter, outbursts do not necessarily occur during every periastron passage.
- In *low-mass X-ray binaries* (LMXBs), the donor is an evolved late type star that fills its Roche lobe. Matter can therefore spill over the inner Lagrange point L_1 and fall toward the compact object. Because of the orbital angular momentum, large accretion disks are usually formed (see below).

When the properties of the accretion process very close to the compact object are considered, it may be more important to distinguish *black hole XRBs* from *neutron star XRBs*. Neutron stars may – unlike black holes, which have *no hair* – bear a (possibly strong) magnetic field, which couples to the accretion flow below some critical distance (the Alfvén radius) and channel the plasma onto the magnetic poles. They furthermore have an extended solid surface, preventing the kinetic energy of accreted matter to 'disappear' (like for black holes; advected beyond the event horizon), as it is deposited in the hot spot when particles crash onto the neutron star.

[10] Because of their fast rotation and high magnetic field, young neutron stars usually emit non-thermal radiation. Due to the anisotropic emission along the magnetic field lines, they appear as (radio) pulsars.

[11] Hawking (1974) radiation of black holes due to quantum effects may evaporate black holes on time scales of $10^{71}\,\mathrm{s}\cdot(M/M_\odot)^3$, but for $M{>}M_\odot$, this effect is negligible within the current lifetime of the Universe of $<5\times10^{17}$ s.

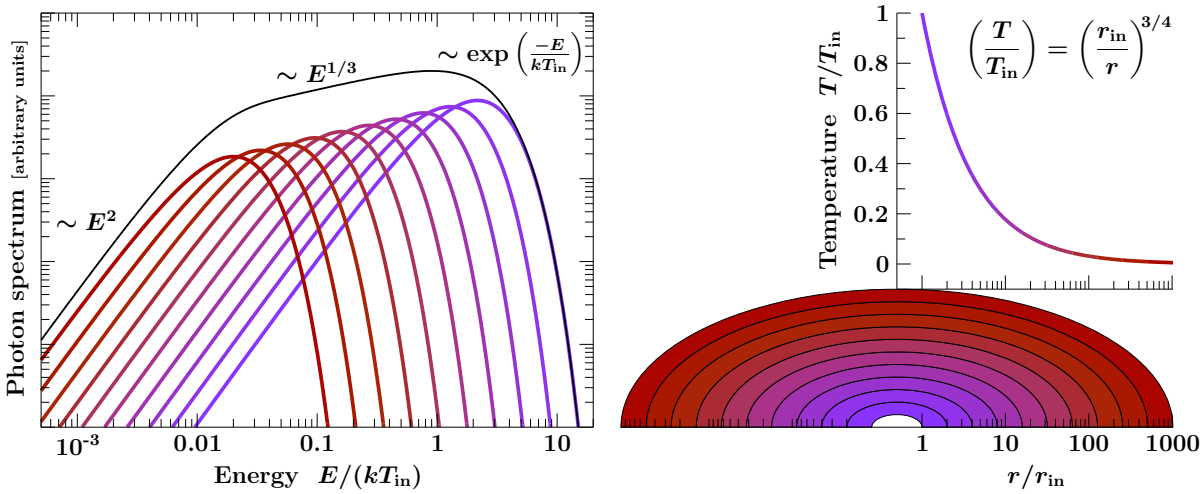

Figure 1.6: Spectrum (left) of an accretion disk with a $T \propto r^{-3/4}$ temperature profile (right). The accretion disk, which is illustrated on a logarithmic scale, has been divided into ten rings, whose blackbody-like contribution to the spectrum on the left is indicated in the same color. The composite spectrum has a Rayleigh-Jeans tail for $E \ll kT_{\rm out}$, a Wien tail for $E \gg kT_{\rm in}$, and a $E^{1/3}$ slope in between (Lynden-Bell, 1969).

Active Galactic Nuclei (AGN). Although not considered in this work, 'supermassive' black holes (with $10^{5-10}\,M_\odot$) in the center of their host galaxies have to be mentioned among the class of accreting compact objects. It was already suggested by Lynden-Bell (1969) that those, when accreting accordingly, may cause *violent events in the nuclei of galaxies* (Burbidge et al., 1963). A detailed description of the broad phenomenology of AGN – and their unification – can be found in the reviews by Antonucci (1993) and Urry & Padovani (1995).

Accretion disks

Matter that posseses angular momentum with respect to the compact object cannot directly fall onto it, but moves on Kepler orbits unless the angular momentum can be transfered via interactions. The standard theory of geometrically thin accretion disks (Shakura & Sunyaev, 1973; reviewed by, e.g., Pringle, 1981) assumes *some form* of viscosity, whose physical origin is unspecified within the α prescription of Shakura & Sunyaev (1973). Many mechanisms have been suggested, including magnetohydrodynamic effects (Schramkowski & Torkelsson, 1996), and in particular the magnetorotational instability (Balbus & Hawley, 1991, 1998; Balbus, 2003). A steady accretion disk needs to dissipate energy at a rate

$$D(r) \;=\; \frac{\mathrm{d}E}{\mathrm{d}A\,\mathrm{d}t} \;=\; \frac{3GM\dot{m}}{4\pi r^3}\left(1-\sqrt{\tfrac{r_0}{r}}\right) \tag{1.33}$$

in order to provide a constant accretion rate $\dot{m}$ (Shakura & Sunyaev, 1973, eq. 2.6; Pringle, 1981, eq. 3.10). The radius r_0 is defined by the inner boundary condition of vanishing torque and dissipation,[12] e.g., $r_0{=}R_\star$ for an accretion disk around a star. The disk's total luminosity

$$\int_{r_0}^{\infty} D(r)\cdot 2\pi r\,\mathrm{d}r \;=\; \frac{GM\dot{m}}{2r_0} \tag{1.34}$$

is just half of the total accretion power; the other part is stored in the kinetic energy of the accreted particles, whose further fate depends on the nature of the compact object, see above.

[12] The factor $(1-\sqrt{r_0/r})$ is often ignored, assuming $r \gg r_0$ or different inner boundary conditions.

If the accretion disk is optically thick, it is locally in thermodynamic equilibrium, and the Stefan-Boltzmann (1884) law applies (to both sides of the disk, hence the factor 2):

$$D(r) \;=\; 2\,\sigma_{\rm SB} T(r)^4 \tag{1.35}$$

which, using Eq. (1.33), leads to

$$T(r) \;=\; 2.7{\times}10^7\,{\rm K}\cdot\left(\frac{\dot{m}/[10^{-10}M_\odot\,{\rm yr}^{-1}]}{(M/M_\odot)^2\cdot(r/R_{\rm g})^3}\right)^{1/4}\cdot\left(1-\sqrt{\tfrac{r_0}{r}}\right)^{1/4} \tag{1.36}$$

For typical values in X-ray binaries, the inner temperature of the accretion disk exceeds 10^6 K and the disk radiates in soft X-rays, whereas the temperatures in AGN disks are much lower.

The disk's composite spectrum from all radii $r_{\rm in} \le r \le r_{\rm out}$ has the shape (see also Fig. 1.6)

$$S_E(E) \;=\; \int_{r_{\rm in}}^{r_{\rm out}} B\big(E,\,T(r)\big)\,2\pi r\,{\rm d}r \tag{1.37}$$

where $B(E,\,T) \propto E^3\cdot\left[\exp\left(E/(kT)\right)-1\right]^{-1}$ is the Planck (1901) function. Approximating $T \approx T_{\rm in}\cdot(r_{\rm in}/r)^{3/4}$ gives the simple *multicolor disk* or *disk blackbody* spectrum, parameterized by the inner radius $r_{\rm in}$ and its temperature $T_{\rm in}$ (Mitsuda et al., 1984; Makishima et al., 1986):[13]

$$S_E(E) \;\approx\; \frac{8\pi}{3}\,r_{\rm in}^2\int_{T_{\rm out}}^{T_{\rm in}}\left(\frac{T_{\rm in}}{T}\right)^{11/3}B(E,\,T)\,\frac{{\rm d}T}{T_{\rm in}} \tag{1.38}$$

Due to the approximations inherent to the multicolor disk formalism e.g., neglecting r_0, the parameter $r_{\rm in}$ in Eq. (1.38) is not the effective inner disk radius, but lacks a so-called "color correction" factor (e.g., Shimura & Takahara, 1995; Kubota et al., 1998; Merloni et al., 2000).

* * *

While the thermal radiation can be reasonably well understood within a simple framework, the non-thermal component due to "Comptonization" requires much more sophisticated calculations and can in general not even be treated analytically. To illustrate the underlying physics, the next section will introduce scattering as the first interaction of radiation with matter.

1.2.2 Compton Scattering, Hard X-ray Spectra, and Spectral States

Scattering off free electrons at rest

As photons are massless and the electromagnetic interaction does not have an intrinsic scale, the quantum mechanical scattering cross section is inversely proportional to the square of the fermion-mass. Light scatters therefore primarily with electrons, the *lightest* free fermions.

Classical electrodynamics. In the non-relativistic limit (named *Thomson scattering*; after the British phycisist and Nobel laureate in 1906, Joseph John Thomson, 1856–1940), photons scatter elastically. This process can be described by classical electrodynamics: the oscillating electric field $\vec{E}$ accelerates the electron, which in turn re-emmits at the same frequency, according to Larmor's formula (1897). As $\vec{E}$ must always be perpendicular to the propagation

[13] The implementation of the multicolor disk in Xspec is called `diskbb`, parameterized by a normalization factor $N_{\rm disk}$ and the inner temperature $T_{\rm in}$. As the observed flux, unlike the emitted intensity of Eq. (1.38), depends on the distance d and the inclination angle θ of the disk, the normalization is $N_{\rm disk} = (r_{\rm in}/\,{\rm km})^2/(d/10\,{\rm kpc})^2\cdot\cos\theta$.

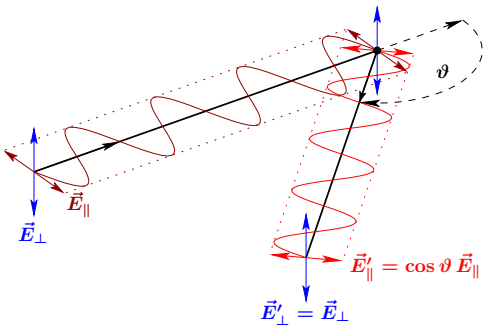

Figure 1.7: Polarization and angle dependency of Thomson scattering. While the electric field $\vec{E}_\perp$ perpendicular to the scattering plane is unchanged (blue), only a projection $\vec{E}'_\parallel = \cos\vartheta\,\vec{E}_\parallel$ of the parallel component (red) can propagate at an angle ϑ. For unpolarized incident light and $|\cos\vartheta| < 1$, the scattered radiation is therefore polarized, and for $\vartheta = 90°$, the degree of polarization is even 100 %. The average intensity is proportional to the mean squared ampitude, i.e., $(1+\cos^2\vartheta)/2$.

direction, its component in the scattering plane is reduced by a factor $\cos\vartheta$ (Fig. 1.7). The average scattering cross section for *unpolarized* electromagnetic waves is therefore:

$$\frac{\mathrm{d}\sigma_\mathrm{T}}{\mathrm{d}\Omega} = \frac{1+\cos^2\vartheta}{2}\cdot r_\mathrm{e}^2 \quad \text{with} \quad r_\mathrm{e} = \frac{e^2}{4\pi\,\epsilon_0\,m_\mathrm{e}\,c^2} = 2.81794\times10^{-15}\,\mathrm{m} \tag{1.39}$$

The integrated Thomson cross section σ_T can be easily obtained from Eq. (1.39):

$$\int_0^{2\pi}\mathrm{d}\phi\int_{-1}^{1}\mathrm{d}(\cos\vartheta)\,\frac{\mathrm{d}\sigma_\mathrm{T}}{\mathrm{d}\Omega} = \frac{8\pi}{3}\,r_\mathrm{e}^2 =: \sigma_\mathrm{T} = 6.6524586\times10^{-25}\,\mathrm{cm}^2 \tag{1.40}$$

Relativistic case. For higher energies, at which the momentum transfer from the photon to the electron cannot be neglected any more, the scattering becomes inelastic. It is then refered to as *Compton scattering* (after its discoverer, the American physicist and Nobel laureate in 1927, Arthur Holly Compton, 1892–1962). A photon scattering off an electron at rest experiences a shift in wavelength λ that solely depends on the scattering angle ϑ (Compton, 1923, eq. 5):

$$\lambda' - \lambda = \underbrace{\frac{h}{m_\mathrm{e}c}}_{2.42631\times10^{-12}\,\mathrm{m}}(1-\cos\vartheta) \quad\Leftrightarrow\quad \frac{E'}{E} = \frac{1}{1+\alpha(1-\cos\vartheta)} \quad \text{with} \quad \alpha := \frac{E}{m_\mathrm{e}c^2} \tag{1.41}$$

The fully relativistic cross section for this process has been derived by Klein & Nishina (1929):

$$\frac{\mathrm{d}\sigma_\mathrm{KN}}{\mathrm{d}\Omega} = \frac{r_\mathrm{e}^2}{2}\left[\left(\frac{E'}{E}\right)^3 + \frac{E'}{E} - \left(\frac{E'}{E}\right)\cdot\sin^2\vartheta\right] \tag{1.42}$$

In the non-relativistic limit $E \ll m_\mathrm{e}c^2$, Eq. (1.41) gives $E' \to E$ and $\mathrm{d}\sigma_\mathrm{KN}/\mathrm{d}\Omega$ recovers $\mathrm{d}\sigma_\mathrm{T}/\mathrm{d}\Omega$. For $E \gg m_\mathrm{e}c^2$, however, scattering occurs preferentially in forward direction, see Fig. 1.8, left. Integration of Eqs. (1.41) and (1.42) gives the total cross section (Klein & Nishina, 1929, eq. 61):

$$\sigma_\mathrm{KN} = \frac{3\sigma_\mathrm{Th}}{4}\left[\frac{1+\alpha}{\alpha^2}\cdot\left(\frac{2\cdot(1+\alpha)}{1+2\alpha} - \frac{\log(1+2\alpha)}{\alpha}\right) + \frac{\log(1+2\alpha)}{2\alpha} - \frac{1+3\alpha}{(1+2\alpha)^2}\right] \tag{1.43}$$

Its energy dependence is shown in Fig. 1.8. The low-energy and ultra-relativisitc limits are:

$$\sigma_\mathrm{KN} \approx \begin{cases} \sigma_\mathrm{Th}\left[1-2\alpha+\frac{26}{5}\alpha^2-\frac{133}{10}\alpha^3+\frac{1144}{35}\alpha^4-\mathcal{O}(\alpha^5)\right] & \text{for } \alpha \ll 1 \\ \frac{3\sigma_\mathrm{T}}{8\alpha}\left[\frac{1}{2}+\log(2\alpha)\right] & \text{for } \alpha \gg 1 \end{cases} \tag{1.44}$$

The photon's average fractional energy-loss by Compton scattering off an electron at rest is:

$$\begin{aligned}\left\langle\frac{\Delta E}{E}\right\rangle &= \frac{1}{\sigma_\mathrm{KN}}\int_0^{2\pi}\mathrm{d}\phi\int_{-1}^{1}\mathrm{d}(\cos\vartheta)\,\frac{\mathrm{d}\sigma_\mathrm{KN}}{\mathrm{d}\Omega}(\vartheta)\cdot\frac{E'(\vartheta)}{E} - 1 \\ &= -\frac{2\alpha\left(3+17\alpha+31\alpha^2+17\alpha^3-\frac{10}{3}\alpha^4\right) - (1+\alpha)\cdot(3-\alpha)\cdot(1+2\alpha)^3\cdot\log(1+2\alpha)}{2\alpha(2+8\alpha+9\alpha^2+\alpha^3)\cdot(1+2\alpha) - (2+2\alpha-\alpha^2)\cdot(1+2\alpha)^3\cdot\log(1+2\alpha)}\end{aligned} \tag{1.45}$$

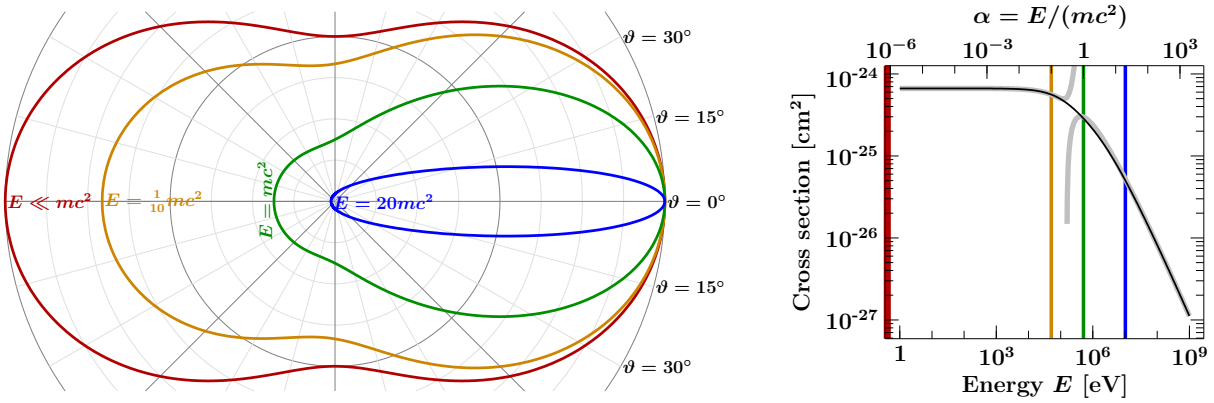

Figure 1.8: Klein-Nishina cross section for Compton scattering. Left: angular dependence of the scattering probability, for different photon energies, according to Eqs. (1.42) and (1.41). Right: integrated total cross section, according to Eq. (1.43). The gray lines show the asymptotic behavior in the low-energy and ultra-relativistic limits according to Eq. (1.44).

Equation (1.45) has the following asymptotic behavior:

$$\left\langle \frac{\Delta E}{E} \right\rangle \approx \begin{cases} -\alpha + \frac{11}{5}\alpha^2 - \frac{51}{10}\alpha^3 + \frac{3931}{350}\alpha^4 - \mathcal{O}(\alpha^5) & \text{for } \alpha \ll 1 \\ -\frac{6\log(2\alpha)-5}{6\log(2\alpha)+3} & \text{for } \alpha \gg 1 \end{cases} \tag{1.46}$$

In the low-energy limit ($\alpha \ll 1$), the energy loss $\langle \Delta E/E \rangle$ is therefore approximately $-E/(m_e c^2)$.

Comptonization by hot electrons

It has already been suggested from the early observations of Cyg X-1 that the innermost region of accretion disks in black hole X-ray binaries, due to the Lightman & Eardley (1974) instability, contains a gas-pressure dominated optically thin plasma (Thorne & Price, 1975, see in particular their fig. 2), with electron temperatures of $\sim 10^9$ K (Eardley et al., 1975).

Photons that Compton scatter with electrons not at rest in the reference frame of the observer, may – as opposed to the results of Eqs. (1.45) and (1.46) from the previous section for electrons at rest – also *gain* energy. This process is called *inverse Compton scattering*. For a thermal electron population at a temperature T_e with $\Theta := kT_e/(m_e c^2) \ll 1$ (where pair production does not matter), the average amplification per scattering is (e.g., Zdziarski, 1985):

$$A = \left\langle \frac{E'}{E} \right\rangle = 1 + \frac{4kT_e - E}{m_e c^2} + \mathcal{O}(\Theta^2) \tag{1.47}$$

The statistical change of a spectrum through *Comptonization* can be described by a Fokker-Planck equation for diffusion in energy space (Kompaneets, 1956; Weymann, 1965, eq. 5). The optical depth τ (and geometry) of the scattering medium determine the average number of scattering acts that photons undergo. Within certain approximations, Shapiro et al. (1976) find for unsaturated Comptonization (i.e., at $y := 4\Theta \max(\tau, \tau^2) \approx 1$) of a soft spectrum $S(E)$ providing copious seed photons below E_s, the emergent hard X-ray spectrum for $E_s < E \ll E_e$ to be a power-law whose index is a function of y,[14] and to have an exponential Wien cutoff for $E > E_e$ – completely independent of $S(E)$. Sunyaev & Titarchuk (1980) were able to find

[14] For non-relativistic multiple scattering of soft radiation in an optically thin medium, the power-law spectrum follows already from heuristic arguments (e.g., Rybicki & Lightman, 1979): For $E \ll kT_e$, Eq. (1.47) gives a constant amplification $A \approx 1 + 4\Theta$ per scattering, such that an energy $E = E_0 \cdot A^k$ is obtained after $k = \log(E/E_0)/\log A$ scatterings, which happen (for $\tau < 1$) with a probability $\propto \tau^k \propto E^{\log \tau / \log A}$.

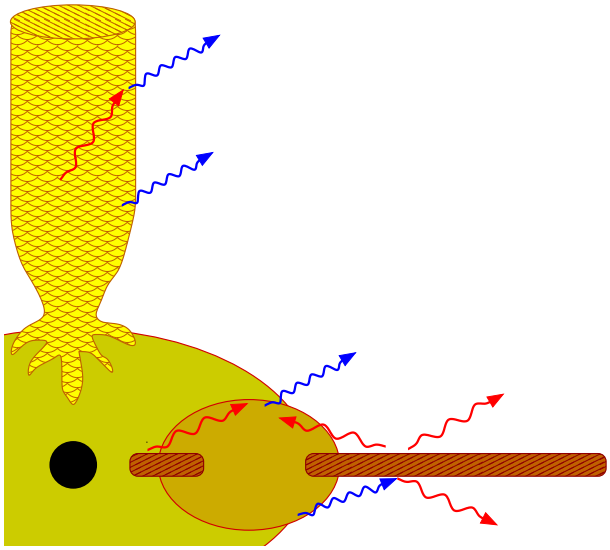

Figure 1.9: Sketch of possible X-ray emission geometries for the black hole X-ray binary Cyg X-1 (Nowak et al., 2011, fig. 9): Soft X-rays (red) from the disk (brown), or from the jet (yellow), are upscattered in a spherical (dark yellow) or toroidal (light brown) corona around the hole (black), or in the base of the jet itself. When hitting the outer disk, these hard X-rays (blue) are reprocessed via Compton scattering and fluorescent line emission. A more detailed discussion is given by Nowak et al. (2011).

more general solutions, releasing some of the previous assumptions, but still within a non-relativistic approximation and for a spherical geometry. Accompanied by Monte-Carlo simulations (e.g., Pozdnyakov et al., 1983), these studies were in the following years extended to the relativistic regime, also including pair-production, for both thermal (e.g., Zdziarski, 1985), and non-thermal electron populations (e.g., Svensson, 1987; Lightman & Zdziarski, 1987).

There are now ample Comptonization models, such as `compTT` allowing for a sphere or disk geometry of the plasma (Titarchuk, 1994; Hua & Titarchuk, 1995; Titarchuk & Lyubarskij, 1995; Titarchuk & Hua, 1995), or `eqpair` for hybrid thermal/non-thermal plasmas (Coppi, 1999, 2004). They can be used to compare observational data with theoretical predictions. However, the direct inference of physical parameters is often limited by the strong degeneracy between different models that describe the data equally well; not only the properties and constitution, but also the location and general nature of the Comptonizing plasma *("corona")* are still uncertain and highly debated (see Nowak et al., 2011, and references therein). Besides the previously mentioned truncated disk model and spherical coronae, the corona could also overlay the inner disk, or be replaced by the base of the jet[15] (Markoff et al., 2005; Maitra et al., 2009). Figure 1.9 shows a sketch of possible X-ray emission geometries (Nowak et al., 2011).

Reflection. An important aspect of the system geometry is that hard X-rays may hit the outer, cool accretion disk when emitted from an elevated region. Those can Compton scatter or excite atomic transitions that lead to flourescent emission, such that reprocessed (commonly called *reflected*) radiation may be emitted into the observer's line of sight. Compton (down) scattering produces the "Compton reflection hump", a hardnening of the spectrum above $\sim$10 keV (see, e.g., Lightman & White, 1988; Done et al., 1992; Magdziarz & Zdziarski, 1995). Among the atomic transitions, the Fe Kα line at 6.4 keV is usually the most prominent one (see the review by Miller, 2007), due to its large fluorescence yield and the high iron abundance (Table 1.2).

X-ray spectral states

The previous sections have identified three major components in the X-ray spectrum of XRBs:

[15] (Black hole) X-ray binaries show radio emission from a colimated relativstic outflow that is strongly linked to the accretion process (e.g., Fender, 2002; Fender et al., 2004, 2009, see also Fig. 1.10). Very Long Baseline Interferometry has allowed to resolve the compact jets of GRS 1915+105 (Dhawan et al., 2000; Fuchs et al., 2003) and Cyg X-1 (Stirling et al., 2001; Fender et al., 2006; Rushton et al., 2011).

1. the thermal emission from the accretion disk,
   in form of a disk blackbody component (at soft X-ray energies),
2. the Compton-upscattered hard X-ray component,
   in form of a (possibly cut-off) power-law (extending to hard X-rays), and
3. the radiation reprocessed by the accretion disk,
   in form of Compton reflection (above ∼10 keV) and fluorescent line emission (at 6.4 keV).

The relative contribution of these components varies between different sources, and may also change for a single source. However, most sources can be classified according to certain *states*, related to different mass accretion rates (e.g., Esin et al., 1997; Bałucińska-Church et al., 2010) and/or configurations of the accretion flow (e.g., Chakrabarti & Titarchuk, 1995; Smith et al., 2002; Yu & Yan, 2009).

Black hole X-ray binaries. Tananbaum et al. (1972) first recognized the *low/hard* and *high/soft* states of Cyg X-1 from its transition in March/April 1971 (see also the review by Oda, 1977). The former is dominated by a hard power-law component with a photon index $\Gamma \approx 1.7$ and a cutoff with a folding energy $E_{\rm fold} \approx 150$ keV (e.g., Wilms et al., 2006). In the soft state of

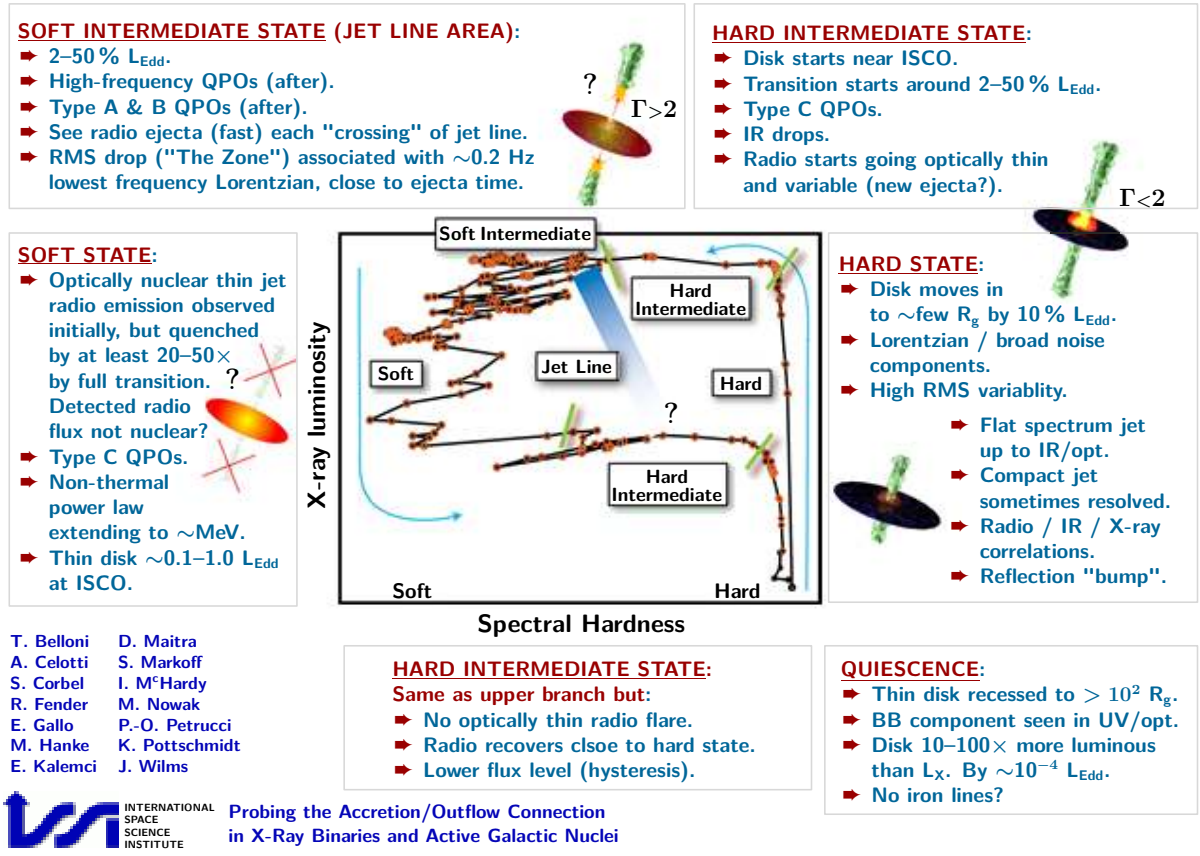

Figure 1.10: Spectral evolution of transient black hole X-ray binaries along an outburst. The hardness-intensity diagram in the center is based on the 2002/2003 outburst of GX 339−4 (Belloni et al., 2005, fig. 2; Homan & Belloni, 2005, fig. 5); such a q-shaped track is, however, common for transient BHBs. The locations in the HID correspond to the states. Some of their spectral/timing/radio properties are listed outside of the diagram. The schematic drawings indicate the properties of the accretion disk and the jet with Lorenz factor Γ. Further details are given by Fender et al. (2004, 2009) and Belloni (2010). This overview has been compiled by the team of T. Belloni et al. during their workshops at the International Space Science Institute in Berne, see `http://www.issibern.ch/teams/proaccretion/`.

Cyg X-1, the power-law is much steeper ($\Gamma \approx 2.5$; e.g., Zhang et al., 1997), but extends up to $\sim$10 MeV without cutoff (e.g., McConnell et al., 2002). While soft X-ray flux in the hard state is thus lower than in the soft state (which originally lead to the nowadays confusing terms 'low' and 'high' states), it is vice versa in the hard X-ray band, and again reversed at γ-ray energies, where the hard state's power-law is exponentially cut off (Gierliński et al., 1999, fig. 1; McConnell et al., 2002, fig. 9). In addition, the disk blackbody component is much stronger in the soft state; however, it never dominates the soft X-ray spectrum of Cyg X-1, unlike for other sources (e.g., GX 339−4; Makishima et al., 1986). The soft state of Cyg X-1 rather resembles their *very high state* (Miyamoto et al., 1991), which Remillard & McClintock (2006) suggest to call *steep power-law state* in order to avoid confusion with the high/soft state, which they in turn call *thermal (dominant) state*.

These spectrally defined states distinguish themselves also in their X-ray timing properties (Belloni et al., 2005; Homan & Belloni, 2005; Belloni, 2010), as well as in the properties of the jet (Fender, 2002). Fender et al. (2004, 2009) have suggested a unified model for the coupling of the accretion flow to the jet for transient black hole XRBs, based on the canonical evolution of an outburst in a hardness-intensity diagram (HID). A concise summary of the properties of different states, which are confined to certain regions of the HID, is shown in Fig. 1.10.

* * *

The large variety of phenomena related to spectral states and the hard X-ray component in general is largely due to the interaction of the primary radiation with matter through electron scattering. The next section describes the other type of interaction, which destroys photons. In this work, it will prove particularly relevant for X-rays produced by *accreting compact objects* on their (long) way to the observer, who can hence use this effect to *probe their environment* – or in general: the medium along the line of sight.

1.2.3 Absorption by Neutral and/or Ionized Matter

As the absorption of a photon by an entirely free electron would violate the conservation of energy and momentum, photoabsorption can only happen at electrons that are either bound in an atom, taking part of the recoil, or interacting with an external field (free-free absorption, also called inverse Bremsstrahlung). The Feynman diagrams for scattering and absorption (Fig. 1.11) look therefore relatively similar. Atomic absorption processes can be classified according to the final state of the electron (and therefore the shape of the feature) into

- bound-bound transitions *(photoexcitations)* at discrete energies (absorption lines), where an electron is lifted from one quantum state into another bound quantum state, and
- continuous bound-free transitions *(photoionizations)* above a certain threshold energy (absorption edges), where an electron is released from the atom or ion.

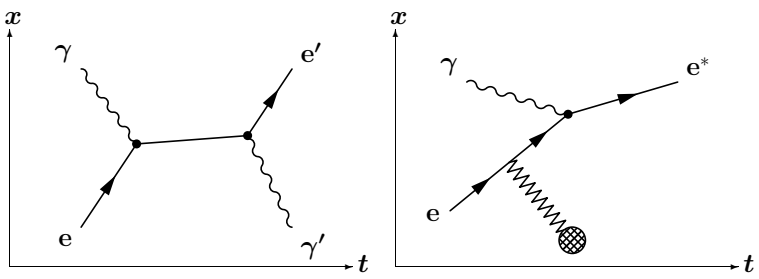

Figure 1.11: Feynman diagrams for Compton scattering (left) and photoabsorption (right). In order to stay on its mass shell, a free electron (left) – unlike a bound or interacting one (right) – cannot really destroy a photon, but *virtually* has to "re-emit"† it.

† The left diagram shows only the '*s*-channel contribution'. For the correct QED description, a '*u*-channel contribution', where the second photon is emitted "before" the first one is absorbed, has to be considered as well.

Absorption provides therefore a vast diagnostic potential, as it allows matter to imprint its atomic signature onto the radiation. In the case of pure absorption, the flux is reduced by a factor $\exp(-\tau)$, where the optical depth $\tau = N \cdot \sigma$ is the product of the absorber's column density N and the quantum mechanical cross section σ for the corresponding process.

Absorption lines

To give an overview on important lines in the 1–25 Å $\approx$ 0.5–13 keV band from a highly ionized medium, Fig. 1.12 shows the position of ground state transitions of the hydrogen- and helium-like ions of oxygen, neon, magnesium, silicon, sulfur, argon, calcium, and iron. Specifically, these are the Lyman series for H-like ions:

$$\mathrm{Ly}\,n: \qquad 1\mathrm{s}\,\left(^2\mathrm{S}_{1/2}\right) \quad \overset{\mathrm{E1}}{\longleftrightarrow} \quad n\mathrm{p}\,\left(^2\mathrm{P}_{3/2} \text{ or } ^2\mathrm{P}_{1/2}\right) \tag{1.48}$$

and the series of resonance lines for He-like ions:

$$\mathrm{He}\,n: \qquad 1\mathrm{s}^2\,\left(^1\mathrm{S}_0\right) \quad \overset{\mathrm{E1}}{\longleftrightarrow} \quad 1\mathrm{s}\,n\mathrm{p}\,\left(^1\mathrm{P}_1\right) \tag{1.49}$$

Figure 1.12 also includes the intercombination (i) and forbidden (f) lines, which form a triplet with the He α resonance (r) line (Gabriel & Jordan, 1969):

$$\mathrm{He\,i}: \qquad 1\mathrm{s}^2\,\left(^1\mathrm{S}_0\right) \quad \overset{\mathrm{M2}}{\longleftarrow} \quad 1\mathrm{s}\,2\mathrm{p}\,\left(^3\mathrm{P}_1\right) \tag{1.50}$$

$$\mathrm{He\,f}: \qquad 1\mathrm{s}^2\left(^1\mathrm{S}_0\right) \quad \overset{\mathrm{M1^{rel}}}{\longleftarrow} \quad 1\mathrm{s}\,2\mathrm{s}\,\left(^3\mathrm{S}_1\right) \tag{1.51}$$

The wavelengths are obtained from the atomic database ATOMDB v.1.3.1 (Smith et al., 2001),[16] or – for transitions beyond Ly δ and He δ – from House (1969).

Line profiles. The absorption cross section for a bound–bound transition $i \rightarrow j$ is given by:

$$\sigma_{ij}(\nu) \;=\; f_{ij} \cdot \tfrac{\pi e^2}{m_\mathrm{e} c} \cdot \phi(\nu) \tag{1.52}$$

where f_{ij} is the absorption oscillator strength (see Hanke, 2007, sect. 2.1, for a semi-classical derivation and references therein), and $\phi(\nu)$ is the normalized line profile, e.g., a Voigt profile

$$\phi(\nu) \;=\; \tfrac{1}{\sqrt{\pi}\,\Delta\nu_\mathrm{D}}\, H\left(\tfrac{\Gamma}{4\pi\,\Delta\nu_\mathrm{D}},\, \tfrac{\nu-\nu_0}{\Delta\nu_\mathrm{D}}\right) \;=\; \tfrac{\Gamma}{4\pi^{5/2}\,\Delta\nu_\mathrm{D}^2} \int_{-\infty}^{\infty} \tfrac{\exp(-y^2)\;\mathrm{d}y}{[(\nu-\nu_0)/\Delta\nu_\mathrm{D}-y]^2+[\Gamma/(4\pi\,\Delta\nu_\mathrm{D})]^2} \tag{1.53}$$

which follows from Gaussian broadening with a Doppler width $\Delta\nu_\mathrm{D}$ of a Lorentzian line profile, whose width Γ equals the Einstein coefficient A_{ji} for the case of pure radiation damping.

A column density N_i creates the following absorption line in the continuum $F_\nu^\mathrm{cont}(\nu)$:

$$F_\nu(\nu) \;=\; \mathrm{e}^{-\tau(\nu)} \cdot F_\nu^\mathrm{cont}(\nu) \qquad \text{with} \qquad \tau(\nu) \;=\; N_i\,\sigma_{ij}(\nu) \tag{1.54}$$

The equivalent width can possibly be measured even when the line profile cannot be resolved:

$$W_\lambda \;:=\; \int \frac{F_\lambda(\lambda) - F_\lambda^\mathrm{cont}(\lambda)}{F_\lambda^\mathrm{cont}(\lambda)}\,\mathrm{d}\lambda \;=\; \int \left(\mathrm{e}^{-\tau(\nu)} - 1\right) \cdot \left|\frac{\mathrm{d}\lambda}{\mathrm{d}\nu}\right|\,\mathrm{d}\nu \;\overset{\text{for narrow lines}}{\approx}\; W_\nu \cdot \frac{\lambda_0}{\nu_0} \tag{1.55}$$

For optically thin lines with $\tau \ll 1$, the equivalent width is independent of the line profile:

$$W_\lambda \;\approx\; -\int N_i\,f_{ij} \cdot \tfrac{\pi e^2}{m_\mathrm{e} c} \cdot \phi(\nu)\;\mathrm{d}\nu \;\cdot\; \tfrac{\lambda_0}{\nu_0} \;=\; -N_i\,f_{ij} \cdot \tfrac{\pi e^2\,\lambda_0^2}{m_\mathrm{e} c^2} \tag{1.56}$$

In this case, N_i can be inferred from W_λ (see also Spitzer, 1978, eq. 3-48; Mihalas, 1978, § 10-3):

$$N_i \;=\; 1.13{\times}10^{17}\,\mathrm{cm}^{-2} \cdot f_{ij}^{-1} \cdot \left(\lambda_0/\text{Å}\right)^{-2} \cdot \left(W_\lambda/\text{mÅ}\right) \tag{1.57}$$

[16] See http://cxc.harvard.edu/atomdb/, and http://www.atomdb.org/ for ATOMDB v.2.0.

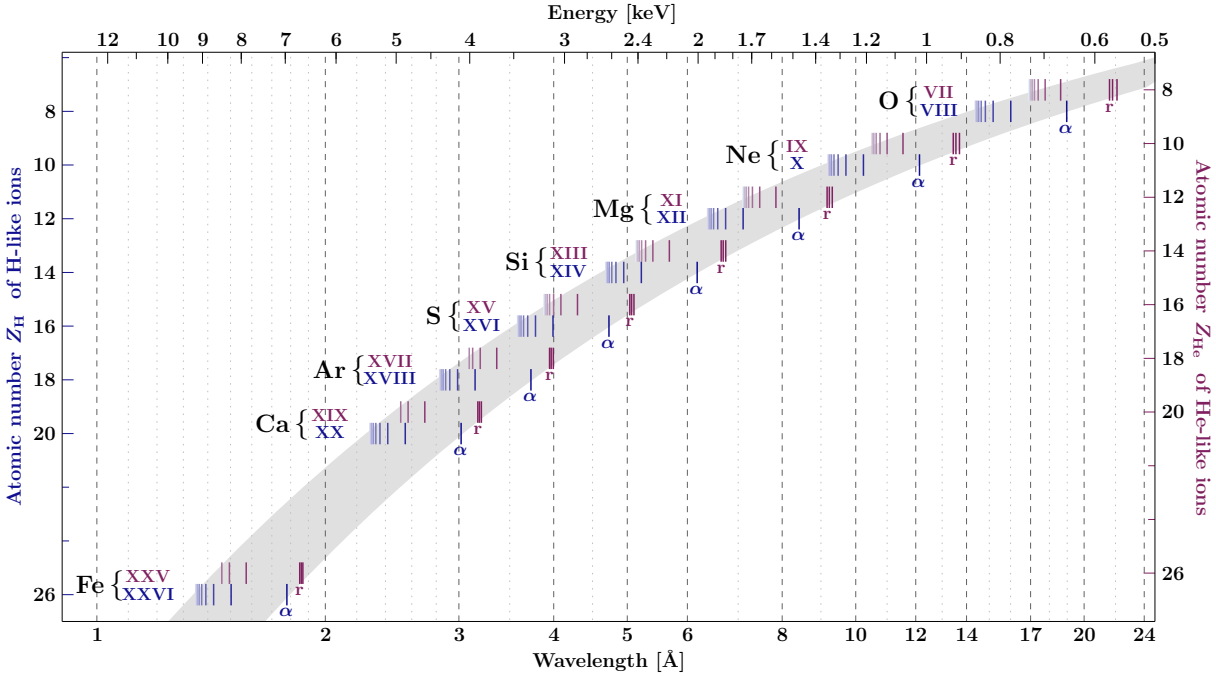

Figure 1.12: Position of ground state transitions of astrophysically relevant K-shell ions, accoring to ATOMDB and House (1969). The lines of H-like ions (Lyman series) are marked in blue, those of He-like ions, including i and f lines, in purple. The ordinate is the atomic number Z, but Z_{He} (right axis) has been offset from Z_{H} (left axis) for visual clarity. The strength of a series' resonance lines decreases from Ly α, respectively He r, at lowest energy, to the corresponding series limit. This region has been shaded in gray for the lines of H-like ions, for which $E \propto Z_{\mathrm{H}}^2$.

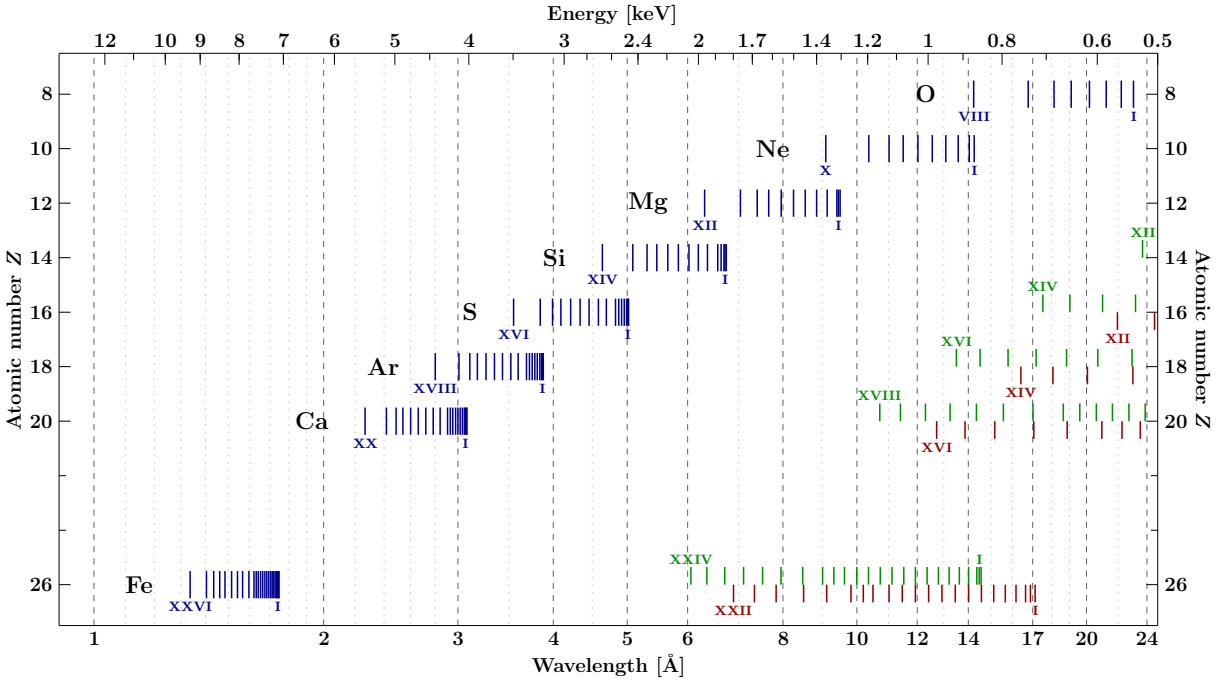

Figure 1.13: Position of K-, L_1-, and L_2-shell ionization thresholds (in blue, green, and red, respectively) of all ions and neutral atoms, according to Verner & Yakovlev (1995, table 1). For each element and for each sequence, the ionization energy increases from the neutral atom (labeled with 'I') to the highest ionization stage (H-, Li-, or B-like ions for K-, L_1-, or L_2-shell ionization of an electron in the 1 s, 2 s, or 2 p state). The K-shell thresholds for H- and He-like ions correspond to the series limits in Fig. 1.12.

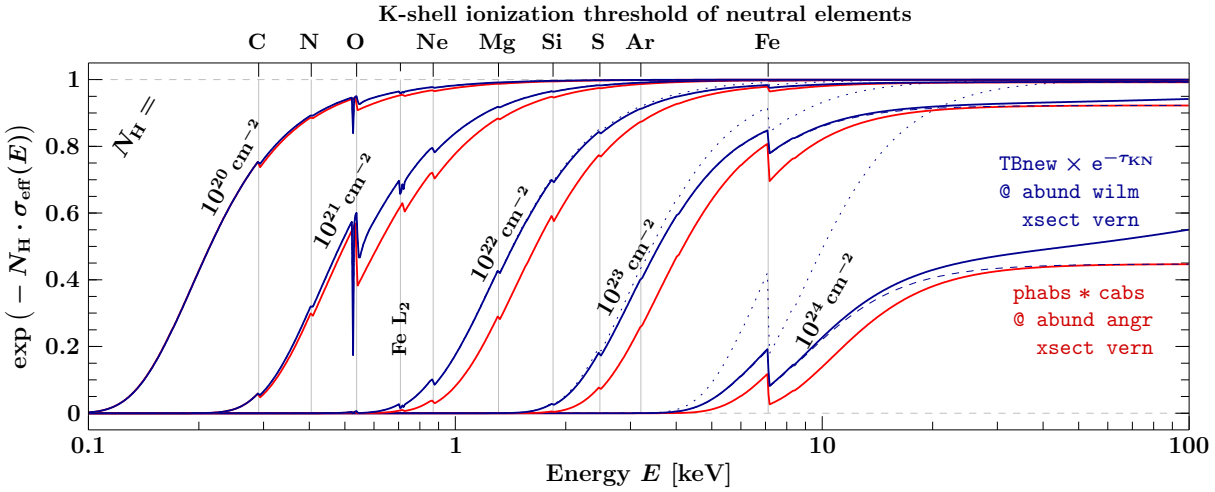

Figure 1.14: Comparison of different models for neutral absorption and (single) Compton scattering in fully ionized material. Blue lines show the `TBnew` model using the abundances of Wilms et al. (2000). Dotted lines display the pure absorption model without a Compton scattering factor. Solid lines include a factor $\exp\left(-N_e \cdot \sigma_{\text{Klein-Nishina}}(E)\right)$ with $N_e = 1.21\,N_H$. Dashed lines include the `cabs` model, using the constant Thomson cross-section. Red lines show the `phabs` model using the abundances of Anders & Grevesse (1989), with higher metal abundances than in the `wilm` table. Unlike `TBnew`, `phabs` does not include fine structure at the O K, Fe L, and Ne K edges. For N_H=10^{24} cm^{-2}, Klein-Nishina effects are seen above ∼10 keV.

Absorption edges

Figure 1.13 shows the position of the K-, L_1-, and L_2-shell thresholds (for ionization of electrons in the 1s, 2s, or 2p state, respectively) according to Verner & Yakovlev (1995), for *all* ions of the same elements as in Fig. 1.12. As absorption in the interstellar medium (ISM) is ubiquitous – e.g., Dickey & Lockman (1990) find at a Galactic latitude b a median of

$$N_H \;=\; (3.84/\sin b - 2.11)\times 10^{20}\,\text{cm}^{-2}\;, \tag{1.58}$$

the soft X-ray band's most important edges are (e.g., Juett et al., 2004, 2006; Hanke et al., 2009):

- the neutral oxygen K edge at 23.5 Å ≈ 0.53 keV,
- the neutral iron L_2 and L_3 edges at 17.2 Å ≈ 0.72 keV and 17.5 Å ≈ 0.71 keV (from the ionization of electrons in the $2p_{1/2}$ and $2p_{3/2}$ states, respectively), and
- the neutral neon K edge at 14.3 Å ≈ 0.87 keV.

The strongest edge at higher energies is clearly (see also Fig. 1.14):

- the neutral iron K edge at 1.74 Å ≈ 7.12 keV.

Modelling absorption

Neutral absorption and equivalent N_H. While absorption edges detected in high-resolution spectra allow for an accurate determination of single elements' column densities N_Z, broad band spectra (at CCD resolution or worse) are usually modelled with an *equivalent* hydrogen column density, assuming a (fixed) set of elemental abundances $A(Z)/A(1)$ relative to H:

$$\mathrm{e}^{-\tau(E)} \;=\; \exp\Big(-\sum_Z N_Z\sigma_Z(E)\Big) \;=\; \exp\Big(-N_H\cdot\underbrace{\sum_Z \tfrac{A(Z)}{A(1)}\,\sigma_Z(E)}_{=:\;\sigma_{\text{eff}}(E)}\Big) \tag{1.59}$$

Table 1.2: Galactic abundances defined by XSPEC, XSTAR, and LMC abundances

Element	Abundances $\varepsilon(Z) = 12 + \log_{10}\left(A(Z)/A(1)\right)$ by number								
	Solar abundances						ISM	xstar	LMC
	aneb	angr	feld	grsa	lodd	aspl	wilm		
$_{1}$H	12.00	12.00	12.00	12.00	12.00	12.00	12.00	12.00	12.00
$_{2}$He	10.90	10.99	10.99	10.93	10.90	10.93	10.99	11.00	10.93
$_{3}$Li	3.34	1.16	*1.10*	1.10	3.28	1.05	—	—	—
$_{4}$B	1.46	1.15	*1.40*	1.40	1.41	1.38	—	—	—
$_{5}$Be	2.95	2.60	*2.55*	2.55	2.78	2.70	—	—	—
$_{6}$C	8.65	8.56	8.60	8.52	8.39	8.43	8.38	8.57	8.03
$_{7}$N	7.96	8.05	8.00	7.92	7.83	7.83	7.88	8.04	7.01
$_{8}$O	8.87	8.93	8.93	8.83	8.69	8.69	8.69	8.83	8.38
$_{9}$F	4.49	4.56	*4.56*	4.56	4.46	4.56	—	4.60	—
$_{10}$Ne	8.14	8.09	8.11	8.08	7.87	7.93	7.94	7.45	7.6
$_{11}$Na	6.32	6.33	6.33	6.33	6.30	6.24	6.16	6.25	*5.86*
$_{12}$Mg	7.60	7.58	7.58	7.58	7.55	7.60	7.40	7.54	7.12
$_{13}$Al	6.49	6.47	6.47	6.47	6.46	6.45	6.33	6.39	*6.03*
$_{14}$Si	7.57	7.55	7.55	7.53	7.54	7.51	7.27	7.54	7.21
$_{15}$P	5.58	5.45	*5.45*	5.45	5.46	5.41	5.42	5.52	*5.12*
$_{16}$S	7.28	7.21	7.21	7.33	7.19	7.12	7.09	7.20	6.7
$_{17}$Cl	5.29	5.27	*5.27*	5.50	5.26	5.50	5.12	5.60	*4.82*
$_{18}$Ar	6.58	6.56	6.65	6.40	6.55	6.40	6.41	6.65	6.2
$_{19}$K	5.14	5.12	*5.12*	5.12	5.11	5.03	—	4.95	—
$_{20}$Ca	6.35	6.36	6.36	6.36	6.34	6.34	6.20	6.32	*5.90*
$_{21}$Sc	3.09	3.10	*3.17*	3.17	3.07	3.15	—	3.22	—
$_{22}$Ti	4.95	4.99	*5.02*	5.02	4.92	4.95	4.81	5.13	*4.51*
$_{23}$V	4.03	4.00	*4.00*	4.00	4.00	3.93	—	4.40	—
$_{24}$Cr	5.69	5.67	*5.68*	5.67	5.65	5.64	5.51	5.85	*5.21*
$_{25}$Mn	5.54	5.39	*5.39*	5.39	5.50	5.43	5.34	5.40	*5.04*
$_{26}$Fe	7.52	7.67	7.51	7.50	7.47	7.50	7.43	7.40	7.2
$_{27}$Co	4.92	4.93	*4.93*	4.92	4.91	4.99	4.92	5.10	*6.62*
$_{28}$Ni	6.26	6.25	6.25	6.25	6.22	6.22	6.05	6.30	*7.75*
$_{29}$Cu	4.28	4.21	*4.21*	4.21	4.26	4.19	—	4.50	—
$_{30}$Zn	4.67	4.60	*4.60*	4.60	4.63	4.56	—	4.20	—

References.

- Solar abundances:
  - `aneb` (Anders & Ebihara, 1982)
  - `angr` (Anders & Grevesse, 1989)
  - `feld` (Feldman, 1992), *elements not listed by* Feldman (1992), *but contained in the* `feld` *table* are claimed† to be from `grsa`, but this is not always the case
  - `grsa` (Grevesse & Sauval, 1998)
  - `lodd` (Lodders, 2003)
  - `aspl` (Asplund et al., 2009)
- Abundances in the Galactic interstellar medium (ISM):
  - `wilm` (Wilms et al., 2000)
- Abundances used by a plasma code / warm absorber model (Kallman & Bautista, 2001):
  - `xstar`
- Abundances assumed for the Large Magellanic Cloud, see Sect. **??**:
  - `LMC` (Hanke et al., 2010b), *elements not explicitly listed by* Hanke et al. (2010b) are assumed to be half as abundant as in the `wilm` table

† See `http://heasarc.nasa.gov/docs/xanadu/xspec/manual/XSabund.html`.

Table 1.2 shows the abundance tables currently available in XSPEC 12.6 (Arnaud, 1996), as well as the abundances employed by XSTAR/`warmabs` (Kallman & Bautista, 2001) and LMC abundances (Hanke et al., 2010b) for comparison. Apart from the set of Wilms et al. (2000), all other XSPEC tables refer to *solar* abundances, which may not be appropriate for the Galactic ISM in general. The set of Anders & Grevesse (1989), which has been the default in XSPEC for many years, contains much higher metal abundances than suggested by Wilms et al. (2000); in particular the oxygen and iron abundances differ by a factor of 1.74. As photoabsorption in the soft X-ray band is dominated by metals (Wilms et al., 2000, fig. 1), using `angr` abundances for interstellar absorption as opposed to `wilm` abundances may overestimate the cross-section (see Fig 1.14), and hence underestimate of the column density.

Ionized absorption. Modelling the absorption by ionized matter requires knowledge of the ionization balance, i.e., the population of each element's ionization states. For photoionized optically thin plasmas, it is determined by the ionization parameter (Tarter et al., 1969, eq. 1)[17]

$$\xi \;=\; \frac{L_X}{n\,r^2}\;, \tag{1.60}$$

where L_X is the ionizing luminosity above 13.6 eV, n is the gas density, and r is the distance from the ionizing source. Plasma codes like XSTAR (Kallman & Bautista, 2001)[18] calculate self-consistently – with the correspondingly large computational effort – the radiative transport, thermal equilibrium, and ionization balance through a cloud of gas. The related warm absorber model `warmabs` uses pre-calculated level populations at given ionization parameter (which is a fit parameter) to calculate all ions' opacities and the finally resulting absorption. To the extent that the ionization balance and inner-ionic level populations are influenced by the irradiating spectrum, the calculation is not self-consistent, but gives a first approximation within greatly reduced computation time. Figure 1.15 shows the ionization balance as a function of ionization parameter, from a pre-calculated table for a photoionized plasma at a density of $n = 10^{12}\,\mathrm{cm}^{-3}$, irradiated by a power-law spectrum with photon index $\Gamma = 2$. The resulting warm absorber models for different ionization parameters, in comparison with the `TBnew` model for neutral absorption,[19] are displayed in Fig. 1.16. Since higher energies are dominated by absorption from higher-Z elements, which are always less strongly ionized as lower-Z elements, a low-resolution spectrum above, e.g., 2 keV, may not allow to distinguish neutral absorption from ionized absorption at $\log\xi \lesssim 2$. The detailed physical conditions in such a plasma can only be measured with high-resolution spectra.

* * *

The previous section has laid the foundations for X-rays from accreting compact objects, including internal and external effects on their radiation. The following section will describe how these X-rays can actually be detected and analyzed.

[17] There are also several other definitions of *an* ionization parameter, e.g.,
$U_1 = F_\nu(1\,\mathrm{Ryd})/n_\mathrm{e}$ (Davidson, 1972, § IV),
$\Xi = F_\mathrm{ion}/(n\,kT\,c)$ (Krolik et al., 1981, eq. 2.2),
or $\Gamma = L_X/(8\pi\,hc\,r^2\,n)$ (Kwan & Krolik, 1981, § II).

[18] Available online at `http://heasarc.nasa.gov/lheasoft/xstar/xstar.html`.

[19] Available online at `http://pulsar.sternwarte.uni-erlangen.de/wilms/research/tbabs/`.

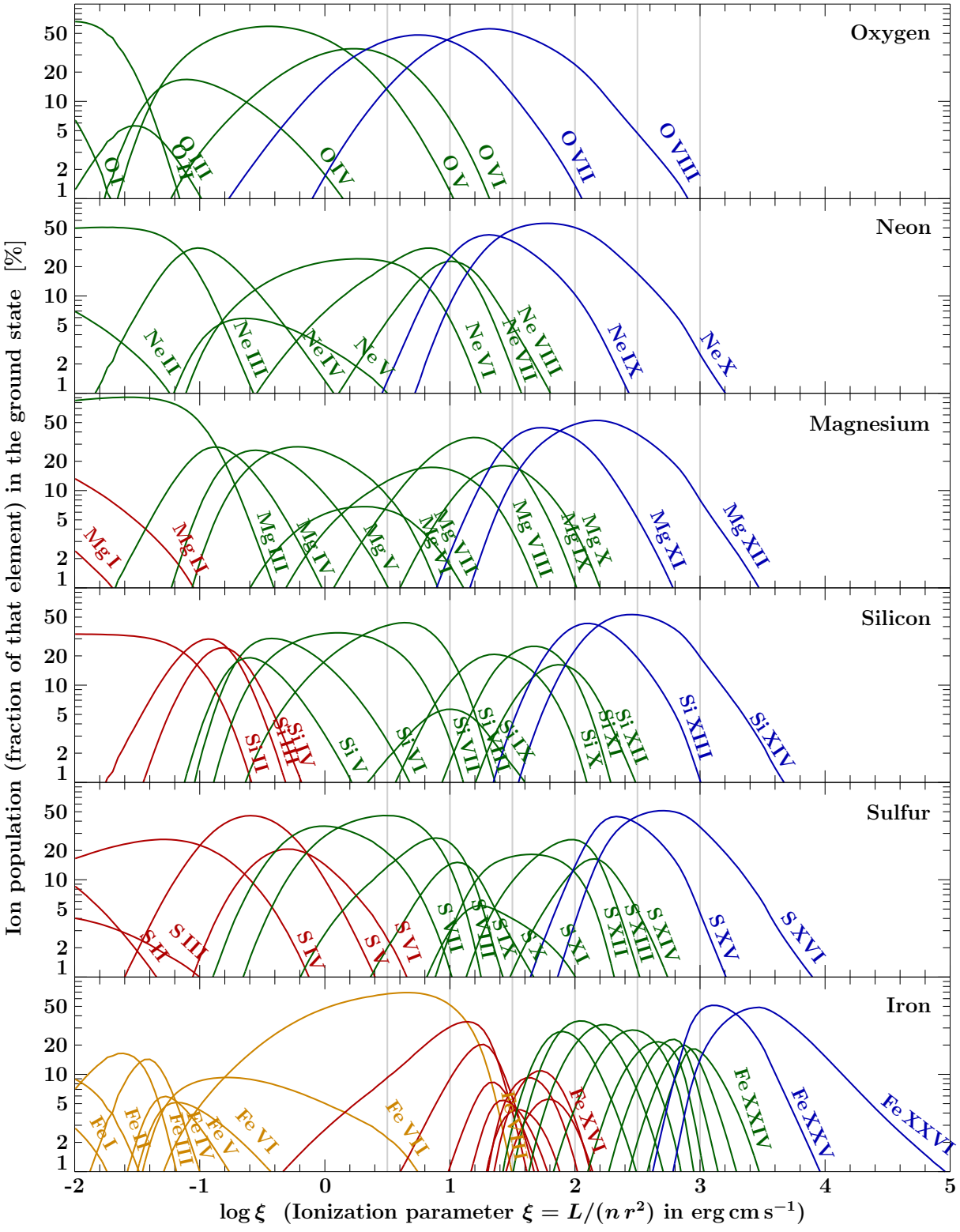

Figure 1.15: Ionization balance for different elements, according to the `pops.fits.n12` file distributed with `warmabs` v2.0 (T. Kallman)[†]. The fraction of each element's ions in their respective ground states is displayed as a function of the ionization parameter (see also, e.g., Kallman & Bautista, 2001, figs. 8 and 13; Kallman, 2010, fig. 4). K-shell ions are depicted in blue, L-shell ions in green, M-shell ions in red, and N-shell ions in orange. The gray vertical lines indicate the ionization parameters for which the `warmabs` model is shown in Fig. 1.16.

[†] Available online at `ftp://legacy.gsfc.nasa.gov/software/plasma_codes/xstar/`.

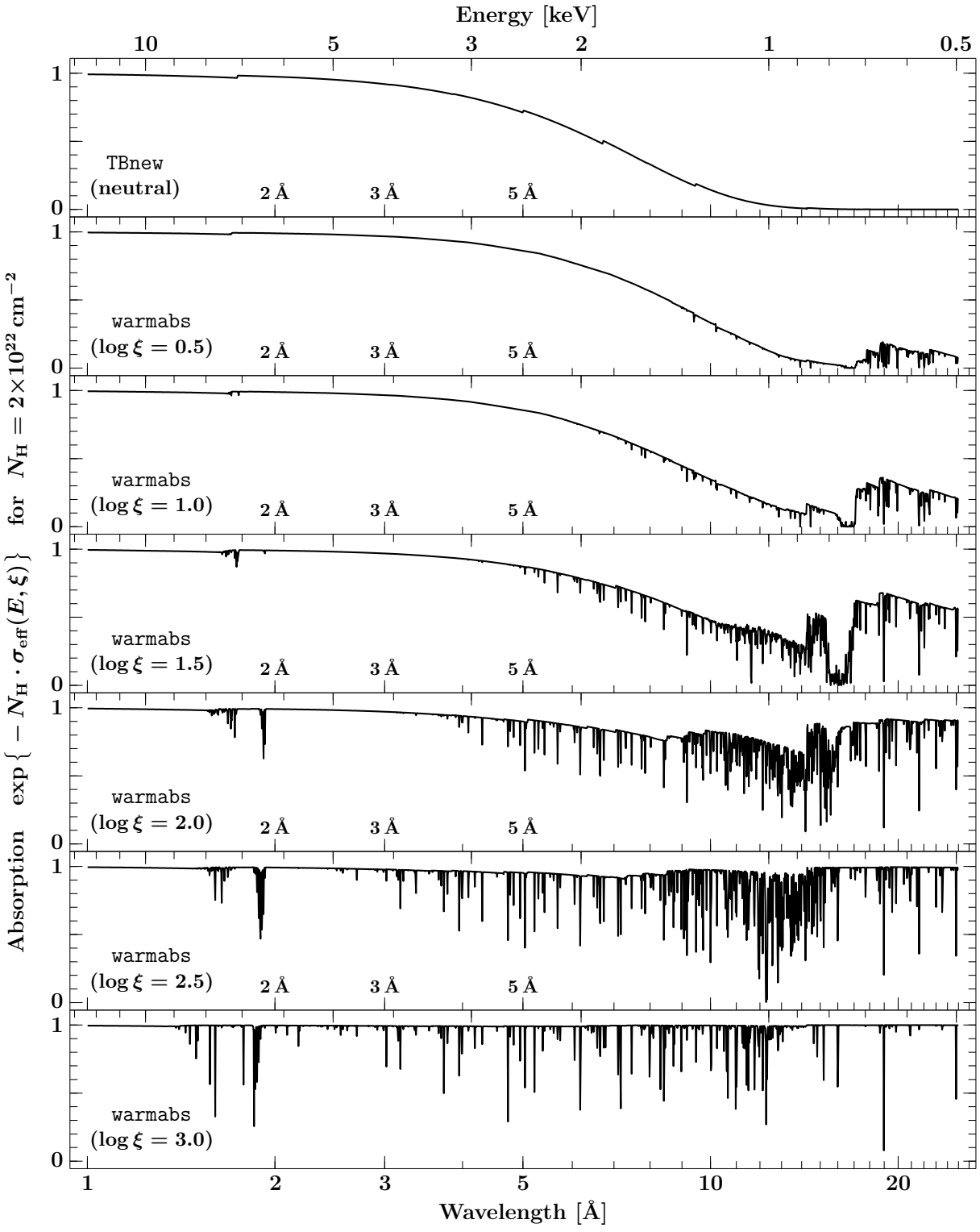

Figure 1.16: Top panel: Neutral absorption according to `TBnew` (see also Fig. 1.14). Other panels: Absorption by photoionized matter for different ionization parameters $\log \xi = 0.5$–3, according to `warmabs` v2.0 (Kallman & Bautista, 2001) using the population file `pops.fits.n12` (see also Fig. 1.15). A common column density of $N_{\rm H} = 2{\times}10^{22}\,{\rm cm}^{-2}$ has been assumed. For low ioniziation parameter, various O ions produce prominent absorption edges and lines at $\lambda{>}14\,$Å. The broad absorption complex at $\sim$16 Å for $\log \xi = 1.5$ is an unresolved transition array of Fe M-shell ions (Behar et al., 2001). With increasing ξ, higher-Z elements get ionized as well, and the features from low-Z elements disappear as these become fully ionized.

1.3 X-ray Observatories and their Instruments

Due to the large number of X-ray satellites carrying different detectors with mutually supplementary capabilities, the beginning of the 21st century may indeed be considered as the golden age of X-ray astronomy. Figure 1.17 shows the spectral coverage of instruments that are currently available to X-ray astronomers. For the soft X-rays, the technologies range from microchannel plate detectors (*Chandra* HRC) with the best spatial, but almost no energy resolution, over proporional counters (*RXTE* PCA) with a relatively bad energy resolution, but very high sensitivity, and CCD detectors (*XMM* EPIC-pn and -MOS, *Chandra* ACIS, *Swift* XRT, *Suzaku* XIS) with moderate energy, but good spatial resolution, to dispersive X-ray gratings (*Chandra* HETGS/LETGS, *XMM* RGS) with lower sensitivity, but the highest spectral resolution currently available. For the hard X-rays, scintillation counters (*RXTE* HEXTE, *Suzaku* GSO), and coded mask detectors (*Swift* BAT, all instruments on *INTEGRAL*) are employed.

1.3.1 The *Rossi X-ray timing Explorer* (*RXTE*)

Since 1995 December 30, NASA's *RXTE* satellite (named after the Italian-American phycisist Bruno Benedetto Rossi, 1905–1993) is in a ∼90 min low-Earth orbit, where it has been decaying from an initial altitude of ≳570 km to ∼490 km in 2006 (Jahoda et al., 2006, fig. 26). *RXTE* carries three instruments:

- The All Sky Monitor (ASM; see Levine et al., 1996; Bradt et al., 2007, for a description of the instrument) contains three scanning shadow cameras with position-sensitive proportional counters that are filled with a 95 % xenon / 5 % CO_2 mixture; its on-axis effective area peaks at $3 \times \sim 30\,\mathrm{cm}^2$ at 5 keV. The cameras have a colimator-limited field of view of $6^\circ \times 90^\circ$ and contain slit masks, such that the ASM operates as a coded-mask detector. As the ASM can be rotated, it monitors (almost) the whole sky; *"a randomly chosen source is scanned typically 5–10 times a day"* (Levine et al., 1996). Data are accumulated during ∼90 s dwells. X-ray light curves in the so-called A-band (1.5–3 keV), B-band (3–5 keV), C-band (5–12 keV), and S-band (1.5–12 keV), derived from all-sky solutions for the shadow patterns, are made available by the *RXTE* ASM team at MIT.[20]

- The Proportional Counter Array (PCA; see Jahoda et al., 1996, 2006) consists of five Proportional Counter Units (PCUs) containing a propane layer and four layers filled with 90 % xenon / 10 % methane below a colimator limiting the field of view to 1°. The first (propane) and last (xenon) layers, as well as the outermost anodes of the middle layers, are used as a veto system to distinguish photons entering the detector from above, from below, or from the side. The three middle xenon layers consitute the main proportional counter; for spectral analysis, one can restrict oneself to data from the first xenon layer ("top layer"), which is best calibrated. From 1996 to 2000, the proportional counters' high voltage has been lowered for four times, which – together with the loss of propane in PCU0 since 2000 May 12, likely after a collision with a micrometeorite – defines the PCA's five gain epochs with different energy-channel conversion.[21]

  Each PCU has a large geometric collecting area of $1\,600\,\mathrm{cm}^2$ and, including quantum efficiencies, an effective area of still $>1\,000\,\mathrm{cm}^2$ per PCU around 8 keV. The PCA is sensitive from ∼2 to ∼100 keV, with the ∼20–50 keV range only being reasonably well calibrated since the recent introduction of pcarmf v.11.7 with the heasoft-6.7 software package in 2009 August.[22]

[20] See http://xte.mit.edu/asmlc/.
[21] See http://heasarc.nasa.gov/docs/xte/e-c_table.html.
[22] See http://astrophysics.gsfc.nasa.gov/xrays/programs/rxte/pca/doc/rmf/pcarmf-11.7/.

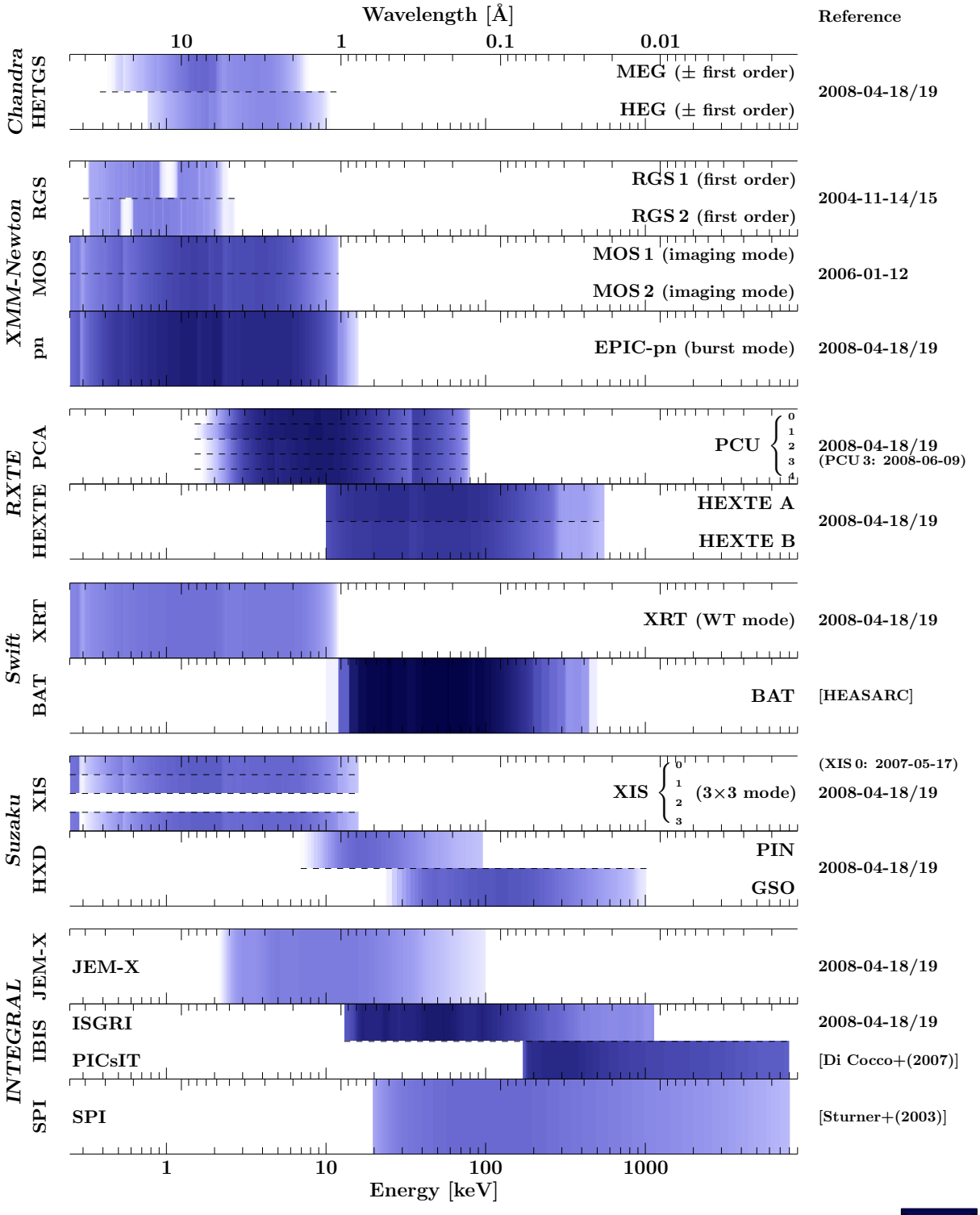

Figure 1.17: Spectral coverage of X-ray detectors currently in orbit. The color scale shows the effective area $A_{\rm eff}$ according to the logarithmic scale on the right. $A_{\rm eff}$ may depend on specific details of the observation; most of the data are from the simultaneous observation of Cyg X-1 on 2008-04-18/19 (Sect. 2.6). $A_{\rm eff}$(*XMM* RGS) is from another observation of Cyg X-1 during which all available CCDs were activated. $A_{\rm eff}$(*XMM* MOS) is from an observation of NGC 1052 by courtesy of M. Böck. $A_{\rm eff}$(*Swift* BAT) is from `http://heasarc.gsfc.nasa.gov/docs/swift/proposals/swift_responses.html`. All $A_{\rm eff}$(*Suzaku*) are by courtesy of M.A. Nowak. $A_{\rm eff}$(*INTEGRAL* JEM-X) is by courtesy of F. Fürst. $A_{\rm eff}$(*INTEGRAL* PICsIT) is from Di Cocco et al. (2007). $A_{\rm eff}$(*INTEGRAL* SPI) is from Sturner et al. (2003).

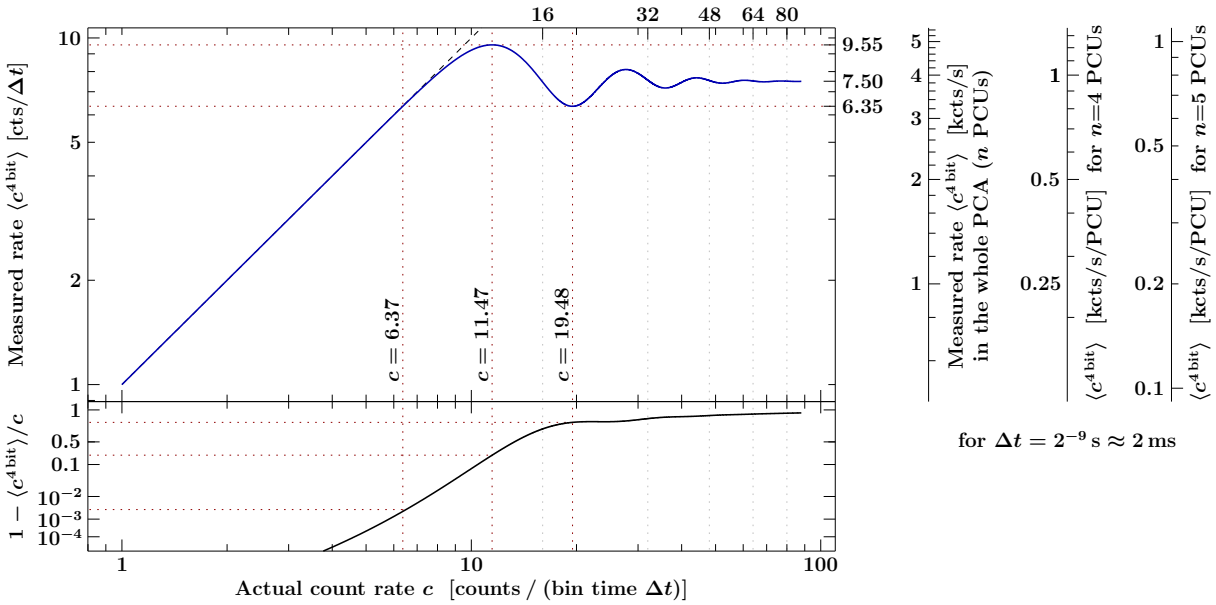

Figure 1.18: Buffer overflow in binned modes of *RXTE* PCA. The upper panel shows the expected average *detected* count rate $\langle c^{4\,\mathrm{bit}} \rangle$ from an *actual* count rate c in presence of a 4 bit overflow according to Eq. (1.61). The lower panel shows the fraction of events lost in overflows. Up to rates of $6.4/\Delta t$, the respsonse function is relatively linear and the losses are less than 0.3 %. At higher rates, it is no more possible to estimate the number of lost events without further assumptions on the count rate c. The axes on the right translate the measured rates in cts/Δt to units of cts/s for $\Delta t = 2^{-9}$ s and cts/s/PCU for $n = 4$ and $n = 5$ active PCUs.

Events recorded by the PCA are digitalized by the Experiment Data System in six Event Analyzers (EAs), with a time resolution that can be as high as 1 μs. The EAs simultaneously bin the same events (*"all six EAs see all events from all detectors"*; Smale, sect. 4.2.7) in different EA modes (which can partly be chosen by the observer), such that different requirements for time or energy resolution can be met at the same time while respecting the telemetry limits. For example, light curves with 2 ms resolution in only few energy bands can be obtained at the same time as 16 s integrated spectra with 129 channels.

In 'binned modes', the event counters for each energy band and time interval may *"roll-over to zero when incremented beyond their maximum (4, 8, or 16 bits according to the configuration). No flag is set to indicate a rollover"* (Smale, sect. 7.5.1). For example, the binned mode `B_2ms_8B_0_35_Q` has a 2 ms (strictly speaking 2^{-9} s) time resolution, uses 8 energy bands covering channels 0–35, and employs 4 bit bins.[23] The highest PCA count rate that can be measured in any one of the 8 energy bands in this mode is thus (15 counts)/(2 ms), i.e., 7.68 kcps. But due to the large fluctuations expected from Poisson statistics in the short time bins, the overflow reduces the mean detected count rate already at much lower fluxes. Figure 1.18 shows the function

$$\langle c^{4\,\mathrm{bit}} \rangle (c) \;=\; \sum_{k=0}^{\infty} P_c(k) \cdot (k \bmod 16) \;=\; \sum_{k=0}^{\infty} \frac{c^k\, \mathrm{e}^{-c}}{k!} \cdot (k \bmod 16) \qquad (1.61)$$

which describes the average $\langle c^{4\,\mathrm{bit}} \rangle$ of the *detected* count rate $(k \bmod 16)$ in presence of the 4 bit buffer overflow, with k being Poisson distributed according to the *actual* count rate c, in units of cts/Δt. The measured rate is thus expected to have a maximum of

[23] *"The naming convention for these configurations is* `B_ttt_ccX_0_hh_B`*, where ttt is the time bin size, cc is the number of energy channels, X selects the channel boundary option, hh specifies the upper channel boundary, and B is one of* `Q`*,* `H` *or* `F` *specifying that 4, 8 or 16 bit bins have been used."* (Smale, appendix Ap.1.4)

$9.55/\Delta t$, which corresponds for the `B_2ms_8B_0_35_Q` mode to 4.89 kcps in the whole PCA (i.e., with up to 5 PCUs). As an example, Gleissner et al. (2004b, fig. A.1) show the rms-flux relation of Cyg X-1 from an observation with 4 active PCUs to deviate from the linear relationship at ∼800 cps, which is in very good agreement with the expectation from Eq. (1.61) and Fig. 1.18.

- The High Energy X-ray Timing Experiment (HEXTE; Gruber et al., 1996; Rothschild et al., 1998) consists of two clusters (called "A" and "B") with four NaI(Tl) / CsI phoswich scintillation counters each. Lead collimators restrict the field of view to 1°, and result in a collecting area of $2 \times 4 \times 200\,\mathrm{cm}^2$ in total. For spectral analysis, however, cluster B has an effective area of $< 600\,\mathrm{cm}^2$, as the pulse-height analyzer of one of the phoswitch detectors failed on 1996 March 6. HEXTE is sensitive from 15 to 250 keV and capable to perform timing studies at 8 μs resolution with an absolute accuracy better than 1 ms.

  In order to measure the instrumental background, a "rocking" mechanism was implemented: each cluster may move independently by 1.5° or 3°. to an off-source pointing The rocking mechanism of cluster A has failed occasionally since 2005 and was finally shut down on 2006 October 20. Cluster B failed rocking on 2009 December 14 as well.

1.3.2 The *Chandra* X-ray Observatory

The *Chandra* X-ray observatory (named after the Indian-American astrophycisist and Nobel laureate in 1983, Subrahmanyan Chandrasekhar, 1910–1995) is one of NASA's "Great Observatories", next to the *Compton Gamma-ray observatory*, the *Hubble Space Telescope*, and and the *Spitzer Space Telescope*. It was launched on 1999, July 23 by the Space Shuttle *Columbia* into an eccentric ∼64 hour orbit around Earth at a distance of ∼10 000–140 000 km.

Chandra has a Wolter (1952a,b) type I telescope, the High Resolution Mirror Assembly (HRMA), of four coaxial pairs of iridum coated parabolic/hyperboloic mirror shells, focussing X-rays that hit the HRMA at grazing incidence. The focal length is 10 m and the field of view is 1° at a resolution of $\lesssim 0.5''$. X-rays are detected by one of two different focal-plane science instruments: the Advanced CCD Imaging Spectrometer (ACIS) or the High Resolution Camera (HRC). In addition, High or Low Energy Transmission Gratings (HETG or LETG) may be brought into the optical path, which disperse part of the photons according to their wavelength and thus render the focal-plane detector into a high-resolution spectrometer.

- The ACIS detector (Garmire et al., 2003) consists of ten CCDs with 1024×1024 pixels of $(24\,\mu\mathrm{m})^2$ size, corresponding to $(0.49'')^2$ of the field of view. At most six chips can be operated at a time. There are two subsystems (see CXC, 2010b, fig. 6.1 for the layout): ACIS-I, an array of 2×2 CCDs (I0–I3 ≡ CCDs 0–3) optimized for imaging, and ACIS-S, a linear array of six CCDs (S0–S5 ≡ CCDs 4–9) optimized for HETG-spectroscopy. The chip gaps between the ACIS-I (ACIS-S) chips correspond to 22 (18) pixels. In order to cover these gaps, the spacecraft usually dithers with a full width of 16" for ACIS observations. All ACIS CCDs but S1 and S3 are front-illuminated. The back-illuminated CCDs have a better quantum efficiency for soft X-rays (see, e.g., Fig. 2.54 on page 100).

  The detector can be read out in either *timed exposure* (TE) or *continuous clocking* (CC) mode. In TE mode, the CCDs are only read out after some integration time: the nominal frame time for full frames is 3.2 s; subarrays allow for shorter frame times at the expense of a reduced field of view. In alternating exposure mode, a short frame with an exposure below 3.2 s is followed by a sequence of longer exposed frames with exposures of > 3.2 s (CXC, 2010b, sect. 6.12.2). In CC mode, on the other hand, the rows are continuously

shifted, reducing the integration time to 2.85 ms per pixel in trade-off against one spatial dimension – as usual in timing modes.

On-board data processing is used to grade detected events, i.e., to determine the pattern in 3×3 pixels surrounding the main event. 'Bad' grades, likely to be caused by background events, are not included in the telemetry stream. For 'good' grades, the transmitted information depends on the telemetry format: in addition to the pulse height amplitude, and the time and position of the main event, only the grade is reported in *graded mode*, whereas all amplitudes of 3×3 (or even 5×5) surrounding pixels are transmitted in *faint mode* (or *very faint mode*, respectively). If the bandwidth is not sufficient to telemeter all data, full frames in TE mode or virtual frames of 512 rows in CC mode will be discarded for individual CCDs, which can thus gather different exposures during an observation (e.g., Feng et al., 2003). Frame dropouts due to telemetry saturation must therefore treated with special care during data analysis, see Sect. 1.3.4. In order to reduce the telemetry rate, event filters can be defined instructing the onboard data processor to include only a certain fraction of events from a given region on the detector into the telemetry stream (CXC, 2010b, sect. 6.20.2).

- The HRC (Murray et al., 2000) consists of CsI-coated microchannel plate detectors, in which photoelectrons are multiplied by a high voltage to a cascade. The energy resolution is very poor ($\Delta E/E \approx 1$; CXC, 2010b, table 7.1), but the sensitivity extends from 0.08 keV to 10 keV. The HRC-S subsystem is thus ideal for LETG spectroscopy, while HRC-I takes advantage of the high spatial resolution of 0.4" matching HRMA's capabilities.

- The HETG (Canizares et al., 2005) comprises two sets of gratings with different resolving powers: the high- and medium-energy gratings (HEG and MEG), consisting of $(25\,\mathrm{mm})^2$ sized grating facets with 120 nm × 510 nm gold bars at a period p_{HEG}=200 nm, and 208 nm × 360 nm bars at p_{MEG}=400 nm, respectively. The dimensions were chosen to optimize the first order diffraction efficiency, and to suppress second order diffraction of the MEG. The gratings are mounted in four annuli on a circular support structure with a diameter of 1.1 m (see Fig. 1.19) that can be inserted after the four mirror shells into the optical path. All gratings of one set are aligned with each other and positioned on a Rowland (1882) torus (see, e.g., Beuermann et al., 1978, fig. 1) to ensure that all photons of wavelength λ that are dispersed in the same order m – i.e., by an angle β according to

$$p \cdot \sin\beta \;=\; m \cdot \lambda \tag{1.62}$$

  – arrive at the same focus. The dispersion directions of HEG and MEG are rotated by ∼10° such that the spectra on both sides of the undispersed image (which will be denoted by sgn $m = \pm 1$) form an 'X' on the detector. The wavelength scales per pixel are

$$\Delta\lambda_{\mathrm{HEG}} \;=\; 11\,\mathrm{m\AA} \qquad \text{and} \qquad \Delta\lambda_{\mathrm{MEG}} \;=\; 5.5\,\mathrm{m\AA} \tag{1.63}$$

  such that the full ACIS-S detector can only cover $m \cdot \lambda_{\mathrm{HEG}} \lesssim 15$ Å and $m \cdot \lambda_{\mathrm{MEG}} \lesssim 31$ Å. ACIS' energy resolution allows to separate different orders m, and also to (first of all) distinguish HEG and MEG first order spectra in CC mode, in which the 'X' is only seen as an 'I' due to the lack of spatial information along the readout direction.

- The LETG (see Brinkman et al., 1997; Predehl et al., 1997, for an extensive description of the instrument) consists of free-standing gold wires of ∼0.5 μm thickness with a period $p_{\mathrm{LETG}} \approx 1\,\mu$m, held by a perpendicular fine-support mesh with a period $p_{\text{fine support}} \approx 25\,\mu$m and triangular coarse-support bars. According to Eq. (1.62), the LETG has a much lower dispersion than the HETG, which allows to cover 1.2–175 Å with the HRC-S detector.

Figure 1.19: A true scale model of *Chandra*'s High Energy Transmission Gratings (right), exhibited at MIT's Space Nanotechnology Laboratory, where the HETG were fabricated, with an X-ray astronomer (left) for size comparison. The two inner annuli contain 144 high-energy grating facets, whose gold transmission gratings have 5000 lines/mm, whereas the two outermost annuli consist of 192 medium-energy grating facets with 2500 lines/mm.

1.3.3 The *X-ray Multi-Mirror Mission (XMM) Newton*

ESA's *XMM-Newton* (named after the English physicist, mathematician, and astronomer Sir Isaac Newton, 1643–1727) was launched on 1999 December 10 by an Ariane 5 rocket in a highly excentric 48 hour orbit around the Earth with a distance of initially ∼7 000–114 000 km (Jansen et al., 2001).[24] The period of exactly 2 days was chosen to keep optimal contact to the ground stations in Kourou (French Guyana), Perth (Australia) and Santiago (Chile).[25]

XMM carries three highly efficient co-aligned X-ray telescopes, and an optical/UV telescope. Each Wolter (1952a,b) type I telescope consists of 58 nested co-axial mirror shells, whose gold coating focuses X-rays from a geometric effective area of $\gtrsim$1 500 cm^2 via total reflection on the paraboloidal and hyperboloidal shape at a focal length of 7.5 m. The X-ray telescopes have a field of view of 30′ and are equipped with different types of CCD arrays in the focal plane – the three European Photon Imaging Cameras (EPIC-pn, -MOS1 and -MOS2) – and with two Reflection Grating Spectrometers (RGS1 and RGS2). The latter disperse ∼40 % of the photons from two of the telescopes onto another linear array CCD detector, while ∼44 % of the photons reach the corresponding MOS detectors (XMM SOC, 2010).

- The EPIC-pn chip (see Strüder et al., 2001, for further details) consists of 2×6 back-illuminated CCDs that have been manufactured on a single $(6\,\mathrm{cm})^2$ silicon wafer by the Max-Planck Insititute for Extraterrestrial Physics (MPE) in Garching, Germany. Each CCD has 64 × 200 pixels with a size of $(150\,\mu\mathrm{m})^2$, corresponding to $(4.1'')^2$ on the sky.

  A parallel readout allows for a very high time resolution, depending on the readout mode: the full frame can already be read out in 73 ms, parts of the detector, in large or small window mode, even in 48 ms or 6 ms. If only one CCD is operated in timing or burst mode, i.e., continuously read out, a time resolution of 30 μs or even 7 μs can be achieved, however, with the drawback of the loss of one spatial dimension, and, in addition for the burst mode, of the low duty cycle of only 3 %.

- The two identical MOS cameras (see Turner et al., 2001, for a characterization of the instrument) consist of seven front-illuminated CCD chips from the English electric Valve

[24] Because of several perturbations, the orbit parameters change with time, such that the perigee and apogee heights vary between (7–22)×10^3 km and (114–100)×10^3 km, respectively, correpsonding to an eccentricity ε of $\varepsilon = 0.88$–0.64. Furthermore, the perigee height was lifted by an orbit correction maneuver in 2003 February.

[25] Due to the evolution of the orbit, the ground station in Santiago has become dispensable in 2006 December (Parmar et al., 2008).

Company (EEV; since 2002 named e2v). The six chips surrounding the central one at the focal point of the telescope are elevated by 4.5 mm in order to follow the focal surface and also to allow for electronic connections to the central chip. All CCDs have 600×600 pixels of $(40\,\mu\mathrm{m})^2$ area, each corresponding to $(1.1'')^2$ on the field of view.

The MOS camera's full frame readout takes 2.6 s, but large and small window modes with frame times of 0.9 s and 0.3 s, as well as a 1.75 ms timing mode, are possible for bright sources.

On 2005 March 9, the peripheral CCD6 was damaged, probably by the impact of a micrometeorite.

- The two identical Reflection Grating Arrays (den Herder et al., 2001) consist of 182 gratings, which have a 2 μm gold coating on an 1 mm thin SiC substrate. The gratings have a groove density of 646 lines/mm. Each dispersed spectrum is collected by a linear array of nine CCDs with 1024×768 pixels (only 1024×384 are exposed, the other half of the CCD serves as a storage) of $(27\,\mu\mathrm{m})^2$ pixelsize, which are located on the Rowland circle.

  Already after the first week of the mission, CCD4 of RGS2 failed, and so did CCD7 of RGS1 in 2000 September. Since then, the 20–24 Å and 10.6–13.8 Å regions of the spectrum are at most covered by one of the – otherwise redundant – RGSs.

  The readout time is 0.6 s per CCD if read out via two nodes. Since 2007 August, single-node readout is applied for RGS2, yielding a readout time of 1.2 s per CCD. Subsequently reading out all eight operative CCDs of RGS1 (RGS2) therefore takes 4.8 s (9.6 s). The readout sequence can, however, (largely) be defined by the observer; one can, for example, omit certain CCDs, or also read out ones more often than others, e.g., in order to reduce the frame time on them and therefore reduce pileup in regions where high fluxes are expected. An example for such an optimization is illustrated in Figs. 2.77 and 2.78.

1.3.4 X-ray Data Analysis

The principles of X-ray data analysis in general, as well as their implementation in the very flexible and powerful *Interactive Spectral Interpretation System* (ISIS; Houck & Denicola, 2000; Houck, 2002; Noble et al., 2006; Noble & Nowak, 2008)[26] have already been described by Hanke (2007, sects. 2.2, 3.2). Therefore, this section only reminds of the 'master formula' before noting a few additional features that are of particular relevance for this work.

Due to the low energy resolution of (non-dispersive) X-ray detectors, the photon flux spectrum $f_E(E) = \mathrm{d}N_\mathrm{ph}/\mathrm{d}t\,\mathrm{d}A\,\mathrm{d}E$ cannot be directly inferred from measured count rates. Instead, models for $f_E(E)$ are folded through the instrumental response, such that predicted numbers of counts in the detector's spectral channels $\#i$:

$$C(i) \;=\; B(i) \;+\; t_\mathrm{exp}\cdot\int\mathrm{d}E\;\; R(i,E)\cdot A(E)\cdot f_\mathrm{E}(E) \;\;=:\;\; B(i)+S(i) \tag{1.64}$$

can be compared with measured ones, based on (e.g.) χ^2 statistics. In Eq. (1.64), $B(i)$ denotes the (properly scaled) background contribution, and $S(i)$ is the source contribution. The latter is composed of the (effective) exposure time t_exp; the *redistribution matrix function* (RMF) $R(i,E)$, which indicates the probability for a photon of energy E to be detected in bin $\#i$; the *ancillary response function* (ARF) $A(E)$, i.e., the effective area at energy E (which is shown in Fig. 1.17). Spectral analysis is therefore reduced to an optimization problem for the model's parameters.

[26] See http://space.mit.edu/cxc/isis.

Background correction

ISIS allows for a very general background correction by defining a hook function *"to modify the computed model* [C] *after the separate source and background contributions* [S and B] *have been computed"*.[27] For instance, the predicted background can be rescaled by a constant factor c_{back}:

$$C(i) \;=\; S(i) \;+\; c_{\mathrm{back}} \cdot B(i) \tag{1.65}$$

c_{back} can be introduced as a fit parameter by coupling it to a parameter that has formally been added to the model, but that does not change the flux, as in the following example:

```
define backcorr_fit(lo, hi, par)              % additive dummy model that has no effect
{ return 0*lo;
}
add_slang_function("backcorr", ["c"]);

define backcorr_hook(lo, hi, S, B)            % background correction according to Eq. (1.65)
{ return S + get_par("backcorr(1).c") * B;
}

fit_fun(get_fit_fun() + "+backcorr(1)");      % add the dummy model to the fit function
set_post_model_hook(id, &backcorr_hook);      % assign background correction to data set id
```

Gainshift correction for CCD detectors

When a photon hits a CCD detector, a number of electron-hole pairs are created. The electrons are initially confined to the pixels, but finally shifted along the columns to an analog-digital-converter at one edge of the CCD. As some charges may be 'lost' (e.g., due to scattering off crystal defects), the charge-transfer efficiency (CTE) is less than 100 %. If the initially recorded pulse-height amplitude were converted to an energy $E_1(\textsc{pha})$, it would usually be smaller than the energy $E_0(\gamma)$ of the event.[28] The calibration of the events during data (re)processing ought to correct the pulse invariant $E_2(\textsc{pi})$ for the charge transfer *inefficiency* (CTI $= 1 -$ CTE):

$$E_0(\gamma) \quad \xrightarrow[\text{CTI}]{\text{CCD readout}} \quad E_1(\textsc{pha}) < E_0(\gamma) \quad \xrightarrow[\text{correction}]{\text{calibration}} \quad E_2(\textsc{pi}) > E_1(\textsc{pha}) \tag{1.66}$$

A wrong gain correction, yielding $E_2(\textsc{pi}) \neq E_0(\gamma)$, may lead to a distorsion of the spectrum – which is a histogram of $E_2(\textsc{pi})$ with respect to the EBOUNDS grid of channel boundaries – in particular close to spectral regions with large variations of the detector efficiency around strong absorption edges. To correct for that, ISIS' `gainshift` kernel allows for a linear relation

$$E_2(\textsc{pi}) \;=\; \texttt{slope} \cdot \big[E_0(\gamma) + \texttt{intercept}\big] \tag{1.67}$$

by rebinning the model counts $C(i)$ to a modified grid of channel energy boundaries:

$$\textsc{ebounds} \quad \xrightarrow[\text{gainshift}]{\text{ISIS}} \quad \textsc{ebounds}' \;=\; \frac{\textsc{ebounds}}{\texttt{slope}} \;-\; \texttt{intercept} \tag{1.68}$$

Binning energies $E_0(\gamma)$ of the model in channel i with modified boundaries $\textsc{e}'(i)$ and $\textsc{e}'(i{+}1)$ is equivalent to binning modfied energies $E_2(\textsc{pi})$ in the original EBOUNDS $\textsc{e}(i)$ and $\textsc{e}(i{+}1)$.

[27] after the ISIS documentation of `set_post_model_hook`, which assigns this hook function to the spectrum

[28] $E_0(\gamma)$ is not necessarily the energy of the original photon, as the latter may already have been redistributed during the detection process, which is accounted for by the RMF.

Computation of confidence maps

Generally, in order to compute a confidence map for two parameters p_1 and p_2 of a model's parameter vector $\vec{p}$ that is fitted to some data according to $\chi^2(\vec{p})$ – or another function to assess the 'goodness of a fit' –, the two parameters $(p_1,\, p_2)$ are subsequently fixed at all points of a predefined grid $\{x_i\}_{(i)} \times \{y_j\}_{(j)}$. In each step, $\chi^2(\vec{p})$ is minimized on the subset of parameter space in which the other (free) parameters are allowed to vary. That is, the fit algorithm has to find the local best fit $\vec{b}_{(i,j)}$ such that

$$\chi^2\big(\vec{b}_{(i,j)}\big) \;\leq\; \chi^2(\vec{p}) \qquad \text{with} \quad p_1 = b_{1(i,j)} = x_i \quad \text{and} \quad p_2 = b_{2(i,j)} = y_j \tag{1.69}$$

for all $\vec{p}$ of the allowed parameter space. If $\vec{B}$ is the global best fit parameter vector (obtained from fitting for p_1 and p_2 as well), the difference $\Delta\chi^2{}_{(i,j)} = \chi^2\big(\vec{b}_{(i,j)}\big) - \chi^2(\vec{B})$ follows a χ^2 distribution with two degrees of freedom, and contours at $\Delta\chi^2{}_{(i,j)} = X$ enclose a confidence region for p_1 and p_2 corresponding to a probability (e.g., Bevington & Robinson, 1992):

$$P_{\chi^2;\,\nu=2}\left(\Delta\chi^2 \leq X\right) \;=\; 1 - \exp\left(-\tfrac{X}{2}\right) \tag{1.70}$$

Thus, $\Delta\chi^2 \leq 2\log(10) \approx 4.61$ defines a 90 % confidence region for two parameters of interest.

As the convergence of many numerical fit algorithms depends strongly on the start parameters (e.g., gradient algorithms may be attracted by a local side minimum of the χ^2 function when starting at an unfortunate parameter vector), the choice of the inital parameters before each step's fitting may be relevant for the computation of confidence maps as well. In earlier implementations of ISIS, the start parameters were always set to the global best fit $\vec{B}$, modified by $p_1 = x_i$ and $p_2 = y_j$, which will be denoted as $\vec{B}_{\perp(i,j)}$ in the following. However, the local best fit $\vec{b}_{(i,j)}$ is a continuous function of $(p_1,\, p_2)$, just as the confidence map $\Delta\chi^2{}_{(i,j)}$ itself. A better choice for the start parameters may therefore be a local best fit $\vec{b}_{(i',j')}$ that has already been obtained at a grid point $(i',\, j')$ that is close to $(i,\, j)$ – that is, to start with $\left(\vec{b}_{(i',j')}\right)_{\perp(i,j)}$. In addition, it is desirable to connect each grid point with the neighbor with lowest $\Delta\chi^2{}_{(i,j)}$. The following "flood" algorithm for the computation of confidence maps expands dynamically (i.e., according to $\Delta\chi^2{}_{(i,j)}$ obtained during the computation) from the global best fit $\vec{B}$:

0. Fit the grid point $(i_0,\, j_0)$ that is closest to the global best fit $\vec{B}$, starting from $\vec{B}_{\perp(i_0,j_0)}$.
1. Save both $\Delta\chi^2{}_{(i_0,j_0)}$ and $\vec{b}_{(i_0,j_0)}$ obtained in the last step, and note that $(i_0,\, j_0)$ is 'done'. If all grid points have been computed, then the computation is finished.
2. Among all grid points $(i,\, j)$ whose status is 'done', find $(i_1,\, j_1)$ with the minimal $\Delta\chi^2{}_{(i,j)}$.
   (a) If $(i_1,\, j_1)$ has a neighbor $(i_0,\, j_0)$ that has not been investigated yet, then fit it starting from $\left(\vec{b}_{(i_1,j_1)}\right)_{\perp(i_0,j_0)}$ and continue with step 1.
   (b) If all neighbors of $(i_1,\, j_1)$ have already been investigated, then set the status of $(i_1,\, j_1)$ to 'cannot grow any more', free the memory for $\vec{b}_{(i_1,j_1)}$, and continue with step 2.

The computation can even be stopped as soon as the interesting region is covered, if step 2 is modified in the following way:

2'. Among all grid points $(i,\, j)$ whose status is 'done', find $(i_1,\, j_1)$ with the minimal $\Delta\chi^2{}_{(i,j)}$. If $\Delta\chi^2{}_{(i_1,j_1)}$ is larger than a predefined threshold, then the computation is finished.

This "flood" algorithm may not only produce more accurate results due to a better convergence of local fits, but it also allows to speed up the calculation significantly when a possibly large

number of grid points do not need to be computed at all – without prior knowledge of the shape of the confidence contours. It has been implemented into ISIS with version 1.6.1-23.[29]

Inferring derived parameters and fluxes

While spectral fitting allows to measure the direct parameters $\vec{p}$ of a model and their confidence limits in one or – as outlined above – more dimensions, one is often also interested in derived parameters $f(\vec{p})$, e.g., the flux of a model (component). If it were possible to define a probability density $P_{\vec{p}}$ on the parameter space (it will be shown below that it is in general not), one could immediately deduce a probability distribution P_f for such a derived quantity $f(\vec{p})$:

$$P_f(f_0) \;=\; \iiint \mathrm{d}^n p \;\; P_{\vec{p}}(\vec{p}) \;\; \delta\big(f(\vec{p}) - f_0\big) \tag{1.71}$$

If $P_{\vec{p}}$ shall follow from the χ^2 statistics defined by the data, it is reasonable to assume that the probability of the whole region in parameter space leading to a certain χ^2 value is given by the probability $P_{\chi^2;\,\nu}(\chi^2)$ of the χ^2 distribution for ν degrees of freedom, and that all parameter vectors in this region are considered to be equally probable. The first requirement reads:

$$\iiint\limits_{\left\{\vec{p}\,\in\,\mathbb{R}^n \;\middle|\; \chi^2_1 \le \chi^2(\vec{p}) < \chi^2_2\right\}} \mathrm{d}^n p \;\; P_{\vec{p}}(\vec{p}) \;\stackrel{!}{=}\; \int_{\chi^2_1}^{\chi^2_2} \mathrm{d}\chi^2 \;\; P_{\chi^2;\,\nu}\left(\chi^2\right) \tag{1.72}$$

For infinitesimal $\left[\chi^2_1,\, \chi^2_2\right] = \left[\chi^2(\vec{p}_0),\, \chi^2(\vec{p}_0)+\mathrm{d}\chi^2\right]$, the left-hand side of Eq. (1.72) becomes $P_{\vec{p}}(\vec{p}_0)$ times the parameter space volume according to the second requirement, and thus:

$$P_{\vec{p}}(\vec{p}_0) \;=\; \frac{P_{\chi^2;\,\nu}\left(\,\chi^2(\vec{p}_0)\,\right) \;\; \mathrm{d}\chi^2}{\iiint\limits_{\left\{\vec{p}\,\in\,\mathbb{R}^n \;\middle|\; \chi^2(\vec{p}_0) \le \chi^2(\vec{p}) < \chi^2(\vec{p}_0)+\mathrm{d}\chi^2\right\}} \mathrm{d}^n p} \;=\; \frac{P_{\chi^2;\,\nu}\left(\,\chi^2(\vec{p}_0)\,\right)}{\oiint\limits_{\left\{\vec{p}\,\in\,\mathbb{R}^n \;\middle|\; \chi^2(\vec{p}) = \chi^2(\vec{p}_0)\right\}} \mathrm{d}^{n-1} p \;\; \left|\vec{\nabla}\chi^2(\vec{p})\right|^{-1}} \tag{1.73}$$

This definition involving parameter space volumina is, however, not invariant under non-linear transformations of the parameters $\vec{p}$. Not to mention the possible inconveniences with a numerical implementation of Eq. (1.73), the probability distribution of a derived parameter $f(\vec{p})$ according to Eq. (1.71) is therefore not even uniquely defined by the data.

Fluxes. Fortunately, the flux of a model (component) *can* be implemented as direct fit parameter of a convolution model that renormalizes the convolved spectral component to the flux demanded by this parameter. Such convolution models – like XSPEC's `cflux` for the energy flux, or the `enflux` (`phflux`) model for the energy (photon) flux developed by M. Böck et al.[30] – provide therefore the only statistically justified way to infer the flux and its confidence interval that is compatible with the data.

Chandra ACIS Grating Light Curves

As the chips of *Chandra*'s ACIS detector transmit their data independently of each other, the good time intervals (GTIs) of the active CCDs may differ from each other when frames are

[29] The "flood" algorithm is applied when `conf_map_counts` (or `conf_map_flux`) is called with the `flood` qualifier. In order to apply step 2', a $\Delta\chi^2$-threshold value can be passed as *value* of the `flood` qualifier.

[30] See `http://www.sternwarte.uni-erlangen.de/git.public/?p=isisscripts;a=commit;h=0b7e15d8a14ef4`.

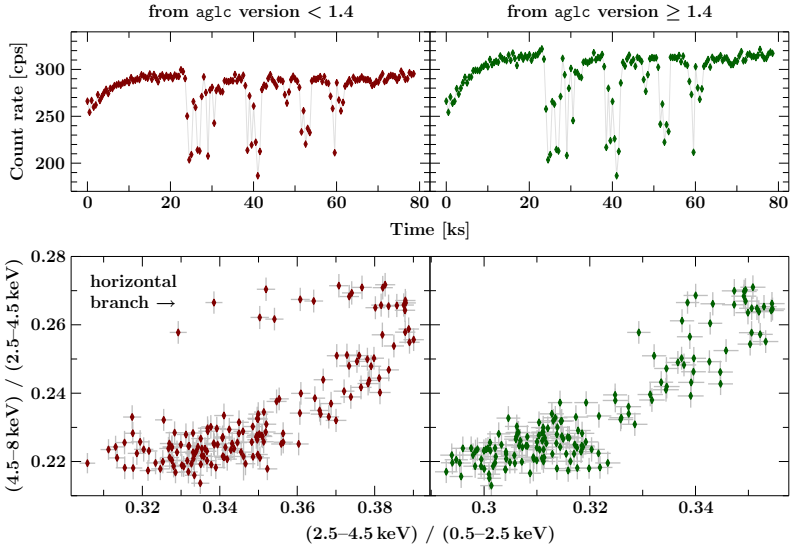

Figure 1.20: Comparison of light curves (upper panel) and color-color diagrams (lower panel) of Cyg X-2 from *Chandra* ObsID 8170 at a time resolution of 500 s (Schulz et al., 2009, fig. 1), computed with `aglc` – according to Eq. (1.75) on the left, and according to Eq. (1.74) on the right. The extension of the horizontal branch is changed by the correction for frame losses.

lost, e.g., because of telemetry saturation. The default tool `dmextract`[31] from the *Chandra* Interactive Analysis of Observations software (CIAO; Fruscione et al., 2006) for light curve extraction, however, considers only the first GTI and may therefore generate incorrect results.[32] Since the dispersed HETG spectra usually extend over all chips, this caveat is relevant for light curves from every observation with frame dropouts. Their spectra, on the other hand, are supposedly handled correctly, since the individual CCDs' exposures are taken into account by the `mkgarf` tool that creates the grating ARF, i.e., $A(E)$ in Eq. (1.64). $A(E)$ should therefore contain a factor for the exposure relative to the *effective* exposure t_{exp} in Eq. (1.64).

ACIS grating light curves can be extracted with ISIS using the `aglc` functions provided by D.P. Huenemoerder.[33] During the course of this work, some major updates were suggested.

Calculation of count rates. Not all parts of the spectrum have necessarily the same exposure. The exposure T_i depends mostly on the CCD i. A much more sophisticated treatment would have to account for a continuously wavelength-dependent exposure, since the dither of the spacecraft moves chip gaps and bad pixels back and forth with time, and small wavelength regions close to chip edges may even appear – subsequently – on two neighbouring CCDs. As light curves are usually uncalibrated count rates, the effect of dither is only a minor one. In a first approximation, the count rate $r(t)$ in a given wavelength interval $[\lambda_1, \lambda_2]$ can therefore be decomposed in a sum over the contributions from the all CCDs. These rates are then calculated from the number $C_i(t)$ of events with $\lambda \in [\lambda_1, \lambda_2]$ on CCD i, and the exposures T_i:

$$r(t) \;=\; \sum_i r_i \;=\; \sum_i \frac{C_i(t)}{T_i} \tag{1.74}$$

In versions of `aglc` prior to 1.4, r was computed from the total counts and an average CCD exposure, which introduces an incorrect weightening that depends on the spectral shape:

$$r(t) \quad \overset{\text{in general}}{\neq} \quad \frac{\sum_i C_i(t)}{\sum_i T_i / n} \tag{1.75}$$

Colors, i.e, hardness ratios between different energy bands, are often more significantly affected than count rates themselves, see, e.g., Fig. 1.20.

[31] See `http://cxc.harvard.edu/ciao/ahelp/dmextract.html`.
[32] See also `http://cxc.harvard.edu/ciao/why/lightcurve.html`.
[33] See `http://space.mit.edu/cxc/analysis/aglc/`.

Times. Each CCD frame, and thus also every event, is associated with an 'exposure number' (`expno`), an integer frame counter. The exposures T_i are determined from the number of unique `expno`s for CCD i in the *exposure statistics file* `acis*_stat1.fits`,[34] and `aglc` also constructs $C_i(t)$ as a histogram of the `expno`s of the events with $\lambda \in [\lambda_1, \lambda_2]$, which is only at the end converted to actual times. The time difference between two (real) frames in TE mode is the sum of the static exposure time for a frame (= 3.2 s for a full frame) and the time required to shift the charges over the CCD into the frame store (= 41.04 ms). The time between two virtual frames in CC mode is 512×2.85 ms. Versions of aglc up to 1.5.2 employed a wrong time conversion factor of 510×2.85 ms in CC mode. (The factor was probably confused due to the fact that only 510 rows of data can be obtained because of the grading in 3×3 pixel islands.) The resulting `aglc` light curves from CC mode data were therefore too short by 0.4 %. Furthermore, the time corresponding to `expno` $= 0$ was misidentified with with the time of the first event, resulting in an additional time shift. These issues have been adressed with `aglc` v. 1.5.3 (priv. comm., submitted to D.P. Huenemoerder).

A simple model for pileup in first order *Chandra* HETG spectra

In addition to the potential telemetry saturation, the spectra of bright sources may be distorted by photon pileup. For the first-order spectra, pileup causes a pure reduction of count rate: a multiple event, i.e., the detection of more than one photon in a CCD pixel during one readout time, which cannot be separated, is either rejected by grade selection during the data processing, or migrates to a higher-order spectrum. The Poissonian probability for single events (i.e., $P_n = \Lambda^n \cdot \mathrm{e}^{-\Lambda}/n!$ for n=1) in an event-detection cell i with a size of 3×3 pixels (see, e.g., Davis, 2002, 2003; CXC, 2010a) is:

$$P_1(i) \;=\; \Lambda(i) \cdot \exp\big(-\Lambda(i)\big) \;, \tag{1.76}$$

where the expected number of events, $\Lambda(i) = \beta_0 \cdot S_{\mathrm{tot}}(i)$, is given by the total spectral count rate, $S_{\mathrm{tot}}(i)$, at this position (in units of counts per Å and s), and where the constant β_0 is

$$\beta_0 \;=\; 3\,\Delta\lambda \cdot t_{\mathrm{frame}} \;, \tag{1.77}$$

with the resolution of the spectrometer $\Delta\lambda$ of Eq. (1.63), and the frame time t_{frame}. Pileup in the first-order spectra can be modelled with the nonlinear convolution model `simple_gpile(2)` in ISIS, which exponentially reduces the predicted count rate $S(\lambda)$ according to Eq. (1.76):

$$S'(\lambda) \;=\; S(\lambda) \cdot \exp\big(-\beta \cdot S_{\mathrm{tot}}(\lambda)\big) \tag{1.78}$$

The scale $\beta \approx \beta_0$ can be left as fit parameter, and $S_{\mathrm{tot}}(\lambda)$ also takes the photons into account which are dispersed in a higher order $m \leq 3$. The count rates are estimated from the corresponding effective areas A_m and the assumed photon flux f_λ, in an approximation of Eq. (1.64):

$$S_{\mathrm{tot}}(\lambda) \;=\; \textstyle\sum_{m=1}^{3} A_m(\lambda/m) \cdot f_\lambda(\lambda/m) \tag{1.79}$$

`simple_gpile2` (Hanke, 2007; Hanke et al., 2009, sect. 2.2) is based on the `simple_gpile` model (CXC, 2005; Nowak et al., 2008, appendix A), which parameterizes the strength of pileup by the (maximum) pileup fraction $p = 1 - \exp(-\beta \cdot \max\{S_{\mathrm{tot}}\})$. Using the parameter β of `simple_gpile2` avoids to have a nonlocal model which depends on the flux at the position of the highest pileup The `simple_gpile2` model has been included in the official '*Chandra* ABC Guide to Pileup' (CXC, 2010a, appendix C). Its operation is demonstrated in fig. 2 of Hanke et al. (2009). Figure 2.50 on page 98 shows an application to a spectrum that is extremely piled up, where `simple_gpile2` still allows to roughly model the spectral shape.

[34] The statement in the CIAO 4.3 'Data Products Guide': *"Most users will never need this file in their analysis"* (`http://cxc.harvard.edu/ciao4.3/data_products_guide/`) is thus wrong in view of (potential) frame losses.

Chapter II

Analysis of Cygnus X-1

Large data sets with good S/N are required *to probe the environment of accreting compact objects* in high-mass X-ray binary systems. Cygnus X-1, the persistently bright black hole XRB, is the ideal target for such an endeavour. Although it has been analyzed for more than 40 years, *"we know very little about some of the most important parameters of this X-ray system, which is one of the best-studied and a prototype for a whole class of objects, and do not understand the behavior of matter leading to accretion"* (Karitskaya et al., 2008). The major part of this thesis is therefore about the analysis of X-ray observations of Cyg X-1, which will be presented in this chapter.

After an introduction of the system in Sect. 2.1, the large database of *RXTE* observations will be investigated in Sects. 2.2 and 2.3. These instruments clearly reveal the orbital modulation of the wind absorption, but their low spectral resolution does not allow to infer the detailed physical properties of the absorber. Dedicated observations with *Chandra* and *XMM-Newton* will therefore be discussed in Sects. 2.4 and 2.5. Section 2.6 finally describes a multi-satellite campaign, joining the forces of *all* X-ray missions available in 2008 April.

2.1 The System

Discovery and identification

Already indicated by the first extrasolar X-ray observations (Giacconi et al., 1962; Gursky et al., 1963), Cyg X-1 was discovered in a rocket flight experiment on 1964 June 16, carrying Geiger counters with a collimator-limited field of view of 8.4° and an effective area of 906 cm^2 in the 1–15 Å range (Bowyer et al., 1965). This X-ray source was detected with further experiments, too – however, Byram et al. (1966) noted a decrease of the 1–10 keV flux by a factor 4 between 1964 June and 1965 April, and Overbeck & Tananbaum (1968) found an increase of the 20–50 keV flux by a factor $\geq$2 between 1966 September (Overbeck et al., 1967) and 1967 May. The position of Cyg X-1 was successively refined to a precision of 1.5° by Fisher et al. (1966), to 10′ by Giacconi et al. (1967), by Tananbaum et al. (1971) using the first X-ray satellite *Uhuru*, and to 30″ by Rappaport et al. (1971). Nevertheless, only the appearance of a radio source (Braes & Miley, 1971; Hjellming & Wade, 1971), which could be identified with the X-ray source due to its simultaneous state transition (Tananbaum et al., 1972), reduced the uncertainty of the position of Cyg X-1 to $\lesssim$5″ and suggested the 9 mag star HDE 226868 ($\equiv$ V1357 Cyg $\equiv$ AGK2 +35° 1910 $\equiv$ BD +34°3815) to be the optical counterpart of Cyg X-1 (Braes & Miley, 1971; Murdin & Webster, 1971). Further refinements of the radio location allowed to exclude another potential counterpart (Wade & Hjellming, 1972). HDE 226868 was subsequently discovered to be a spectroscopic binary with a period of 5.6 d (Webster & Murdin, 1972; Bolton, 1972a,b), which also shows orbital photometric variations due to its ellipsoidal deformation (Walker, 1972; Lyutyi et al., 1973). The orbital elements implied immediately that the dynamically constrained mass of the *unseen* secondary exceeds the maximal mass of neutron stars, and that the compact object in this high-mass X-ray *binary* system must therefore be a black hole – unless Cyg X-1 is a triple system with, e.g., a neutron star and a main sequence star orbiting around HDE 226868 (Fabian et al., 1974; Bahcall et al., 1974). The latter model, as well as other alternatives involving a subluminous stellar secondary (e.g., Bahcall et al., 1973; Avni & Bahcall, 1975), are ruled out by the non-detection of a companion with $\geq$2 % of HDE 226868's luminosity (Shafter et al., 1980). Further evidences (e.g., reviewed by Oda, 1977; Cowley, 1992) lead to a growing accpetance that Cyg X-1 contains a black hole.[1]

2.1.1 Parameters of HDE 226868 / Cyg X-1

Orbit parameters

After the discovery of the radial velocity variability of HDE 226868 (Webster & Murdin, 1972; Bolton, 1972a,b), spectroscopic and photometric follow-up observations allowed to improve the accuracy of the orbital period (e.g., Bolton, 1975; Guinan et al., 1979; Gies & Bolton, 1982; Sowers et al., 1998). The claim of a period change by Ninkov et al. (1987b) could not be confirmed. LaSala et al. (1998) suggest that the supposed much larger value of 5.60172(3) d is just *a typographical error* and should actually read 5.6002 d. The measurement

$$P_{\rm orb} \;=\; 5.599829(16)\,{\rm d} \tag{2.1}$$

of Brocksopp et al. (1999) is also used for the most recent ephemerides, which define an epoch of orbital phase $\phi_{\rm orb}$=0, i.e., superior conjunction of the black hole, at heliocentric dates of

$$T_0 \;=\; {\rm MJD}\;51\,729.949(8) \;\equiv\; \text{2000-07-04, 22:58} \pm 11\,{\rm min} \quad \text{(Gies et al., 2003)} \tag{2.2}$$

$$T_0 \;=\; {\rm MJD}\;52\,872.288(9) \;\equiv\; \text{2003-08-21, 06:54} \pm 13\,{\rm min} \quad \text{(Gies et al., 2008)} \tag{2.3}$$

An eccentric orbit, with an eccentricity up to $e = 0.09 \pm 0.02$ (Bolton, 1972b), was suggested from the first observations (also by Bolton, 1975; Hutchings, 1978, though with lower e values), but could not be confirmed by later studies finding circular orbits. Gies & Bolton (1982) admit that their "*earlier result was an artifact of poor phase distribution of the data and inadequate analysis*". The radial velocity semi-amplitude of HDE 226868,

$$K_\star \;=\; \frac{2\pi\, a_\star \sin i}{P_{\rm orb}} \;=\; 75.6(7)\,{\rm km\,s^{-1}} \qquad \text{(Gies et al., 2003)}\quad , \tag{2.4}$$

determines, with the period from Eq. (2.1), the projected radius $a_\star \sin i$ of HDE 226868's orbit:

$$a_\star \sin i \;=\; \frac{K_\star\, P_{\rm orb}}{2\pi} \;=\; 5.82(5)\times 10^9\,{\rm m} \;=\; 8.36(8)\,R_\odot \tag{2.5}$$

The values given by Eqs. (2.4) and (2.5) are in good agreement with the measurements by LaSala et al. (1998) and Brocksopp et al. (1999), but larger than the value $K_\star = 73.0(7)\,{\rm km\,s^{-1}}$ obtained by Gies et al. (2008), which in turn is closer to the lower values derived by, e.g., Bolton (1975) and Sowers et al. (1998). The systematic uncertainty is therefore larger than the error bars quoted in Eqs. (2.4) and (2.5) – probably due to the fact that the radial velocity is not necessarily the same for different photospheric absorption lines (Canalizo et al., 1995).

The inclination i of the system is, however, not very accurately known. Davis & Hartmann (1983) find $i = 36^\circ - 67^\circ$ from the change of the C IV UV line between the conjunction phases. Gies & Bolton (1986a) infer $i = 28^\circ - 38^\circ$ from the photometric modulation and the rotational broadening of photospheric absorption lines. Dolan & Tapia (1989) obtain $i = 62^\circ$ (with a 90 % confidence interval of $25^\circ - 67^\circ$) from the polarization of the R, G, B fluxes (see also Dolan, 1992). Wen et al. (1999) conclude $i = 10^\circ - 40^\circ$ from the orbital modulation of the X-ray flux. Gies et al. (2003) get $i = 23^\circ - 37^\circ$ from the velocity components of H α P Cygni line profile. Abubekerov et al. (2004) derive $i = 31^\circ - 44^\circ$ from the radial velocity curve of a Roche model. Given all of these estimates, the following often adopted *assumption* seems to be well-justified:

$$i \;=\; 35^\circ \tag{2.6}$$

[1] The famous scientific wager from 1974 (*"Whereas Stephen Hawking has such a large investment in General Relativity and Black Holes and desires an insurance policy, and wheras Kip Thorne likes to live dangerously without an insurance policy, Therefore be it resolved that Stephen Hawking bets one year's subscription to 'Penthouse' as against Kip Thorne's wages of a 4-year subscription to 'Private Eye', that Cygnus X-1 does not contain a black hole of mass above Chandrasekhar limit."*) was conceded by Stephen Hawking in 1990.

Stellar parameters

In a detailed NLTE analysis (i.e., not assuming local thermodynamic equilibrium) of the optical spectrum with spherical non-hydrostatic models (i.e., also including the stellar wind; however, without taking metal line blanketing into account), Herrero et al. (1995) derive a temperature of 32 000 K, a stellar radius of 17 $R_\odot$ (Eq. 2.11), a luminosity of $10^{5.4} L_\odot \approx 10^{39}\,\mathrm{erg\,s^{-1}}$, and a mass loss

$$\dot{M}_\star \;=\; 3{\times}10^{-6} M_\odot\,\mathrm{yr^{-1}} \;=\; 1.9{\times}10^{17}\,\mathrm{kg\,s^{-1}} \;=\; 1.1{\times}10^{44}\,m_\mathrm{p}\,\mathrm{s^{-1}} \tag{2.7}$$

(which is similar to $\dot{M}_\star = 3.5{\times}10^{-6}\,M_\odot\,\mathrm{yr^{-1}}$ obtained from IR photometry; Persi et al., 1980) at a terminal wind velocity

$$v_\infty \;=\; 2\,100\,\mathrm{km\,s^{-1}} \tag{2.8}$$

– close to $2\,300\,\mathrm{km\,s^{-1}}$ obtained from *IUE* spectra in the hard state (Davis & Hartmann, 1983), whereas Vrtilek et al. (2008) obtain only $1\,420\,\mathrm{km\,s^{-1}}$ from *HST* STIS spectra in the soft state. *Assuming* synchronous rotation, and $i = 35°$, Herrero et al. (1995) obtain the following masses:

$$q \;=\; \frac{M_\mathrm{bh} \;=\; 10.1\,M_\odot}{M_\star \;=\; 17.8\,M_\odot} \;=\; 0.567 \tag{2.9}$$

Caballero-Nieves et al. (2009) present an NLTE analysis of HDE 226868's UV spectrum with line-banketed, but plane-parallel models from the TLUSTY grid (not including the stellar wind), giving a lower temperature of $(28\,000 \pm 2\,500)$ K and the masses $(17{-}31)\,M_\odot$ and $(8{-}16)\,M_\odot$ for HDE 226868 and the black hole, respectively. The lower mass limit is in agreement with the black hole mass $(8.7 \pm 0.8)\,M_\odot$ derived from X-ray spectral-timing relations (Shaposhnikov & Titarchuk, 2007). Caballero-Nieves et al. (2009, table 5) also discuss other mass estimates available from the literature, including the one of Ziółkowski (2005), who derives a stellar mass $(40 \pm 5)\,M_\odot$ from the evolutionary state of HDE 226868, which corresponds to a black hole mass of $(20 \pm 5)\,M_\odot$. The values quoted in Eq. (2.9) can therefore only be considered as a working hypothesis. Various other numbers, largely obtained with different methods, can be found in the literature. For example, Gies et al. (2003) claim $q = 0.36{\pm}0.05$ from the velocity of an H α emission component *assumed* to be located near the black hole.

The mass ratio allows to gauge the binary separation a. Equations (2.5), (2.6), and (2.9) give:

$$a \;=\; a_\star + a_\mathrm{bh} \;=\; a_\star \cdot \left(1 + \frac{M_\star}{M_\mathrm{bh}}\right) \;=\; 2.8{\times}10^{10}\,\mathrm{m} \;=\; 40.3\,R_\odot \tag{2.10}$$

Equation (2.10) is again only a working hypothesis, quoted without error bars, as not all of the uncertainties inherent to the values of Eqs. (2.5), (2.6) and (2.9) are mutually independent. Using Eq. (2.10), the effective radius determined by Herrero et al. (1995) measures 42 % of a:

$$R_\star \;=\; 17\,R_\odot \;=\; 1.2{\times}10^{10}\,\mathrm{m} \;=\; 0.42 \cdot a \tag{2.11}$$

which corresponds – according to Table 1.1 on page 5 – to a volume filling factor $v_\mathrm{rel} \gtrsim 90\,\%$ for a Roche lobe with q=0.567 from Eq. (2.9). This is in very good agreement with the linear fill-out factor[2] ρ=0.97 quoted by Gies et al. (2003, fig. 8).

The (focused) wind

Walborn (1973) classified HDE 226868 as O9.7 Iab (p-var) star, as it shows a peculiar and variable emission line at λ=4 686 Å (Brucato & Kristian, 1972; Bolton, 1972b). This line corresponds to the Paschen α transition between the n=4 and n=3 states of singly ionized helium.

[2] *"ρ is the fill-out factor, the ratio of the volume radius (i.e., the radius of a sphere of equivalent volume) of the visible star to the volume radius of its Roche lobe"* (Gies & Bolton, 1986a)

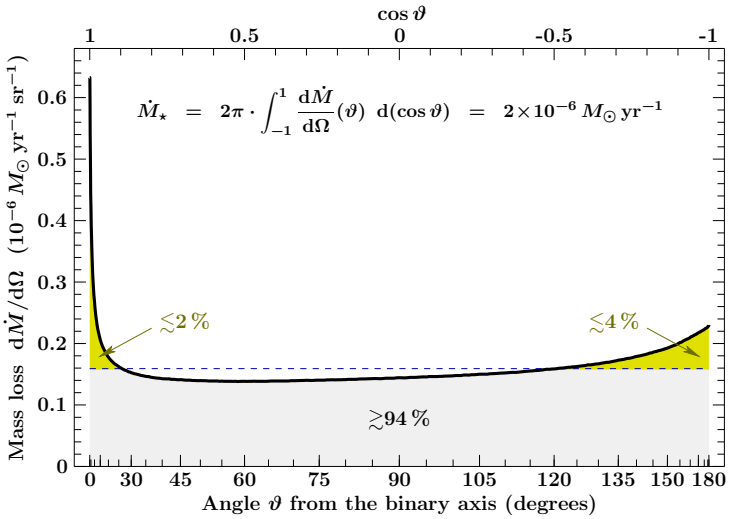

Figure 2.1: Focused wind model of Friend & Castor (1982, fig. 4) for HDE 226868's mass loss rate per solid angle $d\Omega = \sin\vartheta\, d\vartheta\, d\phi$. The total mass loss rate of this model is only $2\times10^{-6}\, M_\odot\,\mathrm{yr}^{-1}$. While $d\dot{M}/d\Omega\,(\vartheta=0)$ is 4 times the average rate (indicated by the dashed line), the excess at $\vartheta\leq27°$ just amounts to 2 % of the total mass loss. The backside excess at $\vartheta\geq120°$ is twice as much.

As its radial velocity curve lags the motion of the primary, the He II λ=4 686 Å emission has been identified with an enhanced flow of matter from the supergiant to the black hole (Hutchings et al., 1973; Bisiacchi et al., 1974; Bolton, 1975; Aab, 1983; Gies & Bolton, 1986a,b; Ninkov et al., 1987a; Karitskaya et al., 2005). Such a *focused wind* is expected for a star in a binary system that almost fills its crictical Roche lobe (Friend & Castor, 1982) and therefore faces a significantly non-spherical potential (Sect. 1.1.1). The angular dependence of HDE 226868's mass loss rate as calculated by Friend & Castor (1982, fig. 4) is displayed in Fig. 2.1. It is supported by the results of Canalizo et al. (1995), who assume that the relation between the radial velocity curve of several lines and their excitation potentials measures the mass loss.

The H α line (at λ=6 563 Å) shows a much more complex variability than He II λ=4 686 Å. Its profile consists of a P Cygni component from the supergiant, and an emission component from the focused wind (Brucato & Zappala, 1974; Hutchings et al., 1974, 1979; Sowers et al., 1998; Hadrava, 2007). As these components follow different radial velocity curves, their superposed profile varies with orbital phase. Furthermore, these components vary in strength. Apart from the orbital variability (because of photoionization; Tarasov et al., 2003, see below) and short-term variability (e.g., because of wind clumping), the strength of the H α emission is loosely anti-correlated with the soft X-ray flux of Cyg X-1 (Voloshina et al., 1997; Tarasov et al., 2003; Gies et al., 2003, 2008; Yan et al., 2008). That is, the H α emission is strongest in the low/hard state; and, vice versa, flares or soft states occur only when the H α emission is weak. Yan et al. (2008) disentangle the H α complex into a P Cygni profile and an emission component, and find that the variation in strength between the soft state in 2004 and the hard state in 2006 is largely due to the focused wind's emission component. Gies et al. (2003), on the other hand, find the strength of the emission to be correlated with that of the P Cygni component. Three mechanisms for the anti-correlation are discussed (Gies et al., 2003; Tarasov et al., 2003):

1. *The H α emissivity is decreased by an enhanced soft X-ray flux due to photoionization.* The detection of a significant drop in H α occurring simultaneously to a short X-ray flare on 1999-09-05 demonstrates that this effect is in operation, as a delay on the order of the system's wind-crossing time ($\sim$10 h) can be excluded (Gies et al., 2003).

As the anti-correlation is not strong enough, and as variability is also seen in the X-ray shadowed part, photoionization cannot be the dominant cause. A second one is therefore required:

2. The H α emission is an indicator for the wind mass loss (Puls et al., 1996).
   2a *The reduced X-ray flux when H α is strong is due to absorption.* This effect is insufficient to explain the anti-correlation, and what is more, hard and soft state spectra differ also at hard X-rays that are not affected by absorption.

2b *A reduced mass-loss triggers an X-ray flare through the following mechanism:* A *lower* wind density and therefore *higher* degree of photoionization by the X-ray source *reduces* the wind acceleration. The *lower* velocity v causes a *higher* accretion rate ($\propto \dot{M}_\star / v^4$; Bondi & Hoyle, 1944), despite the lower wind mass loss $\dot{M}_\star$. This effect is suggested by the finding of a reduction of Hα emission after 1999 August *prior* to a failed transition from the hard state to the soft state in 1999 October (Tarasov et al., 2003).

Vrtilek et al. (2008) point out, however, that hard and soft states do not necessarily differ strongly in mass accretion rate, as the bolometric X-ray luminosity remains roughly constant.

The photoionization and velocity of the wind can be probed with UV observations of line profiles, which usually show wide P Cygni profiles because of the wind acceleration (Sect. 1.1.2). In the presence of the X-ray source, these lines are strongly suppressed at $\phi_{\rm orb} \approx 0.5$ when the line of sight to the supergiant passes through the photoionized region (Hatchett & McCray, 1977). The ions that would give rise to a large opacity in the UV band are superionized, and the wind cannot reach a high velocity. So far, the only measurements in the hard state are from the *International Ultraviolet Explorer* (*IUE*, 1978–1996). These are mostly low-dispersion spectra (Treves et al., 1980), as HDE 226868 was not bright enough to produce a good S/N in high-resolution spectra (Davis & Hartmann, 1983). High-dispersion UV spectra during the soft state were obtained with *HST* STIS (Vrtilek et al., 2008; Gies et al., 2008; Caballero-Nieves et al., 2009). Whereas Davis & Hartmann (1983) derive a terminal velocity of $2\,300\,\mathrm{km\,s^{-1}}$ on the shadowed side and only $\sim 1\,500\,\mathrm{km\,s^{-1}}$ on the hemisphere facing the X-ray source from the hard state *IUE* data, Gies et al. (2008) are able to model their soft state *HST* spectra assuming that the wind of HDE 226868 is fully restricted to the *shadow wind* from the shielded side of the stellar surface (Blondin, 1994). Based on a comparison with low-dispersion *IUE* spectra, Gies et al. (2008) suggest that the orbital variation of the line strength is the same across the states, and therefore conclude that the radiatively driven wind is *"probably always weak or absent"* on the side directed toward the black hole. Nevertheless, the claim that there is no spherical wind at all seems not justified in the hard state, in view of the orbital modulation of the soft X-ray flux due to absorption in the stellar wind, probably not related to the focused wind (according to geometrical considerations discussed in the next section).

The detailed dynamics of the stellar wind and its interaction with the X-ray source are thus still far from being resolved and understood in a self-consistent picture. The hard state is lacking UV spectra comparable to the *HST* STIS data from the soft state, which could firmly constrain the wind structure. Given all the results reviewed above, the latter is clearly sensitive to the X-ray state, if not even the physical cause of hard and soft states in the HMXB Cyg X-1.

* * *

A very simple radial model for the stellar wind in the hard state will be shown in the next section. The situation may be much more complicated if – as suggested by Gies et al. (2008) – non-radial effects due to the Coriolis force on the shadow wind become important, which may lead to a complex dynamics (e.g., Blondin et al., 1990, 1991; Stevens, 1991; Blondin, 1994).

2.1.2 Modelling the Wind Density Field

Before attempts are made to model the wind density for the Cyg X-1 system, it is illustrative to investigate which parts of the wind can in general be probed by observations. Using absorption lines in the spectrum of a point source confines the absorber to the line of sight (LoS), which moves along a cone with a half opening angle given by the inclination i during one orbit of the binary system. Although the following considerations aim to model the Cyg X-1 system, they are largely general and can be transferred to other systems as well.

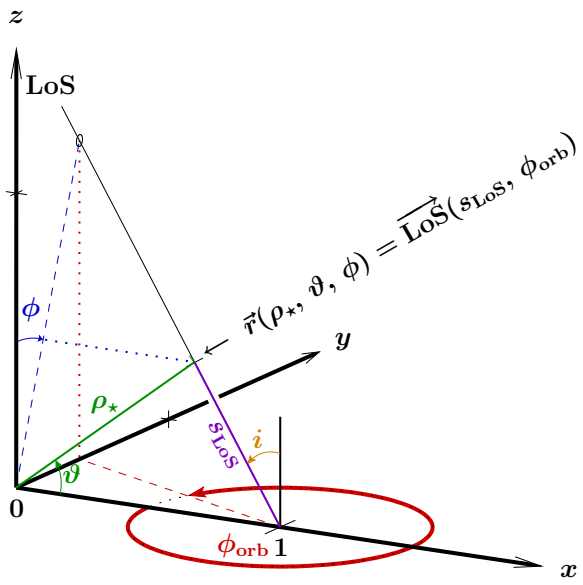

Figure 2.2: Coordinate system definitions: Parameterizing the line of sight in Eq. (2.12), ϕ_{orb} is the orbital phase, the inclination i is the angle between the line of sight and the normal vector to the orbital (x-y) plane, and s_{LoS} is the distance from the secondary along the line of sight. For the spherical coordinate system of Eq. (2.13), $\rho_\star$ is the distance from the primary, ϑ is the angle from the binary axis, and ϕ is the azimuthal angle in the z-y plane, which is constant for an entire line of sight at given ϕ_{orb}, see Eq. (2.14).

Parameterizing the line of sight

Following the convention of Eq. (1.3) for the normalized corotating system with the primary at $(0,\, 0,\, 0)$, the line of sight toward the secondary at $(1,\, 0,\, 0)$ can be parameterized by (Fig. 2.2):

$$\overrightarrow{\mathrm{LoS}}(s_{\mathrm{LoS}},\, \phi_{\mathrm{orb}}) \;=\; \begin{pmatrix} 1 \\ 0 \\ 0 \end{pmatrix} + s_{\mathrm{LoS}} \cdot \begin{pmatrix} -\begin{pmatrix} \cos(2\pi\phi_{\mathrm{orb}}) \\ \sin(2\pi\phi_{\mathrm{orb}}) \end{pmatrix} \cdot \sin i \\ \cos i \end{pmatrix} \tag{2.12}$$

If the stellar wind is radial – admittedly a strong assumption, but adopted in most parts of this section in order to simplify the full 3d hydrodynamical problem – its structure is conveniently expressed in a spherical coordinate system centered on the primary (see also Fig. 2.2):

$$\vec{r}(\rho_\star,\, \vartheta,\, \phi) \;=\; \rho_\star \cdot \begin{pmatrix} \cos\vartheta \\ \sin\vartheta \cdot \begin{pmatrix} -\sin\phi \\ \cos\phi \end{pmatrix} \end{pmatrix} \tag{2.13}$$

The azimuthal angle ϕ is constant for the entire line of sight at any given orbital phase ϕ_{orb}:

$$\sin\phi \;\equiv\; \frac{\sin(2\pi\phi_{\mathrm{orb}})\,\sin i}{\sqrt{1-c^2}} \qquad \text{and} \qquad \cos\phi \;\equiv\; \frac{\cos i}{\sqrt{1-c^2}} \tag{2.14}$$

Here and in the following, c denotes the following expression depending on ϕ_{orb} and i:

$$c \;:=\; \cos(2\pi\phi_{\mathrm{orb}})\,\sin i \tag{2.15}$$

If the system has azimuthal symmetry,[3] every line of sight can be rotated along the x-axis of symmetry in order to obtain an equivalent line in, e.g., the x-z plane:

$$\overrightarrow{\mathrm{LoS}}'(s_{\mathrm{LoS}},\, \phi_{\mathrm{orb}}) \;=\; \begin{pmatrix} 1 & & \\ & \cos\phi & \sin\phi \\ & -\sin\phi & \cos\phi \end{pmatrix} \overrightarrow{\mathrm{LoS}}(s_{\mathrm{LoS}},\, \phi_{\mathrm{orb}}) \;=\; \begin{pmatrix} 1 \\ 0 \\ 0 \end{pmatrix} + s_{\mathrm{LoS}} \cdot \begin{pmatrix} -c \\ 0 \\ \sqrt{1-c^2} \end{pmatrix} \tag{2.16}$$

[3] In principle, the rotation of the binary system in the x-y plane (and thus the whole Roche geometry) does already break the ϕ-invariance. The extensions of the Roche lobe in y- and z-directions do, however, not differ strongly (Table 1.1), and even less in the observable directions at low inclination. And similarly for the dynamics: if the radial wind is much faster than the orbital velocity, azimuthal symmetry may still be a good approximation.

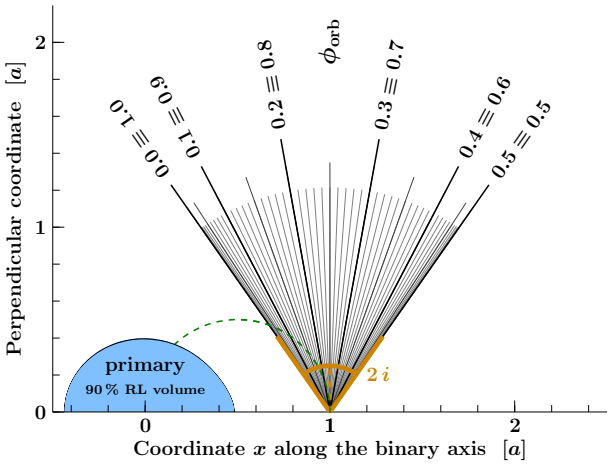

Figure 2.3: Representation of all lines of sight toward the secondary at (1, 0, 0) for a system with azimuthal symmetry, when those can equivalently be rotated into the same plane. The illustration is for an inclination i=35° assumed for the Cyg X-1 system according to Eq. (2.6). The primary is depicted as filling 90 % of the Roche lobe volume for a mass ratio q=0.567 (Eq. 2.9). The green dashed curve traces Thales' circle from x=0 to x=1.

Such a representation allows to visualize all lines of sight in a single plane, as shown in Fig. 2.3, which contains the primary and all radial lines to each location on every line of sight as well. It is notable that the focused wind at $\vartheta \lesssim 20°$ hardly intersects with the lines of sight at $i = 35°$.

In the general case without symmetry regarding ϕ, it is not possible to include the entire cone $\overrightarrow{\text{LoS}}(s_{\text{LoS}},\ \phi_{\text{orb}})$ together with the primary and all radial wind trajectories in a two-dimensional representation. Instead, every line of sight at a given orbital phase ϕ_{orb} defines its own plane (strictly speaking, this plane is identical to the one defined by the orbital phase $0.5 - \phi_{\text{orb}}$), according to Eqs. (2.13) and (2.14). A special transformation of this plane to a generalized polar coordinate system, which is locally Euclidean on the line of sight and therefore particularly suited to measure lengths and angles, is derived in Appendix A on page 147.

Velocity profiles

Section 2.1.1 has illustrated that the velocity profile of the wind in the HDE 226868/Cyg X-1 system is not well known, in particular in the photoionization region between the supergiant and the black hole. Nevertheless, the semi-empirical velocity law of Eq. (1.14) or (1.15) is often used as a starting point to model the velocity – and thus, according to Eq. (1.19), also density – profile. Figure 2.4 shows their functional form for different values of β and $v_0 = 0.01 v_\infty$.

If a spherically symmetric radial wind is assumed, the adoption of a velocity law $v(r)$ defines the space velocity $\vec{v}$ at every location $\vec{r}$. Through the continuity equation of Eq. (1.19), the velocity field defines the wind's density structure, which will be adressed at the end of this section. Another observational consequence is the Doppler shift of wind absorption lines, which reveals only the projection $v_{\parallel}(\vec{r})$ of $\vec{v}(\vec{r})$ against the black hole (Hanke et al., 2008, 2009):

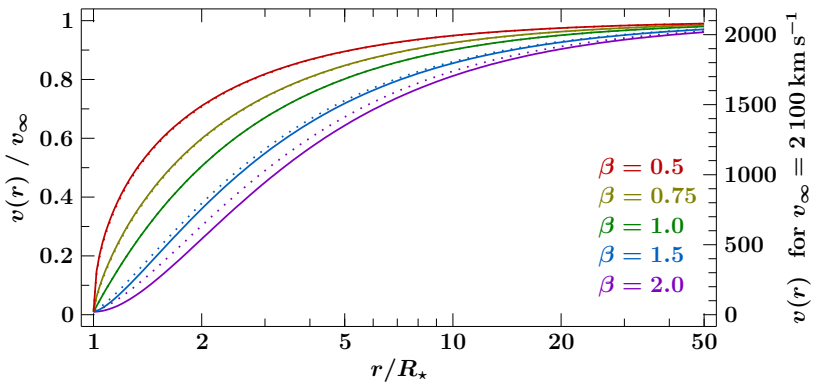

Figure 2.4: Velocity laws of Eq. (1.14) – solid lines, and Eq. (1.15) – dotted lines, for different values of β and $v_0 = 0.01\, v_\infty$. For small β, $r_0 \approx R_\star$ in Eq. (1.15), and both models give very similar wind velocity profiles.

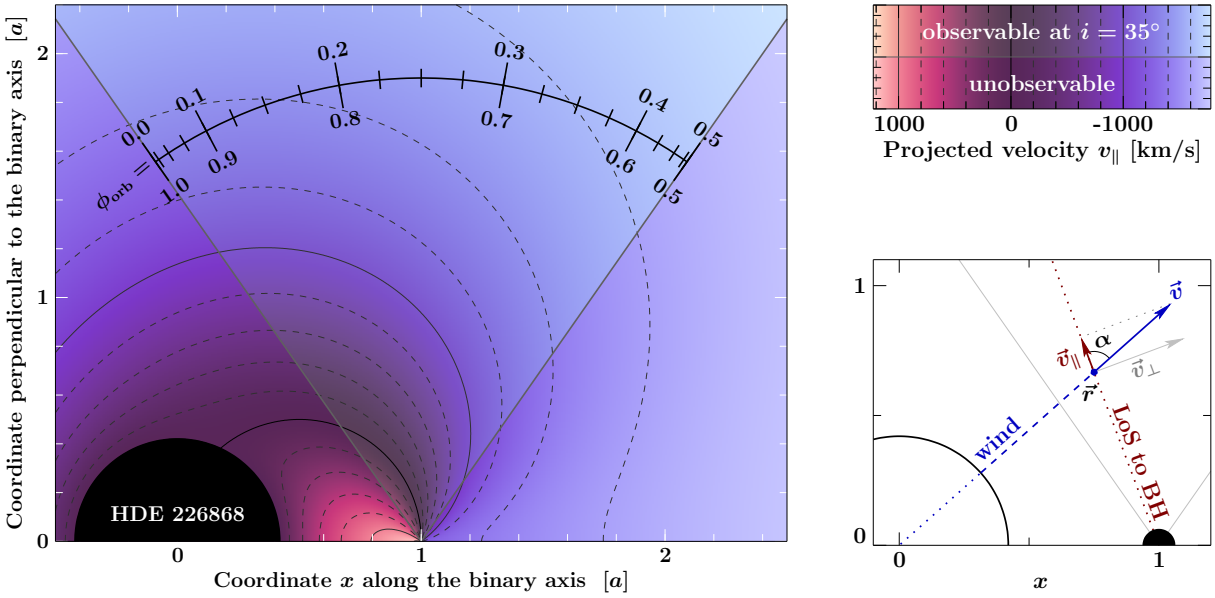

Figure 2.5: Color-coded representation of the projected wind velocity $v_\parallel$ onto the line of sight toward the black hole according to Eq. (2.17); the sketch in the lower right panel illustrates the vector decomposition. Corresponding to $\alpha = 90°$, Thales' circle separates the region of redshifts from the region of blueshifts. The radial wind velocity follows the β-law of Eq. (1.14) with $\beta = 1$, $v_0 = 0.01 v_\infty$, and $v_\infty = 2\,100\,\mathrm{km\,s^{-1}}$ from Eq. (2.8). A spherical star with a radius $R_\star = 0.42\,a$ (Eq. 2.11) is assumed. The gray lines are contours of constant $v_\parallel$ in steps of 200 $\mathrm{km\,s^{-1}}$. The highlighted area with the ϕ_{orb} scale shows the region of all equivalent lines of sight for $i = 35°$, see Fig. 2.3. See text for further details.
(after Hanke et al., 2008, fig. 3; Hanke et al., 2009, fig. 14)

$$v_\parallel(\vec{r}) \quad = \quad \cos\alpha(\vec{r}) \cdot v(\vec{r}) \tag{2.17}$$

where $\alpha(\vec{r})$ is the angle between wind velocity $\vec{v}(\vec{r})$ and the line of sight toward the black hole, see Fig. 2.5. On the circle passing through the center of the star and the black hole, α is 90° by Thales' theorem, and thus $v_\parallel$=0 – independently of the assumed velocity law, as long as the wind flow is radial. The circle separates (possible) absorbing regions of the wind seen at a redshift (inside) from those seen at a blueshift (outside). For a low inclination i=35°, there is only a small region in the vicinity of the secondary – namely for $|\phi_{orb}| < 0.25$ at $0 < s_{LoS} < c$ according to Eqs. (2.15) and (2.16) – which falls into Thales' circle, i.e., where matter in the wind can produce redshifted absorption lines in the secondary's spectrum. Vice versa, absorption lines at $0.25 < \phi_{orb} < 0.75$ that appear redshifted (after correction for the absorber's orbital motion), are incompatible with a radial flow from the primary.

In the focused wind model of Friend & Castor (1982), not only is the mass loss rate a function of the polar angle ϑ (Fig. 2.1), but also the terminal velocity, the β-law index, and likewise – due to the deformation according to the Roche geometry – the stellar radius $R_\star$. Gies & Bolton (1986b, eqs. 1 and 2) investigate a ϑ-dependent β-law for the velocity profile:

$$v(r,\vartheta) \quad = \quad v_\infty(\vartheta) \cdot \left(1 - \frac{R_\star(\vartheta)}{r}\right)^{\beta(\vartheta)} \tag{2.18}$$

Equation (2.18) leads to the following density profile:

$$\rho(r,\vartheta) \quad = \quad \frac{R_\star(\vartheta)^2 \;\cdot\; \rho_0(\vartheta)}{r^2 \cdot [1 - R_\star(\vartheta)/r]^{\beta(\vartheta)}} \tag{2.19}$$

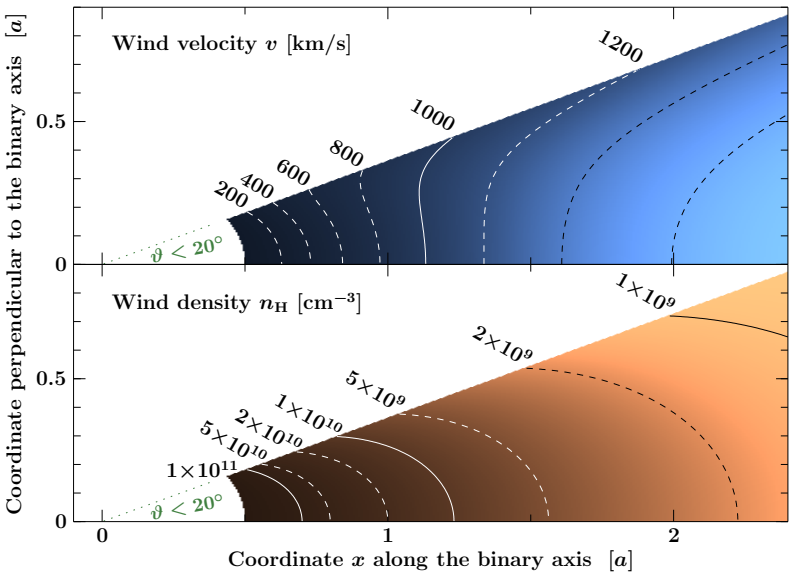

Figure 2.6: Velocity (top) and density (bottom) model for the focused wind at $|\vartheta| < 20°$, parameterized by Gies & Bolton (1986b), see Eqs. (2.18)–(2.20). Close to the black hole, the velocity is $\lesssim 1\,000\,\mathrm{km\,s^{-1}}$, and the density is $n_\mathrm{H} = \mathcal{O}(10^{10}\,\mathrm{cm^{-3}})$.

Only a small part of the line of sight toward the black hole (see Figs. 2.3, 2.5) is at $\vartheta \leq 20°$, in particular at $\phi_\mathrm{orb} \approx 0$.

Gies & Bolton (1986b, eq. 3, table 1) fit the numerical results of Friend & Castor (1982) as:

$$\left.\begin{aligned} R_\star(\vartheta) &= \left[\ 1 \ - \left(\ 1 \ - \tfrac{1.387}{1.496}\ \right)\cdot(\vartheta/20°)^2\right]\cdot 0.5a \\ \beta(\vartheta) &= \left[\ 1.60 \ - \left(\ 1.60 \ - \ 1.05\ \right)\cdot(\vartheta/20°)^2\right] \\ v_\infty(\vartheta) &= \left[2\,540 - \left(2\,540 - 1\,580\right)\cdot(\vartheta/20°)^2\right]\ \mathrm{km\,s^{-1}} \\ \rho_0(\vartheta) &= \left[\ 6.17 \ - \left(\ 6.17 \ - \ 3.72\ \right)\cdot(\vartheta/20°)^2\right]\times10^{14}\,\mathrm{g\,cm^{-3}} \end{aligned}\right\} \quad \text{for} \quad |\vartheta| \leq 20° \ , \tag{2.20}$$

and find that Eq. (2.20) – unlike a less strongly focused wind – can explain the orbital variation of the He II λ=4 686 Å emission line profile from the focused wind in the region $|\vartheta| \leq 20°$. Figure 2.6 illustrates the velocity and density fields resulting from Eqs. (2.18)–(2.20).

Although Eq. (2.20) holds for the focused wind at $|\vartheta| \leq 20°$, the value $\beta(\vartheta{=}20°) = 1.05$ is often used for a spherically symmetrical wind as well (Wen et al., 1999; Lachowicz et al., 2006; Szostek & Zdziarski, 2007; Poutanen et al., 2008). Vrtilek et al. (2008) fit the value $\beta \approx 0.75$, together with $v_\infty \approx 1\,420\,\mathrm{km\,s^{-1}}$ to UV lines in the soft state, but note that *"there may be other local χ^2 minima, and some of the parameters may interact"*.

Column density and photoionization along the line of sight

Figure 2.7 shows the density fields for three different wind velocity models along the line of sight at different orbital phases. The orbital modulation of the total integrated column density is qualitatively very similar; the focused wind model produces a flatter minimum at ϕ_orb=0.5. The quantitative column density is largely determined by the ratio of the mass loss rate and the terminal velocity. The largest contribution to the total column arises from $s_\mathrm{LoS} = \mathcal{O}(a)$, i.e., 10^{12}–10^{13} cm away from the black hole, situated at higher polar angles than the focused wind. For larger $s_\mathrm{LoS} > s_0$, where the wind has already reached its terminal velocity, the density is:

$$n_\mathrm{H}(s_\mathrm{LoS},\,\vartheta) \ \approx \ \frac{\mathrm{d}\dot{M}/\mathrm{d}\Omega(\vartheta)}{\mu\, m_\mathrm{H}\, s_\mathrm{LoS}^2\, v_\infty} \tag{2.21}$$

The contribution of the outer wind to the column density is therefore:

$$\Delta N_\mathrm{H} \ := \ \int_{s_0}^{\infty} \mathrm{d}s_\mathrm{LoS}\ n_\mathrm{H}(s_\mathrm{LoS},\,\vartheta) \ = \ \frac{\mathrm{d}\dot{M}/\mathrm{d}\Omega(\vartheta)}{\mu\, m_\mathrm{H}\, s_0\, v_\infty} \tag{2.22}$$

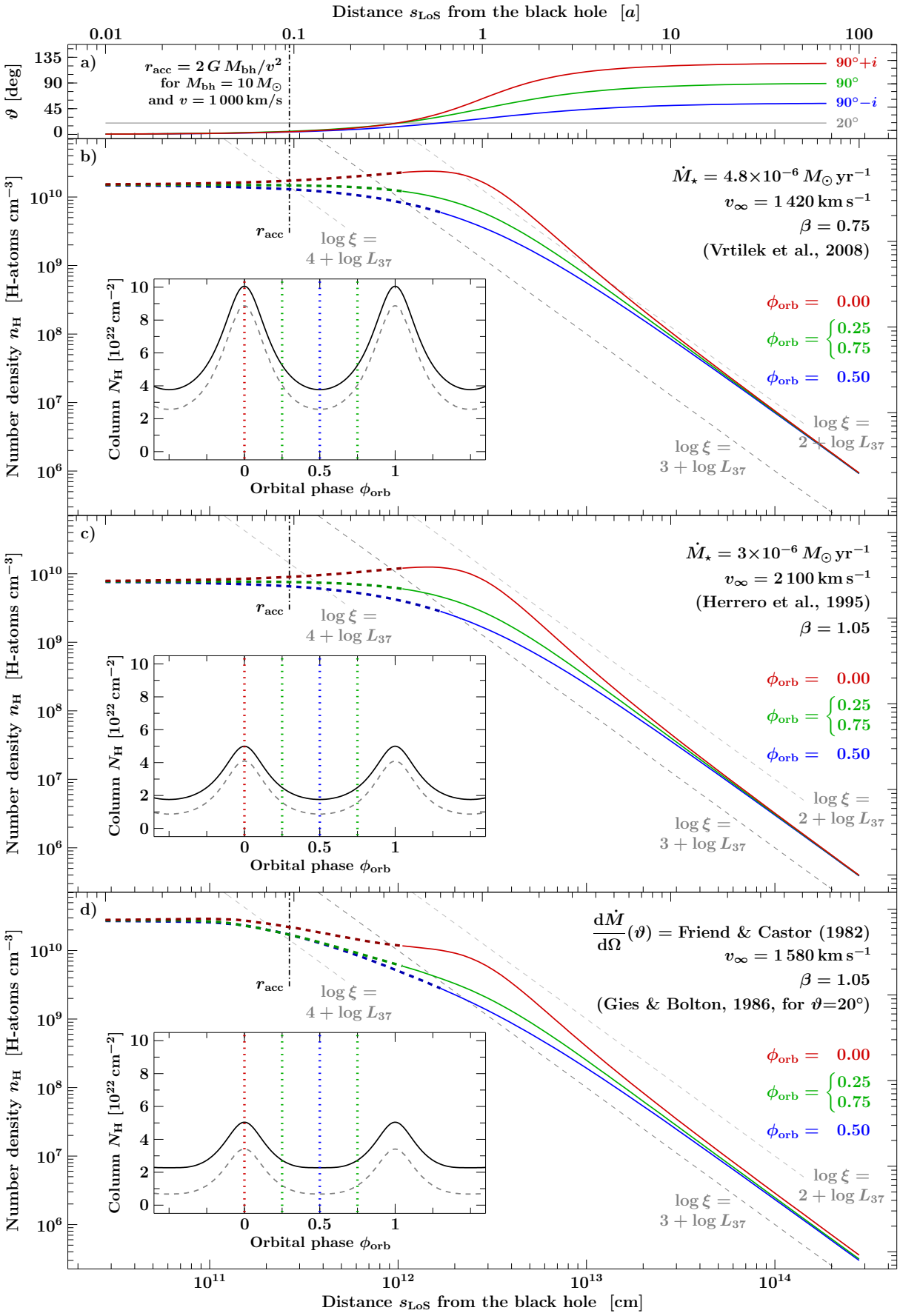

Figure 2.7: Density along the line of sight for three different models of the velocity field. →

Figure 2.7: (continued) **a)** Polar angle ϑ on the line of sight. **b)** Spherical wind model with $\dot{M}_\star{=}4.8{\times}10^{-6}\,M_\odot\,\mathrm{yr}^{-1}$, $v_\infty{=}1\,420\,\mathrm{km\,s}^{-1}$ and $\beta{=}0.75$ (Vrtilek et al., 2008). **c)** Spherical wind model with $\dot{M}_\star{=}3{\times}10^{-6}\,M_\odot\,\mathrm{yr}^{-1}$ and $v_\infty{=}2\,100\,\mathrm{km\,s}^{-1}$ (Herrero et al., 1995), and $\beta{=}1.05$. **d)** Focused wind model with $\dot{M}_\star{=}2{\times}10^{-6}\,M_\odot\,\mathrm{yr}^{-1}$ and $\mathrm{d}\dot{M}/\mathrm{d}\Omega(\vartheta)$ of Friend & Castor (1982), as well as $v_\infty{\equiv}v_\infty(\vartheta{=}20^\circ){=}1\,580\,\mathrm{km\,s}^{-1}$ and $\beta{\equiv}\beta(\vartheta{=}20^\circ){=}1.05$ (Gies & Bolton, 1986b).
The red, green, and blue lines show the density along the line of sight at $\phi_\mathrm{orb}{=}0$, $0.25{\equiv}0.75$, and 0.5. Only the dotted parts occur at $\vartheta \leq 20^\circ$, which may be influenced by the focused wind. The ionization parameter $\xi{=}L_\mathrm{X}/(n\,s_\mathrm{LoS}^2)$ is constant along the gray dashed lines. For an ionizing luminosity of $L_\mathrm{X}{=}10^{37}\,\mathrm{erg\,s}^{-1}$ and $n{=}n_\mathrm{H}$, these correspond to $\log\xi = 4$, 3, and 2. The vertical black dash-dotted lines indicate the accretion radius $r_\mathrm{acc}{=}2GM_\mathrm{bh}/v^2$ of a $10\,M_\odot$ black hole for a relative wind velocity of $1\,000\,\mathrm{km/s}$ (Hoyle & Lyttleton, 1939).
The inset in each panel shows integrated column densities as a function of orbital phase. While the solid black line indicates the total column up to $s_\mathrm{LoS}{=}100\,a$, the dashed gray line only accounts for the material at $\log\xi < 3 + \log L_{37}$, where $L_{37} := L_\mathrm{X}/(10^{37}\,\mathrm{erg\,s}^{-1})$.

As the inner part of the wind is highly photoionized due to the strong irradiation by the X-ray source, the *total* column shown in Fig. 2.7 may include fully ionized plasma and therefore be much larger than the column density detectable with X-ray absorption. Due to the s_LoS^{-2} dependence of the density in Eq. (2.21), the ionization parameter ξ of Eq. (1.60) is constant in the outer wind, provided that its density is homogeneous. If $L_\mathrm{X} \gtrsim 10^{37}\,\mathrm{erg\,s}^{-1}$, the wind may actually not become neutral at all, unless the density is significantly higher than in all models of Fig. 2.7, or the wind is clumpy. Even for the model of Vrtilek et al. (2008), which gives the highest column among the ones considered in Fig. 2.7, $\log\xi$ is larger than $2 + \log(L_\mathrm{X}/10^{37}\,\mathrm{cm}^{-2})$ throughout the entire wind. A large column, $\mathcal{O}(10^{22}\,\mathrm{cm}^{-2})$, of highly ionized ions is therefore expected, which is strongly modulated with orbital phase – however not necessarily because of the focused wind, which only covers a small part of the line of sight in a system seen at small inclination.

* * *

The properties of the stellar wind of HDE 226868 in the photoionization region between the supergiant and the black hole, especially during the hard state, are not well known from optical/UV observations. *If* a wind with high velocity can be launched from the hemisphere facing the black hole, it must be highly photoionized. The orbital effects of the wind of HDE 226868 on the X-ray spectrum of Cyg X-1 will be investigated in the following sections.

2.2 Data from X-ray All-Sky Monitors

2.2.1 Long Term Evolution and Spectral States

X-ray light curves and correlations

As for many other sources, the *RXTE* All-Sky Monitor (ASM) has been very useful to monitor the long term evolution of Cyg X-1 from the beginning of the *RXTE* mission in 1996 on.[4] Since early 2005, the hard X-ray sky in the 15–50 keV band is monitored with the Burst Alert Telescope (BAT; Barthelmy et al., 2005)[5] on the *Swift* satellite. Before that, from 1991 to 2000, the Burst and Transient Source Experiment (BATSE; Harmon et al., 2002)[6] on the *Compton Gamma Ray Observatory* (*CGRO*) delivered light curves using the Earth occultation technique. In late

[4] See http://xte.mit.edu/asmlc/.
[5] See http://swift.gsfc.nasa.gov/docs/swift/results/transients/.
[6] See http://www.batse.msfc.nasa.gov/batse/occultation/.

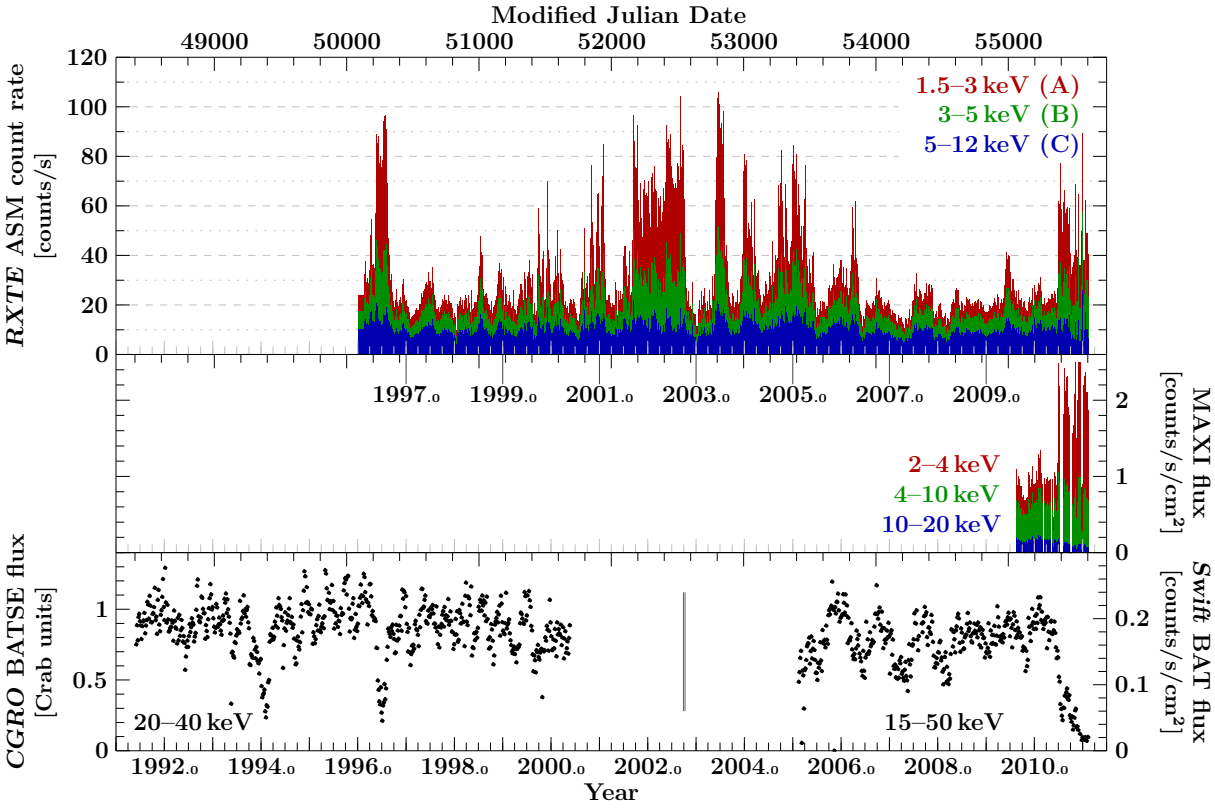

Figure 2.8: Long term evolution of Cygnus X-1, monitored by *RXTE* ASM (top), MAXI (middle), *CGRO* BATSE and *Swift* BAT (bottom panel). While the hardest ASM and MAXI bands hardly change during state transitions, their lowest energy bands are much more sensitive and show a strong increase during soft states. It is only in the hard state that the hard X-ray light curves from *CGRO* BATSE and *Swift* BAT are correlated with the soft X-ray light curves; in the soft state, however, the hard X-ray flux is, contrary to the soft X-ray flux, strongly decreased. All lightcurves have been averaged over 5.6 d.

2009, the Monitor of All-sky X-ray Image (MAXI; Matsuoka et al., 2009)[7] on the International Space Station (ISS) has started to provide additional soft X-ray monitoring. However, MAXI light curves are not necessarily continuous; e.g., for Cyg X-1, there are periods of $\lesssim$1 month when the source is not visible, e.g., obscured by the ISS itself or by the Space Shuttle.

Figure 2.8 shows these light curves of Cyg X-1, averaged over 5.6 days to remove any orbital variations. In the ASM data (top panel), different states are clearly discernible: when the source has settled in the low/hard state,[8] the average 1.5–12 keV count rate is below 30 cps, most often around 20 cps, whereas more than 50 cps on average are reached during flaring periods and outstanding high/soft states.[9] Dring individual measurements on 90 s dwells, Cyg X-1 in the soft state may, however, easily reach more than 100 cps. The brightening in the soft state is mostly due to the steepening of the power-law and the increased flux from the accretion disk in the soft X-ray band. It is therefore the 1.5–3 keV band that shows the largest dynamical range and is best suited to distinguish low/hard from high/soft states. With MAXI, the same holds true for its lowest 2–4 keV band, while the 10–20 keV band is rather insensitive to state transitions. The behavior of the hard X-ray component – as measured with *Swift* BAT at 15–50 keV or similarly with *CGRO* BATSE at (and above) 20–40 keV – is different: while these fluxes are correlated with the soft X-ray light curves in the low/hard state, the hard X-ray flux decreases strongly in the high/soft state (see also McConnell et al., 2002, fig. 1).

[7] See `http://maxi.riken.jp/top/`.
[8] Wilms et al. (2006) define Cyg X-1 to be in the hard state for average *RXTE* ASM count rates below 45 cps.
[9] Wilms et al. (2006) define Cyg X-1 to be in the soft state for average *RXTE* ASM count rates above 80 cps.

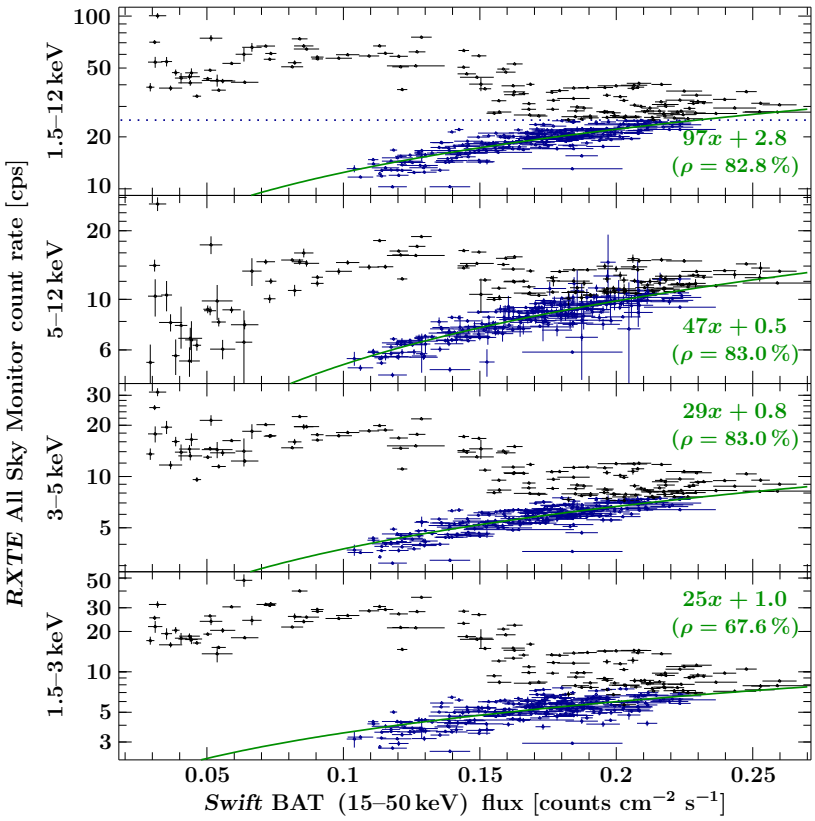

Figure 2.9: Correlation of orbit-averaged *Swift* BAT fluxes of Cyg X-1 and simultaneous *RXTE* ASM count rates in the full 1.5–12 keV band (top), the hard 5–12 keV band, the 3–5 keV band, and the soft 1.5–3 keV band (bottom). The blue data points have a total 1.5–12 keV *RXTE* ASM count rate below 25 cps (dotted line). The linear fits and correlation coefficients (green) refer to those hard state data.

Figure 2.9 shows the correlation between *Swift* BAT fluxes and *RXTE* ASM count rates of Cyg X-1, averaged over one orbital period. In the hard state, the linear correlation coefficient is >80 % for the ASM B, C, and S band. Nonetheless, there is no unique global mapping from BAT fluxes to ASM count rates that extends into the soft state; the *Swift* BAT flux alone does therefore not in general allow to infer the spectral state of Cyg X-1. Very low fluxes of $\lesssim 0.1$ counts cm^{-2} s^{-1} are, however, indicative for the soft state.

Hardness-intensity diagrams

It was mentioned at the end of Sect. 1.2.2 that the spectral evolution of black hole X-ray binaries is commonly depicted in *a* hardness-intensity diagram (HID), where *an* intensity value is plotted on the *y*-axis against *a* hardness ratio on the *x*-axis. If the intensity is just a count rate and the hardness is just the ratio of count rates in two energy bands, the shape of the HID may clearly depend to a large extent on the instrument. Even if source properties are displayed, viz., flux vs. flux-ratio, the HID still depends on the selected energy bands.

Figures 2.10 and 2.11 show *all* HIDs of Cyg X-1 that can be constructed from the *RXTE* ASM and MAXI count rates available in three energy bands each. As these bands may be dominated by different components of the X-ray spectrum, a variety of shapes can be obtained for the HID. Very soft count rates, e.g., in the 1.5–3 keV or 2–4 keV bands, are anticorrelated with spectral hardness – which is why soft states have historically been called high-intensity states (e.g., Tananbaum et al., 1972). On the contrary, MAXI's hardest count rate in the 10–20 keV band is highly correlated with its (10–20 keV)/(4–10 keV) hardness. While hard and soft states seem to be continously connected in the *RXTE* ASM data, they appear much more separated in the MAXI HIDs. This difference is likely due to the fact that only one transition from the hard state to the soft state, at the end of June 2010, is covered by the available MAXI data.

The *RXTE* ASM data will be investigated in more detail in the following section.

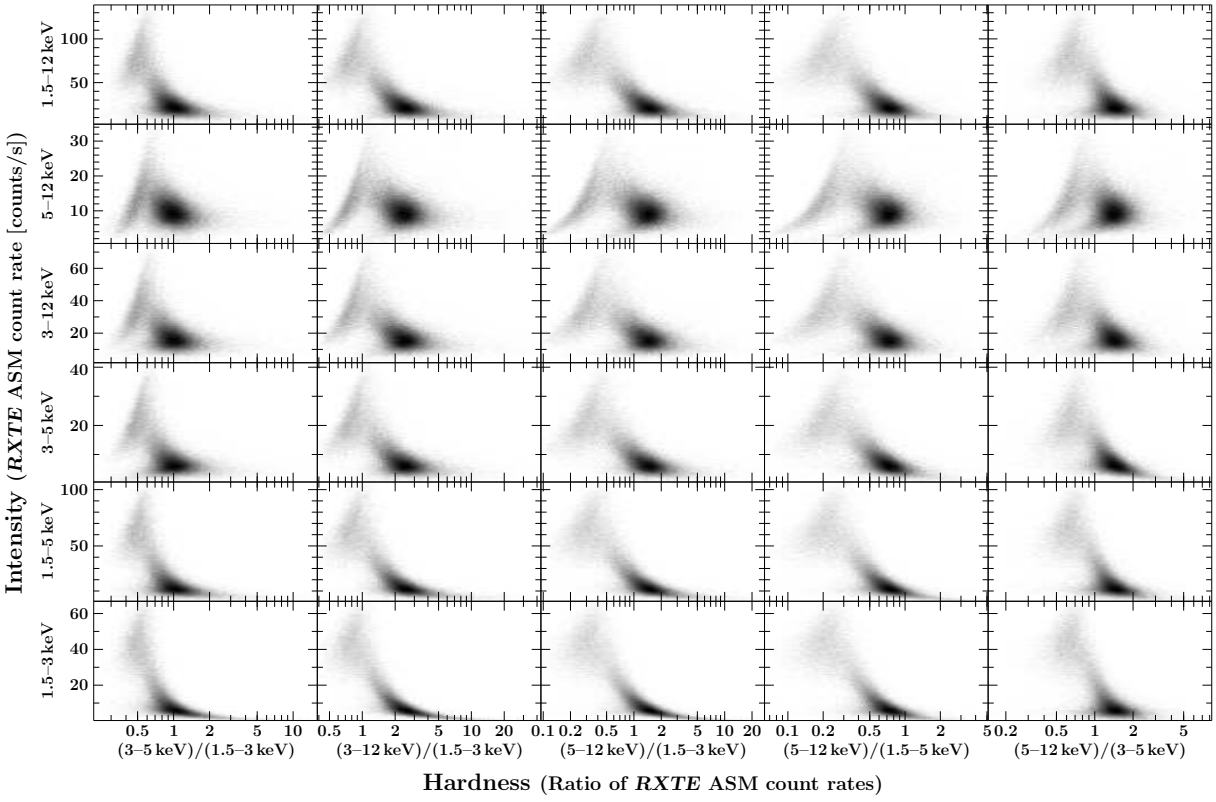

Figure 2.10: Hardness-intensity diagrams of Cyg X-1 using different bands of the *RXTE* ASM. The gray scale indicates the density of data points from 1996-01-05 – 2011-01-01 on 90 s dwells.

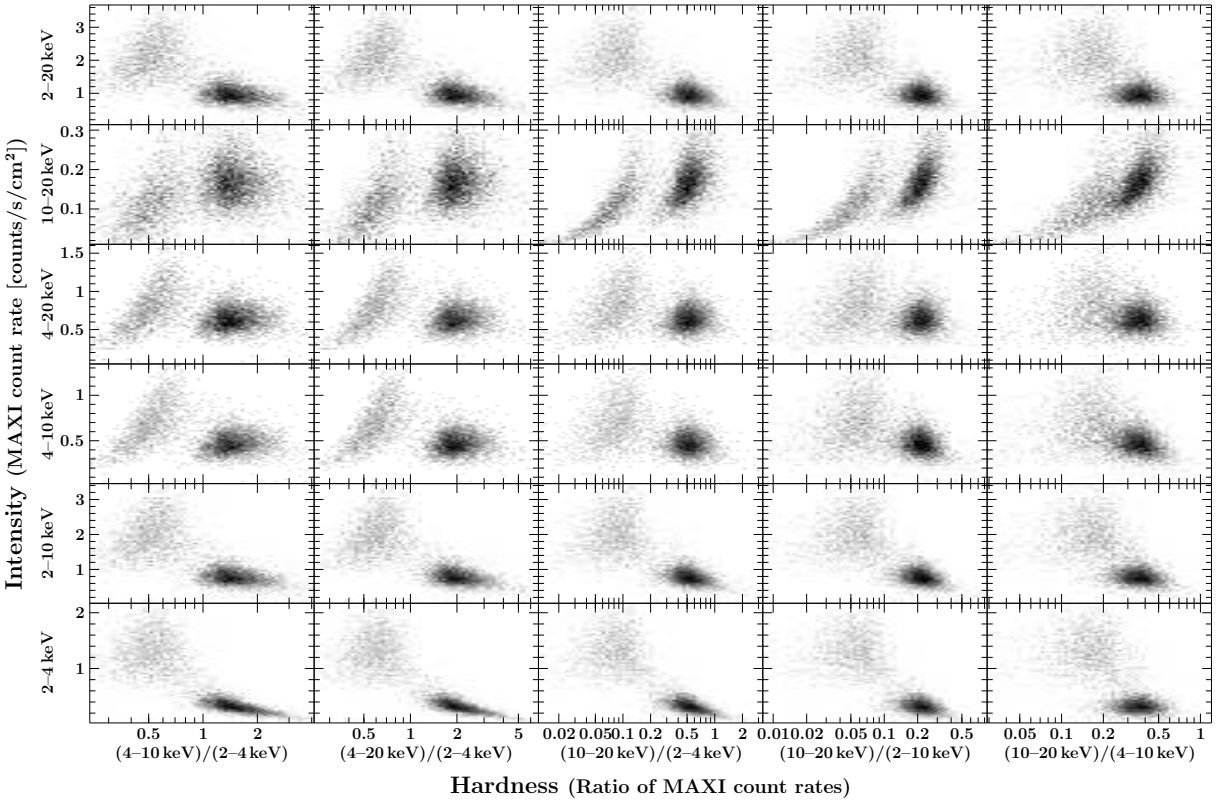

Figure 2.11: Same as Fig. 2.10, but for all MAXI data from 2009-08-15 to 2011-01-01.

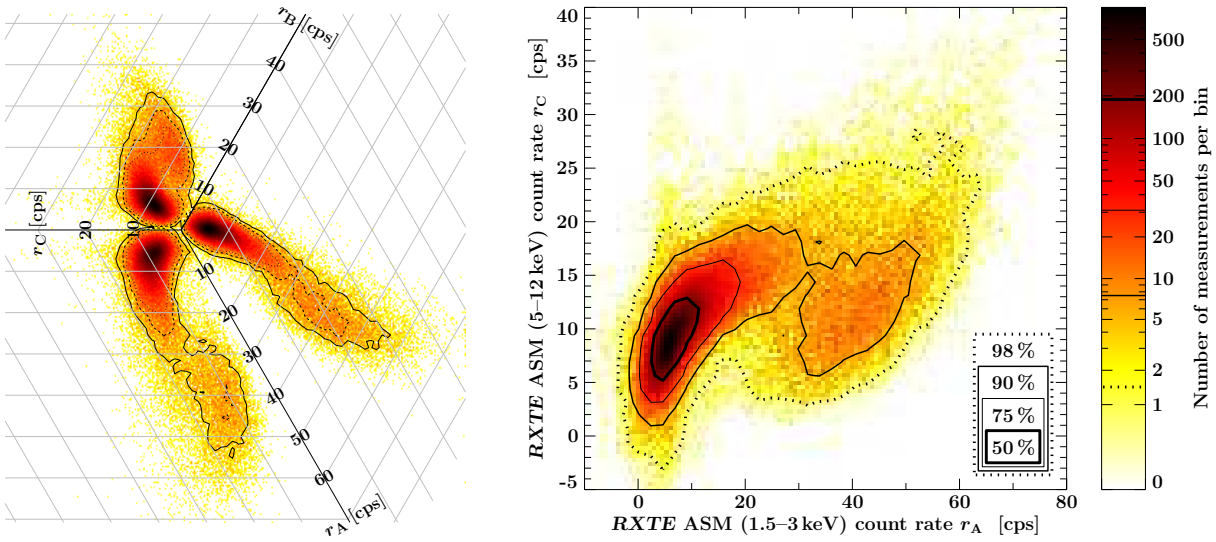

Figure 2.12: Joint distribution of *RXTE* ASM count rates of Cyg X-1. Left: Consecutive distributions of A, B, and C band rates r_A, r_B, and r_C on sheared Cartesian (i.e., tilted) coordinate systems, which can be seen as projections of the three-dimensional distribution of all rates. Right: Joint distribution of r_A and r_C on an orthogonal 2d coordinate system. 98 %, 90 %, 75 %, and 50 % of the data points cluster at higher densities than the contour lines in the righthand plot, which therefore enclose approximately the respective fractions of all measurements.

2.2.2 Orbital Modulation of the *RXTE* ASM Flux Distribution

96 778 *RXTE* ASM measurements of Cyg X-1 have been performed between 1996-01-05 and 2010-07-01 – at 82 564 unique times, as the source was in the field of view of two SSCs during 17.2 % of the observations, resulting in two independent flux measurements. Figure 2.12 displays the joint distribution of the count rates r_A, r_B, and r_C in the three energy bands. Only r_A shows a clearly bimodal distribution, related to the hard and soft states of the source. As the softest rate, r_A, is also most strongly affected by external absorption in the wind, it is best suited for an investigation of the orbital effects of the stellar wind.

Due to the brightness of Cygnus X-1, the data quality is usually very good. In the A-band, the solution to the all-sky shadow pattern had a χ^2/dof of >1.5 for only 111 times (<0.15 %), and 597 measurements (0.6 %) had a count rate of ≤ 0, indicating background oversubtraction. In 4 016 cases (4.1 %), the uncertainty Δr_A was more than half of r_A itself, see Fig. 2.13. As the occurence of measurements with $\Delta r_A > 0.5\, r_A$ depends on orbital phase (indicated by the bluish left side of the heart-like distribution in Fig. 2.13), screening the data with a criterion based on a $\Delta r_A / r_A$ ratio will introduce a bias against low count rates at early orbital phases.

Previous results on the average orbital modulation

The system's emission varies at all wavelengths with the orbital period (Eq. 2.1). While the modulation in the optical/IR (Walker, 1972; Leahy & Ananth, 1992) is due to the ellipsoidal deformation of HDE 226868 (Morris, 1985), the modulation in the radio (Pooley et al., 1999) and X-rays (e.g., Holt et al., 1976; Ling et al., 1990; Paciesas et al., 1997; Kitamoto et al., 2000) is due to its wind. Its effect on *RXTE* ASM light curves has been studied by Wen et al. (1999) from 1996/03 to 1998/09, by Lachowicz et al. (2006) from 1996/09 to 2003/08 (separating hard and soft state data), and by Poutanen et al. (2008) from 1996/01 to 2006/02 (selecting hard states only). These authors detect the orbital variation in the hard state and explain the average folded light curves by wind absorption and scattering models. Later studies have detected the modulation in the soft state as well (Dong et al., 2007; Boroson & Vrtilek, 2010).

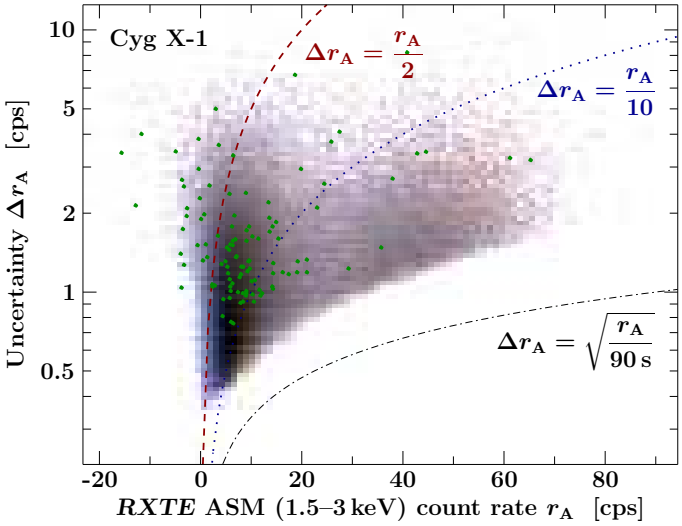

Figure 2.13: Distribution of 96 778 *RXTE* ASM count rates r_A and their uncertainties Δr_A. Darker colors correspond to higher densities of data points; blue (red) indicates an excess of events at early (late) orbital phases. The dashed red (dotted blue) line corresponds to a relative uncertainty of 0.5 (0.1). The dash-dotted line marks the Poisson error for 90 s dwells, which is a lower limit of the total measurement uncertainty. The 111 green data points correspond to sky solutions of $\chi^2_{red} > 1.5$.

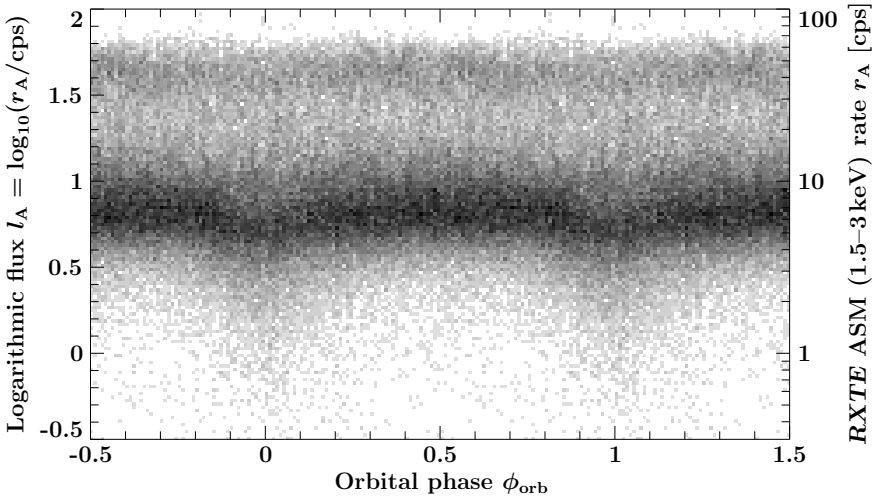

Figure 2.14: Orbital-phase resolved distribution of the 96 778 *RXTE* ASM rates r_A. The color-scale indicates the number of measurements per orbital phase bin and (logarithmic) flux bin. The orbital modulation of the average count rate and the width of the distribution are clearly discernible.

Flux distribution

In this work, the analysis of the orbital modulation of the soft X-ray flux is not restricted to its average value, but extended to the flux distribution, see Figs. 2.14 and 2.15 (top row). The one-dimensional distribution of the ASM (1.5–3 keV) count rate of Cyg X-1 shows two peaks, clearly corresponding to low/hard and high/soft states. The hard state peak follows closely a lognormal distribution (Poutanen et al., 2008), which is also found on short time scales (Uttley et al., 2005). The soft state peak has a stronger cutoff at high fluxes. The excess of the hard state distribution at low fluxes beyond a lognormal shape is largely suppressed if only measurements with $\Delta r_A < r_A/2$ are considered. A quantitative analysis has therefore to account for the uncertainties Δr_A. Fig. 2.13 has, however, shown that screening the data according to $\Delta r_A / r_A$ may introduce a bias and distort the orbital phase dependence.

Another way to account for the measurement uncertainties was therefore investigated: the *histogram of probabilities*. While previous distributions (e.g., Figs. 2.12, 2.13) were calculated from basically adding a delta function for each measurement into the histogram, one can also construct a histogram from probability distributions already for each data point, which can be normalized Gaussians – centered at the measured value and with a standard deviation given by the measurement uncertainty. This method corresponds nearly to a Gaussian smearing of the original histogram, see right column of Fig. 2.15. The data values in such a 'histogram of probabilities' are, however, no more independent of each other.

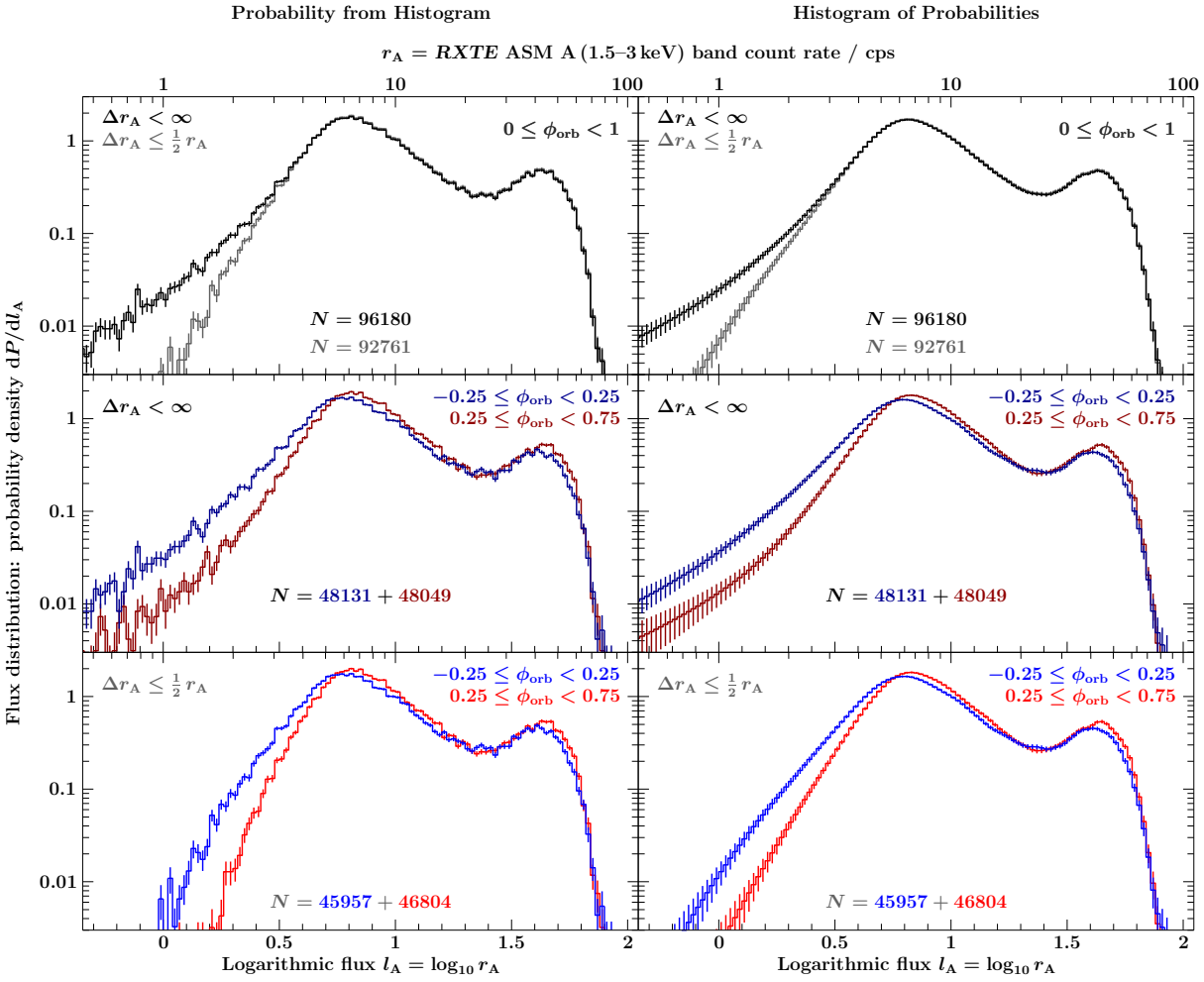

Figure 2.15: Distribution of the logarithm $l_A = \log_{10} r_A$ of the *RXTE* ASM (1.5–3 keV) rate r_A. The left column shows probabilities inferred from histograms of count rates that are assumed to be exact. If at all, uncertainties are only used to screen the measurements. The right column shows histograms of probabilities, where each data point contributes a Gaussian distribution according to its value and uncertainty. The top row compares the effects of data screening: while unfiltered data are shown in dark, light curves result from data with $\Delta r_A \leq r_A/2$. Below that, the orbital modulation is demonstrated for the unfiltered (middle row) and screened data (bottom row): Blue corresponds to early orbital phases ($-0.25 \leq \phi_{orb} < 0.25$), and red to late orbital phases ($0.25 \leq \phi_{orb} < 0.75$).

Orbital phase resolved flux distribution

Throughout this analysis, orbital phases are calculated according the ephemeris of Gies et al. (2003), see Eq. (2.2), where ϕ_{orb}=0 corresponds to the superior conjunction of the black hole.

Due to the orbital modulation, the flux distribution changes with orbital phase. In the lower two rows of Fig. 2.15, the results for *'early'* orbital phases ($-0.25 \leq \phi_{orb} < 0.25$) are compared with those for *'late'* orbital phases ($0.25 \leq \phi_{orb} < 0.75$). The distribution is shifted toward lower fluxes at early orbital phases due to enhanced X-ray absorption or scattering when the line of sight to the X-ray source probes denser regions of the stellar wind. The fact that such a change is also seen for the second peak confirms an orbital modulation even in the soft state.

In the following, an orbital-phase-resolved analysis of the flux distribution in 10 bins covering $\Delta\phi_{orb} = 0.1$ each is presented. At this resolution, the soft state peak becomes rather noisy, but these data are still taken into account and modelled. Fitting lognormal functions

reveals that the flux distribution does not only shift to lower count rates at early orbital phases, but also becomes broader (Fig. 2.16). The shift of the logarithmic flux $l = \log r$ equals (or is proportional to, if $l = \log_{10} r$ is considered) the wind's *effective optical depth* τ,[10] defined by

$$r_{\rm obs} \;=\; {\rm e}^{-\tau} \cdot r_{\rm intrin} \;\;, \tag{2.23}$$

where $r_{\rm obs}$ and $r_{\rm intrin}$ are the observed and source intrinsic count rates. The varying width of the distribution indicates a different structure of the wind at early and late orbital phases: the normalized flux distribution ${\rm d}P/{\rm d}l_{\rm obs}$ (i.e., the probability density with $\int {\rm d}P/{\rm d}l_{\rm obs}\ {\rm d}l_{\rm obs} = 1$) is the convolution of ${\rm d}P/{\rm d}l_{\rm intrin}$ and ${\rm d}P/{\rm d}\tau$, if those are established on the same time scale:

$$\frac{{\rm d}P}{{\rm d}l}_{\rm obs}(l_{\rm obs}) \;=\; \int {\rm d}\tau \;\; \frac{{\rm d}P}{{\rm d}l}_{\rm intrin}(l_{\rm obs}+\tau) \;\cdot\; \frac{{\rm d}P}{{\rm d}\tau}(\tau) \tag{2.24}$$

If the source's intrinsic flux does not depend on the orbital phase, the broadening of the flux distribution at early orbital phases has to reflect a broader distribution of the optical depth for absorption and/or scattering at these phases. For example, the convolution of two normalized Gaussians with widths σ_1 and σ_2 is again a normalized Gaussian with width $(\sigma_1^2+\sigma_2^2)^{1/2}$.

The observed distributions ${\rm d}P/{\rm d}l$ are, however, not necessarily Gaussians, that is, the rate r may not exactly follow a lognormal distribution. Figure 2.16 also shows the results from fitting Voigt functions to the logarithmic flux distribution. A normalized and zero-centered Voigt function $V(x;\,\sigma,\,\gamma)$ is the convolution of a Gaussian $G(x;\,\sigma)$ and a Lorentzian $L(x;\,\gamma)$, i.e.,

$$V(x;\,\sigma,\,\gamma) \;=\; \int {\rm d}t \;\; G(t;\,\sigma)\cdot L(x-t;\,\gamma) \tag{2.25}$$

where

$$G(x;\,\sigma) \;=\; \frac{1}{\sqrt{2\pi}\;\sigma} \;\cdot\; \exp\left(-\frac{x^2}{2\sigma^2}\right) \tag{2.26}$$

and

$$L(x;\,\gamma) \;=\; \frac{\gamma}{\pi} \;\cdot\; \frac{1}{x^2+\gamma^2} \tag{2.27}$$

ISIS' fit-function '`voigt`' (which has the four parameters `norm`, `energy`, `fwhm`[11], and `vtherm`) calculates – in the notation of Eq. (2.25) – the following expression in energy-space:

$$\texttt{norm} \;\times\; V\left(x-\texttt{energy};\;\; \sigma=\frac{\texttt{vtherm}}{\sqrt{2}\;c}\cdot\texttt{energy},\;\gamma=\frac{\texttt{fwhm}}{4\pi}\right) \;/\;{\rm keV} \tag{2.28}$$

where `norm` is given in photons/s/cm^2; x, `energy`, and `fwhm` are given in keV; `vtherm` is given in km/s; and c is the speed of light.

The set of 10 flux distributions ${\rm d}P/{\rm d}l$ is modelled in the $l = 0.2 - 1.78$ range with the sum of either (0a) two Gaussians or (0b) two Voigt functions. In any case, the same normalization of the hard state component, which could be considered as total probability for Cyg X-1 to be in this state, is applied to all of the 10 distributions, and so is the same normalization of the soft state component. However, as the fitting is only carried out in a limited range of fluxes, outside of which the distribution may be cut off more strongly, the resulting "probabilities" do neither add up to 1, nor do they agree between the modelling with Gauss or Voigt functions. The Voigt functions require a systematically higher normalization, which is likely due to the fact that more area "leaks out" into the range not considered.

[10] Due to the broad energy bands and the instrumental response of the ASM, the effective optical depth of Eq. (2.23) cannot be directly converted to a column density.

[11] As also stated in the ISIS documentation for the `voigt` fit-function, the parameter name `fwhm` is misleading, since the true full width at half maximum is $2\times\gamma = \texttt{fwhm}/(2\pi)$.

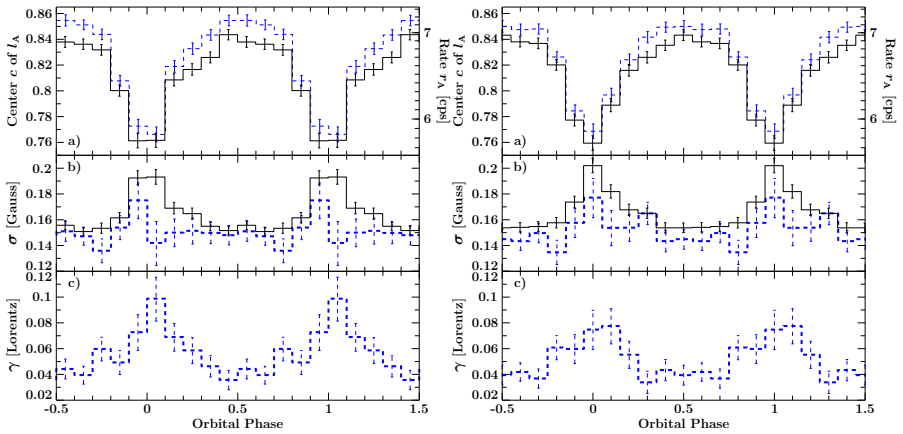

(a) Fit results using all data and conventional histograms.

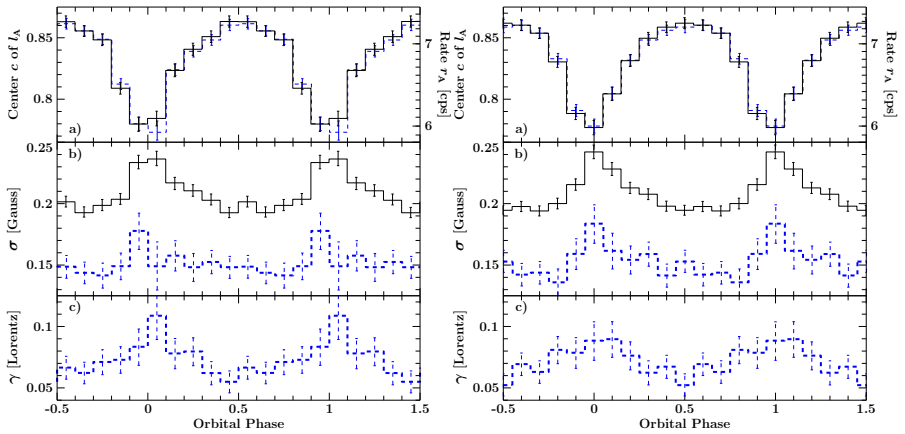

(b) Fit results using all data and histograms of probability distributions.

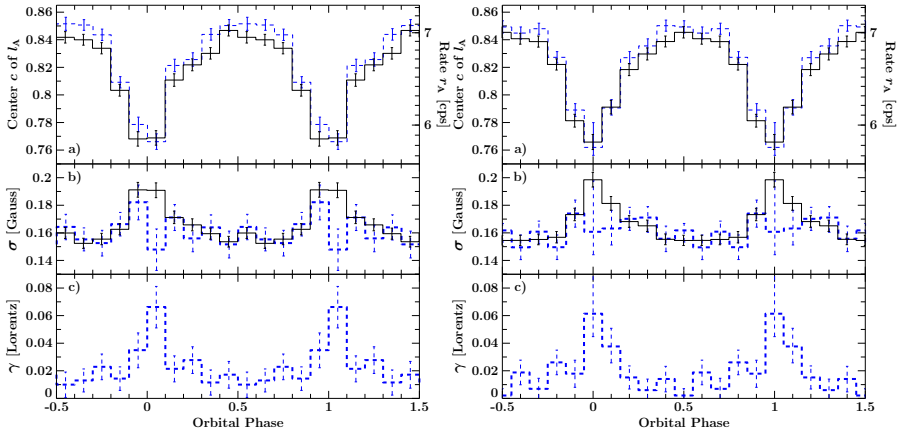

(c) Fit results using only screened data and conventional histograms.

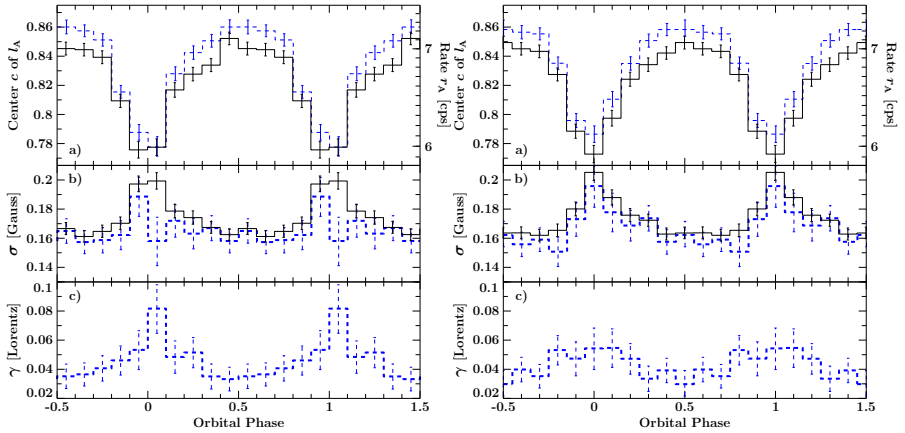

(d) Fit results using only screened data and histograms of probability distributions.

Figure 2.16: Fit results for the hard state peak of orbital-phase resolved *RXTE* ASM-A flux-distributions of Cyg X-1, using logarithmic Gaussian (black) or Voigt (blue) profiles, for the histograms constructed in a conventional way (left) or from probability distributions (right), and from all 96 778 measurements between 1996-01-05 and 2010-07-01 (top) or only from the 92 762 ones with $\Delta r_A < r_A/2$ (bottom). See text for more details.

In order to investigate systematic dependencies and to check the statistical robustness of the results, this procedure is carried out for $2 \times 2 \times 2$ configurations: (1a) using conventional histograms or (1b) using histograms of probability distributions; (2a) using all data or (2b) using only screened data with $\Delta r_A < r_A/2$; and (3a) having the first orbital phase bin start at $\phi_{orb}=0$ or (3b) centered at $\phi_{orb}=0$. The results for the hard state peak are displayed in Fig. 2.16 and given in Table B.1 on page 150. They can be summarized as follows:

(0) The Voigt functions fit better to the observed flux distributions than the Gaussians do. Both descriptions tend to agree on the center of the distribution. The width σ_{Voigt} of the Voigt functions is usually smaller or equal to σ_{Gauss} of the Gauss functions, as the latter do not have an additional Lorentzian width γ.

(1) For the histograms of probabilities (Table B.1 b & d), the formal χ^2 value is much lower than for the conventional histograms (Table B.1 a & c), but as their data are not independent of each other, χ^2 statistics may not apply.

For the unfiltered data (Fig. 2.16 a & b), the width of the distribution is considerably larger if probability distributions are considered, as they are already broadened themselves: while σ_{Gauss} varies between $\sim$0.15–0.2 for the conventional histograms (Table B.1 a), values between $\sim$0.19–0.24 are found for the histograms of probability distributions (Table B.1 b). This effect is less pronounced for the screened data that have smaller uncertainties (Fig. 2.16 c & d). For the fits with Voigt functions, the smearing by the measurement uncertainty results in both cases in a slight increase of γ only.

(2) Likewise, the Voigt profile modelling gives a larger γ for all data (Fig. 2.16 a & b) than for the screened data (Fig. 2.16 c & d). For the conventional histograms, no significant change in σ is found between the two approaches (Table B.1 a & c) – remarkably not even for the Gaussian modelling.

(3) The results are in general statistically stable against shifting the phase bins by $\Delta\phi_{orb}=0.05$, i.e., the fits where the phase bins start at $\phi_{orb}=0.0, 0.1, \ldots, 0.9$ (all Figs. 2.16 a–d, left) show the same trends as the fits with bins centered at $\phi_{orb}=0.0, 0.1, \ldots, 0.9$ (Figs. 2.16 a–d, right) – unless structures that are smaller than $\Delta\phi_{orb}=0.1$ are concerned (see below).

The following results hold (largely) independent of the considered configuration:

- The flux distributions at early orbital phases ($-0.25 \leq \phi_{orb} < 0.25$) are significantly broader than at late orbital phases. Table B.1 shows that $\sigma_{Gauss}(-0.05 \leq \phi_{orb} < 0.05)$ is larger than $\sigma_{Gauss}(0.45 \leq \phi_{orb} < 0.55)$ by 5.7–7.3 times the uncertainty of their difference.

- For the fits with Voigt functions, it appears that the broadening of the distribution at early orbital phases is largely due to an increase of γ, occuring in a larger range of orbital phases, in phase with the flux decrease. This suggestion is supported by Fig. 2.17 showing the correlations between the width of the flux distribution and the optical depth τ in the wind. While there is no significant correlation between σ_{Voigt} and τ (the linear correlation coefficient is only 28–67 %), γ and τ are correlated with coefficients $\geq$83 %.

  The peak at $\phi_{orb} \approx 0$ itself seems to have substructure, which cannot be resolved very well with the current statistics: $\sigma_{Voigt}(0.9 \leq \phi_{orb} < 1)$ is always enhanced compared to the neighbouring bins, and the same is usually seen for $\sigma_{Voigt}(-0.05 \leq \phi_{orb} < 0.05)$. On the other hand, $\gamma(0 \leq \phi_{orb} < 0.1)$ is enhanced compared to the neighbouring bins, which is not detected by $\gamma(-0.05 \leq \phi_{orb} < 0.05)$.

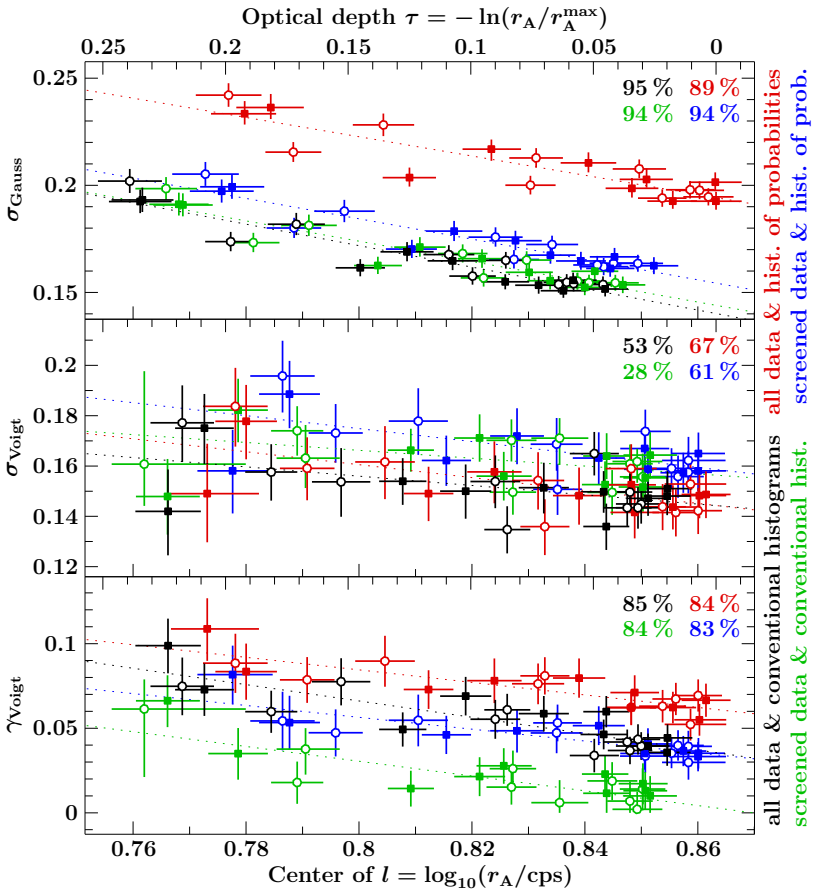

Figure 2.17: Correlation between the width of the hard state peak of the orbital phase-resolved flux distribution of Cyg X-1 and its center position, according to Table B.1. Open circles (filled squares) depict bins centered (starting) at $\phi_{orb} = 0, 0.1,$ etc. While the top panel shows σ from the Gaussian description, the middle and bottom panels show σ_{Voigt} and γ from the Voigt profile modelling. The numbers in each panel's upper right corner specify the linear correlation coefficients for different configurations indicated by colors according to the labels on the right.

To conclude, a higher optical depth in the wind at early orbital phases implies also a broader flux distribution. The broadening seems to be largely caused by a non-Gaussian component.

A possible interpretation of this result is that the wind structure probed at $\phi_{orb} \approx 0$ is significantly more clumpy than the wind seen at the opposite conjunction phase. A clumpy wind can provide a broad distribution of optical depths, if its porosity is such that the number of clumps crossing the line of sight during one 90 s dwell of the ASM is small and therefore subject to large Poisson fluctuations. If the line of sight would always contain a large number of clumps, the relative rms variability would be smaller. A microporous clumpy wind would therefore resemble a homogeneous wind, as long as absorption is optically thin and $\tau \propto N_H$.

The present results on the distribution of the optical depth in the wind can be used to test future quantitative models of a clumpy wind in the HDE 226868/Cyg X-1 system.

* * *

With more than 15 years of operation, the *Rossi X-ray timing Explorer* has been (and currently still is) an extremely successful mission. The large database from the regular monitoring with the ASM has provided the possibility for a detailed statistical analysis of the flux distribution of Cyg X-1, which was presented in the previous section. The two other science instruments aboard *RXTE*, which allow for a spectral analysis, are employed in dedicated pointed observations – a large number of which were also targeted at Cyg X-1. The investigation of the entire PCA data set is the topic of the next section.

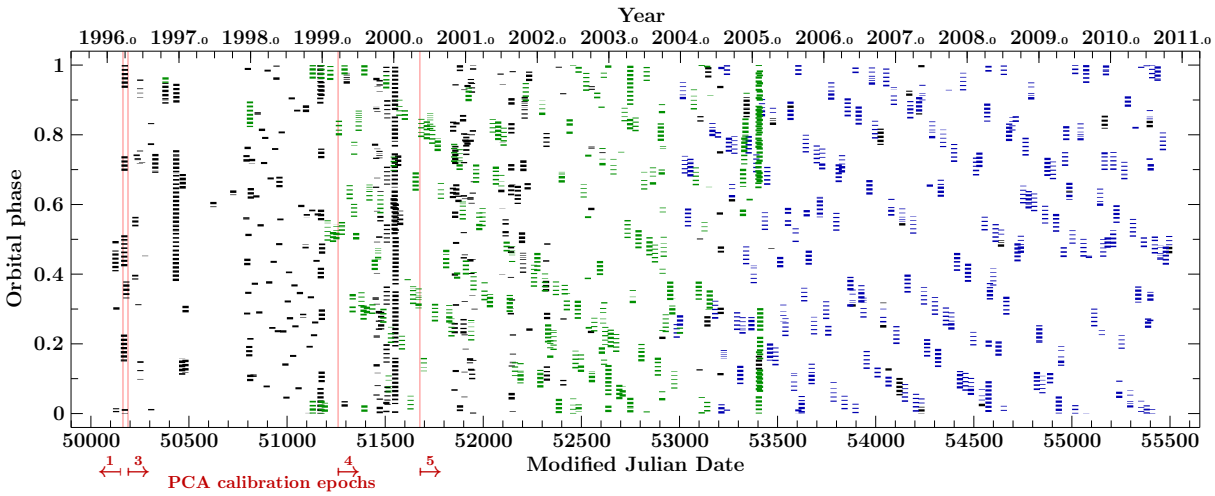

Figure 2.18: *RXTE* observations of Cyg X-1 and their orbital phase coverage, up to 2010 Nov 1. Gaps are due to interruptions by Earth occultations or passages through the South Atlantic Anomaly. All observations shown in green (blue) employ the same PCA configuration 1 (2) of Table 2.1, which only differ in the time bin size of two single bit modes. The red vertical lines separate the five PCA calibration epochs. The top-left to bottom-right pattern arises from the ∼14 day period of the monitoring campaign corresponding to ∼2.5 binary orbits.

Table 2.1: *RXTE* PCA modes used in the Cyg X-1 monitoring campaign

	Mode	
Event Analyzer	configuration 1 employed until 2005-02-10	configuration 2 employed after 2003-12-12
EA 1*	..... `E_125us_64M_36_1s`	
EA 2*	..... `B_2ms_8B_0_35_Q`	
EA 3*	`SB_250us_0_13_2s`	`SB_125us_0_13_1s`
EA 5	..... `Standard1b`	
EA 6	..... `Standard2f`	
EA 7*	`SB_250us_14_35_2s`	`SB_125us_14_35_1s`

Note. The modes of the Event Analyzers marked with * are defined by the guest observer.

2.3 Pointed Observations with *RXTE* (PCA)

Figure 2.18 shows the pointed *RXTE* observations of Cyg X-1 and their orbital phase coverage. The monitoring campaign (Pottschmidt et al., 2003; Gleissner et al., 2004a,b; Wilms et al., 2006) started with short weekly observations in 1998, continued with longer biweekly observations from 1999 on, and was still ongoing in 2011. It has not only greatly extended the archive of Cyg X-1 observations with *RXTE*, but also provides a large data set with a homogeneous configuration of the instruments (see Table 2.1), in particular identical high time-resolution modes, which is desirable for a timing analysis of the source's long term evolution. For a sole spectral analysis on time scales longer than 16 s, the pre-set `Standard2` mode (`Standard2f` after 1996-06-18) is available from Event Analyzer 6 in *all* observations.

As this work focuses mainly on the low-energy spectrum, only data from the PCA are considered, although HEXTE was usually available as well. However, with the improvements of the PCA response matrix (PCARMF 11.7) relased with HEASOFT 6.7 in 2009 August, PCA data up to 50 keV are well calibrated,[12] while previously, data above ∼25 keV were often ignored.

[12] See `http://astrophysics.gsfc.nasa.gov/xrays/programs/rxte/pca/doc/rmf/pcarmf-11.7/`.

Data reduction

All data were reduced using `heasoft 6.9` following standard data screening procedures as recommended by the *RXTE* Guest Observer Facility. Data were ignored when the satellite has passed through the South Atlantic Anomaly (SAA; see Fürst et al., 2009) within the last 10 minutes, or when the elevation of the source over the limb of the Earth was lower than 10°. The brightness of Cyg X-1 allowed to split the data into continuous segments, uninterrupted by Earth occultations or SAA passages, and still obtain spectra with a good S/N (following Böck, 2008; Böck et al., 2008, 2010). In a few instances, PCUs were switched on or off *during* one segment, which will result in more than one spectrum being fitted simultaneously. In total, 2247 such segments were obtained during the 14.5 years between 1996-02-12 and 2010-10-09, see Table B.2 on page 149. The total exposure amounts to more than 4.78 Ms (55.35 days). The distribution of exposure times (Fig. 2.19) shows that one third of these segments have exposures of more than 45 min, with a sharp peak at 3.2 ks, while for the other two thirds, a scheduling in shorter intervals was preferred, resulting in a broad distribution peaking at ∼1.7 ks. While at the beginning of the *RXTE* mission, all five PCUs were usually turned on, the observing policy was changed from ∼1999 on and the number of active PCUs was lowered (see Fig. 2.20) in order to prevent high voltage breakdowns due to organic molecules building up at the anodes (Jahoda et al., 1996).

Data selection and preparation. `Standard2f` spectra can be extracted from the top Xenon layer of the PCA, or from all three layers. For the following analysis, top layer spectra were chosen, as they contain almost all of the soft X-ray photons (see Fig. 2.21), and are more accurately calibrated. For Cyg X-1, the S/N at higher energies is still good, even though 50–68 % of the total events above 16 keV occur *below* the top layer, which can be seen from Fig. 2.21. While the first *three* spectral channels, as well as those above 50 keV, are always ignored according to the recommendations of the PCA calibration team,[12] a detailed investigation of the *fourth* bin[13] was performed (‘`ign 1-3`’ vs. ‘`ign 1-4`’), which will prove crucial for the determination of low-energy spectrum. Similarly, the (earlier) advice[12] to add $s = 0.5\,\%$ “systematic errors” to the data – in order to account for calibration uncertainties – will be scrutinized as well (‘`syst 0.5%`’ vs. ‘`syst 0`’). Specifically, adding a systematic error s in quadrature means to increase the uncertainty of each measured count rate c from the orignal value σ to

$$\sigma' \;=\; \sqrt{\sigma^2 + (s \cdot c)^2} \tag{2.29}$$

Although the signal-to-noise ratio was usually at most in a few channels (if at all) below five, all spectra were rebinned to $S/N \geq 5$ in order to ensure a homogeneous data quality.

2.3.1 Spectral Modelling in Hard and Soft States

Wilms et al. (2006) have previously shown that a simple phenomenological description of the *RXTE* spectrum of Cyg X-1 in the hard state – using a broken power-law with high-energy cutoff, and a Gaussian Fe K α fluorescence line at 6.4 keV – describes the data as good or even better than different physically motivated Comptonization models. From the analysis of four *Suzaku* spectra of Cyg X-1 in the hard state, Nowak et al. (2011) have recently concluded that there is still a strong degeneracy between physical models for Comptonizing coronae with thermal or mixed thermal/non-thermal electron populations, and jets. For these reasons, and as the main focus of this work lies on the external absorption, only phenomenological broken

[13] In PCA calibration epoch 5, since 2000-05-13, covering the largest part of the monitoring campaign by now, the energy correspondence of the fourth channel (i.e., index 3 when counting from 0) was ∼2.8–3.3 keV.

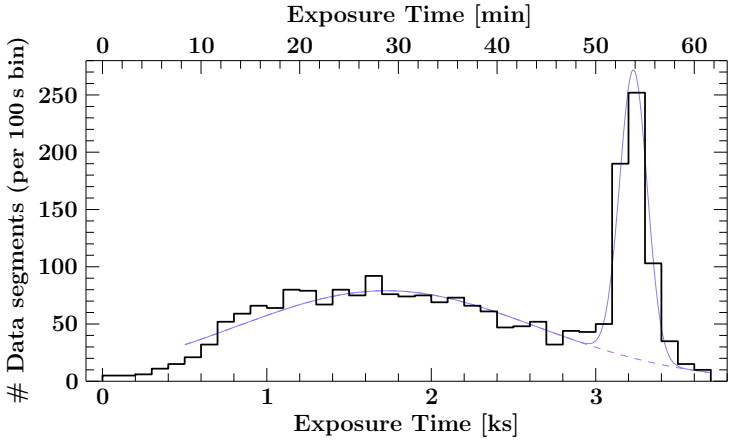

Figure 2.19: Distribution of Cyg X-1 exposure times of the *RXTE* PCA data segments. The blue curve consists of two Gaussian functions centered at 1.73 ks and 3.23 ks with a $1\,\sigma$-width of 0.91 ks and 84 s, respectively, possibly indicating two different ways of scheduling *RXTE* observations.

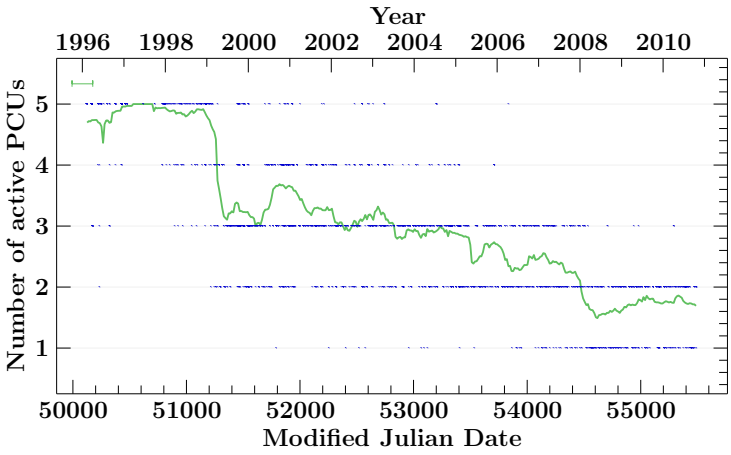

Figure 2.20: Number of PCUs that were active during the *RXTE* observations of Cyg X-1. The blue points show the PCA configuration in all individual segments. The solid green line is a moving average over half a year, corresponding to the horizontal error bar in the upper left corner.

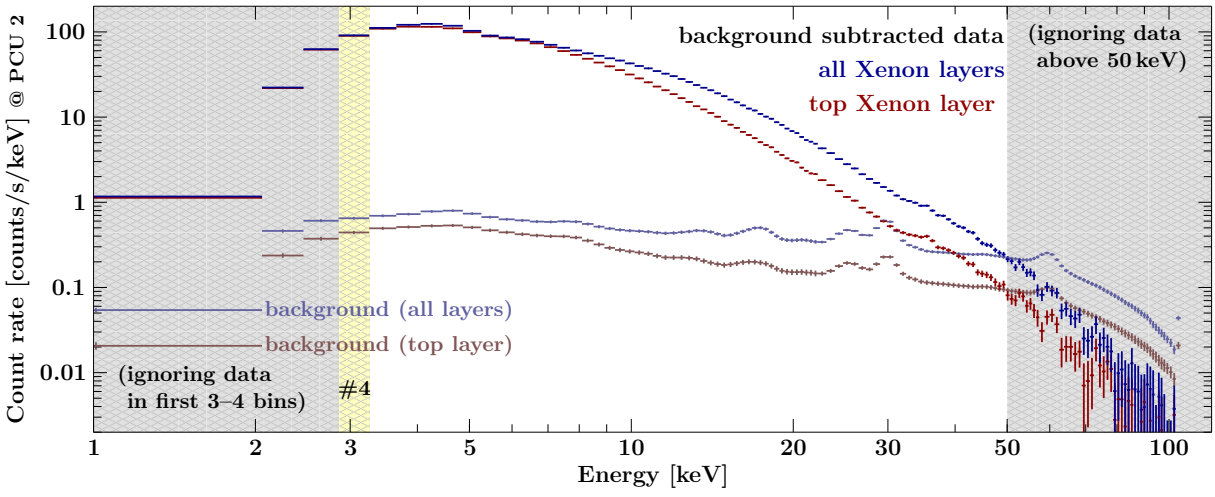

Figure 2.21: (Not rebinned) *RXTE* PCA (`Standard2f`) spectra of Cyg X-1 in the hard state (observed on 2010-01-14, ObsID 95338-07-01-00) from all three Xenon layers (blue) and from the top layer only (red). The top layer records nearly all soft X-ray photons (90–99 % below 8 keV), but less than 50 % of the events above 16 keV. While the palish data points show the estimated background, the darker ones display background subtracted source count rates. Data in the gray crosshatched regions, i.e., the first three *or* four bins ('`ign 1-3`' vs. '`ign 1-4`', see text; the fourth bin is highlighted in yellow), as well those above 50 keV, were not considered for spectral analysis. Due to the decrease of the high voltage of the PCA in 1996 and 1999, all channels corresponded to lower energies in gain epochs earlier than 4.

power-law models are considered in the following. For hard state spectra without a thermal component, the '`bknpower`' model has the form:

$$\left(\texttt{bknpower} * \texttt{highecut} + \texttt{egauss}\right) * \texttt{TBnew} \tag{2.30}$$

Whereas Wilms et al. (2006) concentrate on the hard X-ray spectrum and ignore all data up to 5 keV when Cyg X-1 is in the soft state, the soft X-ray spectrum is crucial for this study of absorption properties. To account for the thermal component that appears in the spectrum, an additional disk blackbody is introduced. The '`bknpower`+`diskbb`' model reads:

$$\left(\texttt{bknpower} * \texttt{highecut} + \texttt{egauss} + \texttt{diskbb}\right) * \texttt{TBnew} \tag{2.31}$$

Hard state spectra

As an example, the analysis of the top-layer spectrum from ObsID 95338-07-01-00 (Fig. 2.21), which is the *RXTE* observation simultaneous to the first *Chandra* observation of Cyg X-1 in the hard state at $\phi_{\mathrm{orb}} \approx 0.5$ on 2010-01-14 (Sect. 2.4.2), is presented in detail. Table 2.2 shows the parameters obtained with the '`bknpower`' model, which gives a perfect description of the data, even when the fourth bin is included, and even when no systematic errors are added. Due to the high flux of Cyg X-1, systematic errors as high as 0.5 % of the count rate are of the same order as the Poissonian uncertainty of the data below ∼10 keV, such that the total uncertainties of the data would be dominated by calibration, rather than statistical uncertainties. The fact that the reduced χ^2 is lowered from 0.9 to 0.6 (Table 2.2) shows that adding systematic errors overestimates the actual uncertainties of the data, which in turn lowers the constraints on derived parameter values, i.e., leads to misleadingly large confidence intervals (Wilms et al., 2006, appendix B). Table 2.2 shows that the error bars of the parameters describing the low energy part of the spectrum, namley the broken power-law's normalization N_{bknpower} and low-energy photon index Γ_1, and in particular the column density N_{H}, are nearly doubled by adding systematic errors. These parameters – N_{bknpower}, Γ_1, and N_{H} – are also very strongly entangled, which can be seen from the confidence maps in Fig. 2.22. As the spectrum only starts at ∼2.8 keV (for '`ign 1-3`'), and due to its low resolution, *RXTE* PCA can hardly distinguish power-law slope below E_{break} and absorption at lowest energies, especially since the Fe line at 6.4 keV can largely compensate for changes in the ∼5–8 keV range. Since the break of the power-law is at 10 keV, and since the spectrum above E_{break} is not affected by $\mathcal{O}\left(10^{22}\,\mathrm{cm}^{-2}\right)$ absorption, an increase of Γ_1 requires an increased N_{bknpower} as well, which is the flux of the low energy power-law at 1 keV. As expected, N_{H} is even more badly constrained if the fourth spectral channel is ignored ('`ign 1-4`'), too, see Table 2.2.

Of course, one can also apply the '`bknpower`+`diskbb`' model (2.31) to a hard state spectrum. The results are shown in Table 2.2. The confidence maps in Figs. 2.23 and 2.24 clearly indicate that the disk parameters cannot be constrained very well. Although the fits are improved, e.g., from $\chi^2/\mathrm{dof} = 64.4/71 = 0.91$ to $55.7/69 = 0.81$ for '`ign 1-3`' and '`syst 0`', virtually any combination of disk temperature and normalization is permissible below the line in the N_{disk}-T_{in} plane of parameter space that limits the contribution of the disk to the first energy bin considered – especially, if systematic errors are applied. The disk in the hard state, if present at all, must clearly be below the energy range covered by the spectrum. An analysis of its systematic effects on other model parameters is still required in order to understand the spectral evolution from the hard state to the soft state, where the disk *is* significant (as will be shown below), in a continuous way. Figure 2.25 illustrates the interplay between the disk component and N_{H}: compared to the model without a disk (green), a more strongly absorbed, extremely bright, cool disk (red), or a much more strongly absorbed and fainter, but hotter disk (blue) describe the data almost equally well. If a disk component is added, N_{H} is systematically increased, and the uncertainty of N_{H} may be enlarged by a factor of ∼10, e.g., from

Table 2.2: Parameters of the '`bknpower`' model (2.30) for the hard state spectrum from ObsID 95338-07-01-00, observed on 2010-01-14 (segment at 05:46–06:31 UT)

Parameter	[Unit]	'ign 1-3'		'ign 1-4'	
		'syst 0'	'syst 0.5%'	'syst 0'	'syst 0.5%'
·····		`bknpower` — broken power-law			·····
N_{bknpower}	$\left[\frac{\mathrm{ph}}{\mathrm{s\,cm^2\,keV}}\right]$	1.70 ± 0.04	1.70 ± 0.07	1.73 ± 0.05	1.73 ± 0.09
Γ_1		1.709 ± 0.010	1.709 ± 0.018	1.715 ± 0.013	1.72 ± 0.02
E_{break}	[keV]	10.2 ± 0.4	10.2 ± 0.5	10.2 ± 0.4	10.2 ± 0.5
Γ_2		$1.49^{+0.02}_{-0.04}$	$1.49^{+0.02}_{-0.04}$	$1.49^{+0.02}_{-0.04}$	$1.50^{+0.02}_{-0.04}$
·····		`highecut` — high-energy cutoff			·····
E_{cut}	[keV]	20^{+6}_{-5}	20^{+6}_{-5}	20^{+6}_{-5}	20^{+6}_{-5}
E_{fold}	[keV]	278^{+198}_{-91}	280^{+221}_{-94}	281^{+205}_{-93}	284^{+229}_{-96}
·····		`egauss` — Fe Kα fluorescence line at 6.4 keV			·····
$A_{\mathrm{Fe\,K}\alpha,-3}$	$\left[10^{-3}\,\frac{\mathrm{ph}}{\mathrm{s\,cm^2}}\right]$	$7.6^{+0.9}_{-0.8}$	$7.5^{+1.5}_{-1.3}$	$7.3^{+0.9}_{-0.8}$	$7.2^{+1.6}_{-1.4}$
$\sigma_{\mathrm{Fe\,K}\alpha}$	[keV]	0.40 ± 0.09	$0.39^{+0.14}_{-0.15}$	0.38 ± 0.09	$0.38^{+0.15}_{-0.17}$
·····		`TBnew` — photoelectric absorption (`abund wilm, xsect vern`)			·····
$N_{\mathrm{H,22}}$	$\left[10^{22}\,\mathrm{cm^{-2}}\right]$	$0.96^{+0.16}_{-0.15}$	1.0 ± 0.3	1.1 ± 0.2	1.1 ± 0.5
χ^2/dof		$\frac{64.4}{71} = 0.91$	$\frac{44.1}{71} = 0.62$	$\frac{62.2}{70} = 0.89$	$\frac{43.5}{70} = 0.62$

Table 2.3: Parameters of the '`bknpower`+`diskbb`' model (2.31) for the hard state spectrum from ObsID 95338-07-01-00, observed on 2010-01-14 (segment at 05:46–06:31 UT)

Parameter	[Unit]	'ign 1-3'		'ign 1-4'	
		'syst 0'	'syst 0.5%'	'syst 0'	'syst 0.5%'
·····		`bknpower` — broken power-law			·····
N_{bknpower}	$\left[\frac{\mathrm{ph}}{\mathrm{s\,cm^2\,keV}}\right]$	2.0 ± 0.2	$1.9^{+0.4}_{-0.2}$	$1.86^{+0.12}_{-0.10}$	$1.86^{+0.20}_{-0.15}$
Γ_1		1.76 ± 0.04	1.76 ± 0.06	$1.74^{+0.04}_{-0.02}$	$1.74^{+0.07}_{-0.04}$
E_{break}	[keV]	10.4 ± 0.4	10.4 ± 0.6	10.2 ± 0.4	$10.2^{+0.6}_{-0.5}$
Γ_2		$1.51^{+0.03}_{-0.04}$	1.51 ± 0.04	$1.50^{+0.02}_{-0.04}$	1.50 ± 0.04
·····		`highecut` — high-energy cutoff			·····
E_{cut}	[keV]	$21^{+7}_{-6^*}$	$21^{+8}_{-6^*}$	$20^{+6}_{-5^*}$	$20^{+7}_{-5^*}$
E_{fold}	[keV]	323^{+351}_{-121}	324^{+459}_{-126}	299^{+254}_{-104}	301^{+308}_{-108}
·····		`egauss` — Fe Kα fluorescence line at 6.4 keV			·····
$A_{\mathrm{Fe\,K}\alpha,-3}$	$\left[10^{-3}\,\frac{\mathrm{ph}}{\mathrm{s\,cm^2}}\right]$	6.0 ± 1.2	6 ± 2	$6.1^{+1.1}_{-1.3}$	6 ± 2
$\sigma_{\mathrm{Fe\,K}\alpha}$	[keV]	0.35 ± 0.13	0.4 ± 0.3	$0.32^{+0.11}_{-0.13}$	$0.3^{+0.2}_{-0.3}$
·····		`diskbb` — disk blackbody component			·····
$\log_{10} N_{\mathrm{disk}}$		$4.1^{+0.9}_{-0.6}$	4^{+1}_{-4}	8^{+2}_{-4}	8^{+2}_{-8}
kT_{in}	[keV]	$0.42^{+0.06}_{-0.17}$	$0.4^{+0.2}_{-0.4}$	$0.2^{+0.2}_{-0.0}$	$0.2^{+0.4}_{-0.2}$
·····		`TBnew` — photoelectric absorption (`abund wilm, xsect vern`)			·····
$N_{\mathrm{H,22}}$	$\left[10^{22}\,\mathrm{cm^{-2}}\right]$	3 ± 2	3^{+3}_{-2}	$2.0^{+1.2}_{-0.6}$	2^{+4}_{-1}
χ^2/dof		$\frac{55.7}{69} = 0.81$	$\frac{41.8}{69} = 0.61$	$\frac{52.5}{68} = 0.77$	$\frac{41.0}{68} = 0.60$

Note. * The cut-off energy was restricted to $E_{\mathrm{cut}} \geq 15\,\mathrm{keV}$.

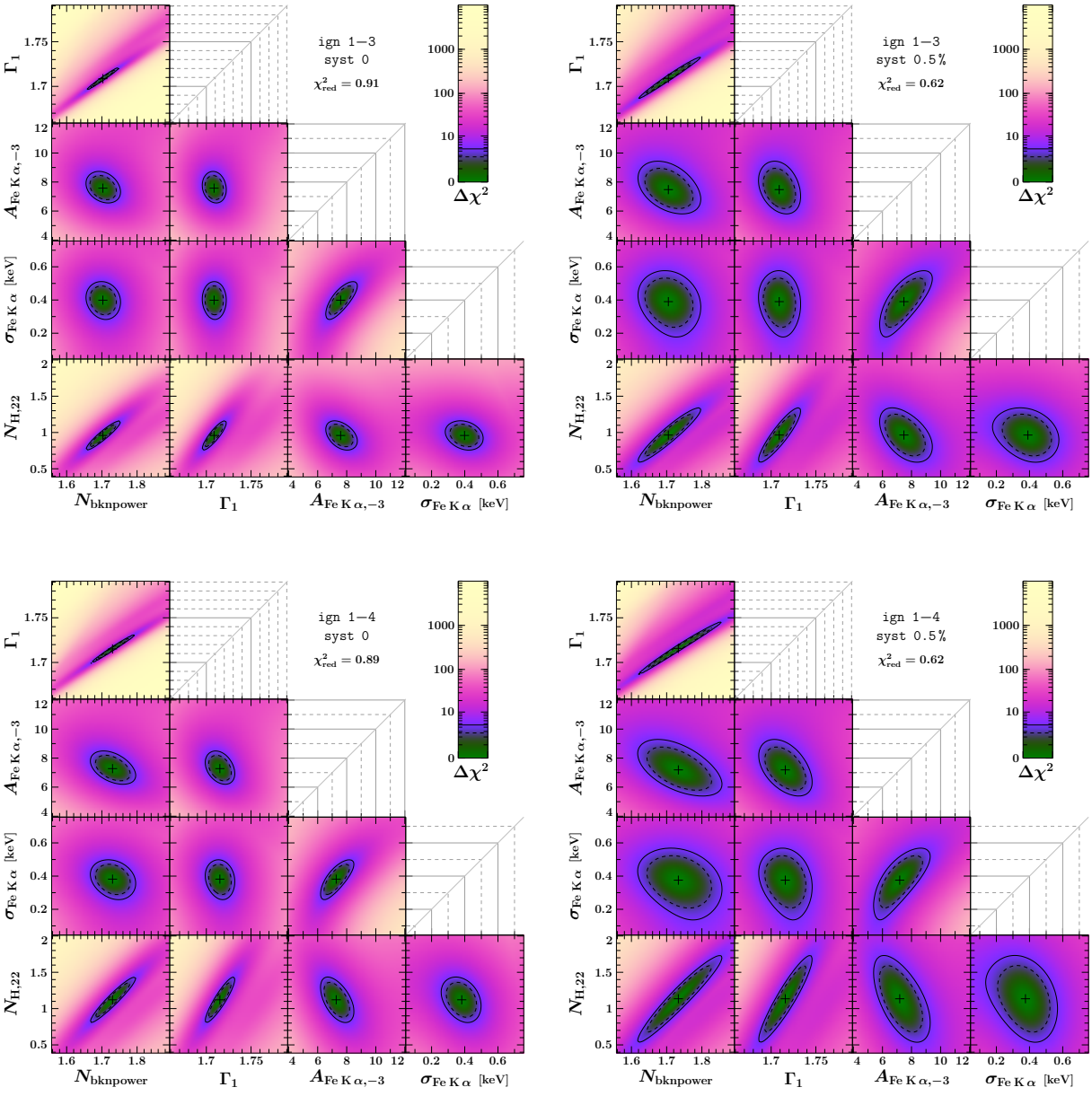

Figure 2.22: Matrices of two-parameter confidence maps for parameters of the '`bknpower`' model (2.30) for the hard state spectrum from ObsID 95338-07-01-00, see Table 2.2. The upper row of matrices was obtained by ignoring the first channels 1–3 at low energies ('`ign 1-3`'), while channel 4 was additionally ignored for the lower row ('`ign 1-4`'). The left column has no systematic errors applied ('`syst 0`'), while the right column has 0.5 % ('`syst 0.5%`'). The color scale of each confidence map indicates the difference of the local best fit χ^2 (when the corresponding two parameters are fixed at their respective values, while all others are left free to vary), relative to χ^2_0 of the global best fit, which is marked by a cross. The solid contour line at $\Delta\chi^2 = 2\log 10 \approx 4.61$ encloses 90 % probability for two parameters of interest; the projection of the dashed contour at $\Delta\chi^2 \approx 2.71$ onto each of the parameter axes gives the 90 % confidence interval for one parameter of interest. As the expansion of the χ^2 function around the global best fit is – in first approximation – a positive definite quadratic form, these confidence contours are nearly elliptic. An ellipse with major axes not parallel to the parameter axes indicates a degeneracy between model parameters that cannot be disentangled by the data. See text for further details.

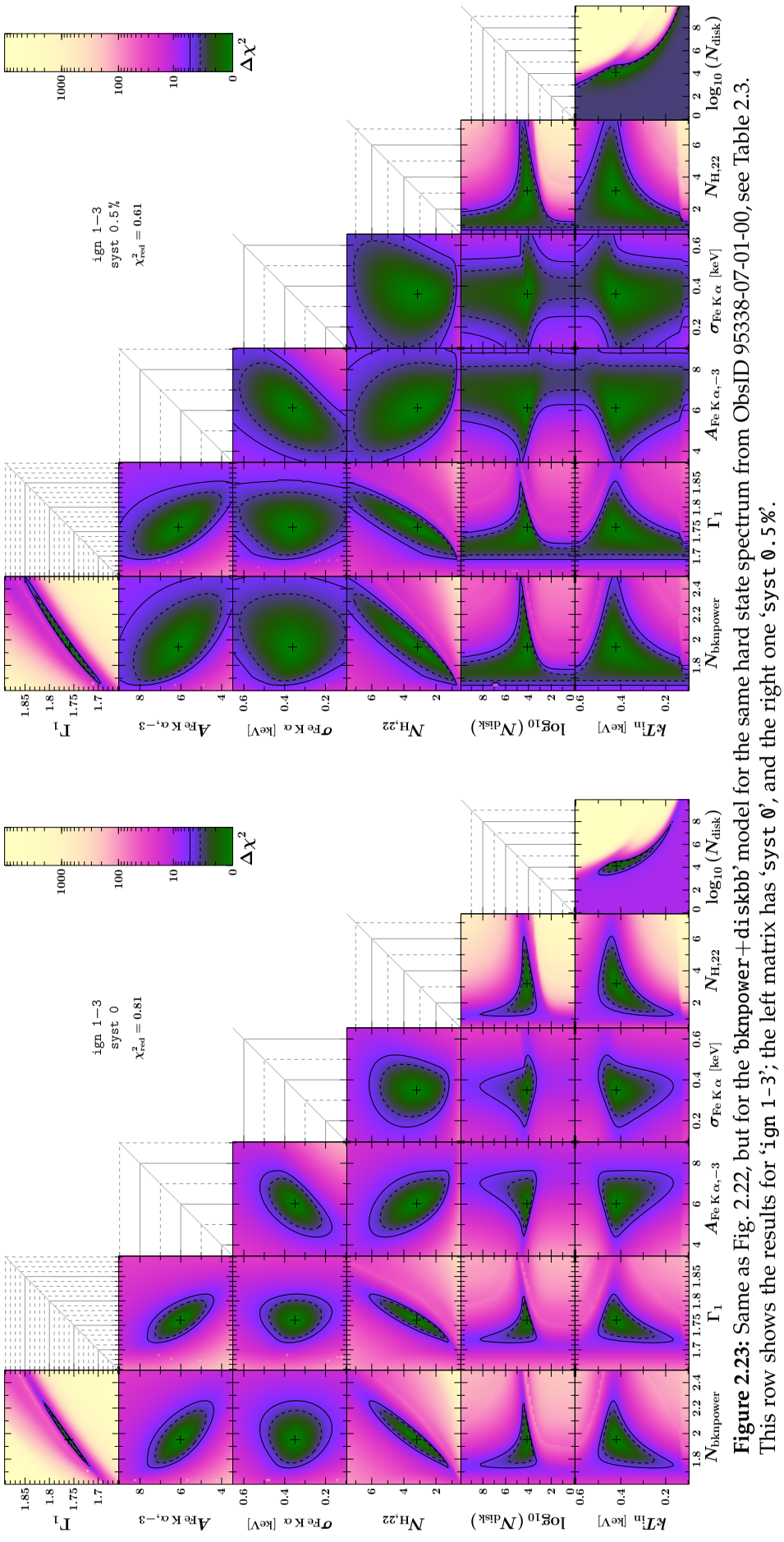

Figure 2.23: Same as Fig. 2.22, but for the '`bknpower+diskbb`' model for the same hard state spectrum from ObsID 95338-07-01-00, see Table 2.3. This row shows the results for '`ign 1-3`'; the left matrix has '`syst 0`', and the right one '`syst 0.5%`'.

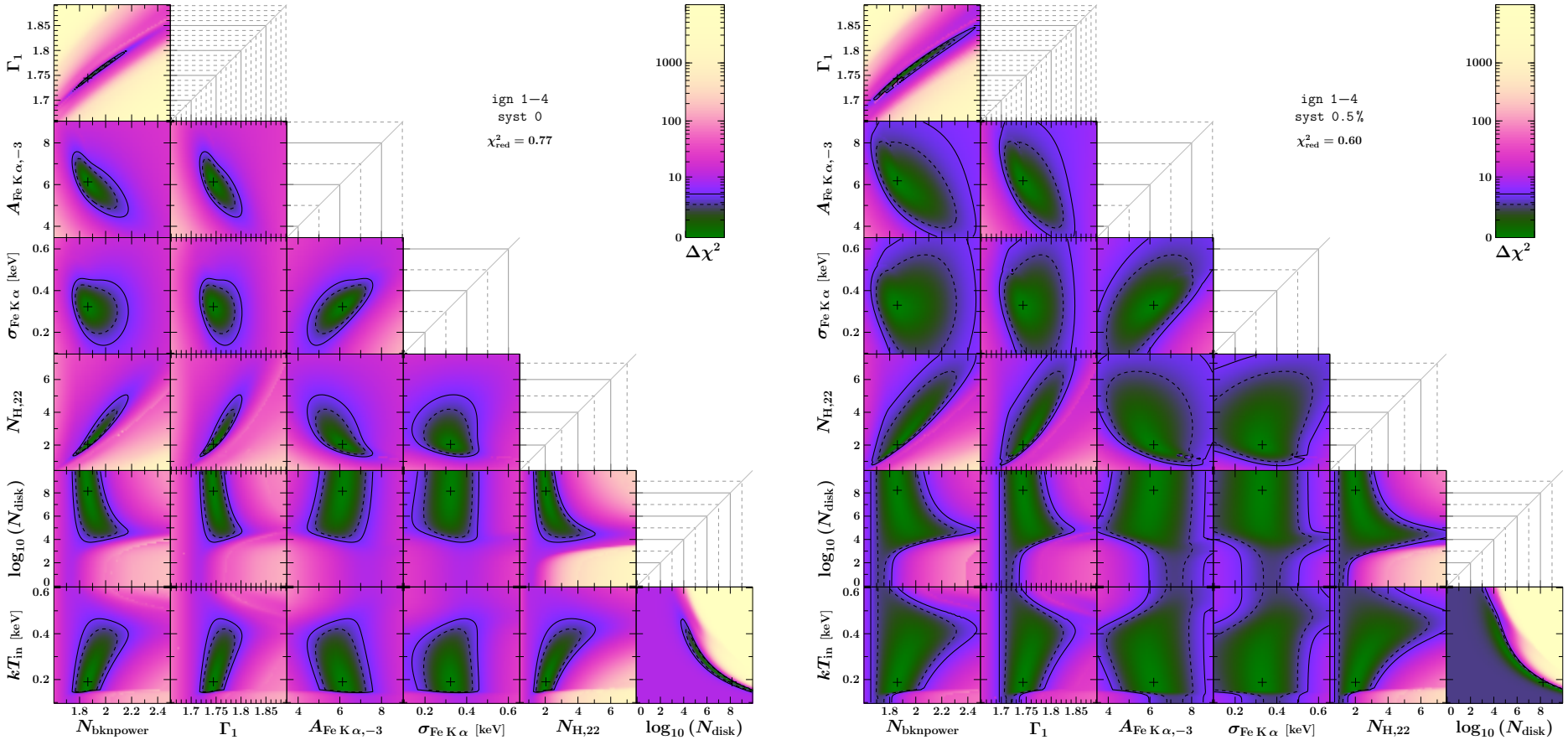

Figure 2.24: Same as Fig. 2.22, but for the '`bknpower`+`diskbb`' model for the same hard state spectrum from ObsID 95338-07-01-00, see Table 2.3. This row shows the results for '`ign 1-4`'; the left matrix has '`syst 0`', and the right one '`syst 0.5%`'.

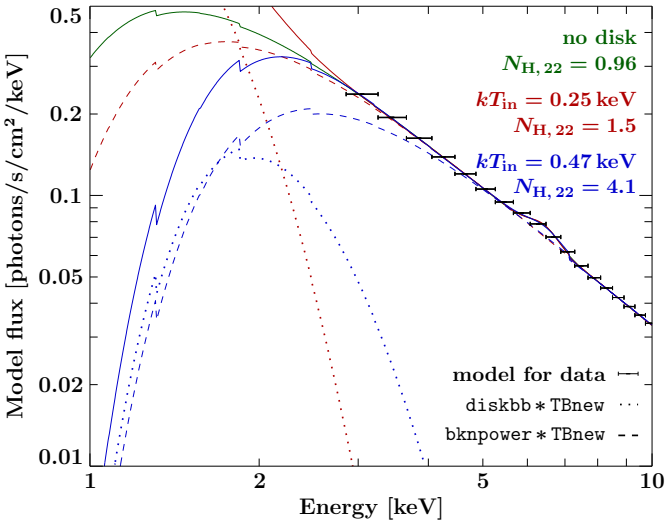

Figure 2.25: Models for the hard-state spectrum from ObsID 95338-07-01-00 with and without disk component. While the green line shows the best-fit '`bknpower`' model to the top-layer spectrum ('`ign 1-3`', '`syst 0`', see Table 2.2), the red and blue curves show the '`bknpower+diskbb`' model with lowest and highest T_{in} from its 90 % confidence interval (Table 2.3). The absorbed disk and power-law components are indicated by dotted and dashed lines, respectively. Adding a disk component increases N_H and its uncertainty.

$N_{H,22}$=$0.96^{+0.16}_{-0.15}$ to $3.2^{+1.5}_{-0.6}$ for '`ign 1-3`' and '`syst 0`'. Due to the correlations between $N_{bknpower}$, Γ_1, and N_H, which still hold for the '`bknpower+diskbb`' model (see Figs. 2.23 and 2.24), the stronger absorption also leads to a systematically steeper power-law at low energies $E<E_{break}$.

Soft state spectra

The observation from ObsID 95121-01-17-02 was chosen as a representative example for Cyg X-1 in the soft state. It was performed seven months after the hard state observation discussed above, on 2010-08-14, but at a very similar orbital phase ($\phi_{orb}\approx0.48$). Figure 2.26 shows that bin #4 (the first one considered with '`ign 1-3`') contains the highest count rate and therefore the largest statistical weight – unlike in Fig. 2.21: the hard state spectrum rises until bin #6 before it drops after #7. The fit results for this soft state spectrum will therefore depend more strongly on the calibration of bin #4 than those of the previous hard state example.

The '`bknpower`' model does not allow for an acceptable fit: even when 0.5 % systematic errors are added, the best fit has $\chi^2_{red}>8$. The '`bknpower+diskbb`' model can describe the spectrum, but comparing the results for the '`ign 1-3`' and '`ign 1-4`' configurations, the parameters relevant for the soft X-ray spectrum ($N_{bknpower}$, Γ_1, N_H) are not ('`syst 0`') or only marginally ('`syst 0.5%`') consistent with each other. In particular for the absorption, an unexpectedly high value $N_H\approx5\times10^{22}\,cm^{-2}$ was found for '`ign 1-3`', whereas the best fit for '`ign 1-4`' is $N_H = 0$, with an upper limit of $2\times10^{22}\,cm^{-2}$ for '`syst 0`'. This finding indicates that the calibration of bin #4 (which was either considered or ignored) may indeed be systematically off, whereas the previous results showed that bins #6 and #7, which have the dominant count rates in the hard state spectrum, do most likely not need systematic errors added. For this soft-state spectrum, it was found that adding systematic errors of 0.5 % to bins #4 and #5 *only* already lead to a significantly decreased N_H. Of course, systematic calibration uncertainties cannot be investigated with a single spectrum, but the large sample will later lead to the same result.

Table 2.4 shows the results from a modification of the '`bknpower+diskbb`' model (Eq. 2.31):

$$\big(\texttt{bknpower} + \texttt{egauss} + \texttt{diskbb}\big) * \texttt{TBnew} \otimes \texttt{backcorr} \qquad (2.32)$$

The convolution '$\otimes$ `backcorr`' is here only used to formally denote background correction as in Eq. (1.65). Although the soft X-ray flux is higher in the soft state, the power-law component falls off much faster than in the hard state – namely with a high-energy photon index $\Gamma_2\approx2.1$, compared to $\Gamma_2\approx1.5$ for the example of Tables 2.2 and 2.3. Above 7.6 keV, the flux in the

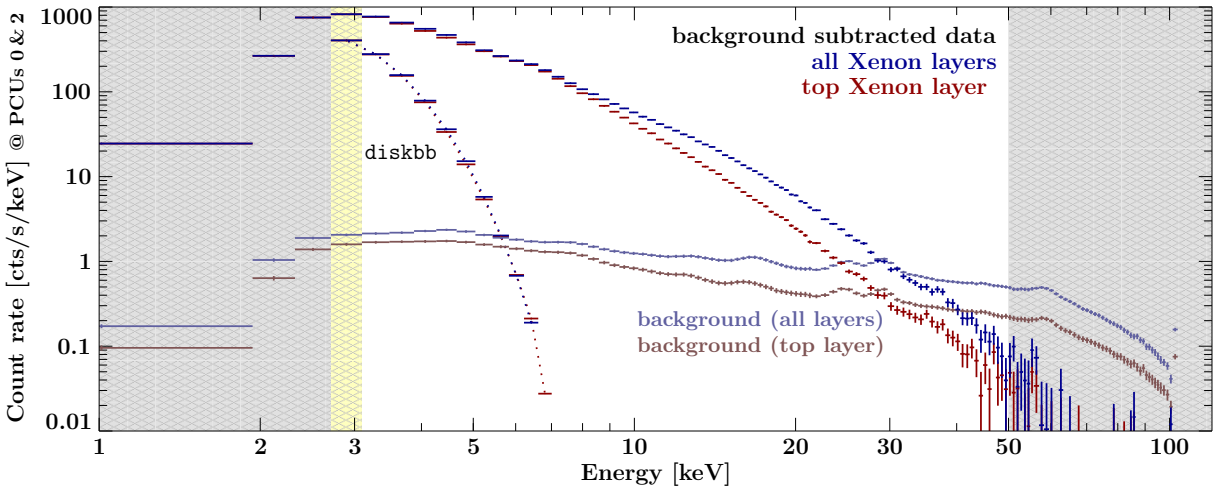

Figure 2.26: Same as Fig. 2.21, but for the soft-state observation from ObsID 95121-01-17-02. Since these data are collected from two PCUs (0 and 2), but the hard state spectrum of Fig. 2.21 is solely recorded with PCU 2, the count rates here are in general approximately twice as high for instrumental reasons, irrespective of the spectral differences. The dotted line illustrates the `diskbb` component, which is clearly required in this spectrum. As the power-law drops much steeper than in the hard state spectrum of Fig. 2.21, the 30–50 keV range is already dominated by the instrumental background.

Table 2.4: Parameters of the '`bknpower`+`diskbb`' model (2.32) for the soft state spectrum from ObsID 95121-01-17-02, observed on 2010-08-14 (segment at 22:35–22:54 UT)

Parameter	[Unit]	'`ign 1-3`'		'`ign 1-4`'	
		'`syst 0`'	'`syst 0.5%`'	'`syst 0`'	'`syst 0.5%`'
·····	`bknpower` — broken power-law	·····			
N_{bknpower}	$\left[\frac{\mathrm{ph}}{\mathrm{s\,cm^2\,keV}}\right]$	$20.4^{+1.6}_{-1.5}$	19^{+4}_{-3}	$16.1^{+0.3}_{-0.4}$	$16.1^{+0.7}_{-0.8}$
Γ_1		2.93 ± 0.03	2.91 ± 0.07	2.845 ± 0.011	2.84 ± 0.02
E_{break}	[keV]	10.61 ± 0.16	10.60 ± 0.19	10.51 ± 0.16	10.50 ± 0.19
Γ_2		2.12 ± 0.03	2.12 ± 0.03	2.09 ± 0.03	2.09 ± 0.03
·····	`egauss` — Fe Kα fluorescence line at 6.4 keV	·····			
$A_{\mathrm{Fe\,K}\alpha,-3}$	$\left[10^{-3}\,\frac{\mathrm{ph}}{\mathrm{s\,cm^2}}\right]$	$28.4^{+1.7}_{-1.6}$	29 ± 3	27.0 ± 1.4	27 ± 2
$\sigma_{\mathrm{Fe\,K}\alpha}$	[keV]	0.70 ± 0.04	$0.69^{+0.08}_{-0.07}$	0.62 ± 0.04	0.62 ± 0.06
·····	`diskbb` — disk blackbody component	·····			
$\log_{10} N_{\mathrm{disk}}$		$5.97^{+0.18}_{-0.20}$	$5.9^{+0.4}_{-0.5}$	5.9 ± 0.2	$5.9^{+0.6}_{-0.5}$
kT_{in}	[keV]	$0.360^{+0.010}_{-0.009}$	$0.37^{+0.03}_{-0.02}$	$0.333^{+0.017}_{-0.016}$	0.33 ± 0.04
·····	`TBnew` — photoelectric absorption (`abund wilm, xsect vern`)	·····			
$N_{\mathrm{H},22}$	$[10^{22}\,\mathrm{cm^{-2}}]$	$5.1^{+1.1}_{-1.2}$	4 ± 3	≤ 1.8	≤ 5
·····	`constant` — background correction factor	·····			
c_{back}		0.92 ± 0.02	0.91 ± 0.03	0.91 ± 0.02	0.91 ± 0.03
χ^2/dof		$\frac{90.0}{62} = 1.45$	$\frac{43.8}{62} = 0.71$	$\frac{71.4}{61} = 1.17$	$\frac{41.5}{61} = 0.68$

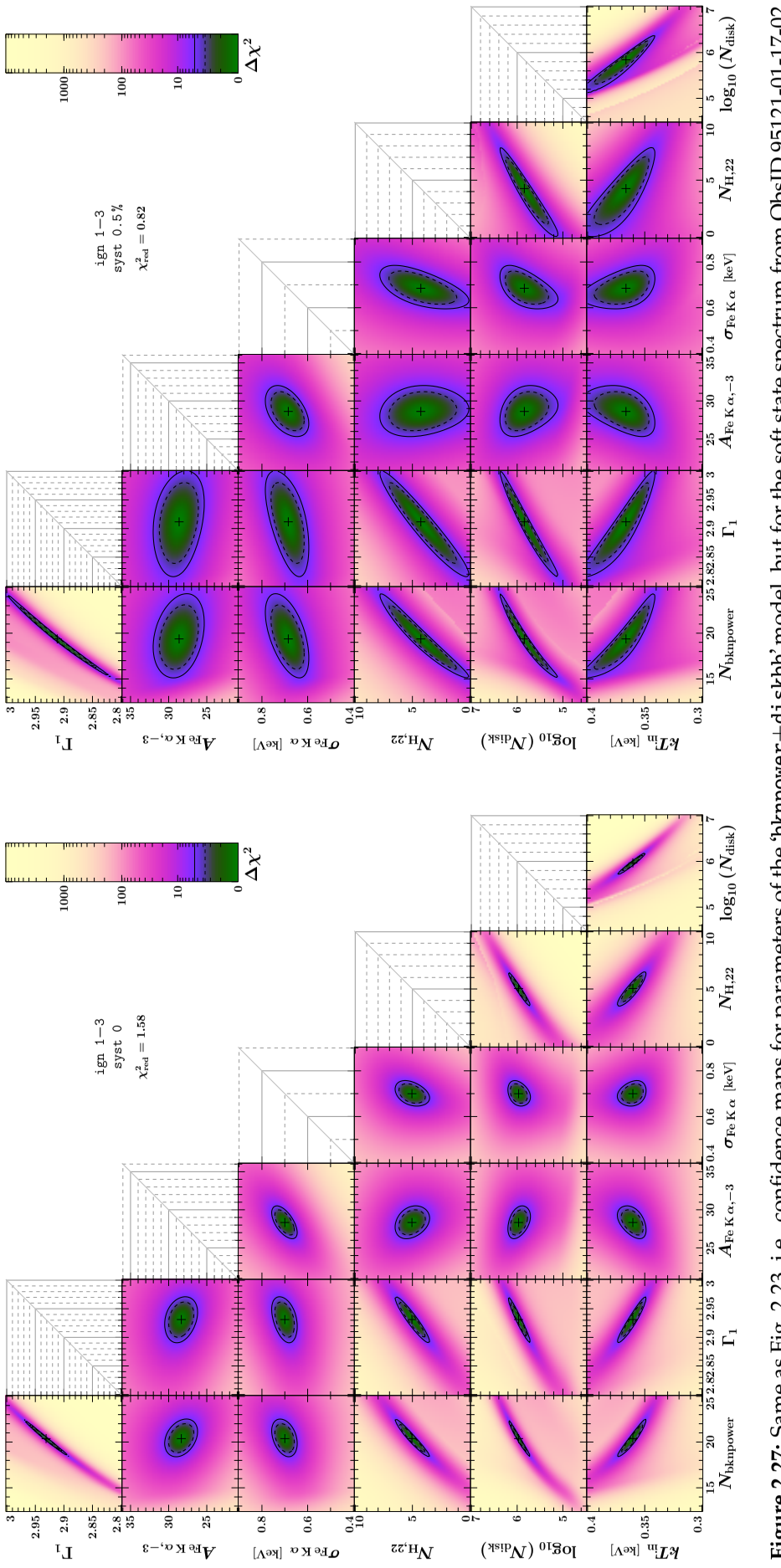

Figure 2.27: Same as Fig. 2.23, i.e., confidence maps for parameters of the '`bknpower+diskbb`' model, but for the soft state spectrum from ObsID 95121-01-17-02, see Table 2.4. This row shows the results for '`ign 1-3`'; the left matrix has '`syst 0`', and the right one '`syst 0.5 %`'.

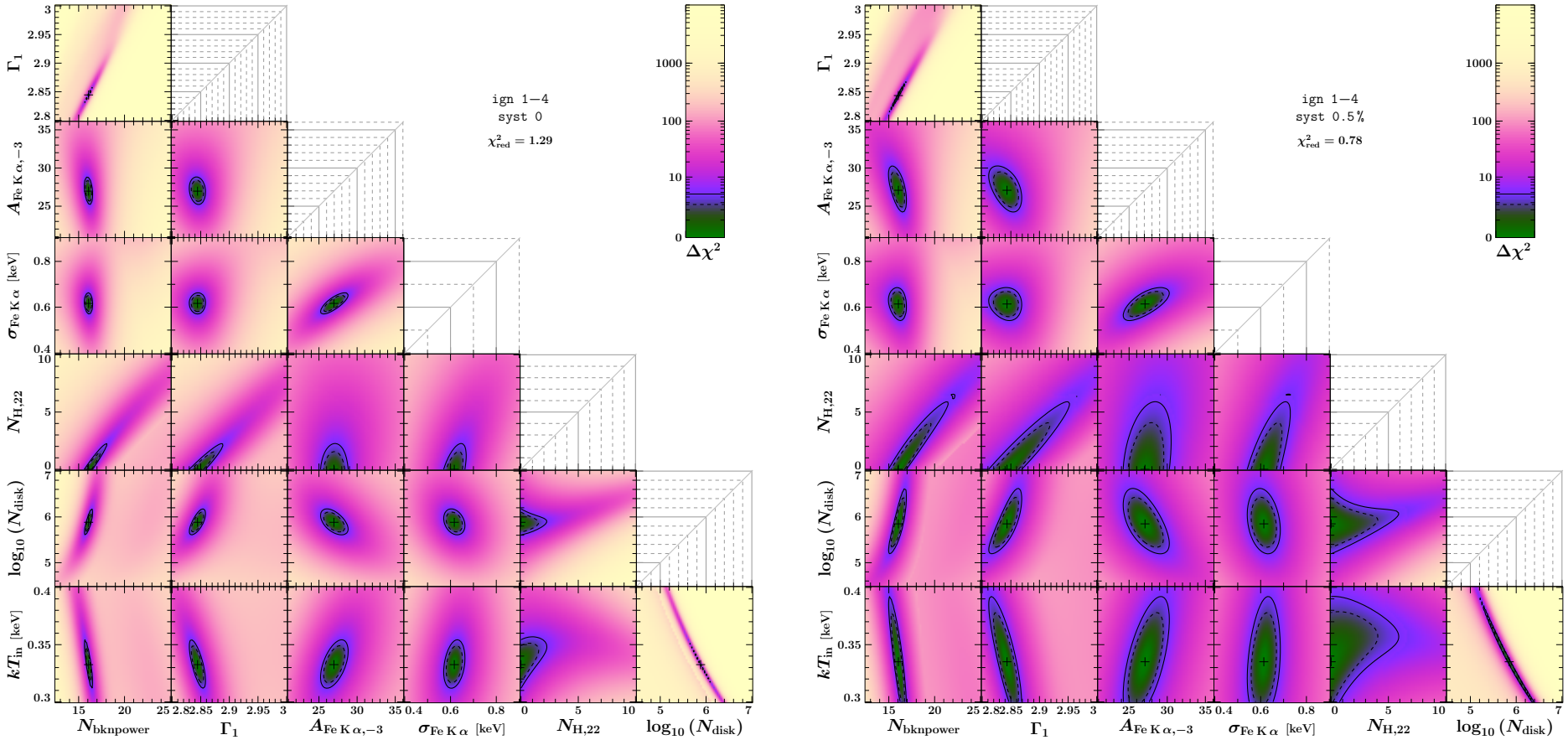

Figure 2.28: Same as Fig. 2.24, i.e., confidence maps for parameters of the '`bknpower`+`diskbb`' model, but for the soft state spectrum from ObsID 95121-01-17-02, see Table 2.4. This row shows the results for '`ign 1-4`'; the left matrix has '`syst 0`', and the right one '`syst 0.5%`'.

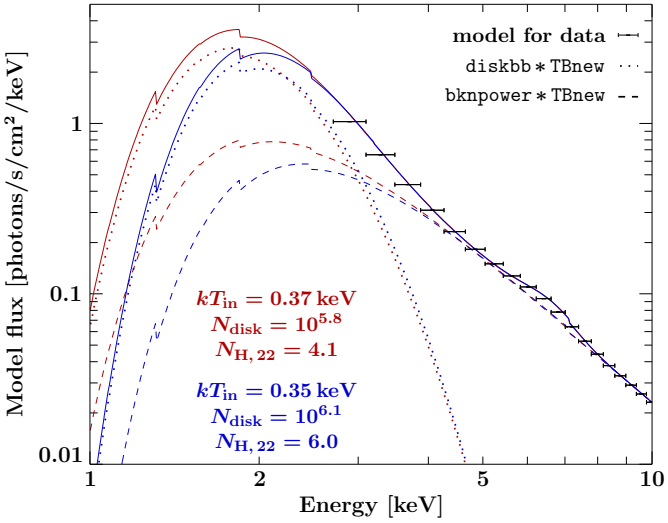

Figure 2.29: '`bknpower`+`diskbb`' models for the soft-state spectrum from ObsID 95121-01-17-02 (for '`ign 1-3`', '`syst 0`'; see also Fig. 2.26). As in Fig. 2.25, the red and blue curves show the models with lowest and highest disk temperature T_{in} from its 90 % confidence interval (Table 2.4). The absorbed disk and power-law components are indicated by dotted and dashed lines, respectively. Unlike in the hard state example, T_{in} is constrained to ±3 %. On the other hand, N_H is still uncertain to ±24 %.

soft state spectrum (Fig. 2.26) is actually *lower* than in the hard state spectrum (Fig. 2.21), and the background of the PCA becomes dominant above 30 keV in the former spectrum, while the latter stays source-dominated up to 50 keV. A detailed modelling of the high-energy spectrum requires therefore an accurate estimation of the instrumental background. For this soft state spectrum – with a relatively short PCA exposure of only 1.1 ks (to be compared with Fig. 2.19) – the *RXTE* PCA data below 50 keV do not constrain the high-energy cutoff, which is nevertheless required – unless a background correction factor c_{back} according to Eq. (1.65) is introduced. If, on the other hand, the count rates predicted by the SkyVLE background model are reduced by ∼9 %, corresponding to $c_{back} \approx 0.91$, the data can be equally well described by the model in Eq. (2.32) without high-energy cutoff. As virtually none of the other parameters are affected – neither in their value, nor in their uncertainties – by the question of how much of the exponential cutoff at high energies is due to improper background modelling, this issue can safely be ignored for the present analysis.

Figures 2.27 and 2.28 show the confidence maps for the model parameters relevant to the soft X-ray spectrum. The `disk` parameters of the soft state spectrum are better constrained and more clearly correlated with the '`bknpower`' parameters than those of the hard state spectrum (Figs. 2.22, 2.23 and 2.24). For the soft state spectrum, the disk normalization N_{disk} follows $N_{bknpower}$, Γ_1, and N_H, which are – as in the hard state – positively correlated themselves. The disk's temperature T_{in} is anticorrelated with all of them. That is, when a disk component is indeed present in the spectrum, it can either be modelled by a brighter (but cooler) disk that is more strongly absorbed or by a fainter (but hotter) disk that is less strongly absorbed, see Figure 2.29. (For the hard state spectrum, the correlations of the `diskbb` parameters with the '`bknpower`' parameters were just vice versa, i.e., a hotter, fainter disk had to be more strongly absorbed than a cooler, brighter one.)

2.3.2 Broken Power-Law Fits to all Data from 14.5 Years

After these preliminary studies of hard and soft state spectra and the systematic effects affecting their fit parameters, *all* 2247 segments (Table B.2 on page 149) were modelled in an automated way with the following combinations of configurations:

1. with background correction factor c_{back} from Eq. (1.65) both fixed to 1 and freely variable,
2. for '`syst 0`' as well as '`syst 0.5 %`',
3. with the '`bknpower`' model as well as with the '`bknpower`+`diskbb`' model, and
4. for '`ign 1-3`' as well as '`ign 1-4`'.

Table 2.5 shows the number of acceptable fits that were obtained with these combinations. The following general conclusions can be drawn:

1. Background correction turns out to be only important for very few of the spectra. The distribution of $\Delta\chi^2$ and $\Delta\chi^2_{\rm red}$ is shown in Fig. 2.30. For most of the spectra, the improvement in χ^2 when letting $c_{\rm back}$ vary is not enough to get a significant improvement in $\chi^2_{\rm red} = \chi^2/\nu$. As the number of degrees of freedom, ν, decreases when additional model parameters are introduced, $\Delta\chi^2_{\rm red} = \chi^2_{\rm red}(c_{\rm back}\equiv 1) - \chi^2_{\rm red}(c_{\rm back}\ \text{free})$ may also become negative. The median of $\Delta\chi^2_{\rm red}$ is in fact -0.004, but on average $\chi^2_{\rm red}$ is improved by $\langle\Delta\chi^2_{\rm red}\rangle = +0.03$. As $\chi^2_{\rm red}$ is not worsened by more than 0.03 for all spectra with $\chi^2_{\rm red}(c_{\rm back}\ \text{free}) < 2$ considered in Fig. 2.30,[14] but since a few fits are significantly improved, background correction will always be considered in the following discussion. Even for fits that are not improved, the systematic change of the parameters describing the low-energy spectrum by the introduction of background correction is generally much lower than their statistical uncertainty.

2. The fact that adding '`syst 0.5%`' gives $\chi^2_{\rm red}<1$ for more than two thirds of the fits (of any configuration) clearly indicates that the uncertainties of the Cyg X-1 data are overestimated by adding 0.5 % systematic errors, i.e., that the calibration of the PCA is now more accurate than 0.5 % for Cyg X-1. Unless explicitly stated otherwise, '`syst 0`' will be assumed in the following. As the actual systematic uncertainties may lie between 0 and 0.5 %, the resulting χ^2 values may be overestimated when systematics are entirely neglected. An additional configuration – adding systematic errors to channels #4 and #5 only – will be investigated in Sect. 2.3.3 (Fig. 2.39, Table 2.6). It is not part of the comparison in the present section.

3. It is already obvious from the preliminary studies that the '`bknpower`' model fails to describe the spectrum in the soft state. Figure 2.31 shows that there is a clear correlation of the quality of the fit and its photon index Γ_1 as a measure for the spectral hardness: the softer the spectrum, the worse its description with the '`bknpower`' model. That is, the disk component becomes gradually stronger and more significant in the energy range of the PCA. With '`syst 0`', two thirds of the '`bknpower`' fits with $\Gamma_1 \le 2$ have $\chi^2_{\rm red}<2$. When 0.5 % systematic errors are added, more than 99 % of the fits with $\Gamma_1 \le 2.2$ have $\chi^2_{\rm red}<2$. 85 % of those have even $\chi^2_{\rm red}<1$, which again shows that adding '`syst 0.5%`' overestimates the actual uncertainties of the data.

   For fits with the '`bknpower+diskbb`' model, on the other hand, the goodness of the fits is independent of the spectral hardness (Fig. 2.31). According to Table 2.5, 91 % of the fits with '`syst 0`' have $\chi^2_{\rm red}<2$, and 94 % of those with '`syst 0.5%`' have $\chi^2_{\rm red}<1$. If the disk modelled in the hard state observations were real, the '`bknpower+diskbb`' model would provide a continuous set of parameter values over the whole parameter space covered by Cyg X-1. However, when changing from the '`bknpower`' model for the hard state to the '`bknpower+diskbb`' model for the soft state, there are systematic differences in the parameters. Figure 2.32 shows the gradual increase of the difference in the photon indices Γ_1 derived with the two models, which is accompanied by a systematic difference in $N_{\rm H}$: fits including the `diskbb` component have a bias toward a steeper power-law that seems unreasonably strong absorbed.

4. In the hard state, '`ign 1-3`' is favored compared to '`ign 1-4`', as the former configuration allows to constrain the low-energy parameters much more tightly than the latter one – especially $N_{\rm H}$, for which the average uncertainty is increased by 66 % if bin #4 is excluded. However, in the soft state, when bin #4 is the dominant one, calibration uncertainties do become relevant. $N_{\rm H}$('`ign 1-3`') tends to be larger than $N_{\rm H}$('`ign 1-4`'), and the difference is growing with the softness of the spectrum, see Fig. 2.33.

[14] If χ^2 is not improved by background correction, $\Delta\chi^2_{\rm red}$ is $\frac{\chi^2}{\nu} - \frac{\chi^2}{\nu-1} = \frac{-\chi^2}{\nu(\nu-1)}$. The formal worsening of unacceptable fits with high χ^2 (e.g., soft state spectra described with the '`bknpower`' model) can be arbitrarily large.

Table 2.5: Number of good / acceptable fits from 2247 *RXTE* PCA spectra of Cyg X-1

	Model	$c_{\rm back}$	'ign 1-3'		'ign 1-4'	
			'syst 0'	'syst 0.5%'	'syst 0'	'syst 0.5%'
$\chi^2_{\rm red} < 1$	'bknpower'	$\equiv 1$	172	1513	236	1696
		free	174	1554	242	1753
	'bknpower+diskbb'	$\equiv 1$	557	2117	802	2117
		free	592	2187	852	2200
$\chi^2_{\rm red} < 1.5$	'bknpower'	$\equiv 1$	755	1821	901	1925
		free	765	1839	920	1945
	'bknpower+diskbb'	$\equiv 1$	1729	2225	1999	2226
		free	1776	2235	2052	2240
$\chi^2_{\rm red} < 2$	'bknpower'	$\equiv 1$	1111	1888	1311	1976
		free	1120	1896	1327	1995
	'bknpower+diskbb'	$\equiv 1$	2049	2229	2174	2233
		free	2076	2237	2205	2242

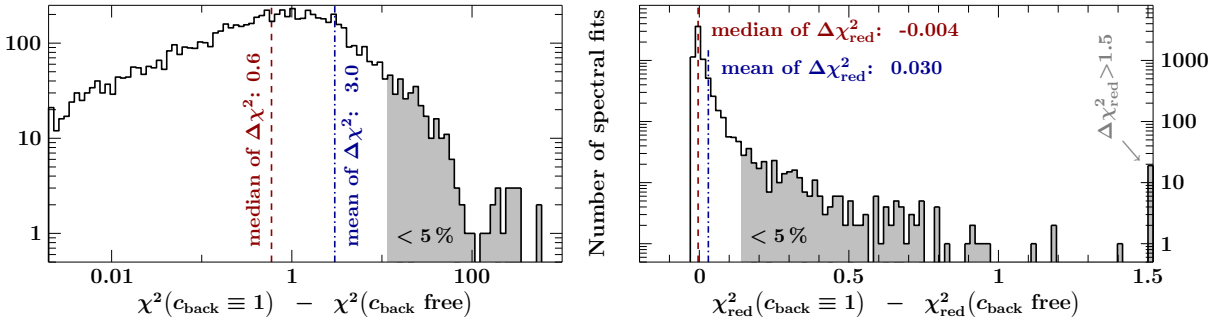

Figure 2.30: Effect of the background normalization factor $c_{\rm back}$ on spectral fits to the 2247 segments of *RXTE* PCA data from Cyg X-1. The histograms show the distribtions of the improvement in χ^2 (left) and $\chi^2_{\rm red}$ (right) when $c_{\rm back}$ was allowed to vary. Only fits that gave $\chi^2_{\rm red}(c_{\rm back}\ {\rm free}) < 2$ were considered. As the distributions for the 'syst 0' / 'syst 0.5%' and 'bknpower' / 'bknpower+diskbb' modelling were very similar, all 1120 + 1896 + 2076 + 2237 results for spectra with 'ign 1-3' (see Table 2.5) have been combined. Only a small fraction of spectra require a background correction $c_{\rm back} \neq 1$; for the majority, the gain in χ^2 is too small to compensate for the additional degree of freedom, and $\chi^2_{\rm red}$ gets worse.

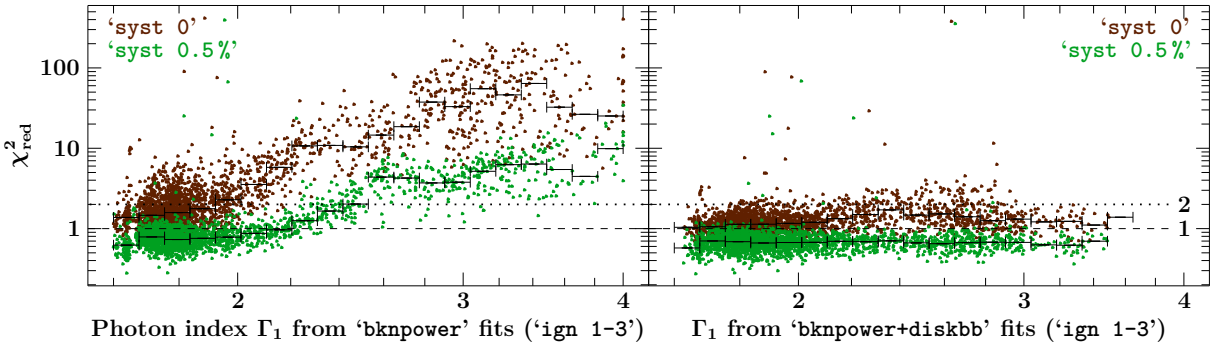

Figure 2.31: Goodness of fits to 2247 *RXTE* PCA top layer spectra ('ign 1-3') of Cyg X-1, obtained with the 'bknpower' (left) or 'bknpower+diskbb' (right) model, for 'syst 0' (blue) and 'syst 0.5%' (red), as a function of the photon index Γ_1 (which is often overestimated by the 'bknpower' model, in particular when fitted to a soft state spectrum, see Fig. 2.32). For each distribution, the histogram indicates the median of the $\chi^2_{\rm red}$ values in 20 bins from Γ_1=1.6–4. The dashed and dotted horizontal lines correspond to $\chi^2_{\rm red}$=1 and 2, respectively.

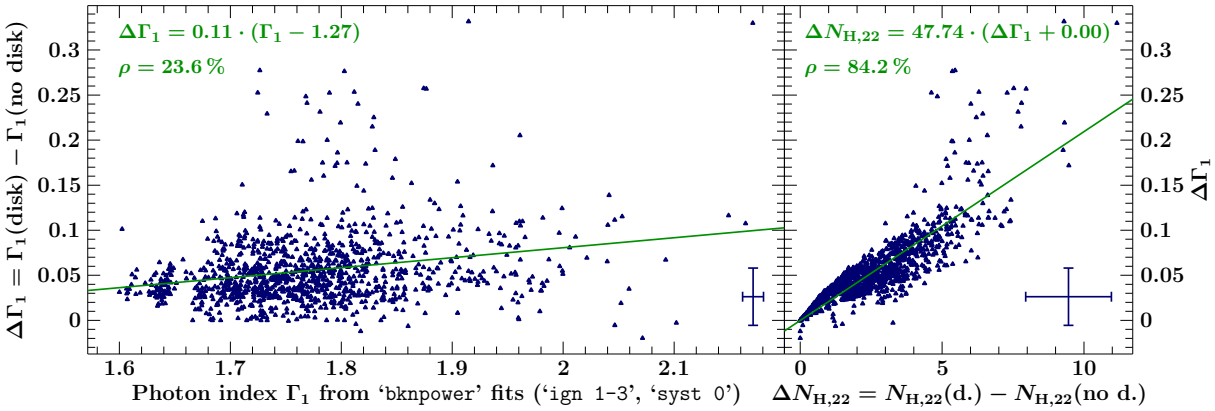

Figure 2.32: Systematic difference in Γ_1 (left) and N_H (right) between the '`bknpower`' model and the '`bknpower+diskbb`' model for those 1120 segments that gave a $\chi^2_{red}<2$ with both models ('`ign 1-3`', '`syst 0`'). Average error bars are indicated in the lower right corner of each panel. The green lines are (unweighted) linear fits to the data. ρ is the linear correlation coefficient.

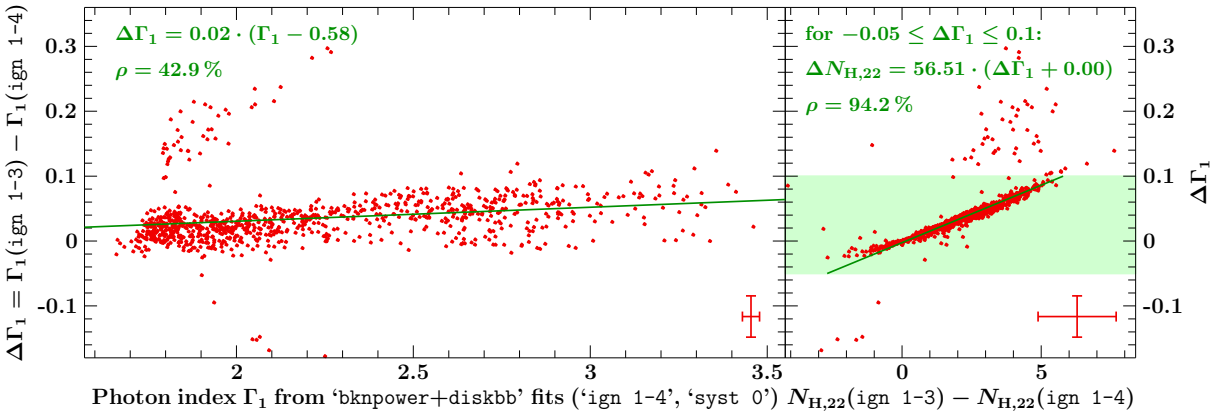

Figure 2.33: Same as Fig. 2.32, but for the systematic difference in Γ_1 (left) and N_H (right) between the '`ign 1-3`' and the '`ign 1-4`' configuration for those 956 segments that gave $\chi^2_{red}\geq 2$ with the '`bknpower`' model, but $\chi^2_{red}<2$ with the '`bknpower+diskbb`' model (using '`syst 0`'). In the right panel, the fit applies only to data with $-0.05 \leq \Delta\Gamma_1 \leq 0.1$ in the shaded region.

Data selection for further analysis

To avoid unnecessary degeneracies between the model parameters, the simpler '`bknpower`' model is used for as many data segments as reasonably possible. 1120 segments (out of 2247, i.e., 50 %; see Table 2.5) allow for a fit with $\chi^2_{red}<2$ (using '`syst 0`' and '`ign 1-3`'), which can be considered to be acceptable given that χ^2 may be overestimated due to systematic calibration uncertainties, which are probably less than 0.5 % for the dominant bins in the hard state spectra, but not necessarily 0. These segments correspond to hard state spectra, and have $\Gamma_1<2.18$ and $\Gamma_2<1.73$, see also Fig. 2.32. They will be referred to as *'the hard sample'* and depicted by blue triangles in Figs. 2.32–2.38. The '`bknpower+diskbb`' model gives an acceptable fit with $\chi^2_{red}<2$ for 956 of the remaining 1127 segments. Although these data comprise most of the soft states, the sample contains hard state spectra as well. The photon indices are only limited by $\Gamma_1>1.64$, and $\Gamma_2>1.42$, see also Fig. 2.33. This selection will still be called *'the soft sample'* and indicated by red circles in Figs. 2.33–2.38.

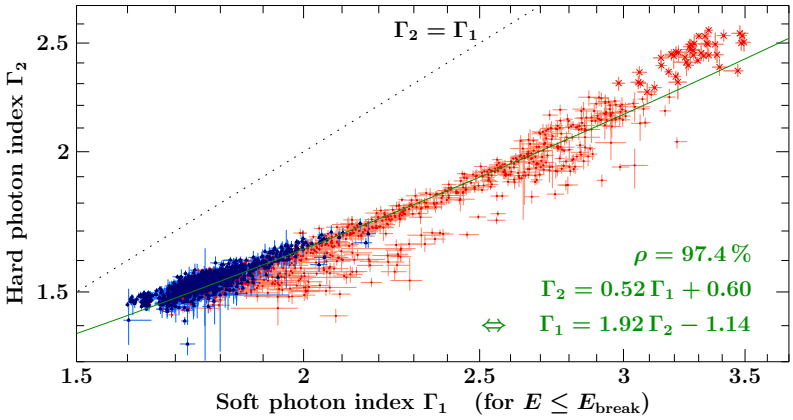

Figure 2.34: Correlation between the photon indices Γ_1 and Γ_2, from 1120 '`bknpower`' fits (blue) and 956 '`bknpower+diskbb`' fits (red). Crosses indicate very soft states with Γ_2>2.25. ρ is the linear correlation coefficient. The green line is an unweighted linear fit.

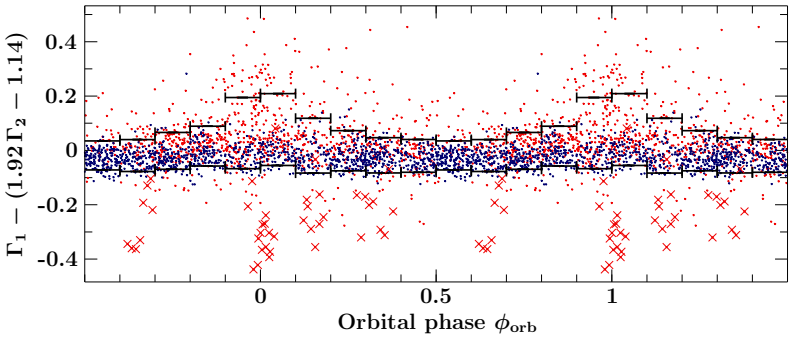

Figure 2.35: Orbital phase dependence of the deviation of the photon indices Γ_1 and Γ_2 from the linear relation of Fig. 2.34, repeated twice for clarity. The black histograms show 10 and 90 % quantiles in ten phase bins.

Spectral evolution from 1996 to 2010

It was already found in previous studies (Wilms et al., 2006, fig. 3; Böck et al., 2008, fig. 3) that the photon indices of Cyg X-1 are tightly correlated, and that the break $\Gamma_1 - \Gamma_2$, which is related to reflection, increases with the softness of the spectrum. Figure 2.34 shows the results obtained from automated fits to this greatly enlarged data set. With a linear correlation coefficient $\rho > 97\,\%$, most of the measurements can well be described by a linear function extending from the hard state to soft-intermediate states at $\Gamma_1 \lesssim 2.6$ and $\Gamma_2 \lesssim 1.95$:

$$\begin{aligned} \Gamma_2 &= 1.7736 + 0.5214 \cdot(\Gamma_1 - 2.26) \quad \text{(unweighted fit)} \\ \text{or} \quad \Gamma_2 &= 1.7736(5) + 0.4977(11)\cdot(\Gamma_1 - 2.26) \end{aligned} \tag{2.33}$$

The second fit has been obtained with the algorithm of Fasano & Vio (1988), which takes the uncertainties into account and gives a slightly different slope as the unweighted linear regression fit. Outliers from the linear correlation in Fig. 2.34 appear in the soft state above the line, and at any hardness below this line. While the former may indicate a Γ_1-Γ_2-relation with a different slope in the soft state, the latter occur preferentially close to orbital phase $\phi_{\rm orb}$=0, see Fig. 2.35. These are therefore likely to be related to absorption events in the stellar wind, which will be discussed in the next section.

The hardness-intensity diagrams (HIDs) of Fig. 2.36 show that the observed soft X-ray flux in the 3–10 keV band (as calculated with the `cflux` model giving proper 90 % confidence limits, see Sect. 1.3.4) increases as the spectrum gets softer, up to $\Gamma_1 \lesssim 2.9$ and $\Gamma_2 \lesssim 2.1$, but decreases again for even softer phases. This behavior is also seen in HIDs from *RXTE*-ASM data or MAXI's soft X-ray data (Figs. 2.10 and 2.11, on page 54). Figure 2.36 also shows that the brightening in the soft state is not only due to the disk component, whose flux is less than 20 % of the total flux in the 3–10 keV band. In contrast, the hard X-ray flux (e.g., in the 20–40 keV band) is correlated with spectral hardness, which was already seen in MAXI HIDs from hard X-ray count rates, such as 10–20 keV vs. (10–20 keV)/(4–10 keV) in Fig. 2.11.

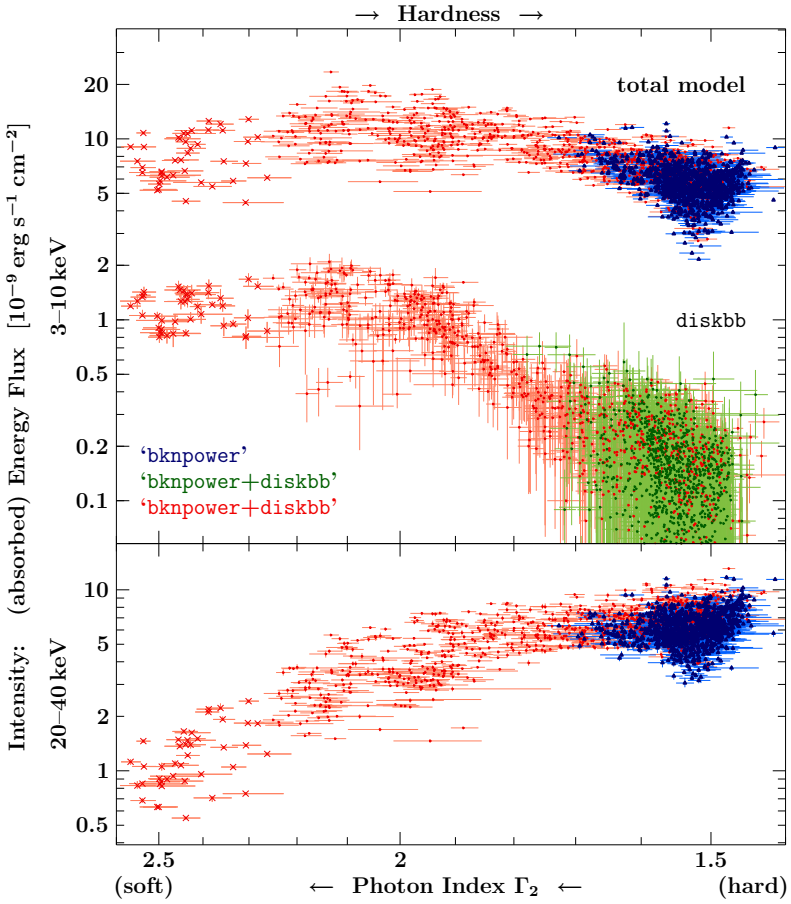

Figure 2.36: Hardness intensity diagrams of Cyg X-1 from *RXTE* PCA spectral fits. The hardness is given by Γ_2, which has a smaller systematic uncertainty than Γ_1. The upper panel shows the absorbed energy flux in the 3–10 keV band for both the total model and the `diskbb` component only, which are (largely) anticorrelated with spectral hardness, except for the very softest states. The lower panel shows the energy flux in the 20–40 keV band, which is correlated with spectral hardness. The data points and their colors correspond to the selection in Fig. 2.34, except for the disk flux of the hard sample (green data points), which has obviously also been measured with the '`bknpower+diskbb`' model.

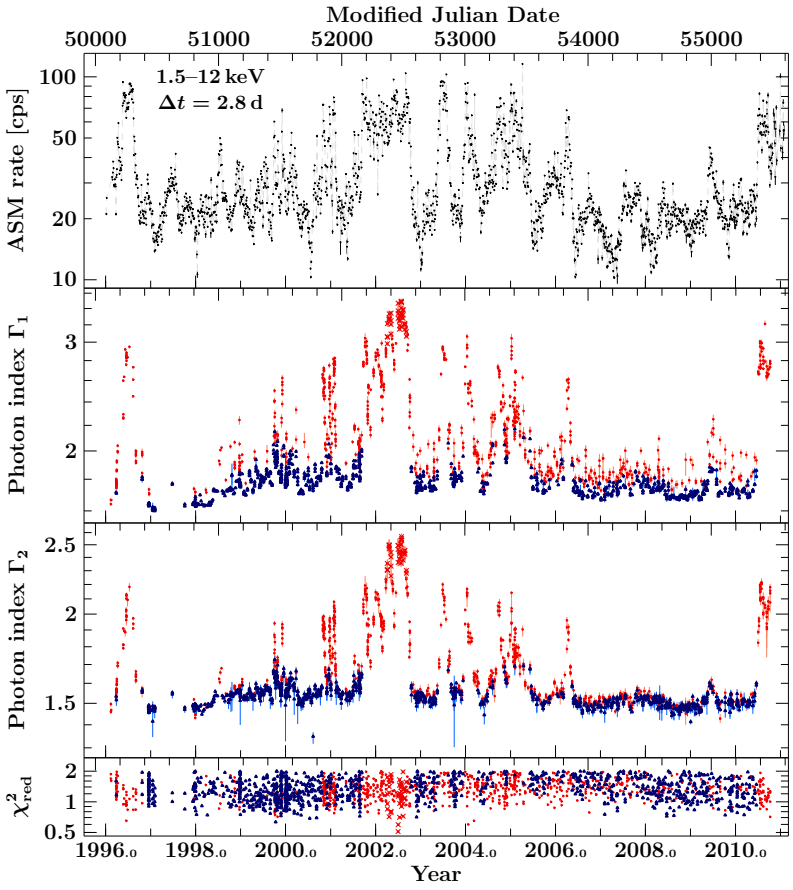

Figure 2.37: Spectral evolution of Cyg X-1 from 1996 to 2010 Oct. The top panel displays the *RXTE* ASM (1.5–12 keV) light curve. The middle panels show the photon indices Γ_1 and Γ_2 from *RXTE* PCA '`bknpower`' and '`bknpower+diskbb`' fits, using the same data and color scheme as in Fig. 2.34. The bottom panel shows $\chi^2_{\rm red}$, which is always below 2 due to the data selection, but does not show a clear evolution with time. As in the previous figures, the crosses mark spectra with $\Gamma_2 \geq 2.25$, which was only reached during the soft state in 2002.

Figure 2.37 shows the spectral evolution of Cyg X-1 from 1996 to 2010 in terms of the power-law's photon indices, in comparison with the *RXTE* ASM long-term light curve. Due to the Γ_1-Γ_2 relation and the correlations between spectral shape and flux from the hardness intensity diagrams (Fig. 2.36), these parameters evolve in a very similar way, except for the fact that Γ_1 appears less continuous than Γ_2 due to the systematic offset between '`bknpower`' and '`bknpower+diskbb`' fits (Fig. 2.32). The major soft states in 1996 (Cui et al., 1997; Zhang et al., 1997), in 2001/2002 (Pooley, 2001; Pottschmidt et al., 2003), and in 2010 (Grinberg et al., 2010, 2011) are clearly discernible, as well as the flaring periods with failed state transitions and brief excursions to the soft state in 1998 (Pottschmidt et al., 2000), in 2000/2001 (Cui et al., 2002; Pottschmidt et al., 2003), from 2003 to 2006 (Wilms et al., 2006; Böck et al., 2008), in 2004 (Miller et al., 2009b) and in 2009 (Grinberg et al., 2011).

The analysis of the spectral properties of Cyg X-1 is, however, not the main topic of this work, but will be presented in a paper by V. Grinberg, M. Böck, M. Hanke et al. (in prep.). Here, the large data set of these fits serves to investigate the orbital modulation of the absorption.

2.3.3 Orbital Modulation of N_{H}

The results for the absorbing column density are presented in Fig. 2.38 and Table 2.6. Due to the systematically increased N_{H} values from '`bknpower+diskbb`' fits compared to '`bknpower`' fits (Fig. 2.32), both configurations need to be treated separately. All of them show, however, very similar trends for the orbital modulation. For the hard sample, described with the '`bknpower`' model (Fig. 2.38, A1), the average of $N_{\mathrm{H},22} := N_{\mathrm{H}}/(10^{22}\,\mathrm{cm}^{-2})$ in bins of $\Delta\phi_{\mathrm{orb}}$=0.1 has a flat baseline at $N_{\mathrm{H},22}$=0.7 and peaks at ϕ_{orb}=0 with $N_{\mathrm{H},22}$=2.3, although still higher values are found for single segments close to ϕ_{orb}=0. This finding is reflected in the standard deviation of N_{H} values in each phase bin, which also peaks at ϕ_{orb}=0. It is therefore reminiscent of the distribution of optical depths in the wind, which was found to be broader at early orbital phases (Sect. 2.2.2). Applied to the same data, the '`bknpower+diskbb`' model gives – as expected from previous considerations – a modulation with higher $N_{\mathrm{H},22}$ of 2.6–6.1 (Fig. 2.38, A2). The spectra from the soft sample show two different behaviors when nevertheless modelled with '`bknpower`' (Fig. 2.38, B1): One part shows a similar modulation as the results in Fig. 2.38 A1, but with underestimated uncertainties due to the bad fit. These are most of the hardest spectra in this sample, for which the '`bknpower`' model without systematic errors gave too large χ^2 values (Fig. 2.31). If systematic errors are added, a large fraction of those segments indeed migrates to the hard sample. For the other part of mostly softer spectra in Fig. 2.38 B1, including those from the soft-state in 2002 (indicated by red crosses), the best fit is $N_{\mathrm{H}}\approx$0; 469 segments have N_{H}=0. Finding $N_{\mathrm{H}}\approx$0 is a typical artifact of the '`bknpower`' model trying to describe an additional soft component. Wilms et al. (2006), who do not model the disk component with '`bknpower+diskbb`' fits, but exclude more low energy channels for soft state spectra, also find N_{H}=0 for 46 out of 202 observations.[15] Properly modelling the soft sample spectra with the '`bknpower+diskbb`' model (Fig. 2.37, B2) leaves only 6 segments with N_{H}=0. However, all $N_{\mathrm{H},22}$ values are systematically increased. The average in phase bins with $\Delta\phi_{\mathrm{orb}}$=0.1 varies in the range 3.1–6.8 – in a more (co-)sinusoidal way than for the hard sample, and also with a less strongly peaked spread at ϕ_{orb}=0. If this effect was indeed due to the different spectral states of the X-ray source and not because of different systematics of the '`bknpower+diskbb`' modelling, it would directly show that the wind structure changes between hard and soft states. An interpretation for the increased standard deviation of N_{H}, viz., the broader distribution of optical depths, is that the line of sight at $\phi_{\mathrm{orb}}\approx$0 in the hard state passes through a region with enhanced wind clumping. If true, its suppression in the soft state could be due to photoionization of the clumps by the increased soft X-ray flux.

[15] Boroson & Vrtilek (2010) erroneously claim that eliminating these 46 out of 202 leaves 133 data points. The 69 lowest values have $N_{\mathrm{H}}<5\times10^{18}\,\mathrm{cm}^{-2}$, i.e., are virtually zero. There are also 9 further values below $10^{21}\,\mathrm{cm}^{-2}$.

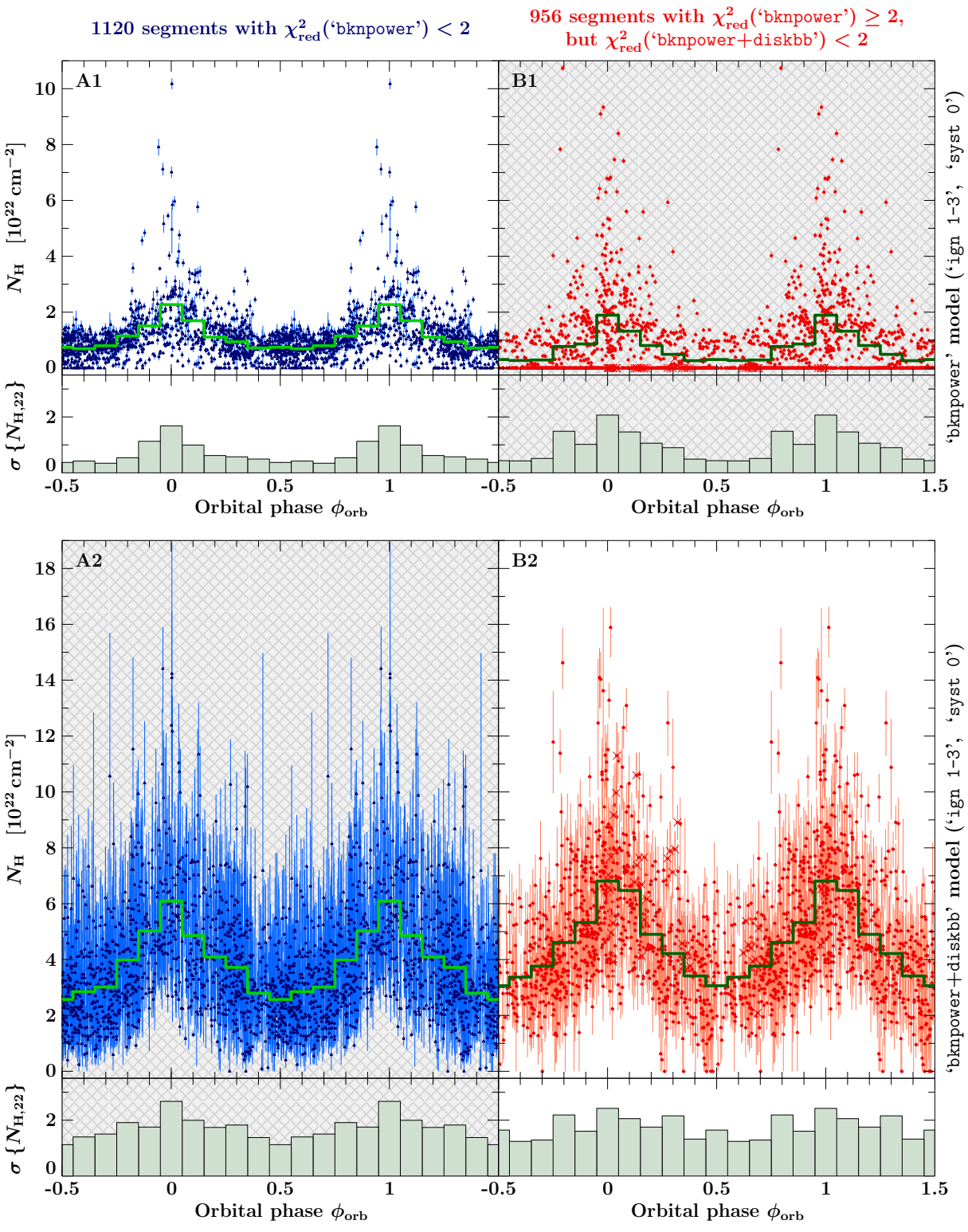

Figure 2.38: Orbital phase dependence of $N_{\rm H}$ from *RXTE* PCA spectral fits ('ign 1-3', 'syst 0'). Whereas the blue triangles in the left column (A) indicate the 1120 segments from the hard sample, the red circles in the right column (B) corrspond to the 956 segments from the soft sample – as in previous Figs. 2.32–2.37. Row 1 (2) shows results from the 'bknpower' ('bknpower+diskbb') model. The panels of bad 'bknpower' fits (B1) and overparameterized 'bknpower+diskbb' fits (A2) are only shown for illustration of the systematic differences between the models, and thus shaded with a gray crosshatched background. The green lines indicate the average $N_{\rm H}$ in ten orbital phase bins. The standard deviation of all column density measurements in each bin, $\sigma\{N_{\rm H}\}$, is shown by the histogram below the corresponding plot.

Table 2.6: Orbital modulation of $N_{\rm H}$ measured for different samples of *RXTE* PCA segments

Syst	Hard Samples			Soft Samples			Model
	n	$\langle N_{\rm H}\rangle$ (10^{22} cm^{-2})	$\sigma\{N_{\rm H}\}$ (10^{22} cm^{-2})	n	$\langle N_{\rm H}\rangle$ (10^{22} cm^{-2})	$\sigma\{N_{\rm H}\}$ (10^{22} cm^{-2})	
'syst 0'	1120	0.69–2.27	0.34–1.68	956	0.26–1.89	0.43–2.07	'bknpower'
	1070†	0.77–2.27	0.32–1.68	481†	0.75–2.67	0.29–1.99	
	1067‡	0.77–2.27	0.32–1.68				
	1120	2.57–6.09	1.13–2.68	956	3.07–6.81	1.24–2.43	'bknpower+diskbb'
	1118†	2.57–6.09	1.13–2.68	950†	3.24–6.81	1.24–2.43	
				447‡	3.91–7.00	0.96–2.53	
'syst 1 (0.5) %' only for #4 (5)	1557	0.93–2.74	0.48-1.79	639	0.15–2.18	0.46–2.46	'bknpower'
	1513†	0.96–2.74	0.44–1.79	275†	1.12–3.12	0.15–2.42	
	1067‡	0.97–2.62	0.38–1.73				
	1557	2.18–5.78	1.07–2.83	639	1.11–6.03	1.25–3.09	'bknpower+diskbb'
	1554†	2.18–5.78	1.07–2.83	535†	1.78–6.09	1.13–3.05	
				447‡	1.80–6.11	1.13–3.03	

Notes. The first column lists the systematic errors applied: either none at all ('syst 0'), or 1 % and 0.5 % only for channels #4 and 5, respectively. The hard samples contain spectra which allow for $\chi^2_{\rm red}<2$ with the 'bknpower' model – which the soft samples do not, but only with the 'bknpower+diskbb' model. n is the number of data segments in each sample, † indicates a selection of segments with $N_{\rm H}>0$, and ‡ indicates, in addition, the intersection of both hard or both soft samples with different systematics. $\langle N_{\rm H}\rangle$ and $\sigma\{N_{\rm H}\}$ indicate the range of the modulation in the average and the standard deviation of $N_{\rm H}$ values in ten orbital phase bins, whose individual values are displayed in Figs. 2.38 and 2.39. Numbers in gray indicate results from the model that is not adequate for the respective sample.

The overall seeming increment of $N_{\rm H}$ in the soft compared to the hard sample must be treated with caution, since the previous study has demonstrated that there is a systematic difference in $N_{\rm H}$ between 'bknpower' and from 'bknpower+diskbb' fits, as well as between configurations with 'syst 0' and 'syst 0.5%'. Figure 2.39 shows the results from a different configuration ignoring channels 1–3, with systematic errors added to channels #4 and #5 (namely 1 % and 0.5 %, respectively), but not to other channels at higher energies. Again defined by cuts at $\chi^2_{\rm red}=2$, the hard sample derived from this configuration comprises now 1557 segments, whereas the soft sample here consists of only 639 segments. The former gives an orbital modulation of $N_{\rm H,22}$ in the range 0.9–2.7, while 1.1–6.0 was obtained from the latter sample. Compared to the results from the previous modelling with 'syst 0', $N_{\rm H}$ is only slightly increased for 'bknpower' fits to the hard sample, but strongly reduced for 'bknpower+diskbb' fits to the soft sample. In order to exclude that the different results are due to the variation of the sample composition, Table 2.6 also includes the modulation observed for the subset of segments which belongs to both samples without and with systematic errors: by adding systematic errors to bins #4 and #5 (of 1 % and 0.5 %, respectively), the modulation for an identical hard state sample (excluding $N_{\rm H}=0$ artifacts) of 1067 segments was changed from $N_{\rm H,22}=0.8$–2.3 to 1.0–2.6. Likewise for a soft state sample of 447 segments, the average $N_{\rm H,22}$ was clearly reduced from 3.9–7.0 to 1.8–6.1.

To conclude, the orbital modulation of $N_{\rm H}$ in the Cyg X-1 system is well detected with *RXTE* PCA, to the extent that the spectrum can be described by "absorption" × "power-law (+disk) continuum". Absolute values, however, are somewhat uncertain because of systematic effects due to modelling and calibration of the spectra. Within this interpretation, a significant part of the absorption at $\phi_{\rm orb}\approx 0$ is caused by material local to the binary system. As *RXTE* PCA does not resolve absorption edges and therefore cannot distinguish absorption from

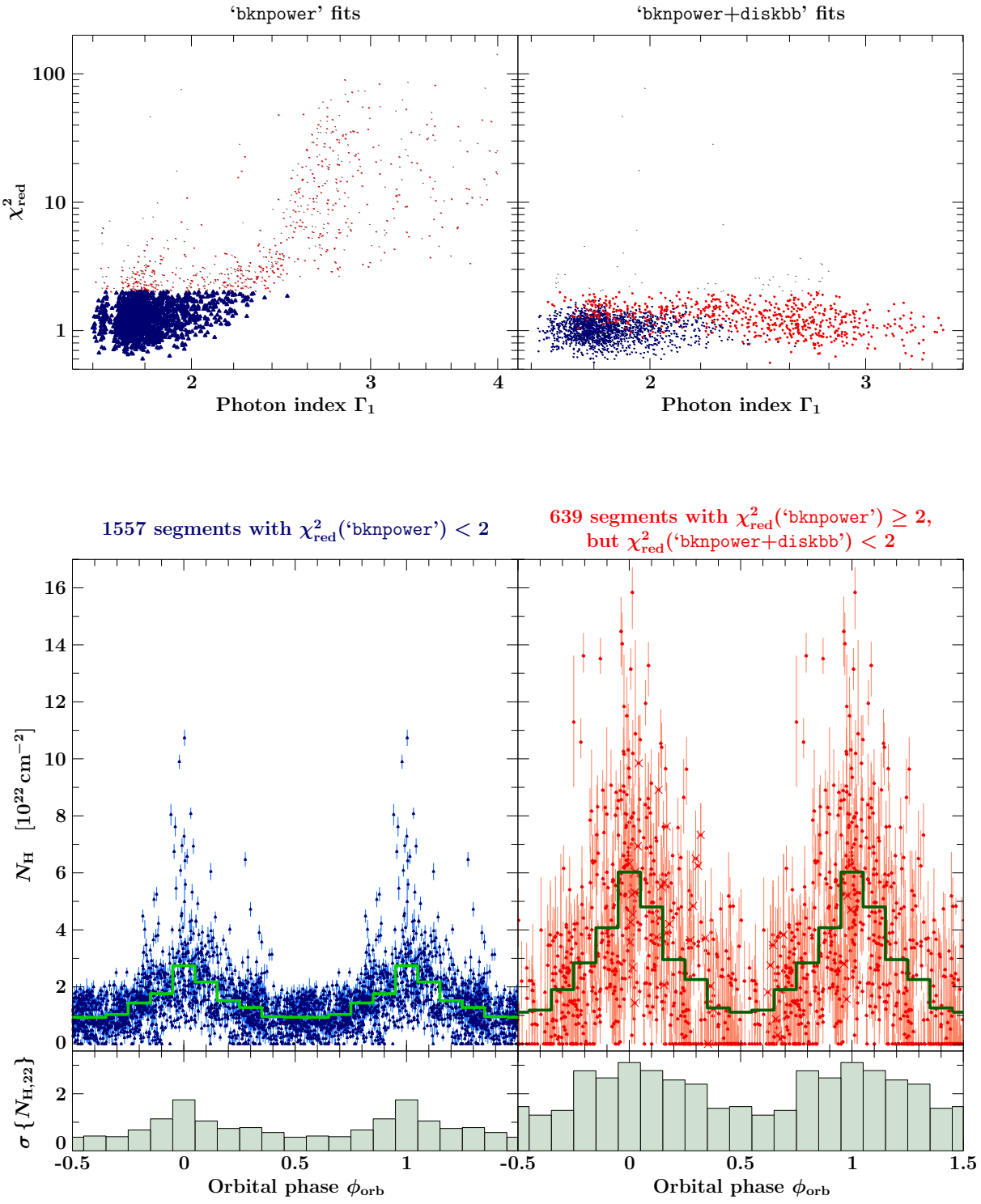

Figure 2.39: Similar to Figs. 2.31 and 2.38, but for the '`ign 1-3`' configuration with 1 % and 0.5 % systematic errors added to bins #4 and #5 only. The same selection criteria, applied to the (new) results from this configuration, leads to another 'hard sample' (left column, blue triangles) of segments, for which the '`bknpower`' model allows fits with $\chi^2_{\rm red}$<2, and another 'soft sample' (right column; red circles) of spectra, which give $\chi^2_{\rm red}$<2 only with the '`bknpower+diskbb`' model. The upper plots show $\chi^2_{\rm red}$ as a function of the derived photon index Γ_1, along with the resulting sample selection. The lower plots show the $N_{\rm H}$ measurements as a function of orbital phase, together with the average orbital modulation (upper panel), as well as the spread $\sigma\{N_{\rm H}\}$ (histograms, lower panel).

other changes in the curvature of the soft X-ray spectrum, such as introduced by a `diskbb` component, the present analysis does neither allow to firmly ascribe the detected modulation to an orbital variation of the *absorbing column density*, nor to discriminate *neutral* from *ionized* absorption. These results are therefore not necessarily in conflict with to the suggestion of Miller et al. (2009a) *"that absorption in the interstellar medium strongly dominates the neutral column density observed in spectra of X-ray binaries"*. These authors conclude their result from the fact that they did not observe changes in neutral absorption edges of five X-ray binary systems (including Cyg X-1) amongst (each) 2–4 *Chandra* observations at different luminosities. Since Miller et al. (2009a) did, however, not investigate the orbital phase dependence of their observations at all, no upper limits on a modulation of the neutral column could be derived.

2.3.4 Variabilty of $N_{\rm H}$ on Short Time Scales

In previous studies, the spectral variability of Cyg X-1 has usually been taken into account on timescales of *RXTE* observations – e.g., Wilms et al. (2006) model the long term variability of Cyg X-1 from the monitoring campaign in 1999–2004 using complete observations with an average exposure of 81 min. A higher temporal resolution, defined by *RXTE*'s orbit around Earth yielding segments of $\sim$50 min, was employed by Böck (2008) and Böck et al. (2008, 2010) to describe the fast variability during a state transition. The analysis of the previous section 2.3.2 is the first systematic study of the whole *RXTE* PCA data set on such short timescales, with an average exposure in continuous data segments of $\mathcal{O}(40\,\mathrm{min})$, see Fig. 2.19. The results of Sect. 2.3.3 have not only shown that $N_{\rm H}$ is variable over the 5.6 d orbit, but also indicated that there is a larger diversity of optical depths around $\phi_{\rm orb}$=0, which is in agreement with the results from Sect. 2.2.2.

Absorption dips

Transient X-ray absorption dips at $\phi_{\rm orb}\approx$0 (Bałucińska-Church et al., 2000), which have already been found in early X-ray observations of Cyg X-1 (e.g., Li & Clark, 1974; Mason et al., 1974; Parsignault et al., 1976; Pravdo et al., 1980; Remillard & Canizares, 1984; Kitamoto et al., 1984), indicate that the medium along this line of sight, i.e., the (focused) wind from the donor star to the black hole, must contain small, overdense structures, often referred to as "clumps" or "blobs". It has been debated for a long time which fraction of the orbital X-ray modulation is caused by discrete dips rather than a continuous wind density (Holt et al., 1976; Wen et al., 1999; Kitamoto et al., 2000; Feng & Cui, 2002). The interpretation of the previous results within the clumpy wind model can already give a first answer: while the increased lower baseline of the bulk of $N_{\rm H}$ measurements at $\phi_{\rm orb}\approx$0 must correspond to absorption by the smooth wind, the increased scatter is likely due to small-scale inhomogeneities, which either happen to cross the line of sight during the integration time – or not. According to Figs. 2.38 or 2.39, the stochastic contribution of clumps at $\phi_{\rm orb}\approx$0 to the total column seems to compare with the one of the continuous flow. However, the amplitude of the spread also depends on the considered timescale, in particular how it relates to the projected size and velocity of the clumps. Measured time scales of dips depend on the employed instrument and its capabilities: e.g., detectors sensitive to soft X-rays at 0.5 keV can detect much weaker dips than *RXTE* PCA above $\sim$2 keV. Furthermore, instruments with a low sensitvity may not be able to resolve the temporal structures. While the timescales reported for the first X-ray dips discovered with *OSO-7* by Li & Clark (1974) and *Copernicus* by Mason et al. (1974) were on the order of 30 minutes and up to $\sim$2 hours, Kitamoto et al. (1984) already observed dips with *Tenma* lasting from more than ten minutes down to several seconds only.

Table 2.7: *RXTE* observations used to analyze $N_{\rm H}$ variations on a 128 s time scale

Name	ObsID	Date	Start (MJD)	Stop (MJD)	Exposure (ks)	*RXTE* orbits	$N_{128\,\rm s}$
R_{1a}	60090-01-30	2003-04-19	52748.086	52748.319	12.6	4	...
R_{1b}	P80111	2003-04-19/20	52748.347	52749.371	46.6	16	...
R_1	...	2003-04-19/20	52748.086	52749.371	59.1	20	438
R_2	P93120	2008-04-18/19	54574.557	54575.837	35.6	10+2	268

Note. $N_{128\,\rm s}$ is the number of complete 128 s intervals of good time.

Table 2.8: Parameters of the joint '`bknpower`' continuum for R_1 and R_2

Parameter	[Unit]	R_1	R_2
.....	`bknpower` — broken power-law		.....
Γ_1		$1.7692(2)$	$1.7383^{+0.0003}_{-0.0002}$
$E_{\rm break}$	[keV]	$9.14(3)$	$9.81^{+0.05}_{-0.06}$
Γ_2		$1.5175(16)$	$1.490(3)$
.....	`highecut` — high-energy cutoff		.....
$E_{\rm cut}$	[keV]	28^{+2}_{-5}	$35(2)$
$E_{\rm fold}$	[keV]	241^{+105}_{-34}	408^{+223}_{-114}
.....	`egauss` — Fe Kα fluorescence line at 6.4 keV		.....
$A_{\rm Fe\,K\alpha,-3}$	$\left[10^{-3}\frac{\rm ph}{\rm s\,cm^2}\right]$	$3.32^{+0.07}_{-0.06}$	$2.73^{+0.09}_{-0.07}$
$\sigma_{\rm Fe\,K\alpha}$	[keV]	$0.573(16)$	$0.39^{+0.03}_{-0.02}$
χ^2/dof		$\frac{36\,400}{32\,133} = 1.13$	$\frac{20\,040}{19\,098} = 1.05$

Note. The individual values of $N_{\rm H}$ for the 128 s spectra are shown in Figs. 2.40 and 2.41.

Evolution of $N_{\rm H}$

To follow the absorption quantitatively by spectral fitting, an exemplary analysis of two long *RXTE* PCA observations was performed on a time scale of 128 s, i.e., 8 integration times within the `Standard2` mode. These observations (Table 2.7) are denoted by R_1 and R_2 in the following; their data were taken simultaneously with the *Chandra* observation 3814 (Sect. 2.4.2), and the multi-satellite campaign (Sect. 2.6), respectively – both close to $\phi_{\rm orb}$=0, when soft X-ray absorption dips were encountered. Although Cyg X-1 was in a very hard state, with $\Gamma_2 \approx 1.5$ during both observations, the analysis of Sect. 2.3.2 did not give acceptable fits with the '`bknpower`' model ('`ign 1-3`', '`syst 0`') for many segments (see Figs. 2.40 and 2.41). Based on its formal χ^2 improvement, the '`bknpower+diskbb`' model had to be prefered in these cases. Here, it will be shown that the apparent disagreement with the simple '`bknpower`' model is solely due to the variability of $N_{\rm H}$ on short time scales. The short-exposed spectra were extracted using `heasoft 6.8` in the way stated above. As the data from an individual short segment cannot accurately constrain all model parameters, all 438 (268) spectra from observation R_1 (R_2) were fitted simultaneously with a joint set of '`bknpower`' continuum parameters (Table 2.8), but an individual value of $N_{\rm H}$ and an individual overall normalization factor for each of the spectra. This approach allows for an excellent fit to the data, and reveals strong variations of $N_{\rm H}$ on $\mathcal{O}(100\,\rm s)$ time scales, see Figs. 2.40 and 2.41. For example, the strongest dip in R_1 consists of an increase of $N_{\rm H,22}$ from $7.60^{+0.14}_{-0.17}$ to $18.4^{+0.2}_{-0.3}$ and back to $7.49^{+0.16}_{-0.20}$ within Δt=128 s each. If this is due to a single spherical clump (with approximately the same lateral extension $r_\perp$ as

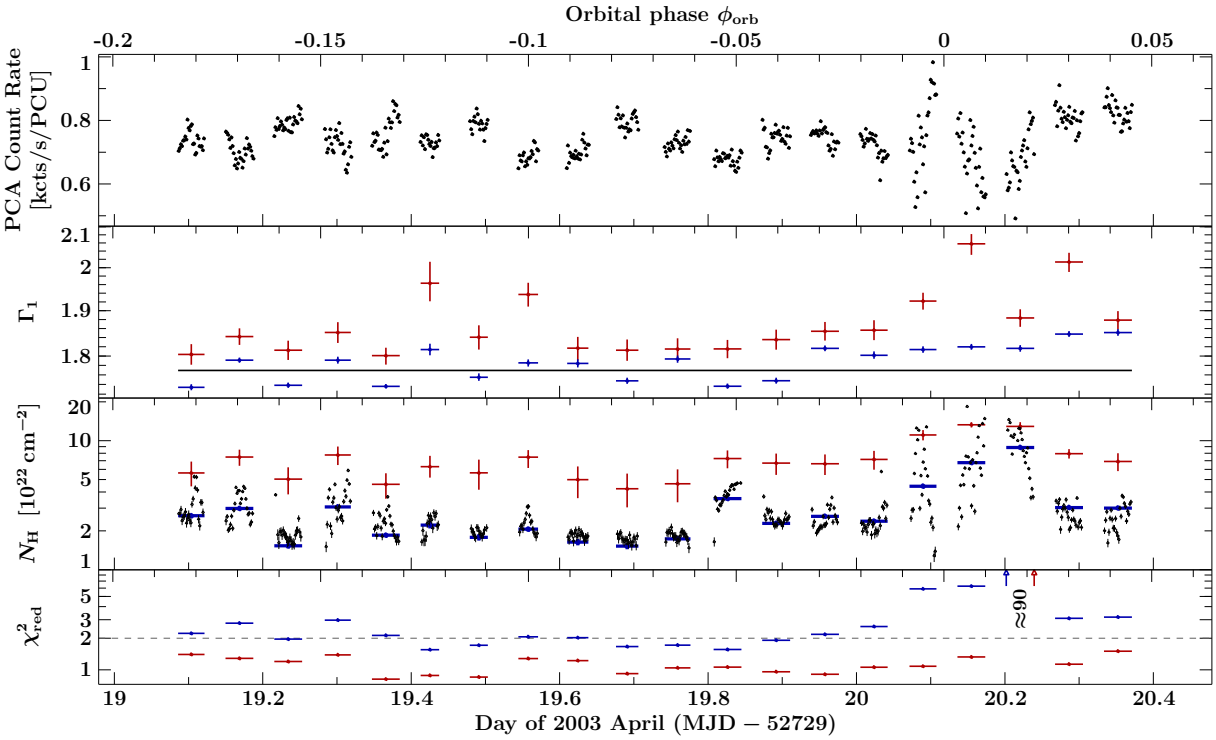

Figure 2.40: Evolution of fit parameters of the *RXTE* observation R_1 on 2003 April 19/20, consisting of 20 subsequent orbits of *RXTE*. The top panel shows the PCA light curve at 128 s time resolution, and the following panels the photon index Γ_1, the column density $N_{\rm H}$, and the reduced χ^2. Whereas the blue (red) data points result from fits with the '`bknpower`' and '`bknpower+diskbb`' model to all continuous segments with 2.4–3.3 ks exposure (Sect. 2.3.2), the black data result from a joint fit to 438 exposures with 128 s that share one '`bknpower`' continuum (solid line for Γ_1), but differ in $N_{\rm H}$ and normalization. See text for further details.

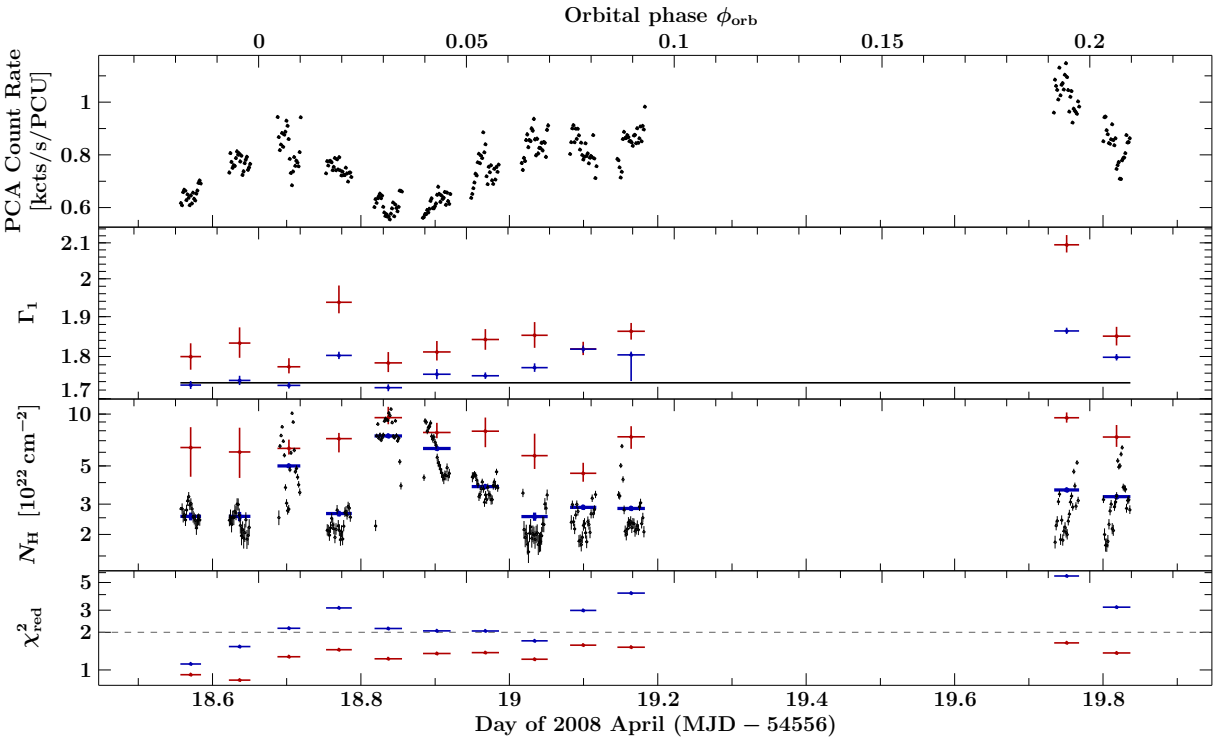

Figure 2.41: Same as Fig. 2.40, but for the $10 + 2$ *RXTE* orbits from R_2 on 2008 April 18/19.

the longitudinal extension $r_\parallel$) passing through the line of sight with a velocity component $v_\perp$, the latter is inversely related to the clump's density of H-atoms, n_H:

$$v_\perp \cdot \Delta t \;=\; r_\perp \;\approx\; r_\parallel \;=\; \mathcal{O}\left(\frac{\Delta N_\mathrm{H}}{n_\mathrm{H}}\right) \tag{2.34}$$

The measurements $\Delta N_\mathrm{H} = \mathcal{O}\left(10^{23}\,\mathrm{cm}^{-2}\right)$ and $\Delta t = \mathcal{O}\left(100\,\mathrm{s}\right)$ predict therefore:

$$n_\mathrm{H} \cdot v_\perp \;=\; \mathcal{O}\left(10^{16}\,\mathrm{cm}^{-3}\cdot\mathrm{km/s}\right) \tag{2.35}$$

Using the mean molecular weight $\mu{\approx}1.4$ from Eq. (1.20), the mass of such a clump is then

$$\begin{aligned} m_\mathrm{cl} \;&=\; \frac{4\pi}{3}\, r^3 \cdot n_\mathrm{H} \cdot \mu\, m_\mathrm{H} \\ &\approx\; \frac{4\pi}{3}\,\mu\, m_\mathrm{H} \cdot \frac{(\Delta N_\mathrm{H})^3}{n_\mathrm{H}^2} \;\approx\; 10^{20}\,\mathrm{g} \cdot \frac{\left(\Delta N_\mathrm{H}/10^{23}\,\mathrm{cm}^{-2}\right)^3}{\left(n_\mathrm{H}/10^{13}\,\mathrm{cm}^{-3}\right)^2} \\ &=\; \frac{4\pi}{3}\,\mu\, m_\mathrm{H} \cdot \Delta N_\mathrm{H} \cdot (\Delta t \cdot v_\perp)^2 \;\approx\; 10^{20}\,\mathrm{g} \cdot \left(\frac{\Delta N_\mathrm{H}}{10^{23}\,\mathrm{cm}^{-2}}\right) \cdot \left(\frac{\Delta t}{100\,\mathrm{s}}\right)^2 \cdot \left(\frac{v_\perp}{10^3\,\mathrm{km/s}}\right)^2 \end{aligned} \tag{2.36}$$

For $n_\mathrm{H} \gtrsim 10^{13}\,\mathrm{cm}^{-3}$, corresponding to $v_\perp \lesssim 10^3\,\mathrm{km/s}$, the clump mass would be $m_\mathrm{cl} \lesssim 10^{20}\,\mathrm{g}$, i.e., the mass that HDE 226868 loses in $\lesssim$0.5 s, which is very similar to the clump masses $5{\times}10^{19} - 10^{21}\,\mathrm{g}$ obtained by Fürst et al. (2010) for Vela X-1 from an analysis of the luminosity during hard X-ray flares.

Close-up view on dips

Figure 2.42 shows a close-up view on this strong dip at high time-resolution: The soft X-ray light curve S comprises the smallest set of PCA channels at low energies that can be extracted from `B_2ms_8B_0_35_Q` mode data, namely channels 0–10 corresponding[16] to energies $\leq$4.5 keV. The hard light curve H is formed from channels 14–35, i.e., energies 5.7–14.8 keV. The fact that H is also significantly reduced during the strong dip indicates an absorbing and/or scattering column in excess of $10^{23}\,\mathrm{cm}^{-2}$ (see also Fig. 1.14). While the light curves at 0.5 s time resolution are dominated by the strong flickering of the source and scatter significantly around their 16 s average, their softness ratio S/H evolves more smoothly (see also Bałucińska-Church et al., 1997). The ratios from the 0.5 s light curves are mostly consistent with those from the 16 s data, but show substructures on time scales $<$10 s.

Short dips are, in fact, not uncommon. In a dedicated study of absorption dips from *RXTE* PCA light curves at 0.125 s time resolution, Strobel (2010) finds dips between 1 s and $\sim$100 s. The number of dips of length Δt scales approximately with $(\Delta t)^{-5/2}$. In his work, dips are identified using the hardness ratio between the 8.2–14.8 keV band (absolute PCA channels 20–35) and the $\leq$5.7 keV band (channels 0–13). After applying a moving average over 7 bins (i.e., 0.875 s) to remove high-frequency fluctuations, a hardness ratio of more than $2\,\sigma$ above its *local* mean μ for longer than 1 s is considered to be indicative for an absorption dip. The values of σ and μ are redetermined for each continuous data segment in order to account for source-intrinsic spectral changes.[17] In the hard state (with $\mu{>}0.3$), Strobel (2010) finds 857 dips at ϕ_orb=0.68–0.30. The lack of dips at $\phi_\mathrm{orb}{\approx}0.5$ is not due to a lack of exposure (Fig. 2.18). Figure 2.43 shows an example of a relatively long event of an isolated strong dip at ϕ_orb=0.756 lasting 34 s, which happens to occur only 17 minutes after the *XMM* observation 020276 03 01.

[16] Note that these are *absolute* PCA channels, not to be confused with `Standard2` energy bins, e.g., shown in Fig. 2.21. Absolute channels 0–10 correspond to the first seven energy bins of `Standard2` mode.

[17] Previous studies, identifying dip events from a hardness ratio that exceeds a *global* threshold (Bałucińska-Church et al., 2000; Poutanen et al., 2008; Boroson & Vrtilek, 2010), are clearly biased against dips in softer states and preferentially detect dips in harder states.

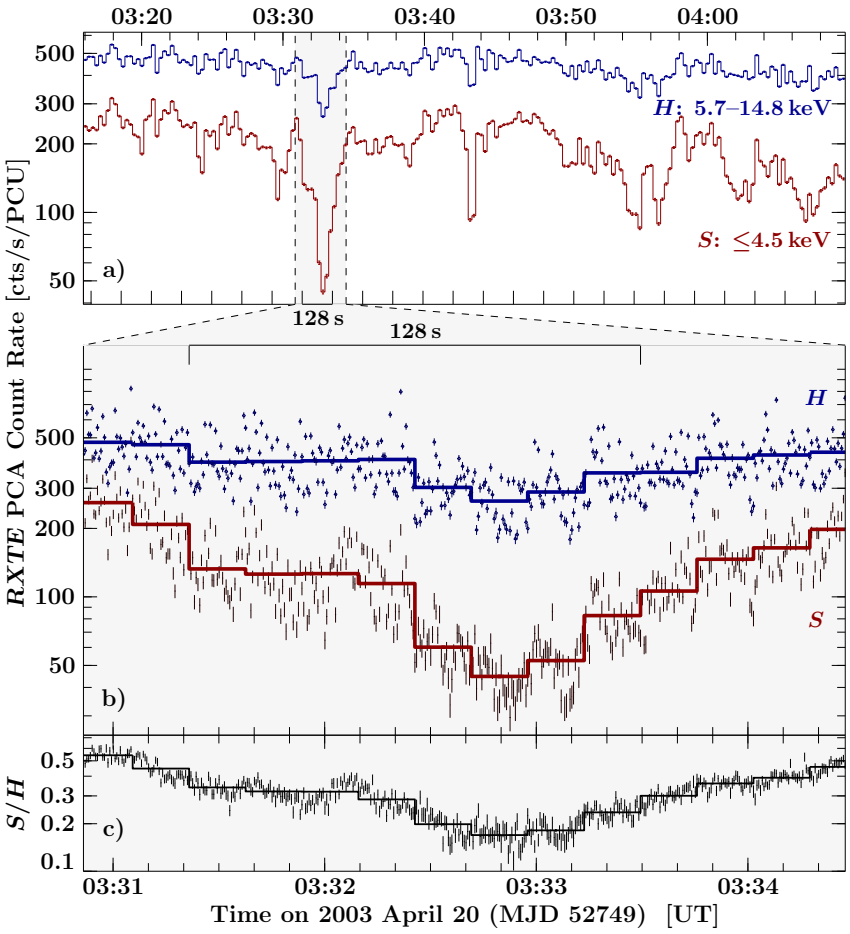

Figure 2.42: Close-up view on the strongest dip in R_1 (Fig. 2.40).
a) *RXTE* PCA light curves at 16 s time resolution of R_1's *RXTE* orbit with the strongest dip. The top curve shows the 5.7–14.8 keV band (H), and the lower curve the $\leq$4.5 keV band (S).
b) Like a), but zooming onto the dip. The data points around the histogram show the light curves at 0.5 s resolution, illustrating the high frequency flickering of the source.
c) Softness ratio S/H from the light curves in b), revealing some substructures in the dip.

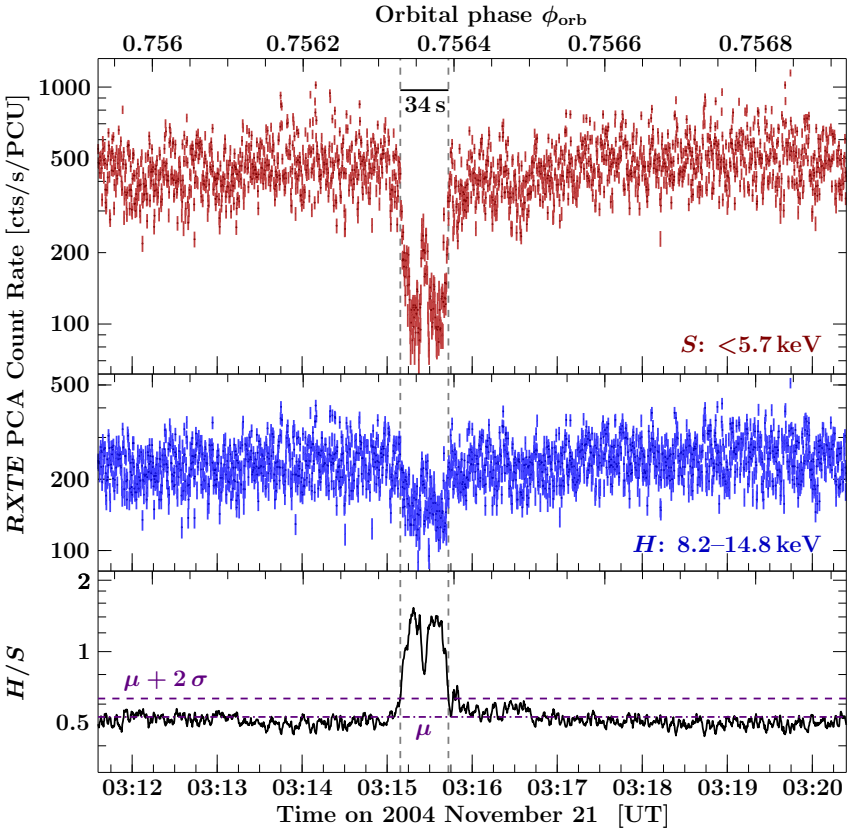

Figure 2.43: Isolated strong absorption dip at ϕ_{orb}=0.756 lasting $\sim$34 s. Its morphology suggests an origin in two major clumps. The top and middle panels show *RXTE* PCA light curves at 0.125 s time resolution, in a soft (S) and hard (H) X-ray band. The bottom panel displays the moving average of the hardness ratio H/S in a window of 0.875 s, used to detect the dip as a $\geq 2\sigma$ increase above the local mean hardness ratio μ for this data segment (after Strobel, 2010, figs. 2.5 and 3.3).

There are multiple implications from this variability of $N_{\rm H}$ on short time scales Δt: First, the clump size inferred from Eq. (2.34) becomes smaller. Kitamoto et al. (1984) have already suggested dimensions of the order of 10^9 cm, assuming $v_\perp \lesssim 2000\,{\rm km/s}$ and Δt of a few seconds only. Second, the value $2\times10^{23}\,{\rm cm}^{-2}$ obtained from the 128 s spectrum is only a lower limit for the peak column density during that dip. Third, it is now evident that the '`bknpower`' model was not able to describe an average spectrum using simple absorption, when many differently strong absorbed spectra are actually accumulated during a long integration. Partial covering models have been suggested to explain the soft excess observed in dip spectra (e.g., Kitamoto et al., 1984; Bałucińska & Hasinger, 1991; Bałucińska-Church et al., 2000), but their interpretation was often a partial *spatial* covering of an extended emission region, which was considered implausible by Pravdo et al. (1980). Kitamoto et al. (1984) also point out that, if *"the absorber is patchy or it consists of blobs"*, *"a large fraction of soft X-rays from the source comes through the space between the blobs without being absorbed, as the blobs pass in front of the source"* – i.e., a point source could likewise be covered during parts of the *time*. Given the fine structure of dip events at short time scales on the order of seconds or even lower, it is virtually impossible to select an integration time such that *only one dip* is contained at *constant absorption*, and still obtain a spectrum with good S/N with the sensitivity of current instruments.

In order to address the spectrum of a single dip, future generation X-ray observatories will be needed that have not only a greatly enlarged collecting area, but also detectors with sufficiently high spatial resolution to separate the source Cyg X-1 itself from its X-ray scattering halo (Predehl & Schmitt, 1995). As Nowak et al. (2011) emphasize, radiation scattered by the dust cloud arrives with a time delay that varies with the angular distance from the X-ray source (Ling et al., 2009; Zhang et al., 2009; J. Xiang, submitted to ApJ). The scattered halo component will therefore in general not follow the absorption of the direct component during dips, but will contribute unabsorbed soft X-ray flux – mimicking an "unconvered" component within a partial covering interpretation – unless the halo is spatially resolved and excluded.

* * *

From the large *RXTE* database, an orbital modulation of the absorbing column density could be inferred. At early orbital phases, however, $N_{\rm H}$ does not vary as smoothly with $\phi_{\rm orb}$ as expected for a homogeneous wind, but turned out to be strongly variable at time scales of <100 s. The broad distribution of optical depths in the wind at $\phi_{\rm orb}\approx0$ can therefore be interpreted as a result from the statistical accumulation of short absorption dips during longer integration times. If spectra from strong dips are coadded with nondip spectra, the spectral distorsion from a simple absorbed continuum is even detected above ~3 keV and with the low energy resolution of *RXTE*'s proportional counters. The inferred low-energy photon index Γ_1, which is often used as a proxy for the source's spectral state, may then be systematically off. It is therefore a side result of this study that the high-energy photon index Γ_2 should better be used as a more reliable indicator, not affected by systematic uncertainties due to absorption – nor due to the accretion disk, which is often not well defined by the *RXTE* data alone.

The next sections will address the soft X-ray spectrum in more detail. The CCDs on *XMM-Newton*, and in particular the gratings on *XMM* and *Chandra*, provide a much higher resolution and cover energies down to 0.5 keV (or even below), allowing for a closer investigation of the properties of the wind in the HDE 226868/Cyg X-1 system. There are, however, much fewer measurements of Cyg X-1 with these great and highly requested observatories than with *RXTE*. From the 17 individual *Chandra* pointings that are available up-to-date, four have been acquired within the course of this work. Section 2.4 gives a concise overview of all *Chandra* data and presents a detailed analysis of the wind structure inferred from the hard state observations. Section 2.5 will then briefly discuss the *XMM* data.

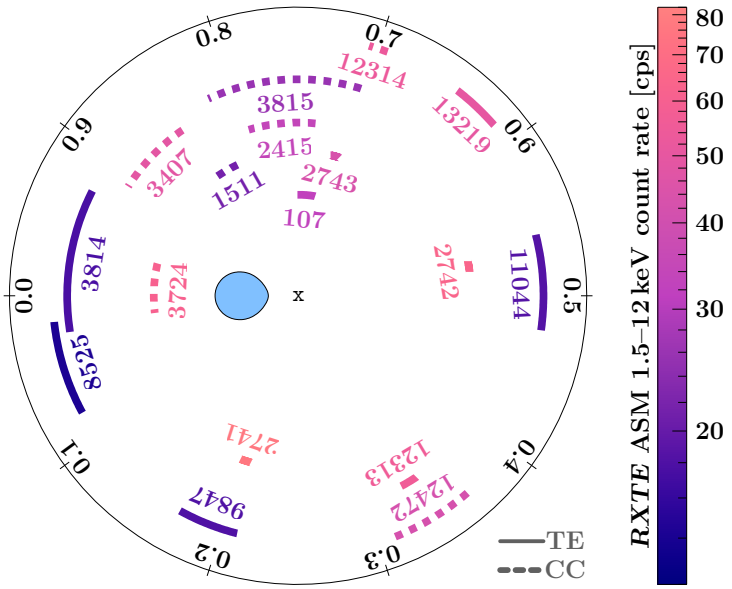

Figure 2.44: Orbital phase coverage of the *Chandra* HETGS observations of Cyg X-1. The color scale indicates the simultaneous *RXTE* ASM flux according to the scale on the right-hand side. Solid (dotted) lines indicate TE (CC) readout modes. Only ObsIDs 12314 and 12472 employ the faint telemetry format, which allows for a better calibration, in particular of CC mode data; all other observations were performed using the graded telemetry format.

2.4 *Chandra* Observations

2.4.1 Overview

During the first four years of the *Chandra* mission, from 1999 October to 2003 April, Cyg X-1 has been observed with the HETGS for ten times. Most pointings took place during intermediate, transitional, or soft states; only the last of those, ObsID 3814, caught a very hard state. No observations were performed in the following five years. New measurements were only obtained in 2008 April, and then in 2010 January, after Cyg X-1 had settled in a long hard state. Four further observations took place in 2010 July and early 2011, when the source had once again entered another deep soft state. Table 2.9 gives an overview of these *Chandra* observations, the flux level measured with the *RXTE* ASM, and the fractional exposure of the individual ACIS-S CCDs. Only the hard state observations are essentially free of frame dropouts; in the soft state, the telemetry stream was regularly saturated by the high flux.

Figure 2.44 illustrates the orbital phase coverage. It is largely accidental that many observations cluster between orbital phases 0.7 and 1.0. ObsIDs 2740–2743 were intended to compare the spectrum at orbital phases 0, 0.25, 0.5, and 0.75, but their data suffer from severe pileup. ObsIDs 3814 and 8525 were conducted by our group (PIs: K. Pottschmidt and J. Wilms) to study the stellar wind of the donor star during superior conjunction of the black hole. ObsID 11044 was then proposed by our group (PI: M.A. Nowak) to get the first (good) *Chandra* data of Cyg X-1 at ϕ_{orb}=0.5, and similarly ObsID 12472 (PI: M. Hanke) to fill the gap at ϕ_{orb}=0.25−0.5.

Figure 2.45 shows an overview of *all* light curves, corrected for the different CCD exposures with `aglc` 1.5.3 (Sect. 1.3.4). The ±first order HEG and MEG spectra were combined, unless the MEG−|m| and HEG+|m| arms were placed off the detector; for ObsIDs 12313, 12314, and 12472, twice the sum of the HEG−1 and MEG+1 light curve is displayed instead. Nevertheless, not all absolute count rates are comparable with each other, since the detector mode and the resulting severity of pileup strongly influence the count rates. For example, the apparent difference in intensity and color between ObsIDs 12313 and 12314, which were performed only two days apart, is largely due to the fact that ObsID 12313's TE mode spectra are heavily damaged by pileup. Even using CC mode in ObsID 12314 could not prevent periodic telemetry dropouts, see Table 2.9. The fact that the spurious reductions in count rate appear only at the beginning and at the end of the good times requires further investigation.

Table 2.9: *Chandra* HETGS observations of Cyg X-1

ObsID	Mode	Start Date T_0		Date $- T_0$	T_{exp}	ϕ_{orb}	r_S	Fractional exposure					
		(YYYY-mm-dd)	(MJD)	(days)	(ks)		(cps)	CCD 4	CCD 5	CCD 6	CCD 7	CCD 8	CCD 9
107	TE graded	1999-10-19	51470	0.829–0.991	$\left\{\begin{smallmatrix}2.4\\11.5\end{smallmatrix}\right\}^*$	0.73–0.76	32.3	100.0 %	100.0 %	100.0 %	100.0 %	100.0 %	100.0 %
1511	CC graded	2000-01-12	51555	0.355–0.502	12.7	0.82–0.85	21.4	0.0 %	100.0 %	100.0 %	100.0 %	100.0 %	100.0 %
2415	CC graded	2001-01-04	51913	0.263–0.612	30.2	0.74–0.80	(34)	99.5 %	100.0 %	99.6 %	99.9 %	99.6 %	99.6 %
3407	CC graded	2001-10-28	52210	0.690–1.038	30.1	0.85–0.91	48.6	84.5 %	100.0 %	44.0 %	55.0 %	49.8 %	85.6 %
2741	TE graded	2002-01-28	52302	0.242–0.301	5.1	0.20–0.21	(77)	87.3 %	79.6 %	28.3 %	37.6 %	36.0 %	78.5 %
2742	TE graded	2002-01-30	52304	0.066–0.128	5.4	0.52–0.53	(64)	88.2 %	76.8 %	27.4 %	35.8 %	35.0 %	77.0 %
2743	TE graded	2002-04-13	52377	0.881–0.941	5.2	0.70–0.71	43.1	90.7 %	88.0 %	37.7 %	53.1 %	43.9 %	83.6 %
3724	CC graded	2002-07-30	52485	0.736–1.074	29.2	0.97–0.03	61.3	64.1 %	90.8 %	22.3 %	29.5 %	25.7 %	58.9 %
3815	CC graded	2003-03-04	52702	0.665–1.340	58.4	0.70–0.82	25.8	99.7 %	100.0 %	95.0 %	95.8 %	98.4 %	99.9 %
3814	TE graded	2003-04-19	52748	0.709–1.269	48.3	0.93–0.03	17.5	100.0 %	100.0 %	100.0 %	100.0 %	100.0 %	100.0 %
8525	TE graded	2008-04-18	54574	0.769–1.118	30.1	0.02–0.08	14.2	100.0 %	100.0 %	100.0 %	100.0 %	100.0 %	100.0 %
9847	TE graded	2008-04-19	54575	0.623–0.846	19.3	0.17–0.21	18.0	100.0 %	100.0 %	100.0 %	100.0 %	100.0 %	100.0 %
11044	TE graded	2010-01-14	55210	0.130–0.479	30.1	0.48–0.54	18.4	100.0 %	100.0 %	100.0 %	100.0 %	100.0 %	100.0 %
12313	TE graded	2010-07-22	55399	0.694–0.764	6.1	0.33–0.34	(56)	100.0 %	92.0 %	41.7 %	36.4 %	63.0 %	100.0 %
12314	CC faint	2010-07-24	55401	0.738–0.805	5.8	0.69–0.71	(53)	27.3 %	43.8 %	21.5 %	14.9 %	21.1 %	27.7 %
12472	CC faint	2011-01-06	55567	0.584–0.863	24.1	0.31–0.36	(42)	30.2 %	47.6 %	21.7 %	13.8 %	23.0 %	30.8 %
13219	TE graded	2011-02-05	55597	0.289–0.429	12.1	0.62–0.65	(50)	82.9 %	69.6 %	28.4 %	37.4 %	37.8 %	76.4 %

Notes: T_{exp} is the exposure time.
ϕ_{orb} is the orbital phase according to Eq. (2.2), i.e., according to the ephemeris of Gies et al. (2003), which is used throughout this work.
r_{S} is the *RXTE* ASM (1.5–12 keV) count rate, averaged over the observation (or the two measurements immediately before and after it)
* For ObsID 107, the alternating readout mode was employed.

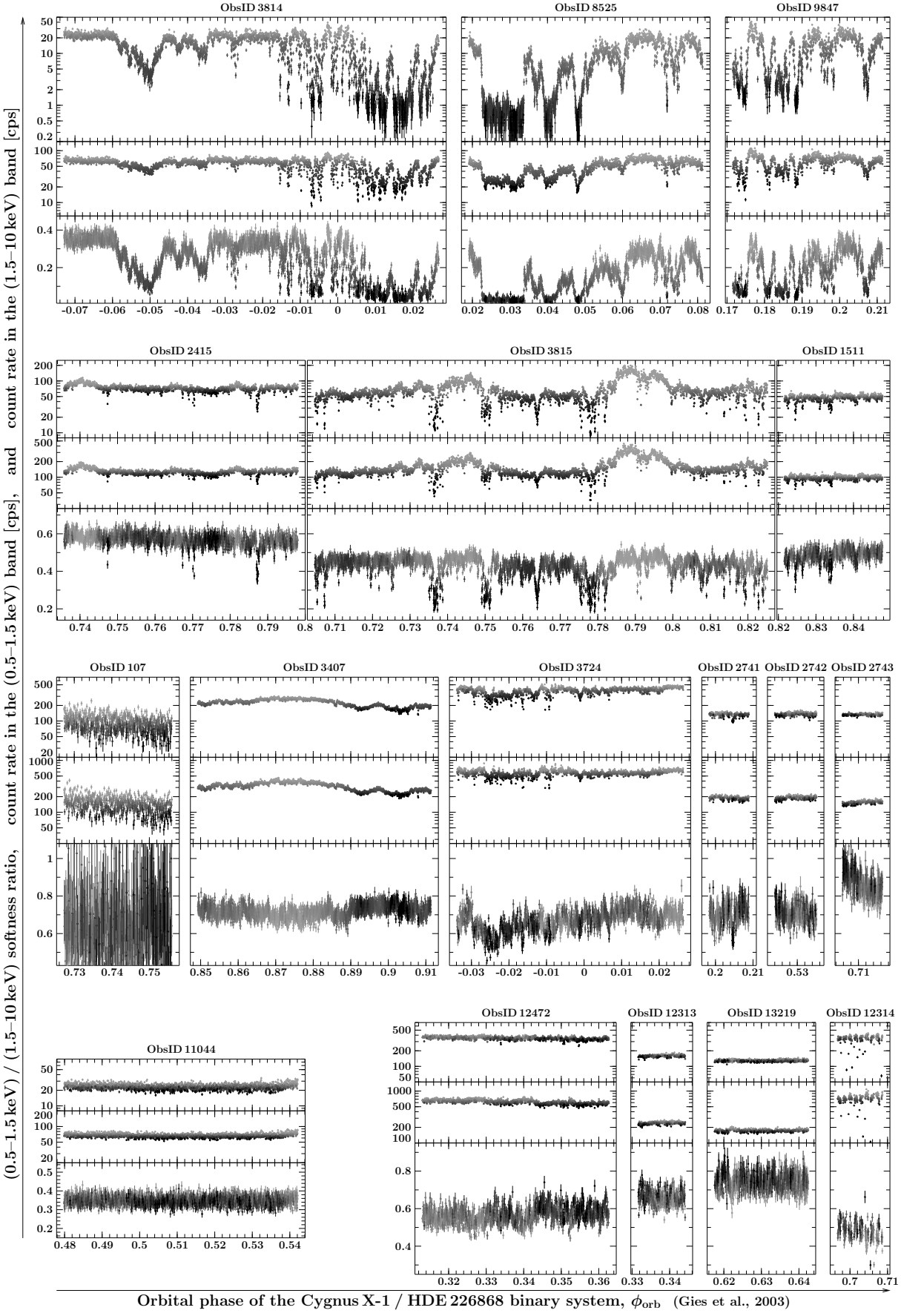

Figure 2.45: Light curves and softness ratios of all *Chandra* observations of Cyg X-1, at ∼16 s. The gray scale encodes the total count rate. See text for a discussion of further details.

The narrow drops in count rate during ObsIDs 2415, 3815, and 1511 (at $\phi_{\rm orb}$=0.70−0.85, in hard-intermediate or transitional states) – and notably also in ObsID 3742 (at $\phi_{\rm orb}\approx$0, in the soft state) – are, however, real and due to short absorption dips. Strong dipping, on the other hand, is encountered in all hard state observations at $\phi_{\rm orb}\approx$0 and $\phi_{\rm orb}\approx$0.2. A more complete orbital phase coverage in the hard state would be desirable to study the evolution of dipping.

A detailed analysis of the very hard state observations will be presented in Sects. 2.4.2–2.4.3. Images from the TE mode observations are shown in appendix C.1 on page 162. Most of the *Chandra* pointings are accompanied by simultaneous *RXTE* observations. Their PCA light curves are displayed in appendix C.2.

ObsID 107

The first *Chandra* HETGS observation of Cyg X-1 was performed from guaranteed time of the instrument PI, Claude Canizares, for 14 ks on 1999-10-19 at orbital phase $\phi_{\rm orb}$=0.73–0.76. Schulz et al. (2002) erroneously cite the date 1999-10-15 and $\phi_{\rm orb}$=0.92 – a confusion adopted by Marshall et al. (2001), Gies et al. (2003), but also Miller et al. (2005), Vrtilek et al. (2008), Nagae et al. (2009), and Boroson & Vrtilek (2010), although the correct phase was already noted by Feng et al. (2003) and Hanke et al. (2009). The misdating was likely due to wrong initial time stamps in the file headers, which were not always correct for observations from early in the *Chandra* mission, especially if there were changes in the short term scheduling (N. Schulz, priv. comm.). Cyg X-1 was simultaneously observed with *RXTE*, with a good time of 3.8 ks, see Fig. C.11.

All six CCDs of the linear ACIS-S array were used in TE mode. Whereas the nominal full frame time is 3.2 s, the ACIS alternating exposure mode was chosen with one frame of 0.3 s primary exposure after five frames of 3.3 s secondary exposure. The short-frame data total to only 2.4 ks of good time, but are significantly less affected by pileup than the long-frame data with a good time of 11.5 ks. (Schulz et al. 2002 quote slightly different numbers.) Figure C.1 shows the detector and sky images from the long-frame data; the undispersed image clearly suffers from severe pileup. But also the first order dispersed spectra from the long-frame data seemingly contain a much lower count rate than those from the short-frame data, see Fig. 2.46.

Cyg X-1 was in a transitional state. Schulz et al. (2002) derive a neutral column density of $N_{\rm H} = 6.2\times10^{21}\,{\rm cm}^{-2}$ from prominent absorption edges. They detect weak emission and absorption lines, mostly from intermediate to highly ionized iron, some of them giving the impression of P Cygni profiles.

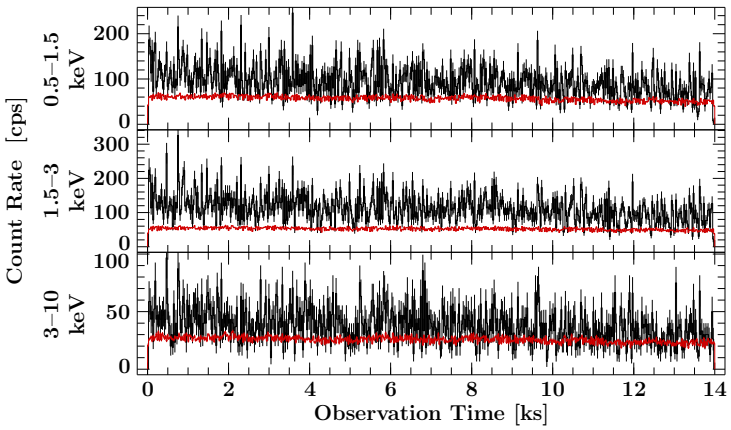

Figure 2.46: Light curves from the *Chandra* observation 107, at 25.5 s resolution. The black lines show the short-frame data, the red lines the long-frame data. Due to the much shorter exposure of 0.3 s instead of 3.3 s, the short-frame data have larger statistical errors, but are much less affected by pileup losses than the long-frame data.

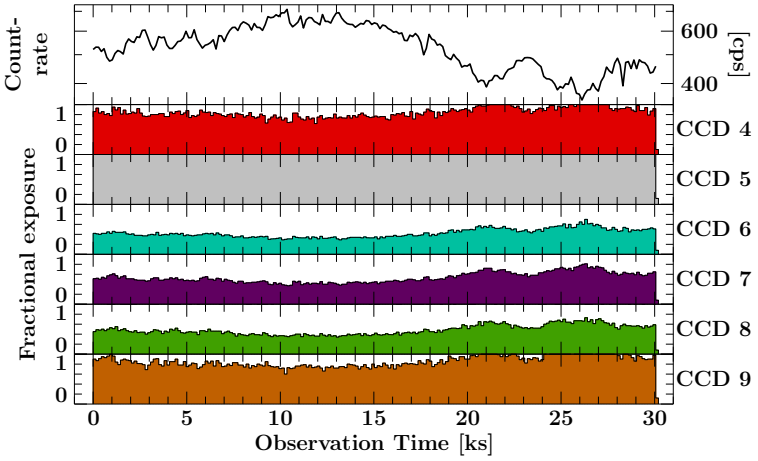

Figure 2.47: Lightcurve (top) and fractional exposure on the six ACIS-S CCDs during the observation 3407, in bins of 100 virtual frames of $512 \times 2.85\,\mathrm{ms} = 1.459\,\mathrm{s}$ each. The frame losses are clearly correlated with the source flux. The average exposures are given in Table 2.9.

ObsID 1511

The second *Chandra* observation of Cyg X-1, also from guaranteed time (PI: Claude Canizares), took place for 13 ks on 2000-01-12[18] at orbital phase ϕ_{orb}=0.82–0.85. CCDs 5–9 were operated in CC mode. Due to the lack of CCD 4, the HEG−1 and MEG−1 spectra do not continue beyond ∼13 Å and 26 Å, respectively. There is no simultanous *RXTE* data, but the observation of a full revolution of Cyg X-1 (Feng & Cui, 2002) was performed in the previous binary orbit, see Fig. C.12.

During ObsID 1511, Cyg X-1 was in a harder state than during ObsID 107, see Table 2.9. Marshall et al. (2001) report Ly α and He α absorption lines, redshifted by $(450 \pm 150)\,\mathrm{km\,s^{-1}}$. The light curve in Fig. 2.45 shows that ∼15 % of the observation is covered by absorption dips.

ObsID 2415

The third *Chandra* observation (30 ks), using director's discretionary time (DDT; PI: Jon Miller), was performed on 2001-01-04, at orbital phase ϕ_{orb}=0.74–0.80. The full six CCDs 4–9 were operated in CC mode. Columns 367–516 on CCD 7, containing the undispersed source image, were not transmitted at all to (successfully) avoid telemetry saturation. Figure C.13 shows the PCA light curve of the simultaneous *RXTE* observation with 13 ks good time.

Cyg X-1 was in an intermediate state during this observation. Miller et al. (2002) infer a column density of $6.2 \times 10^{21}\,\mathrm{cm^{-2}}$, and Miller et al. (2005) report absorption and emission lines of H- and He-like resonance lines of Ne, Na, Mg, and Si with a mean redshift of $\sim$100 $\mathrm{km\,s^{-1}}$, as well as some lines of highly ionized Fe and Ni. Miller et al. (2002, 2005) note *"a prominent 500 s dip"*, which they exclude from their analysis – unlike several other, shorter ones.

ObsID 3407

This DDT observation (PI: Wei Cui) was performed on 2001-10-28/29, for 30 ks at orbital phase ϕ_{orb}=0.85–0.91. The full CCDs 4–9 were employed in CC mode. Due to the high source flux, data from all CCDs except CCD 5 suffered from large telemetry dropouts even though only every tenth event was transmitted from columns 366–465 of CCD 7, see Table 2.9 and Fig. 2.47. Figure C.14 shows the 11 ks PCA light curve of the simultaneous *RXTE* observation.

[18] There is a typo in the date quoted by Hanke et al. (2009). The correct observation date is 2000-01-12, as also originally reported by Marshall et al. (2001), and not one year later.

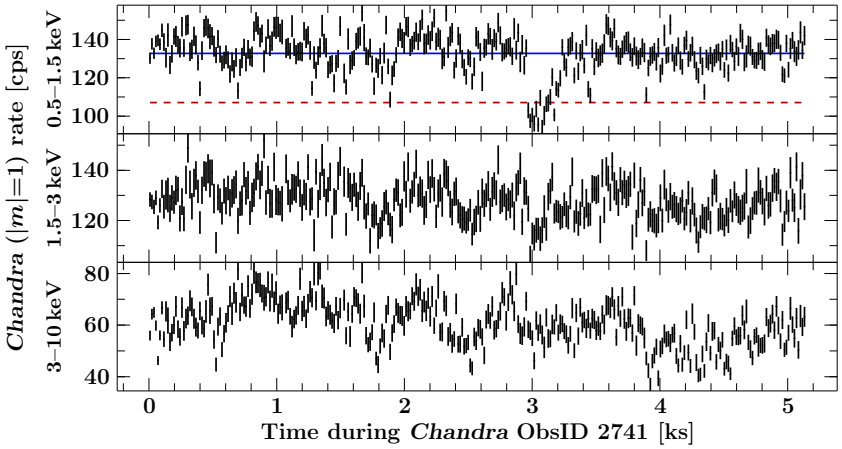

Figure 2.48: Light curve of the *Chandra* observation 2741 in different energy bands, at ∼16 s resolution. The solid blue horizontal line in the first panel for the 0.5–1.5 keV band indicates its average count rate, and the dashed red horizontal line indicates a 2.5 σ lower level.

Chang & Cui (2007) report dramatic variability during this observation in the intermediate state: While a large number of absorption lines (mostly redshifted, but not by a consistent velocity) is identified in the first part of their observation, most of them weaken significantly or cannot be detected at all during the second part. The complete ionization of the wind due to a sudden density decrement is given as a possible explanation.

ObsIDs 2740–2743

Three of those observations – intended to compare the spectrum at orbital phases 0, 0.25, 0.5, and 0.75 through 5 ks snap-shots (proposed by the PI Shuang Nan Zhang as a guest observer, GO) – were performed in early 2002: ObsID 2741 on Jan-28 at $\phi_{\rm orb}$=0.20–0.21, ObsID 2742 only a third of a binary orbit later on Jan-30 at $\phi_{\rm orb}$=0.52–0.53, and ObsID 2743 on Apr-13 at $\phi_{\rm orb}$=0.71–0.72. ObsID 2740, once planned for 2002-07-31, was finally canceled.

Cyg X-1 was in a soft state during the three observations. Despite the high source flux, they were carried out in TE mode using one half subarray of all CCDs 4–6, i.e., with a frame time of 1.7 s, which resulted in large frame losses (see Table 2.9) and pileup, see also Figs. C.2–C.4.

ObsID 2741 contains an interval of ∼2.5 minutes during which the count rate measured in the 0.5–1.5 keV band is continuously less than 81 % of its average value, corresponding to more than 2.5 σ below the mean. While a similar, but much less significant structure can be seen in the 1.5–3 keV band, no reduction is detected in the 3–10 keV band, see Fig. 2.48. These results are consistent with a short absorption dip. If true, the finding of even a weak dip at $\phi_{\rm orb}$=0.205 is very valuable as it may place constraints on the wind structure in the soft state.

ObsID 3724

This 29 ks DDT observation (PI: Yuxin X. Feng) was aimed at catching Cyg X-1 when it entered the high/soft state. It was performed on 2002-07-30/31, at orbital phase $\phi_{\rm orb}$=0.97–0.03. The full ACIS-S array was operated in CC mode, with a 90 % blocking filter applied to the zeroth order image at columns 366–465 on CCD 7. The average fractional exposures of CCDs 6–8 were <30 % (Table 2.9). Figure C.15 shows the simultaneous 10 ks *RXTE* PCA light curve.

Feng et al. (2003) detect asymmetric absorption lines: The line centers are almost at their rest wavelengths, but the red wings are more extended, especially for the transitions of highest ionized ions, which they explain by the inflowing focused wind reaching both the highest redshift and ionization parameter closest to the black hole. The light curve of Fig. 2.45 seems to indicate narrow absorption dips, which have not been investigated yet.

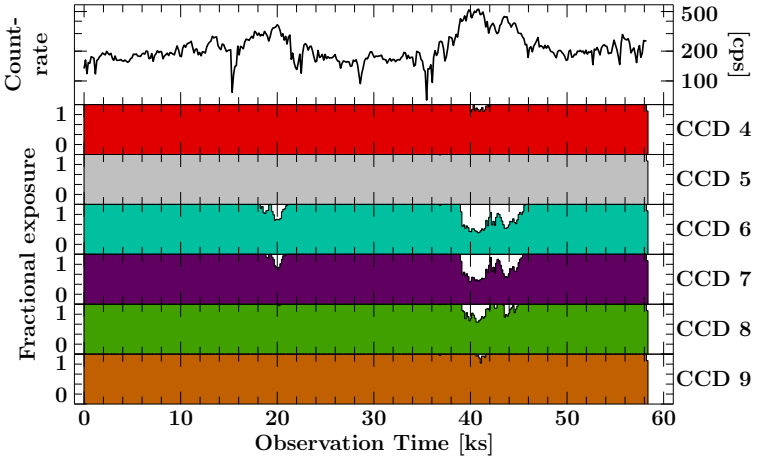

Figure 2.49: Same as Fig. 2.47, but for ObsID 3815. Whereas the telemetry streams of (mostly) CCDs 6 and 7 were saturated during the small flare at t=20 ks, all but CCD 5 were affected during the major flare around t=40 ks. All CCDs' average fractional exposures are given in Table 2.9.

ObsID 3815

This GO observation (PI: Walter Lewin) was performed for 58 ks on 2003-03-04/05 at orbital phase $\phi_{\rm orb}$=0.70–0.82. The chips were operated in CC graded mode. Only 10 % of the events from columns 154–281 on CCD 7 were included in the telemetry stream. ObsID 3815 displays the highest internal source variability, with changes by up to a factor 4. During this major flare, and also during a smaller one, the telemetry limit was reached, see Fig. 2.49. There is a single simultaneous *RXTE* data segment with less than 0.9 ks exposure, see Fig. C.16.

The source was in a hard state, but closer to the intermediate state than ObsID 1511. Miller et al. (2009a) use this observation and ObsID 3724 to compare neutral absorption edges. The spectrum shows absorption lines from the photoionized stellar wind, redshifted by approximately 200–300 km s^{-1}. Narrow absorption dips are encountered, during which lower ionization stages are seen (Miškovičová et al., 2011; I. Miškovičová, M. Hanke, et al., in prep.).

ObsID 3814

This 48 ks GO observation (PI: Katja Pottschmidt) was performed on 2003-04-19/20, at orbital phase $\phi_{\rm orb}$=0.93–1.03. A half subarray of the ACIS detector was operated in TE mode, with a 90 % blocking filter at columns 276–315 × rows 237–274 on CCD 7 for the undispersed source image, see Fig. C.5. The simultaneous *RXTE* observation consisting of 20 successive data segments with a total of 59 ks good time was denoted R_1 in Sect. 2.3.4, see Table 2.7 and Fig. 2.40. The overlap of the PCA light curve and the *Chandra* exposure is shown in Fig. C.17.

Cyg X-1 was in a very hard state. Strong absorption dips occured during the observation. A detailed analysis of the non-dip spectrum has been presented by Hanke et al. (2009) and will be discussed – together with ObsIDs 8525, 9847, and 11044 – in Sect. 2.4.2.

ObsIDs 8525 and 9847

Motivated by the large diagnostic potential of *Chandra* HETGS observations for the photoionized wind and the absorption dips at $\phi_{\rm orb}\approx$0 unveiled by our previous observation, our group initiated a joint *XMM-Chandra* observation (PI: Jörn Wilms), which was later extended to a multi-satellite campaign targeted at Cyg X-1, see Sect. 2.6. The originally proposed 50 ks *Chandra* exposure simultaneous to the *XMM* observation on 2008-04-18/19 had to be split – for scheduling reasons – into ObsID 8525 with 30 ks exposure at $\phi_{\rm orb}$=0.02–0.08 in overlap with *XMM* and ObsID 9847 with 20 ks exposure at $\phi_{\rm orb}$=0.17–0.21 within the same binary orbit.

A similar detector setup was chosen as for our previous observation, ObsID 3814, namely a readout of rows 2–511 in a frame time of 1.7 s, however with a slightly larger blocking window for the zeroth order at columns 195–244 × rows 241–288 of CCD 7, see Figs. C.6 and C.7. The $10 + 2$ simultaneous *RXTE* orbits with 30 ks and 6 ks good time were denoted as R_2 in Sect. 2.3.4, see Table 2.7 and Fig. 2.41. The PCA light curve is shown again in Fig. C.18.

Cyg X-1 was in a comparable hard state during this multi-satellite campaign as during our previous *Chandra* observation. The light curves of ObsIDs 3814 and 8525 nearly adjoin in orbital phase, and show a very similar morphology of strong absorption dips. ObsID 9847 at $\phi_{\rm orb}\approx0.2$, however, contains absorption dips as well; shorter and less deep than those at $\phi_{\rm orb}\approx0$, but longer and more frequent than in the $\phi_{\rm orb}\approx0.75$ observation 3815.

ObsID 11044

Since none of the previous *Chandra* HETGS observations of Cyg X-1– apart from ObsID 2742 with 5 ks, whose spectra are heavily piled up – covered the half of the orbit from $\phi_{\rm orb}=0.2$ to 0.7, we proposed for a dedicated observation near $\phi_{\rm orb}=0.5$ to analyze *"Cygnus X-1 viewed outside of its secondary's wind"*. The proposal (PI: Michael A. Nowak) was accepted and the observation was performed on 2010-01-14, for 30 ks at orbital phase $\phi_{\rm orb}=0.48$–0.54. We again chose a half subarray readout, but this time omitting the event filter for the telemetry stream, since the events from the undispersed image will pile up and be rejected already by onboard grading, see Fig. C.8. The PCA light curve of the simultaneous *RXTE* observation with 11 ks good time is shown in Fig. C.19. It has been analyzed in Sect. 2.3.1, see Tables 2.2–2.3.

Cyg X-1 was again in a similarly hard state as in our previous observations. As expected, the light curve at $\phi\approx0.5$ does not contain absorption dips, but is – quite the opposite – remarkably constant. The spectrum shows for the first time clear P Cygni profiles with a strong emission component at a projected velocity ~0, while the weak absorption components occur at a blueshift of $\sim$500–1 000 km s^{-1} (Miškovičová et al., 2011; M. Hanke et al., in prep.).

ObsID 12472

Given the large differences between the hard state observations at $\phi_{\rm orb}\approx0.7$, 0, and 0.2 on the one hand, and $\phi_{\rm orb}\approx0.5$ on the other hand – in terms of the morphology of dipping, as well as of the line profiles –, we proposed for an observation between $\phi_{\rm orb}=0.25$ and 0.4 in order to *"fill the gap in understanding the wind structure of HDE 226868 / Cyg X-1"* (PI: Manfred Hanke). The proposal was accepted and the observation was performed on 2011-01-06. Since Cyg X-1 had, after having spent more than 4 years in a deep hard state, again entered a very bright soft state at the end of 2010 June (Grinberg et al., 2010, 2011), and as previous observations have clearly demonstrated that the frame times in TE mode lead to an unacceptable amount of pileup in the dispersed spectra (see Fig. 2.50), we chose[19] CC mode for the ACIS detector and the faint telemetry format – which allows for a better calibration of the spectra than CC graded mode. The Science Instrument Module was translated by 11.3 mm in Z direction in order to place the MEG$-|m|$ and $HEG+|m|$ spectra off the detector and thereby reduce the telemetry rate, in addition to the filter for every tenth event from columns 172–271 on CCD 7. Table 2.9 shows that the bandwidth was still saturated and a large number of frames was lost. Figure C.21 presents the 11 ks PCA light curve from the simultaneous *RXTE* observation.

[19] Planning this observation on 2011 January 6 was complicated by the fact that *Chandra*'s short term schedule had to be defined already in mid-December, due to Christmas holidays. Since 2010 November, the *RXTE* ASM light curve was no more regularly updated, and Cyg X-1 was also not in the field of view of MAXI during 2010 December 1–27. The *Swift*-BAT monitor, however, showed that the source was in a very soft state, see Sect. 2.2.1.

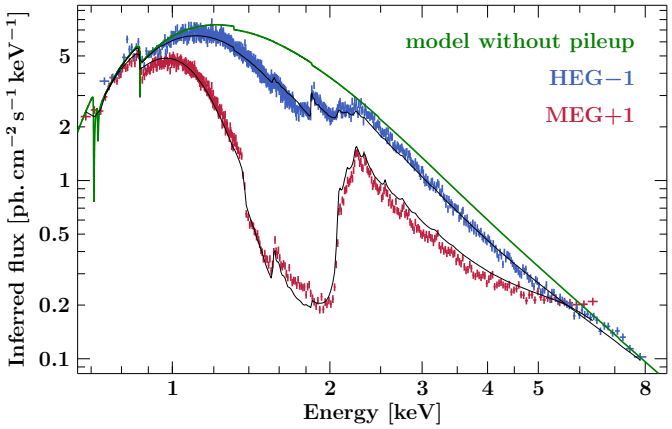

Figure 2.50: Flux-corrected spectra from ObsID 12313, obtained in TE mode during the soft state of Cyg X-1, illustrating the severity of pileup. The thick (green) line is the pileup-corrected model from a fit with `simple_gpile2` (see Sect. 1.3.4), according to which the pileup fraction is more than 40 % in HEG−1 (blue) at 6.8–7.4 Å, and more than 90 % in MEG+1 (red) at 6.1–8.9 Å.

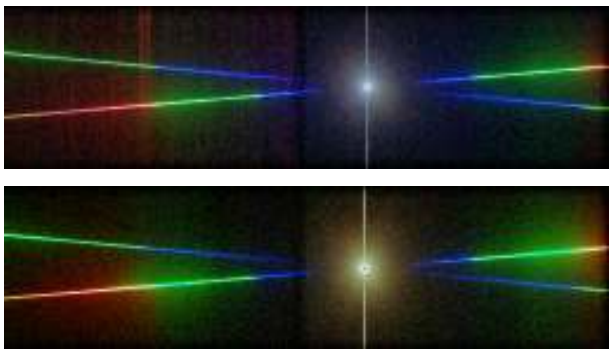

Figure 2.51: Sky images from ObsIDs 11044 (top) and 13219 (bottom), using unfiltered (level 1) events from CCDs 6 and 7. Events with energies 0.5–1.5 keV are displayed in red, 1.5–3 keV in green, and 3–10 keV in blue. Mixed colors in the pure first order spectrum (e.g., yellow in the red region) indicate pileup. The scattering halo reflects the spectrum and appears therefore bluish in the hard state and yellowish in the soft state.

ObsIDs 12313 and 12314

These DDT observations (PI: Jeffrey E. McClintock) were proposed immediately after the transition into the soft state in 2010 June in order to *"measure the spin of the black hole Cygnus X-1"*. They were performed on 2010-07-22 and 24, for 6 ks each, at $\phi_{\rm orb}$=0.33–0.34 and 0.69–0.71. ObsID 12313 employed a third subarray (rows 2–349) in TE mode, with a frame time of 1.3 s. A window with 10 % duty cycle was placed on columns 150–240 × rows 2–99, see Fig. C.9, which could, however, still not prevent frame losses due to telemetry saturation, see Table 2.9. The dispersed spectra are, as expected, heavily piled up (see Fig. 2.50), but these investigators were principally aiming at the undispersed events in the readout streak (J.E. McClintock, priv. comm.). These occur only during the 41 ms while the CCD is read out after each 1.3 s exposure. ObsID 12314, on the other hand, was performed in CC mode, also using the faint telemetry format. A 10 % filter was applied for columns 150–249 on CCD 7. Figure C.20 shows the PCA light curves from the simultaneous RXTE observations with 10 ks and 7 ks good time.

ObsID 13219

A further DDT observation (PI: Jeffrey E. McClintock) was proposed to secure the result from their two DDT observations in 2010 July, yielding a near-maximal spin of Cyg X-1 of $a > 0.97$ (McClintock et al.)[20]. This 12 ks observation 13219 was performed on 2011-02-05, at orbital phase $\phi_{\rm orb}$=0.62−0.65. A half subarray of ACIS was operated in TE mode with a frame time of 1.8 s, again focussing on the undispersed out-of-time events in the readout streak, from a net exposure of ∼20 s (J.E. McClintock, priv. comm.). No event filter was applied to the telemetry stream, see Figs. C.10 and Fig. 2.51, the latter demonstrating that observing Cyg X-1 in its bright soft state using TE mode is also very beneficial for studys of the scattering halo.

[20] See `http://cda.harvard.edu/chaser/viewerContents.do?obsid=13219&operation=propAbstract`.

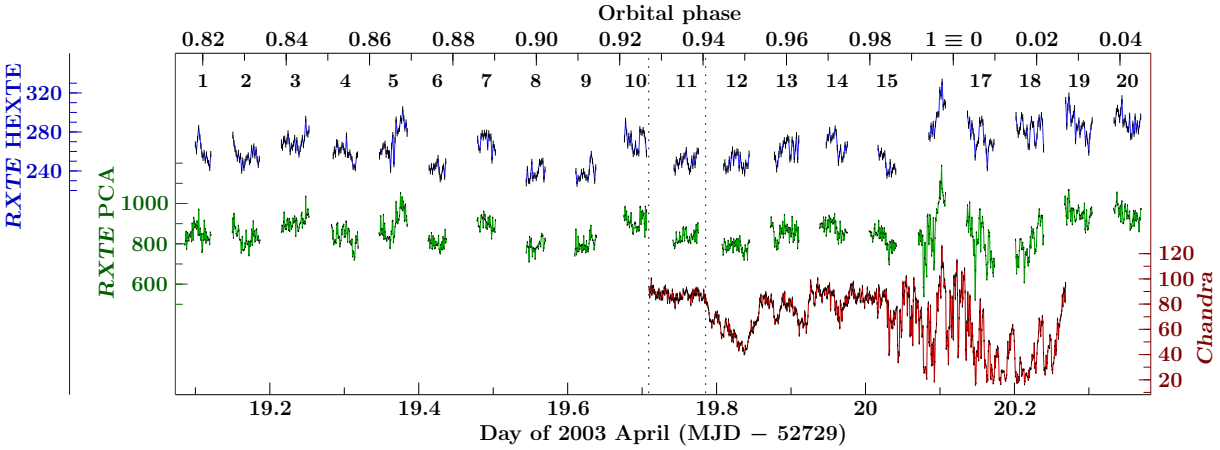

Figure 2.52: Background-subtracted light curves from the simultaneous *RXTE* and *Chandra* observations on 2003 April 19/20. Top: *RXTE*-HEXTE (20–250 keV), at 128 s time resolution (blue). The count rates from cluster A and B have been corrected for detector dead time and combined. Middle: *RXTE*-PCA (PCU 2) rate (green), and bottom: *Chandra*-HETGS (0.5–12 keV, ± first-order rate; red); both at 64 s time resolution. The numbers label the *RXTE* orbits. The vertical lines mark the first nondip part of the *Chandra* light curve (see Fig. 2.53), covering *RXTE* orbit 11. (after Hanke et al., 2009, fig. 3)

After this overview, the hard state observations will be investigated in more detail.

2.4.2 The Photoionized Wind in the Hard State

The observations 3814 and 8525 were performed five years apart, but both close to superior conjunction of the black hole. ObsID 8525 is, together with ObsID 9847, which is only separated by 44 ks, part of the multi-satellite campaign (Sect. 2.6). The simultaneous *RXTE* observations, which have been analyzed in Sect. 2.3.4, show that these spectra were very hard, with $\Gamma_2 \approx 1.5$ (see Table 2.8 on page 86). The same is true for ObsID 11044, whose concurrent *RXTE* data were modelled in Sect. 2.3.1, see Tables 2.2–2.3. All these *Chandra* observations caught Cyg X-1 therefore in the hardest region of the parameter space covered during its long-term evolution (see also Fig. 2.34 on page 78). The *Chandra* light curves of ObsIDs 3814, 8525, and 9847 (Fig. 2.45) display a very similar morphology of soft X-ray absorption dips, which will be discussed in Sect. 2.4.3. This section describes the spectrum from the persistent phases.

Observation 3814 on 2003 April 19/20 at $\phi_{\rm orb} = 0.93$–0.03

The detailed analysis of the joint *Chandra-RXTE* observation (Fig. 2.52) was published by Hanke et al. (2009). The most important results for the wind structure will be summarized in the following. Hanke et al. (2009) select the 'nondip spectrum' from the phases of persistent emission as defined by ± first order HEG + MEG count rates of >82.7 cps, see also Fig. 2.53. Accounting for pileup in the HETGS spectra with the `simple_gpile2` model (Sect. 1.3.4; see also Hanke et al., 2009, fig. 2), their continuum can be described by a power-law, absorbed by $N_{\rm H}$=5.4×10^{21} cm^{-2}. A disk component with $kT_{\rm in}$=0.25 keV was added to describe a weak soft excess. The modelling of the spectrum below 1 keV is, however, complicated by the large number of absorption lines from the photoionized wind, see Figs. 2.54 and 2.55. The systematic uncertainty of both neutral absorption and the disk parameters may therefore exceed the statistical uncertainties quoted by Hanke et al. (2009). Below ∼10.5 Å, the spectrum is dominated by absorption lines from several transitions of H- and He-like ions of Fe, Ca, Ar, S, Si, Al, Mg, and Ne in their ground state (see Fig. 1.12 on page 23). At longer wavelengths, many lines from Fe L-shell ions are often blended and complicate the identification and analysis.

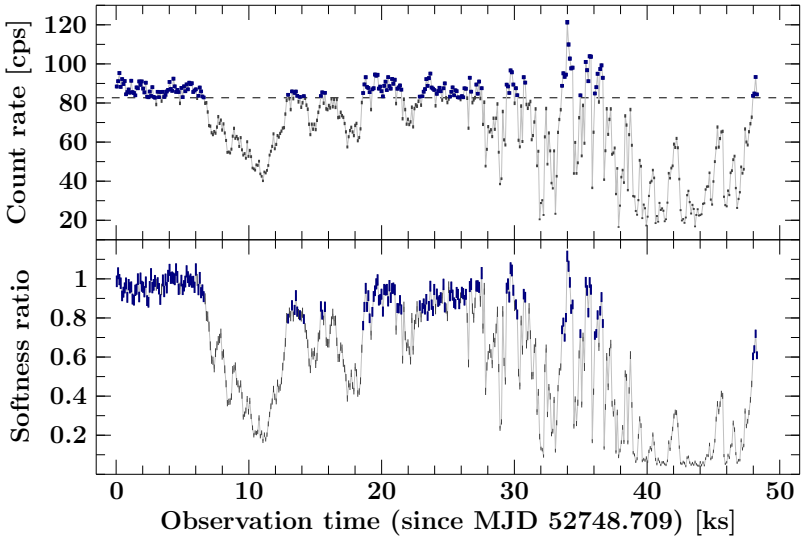

Figure 2.53: Top: *Chandra* (0.5–12 keV) light curve, at 100 s time resolution. Bottom: Softness ratio between the (0.5–1.5 keV) and (3–10 keV) band. Absorption dips – at first compact, then with complex substructure – show up with a reduced flux and spectral hardening. Count rates > 82.7 cts/s define here the nondip data, shown in blue (after Hanke et al., 2009, fig. 4).

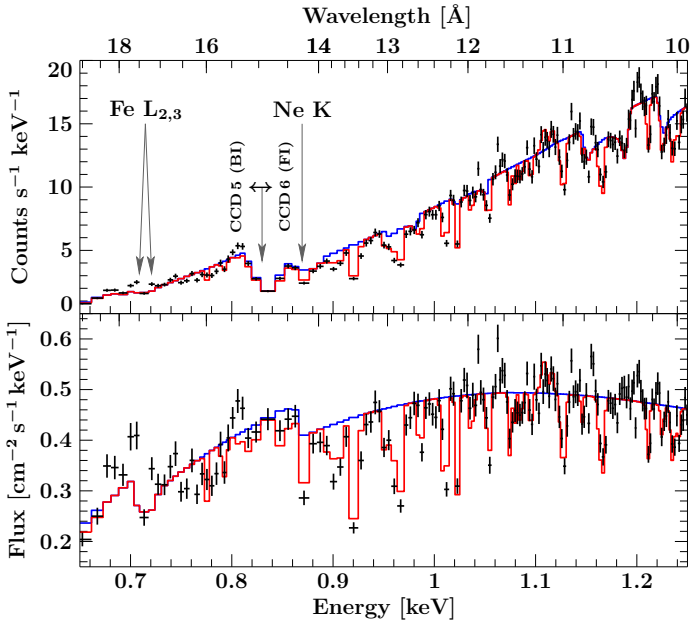

Figure 2.54: Part of ObsID 3814's MEG−1 spectrum from the nondip phase, rebinned to $S/N \geq 15$ below and $S/N \geq 20$ above 0.8 keV. Top: Spectral count rate. Bottom: Flux-corrected spectrum. The red lines are from a model including highly ionized absorption lines (Fig. 2.55); the blue lines show just the continuum. The large step in the raw spectrum at ∼15 Å is not due to an absorption edge, but due to the different sensitivity of back- and front-illuminated CCDs. Neutral absorption edges (marked by arrows) are much weaker than the total absorption by the ionized absorber.

In a first approach, the lines were modelled with Gaussian profiles, which allow to measure velocity shifts (Hanke et al., 2009, table 5) and equivalent widths W_λ according to Eq. (1.55) on page 22. If the lines are optically thin, the ionic column densities N_i are directly proportional to W_λ. Table 6 of Hanke et al. (2009) shows, however, that the strongest lines (Ly α or He α) are often saturated, as their equivalent width is smaller than expected from the linear law of Eq. (1.57) and the column density inferred from weaker transitions into higher levels.

As a second approach, alternatively to a curve of growth analysis, a model was developed that implements Voigt profiles according to Eq. (1.53) for all transitions of a series from a common ground state i. The column density N_i and velocity shift are therefore constrained by *all* lines of a series in a self-consistent way. The results are represented in Table 2.10, which lists in addition also the equivalent H column density corresponding to the sum of each element's ionic columns. For the low-Z elements O and Ne, a relatively small column of He-like ions was detected, compared to the rather large column of H-like ions. Thus, the majority of these *elements* may actually be fully ionized, also because their total equivalent N_H is much lower than for the other elements at higher Z. The fact that the fraction of He-like ions gradually increases with Z is consistent with the expected ionization balance in a photoionized plasma, see Fig. 1.15. The equivalent N_H inferred from H- and He-like ions of the higher-Z elements

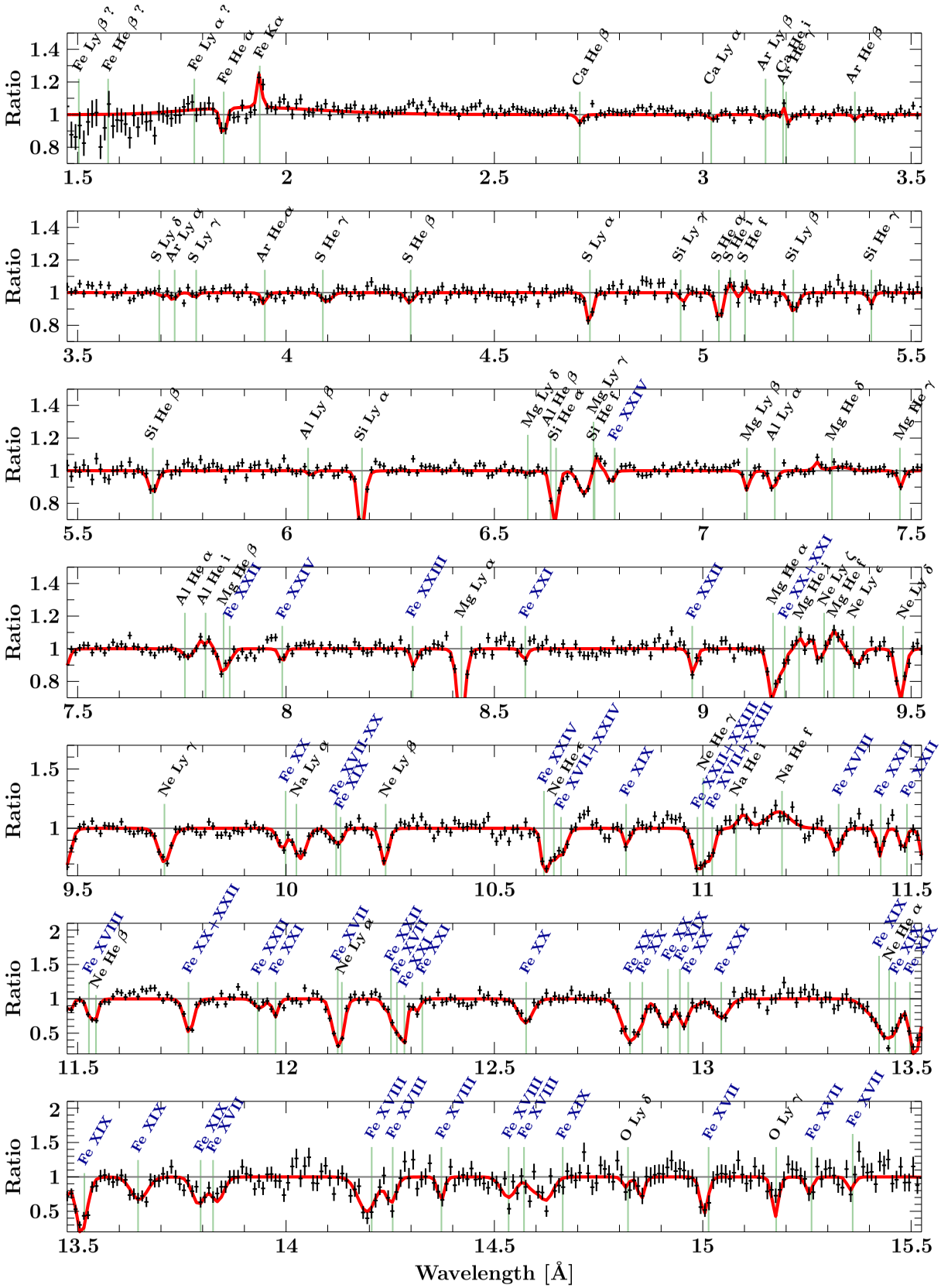

Figure 2.55: Nondip *Chandra* HETGS spectrum (combined HEG±1 and MEG±1; rebinned to 10 mÅ) from ObsID 3814, displayed as ratio of data and continuum model. The red line shows the model with Gaussian line fits, with identifications labeled at their rest wavelengths. Iron L-shell transitions (lines of Fe XVII–XXV) are labeled in blue. (after Hanke et al., 2009, fig. 10)

Table 2.10: Column densities from H- and He-like ions' line series (ObsID 3814, nondip)

	N_i in units of $10^{16}\,\mathrm{cm}^{-2}$						
	O	Ne	Mg	Al	Si	S	Ar
H-like	36^{+18}_{-12}	42^{+10}_{-4}	7.2 ± 0.6	1.4 ± 0.5	10.1 ± 0.8	15^{+12}_{-5}	11^{+1}_{-6}
He-like	0^{+4}_{-0}	$6.3^{+1.3}_{-1.6}$	5^{+2}_{-1}	$0.8^{+0.2}_{-0.4}$	12 ± 3	15^{+2}_{-3}	8^{+1}_{-4}

(from Hanke et al., 2009, table 6)

	equivalent $N_\mathrm{H} = N_i / \big(A(Z)/A(1)\big)^\dagger$ in units of $10^{22}\,\mathrm{cm}^{-2}$						
H- + He-like	$0.07^{+0.04}_{-0.02}$	$0.55^{+0.12}_{-0.05}$	$0.49^{+0.08}_{-0.05}$	$1.03^{+0.25}_{-0.30}$	1.19 ± 0.17	$2.4^{+1.0}_{-0.5}$	$7.4^{+0.6}_{-2.8}$

† using the abundances of Wilms et al. (2000), see also Table 1.2

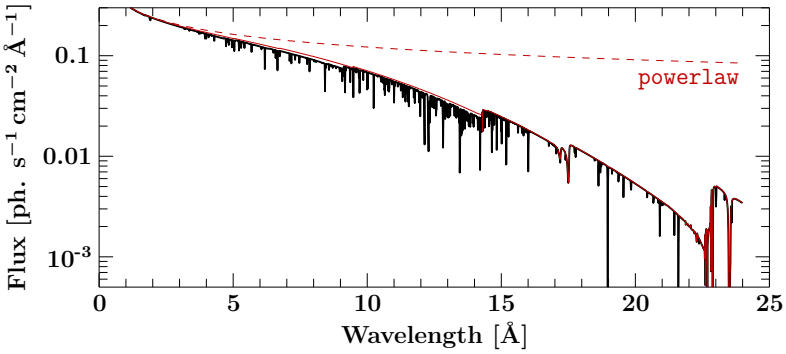

Figure 2.56: The black line shows a warm absorber model that fits the nondip spectrum at $\phi_\mathrm{orb} \approx 0$ from ObsID 3814, see Table 2.11. The dashed (or solid) red line shows the power-law only (or including neutral absorption).

is of the same order of magnitude as the total column through the wind expected from the models of the density profile presented in Sect. 2.1.2, implying that a large fraction of the wind, if not the entire wind, is highly photoionized. There is probably no contribution of the wind to the neutral column density, which is much lower than found by *RXTE* (see Fig. 2.40).

An XSTAR photoionization calculation (Hanke et al., 2009, table 11), see also Fig. 1.15 on page 27, shows that the ionization balance of Table 2.10 is qualitatively consistent with plasma at $\log \xi \approx 2$, e.g., because of the strength of Si XIV compared to Si XIII. A more quantitative result can be obtained, e.g., with the warm absorber model (T. Kallman; see also Fig. 1.16 on page 28). Figure 2.56 shows a first fit with a *single* `warmabs` model with $\log \xi = 2.38$, applied to an absorbed power law, see Table 2.11. The quality of the fit is already very promising, but the depth of the strongest absorption lines is not fully reproduced, even with adjusted individual abundances.[21] A more sophisticated modelling may also have to account for a range of ionization parameters along the line of sight.

Observation 8525 on 2008 April 18/19 at $\phi_\mathrm{orb} = 0.02$–0.08

Figure 2.57 shows that the light curve of ObsID 8525 is, similarly to the one for ObsID 3814 shown in Fig. 2.53, dominated by absorption dips. A selection of four different stages of dipping was performed based on the softness ratio between the count rates in the 0.5–1.5 keV and 3–10 keV bands. In order to achieve a similar S/N ratio, the cuts were defined such that the total number of photon events in the 1.5–3 keV band is approximately the same in all parts.

[21] It was found that `warmabs` v2.0 does not always compute the individual elements' opacities correctly, if the abundances are changed by $\leq 1\,\%$ between two successive model evaluations during fitting. This issue will be addressed by future versions of the `warmabs` model (priv. comm. with T. Kallman).

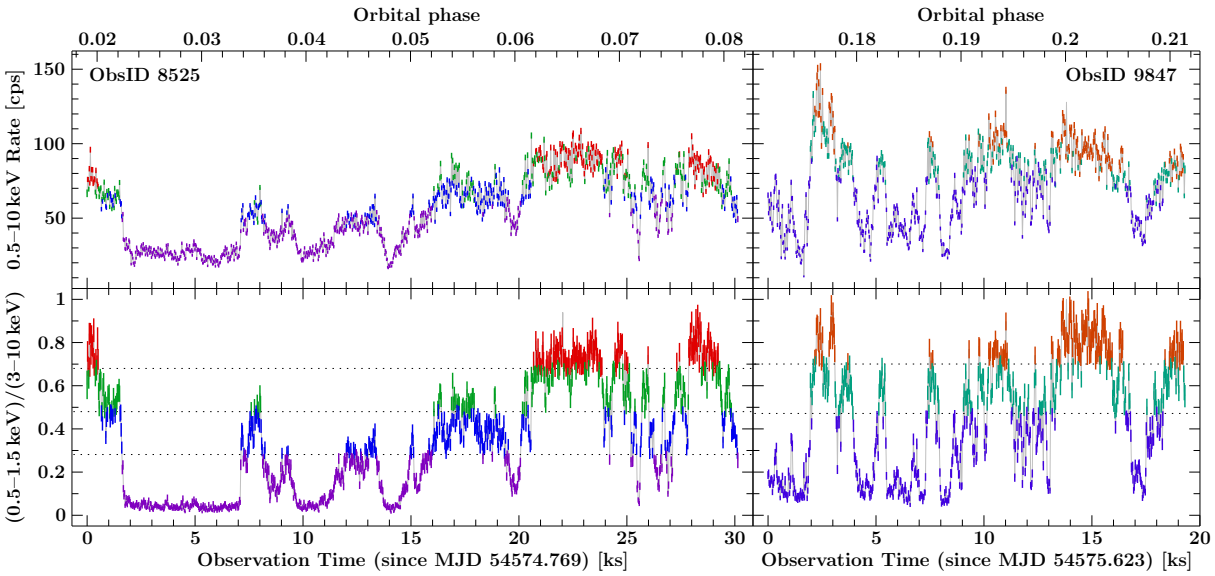

Figure 2.57: Same as Fig. 2.53, but for ObsIDs 8525 (left) and 9847 (right) on 2008 April 18/19: Top: First order *Chandra* HETGS count rate, at 25.5 s time resolution. Bottom: Softness ratio. Different stages of dipping were defined according to the color, see text for further details.

Table 2.11: Parameters of warm absorber models fitted to hard nondip spectra of Cyg X-1

Parameter		Observation (orbital phase)		
		ObsID 3814 (0.93–0.03)	ObsID 8525 (0.02–0.08)	ObsID 9847 (0.17–0.21)
·····	`powerlaw` — power-law continuum			·····
N	$[\mathrm{s^{-1}\,cm^{-2}\,keV^{-1}}]$	1.38	1.36	1.62
Γ_1		1.58	1.51	1.54
·····	`TBnew` — neutral absorption			·····
N_H	$[10^{21}\,\mathrm{cm^{-2}}]$	5.61	6.44	5.80
·····	`warmabs` — ionized absorption			·····
$\log\xi$	$[\mathrm{erg\,cm\,s^{-1}}]$	2.38	2.38	2.30
N_O	$[10^{19}\,\mathrm{cm^{-2}}]$	1.09	1.59	1.72
N_Ne	$[10^{18}\,\mathrm{cm^{-2}}]$	4.60	5.66	5.80
N_Mg	$[10^{17}\,\mathrm{cm^{-2}}]$	5.52	6.92	3.70
N_Al	$[10^{17}\,\mathrm{cm^{-2}}]$	0.12	0.22	0.11
N_Si	$[10^{17}\,\mathrm{cm^{-2}}]$	7.55	4.53	2.86
N_S	$[10^{17}\,\mathrm{cm^{-2}}]$	0.95	1.12	0.45
N_Fe	$[10^{17}\,\mathrm{cm^{-2}}]$	1.05	1.67	1.30
T_exp	[ks]	16.1	4.4	4.4
χ^2/dof		$\frac{11556.7}{8368} = 1.38$	$\frac{4216.0}{3096} = 1.36$	$\frac{4947.0}{3511} = 1.41$

Notes: Only spectra from the nondip phases were considered. The HEG + MEG ± first order spectra were rebinned to $S/N \geq 10$, and the $\lambda > 20$ Å range was ignored. The model

`simple_gpile2` $\otimes$ `powerlaw` $\times$ `TBnew` $\times$ `warmabs`

accounts for pileup in the gratings spectra. The parameters of these fits are still preliminary since no confidence intervals could have been obtained yet, as the `warmabs` model demands very high computational efforts and also requires some improvements (see also footnote 21).

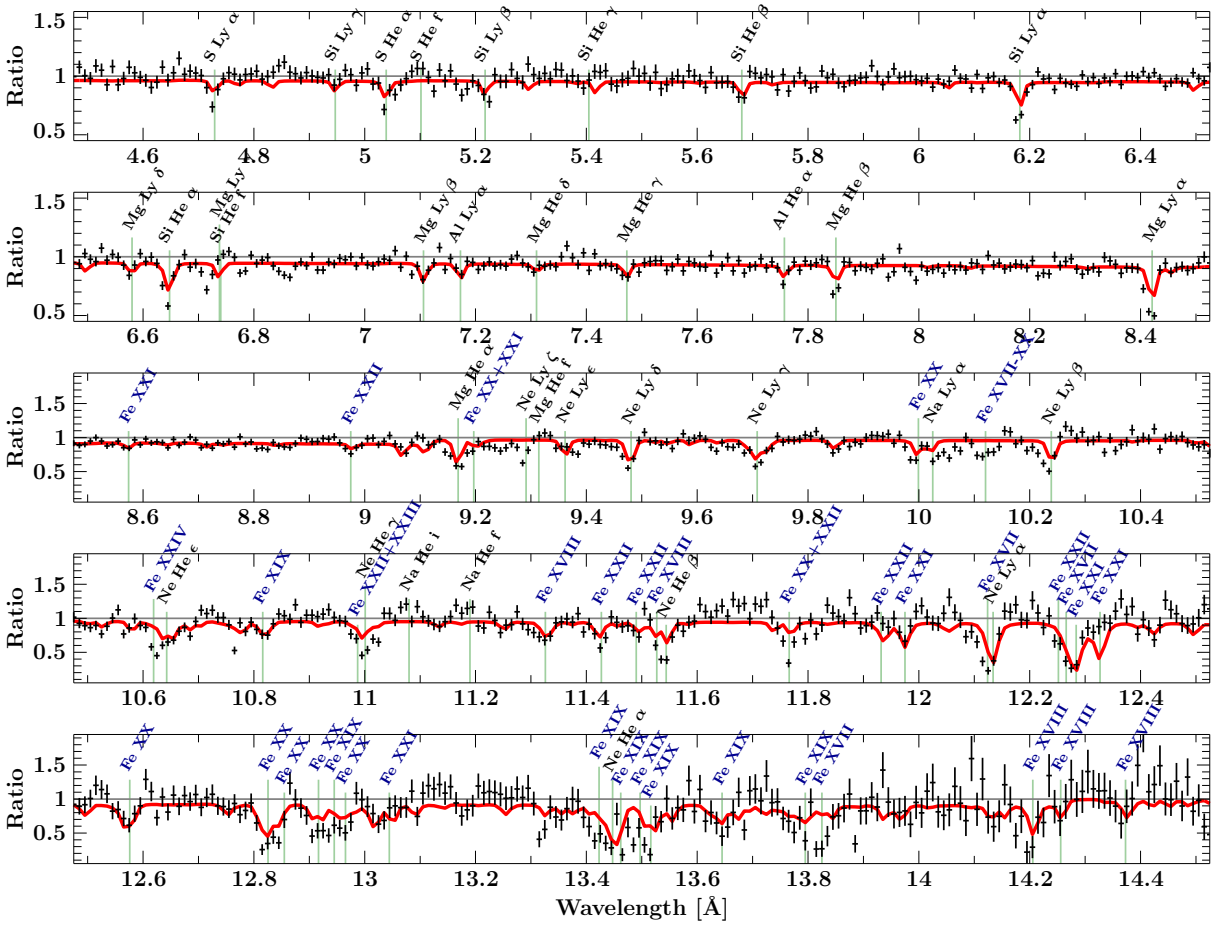

Figure 2.58: Same as Fig. 2.55, but for the nondip spectrum from ObsID 8525, modelled with the `warmabs` model of Table 2.11 (red line). The ratio of data and continuum model (excluding `warmabs`) is shown in black. The `warmabs` factor also contributes to the 'continuum', in particular at $\lesssim 9.1$ Å due to the Ne x absorption edge. The labels are a subset from the identifications in Fig. 2.55 and not directly related to the `warmabs` model.

The 4.4 ks nondip spectrum displays again a large number of absorption lines from the photoionized stellar wind, and a simple `warmabs` model can also provide a relatively good fit ($\chi^2_{\rm red}$=1.36) with similar parameters as for the spectrum of ObsID 3814, see Fig. 2.58 and Table 2.11. As before, the predicted line depths of most of the strongest lines are too small, and not all lines are modeled, but it is still notable that the `warmabs` model is able to largely reproduce the spectrum with very few parameters – $\log \xi$ and the column, and possibly individual abundances. For these fits, the abundance of O, Ne, Mg, Al, Si, S and Fe were left free. The latter is required since the abundances adopted by `warmabs` (see Table 1.2 on page 25) differ from those in the interstellar medium; e.g., the Ne abundance is less than one third of the value adopted by Wilms et al. (2001), whereas the Si abundance is almost double.

Observation 9847 on 2008 April 19 at $\phi_{\rm orb} = 0.17$–0.21

The second part of the *Chandra* exposure during the multi-satellite campaign allows to probe the wind at later orbital phases $\phi_{\rm orb} = 0.17$–0.21. Notably, the light curve is still dominated by absorption dips, see Fig. 2.57. In the same way as for ObsID 8525, different stages of dipping were isolated according to the (0.5–1.5 keV)/(3–10 keV) ratio and the S/N in the 1.5–3 keV band. However, due to its shorter length, this observation was only split into three parts.

The warm absorber model was also applied to the 4.4 ks nondip spectrum of this observation. Table 2.11 shows that the column density in Mg, Si, and S are strongly reduced compared to both observations closer to inferior conjunction of the donor star, whereas the O and Ne columns are slightly higher in ObsID 9847 than in ObsID 8525. If the former effect was significant, it would support the expectation of a reduced column density along the line of sight at later orbital phases. However, the current version of `warmabs` does not allow for a correct calculation of confidence intervals (see footnote 21), hence the answer to this question must be defered to a future version of the model. Further modelling with `warmabs` will also require to allow for a Doppler shift of the ionized absorber. The current version supports only (cosmological) redshifts, but the absorption lines in ObsID 9847 are blue-shifted – more clearly than those at earlier orbital phases. The colum density may therefore be underestimated when measured with `warmabs` at $z = 0$.

While the lines in this observation at $\phi_{\rm orb} = 0.17$–0.21 are blue-shifted, the same absorption lines in ObsID 3815 at $\phi_{\rm orb} = 0.70$–0.82 are redshifted (Miškovičová et al., 2011, fig. 6), often by a similar amount. If the lines were formed in the same region of the wind (assuming azimuthal symmetry) – even though the latter observation occured at a higher flux level, which may shift the ionization balance of the wind outwards – the Doppler shifts could be largely related to the motion of the donor star. At ϕ=0.2, HDE 226868 is approaching with the same velocity as it is receeding at ϕ=0.8, since the systemic velocity is low (Gies et al., 2008).

Observation 11044 on 2010 January 14 at $\phi_{\rm orb} = 0.48$–0.54

The observation is free of absorption dips, and the flux is remarkably constant: in the light curve at 17.4 s (i.e., 10 frame times) resolution, the 0.5–10 keV $\pm$ first order HEG + MEG count rate varies around its mean at 91 cps with a standard deviation of 6.3 cps. A single (nondip) spectrum can therefore be accumulated from the entire 30 ks of data. This spectrum (Fig. 2.59) does not show as many strong absorption lines from the photoionized wind as those at earlier orbital phases (Figs. 2.55 and 2.58), hence ObsID 11044 allows to measure the neutral absorption edges with much smaller systematic uncertainty. The following column densities result from a fit to the first order spectra in the 13–20 Å range, rebinned to $S/N \geq 10$, and including the Ne IX intercombination and O VIII Ly α emission lines at 13.55 Å and 18.97 Å, see Fig. 2.60:

$$\begin{aligned} N_{\rm Ne} &= (8.7 \pm 1.2) \times 10^{17}\,{\rm cm}^{-2} \\ N_{\rm Fe} &= (1.8 \pm 0.3) \times 10^{17}\,{\rm cm}^{-2} \end{aligned} \tag{2.37}$$

These error bars include the uncertainty of the power-law continuum, which was left free to vary as well. The columns of Eq. (2.37) are smaller than those previously found for ObsID 3814, but the systematic uncertainties due to the continuum and the ionized absorber at $\phi_{\rm orb} \approx 0$ may exceed the statistical uncertainties quoted by Hanke et al. (2009, table 3) by far.

The lines from the photoionized wind differ strongly from all previous hard state observations. Whereas resonance transitions were always detected in absorption at early orbital phases, the spectrum at $\phi_{\rm orb} \approx 0.5$ shows *emission* lines. Some of them – most clearly the Ly α transitions of Si XIV, Mg XII, and Ne X (Fig. 2.61), whose detailed parameters are given in Table 2.12 – display P Cygni profiles with a weak blue-shifted absorption component. This is the first detection of *clear* P Cygni profiles for Cyg X-1. Previous findings were restricted to "*absorption features, and many of them seem to be associated with an adjacent emission line that gives the impression of a P Cygni type line profile*" for ObsID 107 at $\phi_{\rm orb}$=0.73–0.76 (Schulz et al., 2002). The fact that the equivalent widths of the absorption lines are much smaller in this observation than at early orbital phases demonstrates that the column density of the ionized absorber is strongly modulated with orbital phase.

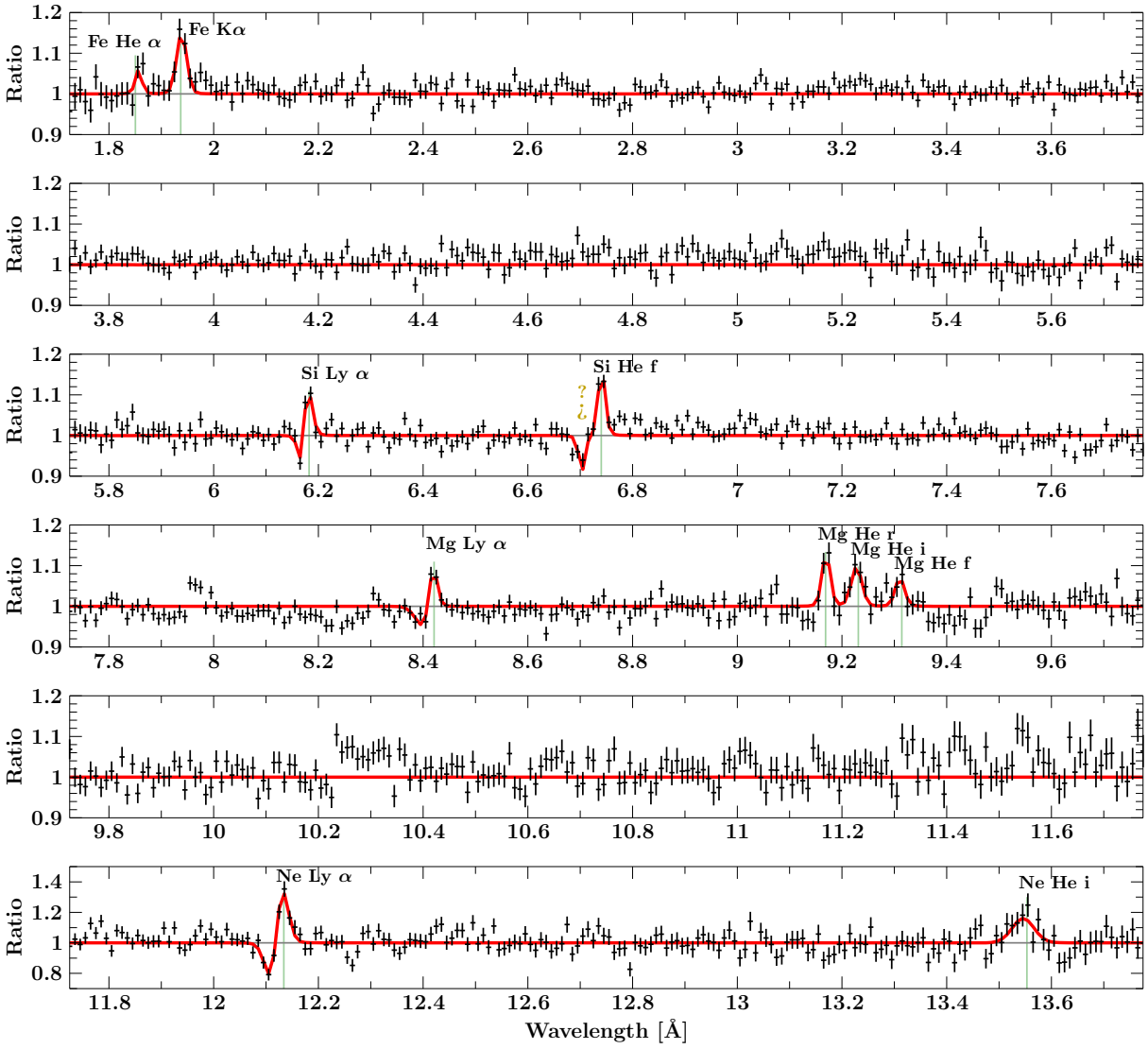

Figure 2.59: Same as Figs. 2.55 and 2.58, but for the spectrum from ObsID 11044, displayed as ratio between data and absorbed power-law continuum model. The most prominent absorption and emission lines have been fitted with Gaussians. The Ly α lines of H-like Si, Mg, and Ne show clear P Cygni profiles. The absorption line at 6.70 Å, however, cannot be related to the emission line at 6.74 Å, if the latter is due to the (dipole-) forbidden transition of Si XIII.

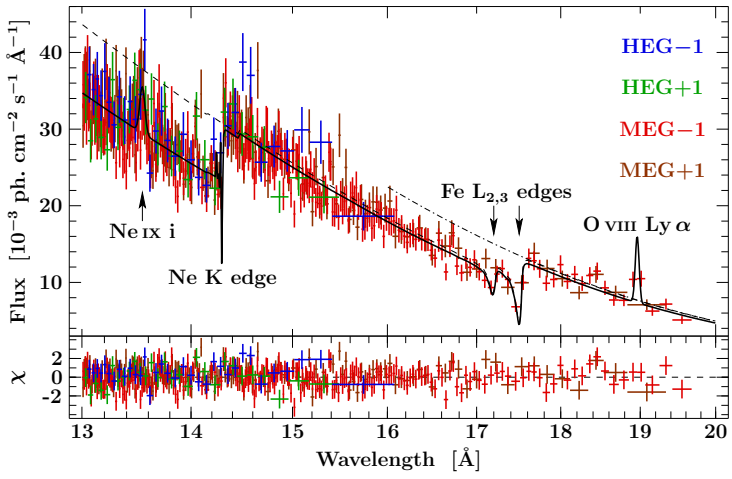

Figure 2.60: Absorption edges in the spectrum from ObsID 11044. The spectra have been rebinned to $S/N \geq 10$ each. The neutral Ne K and Fe $L_{2,3}$ edges are clearly detected at 14.3 Å, and at 17.2 Å and 17.5 Å, respectively. The model without Ne (Fe) absorption is shown by the dashed (dash-dotted) line. The fit includes the Ne IX i and O VIII Ly α emission lines.

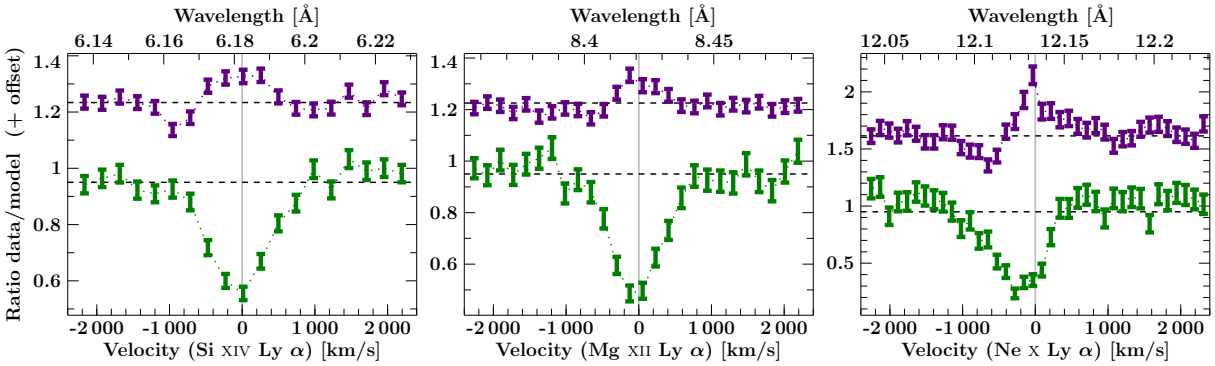

Figure 2.61: Comparison of Ly α line profiles from ObsIDs 11044 (top) and 3814 (bottom). Left: Si XIV. Middle: Mg XII. Right: Ne X. The data are shown as ratio with a continuum model, and the values for ObsID 11044 are shifted according to the horizontal dashed line. The vertical line indicates the rest wavelength λ_0, or projected velocity $v = (\lambda - \lambda_0)/\lambda_0 \cdot c = 0$.

Table 2.12: Parameters of P Cygni line profiles in the spectrum from ObsID 11044

Line	Absorption			Emission		
	λ (Å)	v (km/s)	W_λ (mÅ)	λ (Å)	v (km/s)	$F^\dagger_{-3}$
Si XIV Ly α	$6.165^{+0.011}_{-0.015}$	$-\left(817^{+119}_{-527}\right)$	$-\left(2^{+49}_{-1}\right)$	$6.181^{+0.002}_{-0.005}$	$-\left(75^{+225}_{-115}\right)$	$0.5^{+12.6}_{-0.1}$
Mg XII Ly α	$8.40^{+0.02}_{-0.05}$	$-\left(658^{+566}_{-565}\right)$	$-\left(3^{+34}_{-2}\right)$	$8.419^{+0.003}_{-0.008}$	$-\left(74^{+295}_{-95}\right)$	$0.5^{+12.7}_{-0.2}$
Ne X Ly α	$12.11^{+0.01}_{-0.06}$	$-\left(478^{+322}_{-269}\right)$	$-\left(13^{+87}_{-9}\right)$	$12.128^{+0.007}_{-0.009}$	$-\left(138^{+224}_{-175}\right)$	$1.9^{+9.9}_{-1.1}$

Notes: † F_{-3} is the line flux in units of $10^{-3}\,\mathrm{cm^{-2}\,s^{-1}}$. In this fit, there is a strong degenerary between the absorption line equivalent width and the emission line flux, since both parameters were allowed to vary freely, resulting in large confidence intervals.

Interpretation of the wind structure. The emission component appears at very low velocity, slightly blue-shifted, but with $|v| < 150\,\mathrm{km\,s^{-1}}$. The blue-shift of the absorption lines is much higher, see Table 2.12. It is a direct proof that a non-focused part of the wind exists also on the X-ray irradiated side of the donor star, and that it is accelerated to high velocities (i.e., $\gtrsim 800\,\mathrm{km\,s^{-1}}/\cos\alpha$, where α is the angle between the velocity of the wind's part causing the Si XIV absorption line and the line of sight towards the black hole; see also Fig. 2.5 on page 48). If the different line profiles at $\phi_{\rm orb}{\approx}0$ and $\phi_{\rm orb}{\approx}0.5$ result from the same wind structure, only seen at different viewing angles, the weakness of the absorption lines at $\phi_{\rm orb}{\approx}0.5$ confirms that the line of sight at this phase probes less dense regions of the wind than at the other conjunction phase. Since no net emission is seen at $\phi_{\rm orb}{\approx}0$, any emitting gas must be at small projected velocity, where the emission fills only part of the absorption trough in the continuum radiation created along the line of sight. As this gas is also seen at low velocity from $\phi_{\rm orb}{\approx}0.5$, its full space velocity must be small. It could, e.g., be related to the slow base of the spherical wind (see Fig. 2.62 for a sketch of the geometry), or to the focussed wind. Better disentangling these line profiles in the hard state through a further observation at $\phi_{\rm orb}$=0.25–0.4 was one of the goals for ObsID 12472 (PI: M. Hanke), which could, however, not be achieved as Cyg X-1 was in the soft state.

* * *

High-resolution *Chandra* spectroscopy has allowed to resolve the structure of the homogeneous part of the wind in the hard state: Large columns of highly photoionized gas at low

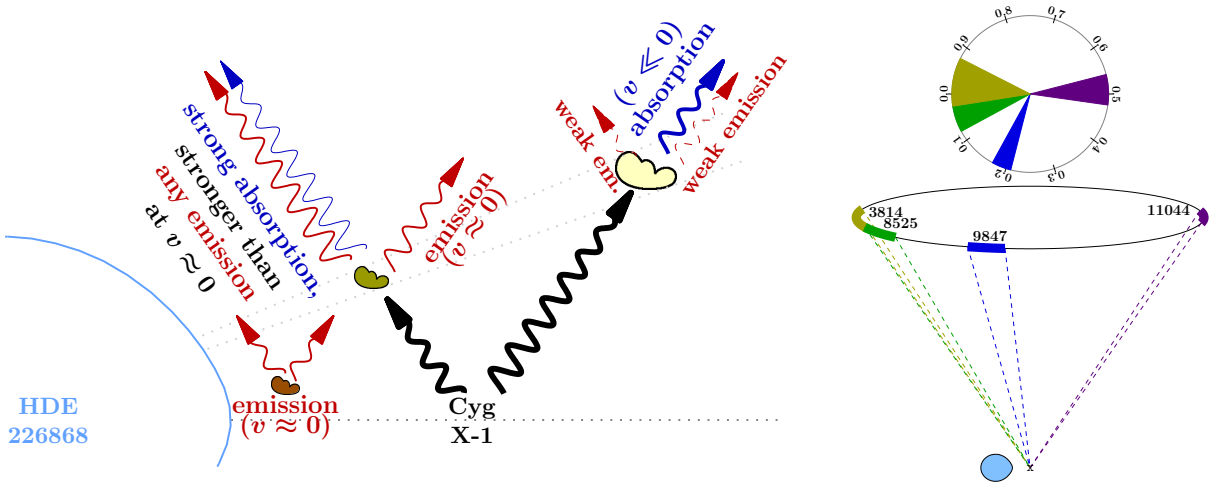

Figure 2.62: Left: Sketch of a possible interpretation of the wind structure. Right: Orbital phase coverage of the hard state observations discussed in this section, in a polar and a side view (top and bottom). The gas seen in front of the X-ray source at $\phi_{\rm orb}\approx0$ (left; dark yellow) is dense and slow, hence it creates deep absorption lines (blue) at low velocities in the X-ray continuum from Cyg X-1 (black). Its emission (red), and also the emission from all other parts of the wind that are dense enough (dark red), occurs at the same velocity, but is not sufficient to fill the absorption troughs. It may, however, be seen at $\phi_{\rm orb}\approx0.5$, where the line of sight toward the black hole probes accelerated gas (right; light yellow); absorption is blue-shifted and does therefores not interfere with the other emission. Since the latter gas is more tenous, no emission is detected. The emission seen at $\phi_{\rm orb}\approx0.5$ is not necessarily due to the same gas that causes the absorption at $\phi_{\rm orb}\approx0$. The emitting gas has to be slow (in both directions), and could, e.g., also be associated with the focused wind.

velocity are detected at $\phi_{\rm orb}\approx0$, whereas the line of sight at $\phi_{\rm orb}\approx0.5$ probes dilluted and accelerated gas further away from the donor. The next section will address the spectra during absorption dips, which are probably due to clumps in the stellar wind, although Poutanen et al. (2008) suggest that *"at least 1/3 of all X-ray dips are caused by the bulge"* at the outer edge of the accretion disk that is formed by its interaction with the accretion flow.

2.4.3 Absorption Dips

It was already seen from the light curves (Figs. 2.45, 2.53, and 2.57) that strong absorption dips were detected in *all* hard state observations at $\phi_{\rm orb}\approx0$ and $\phi_{\rm orb}\approx0.2$, but not at $\phi_{\rm orb}\approx0.5$. The deepest dipping takes place in ObsID 8525: The $\pm$first order HEG + MEG count rate in the 0.5–1.5 keV band is continually reduced from >20 cps in the 'nondip' phases to <2 cps during the first 'deep dip' lasting 90 min. At this time, the column density inferred from the fits to *RXTE* PCA spectra on 128 s time scales is $>6.8\times10^{22}\,{\rm cm}^{-2}$, see Fig. 2.41 on page 85.

Color-color diagrams and partial covering

Figure 2.63 addresses the spectral evolution in dipping using color photometry in broader energy bands. Whereas pure absorption with increasing column density would produce a track from the (soft) upper right to the (hard) lower left corner of these color-color diagrams, a bend of the track during the deepest dips is observed. This behavior can be caused by partially covering absorption (e.g., Stelzer et al., 1999; Bałucińska-Church et al., 2000):

$$f_{\rm c}\cdot\exp\Big(-N_{\rm H}\cdot\sigma_{\rm eff}(E)\Big)\;+\;(1-f_{\rm c})\cdot\exp\Big(-N_{\rm H}^{(0)}\cdot\sigma_{\rm eff}(E)\Big) \qquad (2.38)$$

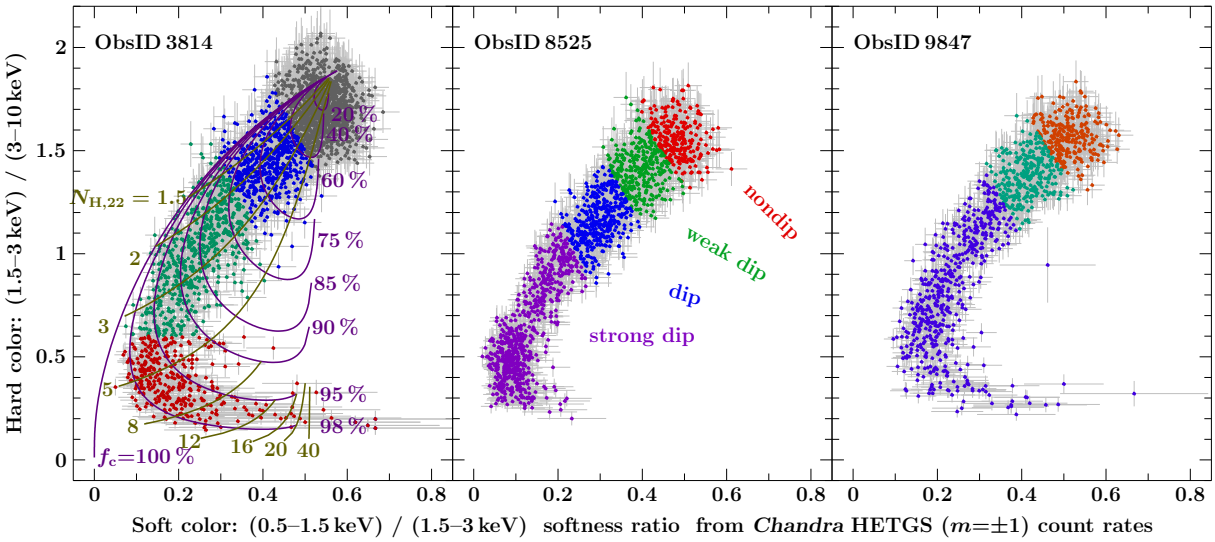

Figure 2.63: Color-color diagrams from ObsIDs 3814 (left), 8525 (middle), and 9847 (right) with strong dipping. The colors are calculated as consecutive softness ratios between the count rates in the energy bands 0.5–1.5 keV, 1.5–3 keV, and 3–10 keV, at a resolution of 17.4 s (10 frame times). A grid of partial covering models (Eq. 2.38) with covering fraction f_c (labeled in purple) and column density $N_{H,22} := N_H/(10^{22}\,cm^{-2})$ (dark yellow) from Hanke et al. (2008, fig. 5b) is plotted for ObsID 3814, see text for further details. For ObsIDs 8525 and 9847, different stages of dipping are colorized as in Fig. 2.57.

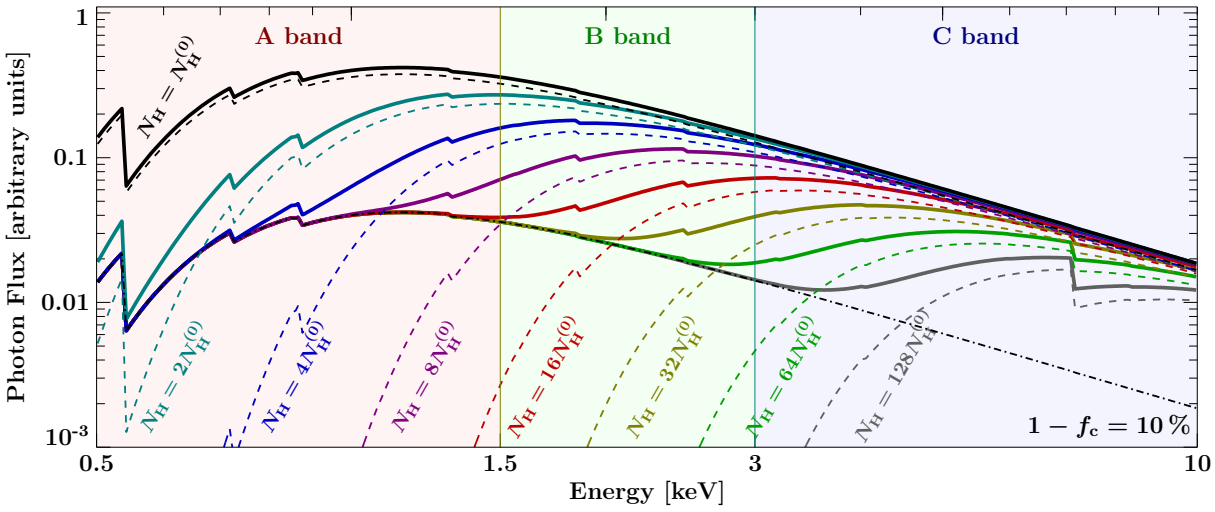

Figure 2.64: Partial absorption at constant covering factor. A constant fraction $1 - f_c = 10\,\%$ of a power-law spectrum with $\Gamma = 1.73$ is absorbed by a fixed column density $N_H^{(0)}$ (dash-dotted line), and the covered fraction f_c is absorbed by varying N_H (dashed lines). The behavior of the sum of these two components (solid lines) is considered in three bands – denoted as A, B, and C with increasing energy. At low $N_H \gtrsim N_H^{(0)}$, the covered component dominates the spectrum, and an increasing N_H decreases both ratios A/B and B/C of the fluxes in these bands, due to the energy dependence of the photoabsorption cross section. At intermediate N_H, the A band is dominated by the (constant) uncovered fraction, but increasing N_H still decreases B and C. A/B *increases* therefore again, while B/C continues to decrease. When the contribution of the covered component to both A and B bands is finally negligible, A/B remains constant, and B/C grows with increasing N_H, until the entire covered fraction is removed. In bands that are dominated by the uncovered component, partial covering acts as a mere reduction of the flux, and no increased optical depth can be detected in absorption edges.

The grid in Fig. 2.63 for ObsID 3814 (left) is calculated for a power law with photon index $\Gamma = 1.73$, of which a fraction f_c is absorbed by a column density N_H, whereas the remaining fraction is only absorbed by a constant $N_H^{(0)} \equiv 5.4\times10^{21}\,\mathrm{cm}^{-2}$. The track for $f_c = 100\,\%$ corresponds to the case of pure absorption and evolves strictly monotonically in the color-color diagram, whereas any track for $f_c < 100\,\%$ bends (twice) with increasing N_H, namely when the first (or the second) energy band starts to become dominated by the uncovered fraction $(1 - f_c)$ of the spectrum instead of the more strongly absorbed part, see Fig. 2.64.

The strongest dips in ObsID 3814 can be described by an additional absorber with $N_H = \mathcal{O}(10^{23}\,\mathrm{cm}^{-2})$ and a covering fraction $f_c = 95$–$98\,\%$ (Hanke et al., 2008). As already mentioned in Sect. 2.3.4, at least two mechanisms can lead to the detection of a partially absorbed spectrum without requiring an absorber to cover only a *spatial* part of an extended X-ray source:

1. *Time-delayed radiation scattered by a dust cloud.*
   If the scattering halo is not spatially resolved by the detector or not properly excluded, it will contribute radiation delayed by $\mathcal{O}(1-10)$ ks. That is, while the direct component shows absorption dips, the scattered component may still display an unabsorbed nondip spectrum. Nowak et al. (2011) find 20–30 % uncovered emission (i.e., $f_c = 70$–$80\,\%$ only) in similar color-color diagrams from *Suzaku* data (see also Fig. 2.87), which do not allow to discriminate the halo – unlike *Chandra* (see Fig. 2.51), with its narrow point-spread-function and high pointing accuracy. Here, particularly narrow spectral extraction regions were chosen to minimize the halo contribution in cross-dispersion direction, but the fraction of the halo that extends in dispersion direction is inevitably included. Extractions with different widths in cross-dispersion direction suggest, however, that this halo contribution is very small.

2. *Short-lived nature of absorption dips.*
   If the strongest absorption in a dip only occurs during a time shorter than the bin size used to record the light curves, various differently absorbed spectra are integrated on top of each other. Within this interpretation, the covering fraction f_c denotes the part of the *time* covered by the dip. Notably, ObsID 8525, whose light curve shows the least dipping activity on very short time scales but – especially in its first 20 ks – rather long, deep absorption dips (Fig. 2.57), displays the least pronounced deviation from the pure absorption track in the color-color diagram. The same is true for ObsID 3814 when only the compact dips in the first 26 ks are considered. This interpretation is therefore clearly favored for low covering fractions during times of fast dipping variability.

The following detailed analysis of dip spectra will suggest that the *environment of the accreting compact object* may indeed contribute *spatially* uncovered emission with $\sim$2 % of the flux.

Spectral analysis of dipping in ObsID 8525

The spectral evolution during dipping in ObsID 8525 is investigated based on the four selections of Figs. 2.57 (left) and Fig. 2.63 (middle): the 4.4 ks 'nondip' spectrum, which was already investigated in the previous section, as well as 'weak dip', 'dip', and 'strong dip' spectra with exposures of 5.0 ks, 6.3 ks, and 13.7 ks, respectively. All HEG and MEG $\pm$first order spectra from each of these four data sets are simultaneously modeled with a joint continuum, consisting of an absorbed power-law, but different (partial) absorption. The ionized absorber is taken into account by a `warmabs` model with parameters fixed to the values obtained in Sect. 2.4.2 (Table 2.11). In addition, a multiplicative flux normalization constant is applied to each of the data sets. The results are listed in Table 2.13, and the corresponding models and residuals are shown in Fig. 2.65.

Table 2.13: Parameters for the partial covering model fit to the spectra from ObsID 8525

Joint parameters		Value
.....	`powerlaw`	.....
N	$[\mathrm{s^{-1}\,cm^{-2}\,keV^{-1}}]$	1.47 ± 0.03
Γ_1		$1.568^{+0.013}_{-0.010}$
.....	$\texttt{TBnew}^{(0)}$	.....
$N_\mathrm{H}^{(0)}$	$[10^{21}\,\mathrm{cm^{-2}}]$	$6.48^{+0.15}_{-0.07}$
.....	`warmabs`	.....
as in Table 2.11 for ObsID 8525		

Data set i	Individual parameters		
	$f_\mathrm{c}^{(i)}$ (%)	$N_\mathrm{H}^{(i)}$ ($10^{22}\,\mathrm{cm^{-2}}$)	$c^{(i)}$ (%)
'nondip'	8 ± 2	$3.0^{+1.0}_{-0.6}$	$\equiv 100$
'weak dip'	$37.4^{+1.3}_{-2.0}$	$2.1^{+0.2}_{-0.1}$	$96.7^{+1.0}_{-0.9}$
'dip'	$66.4^{+0.7}_{-1.1}$	$2.29^{+0.10}_{-0.07}$	$92.3^{+0.9}_{-0.8}$
'strong dip'	91.0 ± 0.2	$4.49^{+0.06}_{-0.05}$	$79.7^{+0.7}_{-0.6}$

Notes: Each four spectra (±first order HEG + MEG) from the four different stages of dipping as selected in Fig. 2.57 (left) or Fig. 2.63 (middle), rebinned to $S/N \geq 10$ and ignoring $\lambda > 20$ Å, were fitted simultaneously with a joint continuum (left table; the parameters of the `warmabs` model were fixed at the values obtained for the nondip spectrum), and individual partial covering models (right table; index i) with individual flux normalization constants $c^{(i)}$:

$$\texttt{simple\_gpile2} \otimes \texttt{powerlaw} \times \texttt{TBnew}^{(0)} \times \texttt{warmabs} \times \left(f_\mathrm{c}^{(i)} \cdot \texttt{TBnew}^{(i)} + \left(1 - f_\mathrm{c}^{(i)}\right) \right) \cdot c^{(i)}$$

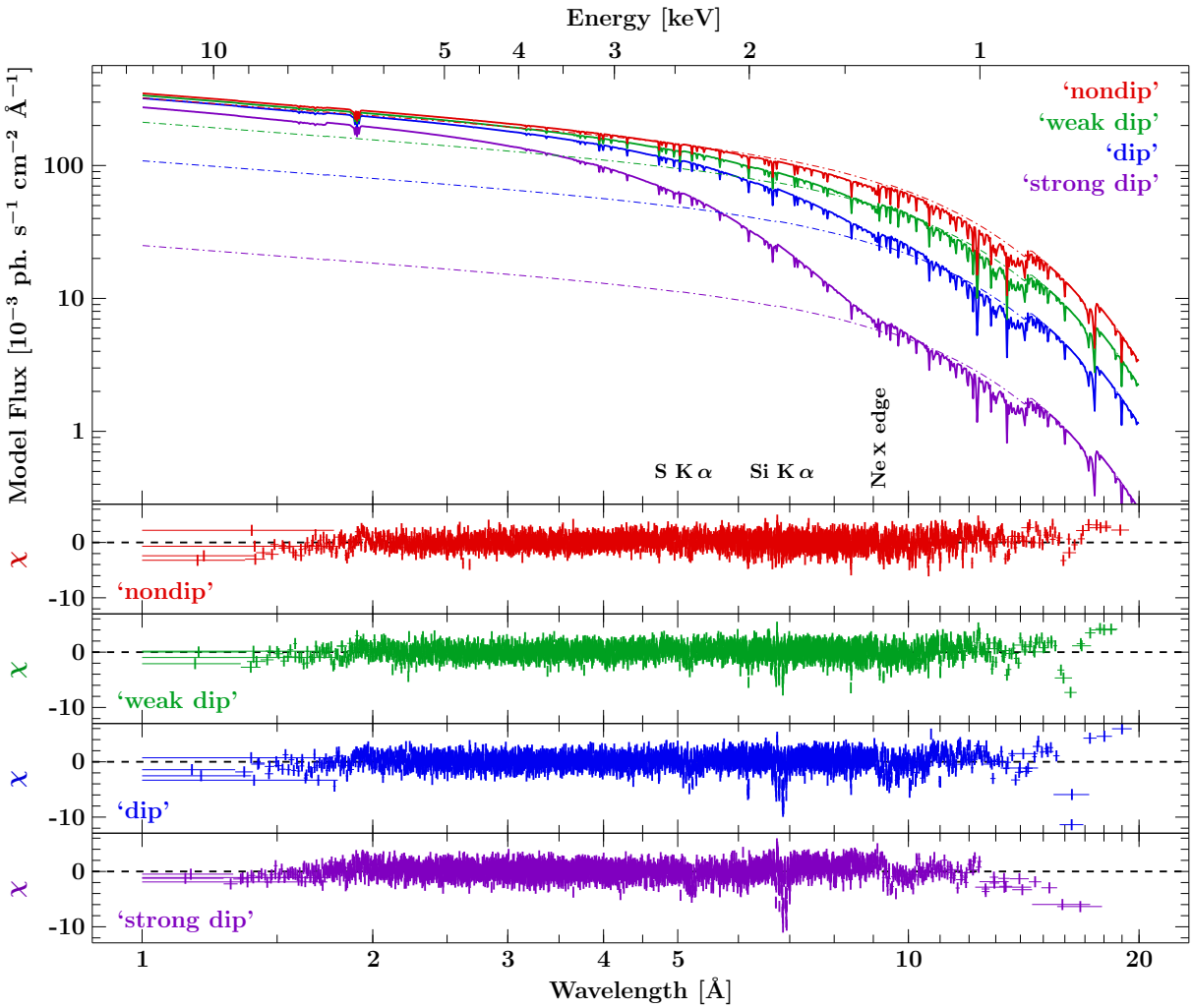

Figure 2.65: Fit to the spectra from ObsID 8525 at different stages of dipping. The top panel shows the models from Table 2.13 (solid lines), and the uncovered component without warm absorber, viz., $\texttt{powerlaw} \times \texttt{TBnew}^{(0)} \times (1 - f_\mathrm{c}^{(i)}) \cdot c^{(i)}$ (dash-dotted lines). The lower panels show the residuals of the ± first order HEG + MEG spectra from the corresponding models.

Partial covering absorption gives in general a good description for the spectral continuum, with limitations discussed below. The covering fraction increases with the degree of dipping, reaching 91 % for the 'strong dip' spectra. At the same time, the overall flux normalization decreases monotonically to 80 % of the nondip value. Although source-intrinsic flux variability cannot be ruled out as an explanation, the clear correlation with the appearance of dipping suggests a closer physical relation. A possible interpretation of this finding is that the flux reduction is due to electron scattering in an ionized cloud accompanying the dense clumps, which is consistent with hard X-ray light curves investigated in Sect. 2.6. The largest *additional*[22] neutral column density is $4.5\times10^{22}\,\mathrm{cm}^{-2}$ for the 'strong dip' spectrum. This value is lower than the $> 6.8\times10^{22}\,\mathrm{cm}^{-2}$ inferred from PCA spectra for the *RXTE* orbit during the first deep dip, but it is already obvious from Fig. 2.63 that each of the selections – and in particular the one of the 'strong dips', with the long exposure of 13.7 ks, which was chosen to achieve the same S/N in the 1.5–3 keV band – cover a broad range of absorbing column densities.

The simple partial covering of a power-law model, including ionized absorption at fixed column and ionization parameter, fails to describe the following changes in the spectrum:

- An absorption feature at $\sim$16 Å develops already during the 'weak dips', and stays significant during the stronger dips in spite of the large drop in S/N at long wavelengths.
- The jump at 9.1 Å in the residuals of the 'strong dip' spectrum, and to a weaker extent also in the 'dip' spectrum, indicates an overcorrection of the Ne x absorption with the `warmabs` model for the 'nondip' spectrum. The ionization balance must therefore change during dips such that Ne x is depopulated (either, and most likely, less strongly excited – or superionized), unless the column density of the photoionized absorber is *reduced*.
- During the dips, a sequence of strong absorption lines appears at $\lambda \lesssim 7$ Å, and a weaker one at $\lambda \gtrsim 5$ Å. They will be identified in the following and give valuable hints on the nature of the absorber.

Lower ionization stages of silicon and sulfur. Figure 2.66 shows a zoom onto the Si region of Fig. 2.65. Since the Ly α and He r transitions are contained in the `warmabs` model, its Si abundance was set to zero in order to illustrate their line depth and to compute equivalent widths in Table 2.14. In the non-dip spectrum, the strongest lines are due to H- and He-like Si XIV and XIII. The absorption lines of Li-like Si XII and Be-like Si XI may also be present in the nondip spectrum (Fig. 2.55), and have probably been misidentified by Hanke et al. (2009) as Mg XII Ly γ and the $2\,\mathrm{s} \rightarrow 6\,\mathrm{p}$ transition of Li-like Fe XXIV. During the dips, lower ionization stages appear and become gradually stronger with increasing degree of dipping. Figure 2.67 shows that the detection of strong Si VIII–X absorption is common during dips and not restricted to orbital phase $\phi\approx0$, at which those were already found for ObsID 3814 (Hanke et al., 2008, fig. 6). The analysis of ObsID 3815 shows that lower ionization stages of silicon are also detected during dips at $\phi_{\mathrm{orb}}\approx0.75$ (Miškovičová et al., 2011, fig. 4; I. Miškovičová, M. Hanke, et al., in prep.). Figure 2.68 shows that the same trend is observed for the $1\,\mathrm{s} \rightarrow 2\,\mathrm{p}$ transitions of sulfur, although at lower S/N. Strong S X–XII absorption is only observed during the dips.

The detection of lower ionization stages during absorption dips than in the highly photoionized wind seen during nondip phases has direct implications on the wind structure. The former ions can only be in equilibrium with the radiation field if they exist in correspondingly dense clumps, since the ionization parameter ξ defined by Eq. (1.60) on page 26 scales with L/n, but no big change of the ionizing hard X-ray spectrum is observed. The results presented above constitute therefore further spectroscopic evidence that the dips in Cyg X-1 are due to dense, cool matter – in addition to the finding of the nearly neutral iron absorption edge during dips (Kitamoto et al., 1984).

[22] Unlike N_{H} in Eq. (2.38), $N_{\mathrm{H}}^{(i)}$ in the model of Table 2.13 is not an absolute column, but relative to $N_{\mathrm{H}}^{(0)}$.

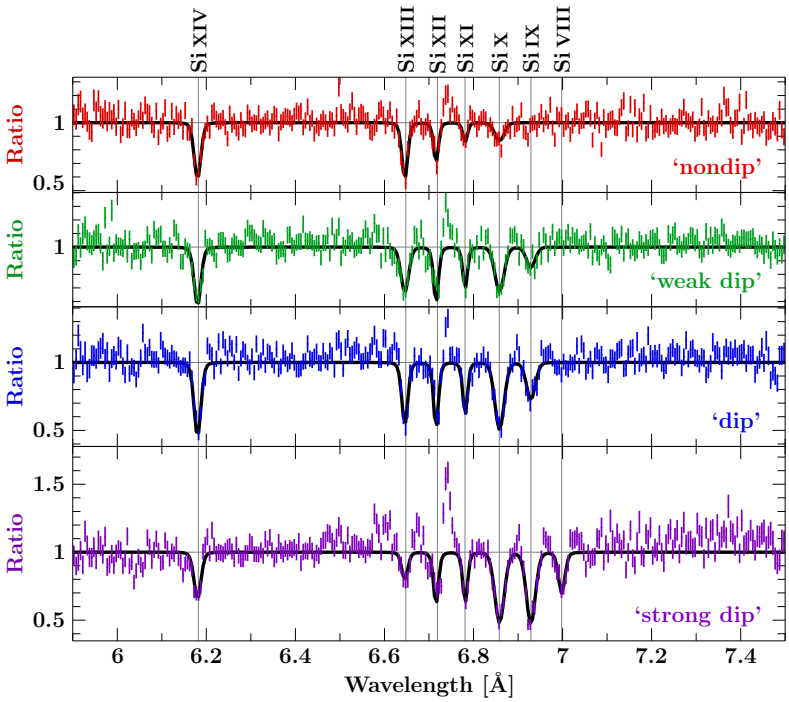

Figure 2.66: Evolution of the 5.9–7.5 Å spectrum from ObsID 8525 with dipping. The four panels show the combined HEG and MEG ±first order residuals of the data from the four data sets rebinned to 5 mÅ resolution, and the corresponding continuum model shown in Table 2.13 and Fig. 2.65. The black line is the model with Gaussian profiles described in Table 2.14. The emission at 6.74 Å is due to the Si XIII forbidden line, which was not included in the model.

[A similar version of this figure, based on the contribution to the "High-resolution X-ray spectroscopy" conference in Utrecht by I. Miškovičová, M. Hanke, et al. (2010), will appear in the 18. Newsletter about the *Chandra* mission.†
† Note added in proof: See `http://cxc.cfa.harvard.edu/newsletters/news_18/`, Fig. 13.]

Table 2.14: Parameters of silicon 1 s → 2 p absorption lines in ObsID 8525

Ion	Wavelength (Å)			Equivalent Width (mÅ)			
	(atdb)	(H69)	(measured)	'nondip'	'weak dip'	'dip'	'strong dip'
XIV	6.1822	···	6.1803(7)	-9.7 ± 1.2	-9.9 ± 1.2	$-12.1^{+1.1}_{-1.2}$	$-7.5^{+1.1}_{-1.2}$
XIII	6.6479	6.684	$6.6459^{+0.0012}_{-0.0011}$	-8 ± 2	$-8.8^{+1.8}_{-1.9}$	-9.0 ± 1.1	-3.9 ± 1.3
XII†	···	6.750	$6.7160^{+0.0013}_{-0.0010}$	$-5.1^{+1.2}_{-1.3}$	$-6.7^{+1.2}_{-1.4}$	$-7.8^{+1.2}_{-1.3}$	$-6.3^{+1.2}_{-1.3}$
XI	···	6.813	$6.7813^{+0.0010}_{-0.0009}$	-2.6 ± 1.0	-5.0 ± 0.9	$-6.1^{+0.8}_{-0.9}$	-5.8 ± 1.0
X	···	6.882	6.8584(8)	$-4.8^{+1.6}_{-1.5}$	-10.5 ± 1.3	$-14.9^{+1.2}_{-1.3}$	$-15.0^{+1.2}_{-1.3}$
IX	···	6.947	$6.9289^{+0.0012}_{-0.0011}$	···	-4.8 ± 1.4	-8.1 ± 1.3	-14.3 ± 1.3
VIII	···	7.007	6.998(3)	···	···	···	-6.2 ± 1.5

Notes: (atdb) Wavelength according to the `atomdb`. (H69) Wavelengths according to House (1969, table 2), which follow from Hartree-Fock calculations that have been *"corrected by arbitrarily forcing agreement between the wavelength of the first ion treated in the calculations and the observed normal Kα transition"*. The values for the highly ionized ions are generally larger than those of more recent calculations (e.g., Palmeri et al., 2008, who list a large number of *different* 1 s → 2 p transitions).
† The emission due to the forbidden line of Si XIII is very close to the Si XII absorption line. Modelling *both* lines with their positions and strengths allowed to vary freely at the same time would give rise to a strong degeneracy between their equivalent widths.

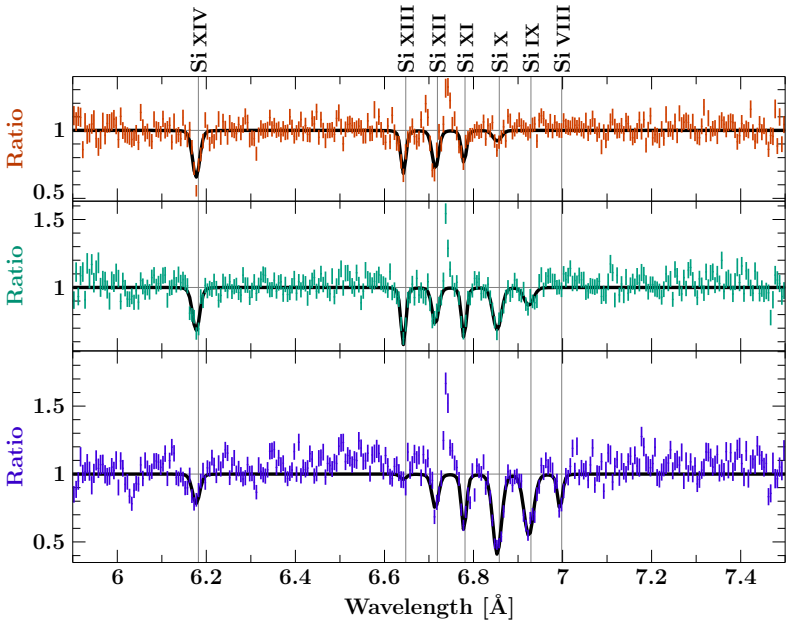

Figure 2.67: Same as Fig. 2.66, but for ObsID 9847 and the selection of three different stages of dipping from Figs. 2.57 and 2.63. As for ObsID 8525, a partially absorbed power-law continuum, including ionized absorption fixed to the parameters obtained for the nondip spectrum (Table 2.11), has been assumed.

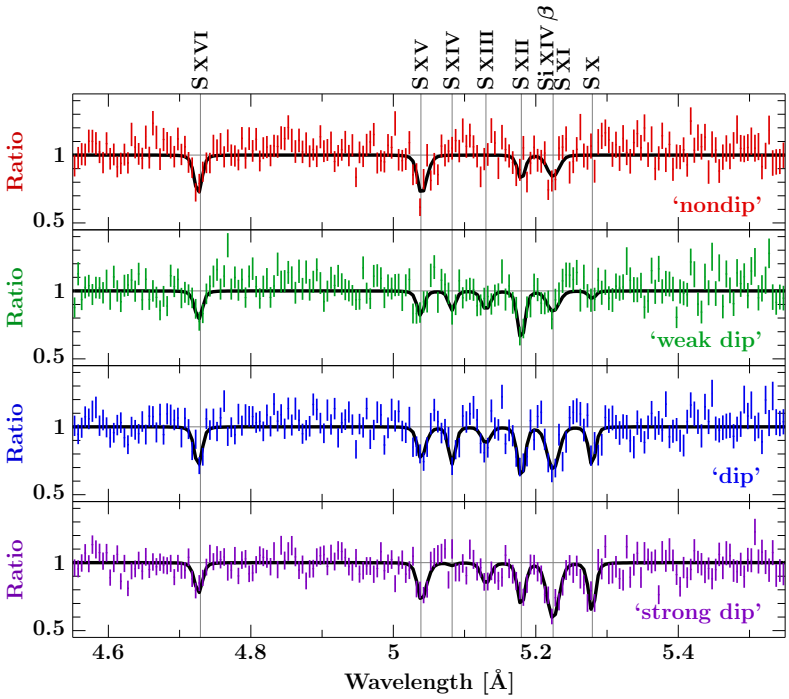

Figure 2.68: Same as Fig. 2.66, but for the 4.6–5.5 Å region of the spectrum including the $1s \rightarrow 2p$ transitions of sulfur. The S XI line is probably blended with Si XIV Ly β at 5.2172 Å. These lines show the same trend as the Si lines: strong absorption lines from lower ionization stages are only detected during the dips.

Spectrum during the deepest dip. Since the finding of partial covering during absorption dips has important implications for the interpretation of the wind structure, the uncovered emission is investigated in further detail. ObsID 8525 provides the opportunity to analyze an extremely absorbed spectrum. 5.3 ks of data were therefore extracted from the first 'deep dip' at the beginning of the observation. The spectrum is so strongly absorbed that pileup is negligible, and the flux-corrected HEG and MEG spectra agree with each other, see Fig. 2.69. As for the previous dip spectra, there is again a soft excess beyond an absorbed power-law with 100 % covering. A partially absorbed power-law model, however, gives a good overall description of the spectrum, with $\chi^2/\mathrm{dof} = 4193.5/3816 = 1.1$. Both the covered fraction $f_c = \left(97.5^{+0.2}_{-0.3}\right)$ % and $N_H = \left(6.20^{+0.14}_{-0.12}\right) \times 10^{22}\,\mathrm{cm}^{-2}$ – defined as in Eq. (2.38) – are larger than for the 'strong dip' spectrum (Table 2.13). This N_H value is therefore closer to those inferred from *RXTE* PCA fits ($> 6.8 \times 10^{22}\,\mathrm{cm}^{-2}$). However, there are large residuals in the 9–12 Å range,

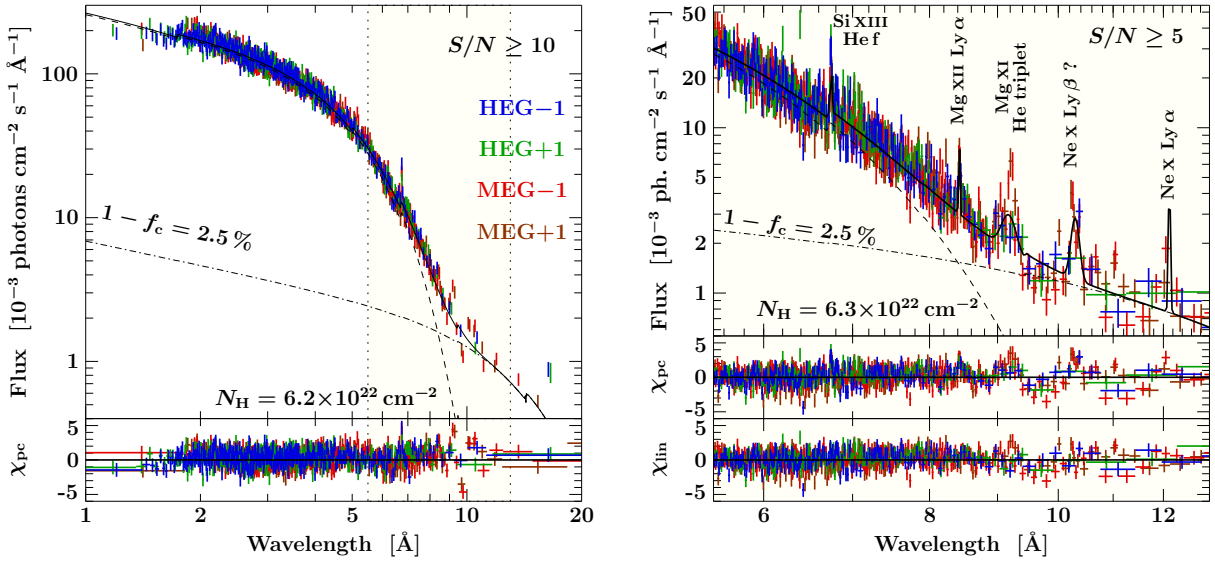

Figure 2.69: 'Deep dip' spectrum from ObsID 8525, from a subset of the 'strong dip' data of Table 2.13 and Fig. 2.65. Left: Partially absorbed power-law fit to the first order *Chandra* HETGS data, rebinned to $S/N \geq 10$. The upper panel shows the flux corrected data together with the model. The dashed and dash-dotted lines display the absorbed and uncovered components. The lower panel shows the residuals $\chi_{\rm pc}$, with strong discrepancies around 10 Å. Right: Zoom onto the 5.5–13 Å range, with the data only rebinned to $S/N \geq 5$, revealing emission lines. The lower two panels shows residuals $\chi_{\rm pc}$ for the pure partial covering model, and $\chi_{\rm lin}$ for the model including the five strongest emission lines of Si XIII, Mg XII, Mg XI, and Ne X (α and β?).

where the *un*covered component dominates. A more detailed analysis of this region (Fig. 2.69, right) clearly demonstrates the presence of *emission* lines. The most prominent ones are due to Si XIII He f (at 6.744 ± 0.002 Å), Mg XII Ly α (at 8.424 ± 0.003 Å), Mg XI He α (at 9.17 ± 0.04 Å) and probably the entire triplet, as well as Ne X Ly β (at 10.3 Å) and Ne X Ly α (at $12.13^{+0.02}_{-0.03}$ Å).

Origin of the uncovered emission. The fit including these lines gives the impression that there might still be broader line emission on top of a much lower continuum level, especially since a larger number of lines, which are not resolved given the limited statistics of the spectrum in this strongly absorbed region, might contribute. The uncovered fraction of (2.52 ± 0.13) % is therefore yet only an upper limit. One can speculate whether the little uncovered emission is fully due to the wind's reprocessed radiation. In this case, the interpretation of the residual *effective* partial covering requires indeed partial *spatial* covering by the absorbing clump(s), though not necessarily of the primary X-ray source, but probably of the entire part of the wind that is dense enough to re-emit a significant amount of secondary radiation.

* * *

The spectroscopy of absorption dips has confirmed the interpretation of the wind structure sketched in Fig. 2.62 on page 108. Just as at $\phi_{\rm orb} \approx 0.5$, secondary emission *is* present also at $\phi_{\rm orb} \approx 0$, but could only be isolated from the continuum during the 'deep dip' when the direct component is heavily blocked. Figures 2.66 and 2.67 show that the *emission line equivalent width* of the Si XIII forbidden line increases with the degree of dipping, demonstrating that not all of the emission is subject to the same strong absorption as the continuum. Since the *total line flux* is nevertheless decreasing (see Fig. 2.65), part of the emission must still be covered by

the absorber. This effect may also cause the decrease of the equivalent width of absorption lines from the highly ionized ions Si XIV and Si XIII (see Table 2.14). If no partial covering of line *emission* took place, the reduction of their *absorption* line depth would imply a smaller column density of H- and He-like ions during dips than in the nondip phase, which would be consistent with the decrease of the Ne X absorption edge that is indicated in Fig. 2.65. In the latter interpretation, absorption dips could be related to a change in the ionization balance of (part of) the wind, without necessarily requiring an additional, less highly ionized absorber passing through the line of sight.

The next section proceeds to the *XMM* observations of Cyg X-1, which are even less numerous than those by *Chandra*. In particular, the hard state at an *RXTE* ASM (1.5–12 keV) rate of <30 cps is solely covered by three X-ray observations. Only the one from our multi-satellite campaign took place at $\phi_{\rm orb} \approx 0$ and in a very hard state, and will therefore be analyzed in more detail, after a preliminary study of the other observation using EPIC-pn in burst mode.

2.5 *XMM-Newton* Observations

2.5.1 Overview

The first *XMM* observations of Cyg X-1 were performed in 2004, as part of two larger observing programs[23]: (formally) nine observations from proposal 20240 (PI: Jon Miller), and four from proposal 20276 (PI: Jörn Wilms), with exposures of $\sim$9–22 ks each. The *RXTE* ASM light curve in Fig. 2.71 shows that Cyg X-1 was in intermediate or soft states during all *XMM* observations of 2004. After those, the next one was the $\sim$60 ks observation in 2008 April, which is part of our multi-satellite campaign (Sect. 2.6). Two further 26–34 ks *XMM* pointings to Cyg X-1 were performed in 2009, see also Table 2.15 and Fig. 2.70.

Jon Miller's observations 020240 oo 01

XMM was not directly pointed toward Cyg X-1 during the first seven observations of this campaign (oo = 01 and 05–10), but 10–11 arcminutes off-source. As a result, Cyg X-1 was not in the field of view (FoV) of both RGSs, but at most[24] in the FoV of the pn camera, which was operated timing mode with the medium filter for these exposures. Although the MOS cameras were switched off such that their telemetry capacity could be reallocated to the pn instrument, all timing mode observations still suffered from frame dropouts, yielding fractional exposures of only $\sim$0.5. Unlike observations oo = 09–12, the five earlier observations have (quasi-) simultaneous *RXTE* coverage.

For the last two observations in 2004 October (oo = 11–12), when the source was in the high/soft state (Miller et al., 2009b), the EPIC-pn burst mode was applied, using the medium filter, too. For the burst mode's special readout, the pointing position is more strongly constrained. Cyg X-1 was therefore also in the field of view of both RGSs. Their first order spectra, however, suffer from strong pileup due to the high flux. Miller et al. (2009b) infer from the EPIC-pn burst mode spectra of these latter two observations – probably without correcting for a gain shift (see Sect. 2.5.2), as Miller et al. (2009b, fig. 15) find large *"features around 2 keV [that] are instrumental"* – that the spin of the black hole in Cyg X-1 is very low, namely $a = 0.05(1)$.

[23] *XMM* ObsIDs are in the format PPPPPP 00 LL, with the proposal number PPPPPP, and the identifier of the individual observation 00 LL, see http://xmm.esa.int/external/xmm_user_support/documentation/dfhb/.

[24] For each of the 9 ks ObsIDs 020240 07 01 and 020240 08 01 with 7 ks and 2 ks of pn exposure, the region on the chip that is active in timing mode did not measure more than one outer wing of the PSF from an off-axis source.

Table 2.15: *XMM-Newton* observations of Cyg X-1

PI, ObsID	Start Date T_0 (YYYY-mm-dd)	(MJD)	Date$^\dagger - T_0$ (days)	$\phi_{\rm orb}{}^\dagger$	$r_{\rm S}$ (cps)	Instruments‡
PI: Jon Miller (propsal 20240):						
020240 01 01	2004-04-07	53102	0.588–0.736	0.12–0.15	45.5	pn(ti), [RGS 1&2], OM
020240 05 01	2004-04-09	53104	0.581–0.729	0.48–0.50	38.7	pn(ti), [RGS 1&2], OM
020240 06 01	2004-04-11	53106	0.571–0.719	0.83–0.86	32.1	pn(ti), [RGS 1&2], OM
020240 07 01	2004-05-17	53142	0.515–0.622	0.25–0.27	(23)	[pn(ti)], [RGS 1&2], OM
020240 08 01	2004-05-21	53146	0.496–0.603	0.96–0.98	(23)	[pn(ti)], [RGS 1&2], OM
020240 09 01	2004-06-02	53158	0.458–0.565	0.10–0.12	23.6	OM
020240 10 01	2004-06-08	53164	0.455–0.562	0.17–0.19	(29)	pn(ti), [RGS 1&2], OM
020240 11 01	2004-10-06	53284	0.023–0.247	0.52–0.56	80.7	pn(bu), RGS 1&2, OM
020240 12 01	2004-10-08	53286	0.018–0.241	0.88–0.92	67.6	pn(bu), RGS 1&2, OM
PI: Jörn Wilms (proposal 20276):						
020276 02 01	2004-11-14	53323	0.909–1.140	0.64–0.69	35.7	pn(ti*), RGS 1&2, OM
020276 03 01	2004-11-20	53329	0.893–1.125	0.71–0.75	(33)	pn(ti*), RGS 1&2, OM
020276 04 01	2004-11-26	53335	0.878–1.136	0.78–0.83	44.8	pn(ti*), RGS 1&2, OM
020276 05 01	2004-12-02	53341	0.862–1.005	0.85–0.88	36.9	pn(ti*), RGS 1&2, OM
PI: Jörn Wilms (proposal 50088):						
050088 02 01	2008-04-18	54574	0.484–1.185	0.97–0.09	14.7	pn(bu), RGS 1&2
PI: Norbert Schartel (Project Scientist):						
061000 04 01	2009-05-16	54967	0.969–1.270	0.24–0.29	27.3	pn(bu), RGS 1&2, OM
PI: Phil Uttley (proposal 60561):						
060561 04 01	2009-12-02	55167	0.144–0.537	0.80–0.87	20.8	pn(ti), RGS 1&2, OM

† The quoted dates specify the total *observation* time, which may exceed the individual exposures. $r_{\rm S}$ is the *RXTE* ASM (1.5–12 keV) count rate as in Table 2.9.
‡ pn(ti), pn(ti*), and pn(bu) refer to the EPIC-pn timing, modified timing, and burst mode. [RGS] and [pn] indicate that Cyg X-1 was not in the corresponding FoV due to offset-pointing.

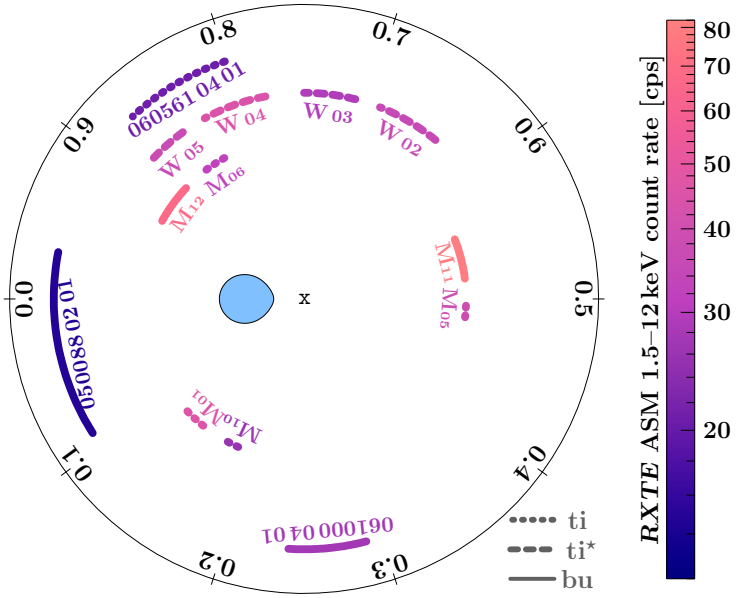

Figure 2.70: Orbital coverage of the *XMM* observations of Cyg X-1 prior to 2010. The color scale indicates the source's (quasi-) simultaneous *RXTE* ASM flux according to the scale on the right. Dotted / dashed / solid lines indicate the EPIC-pn camera operated in timing / modified timing / burst mode. The labels 'M' and 'W' refer to the series of observations by Jon Miller and Jörn Wilms, respectively. All single observations are labeled with their full ObsID.

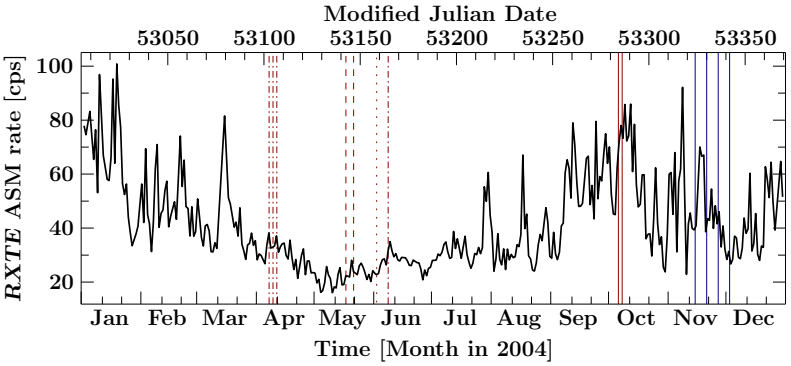

Figure 2.71: *RXTE* ASM (1.5–12 keV) 1-day average count rate of Cyg X-1 in 2004. The red and blue vertical lines mark the times of the *XMM* observations from Jon Miller's proposal 20240 and Jörn Wilms' proposal 20276, respectively.

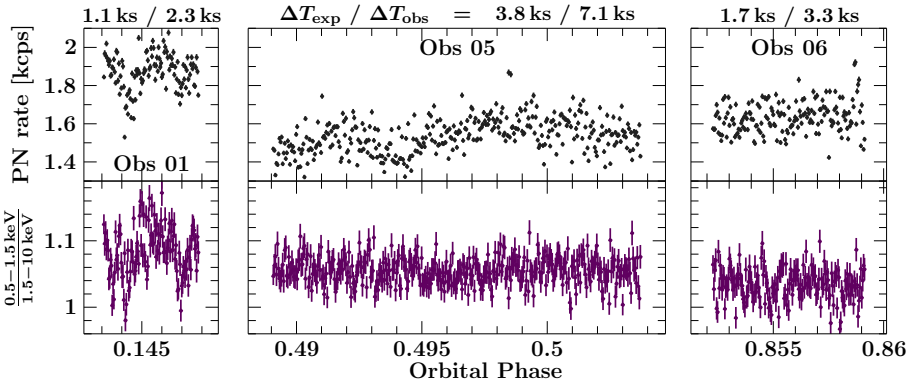

Figure 2.72: EPIC-pn light curves (corrected for the exposure time), and softness ratios from the timing mode observations in 2004 April, at 20 s time resolution.

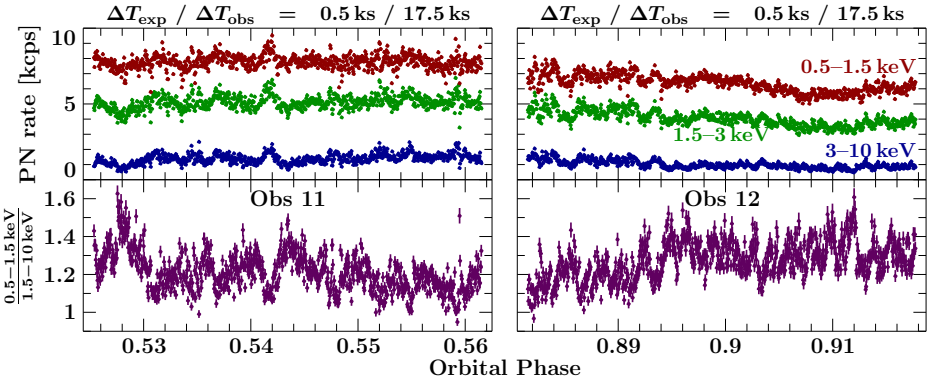

Figure 2.73: Same as Fig. 2.72, but for the burst mode observations in 2004 October. The count rate is displayed in the energy bands 0.5 – 1.5 keV (red), 1.5 – 3 keV (green), and 3–10 keV (blue).

(Note that the x-axis in Fig 2.73 is compressed by a factor of 2.5 compared to Fig. 2.72.)

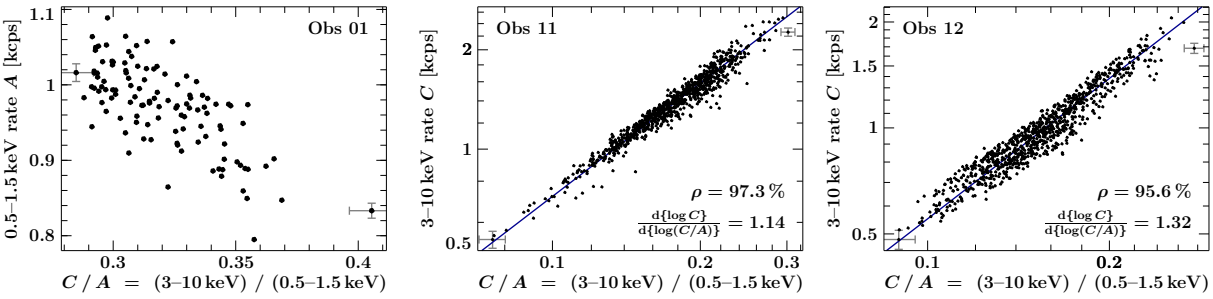

Figure 2.74: Hardness-intensity diagrams for observations oo = 01, 11 and 12 from proposal 20240. Representative error bars are indicated for the two data points at extreme hardness values. While the first one contains absorption dips, as decreased soft X-ray flux accompanied by spectral hardening, the latter two soft state observations show a remarkable correlation between the hard X-ray flux and the hardness, although with a different slope. The linear correlation coefficient ρ has been calculated from the logarithm of both hardness and count rate, i.e., the linear fit of Eq. (2.39) corresponds to the power-law correlation of Eq. (2.40).

The pn light curves from observations oo = 01, 05, and 06 in timing mode (oo = 10 is omitted here because of the short duration of the pn observation of 405 s) are shown in Fig. 2.72, and likewise the burst mode light curves from observations oo = 11 and 12 in Fig. 2.73. The oo = 01 observation seems to contain absorption dips at orbital phases $\phi_{\rm orb} = 0.144$ and $\phi_{\rm orb} = 0.147$. The hardness-intensity diagram (Fig. 2.74) confirms that the reduction in soft X-ray count rate is weakly correlated (linear correlation coefficient $\rho = 72\,\%$) with the hardness. The source variability in the soft state observation oo = 11 (oo = 12) presents a pronounced correlation between hard X-ray flux and spectral hardness, with a correlation coefficient of 97.3 % (95.6 %). Denoting the count rate in the 0.5–1.5 keV and 3–10 keV bands with A and C, the 'linear' fit

$$\log(C) \;=\; a \;+\; b \cdot \log(C/A) \tag{2.39}$$

with $b = 1.14$ (1.32) for oo = 11 (oo = 12) corresponds to the weak power-law dependence

$$A \;\propto\; C^{(b-1)/b} \tag{2.40}$$

with 'power-law index' $(b-1)/b = 0.12$ (0.24), i.e., the soft X-ray band at 0.5–1.5 keV, in which the accretion disk strongly contributes to the emission, does not depend very strongly on the hard X-ray band at 3–10 keV, which is dominated by the Comptonized component. In other words, any variability is mostly due to the hard X-ray band. And indeed, the relative root mean square variability, $\sigma_A/\langle A\rangle$, is only 5.8 % (8.9 %), whereas $\sigma_C/\langle C\rangle$ is 23.0 % (26.9 %).

Jörn Wilms' modified timing mode observations 020276 oo 01

During all four *XMM* observations, Cyg X-1 was simultaneously observed with *RXTE* and *INTEGRAL* (see, e.g., Fritz, 2008, fig. 3.4). While both RGSs were operated in their usual spectroscopy mode, the MOS detectors were switched off in order to allocate more telemetry for the EPIC-pn camera. The latter was operated with the thick filter and in *modified* timing mode, where the lower energy threshold for events to be at all transferred from the satellite is increased from 200 eV to 2.8 keV. That is, all events below 2.8 keV are ignored – which greatly reduces the total count rate and allows to obtain a high-S/N spectrum above 3 keV while meeting *XMM*'s telemetry capacities even for a(n otherwise too) bright source (Kendziorra et al., 2004). However, the modified timing mode requires recalibration, as not only soft X-ray photons are discarded, but also low-energy split-events[25], such that the probability to detect photons with energies even above the threshold is modified, too (Fritz, 2008; R. Duro et al., in prep.).

The EPIC-pn light curves of these observations (see also Fritz, 2008, fig. 5.6) are shown in Fig. 2.75, together with a softness ratio and the corresponding hardness-intensity-diagram. The temporal sequence of the four observations happens to coincide with their orbital phase ordering, as subsequent observations were separated by 3 *XMM*-revolutions, corresponding to 6 days or 1.07 orbits of the Cyg X-1/HDE 226868 system. The X-ray colors were computed from the count rates in the 3–4 keV and 4–10 keV bands, with the lower limit of the 'soft' band in this case given by the threshold of the modified timing mode – a circumstance that has to be taken into account when comparing the colors with those of other observations.

The observation oo = 02 occured during a softer phase of the source, although its intensity and flaring behavior were very similar to those in oo = 04 and 05. Observation oo = 02 covers therefore a distinctly different region in the hardness-intensity-diagram (Fig. 2.75, right),

[25] Split-events are generated when the charge cloud created by the absorption of a photon is deposited in more than one pixel of the CCD (e.g., Schmid et al., 2010). Recognition of simultaneous events in neighbouring pixels by the ground-based data-processing software is thus required in order to reconstruct the full energy of the photon from the energies of all involved split-partners.

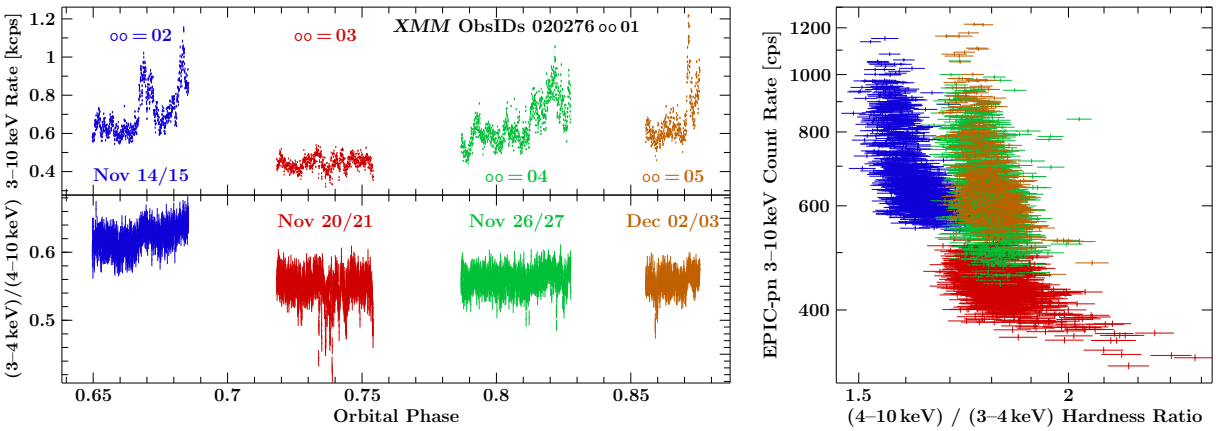

Figure 2.75: Left: *XMM* EPIC-pn light curves and softness ratios of the observations in autumn 2004, at 20 s time resolution. Due to the modified timing mode, no data below ∼3 keV are available. Right: Hardness-intensity-diagram from these data. The colors are chosen similarly to those of Fritz (2008, e.g., figs. 3.3 and 5.5) to identify the four observations.

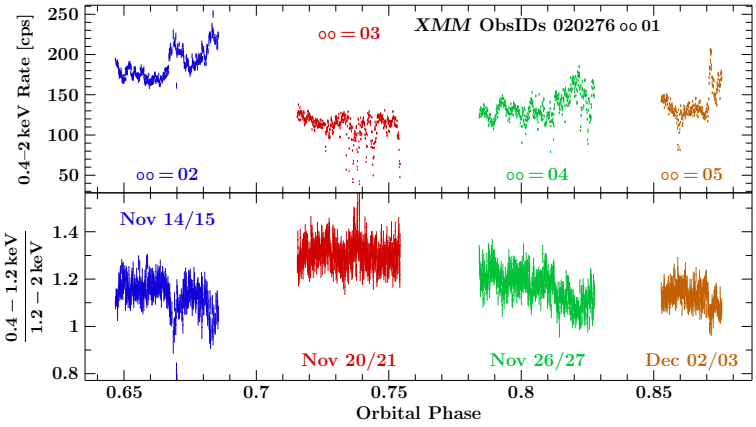

Figure 2.76: *XMM* RGS light curves of the observations in autumn 2004, at 40 s time resolution. The light curves (top panel) confirm the drops in count rate seen in Fig. 2.75. The (0.4–1.2 keV)/(1.2–2 keV) color (bottom panel) does not harden during these events, which can be caused by partially covering, strong absorption.

though still in the hard-intermediate state, where flaring is accompanied by softening unlike in Figs. 2.74b and c. Cyg X-1 was also less bright than in the soft state of ObsIDs 020240 11 01 and 020240 12 01, see also Fig. 2.71. The observation oo = 03, which took place at a lower flux level of the source, contains sudden (i.e., on shorter time scales than the flaring activity) reductions in the count rate with correlated strong hardening. A similar event is also present in the oo = 05 observation shortly before $\phi_{\rm orb}$=0.86, and, to weaker extent, also a few times in the oo = 04 observation. While the RGS light curves (Fig. 2.76) confirm the reduction in count rate, the color in the RGS band does not harden simultaneously. Further investigations are therefore required to identify these events as absorption dips – or not.

ObsID 050088 02 01 – the joint *XMM-Chandra* observation of Cyg X-1

This observation is part of our multi-satellite campaign (Sect. 2.6). It was performed on 2008 April 18/19, at orbital phase 0.97–0.09. The MOS detectors were switched off to save telemetry capacity for the other science instruments. Due to the brightness of the source and the need to observe the soft X-ray spectrum, the EPIC-pn camera was operated in burst mode – the fastest timing mode, however with a lifetime of 3 % only (Kirsch et al., 2006). The thick optical blocking filter was applied. A custom readout sequence was chosen for the CCD array of the Reflection Grating Spectrometer in order to minimize the effects of pileup on the spectrum. As sequentially reading out *all* eight CCDs would have taken almost 5 s for RGS1 (with a two-

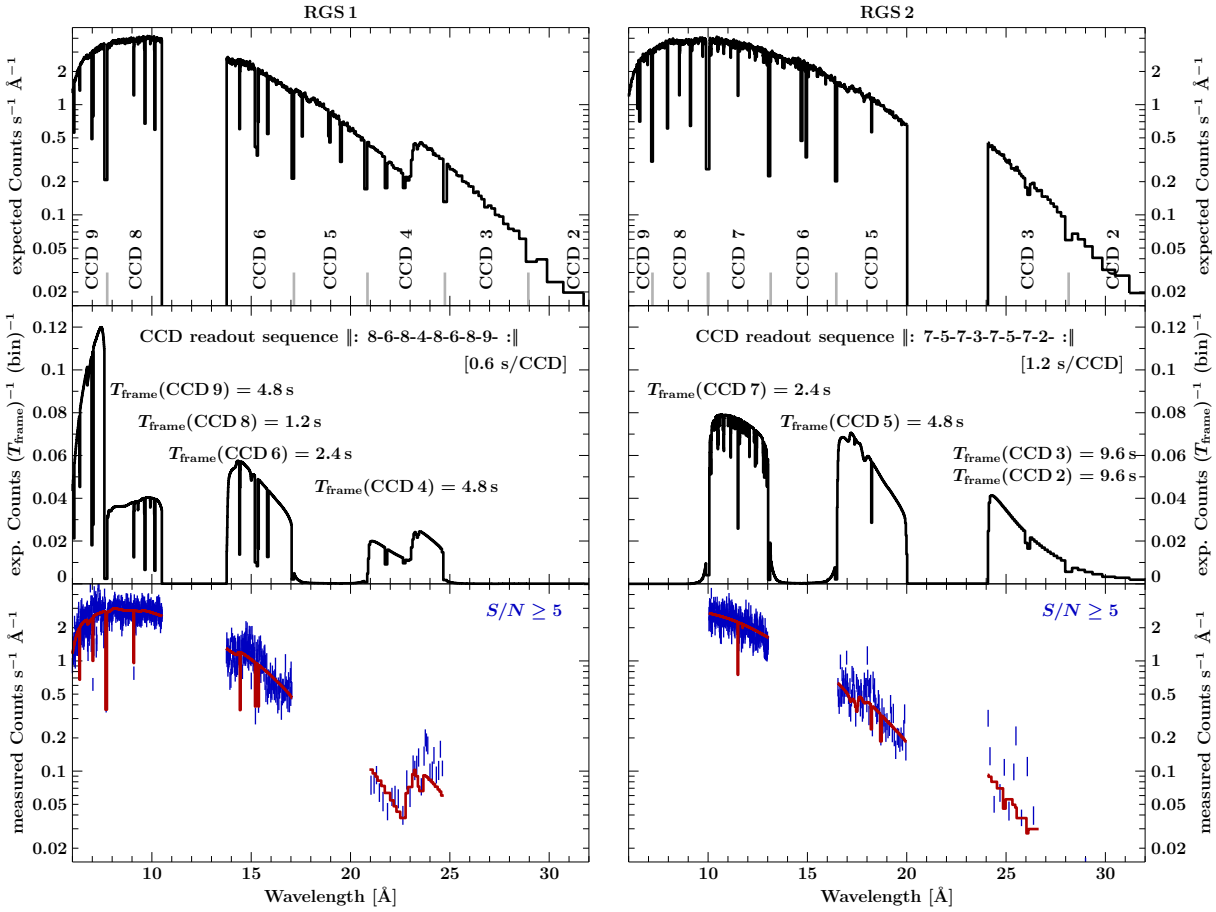

Figure 2.77: Design of the RGS readout sequence for *XMM* ObsID 0500880201. While the left column applies to RGS1, the right one holds for RGS2. In each column, the top panel shows the expected spectral count rate from the simulation of a (rather weakly) absorbed ($N_{\rm H} \lesssim 4\times10^{21}\,{\rm cm}^{-2}$) power-law spectrum. The second panel shows the rate in units of counts per frame time and 3×3 pixel readout bin, which is a measure for the expected pileup fraction. The frame times result from the readout sequence optimized such that RGS1 and RGS2 together cover the 8–34 Å spectrum while suffering from as little pileup as possible. The bin size has been linearly interpolated between 7, 10, and 14 mÅ at 5, 15, and 38 Å (XMM SOC, 2010, sect. 3.4). The bottom panel shows the spectral count rate that finally resulted from the nondip part of the observation, largely confirming the assumed spectrum in the top panel.

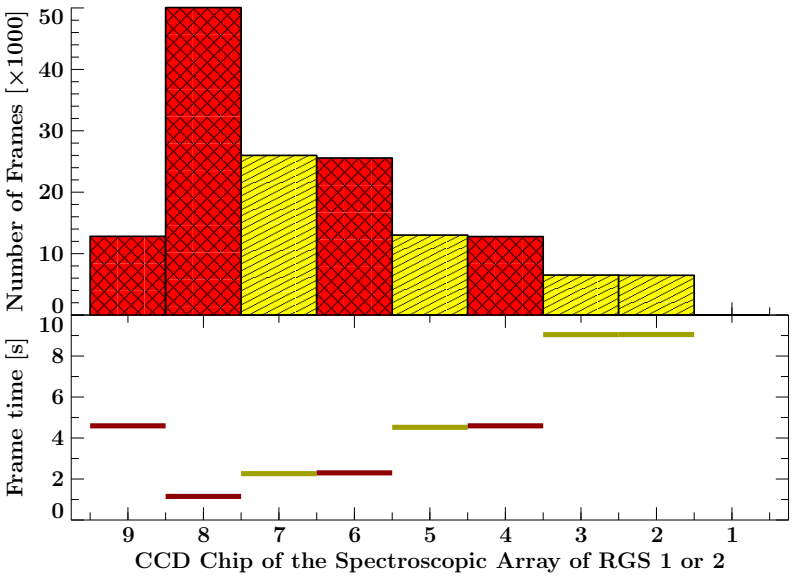

Figure 2.78: Number of frames (top) and frame times (bottom) for the RGS chips in ObsID 0500880201, using the readout sequences of Eq. (2.41). Red color indicates RGS1; yellow RGS2. CCD 8 of RGS1 was read most often to minimize pileup in the 7.8 – 10.6 Å band of high flux. The longest frame times were accepted for CCDs 2 and 3 of RGS2, covering the 24–32 Å spectrum with lower flux.

node readout in $\lesssim$0.6 s/CCD) and more than 9 s for RGS2 (for which a single-node readout in $\gtrsim$1.1 s/CCD is employed since 2007 August), it was decided to ignore certain CCDs of RGS1 and RGS2 with – as far as possible – mutually exclusive wavelength regions and therefore achieve shorter exposure times for the remaining CCDs, see Fig. 2.77. The readout sequence was optimized such that the CCDs that contain the part of the spectrum with the highest flux are read out most often, see Fig. 2.78. Finally taking into account the fact that reading out CCD9 of RGS1 is required by the *XMM* Science Operations Center in order to monitor the radiation background even though the MOS detectors are off, the following readout sequences were chosen, which provide together the 8–34 Å spectrum that is the least affected by pileup:

$$\begin{aligned} &\|\text{: 8 - 6 - 8 - 4 - 8 - 6 - 8 - 9 - :}\| \quad \text{for RGS1} \\ \text{and} \quad &\|\text{: 7 - 5 - 7 - 3 - 7 - 5 - 7 - 2 - :}\| \quad \text{for RGS2} \end{aligned} \tag{2.41}$$

This setup has subsequently been used for further observations of bright sources as well.

ObsID 061000 04 01 – a calibration observation

This $\sim$25 ks observation was performed for calibration purposes on 2009-05-16/17 at orbital phase $\phi_{\rm orb} = 0.24$–0.29. The time of the this measurement encloses a $<$1 ks short *Swift* pointing to Cyg X-1, but there are no simultaneous *RXTE* data. As in our previous observation, the EPIC-pn camera was operated in burst mode, however here with the medium filter. The MOS cameras were also switched off, and the same readout cycle as in Eq. (2.41) was employed for the RGS CCDs. Cyg X-1 was in a hard state, with an exposure-corrected EPIC-pn count rate of $(2.4 \pm 0.3) \times 10^3$ cps in the full band. No absorption dips are detected.

Phil Uttley's BH XRB observation 060561 04 01

The currently most recent *XMM* observation of Cyg X-1 is part of Phil Uttley's program extending the timing analysis of hard state BH XRBs to the soft X-ray band (Wilkinson & Uttley, 2009; P. Uttley, et al., accepted for publication by MNRAS). It was performed on 2009-12-02 for $\sim$30 ks at $\phi_{\rm orb}$=0.80–0.87, simultaneous to an infrared observation with the *Spitzer Space Telescope*, accompanied by *RXTE* pointings, and only one day after a *Suzaku* observation (PI: Jon Miller). The EPIC-pn camera was operated in timing mode with the thick filter, the MOS detectors were turned off, and the RGS CCDs were read out in the optimized sequence of Eq. (2.41).

Cyg X-1 was in a very hard state: the high-energy photon index from the *RXTE* PCA spectra (Sect. 2.3.2) is $\Gamma_2 \approx 1.5$, and the pn count rate is with $(1.32 \pm 0.13) \times 10^3$ cps only half of the count rate in ObsID 061000 04 01. There is possibly a weak absorption dip at $\phi_{\rm orb}$=0.826, when the soft X-ray count rate is reduced (though with marginal significance) for $\sim$20 min.

Phil Uttley's large program proposal 067464

Based on the success of the spectral-timing analysis of the accretion disk in hard state BH XRBs with *XMM-Newton*, a legacy project was proposed as a large program (PI: Phil Uttley) and accepted in AO 10. Cyg X-1 will be observed, probably still in 2011, for four consecutive satellite orbits with 113 ks exposure each. This data set will allow to measure energy- and frequency-resolved time lags with unprecedented accuracy, and thus provide a reverberation mapping of the Fe Kα line. Since these observations will cover almost the entire binary orbit, they will also be ideally suited to study the wind structure in further details.

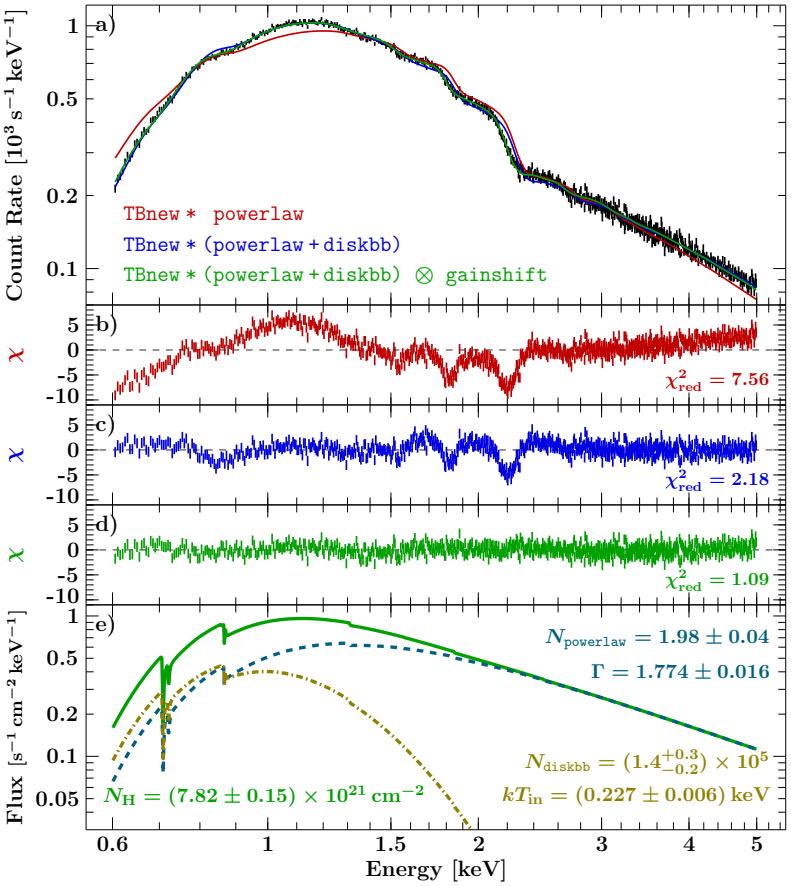

Figure 2.79: EPIC-pn (burst mode) spectrum from *XMM* ObsID 0610000401 in the 0.6–5 keV range, rebinned to $S/N \geq 20$.
a) Measured spectral count rate (black), together with the best fits for three models, whose residuals are displayed in the lower panels:
b) absorbed `powerlaw` (red),
c) absorbed `powerlaw` + `diskbb` model (blue),
d) absorbed `powerlaw` + `diskbb` model, including gain shift correction (green).
e) The bottom panel shows the best fit model and its components: an absorbed power-law (dashed; dark cyan), and an absorbed disk blackbody (dash-dotted; dark yellow).

2.5.2 A Calibration Observation

The observation 0610000401 was performed for a duration of ∼25 ks on 2009 May 16/17, at orbital phase $\phi_{orb} = 0.24$–0.29. Since the same instrumental setup was employed as for ObsID 0500880201, whose analysis will be presented in the next section, it serves as an ideal preliminary study of the hard state spectrum of Cyg X-1 observed with EPIC-pn's burst mode.

EPIC-pn (burst mode) data

The gain correction – viz., the conversion from raw PHA values (pulse-height invariants from the CCD, read by its analog-digital converter) to pulse invariant energies – must be treated with caution for fast readout (timing or burst) modes. It may be necessary to apply a gain shift in order to model the spectrum, see Sect. 1.3.4 (page 36). Figure 2.79 shows that a simple absorbed power-law is not able to describe the 0.6–5 keV spectrum (Fig. 2.79b). To avoid a detailed modelling of the relativisically broadened iron line, which is highly significant in the EPIC-pn data, the 5–10 keV data have been ignored for this present study of the soft X-ray spectrum. The curvature of the residuals below 1.5 keV suggests that an additional thermal component is required. A model including a `diskbb` component allows for a drastically improved fit (Fig. 2.79c), but still leaves strong wiggles in the residuals at 2.2 keV and 1.8 keV. These positions coincide with the absorption edges of gold (M shell) and silicon (K shell), where the effective areas of the telescope, respectively of the CCD detector, change very steeply. The residuals are therefore indicative of an incorrect gain correction. Applying the `gainshift` kernel to fit the EPIC-pn spectrum allows for a very good description of the data (Fig. 2.79d). The slope of the gain relation according to Eq. (1.67) was found to be $(97.26^{+0.16}_{-0.14})$ % with an intercept fixed to zero. That is, the PI energies are 2.7 % lower than the actual event energies.

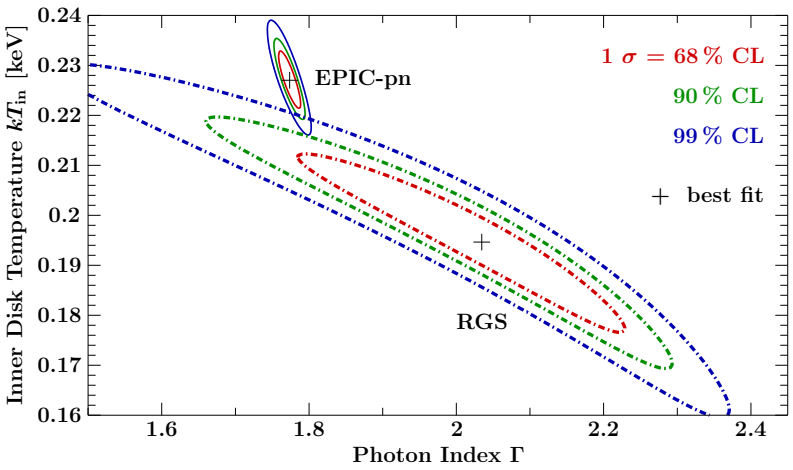

Figure 2.80: Confidence contours for the photon index and the disk temperature in *XMM* ObsID 0610000401, independently determined from RGS 8–28 Å spectra (dash-dotted lines), and EPIC-pn spectra as in Fig. 2.79 (solid lines).

According to the best fit model (Fig. 2.79e), the 1–2 keV photon flux of the `diskbb` component (with $kT_{\rm in} = 227 \pm 6$ eV) is less than one third of the `powerlaw` flux. The contribution of the disk is therefore much lower than in the *RXTE* PCA fit with the '`bknpower+diskbb`' model to a similarly hard state spectrum shown in Fig. 2.25 on page 70. For this *RXTE* observation, the photon index was $\Gamma_1 \approx 1.75$ (see Table 2.3), and for the present *XMM* spectrum, 1.774 ± 0.016 is obtained. If there was a 1:1 mapping between the properties of the accretion disk and the spectral slope of the power-law, i.e., if the spectra from both observations could be expected to be reasonably similar, the '`bknpower+diskbb`' solution with strong disk contribution could be ruled out for *RXTE* PCA spectra at this hardness; the '`bknpower`' model should provide a sufficient description for the PCA data above ∼3 keV. The same result was obtained in Sect. 2.3.2 based on statistical arguments.

Nevertheless, the `diskbb` component in the model of Fig. 2.79e dominates the spectrum below 0.87 keV – i.e., just below the Ne edge – and formally down to 0.2 keV. If the power-law is due to Comptonization of thermal photons from the accretion disk, a deviation of the spectrum from the phenomenological `diskbb+powerlaw` description may occur in this range.

Soft X-ray spectroscopy with the RGS

A large part of the 8–28 Å ≡ 0.44–1.55 keV RGS spectra covers the region where the contributions of `powerlaw` and `diskbb` are similar, and these two components are not well defined by the RGS data alone. Figure 2.80 shows that the data are compatible with a broad range of photon indices and inner disk temperatures, marginally consistent with the parameters obtained from the EPIC-pn spectrum at (mostly) higher energies. This result may indicate that the shape of the Comptonized hard X-ray spectrum deviates from a simple power-law at lower energies, even though the `powerlaw+diskbb` still allows for a good description of both the EPIC-pn and the RGS data sets. Figure 2.81 shows the RGS spectra with the model obtained from a joint fit (with a photon index $\Gamma = 1.780 \pm 0.014$, and a disk temperature $kT_{\rm in} = 220 \pm 4$ eV). The Ne-K, Fe-L, and O-K absorption edges are clearly detected. The following results are obtained from the joint fit with freely variable Ne, Fe, and O column densities:

$$\begin{aligned} N_{\rm Ne} &= (8.5 \pm 0.3) \times 10^{17}\,{\rm cm}^{-2} \\ N_{\rm Fe} &= (1.83 \pm 0.10) \times 10^{17}\,{\rm cm}^{-2} \\ N_{\rm O} &= (4.64 \pm 0.07) \times 10^{18}\,{\rm cm}^{-2} \end{aligned} \qquad (2.42)$$

These values obtained here at $\phi_{\rm orb} = 0.24$–0.29 are fully consistent with those of Eq. (2.37) obtained from the *Chandra* spectrum at $\phi_{\rm orb} \approx 0.5$. The statistical uncertainties in Eq. (2.42) are

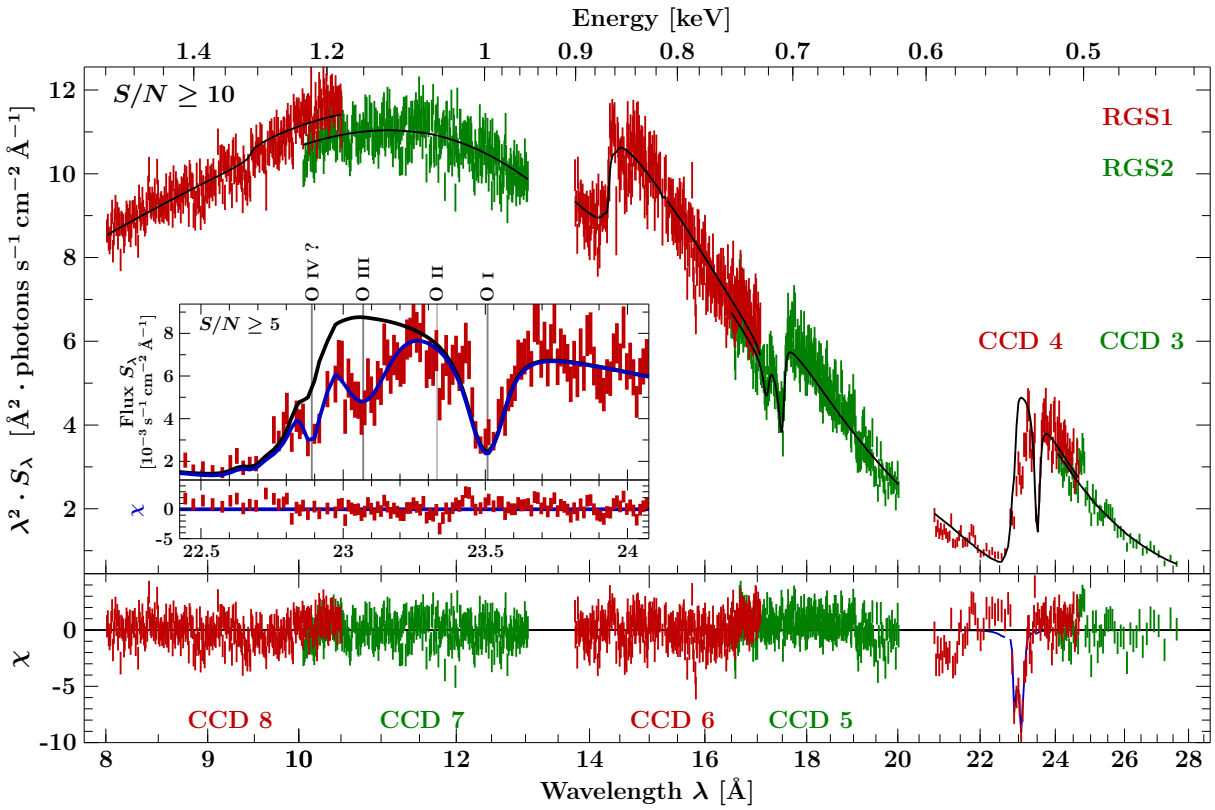

Figure 2.81: RGS spectra from *XMM* ObsID 0610000401; data from RGS1 (RGS2) are depicted in red (green). The top panel shows the flux corrected spectra S_λ at $S/N \geq 10$, multiplied with λ^2 in order to reduce the steep drop at higher wavelengths due to absorption. The bottom panel shows the residuals from the `TBnew*(powerlaw+diskbb)` continuum model (black) that was fitted jointly to the RGS and EPIC-pn data. A different flux normalization was allowed for each of the spectra. The complete model (blue) includes two Gaussian absorption lines at 22.9 Å and 23.1 Å. The inset displays S_λ at $S/N \geq 5$ in units of 10^{-3} photons s^{-1} cm^{-2} $Å^{-1}$, zoomed onto the 22.5–24 Å region. The lower panel shows the final resdiuals. The two lines can be identified with the $1s \rightarrow 2p$ transition of O III and probably O IV. The strong line of O I at ∼23.5 Å is already included in the `TBnew` model. There is only weak evidence for the O II absorption line, expected at ∼23.33 Å (Juett et al., 2004, table 1).

much lower than in Eq. (2.37) due to the larger effective area of *XMM* RGS compared to *Chandra* HETGS in this wavelength band. Besides the neutral absorption edges, further structure is decteded at the oxygen edge in form of two strong absorption lines at $23.070^{+0.015}_{-0.018}$ Å and $22.89^{+0.02}_{-0.01}$ Å, with equivalent widths of -0.11 ± 0.02 Å and $-0.10^{+0.07}_{-0.08}$ Å, respectively. They can be identified with the $1s \rightarrow 2p$ transition of O III and probably O IV (e.g., Juett et al., 2004, table 1). An absorption line of O II at ∼23.33 Å may also be present, but is far less significant.

* * *

The investigation of this observation of Cyg X-1 during an exclusively nondip phase has demonstrated that the EPIC-pn spectra from burst mode data may require a correction of the CCD's gain factor during data analysis. The grating spectra have allowed to derive neutral column densities of O, Ne, and Fe, from absorption edges with ∼3-fold reduced uncertainties compared to the *Chandra* HETGS measurements (from comparable exposures), due to the high sensitivity of *XMM* RGS in the soft X-ray band. The upcoming large program observation almost covering one binary orbit will therefore either allow to constrain the orbital modulation of the neutral column, or tighten the upper limits if a constant neutral absorption is found.

The next section addresses the spectroscopy of absorption dips.

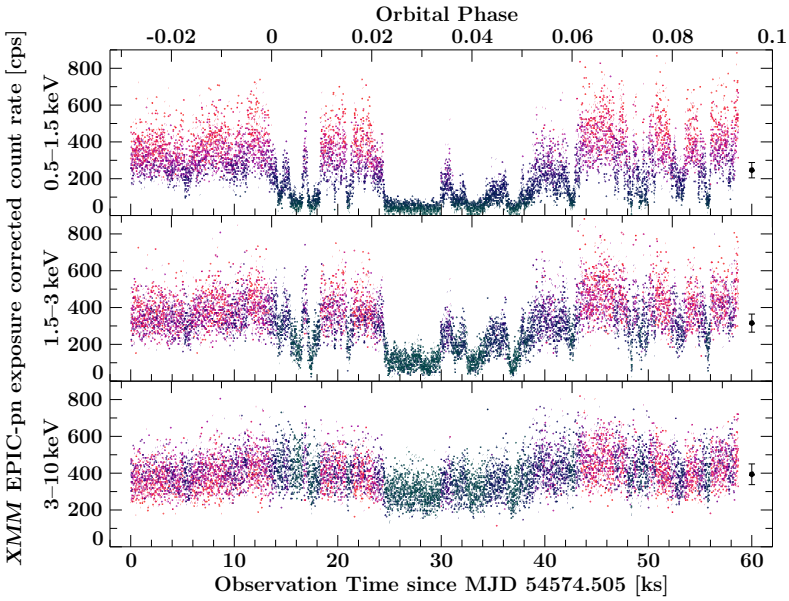

Figure 2.82: EPIC-pn light curves of ObsID 050088 02 01 in three energy bands at a time resolution of 5 s. The count rates have been corrected for the burst mode's duty cycle of 3 %. The isolated data points at 60 ks show the mean count rates and their statistical uncertainties. The color scale from light red to dark cyan indicates the degree of dipping according to the hardness ratio between the 0.5–1.5 keV band and the 3–10 keV band.

2.5.3 Spectral Changes during Absorption Dips

Observation 050088 02 01 is part of our multi-satellite campaign (Sect. 2.6). It was performed on 2008 April 18/19 for almost 60 ks at orbital phase $\phi_{\rm orb} = 0.97$–0.09 in order to investigate the wind structure and absorption dips. It is already clear from the simultaneous *RXTE* and *Chandra* data previously discussed in Sects. 2.3.4 and 2.4.3 that strong absorption dips are present during this observation. Figure 2.82 shows EPIC-pn light curves. The large statistical uncertainties are due to the burst mode's low duty cycle: for a 5 s bin of the light curve, only $\sim$0.15 s of exposure are effectively integrated. Due to the fast variability during the dips, such a high time resolution is nonetheless desirable – and also feasible, since the average EPIC-pn count rate during the nondip phases exceeds 1 000 counts/s. Similarly as in Fig. 2.57, the ratio between the count rates in the 0.5–1.5 keV and 3–10 keV bands is used to define different stages of dipping. The entire *XMM* observation is split into eight parts, which are not necessarily continuous, but combined from different times of corresponding spectral hardness. Unlike for *Chandra* ObsIDs 8525 and 9847, these parts were selected to cover approximately the same time. The resulting subsets of the data contain $\sim$220 s of pn exposure, see Fig. 2.83.

Spectral analysis

Taking the `gainshift` correction into account, the least absorbed spectrum can be well described by an absorbed power-law. Unlike for ObsID 061000 04 01, no `diskbb` component is required. In comparison with this previously considered spectrum at $\Gamma = 1.77$, the present spectrum is also significantly harder, with a photon index of $\Gamma = 1.53$. This value is consistent with the range 1.51–1.57 derived from *Chandra* ObsIDs 8525 and 9847 (Tables 2.11 and 2.13).

In agreement with the results from the *Chandra* analysis, and expected from the selection of non-continuous time intervals, the spectra from the dipping periods can be described as being partially absorbed with successively increasing covering fraction and column density. Figure 2.83 shows the EPIC-pn count rate spectra from eight data selections, and the models that give the best joint fit with the RGS spectra (Table 2.16). There is a weak correlation of the slope of the gain relation according to Eq. (1.67) with the flux level of the source, whose origin remains unknown. A more detailed investigation of the gain corrections applied to burst mode data by the *XMM* Science Analysis Software (SAS) during data processing is required.

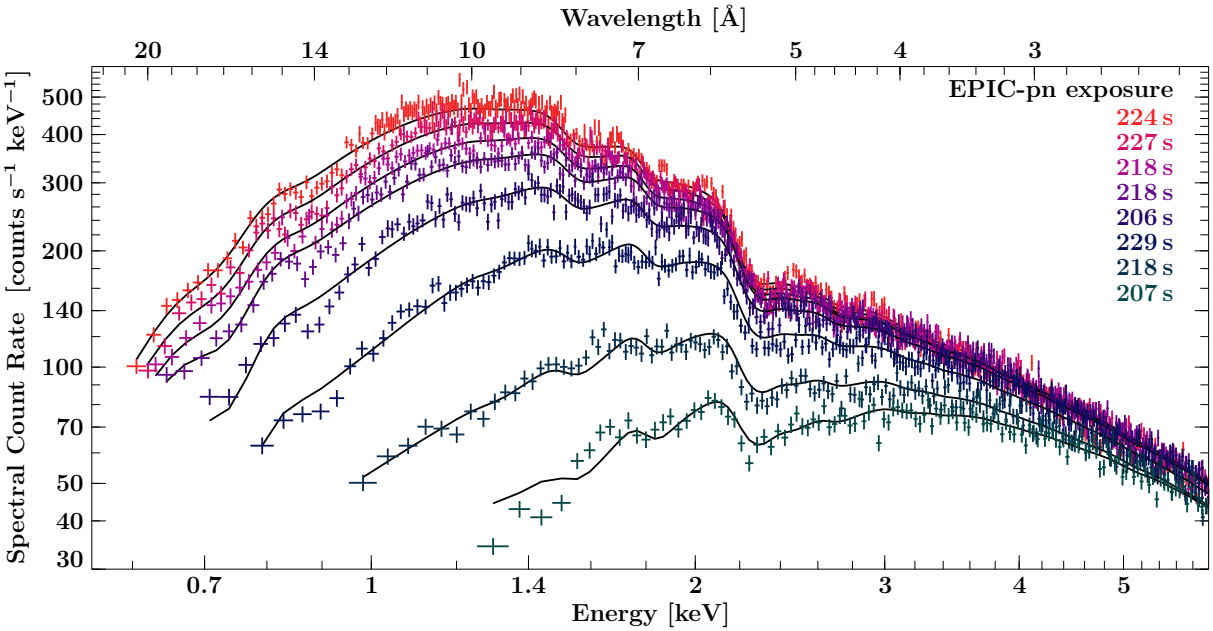

Figure 2.83: EPIC-pn count rate spectra from eight selections of different levels of dipping in *XMM* ObsID 0500880201, indicated by colors from light red (nondip) to dark cyan (deep dip). The spectra have been rebinned to $S/N \geq 20$, and resulting bins broader than 1 Å were ignored. All data sets are described by the same continuum, but individual flux normalization, (partial) absorption, and gain shift. In addition, a broad absorption line at ∼16 Å ≡ 0.77 keV, which is most significant in the RGS spectra (Fig. 2.84), has been taken into account, see Table 2.16. Further absorption lines developing during the dips are indicated by the EPIC-pn data at ∼0.85 keV and, during the deepst dip, at ∼1.4 keV.

The evolution of the gratings spectra is displayed in Fig. 2.84. The optical depths at the Ne and O edges are probably underestimated since the model for the continuum (Table 2.16) assumes fixed elemental abundances (Wilms et al., 2000). The most striking feature is, however, the broad absorption trough at ∼16.2 Å and its growth with the degree of dipping, which was already indicated by the *Chandra* spectra (Fig. 2.65). Here, it is included in the model for the EPIC-pn and RGS spectra as a single broad Gaussian absorption line, whose parameters are listed in Table 2.16. Since the two most strongly absorbed spectra lack signal at long wavelengths, the line is not well constrained in these cases. For the other spectra at lower hardness level $i \leq 6$, there is a clear increase of the equivalent width $\mathrm{EW}^{(i)}$, and probably also the Gaussian width $\sigma^{(i)}$, of the line with the degree of dipping i. For the nondip spectrum ($i = 1$), the centroid wavelength is $\lambda^{(1)} = 16.17 \pm 0.05$ Å, and there is a weak trend of increasing $\lambda^{(i)}$ during the dips, but the significance of this effect is low ($< 2\sigma$). A possible identification of the absorption trough lies in unresolved transition arrays (UTAs) of Fe M-shell ions' n=2 → n=3 transitions (e.g., Behar et al., 2001; Netzer, 2004). Within such an interpretation, the growth of the broad absorption line's equivalent width from 0.2 Å during the least absorbed phase up to ∼1 Å during the strongest dip would be another indication for an increased column density of an absorber at lower ionization state during dips than the highly photoionized wind detected during the nondip phases. Figure 1.16 on page 28 suggests that the Fe UTA at ∼16 Å corresponds to $\log \xi \approx 1.5$, but a more detailed modelling of the ionized absorption using more physical models (like `warmabs`) is required for a quantitative statement on the ionization parameter.

The analysis of the spectra is complicated by the high and fast variability of absorption dips, demanding fine selections in order to avoid a blending of features from different stages of dipping. Further observations covering more absorption dips will allow to combine all data at the same level of dipping and therefore obtain spectra with (even) higher S/N.

Table 2.16: Parameters of partially absorbed power-law models, jointly fit to EPIC-pn and RGS spectra at eight levels of dipping

The EPIC-pn spectra have been rebinned to $S/N \geq 20$, the first order spectra from RGS1 and RGS2 to $S/N \geq 5$, and resulting bins broader than 1 Å were ignored. RGS data below 8 Å were not used either in order to avoid pileup on CCD 9 of RGS1, which was operated with a long frame time of 4.8 s (see Fig. 2.78). All data from different levels of dipping were fitted simultaneously with the model

$$\texttt{(powerlaw + egauss)} \times \texttt{TBnew}^{(0)} \times \left(f_c \cdot \texttt{TBnew}^{(i)} + \left(1 - f_c^{(i)}\right)\right) \cdot c^{(i)} \times \left(1 + \texttt{gauss}^{(i)}\right) \quad \otimes \quad \texttt{gainshift}_{\rm pn}^{(i)}$$

sharing common parameters for the continuum spectrum (left table), but separate parameters (index i) for the partial covering model and the broad absorption line at ∼16.2 Å (right table). The `gainshift` kernel was applied to the EPIC-pn (burst mode) data only.

Joint parameters		Value
·····	`powerlaw`	·····
N	$\left[\mathrm{s^{-1}\,cm^{-2}\,keV^{-1}}\right]$	1.125 ± 0.008
Γ_1		$1.534^{+0.007}_{-0.006}$
·····	`egauss`	·····
E	[keV]	$\equiv 6.4$
A	$\left[10^{-3}\,\mathrm{s^{-1}\,cm^{-2}}\right]$	$6.5^{+1.3}_{-1.1}$
σ	[keV]	$0.59^{+0.12}_{-0.10}$
·····	$\texttt{TBnew}^{(0)}$	·····
$N_{\rm H}^{(0)}$	$\left[10^{21}\,\mathrm{cm^{-2}}\right]$	0.53
· relative flux normalization ·		
RGS1/EPIC-pn [%]		92.9 ± 0.4
RGS2/EPIC-pn [%]		91.3 ± 0.5

Level of dipping	Individual parameters						
	partial absorption			`gauss`			`gainshift`
	$f_c^{(i)}$	$N_{\rm H}^{(i)}$	$c^{(i)}$	$\lambda^{(i)}$	$\mathrm{EW}^{(i)}$	$\sigma^{(i)}$	$\texttt{slope}^{(i)}$
i	(%)	$(10^{22}\,\mathrm{cm^{-2}})$	(%)	(Å)	(Å)	(Å)	(%)
1	$\equiv 0$	—	$\equiv 100$	16.17 ± 0.05	-0.22 ± 0.03	$0.32^{+0.05}_{-0.04}$	96.7 ± 0.2
2	$12.5^{+1.7}_{-1.4}$	1.1 ± 0.3	$99.1^{+0.8}_{-0.4}$	16.18 ± 0.04	-0.25 ± 0.03	0.26 ± 0.03	97.0 ± 0.2
3	24.7 ± 1.2	$1.33^{+0.17}_{-0.15}$	$99.1^{+0.8}_{-0.4}$	16.21 ± 0.04	-0.29 ± 0.03	0.26 ± 0.03	$97.0^{+0.2}_{-0.3}$
4	33.6 ± 0.9	$1.84^{+0.15}_{-0.14}$	$100.8^{+0.9}_{-0.8}$	16.20 ± 0.03	-0.43 ± 0.03	0.32 ± 0.03	$97.4^{+0.2}_{-0.3}$
5	$53.6^{+0.8}_{-0.7}$	$1.82^{+0.09}_{-0.08}$	99.7 ± 0.8	16.26 ± 0.03	-0.59 ± 0.04	0.35 ± 0.03	97.2 ± 0.3
6	72.3 ± 0.5	$2.26^{+0.07}_{-0.06}$	95.3 ± 0.8	16.23 ± 0.04	-0.75 ± 0.06	0.39 ± 0.04	97.4 ± 0.3
7	85.4 ± 0.3	3.85 ± 0.09	90.7 ± 0.9	$16.30^{+0.14}_{-0.13}$	-1.0 ± 0.2	0.7 ± 0.2	$97.6^{+0.3}_{-0.4}$
8	91.3 ± 0.2	5.75 ± 0.11	92.0 ± 1.0	$16.11^{+0.14}_{-0.15}$	-0.58 ± 0.17	$0.35^{+0.15}_{-0.14}$	97.5 ± 0.4

Notes. The data set denoted as i=1 (i=8) corresponds to the least absorbed phase (the deepest dip). The sequence $i = 1 \rightarrow 8$ is the same as shown in Figs. 2.83 and 2.84 from the top to the bottom.

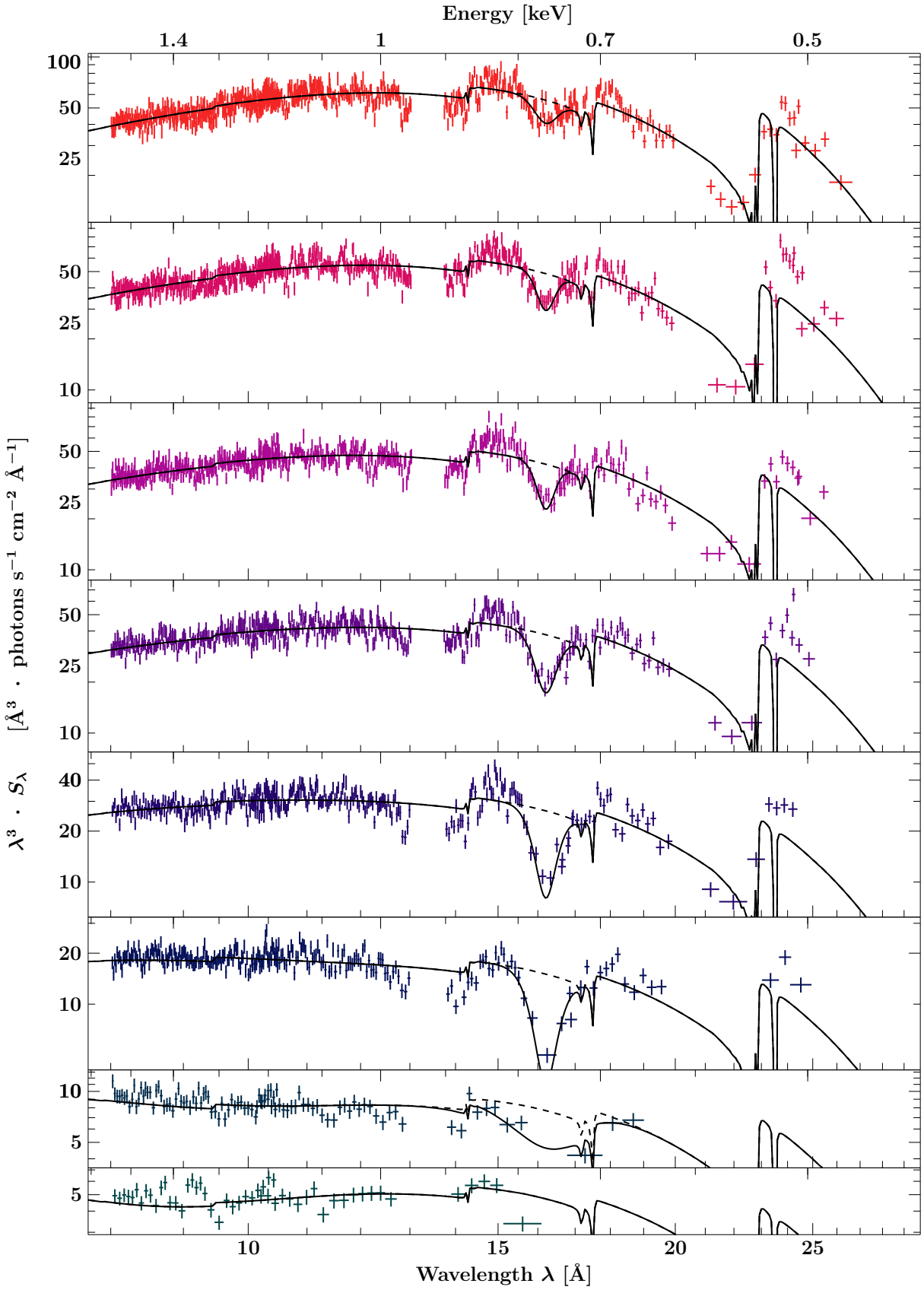

Figure 2.84: Flux-corrected RGS spectra at $S/N \geq 5$ from the same eight selections of different levels of dipping in *XMM* ObsID 0500880201 as in Fig. 2.83, from light red on top to dark cyan on the bottom. For visual clarity, the spectra have been multiplied with λ^3. The joint fit with the corresponding EPIC-pn data includes individual broad Gaussian lines to model the absorption at $\sim$16 Å (Table 2.16).

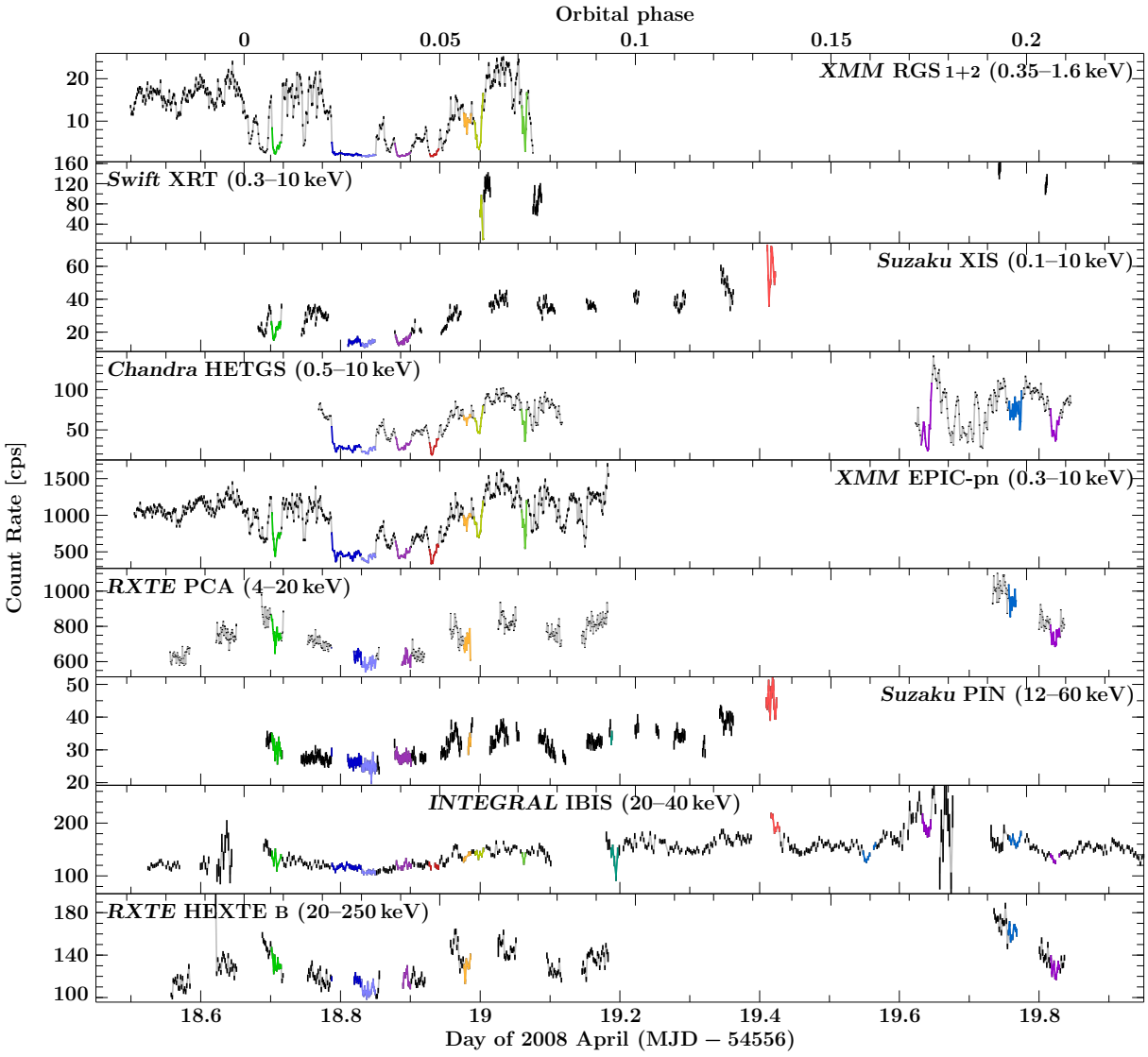

Figure 2.85: Simultaneous light curves from the multi-satellite observation of Cyg X-1 on 2008 April 18/19. Several absorption dips with complex substructure severely reduce the count rate in the soft X-ray band (*XMM* RGS, *Suzaku* XIS, *Chandra* HETGS, *XMM* EPIC-pn). Some of the dips are also apparent above 4 keV (*RXTE* PCA), and few appear even above 12 keV (*Suzaku* PIN) or above 20 keV (*INTEGRAL* IBIS, *RXTE* HEXTE). Selected time intervals are colorized in all light curves in order to highlight some individual structures. The *Swift*, *Suzaku*, and *INTEGRAL* light curves are by courtesy of L. Barragán, and F. Fürst, respectively.

2.6 The Multi-Satellite Campaign

Our group (PI: J. Wilms) has initiated a multi-satellite observation of Cyg X-1, involving largely simultaneous measurements with every X- or γ-ray mission flying in 2008 April.[26] Specifically, the participating observatories were: *XMM*, *Chandra*, *RXTE*, *Suzaku*, *INTEGRAL*, *Swift*, and *AGILE*. Figure 2.85 displays the light curves from most of the instruments. Some of the data have already been investigated in this work, i.e., in Sect. 2.3.4 (*RXTE* ObsID P93120), in Sects. 2.4.2 and 2.4.3 (*Chandra* ObsIDs 8525, 9847), and in Sect. 2.5.3 (*XMM* ObsID 050088 02 01). This section presents further results inspired by the combination of several instruments.

[26] I would like to thank all schedulers for their tremendous coordinative efforts to make this campaign possible – in spite of the overwhelmingly large number of constraints.

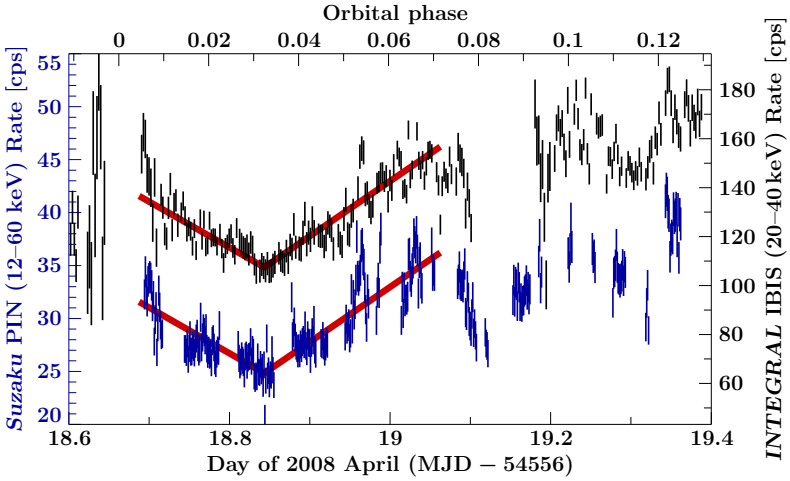

Figure 2.86: Zoom on the hard X-ray light curves from *Suzaku* PIN (blue) and *INTEGRAL* IBIS (black) from Fig. 2.85. Two linear functions (red) describe their decline towards and their rise after the minimum at $\phi_{\rm orb}$=0.03, which coincides with the deepest dip at soft X-ray energies. The lowest count rates of this fit measure 69 % of its highest values.
(Hanke et al., 2010a, fig. 1)

Hard X-ray light curves

Between $\phi_{\rm orb} \approx 0$ and $\phi_{\rm orb} \approx 0.07$, the hard X-ray light curves from three independent detectors – namely *Suzaku* PIN at 12–60 keV, *INTEGRAL* IBIS at 20–40 keV, and *RXTE* HEXTE at 20–250 keV – display a broad trough, with a nearly linear decline and likewise linear rise. Figure 2.86 shows a zoom of the light curves from *Suzaku* PIN and *INTEGRAL* IBIS, with a simultaneous fit of a piecewise linear function between MJD=54574.6875 and 54575.0625. Extending over 9 h, this trough lasts much longer than the soft X-ray absorption dips, but its minimum coincides with the 1.5 h long, deepest dip at $\phi_{\rm orb} \approx 0.03$ (see Sect. 2.4.3). While the dips are caused by photoabsorption by dense clumps in the wind, this process is non-effective for energies above 12 keV or even 20 keV, see also Fig. 1.14 on page 24.

Although source-intrinsic variability cannot be ruled out as an explanation for the shape of the light curves, Compton scattering in an ionized cloud in the wind, much larger than the clumps that cause absorption dips, is another possibility, which is supported by its close relation to the dips. If due to single scattering, the attenuation by 31 % (inferred from the linear fit in Fig. 2.86) corresponds to an additional electron column density of $\Delta N_{\rm e} = 6{\times}10^{23}\,{\rm cm}^{-2}$. In this case, the scattering cloud would have to be almost fully ionized, since the value of $\Delta N_{\rm e}$ exceeds the column seen in (assumedly) neutral absorption by at least one order of magnitude. Such a finding is, however, not necessarily in disagreement with the ionization balance in a highly photoionized gas. For example, the analysis of the nondip *Chandra* spectrum from ObsID 3814 in Sect. 2.4.2 (Table 2.10 on page 102) has shown that already the H- and He-like ions correspond to an equivalent hydrogen column of $\mathcal{O}(10^{22}\,{\rm cm}^{-2})$, whose contribution to the neutral column density $N_{\rm H} = 5.4{\times}10^{21}\,{\rm cm}^{-2}$ inferred from this spectrum is negligble. Within the scattering interpretation, the hard X-ray light curves trace the ionized column density, i.e., the projection of the cloud's density profile *along* the line of sight, as the cloud passes *through* the line of sight. In this scenario, the cloud has a dense core containing lower ionized matter that causes the deep absorption dip. In order to X-ray further substructures, the goal of the following part is to isolate the cloud's (nearly) neutral content.

Time resolved soft X-ray spectroscopy

In Sect. 2.3.4, a spectral analysis of *RXTE* PCA data was performed based on 128 s long integrations (see Fig. 2.41 on page 85). Since the quality of the spectra from short time segments would not allow to measure both the continuum parameters and the absorption properties with high accuracy, all spectra were modeled simultaneously with a joint continuum. Due to

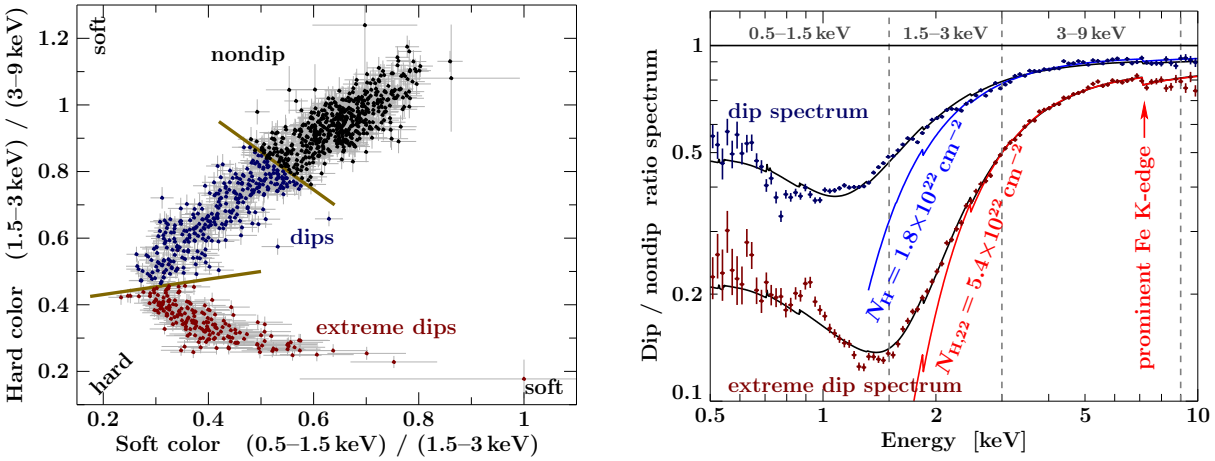

Figure 2.87: Left: *Suzaku* XIS color-color diagram, from light curves at 32 s resolution in the 0.5–1.5 keV, 1.5–3 keV and 3–9 keV bands (see also Nowak et al., 2011, fig. 2d). Three selections, denoted as 'nondip' (black), 'dip' (blue), and 'extreme dip' (red), are defined based on simple cuts in the color-color diagram. Right: Ratios of the dip spectra and the 'nondip' spectrum. Above ∼2 keV, they can be described by simple absorption curve (blue and red solid lines). The model of Eq. (2.44) accounting for partial covering, also in the 'nondip' spectrum, is largely able to describe lower energies as well (black lines). (after Hanke et al., 2010a, fig. 3)

their better energy resolution, it is of interest to repeat such a study with data from the CCD detectors (*XMM* EPIC-pn, *Suzaku* XIS) at even shorter time scales. In terms of the computational effort, the former approach of full spectral fitting $\mathcal{O}(1000)$ data sets (simultaneously) at much higher resolution (e.g., 4096 bins for *XMM* EPIC-pn spectra, compared to 129 channels for *RXTE* PCA `Standard2` mode spectra) would be very demanding and not feasible on current desktop computers. Another method was therefore employed, which simplifies the problem drastically. Since the main interest here lies in the spectral changes, and not in the continuum spectrum, it is – provided that the instrumental response does not change with time – sufficient to describe the ratio of measured spectra and the continuum. The latter is unknown, but can be considered to be given by the least absorbed spectrum among the measurements. Such an approach ignores the redistribution of photon energies among the detector's spectral channels, but is a reasonable approximation for CCDs with good energy resolution – in contrast to proportional counters with a very broad response.

Ratio spectra from *Suzaku* XIS CCDs

This method is at first illustrated with *Suzaku* XIS data: Figure 2.87 (left) shows a color-color diagram, with the typical track seen during absorption dips of Cyg X-1 (see also Fig. 2.63 on page 109). The data were split into three selections of 'nondip', 'dip', and 'extreme dip' phases covering regions of approximately the same size in the color-color diagram. As the data points spread continously along the partial absorption track, there is no well defined, intrinsic 'nondip' selection. The chosen selection will therefore include some weak dipping as well. The right panel of Fig. 2.87 displays the ratios between each of the two dip spectra and the 'nondip' spectrum obtained from the previous selection. It is apparent that the shape of the ratio at $E \gtrsim 2.5$ keV follows the form of an absorption curve $\exp\{-N_\mathrm{H}\sigma_\mathrm{eff}(E)\}$, where σ_eff denotes the total absorption cross section as in Eq. (1.59). The fact that the ratio does not recover at 1 at high energies demonstrates, in agreement with previous results from spectral fitting (Tables 2.13 and 2.16) and the hard X-ray light curves, that dipping is accompanied with an energy independent attenuation. At lower energies, the ratio obviously deviates from a pure absorption curve. It is assumed that the dip spectra ($i = 1, 2$) can, in a first approximation

ignoring the effects of line absorption, be described by a partial covering model:

$$S^{(i)}(E) \;=\; \left[\, f_{\rm c}^{(i)} \cdot \exp\left\{ -N_{\rm H}^{(i)} \sigma_{\rm eff}(E) \right\} \;+\; \left(1 - f_{\rm c}^{(i)}\right) \right] \cdot c^{(i)} \;\times\; S^{\rm cont}(E) \qquad (2.43)$$

with individual covering fractions $f_{\rm c}^{(i)}$, column densities $N_{\rm H}^{(i)}$, and relative flux normalizations $c^{(i)}$, but the same continuum spectrum $S^{\rm cont}(E)$. *If* the 'nondip' spectrum $S^{(0)}(E)$ had directly measured this continuum $S^{\rm cont}(E)$, a flattening of the ratio $S^{(i)}/S^{(0)}$ at $(1 - f_{\rm c}^{(i)}) \cdot c^{(i)}$ would be expected at low energies. The actually detected upturn of the ratio toward lower energies indicates that the 'nondip' spectrum here is partially absorbed itself, as in Eq. (2.43). The ratio

$$\frac{S^{(i)}(E)}{S^{(0)}(E)} \;=\; \frac{f_{\rm c}^{(i)} \cdot \exp\left\{ -N_{\rm H}^{(i)} \sigma_{\rm eff}(E) \right\} \;+\; \left(1 - f_{\rm c}^{(i)}\right)}{f_{\rm c}^{(0)} \cdot \exp\left\{ -N_{\rm H}^{(0)} \sigma_{\rm eff}(E) \right\} \;+\; \left(1 - f_{\rm c}^{(0)}\right)} \;\times\; \left(c^{(i)} / c^{(0)} \right) \qquad (2.44)$$

is able to qualitatively reproduce such a shape, see Fig. 2.87. Even though the ratio spectrum is not suited to infer the detailed structure of the soft X-ray spectrum, the "absorption line" in the 'dip' spectrum at 0.77 keV is probably related to the strong feature also seen in the RGS spectra (Fig. 2.84), which was identified with a growing UTA of Fe M-shell ions in Sect. 2.5.3.

Ratio spectroscopy with *XMM* EPIC-pn data on 48 s time scales

The method of fitting ratios is now applied to spectra from *XMM* EPIC-pn that were extracted in 25 logarithmically spaced bins between 2 keV and 10 keV, for every continuous 48 s interval. These histograms were divided by the 'nondip' spectrum formed from the average of the five spectra with highest count rate. These 2–10 keV ratio spectra (i) can be well described by

$$\frac{S^{(i)}(E)}{S^{(0)}(E)} \;=\; \exp\left\{ -\Delta N_{\rm H}^{(i)} \cdot \sigma_{\rm eff}(E) \right\} \;\times\; c^{(i)} \qquad (2.45)$$

– which is equivalent to Eq. (2.44) for $c^{(0)} = f_{\rm c}^{(0)} = f_{\rm c}^{(i)} \equiv 1$ and $\Delta N_{\rm H}^{(i)} := N_{\rm H}^{(i)} - N_{\rm H}^{(0)}$. The time evolution of the parameters, viz., $\Delta N_{\rm H}^{(i)}$ and the relative flux normalization $c^{(i)}$, is displayed in Fig. 2.88. $\Delta N_{\rm H}$ obviously traces the dips in the soft X-ray light curve very well. The relative column densities obtained here are lower than the absolute values from the *RXTE* PCA data analysis in Sect. 2.3.4 (Fig. 2.3.4 on page 84). This discrepancy cannot be due to an inadequate selection of a 'nondip' spectrum that is already strongly absorbed, since $\Delta N_{\rm H}$ would in this case become (more significantly) negative outside of the dipping periods. The values obtained from ratio spectra during the deep dip, $\Delta N_{\rm H} \approx (4 \pm 1) \times 10^{22}\,{\rm cm}^{-2}$, are also lower than the absorption measured during the hardest spectrum in the sample of eight levels of dipping investigated in Sect. 2.5.3. Table 2.16 on page 128 lists a column density of $(5.75 \pm 0.11) \times 10^{22}\,{\rm cm}^{22}$, as in Eq. (2.45) *in addition* to the absorption during the nondip phase, however only at 91 % covering fraction. The reason for the bias of the relative column densities towards lower values is therefore rather the assumption $f_{\rm c}^{(i)} \equiv 1$, which was chosen to avoid a degeneracy between the model parameters of the ratio spectra. A fraction of $(1 - f_{\rm c}) \approx 10\,\%$ of uncovered emission is consistent with the contribution by the scattering halo, which is unresolved in the *XMM* data: Predehl & Schmitt (1995, fig. 10-3) quote a relative halo brightness of 11.6 %.

The relative flux normalization $c^{(i)}$ is in very good agreement with the hard X-ray light curves: The linear fit from Fig. 2.86 is also displayed in Fig. 2.88c, after identifying the nondip flux level $c = 1$ with an (20–40 keV) IBIS count rate of 175 cps. Such a consistency is expected because both the 2–10 keV band and the hard X-ray band are dominated by the same emission component, namely the Comptonized power-law and its reflection. It does therefore not allow

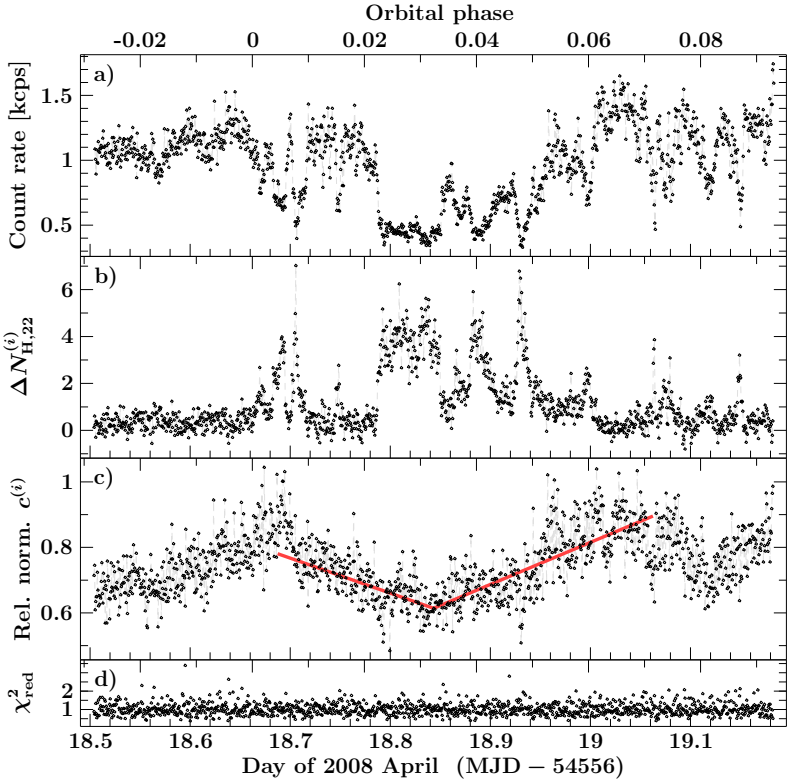

Figure 2.88: Time evolution of the absorption during dips, measured with *XMM* EPIC-pn.
a) Exposure corrected 0.3–10 keV light curve at a time resolution of 48 s.
Spectra were created for every 48 s interval and divided by the 'nondip' spectrum. As in Fig. 2.87 for *Suzaku*-XIS, the 2–10 keV ratio spectrum can be well described by the model of Eq. (2.45) with the following parameters:
b) Column density.
c) Relative flux normalization. The red line is the linear model from Fig. 2.86 for the hard X-ray light curves.
d) χ^2/dof of each fit.
(Hanke et al., 2010a, fig. 2)

to discriminate source-intrinsic flux variability from scattering in an ionized cloud either. The sample of absorption dips that are covered by simultaneous soft and hard X-ray observations is currently very small. Hence it is not yet possible to make a statistical statement on the occurence of absorption dips and scattering troughs. Establishing a connection between dense, cool clumps and the tenous, hot gas with future observations might give further insights in the structure of the wind in high-mass X-ray binaries and in the processes of wind clumping.

* * *

Our multi-satellite observation has given many insights to the wind structure of Cyg X-1, making use of the synergy of different instruments' capabilities. While partial covering absorption during the dips is suggested by the color-color diagrams from all soft X-ray instruments, only *Chandra* was able to address its origin, since it allows to resolve and exclude the scattering halo, and therefore obtain much lower covering fractions and even detect line emission, reprocessed by the wind, when the direct component is heavily blocked during the deepest dip. *Chandra* HETGS spectroscopy of the dips below 1 keV suffers, however, from the strong drop in signal. Due to *XMM*'s much larger effective area, spectroscopy with the RGS could continue at this point and detect the Fe M shell UTA at 16.2 Å, which will prove valuable to constrain the ionization parameter of the clump. On its own, however, the RGS would have missed the lower ionization stages of Si and S, revealed by the *Chandra* high energy grating spectra. Only the simultaneous observation with soft and hard X-ray detectors has allowed to suggest a connection between the variation of the hard X-ray flux and the soft X-ray absorption. If the trough in the hard X-ray light curve was only observed with a single detector, it might not even have been noticed, but confused with instrumental artifacts.

The joint observation has helped to establish a consistent picture of the wind structure during the hard state of Cyg X-1, which will be summarized in chapter 4. But even more, it provides a unique data set in the history of X-ray observations of Cyg X-1 that will certainly prove advantageous for many further studies as well. The next chapter will briefly describe results results from the investigation of the environment of another X-ray binary system.

Chapter III

Investigation of LMC X-1

Extending the study of the environment of X-ray binaries to other systems is desirable; however, the available data set is not for all sources as large as for Cyg X-1, and the S/N of the data from less bright sources is, of course, lower as well. Nonetheless, every high-mass X-ray binary system that shows orbital modulation is a potential target for an investigation of the wind environment. The fact that, e.g., photoionized absorption by the wind is *not detected* in a spectrum at lower S/N does not necessarily imply that it is *not present* and does hence not have a *systematic* effect on the parameters infered. Liu et al. (2005, 2006) have – updating earlier work of Bradt & McClintock (1983), van Paradijs (1995), and Liu et al. (2000) – compiled two catalogues with 128 and 114 HMXBs in the Magellanic Clouds and in the Galaxy, respectively. The sources with known orbital period are listed in Table D.1 on page 169 together with their identifications in the *RXTE* ASM and *Swift* BAT source catalogues – as far as available.

This section briefly presents an analysis of the absorption towards LMC X-1 – the first X-ray source discovered in the Large Magellanic Cloud (LMC), our ∼48 kpc distant neighboring galaxy – which is also a high-mass X-ray binary system with a black hole as compact object. These results have been published by Hanke et al. (2010b).

Introduction

The extragalactic X-ray sources in the LMC were discovered in the late 1960s (Mark et al., 1969; Price et al., 1971). Since the density of stars is high, their optical identifications were uncertain for a long time. LMC X-1 is located $\sim 0\overset{\circ}{.}5$ south-southeast of the 30 Doradus star-formation region, in the NGC 2078 (LMC N159F) nebula. Pakull (1980), Hutchings et al. (1983, 1987), and Cowley et al. (1995) were able to identify the counterpart of LMC X-1 with an m_{V}=14.5 mag O7/8 giant (Hutchings et al., 1983; Negueruela & Coe, 2002). This has allowed the placement of strong dynamical constraints on the compact object's mass. Orosz et al. (2009) have recently used optical spectra of this star – labeled as 'star #32' by Cowley et al. (1978) and also often called Pakull's star – to confirm the black hole candidacy of LMC X-1. They derive an orbital period of 3.909 d, which is consistent with the modulation of the soft X-ray flux of LMC X-1 (Levine & Corbet, 2006). Deriving an extinction of $A_V = 2.28 \pm 0.06$ – much more than previously assumed – from the $V-K$ color excess, Orosz et al. (2009) infer a black hole mass of $10.9 \pm 1.6\,M_{\odot}$.

The persistent XRB LMC X-1 is the only dynamically confirmed black hole candidate that so far has only been found in the high/soft (thermal dominant) X-ray spectral state; that is, its X-ray spectrum can be described by a multi-temperature disk blackbody component plus a weak soft ($\Gamma \gg 2$) power-law component (Ebisawa et al., 1989; Schlegel et al., 1994; Wilms et al., 2001; Nowak et al., 2001; Haardt et al., 2001; Cui et al., 2002; Yao et al., 2005). In comparison, LMC X-3 usually shows a similarly soft X-ray spectrum, but also (partial) transitions to the low/hard state (Wilms et al., 2001; Smith et al., 2007), while Cyg X-1 regularly transits between the low/hard and a soft-intermediate state and never reaches the thermal dominant one (see, e.g., Figs. 2.36–2.37 on page 79). LMC X-1 is therefore an ideal target for measuring the black hole's spin parameter a from the soft X-ray continuum produced by the relativistic accretion disk. Gierliński et al. (2001) constrained a to be less than 0.998 from a 24 ks 0.7–10 keV *ASCA*-SIS spectrum. Gou et al. (2009) have recently reported a=$0.90^{+0.04}_{-0.09}$ from 18 selected *RXTE*-

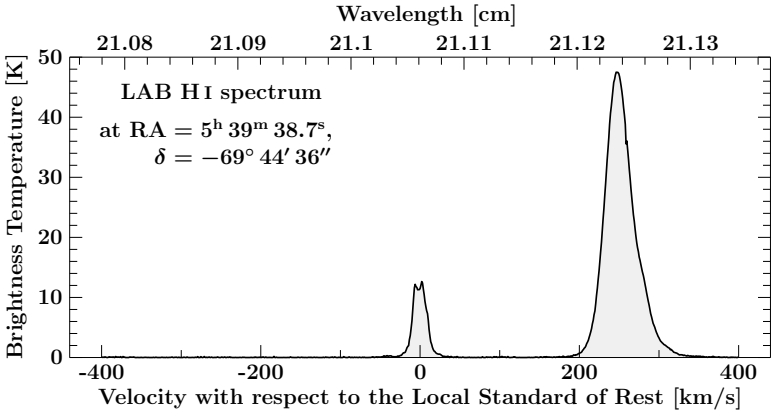

Figure 3.1: 21 cm H I spectrum of LMC X-1 from the LAB survey (Kalberla et al., 2005; Bajaja et al., 2005).† Only <12 % of the H column density resides at $v_{\rm LSR} \approx 0$, while the remaining part is located at a redshift of 200–300 km/s, consistent with the LMC (Richter et al., 1987).

† See http://www.astro.uni-bonn.de/~webaiub/english/tools_labsearch.php?alpha=05+39+38.7&beta=-69+44+36.

Table 3.1: Comparison of elemental abundances in the Galactic ISM and in the LMC $\epsilon(Z) = 12 + \log_{10}\big(A(Z)/A(1)\big)$, see also Table 1.2 on page 25.

	He	C	N	O	Ne	Mg	Si	S	Ar	Fe
$\epsilon_{\rm gal}(Z)^{(1)}$	10.99	8.38	7.88	8.69	7.94	7.40	7.27	7.09	6.41	7.43
$\epsilon_{\rm LMC}(Z)$	$10.93^{(5)}$	$8.03^{(2)}$	$7.01^{(2)}$	$8.38^{(2)}$	$7.6^{(4)}$	$7.12^{(2)}$	$7.21^{(2)}$	$6.7^{(4)}$	$6.2^{(4)}$	$7.2^{(3)}$
$\frac{A_{\rm LMC}(Z)}{A_{\rm gal}(Z)}$	0.87	0.45	0.13	0.49	0.46	0.53	0.87	0.41	0.62	0.59

References: (1) Wilms et al. (2000). (2) Przybilla (priv. comm.): average of 7 B-stars in the LMC (see also Korn et al., 2002, 2005). (3) Przybilla (priv. comm.): 1 star in the LMC (see also Przybilla et al., 2008). (4) Garnett (1999): H II regions in the LMC. (5) Dufour (1984).
Note. The LMC abundances relative to the Galactic ones, $A_{\rm LMC}(Z)/A_{\rm gal}(Z)$, can be used as parameters of the `TBnew` absorption model, provided that the abundances of Wilms et al. (2000) are set as default; i.e., using `xspec_abund("wilm");` in ISIS. For all other elements, which hardly contribute to the absorption in the soft X-ray band, the average value $A_{\rm LMC}(Z)/A_{\rm gal}(Z) = 0.5$ is assumed.
(from Hanke et al., 2010b, table 2)

PCA spectra with exposures between 5 and 11 ks and covering 2.5–20 keV. These authors fix the column density for the photoelectric absorption to $N_{\rm H}$=4.6×10^{21} cm^{-2} as reported by Cui et al. (2002) based on low statistics.

An appropriate description of the absorption is, however, indispensable for modeling the soft X-ray continuum and likewise for modeling the visual extinction, hence the derivation of the system parameters from the dereddened optical spectrum of the companion star. An overview of previous $N_{\rm H}$ measurements for LMC X-1 is given by Orosz et al. (2009, table 2). Figure 3.1 shows the 21 cm spectrum in direction of LMC X-1 measured in the Leiden/Argentine/Bonn survey (Kalberla et al., 2005; Bajaja et al., 2005), demonstrating that only <12 % of the neutral hydrogen column density towards the LMC, $N_{\rm H}$=4×10^{21} cm^{-2}, is of Galactic origin. The largest part is, however, detected at a velocity $v_{\rm LSR}$=200–300 km s^{-1} with respect to the Local Standard of Rest, consistent with the redshift of the Large Magellanic Cloud (Richter et al., 1987) and therefore probably local to the LMC. As the absorption in the 0.5–10 keV band is, however, mostly caused by metals (Wilms et al., 2000), the much lower metallicity of the LMC compared to our Galaxy (see Table 3.1) has to be taken into account.

Absorption measurements

This section describes the analysis of six archival soft X-ray spectra obtained with the gratings and/or CCD detectors on *Chandra*, *XMM-Newton*, or *Swift*. They are referred to as C1, X1–2,

Table 3.2: Observations of LMC X-1 with *Chandra* HETGS, *XMM*, *Swift* XRT, or *Suzaku* XIS

Obs.	Satellite	ObsID	Start Date (YYYY-mm-dd)	(MJD)	Exposure (ks)	$\phi_{\rm orb}{}^{(\rm T3)\dagger}$	$\phi_{\rm orb}{}^{(\rm F9)\ddagger}$
C1	*Chandra*	93	2000-01-16	51559.2	19	0.45–0.51	0.50–0.56
X1	*XMM*	0112900101	2000-10-21	51838.7	5–7	0.94–0.96	0.98–0.01
X2	*XMM*	0023940401	2002-09-26	52543.2	35	0.17–0.28	0.21–0.32
S1	*Swift*	00037079001	2007-10-31	54404.7	2.4	0.37–0.42	0.37–0.43
S2	*Swift*	00037079002	2007-12-06	54440.4	9.8	0.49–0.61	0.50–0.62
S3	*Swift*	00037079003	2007-12-10	54444.1	4.4	0.43–0.50	0.43–0.50
	Suzaku	404061010	2009-07-21	55033.8	108	0.28–0.07	0.28–0.07
	Chandra	11074	2010-01-02	55198.7	17.6	0.47–0.52	0.47–0.52
	Chandra	12068	2010-01-04	55200.4	13.2	0.90–0.94	0.90–0.94
	Chandra	12072	2010-01-05	55201.4	18.6	0.15–0.20	0.15–0.20
	Chandra	11986	2010-01-07	55203.0	8.2	0.58–0.60	0.57–0.60
	Chandra	12069	2010-01-08	55204.0	18.6	0.82–0.88	0.82–0.88
	Chandra	12071	2010-01-09	55205.7	4.2	0.26–0.27	0.25–0.27
	Chandra	12070	2010-01-10	55206.6	17.8	0.50–0.55	0.49–0.55
	Chandra	11987	2010-01-18	55214.6	19.1	0.53–0.58	0.52–0.58
	Chandra	12089	2010-01-21	55217.2	15.1	0.20–0.24	0.20–0.24
	Chandra	12090	2010-02-26	55253.5	13.2	0.49–0.53	0.48–0.52

† using the ephemeris of Orosz et al. (2009, Table 3): $T_0 =$ MJD 53390.8436, $P = 3.90917\,$d
‡ using the ephemeris of Orosz et al. (2009, Fig. 9): $T_0 =$ MJD 53390.75174, $P = 3.9094\,$d

and S1–3 in the following, see Table 3.2. The *Suzaku* data set also listed in this table was not public at the time of the analysis, and the *Chandra* observations in 2010 were successfully proposed by our group (PI: M.A. Nowak) based on the results presented in the following.

Observations. The *Chandra* HETGS observation C1 was performed with the detector CCDs operated in timed exposure mode. The ±first order HEG and MEG spectra, as well as the corresponding response matrices, were taken from the *Chandra* Transmission Grating Catalog archive TGCat (Huenemoerder et al., 2011)[1]. All instruments of *XMM-Newton* were active during the first (shorter) *XMM* observation X1. The EPIC-pn camera was operated in timing mode. Its data are therefore not affected by photon pileup (Wilms et al., 2003). The same is true for data from the Reflection Grating Spectrometers due to their dispersion of the photons, but not for data from the MOS cameras, which were operated in full frame imaging mode. For this reason, only the EPIC-pn spectrum and the first and second order spectra of RGS 1 and 2 were used. No EPIC-pn data are available for the second *XMM* observation X2. *Swift*'s X-ray telescope (XRT; Burrows et al., 2005) was operated in photon counting (PC) mode during the first *Swift* observation S1, which resulted in pileup. For S2 and S3, the windowed timing (WT) mode was used. For the PC mode observation S1, the spectrum had to be extracted from an annulus in order to exclude the region affected by pileup. The resulting spectrum has therefore a lower S/N. The WT mode spectra are not as well calibrated as the PC mode one around the Si edge (Fig. 3.2). Since a gain correction (as in Sects. 2.5.2, 2.5.3) could not remove all residuals in the 1.5–2 keV band, these data were excluded from the fit. Further details of the data extraction are given by Hanke et al. (2010b).

[1] See `http://tgcat.mit.edu`.

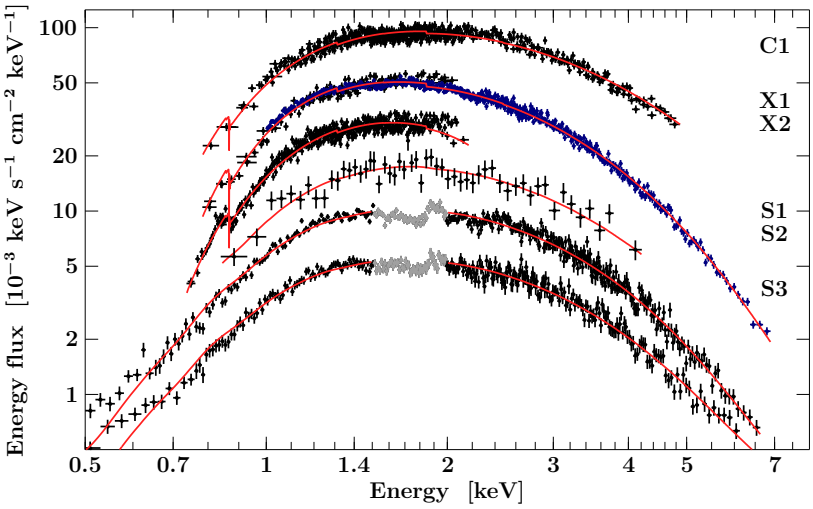

Figure 3.2: Flux-corrected spectra of LMC X-1 from the six observations, shifted in flux according to the labels with respect to C1 for visual clarity. The gray data have been ignored because of calibration issues. The models shown here for illustrative purposes are also broadened by the instrumental response.
(Hanke et al., 2010b, fig. 1)

Table 3.3: Column density in units of $10^{22}\,\mathrm{cm}^{-2}$ for the six observations and the sine fit

Observation	ϕ_{orb} (T3)	Continuum Model			
		`diskbb+powerlaw`*	`eqpair`	`simpl(kerrbb)`	`simpl(diskbb)`
X2	0.17–0.28	$\left(2.00^{+0.17}_{-0.19}\right)^{*}$	1.279 ± 0.005	1.278 ± 0.005	$1.288 \pm 0.016^{\dagger}$
S1	0.37–0.42	$\left(1.2^{+0.5}_{-0.2}\right)^{*}$	$1.17^{+0.15}_{-0.10}$	$1.17^{+0.11}_{-0.10}$	$1.14^{+0.15}_{-0.11}$
S3	0.43–0.50	$0.96^{+0.03}_{-0.02}$	1.02 ± 0.02	$1.01^{+0.03}_{-0.02}$	0.97 ± 0.02
C1	0.45–0.51	$\left(1.25^{+0.04}_{-0.01}\right)^{*}$	$1.065^{+0.000}_{-0.019}$	$1.085^{+0.018}_{-0.016}$	$1.009^{+0.018}_{-0.017}$
S2	0.49–0.61	1.031 ± 0.017	1.088 ± 0.017	1.088 ± 0.017	1.038 ± 0.017
X1	0.94–0.96	$\left(1.81^{+0.06}_{-0.05}\right)^{*}$	$1.191^{+0.006}_{-0.007}$	$1.187^{+0.014}_{-0.012}$	$1.133^{+0.005}_{-0.004}$
Sine Fit	full orbit	$(1.43 \pm 0.43)^{*}$	1.15 ± 0.15	1.15 ± 0.14	1.10 ± 0.18

Notes. Quoted error bars are statistical uncertainties at the 90 % confidence level for the observations, but semi-amplitudes for the sine fits. * The `diskbb+powerlaw` model overestimates N_{H} more, the more the `powerlaw` contributes at low energies, see text. † As the lack of data above 2 keV did not allow to constrain the power-law with the `simpl` model, only `diskbb` was used in this case.

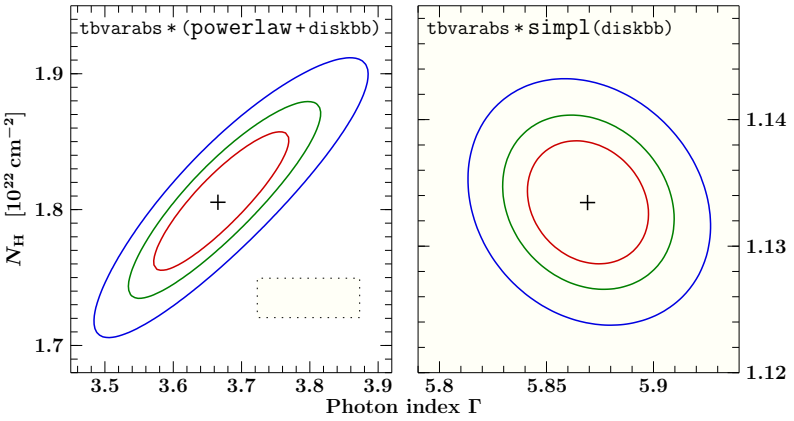

Figure 3.3: Correlation of the column density N_{H} and the photon index Γ, derived with the `powerlaw` model (left) and the `simpl` model (right) for observation X1. The contours show the 68 %, 90 %, and 99 % confidence regions for two parameters of interest (i.e., $\Delta\chi^2 = 2.30$, 4.61, and 9.21). The size of the right plot is indicated within the left one.
(Hanke et al., 2010b, fig. 2)

Analysis. As for all previous observations, the X-ray spectra of LMC X-1 investigated here are very soft (see Fig. 3.2). A hard (albeit very steep) component in addition to a thermal one is nonetheless needed to describe the data, except for S2 and S3. The `powerlaw` model, however, becomes unphysically strong at low energies (e.g., Shrader & Titarchuk, 1998; Done et al., 2002). A steep photon index $\Gamma \gg 2$ (e.g., $\Gamma = 3.7 \pm 0.1$ as measured for X1, which has the best high-energy coverage due to the EPIC-pn spectrum) is compensated for in spectral fits by an incorrectly strong absorption (e.g., Yao et al., 2005; Suchy et al., 2008; Gou et al., 2009). In contrast, the empirical convolution model `simpl` (Steiner et al., 2009) has an intrinsic *low-energy* cut-off when convolving an input spectrum modeled by, e.g., `diskbb` or `kerrbb`.[2] Figure 3.3 shows that the (well known) correlation between $N_{\rm H}$ and Γ vanishes when `simpl` is used instead of `powerlaw`. Although an even steeper photon index was found using `simpl`, the value of $N_{\rm H}$ is lower and is more narrowly constrained.

Because the derived absorption might depend on the shape of the continuum, different models were investigated, namely empirical ones – such as `diskbb + powerlaw`, `simpl(diskbb)`, and `simpl(kerrbb)` (Li et al., 2005) – and the physical Comptonization model `eqpair` (Coppi, 2000). For X1, the $N_{\rm H}$ derived with `diskbb + compTT` (Titarchuk, 1994) is also consistent with the one from, e.g., `simpl(diskbb)`. These models typically describe the data equally well. In all fits, the disk has a temperature between 0.65 and 1.1 keV. The other parameters, too, are similar to previously obtained values. Table 3.3 and Fig. 3.4 show the results for the column density (assuming the LMC abundances given in Table 3.1) as a function of orbital phase $\phi_{\rm orb}$ for each of the six observations and all four of the aforementioned continuum models. In all cases where a steep power-law substantially contributes to the model, the `diskbb + powerlaw` model gives a much higher $N_{\rm H}$ than the other models, because of the systematic error of the `powerlaw` model. These values can consequently be ignored. The other models, however, are quite consistent with one another: their agreement on $N_{\rm H}$ is within $<8\times10^{20}\,{\rm cm}^{-2}$, which is therefore an upper limit of the systematic error due to the choice of the continuum. Using the LMC abundances (Table 3.1), the column densities are in the range of $(1.0-1.3)\times10^{22}\,{\rm cm}^{-2}$. The *equivalent* hydrogen column density inferred from this X-ray absorption study is therefore much higher than the H-column resolved by the LAB survey (at a half-power beam-width of $0.^{\circ}6$; Kalberla et al., 2005), which is likely caused by additional material in the environment of LMC X-1 and in the system itself. This result was not obtained in earlier X-ray absorption measurements, as erroneously applying Galactic abundances resulted in lower $N_{\rm H}$ values.

Evidence for orbital modulation. There is an indication for a modulation of $N_{\rm H}$ with orbital phase. The observations X1 and X2 close to $\phi_{\rm orb}\approx0$, when the black hole is behind the donor star, require a systematically higher $N_{\rm H}$ than S3, C1, and S2 close to $\phi_{\rm orb}\approx0.5$. To quantify this modulation by its mean and amplitude (Table 3.3), sine curves were fit to the six measurements for each continuum model (see Fig. 3.4), although these do not describe the data very well and also predict the strongest absorption at $\phi_{\rm orb}=0.15-0.17$, which is not expected for the absorption in the stellar wind of the donor giant. The amplitude of the modulation is, however, consistent with the orbital modulation of the X-ray flux. Orosz et al. (2009) assume that the latter is mostly caused by Thomson scattering in the stellar wind since they find similar fractional full amplitudes $A = ({\rm max}-{\rm min})/{\rm mean}$ in all three *RXTE*-ASM energy bands, namely $A_{\rm A(1.5-3\,keV)} = 7.2\pm1.0\,\%$, $A_{\rm B(3-5\,keV)} = 7.7\pm1.1\,\%$, and $A_{\rm C(5-12\,keV)} = 3.8\pm2.9\,\%$. From a modulation of $N_{\rm H}$ with a full amplitude of $3\times10^{21}\,{\rm cm}^{-2}$, $A_{\rm A} = 7.7-6.9\,\%$, $A_{\rm B} = 1.6-2.7\,\%$, and $A_{\rm C} = 0.4-1.7\,\%$ are expected, depending on the assumptions about the ASM response; i.e., the variation seen with the ASM is almost consistent with the suggested neutral absorption.

[2] As a convolution model that relies upon a spectral model outside of the energy range spanned by the noticed data, `simpl` must be evaluated on a suitably extended grid, i.e., using `set_eval_grid_method` with `USER_GRID` in ISIS.

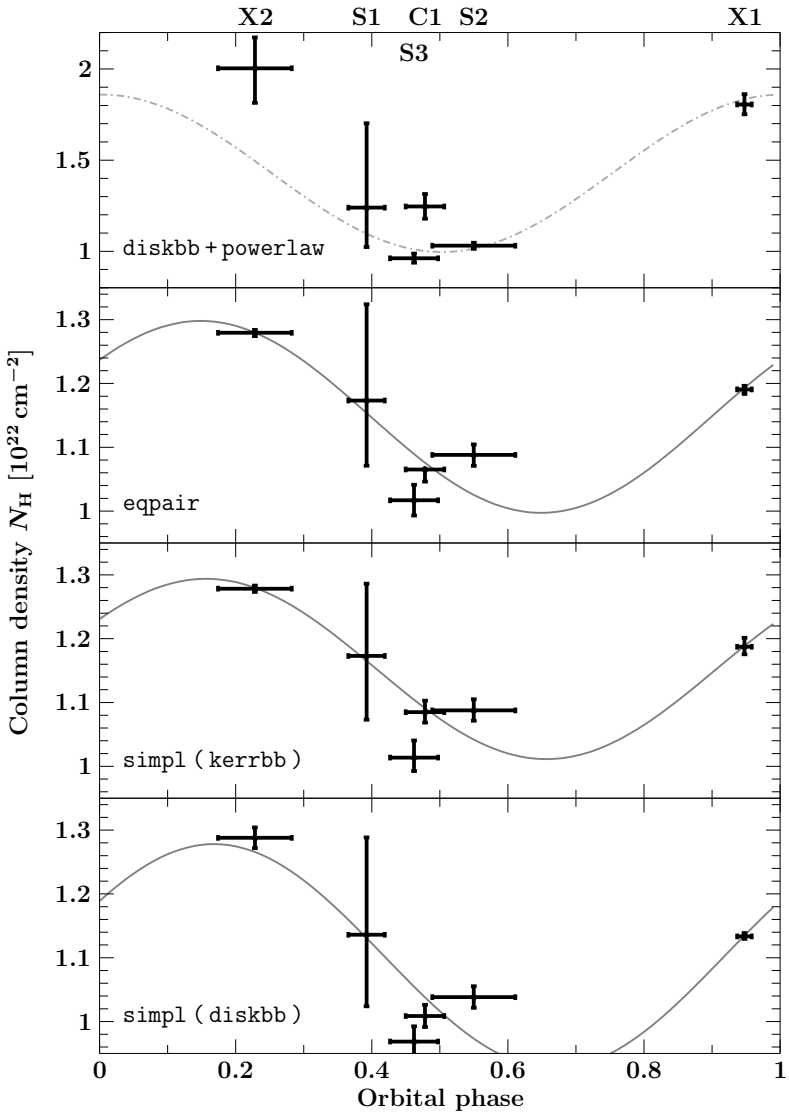

Figure 3.4: N_H as a function of orbital phase $\phi_{orb}{}^{(T3)}$ (see Table 3.2) using various continuum models. Note the different scale for the `diskbb+powerlaw` model, which may predict an unreliably large N_H (see text). The gray lines fit the results with sine curves. (Hanke et al., 2010b, fig. 3)

Chapter IV

Summary and Outlook

X-ray studies of accreting black holes or neutron stars do not only allow to investigate the effects of strong gravity, but also to probe the environment of these objects. A summary of the key results from this thesis is given below, followed by an outlook on still open questions that remain to be resolved by future research.

4.1 Conclusions

The main focus of this work is on the wind structure of the high-mass X-ray binary system Cyg X-1/HDE 226868, which has been addressed with the following methods and results:

Statistical analysis of the *RXTE* ASM flux distribution

The orbital modulation has been known since the first long-term observations in the 1970s, and recent investigations have shown that the X-ray flux in the hard state follows a lognormal distribution (Poutanen et al., 2008). The present study is the first analysis of the combined effect, namely of how the orbital modulation affects the flux distribution. It was found that not only the average optical depth peaks at early orbital phases, but that also the width of its distribution becomes larger at $\phi_{\rm orb}\approx 0$. If the optical depth is due to the wind, and not due to structures in the accretion disk as suggested by Poutanen et al. (2008), the interpretation of this result is that the wind must be more clumpy in the region close to the star than on the other side of the black hole – which is a complementary confirmation of the same conclusion drawn from earlier studies, based on the occurence of absorption dips along the orbit (Bałucińska-Church et al., 2000).

Spectral analysis of all *RXTE* PCA monitoring observations within 14.5 years

Despite the low resolution of proportional counters, the high quality data of Cyg X-1 allow to measure absorption even in the spectrum above $\sim$3 keV. The orbital modulation of the column density, which was already indicated in previous studies, could be confirmed with highly improved significance. This is due to a careful investigation of the soft X-ray spectrum, its systematic errors, and because of the integration of spectra from *shorter* time segments than in earlier studies ($<$60 min; compared to entire observations), allowing for a spectral variability on the time scale of 1 h. Furthermore, the scatter of the column density measurements at $\phi_{\rm orb}\approx 0$ was found to be much larger than at the opposite phase $\phi_{\rm orb}\approx 0.5$, in agreement with aforementioned results from the flux distribution.

Unlike these trends, quantitative column densities depend systematically on the error bars assigned to the spectral count rates in the low energy channels, whose calibration is the least certain. This effect is especially strong in the soft state, when the accretion disk significantly contributes to the Comptonized power-law spectrum, and the low energy count rates are highest. Assuming neutral absorption, the average column density at $\phi_{\rm orb}\approx 0$ is $(2.3-2.7)\times 10^{22}\,{\rm cm}^{-2}$ in the hard state, with a standard deviation of $(1.7-1.8)\times 10^{22}\,{\rm cm}^{-2}$ – compared to only $(0.7-1.0)\times 10^{22}\,{\rm cm}^{-2}$ at $\phi_{\rm orb}\approx 0.5$, with a scatter of $(0.3-0.5)\times 10^{22}\,{\rm cm}^{-2}$.

Spectral analysis of *RXTE* PCA observations during dips on short time scales

For two observations containing strong absorption dips, the evolution of the absorption was traced by means of time resolved spectroscopy based on segments from 128 s of data. It was found that the column density may vary violently on such short time scales.

In hardness ratios from light curves at sub-second time scales (i.e., at the limit of current detectors' capabilities in terms of high time resolution photometry at good S/N), absorption dips appear still structured. It is cautioned that the simple analysis of an average spectrum, integrated from periods of different absorption, may give misleading spectral parameters.

High-resolution X-ray spectroscopy of the wind in the hard state

Due to their high resolution and good coverage of the 0.5–8 keV band, *Chandra* HETGS observations allow to measure absorbing column densities directly from absorption lines and/or edges, without the need to rely on the curvature of the (broad band) continuum that is also detected at lower resolution. The analysis of *Chandra* HETGS observations on 2003 April 19/20 and 2008 April 18/19 at $\phi_{\rm orb}{\approx}0$ in the hard state has demonstrated that the column density of the neutral absorber (outside of absorption dips) is $\sim 6{\times}10^{21}\,{\rm cm}^{-2}$, i.e., much lower than expected from the *RXTE* analysis. Instead, an ionized absorber is detected in strong absorption lines from K-shell ions of Ne, Mg, Si, S, Ar and Ca, as well as a wealth of transitions below 1.2 keV from L-shell ions of Fe. The latter often form complex blends of weaker, unresolved lines that prevent an identification and interpretation of single features. An instructive description of the spectrum requires therefore physical models involving a complete atomic database, such as the photoionization code `xstar`. Within this work, first results have been obtained from the application of the warm absorber model `warmabs`, which is based on `xstar`. These results imply that the stellar wind is highly photoionized, with $\log\xi \approx 2.3$. Therefore, large fractions of low-Z elements up to O are already fully ionized and do not cause strong absorption in the soft X-ray band as they would at lower ionization. The equivalent H column density of the ionized absorber inferred from the *Chandra* spectra amounts to a few times $10^{22}\,{\rm cm}^{-2}$. Higher-Z elements, which contribute to the absorption in the *RXTE* PCA bandpass at $\gtrsim$3 keV, are less strongly ionized, hence the column densities measured with *RXTE* and *Chandra* are not necessarily inconsistent with each other. For a detailed quantitative comparison, the column densities that were previously derived from *RXTE* data assuming neutral absorption have to be corrected for the modified effective opacities of an ionized absorber.

The analysis of a further *Chandra* HETGS observation successfully proposed by our group (PI: M.A. Nowak), which was performed on 2010 January 14 in a similar hard state as the previous ones, has revealed that the absorption line equivalent widths at $\phi_{\rm orb}{\approx}0.5$ are significantly reduced compared to the $\phi_{\rm orb}{\approx}0$ spectrum. This result is consistent with the orbital modulation detected with *RXTE* being due to absorption in the ionized wind.

Moreover, the observation at $\phi_{\rm orb}{\approx}0.5$ displays for the first time clear P Cygni line profiles in the X-ray spectrum of Cyg X-1. These demonstrate the acceleration of the stellar wind even on the photoionized hemisphere of the star, and therefore disprove the conjecture by Gies et al. (2008) that the wind from this side might be absent. In a consistent picture of the hard state observations (Fig. 2.62 on page 108), the emission from the slow base of the wind is not detected at $\phi_{\rm orb}{\approx}0$ because it merely fills a small part of the strong absorption lines in the continuum from Cyg X-1.

Chandra HETG spectroscopy of absorption dips

Soft X-ray absorption dips were recorded during the *Chandra* observations in 2003 April and 2008 April at $\phi_{\rm orb}\approx 0$, as well as at $\phi_{\rm orb}\approx 0.2$. The spectral evolution in a color-color diagram shows a characteristic track that is inconsistent with pure absorption: While the hard color hardens during with increasing level of dipping, the soft color softens during the deepest dips after an initial hardening – a behavior that can be explained by partial absorption of the continuum. A closer investigation has shown three effects to contribute to the partial covering:

1. *Partial temporal covering.* During times of fast time variability of the absorber, the integration time for a single data point in the color-color diagram, which is limited by the detector's readout mode and in particular sensitivity, may already include several dips of different absorption. It was found that the color-color diagram from these phases deviates more strongly from the pure absorption track than during longer, less structured dips.
2. *Partial spatial covering on the detector.* Cyg X-1 is surrounded by an X-ray scattering halo that contributes $\sim 1/10$ of the flux, however arriving with different time delays that may exceed the duration of absorption dips. Instruments that cannot spatially resolve and exclude the halo integrate its – potentially unabsorbed – contribution, while the direct component shows absorption dips. The covering fractions found with *XMM* or *Suzaku* are therefore generally larger than those derived from *Chandra* data.
3. *Partial spatial covering by the absorber.* The analysis of the *Chandra* spectrum during a long, deep absorption dip (i.e., minimizing effects 1 and 2) has revealed emission lines from K-shell ions of Ne and Mg, which had, among the previously discussed hard state observations, only been seen at $\phi_{\rm orb}\approx 0.5$ in emission, but otherwise in absorption. They are, however, expected from the model of the hard state wind developed in the previous section. These lines demonstrate that some emission from the radiating dense part of the wind is indeed not covered by the absorber. They furthermore suggest the hypothesis that the entire uncovered soft X-ray emission could be due to radiation reprocessed by the wind environment in form of line emission from unresolved, weaker transitions, which were likewise blended in the (nondip) absorption spectrum.

The spectral evolution with dipping was investigated in further detail. Because of the fast time variability of the absorber, time intervals from different dips, but at approximately the same level of dipping according to the hardness ratio, had to be integrated to obtain a spectrum with good S/N. While a partial covering model provides a good description of the continuum, line features are emerging at $\sim$6.8 Å, and $\sim$5.2 Å, which could be identified with $1\,\mathrm{s} \rightarrow 2\,\mathrm{p}$ transitions of various ionization stages of Si and S, respectively. The equivalent widths at different levels of dipping show that the ionization balance shifts to lower ionization during dips. This result constitutes the first direct spectroscopic evidence that the ionization parameter of the absorber changes continously.

Spectroscopy of absorption dips with *XMM-Newton*

The analysis of the *XMM* observation simultaneous to the *Chandra* pointing in 2008 April complements the previous results. Because of *XMM*'s large effective area, the RGS spectrum allows to follow the spectral evolution even deeper into the dips at still good S/N. A broad absorption feature is found at $\sim$16.2 Å, whose equivalent width grows from $\lesssim$0.2 Å during the least absorbed parts of the observation to $\gtrsim$1 Å during the deepest dips. A tentative identification can be found in unresolved transition arrays of Fe M-shell ions. The growth of this absorption complex confirms that the column density of a less strongly ionized absorber increases during the dips. No significant change of the centroid position of the absorption complex is detected, although a weak trend hints at a lower ionization parameter while dipping.

Analysis of the multi-satellite campaign

The abovementioned *XMM-Chandra* observation of Cyg X-1 was part of the largest X-ray satellite campaign ever performed; with simultaneous data acquisition by *every* X-ray mission available in 2008 April (i.e., *XMM*, *Chandra*, *RXTE*, *Suzaku*, *INTEGRAL*, *Swift*, and *AGILE*). Both the analysis of hard X-ray light curves from different instruments, and time-resolved soft X-ray spectroscopy show a linear decline of the broad band flux for $\sim$4 h towards the time of the 1.5 h long, deepest absorption dip, followed by a linear rise for more than 5 h afterwards. Although source intrinsic variability cannot be ruled out, the coincidence with the dipping activity suggests a physical connection. An interpretation is given by X-ray scattering in an ionized cloud. Only the dense core and a few further clumps, which may have fragmented out of the hot cloud of fully ionized gas, are cool enough to produce absorption dips. The column density required to explain the conjectured scattering optical depth is more than one order of magnitude larger than those inferred from the absorption of the continuum during dips – if modelled as neutral. Since the previous spectroscopy has demonstrated that the absorber is still highly ionized, even though less strongly than during the nondip phases, the column density infered from continuum absorption is, however, only a lower limit.

Analysis of the absorption towards LMC X-1

The spectra from six archival observations with *Chandra*, *XMM*, and *Swift* have been analyzed in view of the absorption. An indication for an orbital modulation was found, which can nearly explain the observed orbital modulation of the *RXTE* ASM flux.

4.2 Future work

Some interesting questions are left open, which deserve to be followed up on in the future:

More detailed modelling of the ionized absorption in Cyg X-1

A self-consistent simulation of the highly photoionized wind, taking a complete database of atomic transitions into account, is desired to interpret the complex absorption line spectrum below 1.2 keV – in particular at early orbital phases when the absorption is strong. The first results with the warm absorber model are already very promising, but a meaningful spectral fitting, including the calculation of parameter confidence intervals, requires further improvements of the model. Currently, no scaled opacities are returned when elemental abundances are changed by 1 % or less, which is problematic for numerical optimization algorithms.[1]

An inclusion of the Si and S $1\,s \rightarrow 2\,p$ transitions, also for the lower ionization stages than He-like ions (e.g., from Palmeri et al., 2008), in the `xstar` atomic database would be very valuable for the interpretation of the dip spectra, especially in order to infer the column density and ionization parameter.[2]

A self-consistent description of the ionized absorber during the dips will then allow to estimate the total column of fully ionized gas and thereby confirm or disprove the hypothesis of the scattering cloud causing the reduction of the broad band flux.

[1] Note added in proof: With `warmabs` v2.01 (`xstar` version 2.2.1bf), a full recalculation of the opacities is triggered by abundances changed by more than 1 ‰, but smaller changes are still ignored.

[2] Note added in proof: These K transitions have been included with `warmabs` v2.01.

Already in its current version, the `warmabs` model might allow to fit *Chandra* and *RXTE* spectra together. Besides the correction of the previous column densities measured with *RXTE* assuming neutral absorption, a successful joint fit could also resolve previous discrepancies of their spectral slope (Hanke et al., 2009, table 2).

Analysis of new observations

The upcoming *XMM-Newton* large program observation of Cyg X-1 (PI: P. Uttley) will provide the unique opportunity to study the changes of wind absorption within a single orbit, hence with maximally constant continuum spectrum. The almost complete coverage of the orbit will give new insights in the frequency and structure of absorption dips as a function of ϕ_{orb}.

The LMC X-1 study can immediately be continued with new observations that have not been analyzed yet. In particular the long *Suzaku* pointing in 2009 (PI: J.E. McClintock) is well suited because of its broad orbital phase coverage, but also the *Chandra* observations in 2010 obtained by our group (PI: M.A. Nowak).

Analysis of other targets

Finally, the investigation of the wind environment of high-mass X-ray binaries can of course be extended to other sources as well. A list of interesting targets is given in appendix D.

Appendix

A A special polar coordinate system for the line of sight in binaries

A Cartesian parameterization of the line of sight toward the secondary was given in Sect. 2.1.2, by Eq. (2.12) on page 46. In order to investigate the structure of the primary's radial wind, the plane defined by the line of sight at a given orbital phase $\phi_{\rm orb}$ and the primary is suitably described by a polar coordinate system as in Eq. (2.13), with fixed azimuthal angle ϕ, given by Eqs. (2.14) and (2.15). This section derives a transformation of the polar angle ϑ to obtain a generalized polar coordinate system $(\rho_\star,\, \vartheta(\lambda))$ that is locally Euclidean on the line of sight:

$$\vec{r}(\rho_\star,\, \lambda) \;=\; \rho_\star \cdot \begin{pmatrix} \cos\vartheta(\lambda) \\ \sin\vartheta(\lambda) \cdot \begin{pmatrix} -\sin\phi \\ \cos\phi \end{pmatrix} \end{pmatrix} \quad , \tag{A.1}$$

The mapping of Eq. (A.1) has a more general line element than polar coordinates have, namely:

$$|\mathrm{d}\vec{r}|^2 \;=\; \sum_{i=1}^{3} \left(\frac{\partial r_i}{\partial \rho_\star}\,\mathrm{d}\rho_\star + \frac{\partial r_i}{\partial \lambda}\,\mathrm{d}\lambda \right)^2 \;=\; \mathrm{d}\rho_\star^2 + \left(\rho_\star \,\frac{\mathrm{d}\vartheta}{\mathrm{d}\lambda}\,\mathrm{d}\lambda \right)^2 \tag{A.2}$$

The metric of the $(\rho_\star,\, \lambda)$ space is locally Euclidean – i.e., (infinitesimal) lengths and angles are the same as in real space $\vec{r}(\rho_\star,\, \lambda)$ – wherever $|\mathrm{d}\vec{r}|^2 = \mathrm{d}\rho_\star^2 + \mathrm{d}\lambda^2$. It is possible to construct $\lambda(\vartheta)$ such that $\mathrm{d}\lambda/\mathrm{d}\vartheta = \rho_\star$ at the line of sight. Namely, from Eqs. (2.12) and (A.1) follows

$$\tan\vartheta(s_{\rm LoS}) \;=\; \frac{\sqrt{1-c^2}\,s_{\rm LoS}}{1-c\,s_{\rm LoS}} \qquad\Longleftrightarrow\qquad s(\vartheta_{\rm LoS}) \;=\; \frac{\tan\vartheta_{\rm LoS}}{\sqrt{1-c^2}+c\tan\vartheta_{\rm LoS}} \tag{A.3}$$

and therefore

$$\rho_\star(s_{\rm LoS}) \;=\; \sqrt{1-2c\,s_{\rm LoS}+s_{\rm LoS}^2} \;=\; \frac{1}{\cos\vartheta_{\rm LoS} + \frac{c}{\sqrt{1-c^2}}\sin\vartheta_{\rm LoS}} \quad . \tag{A.4}$$

The solution of $\mathrm{d}\lambda/\mathrm{d}\vartheta\,(\vartheta_{\rm LoS}) = \rho_\star(s_{\rm LoS})$ with the initial condition $\lambda(\vartheta{=}0) = 0$ is:

$$\begin{aligned} \lambda(\vartheta) \;&=\; 2\sqrt{1-c^2}\left[\operatorname{artanh}\left(\sqrt{1-c^2}\,\tan\left(\frac{\vartheta}{2}\right) - c \right) + \operatorname{artanh}(c) \right] \\ &=\; \sqrt{1-c^2}\,\log\left(\frac{\sqrt{1-c^2} + (1+c)\,\tan\left(\frac{\vartheta}{2}\right)}{\sqrt{1-c^2} - (1-c)\,\tan\left(\frac{\vartheta}{2}\right)} \right) \end{aligned} \tag{A.5}$$

$\lambda(\vartheta)$ diverges for $\tan(\vartheta/2) \geq \sqrt{(1+c)/(1-c)}$, i.e., $\cos\vartheta \leq -c$, which is a parallel to the line of sight through the primary. The $(\rho_\star,\, \lambda)$ coordinate system covers thus only a half plane in real space. Inverting Eq. (A.5) gives

$$\tan\left(\frac{\vartheta(\lambda)}{2}\right) \;=\; \frac{\sqrt{1-c^2}}{\coth\left(\frac{\lambda}{2\sqrt{1-c^2}}\right) - c} \quad . \tag{A.6}$$

Expressing $\cos\vartheta$ and $\sin\vartheta$ more explicitly does not necessarily give a computational benefit:

$$\begin{aligned} \cos\vartheta(\lambda) \;&=\; \frac{1-\tan\left(\vartheta(\lambda)/2\right)^2}{1+\tan\left(\vartheta(\lambda)/2\right)^2} \;=\; \frac{c\,(1{+}c) \;+\; 2\,(1{-}c^2)\,e \;-\; c\,(1{-}c)\,e^2}{(1{+}c) \;+\; (1{-}c)\,e^2} \\ \sin\vartheta(\lambda) \;&=\; \frac{2\,\tan\left(\vartheta(\lambda)/2\right)}{1+\tan\left(\vartheta(\lambda)/2\right)^2} \;=\; \frac{\sqrt{1-c^2}\,(e{-}1)\left[(1{-}c)\,e \;+\; (1{+}c)\right]}{(1{+}c) \;+\; (1{-}c)\,e^2} \\ &\qquad \text{where} \quad e \;:=\; \exp\left(\frac{\lambda}{\sqrt{1-c^2}}\right) \end{aligned} \tag{A.7}$$

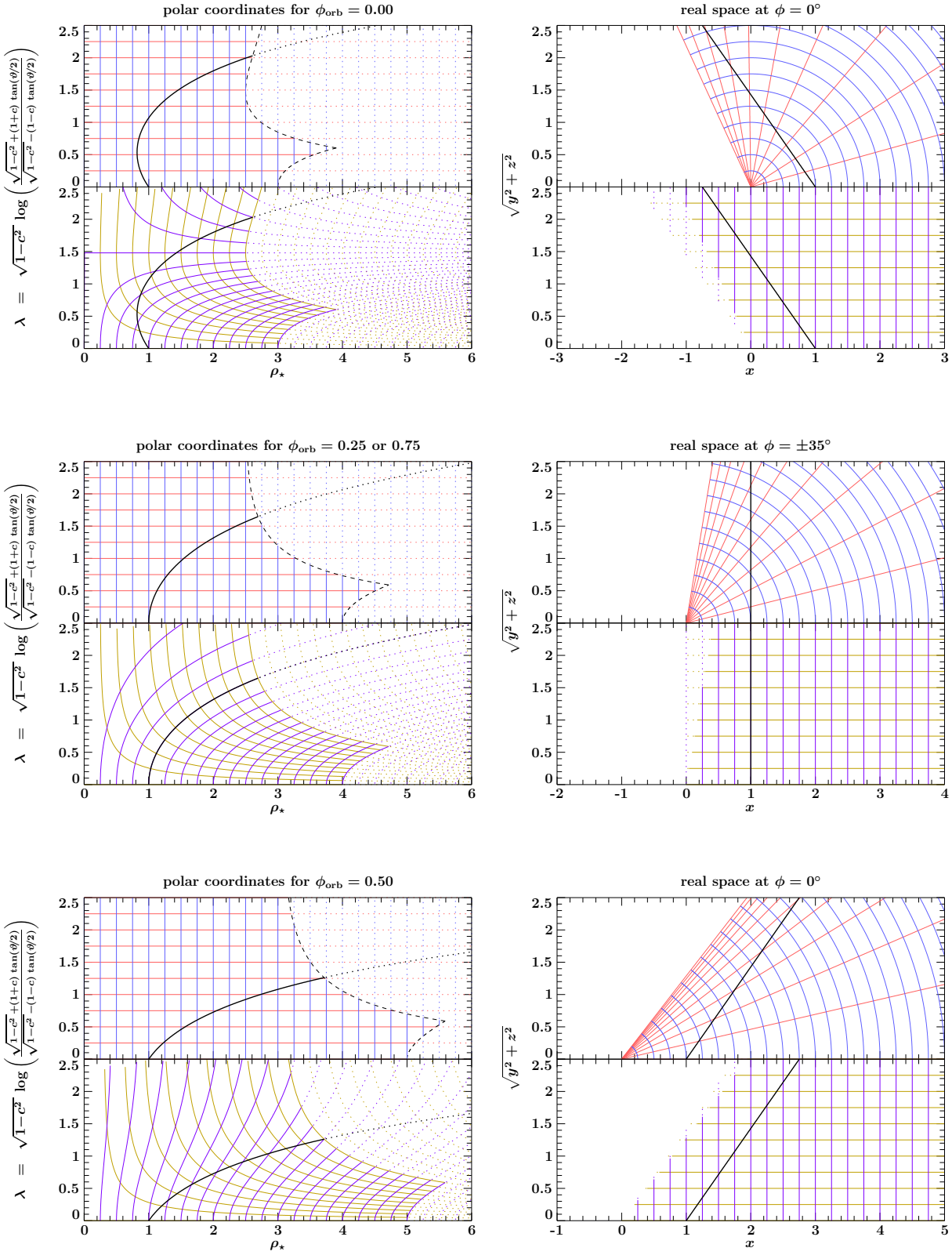

Figure A.1: Mapping between polar coordinates $(\rho_\star, \lambda)$ on the left, and real space $\vec{r} = (x, y, z)$ on the right, for orbital phases $\phi_{\rm orb} = 0$ (top), 0.25 or 0.75 (middle), and 0.5 (bottom). An inclination $i = 35°$ is assumed. While the colored lines show coordinate grids in both systems, the black line correpsonds to the line of sight, where the metric is locally Euclidean. Dotted lines correspond to regions outside of the visible range of the other coordinate system.

Figure A.1 shows the mapping $(\rho_\star, \lambda) \mapsto \rho_\star \cdot \Big(\cos\vartheta(\lambda),\ \sin\vartheta(\lambda)\Big)$ for fixed inclination, but different orbital phases. Although the top and bottom rows show the same plane in real space (of azimuthal angle ϕ=0°) for $\phi_{\rm orb}$=0 and $\phi_{\rm orb}$=0.5 (Eq. 2.14), the mapping is a different one.

B Bulky tables from the *RXTE* analysis of Cyg X-1

B.1 Orbital phase resolved *RXTE*-ASM (1.5–3 keV) flux distribution

Table B.1 shows the results from modelling the orbital phase resolved distribution of *RXTE* ASM A-band count rate of Cyg X-1, which is discussed in Sect. 2.2.2.

B.2 *RXTE*-PCA observations from 1996-02-12 to 2010-10-12

Table B.2 shows all 2247 continuous segments from *RXTE*-PCA observations of Cyg X-1 in the 14.5 years between 1996-02-12 and 2010-10-12. The five gain calibration epochs are identified.

Table B.1: Fit results for the hard state peak of orbital-phase resolved *RXTE* ASM-A flux-distributions of Cyg X-1.

(a) Fit results using all data and conventional histograms, see Fig. 2.16(a)

ϕ_{orb}	center		σ		γ
	Gauss	Voigt	Gauss	Voigt	
0.00–0.10	$0.762^{+0.006}_{-0.005}$	0.766 ± 0.006	0.193 ± 0.006	0.142 ± 0.017	0.099 ± 0.016
0.10–0.20	0.809 ± 0.005	0.819 ± 0.005	$0.169^{+0.005}_{-0.004}$	0.150 ± 0.011	0.069 ± 0.011
0.20–0.30	0.817 ± 0.004	0.833 ± 0.004	0.165 ± 0.004	0.151 ± 0.010	$0.059^{+0.010}_{-0.011}$
0.30–0.40	0.826 ± 0.004	0.843 ± 0.004	$0.155^{+0.004}_{-0.003}$	0.150 ± 0.008	0.046 ± 0.009
0.40–0.50	0.844 ± 0.004	0.855 ± 0.004	0.152 ± 0.003	$0.148^{+0.007}_{-0.008}$	0.036 ± 0.008
0.50–0.60	0.838 ± 0.004	0.855 ± 0.004	$0.156^{+0.004}_{-0.003}$	0.151 ± 0.008	0.044 ± 0.008
0.60–0.70	0.836 ± 0.004	0.851 ± 0.004	0.151 ± 0.003	0.147 ± 0.007	0.039 ± 0.007
0.70–0.80	0.832 ± 0.004	0.844 ± 0.004	0.153 ± 0.004	0.136 ± 0.009	0.060 ± 0.009
0.80–0.90	0.800 ± 0.004	0.808 ± 0.004	0.162 ± 0.004	0.154 ± 0.009	0.049 ± 0.010
0.90–1.00	0.761 ± 0.006	0.773 ± 0.005	$0.192^{+0.006}_{-0.005}$	0.175 ± 0.014	0.073 ± 0.015
	normalization		χ^2/dof		
	Gauss	Voigt	Gauss	Voigt	
joint	0.641 ± 0.007	0.843 ± 0.008	2010.3/683 $= 2.94$	1697.4/663 $= 2.56$	

ϕ_{orb}	center		σ		γ
	Gauss	Voigt	Gauss	Voigt	
-0.05–0.05	0.759 ± 0.006	0.769 ± 0.006	0.202 ± 0.006	$0.177^{+0.015}_{-0.016}$	0.075 ± 0.017
0.05–0.15	0.789 ± 0.005	0.797 ± 0.005	0.182 ± 0.005	$0.154^{+0.013}_{-0.014}$	0.078 ± 0.014
0.15–0.25	$0.816^{+0.005}_{-0.004}$	0.824 ± 0.004	0.168 ± 0.004	$0.154^{+0.010}_{-0.011}$	$0.055^{+0.011}_{-0.012}$
0.25–0.35	0.826 ± 0.004	0.842 ± 0.004	0.165 ± 0.004	0.165 ± 0.009	0.034 ± 0.010
0.35–0.45	0.835 ± 0.004	0.849 ± 0.004	0.154 ± 0.004	0.143 ± 0.008	0.043 ± 0.009
0.45–0.55	0.843 ± 0.004	$0.850^{+0.005}_{-0.004}$	0.154 ± 0.004	0.145 ± 0.008	0.039 ± 0.008
0.55–0.65	0.838 ± 0.004	0.848 ± 0.004	0.154 ± 0.004	0.143 ± 0.007	0.042 ± 0.007
0.65–0.75	0.837 ± 0.004	0.848 ± 0.004	0.155 ± 0.004	$0.150^{+0.007}_{-0.008}$	0.037 ± 0.008
0.75–0.85	0.820 ± 0.004	0.826 ± 0.004	0.158 ± 0.004	$0.135^{+0.009}_{-0.010}$	0.061 ± 0.009
0.85–0.95	0.777 ± 0.005	0.784 ± 0.005	$0.174^{+0.005}_{-0.004}$	0.158 ± 0.011	$0.060^{+0.012}_{-0.013}$
	normalization		χ^2/dof		
	Gauss	Voigt	Gauss	Voigt	
joint	0.650 ± 0.007	$0.827^{+0.009}_{-0.010}$	1931.6/679 $= 2.84$	1694.0/659 $= 2.57$	

Table B.1: (continued)

(b) Fit results using all data and histograms of probability distributions, see Fig. 2.16(b).

ϕ_{orb}	center		σ		γ
	Gauss	Voigt	Gauss	Voigt	
0.00–0.10	0.784 ± 0.006	$0.773^{+0.009}_{-0.006}$	$0.236^{+0.006}_{-0.005}$	$0.149^{+0.020}_{-0.019}$	$0.109^{+0.018}_{-0.019}$
0.10–0.20	0.823 ± 0.005	0.824 ± 0.005	$0.217^{+0.004}_{-0.005}$	0.158 ± 0.012	0.078 ± 0.013
0.20–0.30	0.841 ± 0.005	0.839 ± 0.005	$0.210^{+0.005}_{-0.004}$	$0.148^{+0.011}_{-0.012}$	0.080 ± 0.012
0.30–0.40	0.851 ± 0.005	0.848 ± 0.004	$0.203^{+0.005}_{-0.004}$	$0.153^{+0.009}_{-0.010}$	0.062 ± 0.010
0.40–0.50	0.863 ± 0.005	$0.860^{+0.005}_{-0.004}$	0.193 ± 0.004	0.148 ± 0.009	0.055 ± 0.009
0.50–0.60	0.863 ± 0.005	0.861 ± 0.004	$0.201^{+0.005}_{-0.004}$	0.149 ± 0.009	0.067 ± 0.010
0.60–0.70	0.856 ± 0.004	0.856 ± 0.004	$0.193^{+0.005}_{-0.004}$	0.144 ± 0.009	0.062 ± 0.009
0.70–0.80	0.848 ± 0.005	0.849 ± 0.004	$0.199^{+0.005}_{-0.004}$	0.142 ± 0.010	0.071 ± 0.010
0.80–0.90	0.809 ± 0.005	0.812 ± 0.004	$0.204^{+0.005}_{-0.004}$	0.149 ± 0.011	0.073 ± 0.011
0.90–1.00	0.780 ± 0.006	0.780 ± 0.005	$0.233^{+0.006}_{-0.005}$	$0.178^{+0.014}_{-0.015}$	0.083 ± 0.017

	normalization		χ^2/dof	
	Gauss	Voigt	Gauss	Voigt
joint	0.809 ± 0.006	0.872 ± 0.009	1251.5/695 $= 1.80$	562.9/675 $= 0.83$

ϕ_{orb}	center		σ		γ
	Gauss	Voigt	Gauss	Voigt	
-0.05–0.05	0.777 ± 0.006	0.778 ± 0.006	$0.242^{+0.006}_{-0.005}$	$0.184^{+0.015}_{-0.016}$	$0.088^{+0.017}_{-0.018}$
0.05–0.15	0.804 ± 0.005	0.805 ± 0.005	0.228 ± 0.005	$0.162^{+0.014}_{-0.015}$	0.090 ± 0.015
0.15–0.25	0.831 ± 0.005	0.832 ± 0.005	0.213 ± 0.005	$0.154^{+0.011}_{-0.012}$	0.076 ± 0.012
0.25–0.35	0.850 ± 0.005	0.848 ± 0.005	0.208 ± 0.004	0.159 ± 0.010	0.062 ± 0.011
0.35–0.45	0.859 ± 0.004	0.856 ± 0.004	0.198 ± 0.004	$0.142^{+0.009}_{-0.010}$	0.067 ± 0.010
0.45–0.55	0.862 ± 0.004	$0.859^{+0.006}_{-0.005}$	0.195 ± 0.004	0.153 ± 0.009	0.052 ± 0.009
0.55–0.65	0.860 ± 0.004	0.860 ± 0.004	0.198 ± 0.004	0.142 ± 0.009	0.069 ± 0.009
0.65–0.75	0.854 ± 0.004	0.854 ± 0.004	0.194 ± 0.004	0.144 ± 0.009	0.063 ± 0.010
0.75–0.85	0.830 ± 0.004	0.833 ± 0.004	0.200 ± 0.004	0.136 ± 0.011	0.081 ± 0.011
0.85–0.95	0.788 ± 0.005	0.791 ± 0.005	0.215 ± 0.005	$0.159^{+0.012}_{-0.013}$	$0.079^{+0.013}_{-0.014}$

	normalization		χ^2/dof	
	Gauss	Voigt	Gauss	Voigt
joint	0.809 ± 0.006	$0.872^{+0.009}_{-0.011}$	1285.2/696 $= 1.85$	584.5/676 $= 0.86$

Table B.1: (continued)

(c) Fit results using only screened data and conventional histograms, see Fig. 2.15(c)

ϕ_{orb}	center		σ		γ
	Gauss	Voigt	Gauss	Voigt	
0.00–0.10	0.769 ± 0.005	0.766 ± 0.006	0.191 ± 0.005	0.148 ± 0.015	$0.066^{+0.015}_{-0.016}$
0.10–0.20	0.811 ± 0.005	0.821 ± 0.005	$0.171^{+0.005}_{-0.004}$	0.171 ± 0.009	$0.021^{+0.011}_{-0.012}$
0.20–0.30	0.822 ± 0.004	0.826 ± 0.005	0.166 ± 0.004	0.156 ± 0.010	$0.028^{+0.010}_{-0.011}$
0.30–0.40	0.830 ± 0.004	0.844 ± 0.004	0.159 ± 0.004	0.164 ± 0.009	0.012 ± 0.012
0.40–0.50	0.847 ± 0.004	0.850 ± 0.004	0.154 ± 0.004	0.152 ± 0.010	0.017 ± 0.012
0.50–0.60	0.842 ± 0.004	0.852 ± 0.005	0.160 ± 0.004	0.164 ± 0.009	$(1.0^{+1.2}_{-1.0}) \times 10^{-2}$
0.60–0.70	0.840 ± 0.004	0.851 ± 0.004	0.152 ± 0.004	0.155 ± 0.008	0.013 ± 0.011
0.70–0.80	0.834 ± 0.004	0.844 ± 0.004	0.155 ± 0.004	0.153 ± 0.009	$0.023^{+0.011}_{-0.012}$
0.80–0.90	0.803 ± 0.004	0.809 ± 0.004	0.163 ± 0.004	0.166 ± 0.009	0.014 ± 0.011
0.90–1.00	0.768 ± 0.005	0.779 ± 0.005	0.191 ± 0.005	$0.182^{+0.012}_{-0.013}$	0.035 ± 0.015
	normalization		χ^2/dof		
	Gauss	Voigt	Gauss	Voigt	
joint	$0.684^{+0.011}_{-0.010}$	0.778 ± 0.012	1917.4/652 $= 2.94$	1735.9/632 $= 2.75$	

ϕ_{orb}	center		σ		γ
	Gauss	Voigt	Gauss	Voigt	
-0.05–0.05	0.766 ± 0.005	$0.762^{+0.018}_{-0.006}$	0.198 ± 0.005	$0.16^{+0.04}_{-0.02}$	$0.06^{+0.02}_{-0.04}$
0.05–0.15	0.791 ± 0.005	$0.791^{+0.006}_{-0.005}$	0.181 ± 0.005	$0.163^{+0.013}_{-0.012}$	$0.038^{+0.012}_{-0.015}$
0.15–0.25	0.818 ± 0.004	0.827 ± 0.004	0.168 ± 0.004	0.170 ± 0.008	0.015 ± 0.010
0.25–0.35	0.830 ± 0.004	0.836 ± 0.005	0.165 ± 0.004	$0.171^{+0.008}_{-0.011}$	$(0.6^{+1.3}_{-0.6}) \times 10^{-2}$
0.35–0.45	0.839 ± 0.004	0.850 ± 0.004	0.155 ± 0.004	0.156 ± 0.009	$0.014^{+0.012}_{-0.013}$
0.45–0.55	0.845 ± 0.004	0.849 ± 0.004	0.154 ± 0.004	$0.162^{+0.005}_{-0.008}$	$(2^{+10}_{-2}) \times 10^{-3}$
0.55–0.65	0.841 ± 0.004	0.845 ± 0.004	0.155 ± 0.004	0.150 ± 0.009	0.019 ± 0.011
0.65–0.75	0.839 ± 0.004	0.848 ± 0.004	0.155 ± 0.004	$0.161^{+0.008}_{-0.009}$	$(0.7^{+1.2}_{-0.7}) \times 10^{-2}$
0.75–0.85	0.822 ± 0.004	0.827 ± 0.004	0.157 ± 0.004	0.150 ± 0.009	0.026 ± 0.011
0.85–0.95	0.781 ± 0.005	0.789 ± 0.005	$0.173^{+0.005}_{-0.004}$	0.174 ± 0.010	$0.018^{+0.012}_{-0.013}$
	normalization		χ^2/dof		
	Gauss	Voigt	Gauss	Voigt	
joint	0.684 ± 0.009	$0.764^{+0.014}_{-0.016}$	1876.6/650 $= 2.89$	1755.0/630 $= 2.79$	

Table B.1: (continued)

(d) Fit results using only screened data and histograms of probability distributions, see Fig. 2.15(d)

ϕ_{orb}	center		σ		γ
	Gauss	Voigt	Gauss	Voigt	
0.00–0.10	0.778 ± 0.006	$0.778^{+0.007}_{-0.006}$	0.199 ± 0.006	$0.158^{+0.016}_{-0.017}$	0.082 ± 0.017
0.10–0.20	0.817 ± 0.005	0.828 ± 0.005	0.179 ± 0.005	0.172 ± 0.011	0.048 ± 0.013
0.20–0.30	0.828 ± 0.005	0.842 ± 0.005	$0.174^{+0.005}_{-0.004}$	0.163 ± 0.010	$0.052^{+0.011}_{-0.012}$
0.30–0.40	0.834 ± 0.004	0.851 ± 0.004	0.167 ± 0.004	0.167 ± 0.009	0.035 ± 0.010
0.40–0.50	0.852 ± 0.004	$0.860^{+0.005}_{-0.004}$	0.162 ± 0.004	0.158 ± 0.008	0.033 ± 0.009
0.50–0.60	0.845 ± 0.004	0.860 ± 0.005	0.167 ± 0.004	0.165 ± 0.008	0.035 ± 0.009
0.60–0.70	0.844 ± 0.004	0.857 ± 0.004	0.161 ± 0.004	0.157 ± 0.008	0.037 ± 0.009
0.70–0.80	0.839 ± 0.004	0.851 ± 0.004	0.165 ± 0.004	0.159 ± 0.009	0.041 ± 0.009
0.80–0.90	$0.809^{+0.004}_{-0.005}$	0.815 ± 0.004	0.170 ± 0.004	0.162 ± 0.010	0.046 ± 0.011
0.90–1.00	0.776 ± 0.006	0.788 ± 0.005	0.197 ± 0.005	$0.189^{+0.013}_{-0.014}$	0.053 ± 0.016

	normalization		χ^2/dof	
	Gauss	Voigt	Gauss	Voigt
joint	0.660 ± 0.007	0.832 ± 0.009	991.2/679 $= 1.46$	635.4/659 $= 0.96$

ϕ_{orb}	center		σ		γ
	Gauss	Voigt	Gauss	Voigt	
-0.05–0.05	0.773 ± 0.006	0.786 ± 0.006	0.205 ± 0.006	$0.196^{+0.014}_{-0.015}$	0.054 ± 0.017
0.05–0.15	0.797 ± 0.005	0.810 ± 0.005	0.188 ± 0.005	0.178 ± 0.013	0.055 ± 0.015
0.15–0.25	0.824 ± 0.005	0.835 ± 0.005	$0.176^{+0.005}_{-0.004}$	$0.169^{+0.010}_{-0.011}$	0.047 ± 0.012
0.25–0.35	0.834 ± 0.005	$0.851^{+0.005}_{-0.004}$	0.172 ± 0.004	0.174 ± 0.009	0.034 ± 0.010
0.35–0.45	0.842 ± 0.004	0.858 ± 0.004	0.163 ± 0.004	0.158 ± 0.008	0.039 ± 0.009
0.45–0.55	0.849 ± 0.004	$0.858^{+0.007}_{-0.005}$	0.164 ± 0.004	$0.162^{+0.009}_{-0.008}$	$0.030^{+0.009}_{-0.010}$
0.55–0.65	0.845 ± 0.004	0.856 ± 0.005	0.164 ± 0.004	0.156 ± 0.008	0.040 ± 0.009
0.65–0.75	0.843 ± 0.004	0.855 ± 0.004	0.162 ± 0.004	0.159 ± 0.008	0.035 ± 0.009
0.75–0.85	0.827 ± 0.004	0.835 ± 0.004	0.165 ± 0.004	0.151 ± 0.010	0.053 ± 0.011
0.85–0.95	0.788 ± 0.005	0.796 ± 0.005	0.180 ± 0.005	0.173 ± 0.012	0.047 ± 0.014

	normalization		χ^2/dof	
	Gauss	Voigt	Gauss	Voigt
joint	$0.659^{+0.007}_{-0.008}$	$0.829^{+0.009}_{-0.010}$	966.5/677 $= 1.43$	663.2/657 $= 1.01$

Table B.2: Continuous segments from *RXTE* PCA observations of Cyg X-1 between 1996-02-12 and 2010-10-12

T_{RXTE} (s)	Date (Y-m-d, H:M)	ObsID	PCUs 0 1 2 3 4
— Calibration epoch 1 (starting with the *XTE* mission) —			
066707971	1996-02-12, 02:00	10240-01-01-000	+ + + + +
066712371	1996-02-12, 03:13	10240-01-01-000	+ + + + +
066718243	1996-02-12, 04:51	10240-01-01-000	+ + + + +
066724067	1996-02-12, 06:28	10240-01-01-000	+ + + + +
066729827	1996-02-12, 08:04	10240-01-01-000	+ + + + +
066735395	1996-02-12, 09:37	10240-01-01-00	+ + + + +
066746723	1996-02-12, 12:46	10235-01-01-00	+ + + + +
066996099	1996-02-15, 10:02	10235-01-02-00	+ + + + +
067000275	1996-02-15, 11:12	10235-01-02-00	+ + + + +
067138579	1996-02-17, 01:37	10235-01-03-00	+ + + + +
— Calibration epoch 2 (starting on 1996-03-21, 18:33) —			
070452963	1996-03-26, 10:17	10238-01-08-000	+ + + + +
070454259	1996-03-26, 10:38	10238-01-08-000	+ + + + +
070458723	1996-03-26, 11:53	10238-01-08-000	+ + + + +
070464483	1996-03-26, 13:29	10238-01-08-000	+ + + + +
070470243	1996-03-26, 15:05	10238-01-08-000	+ + + + +
070476003	1996-03-26, 16:41	10238-01-08-000	+ + + + +
070481763	1996-03-26, 18:17	10238-01-08-00	+ + + + +
070487523	1996-03-26, 19:53	10238-01-08-00	+ + + + +
070585539	1996-03-27, 23:06	10238-01-07-000	+ + + + +
070591715	1996-03-28, 00:49	10238-01-07-000	+ + + + +
070597603	1996-03-28, 02:27	10238-01-07-000	+ + + + +
070603715	1996-03-28, 04:09	10238-01-07-000	+ + + + +
070609651	1996-03-28, 05:48	10238-01-07-00	+ + + + +
070615411	1996-03-28, 07:24	10238-01-07-00	+ + + + +
070620067	1996-03-28, 08:42	10238-01-07-00	+ + + + +
070621171	1996-03-28, 09:00	10238-01-07-00	+ + + + +
070625827	1996-03-28, 10:18	10238-01-07-00	+ + + + +
070718051	1996-03-29, 11:55	10238-01-06-00	+ + + + +
070723795	1996-03-29, 13:30	10238-01-06-00	+ + + + +
070729555	1996-03-29, 15:06	10238-01-06-00	+ + + + +
070735315	1996-03-29, 16:42	10238-01-06-00	+ + + + +
070833283	1996-03-30, 19:55	10238-01-05-000	+ + + + +
070839043	1996-03-30, 21:31	10238-01-05-000	+ + + + +
070844915	1996-03-30, 23:09	10238-01-05-000	+ + + + +
070850867	1996-03-31, 00:48	10238-01-05-000	+ + + + +
070856979	1996-03-31, 02:30	10238-01-05-00	+ + + · ·
		10238-01-05-00	+ + + + +
070862915	1996-03-31, 04:09	10238-01-05-00	+ + + · ·
070868675	1996-03-31, 05:45	10238-01-05-00	+ + + · ·
071508675	1996-04-07, 15:32	10238-01-04-00	+ + + · ·
071513235	1996-04-07, 16:48	10238-01-04-00	+ + + · ·
071518995	1996-04-07, 18:24	10238-01-04-00	+ + + · ·
071524755	1996-04-07, 20:00	10238-01-04-00	+ + + · ·
071530531	1996-04-07, 21:36	10238-01-04-00	+ + + · ·
075405443	1996-05-22, 17:58	10412-01-02-00	+ + · + +
		10412-01-02-00	+ + + + +
— Calibration epoch 3 (starting on 1996-04-15, 23:05) —			
075409555	1996-05-22, 19:06	10412-01-02-00	+ + + + +
075479299	1996-05-23, 14:29	10412-01-01-00	+ + + + +
075484467	1996-05-23, 15:55	10412-01-01-00	+ + + + +
075490227	1996-05-23, 17:31	10412-01-01-00	+ + + + +
076060675	1996-05-30, 07:58	10412-01-03-00	+ + + + +
076538931	1996-06-04, 20:49	10512-01-05-00	+ + · + +
		10512-01-05-00	+ + + + +
076821267	1996-06-08, 03:15	10257-01-01-00	+ + + + +
077501299	1996-06-16, 00:09	10512-01-07-00	+ + + + +
077518595	1996-06-16, 04:57	10512-01-07-02	+ + + + +
077593539	1996-06-17, 01:46	10512-01-08-01	+ + + + +
077599299	1996-06-17, 03:22	10257-01-02-00	+ + + + +
077605075	1996-06-17, 04:58	10512-01-08-02	+ + + + +
077616595	1996-06-17, 08:10	10512-01-08-00	+ + + + +
077685795	1996-06-18, 03:24	10512-01-09-02	+ + + + +
077697331	1996-06-18, 06:36	10512-01-09-00	+ + + + +
077708867	1996-06-18, 09:48	10512-01-09-01	+ + + + +
078470099	1996-06-27, 05:15	10257-01-03-00	+ + + + +
079792291	1996-07-12, 12:32	10257-01-04-00	+ + + + +
082365779	1996-08-11, 07:23	10412-01-05-00	+ + + + +
082394707	1996-08-11, 15:26	10412-01-06-00	+ + + + +
082481107	1996-08-12, 15:26	10412-01-07-00	+ + + + +
084262291	1996-09-02, 06:12	10240-01-02-00	+ + + + +
084264067	1996-09-02, 06:42	10240-01-02-00	+ + + · ·
		10240-01-02-00	+ + + + ·
		10240-01-02-00	+ + + + +
084268051	1996-09-02, 07:48	10240-01-02-00	+ + + · ·
084273811	1996-09-02, 09:24	10240-01-02-00	+ + + · ·
084279571	1996-09-02, 11:00	10240-01-02-00	+ + + + +
084285347	1996-09-02, 12:36	10240-01-02-00	+ + + + +
088712979	1996-10-23, 18:30	10241-01-01-000	+ + + + +
088717363	1996-10-23, 19:43	10241-01-01-000	+ + + + +
088718675	1996-10-23, 20:05	10241-01-01-000	+ + + + +
088723123	1996-10-23, 21:19	10241-01-01-000	+ + + + +
088728899	1996-10-23, 22:55	10241-01-01-000	+ + + + +
088734659	1996-10-24, 00:31	10241-01-01-000	+ + + + +
088740419	1996-10-24, 02:07	10241-01-01-00	+ + + + +
		10241-01-01-000	+ + + + +
088746179	1996-10-24, 03:43	10241-01-01-00	+ + + · +
		10241-01-01-00	+ + + + +
093304899	1996-12-15, 22:02	10236-01-01-000	+ + + + +
093310659	1996-12-15, 23:38	10236-01-01-000	+ + + + +
093316419	1996-12-16, 01:14	10236-01-01-000	+ + + + +
093322179	1996-12-16, 02:50	10236-01-01-000	+ + + + +
093327939	1996-12-16, 04:26	10236-01-01-000	+ + + + +
093333747	1996-12-16, 06:03	10236-01-01-00	+ + + + +
093339923	1996-12-16, 07:46	10236-01-01-00	+ + + + +
093345859	1996-12-16, 09:25	10236-01-01-00	+ + + + +
093351987	1996-12-16, 11:07	10236-01-01-00	+ + + + +
093357923	1996-12-16, 12:46	10236-01-01-00	+ + + + +
093363715	1996-12-16, 14:22	10236-01-01-01	+ + + + +
093369475	1996-12-16, 15:58	10236-01-01-020	+ + + + +
093374035	1996-12-16, 17:14	10236-01-01-020	+ + + + ·
		10236-01-01-020	+ + + + +
093379795	1996-12-16, 18:50	10236-01-01-020	+ + + + ·
		10236-01-01-020	+ + + + +
093385555	1996-12-16, 20:26	10236-01-01-020	+ + + + +
093391315	1996-12-16, 22:02	10236-01-01-020	+ + + + +
093397091	1996-12-16, 23:39	10236-01-01-021	+ + + + +
093402851	1996-12-17, 01:15	10236-01-01-021	+ + + + +
093408611	1996-12-17, 02:51	10236-01-01-021	+ + + + +
093414371	1996-12-17, 04:27	10236-01-01-021	+ + + + +
093420211	1996-12-17, 06:04	10236-01-01-02	+ + + + +
093426387	1996-12-17, 07:47	10236-01-01-02	+ + + + +
093432323	1996-12-17, 09:26	10236-01-01-02	+ + + + +
093438323	1996-12-17, 11:06	10236-01-01-02	+ + + + +
093444291	1996-12-17, 12:45	10236-01-01-03	+ + + + +
093450051	1996-12-17, 14:21	10236-01-01-040	+ + + + +
093454707	1996-12-17, 15:39	10236-01-01-040	+ + + + +
093455779	1996-12-17, 15:57	10236-01-01-040	+ + + + +
093460467	1996-12-17, 17:15	10236-01-01-040	+ + + + +
093466227	1996-12-17, 18:51	10236-01-01-040	+ + + + +
093471987	1996-12-17, 20:27	10236-01-01-040	+ + + + +
093477747	1996-12-17, 22:03	10236-01-01-04	+ + + + +
		10236-01-01-040	+ + + + +
093483507	1996-12-17, 23:39	10236-01-01-04	+ + + + +
093552691	1996-12-18, 18:52	10240-01-03-00	+ + + + +
093558419	1996-12-18, 20:27	10240-01-03-00	+ + + + +
093564179	1996-12-18, 22:03	10240-01-03-00	+ + + + +
093569955	1996-12-18, 23:40	10240-01-03-00	+ + + + +
093575715	1996-12-19, 01:16	10240-01-03-00	+ + + + +
096077603	1997-01-17, 00:14	20173-01-01-00	+ + + + +
096082355	1997-01-17, 01:33	20173-01-01-00	+ + + + +
096088131	1997-01-17, 03:09	20173-01-01-00	+ + + + +
096093891	1997-01-17, 04:45	20173-01-01-00	+ + + + +
096099667	1997-01-17, 06:22	20173-01-01-00	+ + + + +
096336115	1997-01-20, 00:02	20173-01-02-00	+ + + + +
096341875	1997-01-20, 01:38	20173-01-02-00	+ + + + +
096347651	1997-01-20, 03:15	20173-01-02-00	+ + + + +
096353555	1997-01-20, 04:53	20173-01-02-00	+ + + + +
097531939	1997-02-02, 20:13	10239-01-01-00	+ + + + +
097535091	1997-02-02, 21:05	10239-01-01-00	+ + + + +
097540851	1997-02-02, 22:41	10239-01-01-00	+ + + + +
097546611	1997-02-03, 00:17	10239-01-01-00	+ + + + +
097615747	1997-02-03, 19:30	10238-01-03-00	+ + + + +
097621523	1997-02-03, 21:06	10238-01-03-00	+ + + + +
109857523	1997-06-25, 11:59	20175-01-01-00	+ + + + +
109861587	1997-06-25, 13:07	20175-01-01-00	+ + + + +
118583075	1997-10-04, 11:45	20175-01-02-00	+ + + + +
118586099	1997-10-04, 12:35	20175-01-02-00	+ + + + +
124355235	1997-12-10, 07:08	30158-01-01-00	+ + + · +
		30158-01-01-00	+ + + + +
124435459	1997-12-11, 05:25	30157-01-01-00	+ + + + ·
124441651	1997-12-11, 07:08	30158-01-02-00	+ + + + +
124707011	1997-12-14, 08:51	30158-01-03-00	+ + + + +
124775427	1997-12-15, 03:51	30158-01-04-00	+ + + + +
124781251	1997-12-15, 05:28	30158-01-05-00	+ + + + +
124936755	1997-12-17, 00:40	30158-01-06-00	+ + + + +
125046515	1997-12-18, 07:09	30157-01-02-00	+ + + + +
125219427	1997-12-20, 07:11	30158-01-07-00	+ + + + +
125299779	1997-12-21, 05:30	30158-01-08-00	+ + + + +
125616547	1997-12-24, 21:30	30157-01-03-00	+ + + + +
125622307	1997-12-24, 23:06	30158-01-09-00	+ + + + +
125628067	1997-12-25, 00:42	30158-01-10-00	+ + + + +
125934915	1997-12-28, 13:56	30161-01-01-000	+ + + + +
125939155	1997-12-28, 15:06	30161-01-01-000	+ + + + +
125944915	1997-12-28, 16:42	30161-01-01-000	+ + + + +
125950675	1997-12-28, 18:18	30161-01-01-000	+ + + + +
125956435	1997-12-28, 19:54	30161-01-01-000	+ + + + +
125962195	1997-12-28, 21:30	30161-01-01-00	+ + + + +
125967955	1997-12-28, 23:06	30161-01-01-00	+ + + + +
126065891	1997-12-30, 02:19	30158-01-11-00	+ + + + +
126071651	1997-12-30, 03:55	30158-01-12-00	+ + + + +
126123507	1997-12-30, 18:19	30157-01-04-00	+ + + + +
126319395	1998-01-02, 00:44	20175-01-03-00	+ + + + +
126325123	1998-01-02, 02:19	20175-01-03-00	+ + + + +
126330883	1998-01-02, 03:55	20175-01-03-00	+ + + + +
126852291	1998-01-08, 04:45	30157-01-05-00	+ + + + +
126855107	1998-01-08, 05:32	30157-01-05-00	+ + + + +
127523347	1998-01-15, 23:10	30157-01-06-00	+ + + + ·
		30157-01-06-00	+ + + + +
128135123	1998-01-23, 01:06	30157-01-07-00	+ + + + +
128740163	1998-01-30, 01:10	30157-01-08-00	+ + + + +
129339091	1998-02-05, 23:32	30157-01-09-00	+ + + + +
		30157-01-09-01	+ + + + +
130030259	1998-02-13, 23:31	30157-01-10-00	+ + + · +
		30157-01-10-00	+ + + + +
130635123	1998-02-20, 23:33	30157-01-11-00	+ + + + +
131251491	1998-02-28, 02:45	30157-01-12-00	+ + + + +
132173283	1998-03-10, 18:49	30157-01-13-00	+ + + + +
132691923	1998-03-16, 18:53	30157-01-14-00	+ + + + +
133314723	1998-03-23, 23:53	30157-01-15-00	+ + + + +
133753235	1998-03-29, 01:41	30157-01-16-00	+ + + + +
134426467	1998-04-05, 20:42	30157-01-17-00	+ + + + ·
		30157-01-17-00	+ + + + +
135054979	1998-04-13, 03:17	30157-01-18-00	+ + + + ·
135815107	1998-04-21, 22:26	30157-01-19-00	+ + + · +
136390627	1998-04-28, 14:18	30157-01-20-00	+ + + + ·
137031123	1998-05-06, 00:13	30157-01-21-00	+ + + + +
137612403	1998-05-12, 17:41	30157-01-22-00	+ + + + +
		30162-01-01-00	+ + + + +
137630675	1998-05-12, 22:45	30162-01-01-01	+ + + + +
138229555	1998-05-19, 21:06	30157-01-23-00	+ + + + +
138834275	1998-05-26, 21:05	30157-01-24-00	+ + + + +
138914627	1998-05-27, 19:24	30162-01-02-00	+ + + + +
138920691	1998-05-27, 21:05	30162-01-02-00	+ + + + +
138926691	1998-05-27, 22:45	30162-01-02-00	+ + + + +
139352627	1998-06-01, 21:04	30157-01-25-00	+ + + + +
139957235	1998-06-08, 21:01	30157-01-26-00	+ + + + ·
140648163	1998-06-16, 20:57	30157-01-27-00	+ + + + +
141569827	1998-06-27, 12:58	30157-01-28-00	+ + + + +
142007907	1998-07-02, 14:39	30157-01-29-00	+ + + + +
142625267	1998-07-09, 18:08	30157-01-30-00	+ + + + +
143149731	1998-07-15, 19:49	30157-01-31-00	+ + + + +
143569491	1998-07-20, 16:25	30157-01-32-00	+ + + + +
144358723	1998-07-29, 19:39	30157-01-33-00	+ + + + +
144968819	1998-08-05, 21:07	30157-01-34-00	+ + + + +
145550451	1998-08-12, 14:41	30157-01-35-00	+ + + + +
145977523	1998-08-17, 13:19	30157-01-36-00	+ + + + +
146761123	1998-08-26, 14:59	30157-01-37-00	+ + + + ·
147342979	1998-09-02, 08:37	30157-01-38-00	+ + + + +
147958867	1998-09-09, 11:42	30157-01-39-00	+ + + + +
148563523	1998-09-16, 11:39	30157-01-40-00	+ + + + +
149377923	1998-09-25, 21:53	30157-01-42-00	+ + + + ·
149381171	1998-09-25, 22:47	30157-01-42-00	+ + + + ·
150441587	1998-10-08, 05:20	30157-01-43-00	+ + + · ·
		30157-01-43-00	+ + + + +
150446515	1998-10-08, 06:42	30157-01-43-00	+ + + + +
150630851	1998-10-10, 09:55	30162-01-03-00	+ + + + +
150636611	1998-10-10, 11:31	30162-01-03-00	+ + + + +
150968595	1998-10-14, 07:44	30157-01-44-00	+ + + + ·
150970819	1998-10-14, 08:21	30157-01-44-00	+ + + + ·
151664323	1998-10-22, 08:59	30157-01-45-00	+ + + + +
151665267	1998-10-22, 09:15	30157-01-45-00	+ + + + +
152239123	1998-10-29, 00:39	30157-01-46-00	+ + + + +
152791443	1998-11-04, 10:05	30157-01-47-00	+ + + + +
153395987	1998-11-11, 10:00	30157-01-48-00	+ + + + +
153580243	1998-11-13, 13:11	30161-01-02-000	+ + + + +
153585939	1998-11-13, 14:46	30161-01-02-000	+ + + + +
153591411	1998-11-13, 16:17	30161-01-02-000	+ + + + +
153597171	1998-11-13, 17:53	30161-01-02-000	+ + + + +
153602931	1998-11-13, 19:29	30161-01-02-000	+ + + + +
153608691	1998-11-13, 21:05	30161-01-02-00	+ + + + +
		30161-01-02-000	+ + + + +
153614435	1998-11-13, 22:41	30161-01-02-01	+ + + + +
154190179	1998-11-20, 14:37	30157-01-49-01	+ + + + +
154691715	1998-11-26, 09:56	30157-01-50-00	+ + + + ·
155261203	1998-12-03, 00:07	30157-01-51-00	+ + + + +
155809299	1998-12-09, 08:22	30157-01-52-00	+ + + + +
156932291	1998-12-22, 08:19	30155-01-01-01	+ + + + +
156938387	1998-12-22, 10:00	30155-01-01-01	+ + + + +
156944387	1998-12-22, 11:40	30155-01-01-01	+ + + + +
156950307	1998-12-22, 13:19	30155-01-01-04	+ + + + +
156956291	1998-12-22, 14:59	30155-01-01-03	+ + + + +
156960435	1998-12-22, 16:08	30155-01-01-00	+ + + + +
156961987	1998-12-22, 16:34	30155-01-01-00	+ + + + +
156966195	1998-12-22, 17:44	30155-01-01-00	+ + + + +
156967731	1998-12-22, 18:09	30155-01-01-00	+ + + + +
156971955	1998-12-22, 19:20	30155-01-01-00	+ + + + ·
		30155-01-01-00	+ + + + +
156977715	1998-12-22, 20:56	30155-01-01-00	+ + + + ·
156983459	1998-12-22, 22:31	30155-01-01-00	+ + + + ·
		30155-01-01-00	+ + + + +
156989219	1998-12-23, 00:07	30155-01-01-020	+ + + + +
156994979	1998-12-23, 01:43	30155-01-01-020	+ + + + +
157000739	1998-12-23, 03:19	30155-01-01-020	+ + + + +
157006595	1998-12-23, 04:57	30155-01-01-020	+ + + + +
157012531	1998-12-23, 06:36	30155-01-01-02	+ + + + +
157018643	1998-12-23, 08:18	30155-01-01-02	+ + + + +
157173443	1998-12-25, 03:18	40100-01-01-00	+ + + + +
157179331	1998-12-25, 04:56	40100-01-01-00	+ + + + +
157185267	1998-12-25, 06:35	40100-01-01-00	+ + + + +
157254099	1998-12-26, 01:42	40100-01-02-00	+ + + + +
157259811	1998-12-26, 03:17	40100-01-02-00	+ + + + +
157265619	1998-12-26, 04:54	40100-01-02-00	+ + + + +
157340403	1998-12-27, 01:41	40100-01-03-00	+ + + + +
157346163	1998-12-27, 03:17	40100-01-03-00	+ + + + +
157351923	1998-12-27, 04:53	40100-01-03-00	+ + + + +
157426755	1998-12-28, 01:40	30155-01-02-00	+ + + + +
157432515	1998-12-28, 03:16	30155-01-02-00	+ + + + +
157438275	1998-12-28, 04:52	30155-01-02-00	+ + + + +
157444403	1998-12-28, 06:34	30155-01-02-00	+ + + + +
157450355	1998-12-28, 08:13	30161-01-03-00	+ + + + +
157456355	1998-12-28, 09:53	30161-01-03-00	+ + + + +
157462291	1998-12-28, 11:32	30161-01-03-00	+ + + + +

Table B.2: Continuous segments from *RXTE* PCA observations of Cyg X-1 between 1996-02-12 and 2010-10-12 (continued)

T_{RXTE} (s)	Date (Y-m-d, H:M)	ObsID	PCUs 0 1 2 3 4
157468067	1998-12-28, 13:08	30161-01-03-01	+ + + + +
157472819	1998-12-28, 14:27	30161-01-03-01	+ + + + +
157473827	1998-12-28, 14:44	30161-01-03-01	+ + + + +
157478579	1998-12-28, 16:03	30161-01-03-01	+ + + + +
157484339	1998-12-28, 17:39	30161-01-03-01	+ + + + +
157513123	1998-12-29, 01:39	40100-01-04-00	+ + + + +
157518883	1998-12-29, 03:15	40100-01-04-00	+ + + + +
157524659	1998-12-29, 04:51	40100-01-04-00	+ + + + +
157599475	1998-12-30, 01:38	40100-01-05-00	+ + + + +
157605219	1998-12-30, 03:14	40100-01-05-00	+ + + + +
157611027	1998-12-30, 04:51	40100-01-05-00	+ + + + +
157691587	1998-12-31, 03:14	40100-01-06-00	+ + + + +
157697443	1998-12-31, 04:51	40100-01-06-00	+ + + + +
157703379	1998-12-31, 06:30	40100-01-06-00	+ + + + +
158923475	1999-01-14, 09:25	40099-01-01-00	+ + + + +
158929235	1999-01-14, 11:01	40099-01-01-00	+ + + + +
158934995	1999-01-14, 12:37	40099-01-01-00	+ + + + +
160128771	1999-01-28, 08:13	40099-01-02-00	+ + + + +
160134947	1999-01-28, 09:56	40099-01-02-01	+ + + + ·
160140947	1999-01-28, 11:36	40099-01-02-02	+ + + + +
160147011	1999-01-28, 13:17	40099-01-02-04	+ + + + +
160152963	1999-01-28, 14:57	40099-01-02-03	+ + + + +
160155747	1999-01-28, 15:43	40099-01-02-03	+ + + + +
161319459	1999-02-11, 02:58	40099-01-03-00	+ + + + +
161325443	1999-02-11, 04:38	40099-01-03-00	+ + + + +
161331507	1999-02-11, 06:19	40099-01-03-00	+ + + + +
161337523	1999-02-11, 07:59	40099-01-03-01	+ + + + ·
162546067	1999-02-25, 07:42	40099-01-04-00	+ + + + +
162551379	1999-02-25, 09:10	40099-01-04-00	+ + + + +
162556675	1999-02-25, 10:38	40099-01-04-00	+ + + + +
164001315	1999-03-14, 03:56	40099-01-05-00	+ · + + +
164007059	1999-03-14, 05:31	40099-01-05-01	+ · + + ·
164012835	1999-03-14, 07:08	40099-01-05-02	+ · + + +
164018579	1999-03-14, 08:43	40099-01-05-03	+ · + + +
164021603	1999-03-14, 09:34	40099-01-05-03	+ · + + +
— Calibration epoch 4 (starting on 1999-03-22, 17:37) —			
165113251	1999-03-27, 00:48	40099-01-06-00	+ · + + +
165119667	1999-03-27, 02:35	40099-01-06-00	+ · + + +
165125795	1999-03-27, 04:17	40099-01-06-01	+ · + · ·
165131731	1999-03-27, 05:56	40099-01-06-02	+ · + + ·
166426451	1999-04-11, 05:35	40099-01-07-00	+ + + + +
166432211	1999-04-11, 07:11	40099-01-07-01	+ · + + ·
166436771	1999-04-11, 08:27	40099-01-07-01	+ · + + ·
166437939	1999-04-11, 08:46	40099-01-07-01	+ · + + ·
166442515	1999-04-11, 10:02	40099-01-07-01	+ + + · +
167617043	1999-04-25, 00:18	40099-01-08-00	+ · + + +
167622243	1999-04-25, 01:45	40099-01-08-00	+ · + + +
167628003	1999-04-25, 03:21	40099-01-08-00	+ · + + +
167639539	1999-04-25, 06:33	40417-01-01-00	+ + + + ·
167645267	1999-04-25, 08:08	40417-01-01-00	+ + + + ·
168571763	1999-05-06, 01:30	40099-01-09-00	+ · + · ·
168577507	1999-05-06, 03:06	40099-01-09-00	+ · + · ·
168579811	1999-05-06, 03:44	40099-01-09-00	+ · + · ·
168583267	1999-05-06, 04:42	40099-01-09-00	+ · + · ·
168586163	1999-05-06, 05:30	40099-01-09-00	+ · + · ·
169862867	1999-05-21, 00:08	40099-01-10-01	+ + + + ·
169868739	1999-05-21, 01:46	40099-01-10-03	+ + + + ·
169874915	1999-05-21, 03:29	40099-01-10-02	+ + + + ·
169880851	1999-05-21, 05:08	40099-01-10-00	+ · + + +
171157251	1999-06-04, 23:41	40099-01-11-00	+ · + + ·
171163187	1999-06-05, 01:20	40099-01-11-02	+ · + + ·
171175043	1999-06-05, 04:38	40099-01-11-01	+ · + + +
171179443	1999-06-05, 05:51	40099-01-11-01	+ · + + +
171773619	1999-06-12, 02:54	40417-01-02-00	+ · + · ·
171779379	1999-06-12, 04:30	40417-01-02-01	+ · + · ·
171785139	1999-06-12, 06:06	40417-01-02-02	+ · + · ·
171790179	1999-06-12, 07:30	40417-01-02-03	+ · + · ·
171859971	1999-06-13, 02:53	40417-01-03-00	+ · + · ·
171872675	1999-06-13, 06:25	40417-01-03-02	+ · + · ·
171876595	1999-06-13, 07:30	40417-01-03-03	+ · + · ·

T_{RXTE} (s)	Date (Y-m-d, H:M)	ObsID	PCUs 0 1 2 3 4
172709907	1999-06-22, 22:59	40099-01-12-00	+ · + + ·
172715667	1999-06-23, 00:35	40099-01-12-00	+ · + · +
173828259	1999-07-05, 21:38	40099-01-13-00	+ · + + ·
173834403	1999-07-05, 23:21	40099-01-13-01	+ · + + ·
173840371	1999-07-06, 01:00	40099-01-13-03	+ · + + ·
173843811	1999-07-06, 01:57	40099-01-13-02	+ · + + ·
173846451	1999-07-06, 02:41	40099-01-13-02	+ · + + ·
173849539	1999-07-06, 03:33	40099-01-13-02	+ · + + ·
173852451	1999-07-06, 04:21	40099-01-13-02	+ · + + ·
173855299	1999-07-06, 05:09	40099-01-13-02	+ · + + ·
175036403	1999-07-19, 21:14	40099-01-14-00	+ · + + ·
175042531	1999-07-19, 22:56	40099-01-14-01	+ · + + ·
175048355	1999-07-20, 00:33	40099-01-14-02	+ · + + ·
175054291	1999-07-20, 02:12	40099-01-14-03	+ · + + ·
175985283	1999-07-30, 20:49	40099-01-15-00	+ · + + ·
175991075	1999-07-30, 22:25	40099-01-15-00	+ · + + ·
175996035	1999-07-30, 23:48	40099-01-15-00	+ · + + ·
176001795	1999-07-31, 01:24	40099-01-15-00	+ · + + ·
176324355	1999-08-03, 19:00	30161-01-04-00	+ · + + ·
176330003	1999-08-03, 20:34	30161-01-04-00	+ · + + ·
176335587	1999-08-03, 22:07	30161-01-04-00	+ · + + ·
176341203	1999-08-03, 23:41	30161-01-04-00	+ · + + ·
176346963	1999-08-04, 01:17	30161-01-04-00	+ · + + ·
177445667	1999-08-16, 18:28	40099-01-16-00	+ · + + ·
177451427	1999-08-16, 20:04	40099-01-16-00	+ · + + ·
178569763	1999-08-29, 18:43	40099-01-17-00	+ · + + ·
178575763	1999-08-29, 20:23	40099-01-17-02	+ · + + ·
178581763	1999-08-29, 22:03	40099-01-17-01	+ · + + ·
178585251	1999-08-29, 23:01	40099-01-17-01	+ · + + ·
178587827	1999-08-29, 23:44	40099-01-17-01	+ · + + ·
178591011	1999-08-30, 00:37	40099-01-17-01	+ · + + ·
179863907	1999-09-13, 18:12	40099-01-18-00	+ · + + ·
179869763	1999-09-13, 19:50	40099-01-18-01	+ · + + ·
179875603	1999-09-13, 21:27	40099-01-18-02	+ · + + ·
180892531	1999-09-25, 15:56	40099-01-19-00	+ · + · +
180898355	1999-09-25, 17:33	40099-01-19-01	+ · + · +
180903699	1999-09-25, 19:02	40099-01-19-01	+ · + · +
181064995	1999-09-27, 15:50	40101-01-01-00	+ · + + ·
181335043	1999-09-30, 18:51	40101-01-14-00	+ · + · +
		40101-01-14-00	+ + + · +
181450083	1999-10-02, 02:49	40101-01-02-00G	+ · + + +
		40101-01-02-00G	+ + + + +
181490339	1999-10-02, 13:59	40101-01-03-00	+ · + + ·
181530579	1999-10-03, 01:10	40101-01-04-00	+ · + + ·
181599603	1999-10-03, 20:21	40101-01-05-00	+ · + + ·
181639859	1999-10-04, 07:31	40101-01-06-00	+ + + + +
181685875	1999-10-04, 20:18	40101-01-07-00	+ · + · +
181726131	1999-10-05, 07:29	40101-01-08-00	+ + + + +
181766371	1999-10-05, 18:40	40101-01-09-00	+ · + + ·
181768947	1999-10-05, 19:23	40101-01-09-00	+ · + + ·
181812387	1999-10-06, 07:27	40101-01-10-00	+ + + + +
181855283	1999-10-06, 19:22	40101-01-11-00	+ · + + ·
181898659	1999-10-07, 07:25	40101-01-12-00	+ + + + +
181941571	1999-10-07, 19:20	40101-01-13-00	+ · + + ·
181987587	1999-10-08, 08:07	40101-01-15-00	+ + + + +
182028099	1999-10-08, 19:22	40101-01-20-00	+ + + + +
182079635	1999-10-09, 09:41	40101-01-16-00	+ + + + +
182114387	1999-10-09, 19:20	40101-01-17-00	+ + + · +
182182819	1999-10-10, 14:21	40101-01-19-00	+ · + + ·
182200707	1999-10-10, 19:19	40101-01-18-00	+ · + + ·
182358803	1999-10-12, 15:14	40099-01-20-00	+ + + · +
182360547	1999-10-12, 15:43	40099-01-20-00	+ + + · +
182367155	1999-10-12, 17:33	40099-01-20-01	+ · + + ·
182370307	1999-10-12, 18:26	40099-01-20-01	+ · + + ·
182373283	1999-10-12, 19:15	40099-01-20-01	+ · + + ·
182744771	1999-10-17, 02:27	40100-01-07-01	+ + + + +
182755907	1999-10-17, 05:32	40100-01-07-02	+ + + + +
182767347	1999-10-17, 08:43	40100-01-07-00	+ · + + ·
182872483	1999-10-18, 13:55	40100-01-08-01	+ · + · +
182983123	1999-10-19, 20:39	40100-01-08-00	+ + + + +
182986083	1999-10-19, 21:29	40100-01-08-00	+ + + + +
182989123	1999-10-19, 22:19	40100-01-08-00	+ · + + +
		40100-01-08-00	+ + + + +

T_{RXTE} (s)	Date (Y-m-d, H:M)	ObsID	PCUs 0 1 2 3 4
182991827	1999-10-19, 23:04	40100-01-08-00	+ · + + +
183075443	1999-10-20, 22:18	40100-01-08-03	+ + + + +
183083923	1999-10-21, 00:39	40100-01-08-05	+ · + · ·
183089683	1999-10-21, 02:15	40100-01-09-01	+ + + · +
183112707	1999-10-21, 08:39	40100-01-09-02	+ · + + ·
183118467	1999-10-21, 10:15	40100-01-09-00	+ · + + ·
183131539	1999-10-21, 13:53	40100-01-09-03	+ · + · +
		40100-01-09-03	+ · + + +
183379155	1999-10-24, 10:40	40100-01-10-00	+ · + + ·
183384099	1999-10-24, 12:02	40100-01-10-00	+ · + + ·
183390211	1999-10-24, 13:44	40099-01-21-03	+ · + + ·
183396227	1999-10-24, 15:24	40099-01-21-00	+ · + + ·
183402275	1999-10-24, 17:05	40099-01-21-01	+ · + + ·
183408291	1999-10-24, 18:45	40099-01-21-02	+ · + + ·
183414387	1999-10-24, 20:27	40099-01-21-04	+ · + + ·
183420211	1999-10-24, 22:04	40100-01-09-04	+ · + + ·
183713059	1999-10-28, 07:25	40100-01-11-00	+ · + + ·
183716883	1999-10-28, 08:29	40100-01-11-00	+ · + + ·
183725139	1999-10-28, 10:46	40100-01-11-01	+ · + + ·
183729219	1999-10-28, 11:54	40100-01-11-01	+ · + + ·
183735171	1999-10-28, 13:33	40100-01-11-01	+ · + + ·
184689827	1999-11-08, 14:44	40099-01-22-00	+ · + + ·
184695619	1999-11-08, 16:21	40099-01-22-01	+ · + · +
184701395	1999-11-08, 17:57	40099-01-22-02	+ + + · ·
184707171	1999-11-08, 19:33	40099-01-22-03	+ + + + +
185982835	1999-11-23, 13:54	40099-01-23-00	+ + + + +
185988339	1999-11-23, 15:26	40099-01-23-01	+ + + + +
185993955	1999-11-23, 17:00	40099-01-23-01	+ · + + ·
185999699	1999-11-23, 18:35	40099-01-23-02	+ · + + ·
186005459	1999-11-23, 20:11	40100-01-12-00	+ · + + ·
186011331	1999-11-23, 21:49	40100-01-12-01	+ · + + ·
186017091	1999-11-23, 23:25	40100-01-12-02	+ · + + ·
186028451	1999-11-24, 02:35	40100-01-12-03	+ · + + ·
186034195	1999-11-24, 04:10	40100-01-12-03	+ · + · ·
186085939	1999-11-24, 18:33	40100-01-13-00	+ · + + +
186091699	1999-11-24, 20:09	40100-01-13-01	+ · + + +
186097603	1999-11-24, 21:47	40100-01-13-02	+ · + + +
186103299	1999-11-24, 23:22	40100-01-13-03	+ · + + +
186109123	1999-11-25, 00:59	40100-01-13-04	+ · + + +
186166419	1999-11-25, 16:54	40100-01-14-00	+ · + + ·
186172163	1999-11-25, 18:30	40100-01-14-01	+ · + + ·
186177923	1999-11-25, 20:06	40100-01-14-02	+ · + + ·
186183667	1999-11-25, 21:42	40100-01-14-03	+ · + + ·
186189587	1999-11-25, 23:20	40100-01-14-04	+ · + + ·
186252659	1999-11-26, 16:51	40100-01-15-00	+ + + + ·
186258403	1999-11-26, 18:27	40100-01-15-01	+ + + + ·
186264163	1999-11-26, 20:03	40100-01-15-02	+ · + + +
186269971	1999-11-26, 21:40	40100-01-15-03	+ · + + +
186275651	1999-11-26, 23:15	40100-01-15-04	+ + + + +
186333155	1999-11-27, 15:13	40100-01-16-04	+ · + + ·
186338883	1999-11-27, 16:49	40100-01-16-00	+ · + + ·
186344643	1999-11-27, 18:25	40100-01-16-01	+ · + + ·
186350403	1999-11-27, 20:01	40100-01-16-02	+ · + + ·
186356259	1999-11-27, 21:38	40100-01-16-03	+ · + + ·
186425123	1999-11-28, 16:46	40100-01-17-00	+ · + + +
186430883	1999-11-28, 18:22	40100-01-17-01	+ · + + +
186436627	1999-11-28, 19:58	40100-01-17-02	+ + + + ·
186442371	1999-11-28, 21:33	40100-01-17-03	+ + + + ·
186448243	1999-11-28, 23:11	40100-01-17-04	+ + + + ·
186511363	1999-11-29, 16:43	40100-01-18-00	+ · + + +
186517123	1999-11-29, 18:19	40100-01-18-01	+ · + + +
186522867	1999-11-29, 19:55	40100-01-18-02	+ · + + +
186528611	1999-11-29, 21:31	40100-01-18-03	+ + + + ·
186534515	1999-11-29, 23:09	40100-01-18-04	+ · + + +
187011603	1999-12-05, 11:41	40099-01-24-00	+ + + + +
187013491	1999-12-05, 12:12	40099-01-24-00	+ + + + +
187017507	1999-12-05, 13:19	40099-01-23-03	+ + + + +
187019907	1999-12-05, 13:59	40099-01-23-03	+ + + + +
187028979	1999-12-05, 16:30	40099-01-23-04	+ · + + ·
187034627	1999-12-05, 18:04	40099-01-24-01	+ · + + ·
188048515	1999-12-17, 11:42	40099-01-25-00	+ · + · ·
188054691	1999-12-17, 13:25	40099-01-20-02	+ · + · ·
188060563	1999-12-17, 15:03	40099-01-20-03	+ · + · ·

T_{RXTE} (s)	Date (Y-m-d, H:M)	ObsID	PCUs 0 1 2 3 4
188070163	1999-12-17, 17:43	40099-01-19-02	+ · + · ·
189202691	1999-12-30, 20:19	40100-01-19-00	+ · + + ·
189208451	1999-12-30, 21:55	40100-01-19-00	+ · + + ·
189214195	1999-12-30, 23:30	40100-01-19-00	+ · + + ·
		40100-01-19-01	+ · + + +
189255395	1999-12-31, 10:57	40099-01-26-02	+ · + · ·
189261283	1999-12-31, 12:35	40099-01-26-00	+ · + + ·
189265923	1999-12-31, 13:53	40099-01-26-00	+ · + · ·
189267107	1999-12-31, 14:12	40099-01-26-00	+ · + + ·
189273667	1999-12-31, 16:02	40099-01-26-01	+ · + + ·
189651043	2000-01-05, 00:51	40102-01-02-00	+ · + + ·
189656787	2000-01-05, 02:27	40102-01-02-00	+ · + + ·
189662531	2000-01-05, 04:03	40102-01-02-00	+ · + + ·
189668451	2000-01-05, 05:41	40102-01-02-00	+ · + + ·
189674499	2000-01-05, 07:22	40102-01-02-00	+ · + + ·
189680451	2000-01-05, 09:01	40102-01-02-04	+ · + · +
189686147	2000-01-05, 10:36	40102-01-02-05	+ · + · +
189691907	2000-01-05, 12:12	40102-01-02-01	+ · + + ·
189697011	2000-01-05, 13:37	40102-01-02-01	+ · + + ·
189702771	2000-01-05, 15:13	40102-01-02-01	+ · + + ·
189708515	2000-01-05, 16:49	40102-01-02-01	+ · + + ·
189716019	2000-01-05, 18:54	40102-01-02-06	+ · + · ·
189720003	2000-01-05, 20:01	40102-01-02-020	+ + + · +
189725763	2000-01-05, 21:37	40102-01-02-020	+ + + + +
189731507	2000-01-05, 23:12	40102-01-02-020	+ · + + ·
189737251	2000-01-06, 00:48	40102-01-02-020	+ · + + ·
189742995	2000-01-06, 02:24	40102-01-02-020	+ · + + ·
189748739	2000-01-06, 03:59	40102-01-02-02	+ · + + ·
189754643	2000-01-06, 05:38	40102-01-02-02	+ · + + ·
189760595	2000-01-06, 07:17	40102-01-02-02	+ · + + ·
189772771	2000-01-06, 10:40	40102-01-02-08	+ · + · +
189779571	2000-01-06, 12:33	40102-01-02-03	+ · + + ·
189783235	2000-01-06, 13:34	40102-01-02-03	+ · + + ·
189788979	2000-01-06, 15:10	40102-01-02-03	+ · + + ·
189794723	2000-01-06, 16:46	40102-01-02-03	+ · + + ·
189800467	2000-01-06, 18:22	40102-01-02-03	+ · + + ·
189806435	2000-01-06, 20:01	40102-01-02-09	+ · + · +
189811971	2000-01-06, 21:33	40102-01-02-10	+ · + · +
189823523	2000-01-07, 00:46	40102-01-01-00	+ · + + ·
189829219	2000-01-07, 02:21	40102-01-01-00	+ · + + ·
189834963	2000-01-07, 03:57	40102-01-01-00	+ · + + ·
189840963	2000-01-07, 05:37	40102-01-01-00	+ · + + ·
189846755	2000-01-07, 07:13	40102-01-01-00	+ · + + ·
189852691	2000-01-07, 08:52	40102-01-01-23	+ · + + ·
189858483	2000-01-07, 10:29	40102-01-01-05	+ · + · +
189864147	2000-01-07, 12:03	40102-01-01-15	+ + + · ·
189869907	2000-01-07, 13:39	40102-01-01-01	+ · + · +
189875491	2000-01-07, 15:12	40102-01-01-24	+ + + · ·
189881347	2000-01-07, 16:50	40102-01-01-08	+ · + · +
189886707	2000-01-07, 18:19	40102-01-01-09	+ + + · ·
189899123	2000-01-07, 21:46	40102-01-01-11	+ · + + ·
189904243	2000-01-07, 23:11	40102-01-01-020	+ · + + ·
189909683	2000-01-08, 00:42	40102-01-01-020	+ · + + ·
189915427	2000-01-08, 02:18	40102-01-01-020	+ · + + ·
189921187	2000-01-08, 03:54	40102-01-01-020	+ · + + ·
189927091	2000-01-08, 05:32	40102-01-01-020	+ · + + ·
189933027	2000-01-08, 07:11	40102-01-01-02	+ · + + ·
189938787	2000-01-08, 08:47	40102-01-01-02	+ · + + ·
189944547	2000-01-08, 10:23	40102-01-01-17	+ · + + ·
189950083	2000-01-08, 11:55	40102-01-01-16	+ + + + +
189955667	2000-01-08, 13:28	40102-01-01-16	+ + + + +
189961411	2000-01-08, 15:04	40102-01-01-16	+ + + + +
189979075	2000-01-08, 19:58	40102-01-01-18	+ · + + ·
189984403	2000-01-08, 21:27	40102-01-01-030	+ · + + ·
189990147	2000-01-08, 23:03	40102-01-01-030	+ · + + ·
189995907	2000-01-09, 00:39	40102-01-01-030	+ · + + ·
190001651	2000-01-09, 02:15	40102-01-01-030	+ · + + ·
190007395	2000-01-09, 03:50	40102-01-01-030	+ · + + ·
190013251	2000-01-09, 05:28	40102-01-01-03	+ · + + ·
190019187	2000-01-09, 07:07	40102-01-01-03	+ · + + ·
190024947	2000-01-09, 08:43	40102-01-01-19	+ · + · +
190030659	2000-01-09, 10:18	40102-01-01-13	+ + + · ·
190037283	2000-01-09, 12:09	40102-01-01-12	+ · + · +

Table B.2: Continuous segments from *RXTE* PCA observations of Cyg X-1 between 1996-02-12 and 2010-10-12 (continued)

T_{RXTE} (s)	Date (Y-m-d, H:M)	ObsID	PCUs 0 1 2 3 4
190041875	2000-01-09, 13:25	40102-01-01-12	+ + + · ·
190047619	2000-01-09, 15:01	40102-01-01-12	+ · + · +
190053379	2000-01-09, 16:37	40102-01-01-12	+ + + · ·
190065155	2000-01-09, 19:53	40102-01-01-20	+ · + + ·
190070627	2000-01-09, 21:24	40102-01-01-040	+ · + + ·
190076371	2000-01-09, 23:00	40102-01-01-040	+ · + + ·
190082115	2000-01-10, 00:36	40102-01-01-040	+ · + + ·
190087859	2000-01-10, 02:11	40102-01-01-040	+ · + + ·
190093603	2000-01-10, 03:47	40102-01-01-040	+ · + + ·
190099347	2000-01-10, 05:23	40102-01-01-04	+ · + + ·
190105283	2000-01-10, 07:02	40102-01-01-04	+ · + + ·
190111075	2000-01-10, 08:38	40102-01-01-25	+ · + + ·
190116803	2000-01-10, 10:14	40102-01-01-21	+ · + · +
190122339	2000-01-10, 11:46	40102-01-01-21	+ · + · ·
190128099	2000-01-10, 13:22	40102-01-01-21	+ + + · +
190136723	2000-01-10, 15:46	40102-01-01-27	+ · + · ·
190139587	2000-01-10, 16:34	40102-01-01-27	+ · + · +
190151363	2000-01-10, 19:50	40102-01-01-26	+ · + + ·
190156835	2000-01-10, 21:21	40102-01-01-22	+ · + + ·
190162579	2000-01-10, 22:57	40102-01-01-22	+ · + + ·
190168339	2000-01-11, 00:33	40102-01-01-22	+ · + + ·
190174083	2000-01-11, 02:09	40102-01-01-22	+ · + + ·
191197187	2000-01-22, 22:20	40100-01-20-00	+ · + + ·
191202851	2000-01-22, 23:55	40100-01-20-00	+ · + + ·
191208611	2000-01-23, 01:31	40100-01-20-00	+ · + + ·
191750755	2000-01-29, 08:06	40099-01-28-00	+ · + + ·
191757171	2000-01-29, 09:53	40099-01-28-01	+ · + + ·
191763283	2000-01-29, 11:35	40099-01-28-02	+ · + + ·
191772035	2000-01-29, 14:01	40099-01-28-03	+ · + + ·
192082915	2000-02-02, 04:22	40100-01-21-00	+ · + · ·
192089507	2000-02-02, 06:12	40100-01-21-01	+ · + · ·
192095907	2000-02-02, 07:59	40100-01-21-02	+ · + · ·
192102035	2000-02-02, 09:41	40100-01-21-03	+ · + · ·
192877731	2000-02-11, 09:09	50110-01-28-01	+ · + · +
192883715	2000-02-11, 10:49	50110-01-28-02	+ · + · +
192889619	2000-02-11, 12:27	50110-01-28-03	+ · + + ·
192895635	2000-02-11, 14:08	50110-01-28-00	+ · + + ·
194164243	2000-02-26, 06:31	50110-01-27-00	+ · + + ·
194169971	2000-02-26, 08:07	50110-01-27-01	+ · + + ·
194175859	2000-02-26, 09:45	50110-01-27-02	+ · + + ·
195370115	2000-03-11, 05:29	50110-01-01-00G	+ · + · +
195373379	2000-03-11, 06:23	50110-01-01-00G	+ · + · +
195375859	2000-03-11, 07:05	50110-01-01-00G	+ + + · ·
195381603	2000-03-11, 08:41	50110-01-01-00G	+ · + · +
195384291	2000-03-11, 09:25	50110-01-01-00G	+ · + · +
195387347	2000-03-11, 10:16	50110-01-01-00G	+ + + · ·
195393091	2000-03-11, 11:52	50110-01-01-01	+ · + · +
196665155	2000-03-26, 05:13	50110-01-02-00	+ · + + ·
196671203	2000-03-26, 06:54	50110-01-02-01	+ · + + ·
196677203	2000-03-26, 08:34	50110-01-02-02	+ · + + ·
196683251	2000-03-26, 10:15	50110-01-02-03	+ · + + ·
197779091	2000-04-08, 02:39	50110-01-03-00	+ · + + ·
197785011	2000-04-08, 04:17	50110-01-03-01	+ · + + ·
197791091	2000-04-08, 05:59	50110-01-03-02	· · + + ·
197797027	2000-04-08, 07:38	50110-01-03-03	· · + + ·
197801075	2000-04-08, 08:45	50110-01-03-03	· · + + ·
197802739	2000-04-08, 09:13	50110-01-03-03	· · + + ·
198904227	2000-04-21, 03:11	50110-01-04-02	+ · + + ·
198910003	2000-04-21, 04:47	50110-01-04-00	+ · + + ·
198915251	2000-04-21, 06:15	50110-01-04-00	+ · + + ·
198921539	2000-04-21, 07:59	50110-01-04-01	+ · + + ·
198926739	2000-04-21, 09:26	50110-01-04-01	+ · + + ·
200192307	2000-05-06, 00:59	50110-01-05-00	+ · + + ·
200195747	2000-05-06, 01:56	50110-01-05-00	+ · + + ·
200203827	2000-05-06, 04:11	50110-01-05-01	+ · + + ·
200207235	2000-05-06, 05:08	50110-01-05-02	+ · + + ·
200210243	2000-05-06, 05:58	50110-01-05-02	+ · + · ·
200213395	2000-05-06, 06:50	50110-01-05-03	+ · + + ·
200218707	2000-05-06, 08:19	50110-01-05-04	+ · + + ·

T_{RXTE} (s)	Date (Y-m-d, H:M)	ObsID	PCUs 0 1 2 3 4
— Calibration epoch 5 (starting on 2000-05-13, 00:00) —			
201397763	2000-05-19, 23:50	50110-01-06-00	· · + + ·
201403891	2000-05-20, 01:32	50110-01-06-00	+ · + + ·
201409779	2000-05-20, 03:10	50110-01-06-01	· · + + ·
201415955	2000-05-20, 04:53	50110-01-06-02	· · + + ·
201421827	2000-05-20, 06:31	50110-01-06-03	· · + + ·
202524131	2000-06-02, 00:43	50110-01-07-00	+ · + + ·
202529027	2000-06-02, 02:04	50110-01-07-01	+ · + + ·
202534947	2000-06-02, 03:43	50110-01-07-02	+ · + + ·
202540723	2000-06-02, 05:19	50110-01-07-03	+ + + + +
203813795	2000-06-16, 22:57	50110-01-08-00	+ · + + +
203819411	2000-06-17, 00:31	50110-01-08-00	+ · + + +
203826371	2000-06-17, 02:27	50110-01-08-01	+ · + + +
203830899	2000-06-17, 03:42	50110-01-08-01	+ + + + ·
203836643	2000-06-17, 05:18	50110-01-08-02	+ · + + +
205279331	2000-07-03, 22:03	50110-01-09-00	+ · + + +
205283251	2000-07-03, 23:08	50110-01-09-01	+ · + + +
205285651	2000-07-03, 23:48	50110-01-09-01	+ · + + +
205291795	2000-07-04, 01:30	50110-01-09-02	+ + + + +
205294739	2000-07-04, 02:19	50110-01-09-02	+ · + + +
205297731	2000-07-04, 03:09	50110-01-09-02	+ · + + +
205300867	2000-07-04, 04:02	50110-01-09-03	+ · + + +
206226595	2000-07-14, 21:10	50110-01-10-00	+ · + · ·
206232595	2000-07-14, 22:50	50110-01-10-02	+ · + · ·
206238595	2000-07-15, 00:30	50110-01-03-04	+ + + + +
206244643	2000-07-15, 02:11	50110-01-10-01	+ · + + ·
206250467	2000-07-15, 03:48	50110-01-10-03	+ · + + ·
207431507	2000-07-28, 19:52	50110-01-11-00	+ · + + +
207437427	2000-07-28, 21:31	50110-01-11-00	+ · + + +
207443155	2000-07-28, 23:06	50110-01-11-01	+ · + + +
207448915	2000-07-29, 00:42	50110-01-11-02	+ · + + +
207453587	2000-07-29, 02:00	50110-01-11-03	+ · + + +
208635683	2000-08-11, 18:22	50110-01-12-00	+ + + + ·
208641411	2000-08-11, 19:57	50110-01-12-00 50110-01-12-00	+ · + · + + · + + +
208647155	2000-08-11, 21:33	50110-01-12-00	+ + + · ·
208652899	2000-08-11, 23:09	50110-01-12-00	+ · + · +
210020867	2000-08-27, 19:08	50110-01-13-00	+ · + + +
210026979	2000-08-27, 20:50	50110-01-13-01	+ · + + +
210032867	2000-08-27, 22:28	50110-01-13-02	+ · + + +
210041747	2000-08-28, 00:56	50110-01-13-03	+ · + + +
211047267	2000-09-08, 16:15	50110-01-14-00F	+ · + · +
211053395	2000-09-08, 17:57	50110-01-14-00F	+ · + · +
211059331	2000-09-08, 19:36	50110-01-14-01F	+ · + · +
211065507	2000-09-08, 21:19	50110-01-14-02F	+ · + · ·
211071283	2000-09-08, 22:55	50110-01-14-03F	+ · + + ·
211077155	2000-09-09, 00:33	50110-01-14-04F	+ · + + ·
212343635	2000-09-23, 16:21	50110-01-15-02	+ · + + ·
212349379	2000-09-23, 17:57	50110-01-15-00	+ · + + ·
212355107	2000-09-23, 19:32	50110-01-15-00	+ · + + ·
212362467	2000-09-23, 21:35	50110-01-15-01	+ · + + ·
212365939	2000-09-23, 22:33	50110-01-15-01	+ · + + +
213719603	2000-10-09, 14:34	50110-01-16-00	+ + + + +
213725347	2000-10-09, 16:10	50110-01-16-00	+ + + + ·
213731571	2000-10-09, 17:53	50110-01-16-01	+ · + · ·
213733523	2000-10-09, 18:26	50110-01-16-01	+ · + · ·
213736803	2000-10-09, 19:21	50110-01-16-02	+ · + · ·
213742739	2000-10-09, 20:59	50110-01-16-03	+ · + + ·
214667923	2000-10-20, 13:59	50110-01-17-00	+ + + + ·
214674083	2000-10-20, 15:42	50110-01-17-03	+ · + + +
214680163	2000-10-20, 17:23	50110-01-17-01	+ · + + +
214686051	2000-10-20, 19:01	50110-01-17-02	+ · + + +
214692179	2000-10-20, 20:43	50110-01-17-04	+ · + + +
215343939	2000-10-28, 09:46	50119-01-01-00	+ + + + ·
215349987	2000-10-28, 11:27	50119-01-01-00	+ + + + ·
215356115	2000-10-28, 13:09	50119-01-01-00	+ + + + ·
215436067	2000-10-29, 11:22	50119-01-02-00	+ + + + ·
215442099	2000-10-29, 13:02	50119-01-02-00	+ · + + +
215448051	2000-10-29, 14:41	50119-01-02-00	+ + + + ·
215878051	2000-11-03, 14:08	50119-01-03-00	+ · + + +
215884115	2000-11-03, 15:49	50119-01-03-01	+ · + + +

T_{RXTE} (s)	Date (Y-m-d, H:M)	ObsID	PCUs 0 1 2 3 4
215889891	2000-11-03, 17:25	50119-01-03-02	+ · + + +
215895827	2000-11-03, 19:04	50119-01-03-03	+ · + + +
215899859	2000-11-03, 20:11	50119-01-03-03	+ · + + +
215901603	2000-11-03, 20:41	50119-01-03-03	+ · + + +
216044099	2000-11-05, 12:15	50109-03-01-00	+ · + + +
216123923	2000-11-06, 10:26	50109-03-02-00	+ · + + +
216129987	2000-11-06, 12:07	50109-03-02-00	+ · + + +
216135987	2000-11-06, 13:47	50109-03-02-00	+ · + + +
216203907	2000-11-07, 08:39	50109-03-03-00	+ · + + ·
216284051	2000-11-08, 06:55	50109-03-04-00	+ · + · +
216289827	2000-11-08, 08:31	50109-03-04-00	+ · + · ·
216358963	2000-11-09, 03:43	50109-03-05-00	+ · + + ·
216364323	2000-11-09, 05:13	50109-03-05-00	+ · + + +
216370051	2000-11-09, 06:48	50109-03-05-00	+ + + + ·
216375875	2000-11-09, 08:25	50109-03-05-00	+ · + + +
216381987	2000-11-09, 10:07	50109-03-05-00	+ + + + ·
216468019	2000-11-10, 10:01	50109-03-06-00	+ · + + ·
216553891	2000-11-11, 09:52	50109-03-07-00	+ · + + +
216645955	2000-11-12, 11:26	50109-03-08-00	+ · + + +
216731891	2000-11-13, 11:19	50109-03-09-00	+ · + + +
216800083	2000-11-14, 06:15	50109-03-10-00	+ · + + ·
216805891	2000-11-14, 07:52	50109-03-10-00	+ · + + +
216811827	2000-11-14, 09:31	50109-03-10-00	+ + + + ·
216897811	2000-11-15, 09:24	50109-03-11-00	+ · + + ·
217167347	2000-11-18, 12:16	50110-01-19-01	+ · + + ·
217173059	2000-11-18, 13:51	50110-01-19-02	+ · + + ·
217178499	2000-11-18, 15:22	50110-01-19-00G	+ + + + +
217184227	2000-11-18, 16:58	50110-01-19-00G	+ · + + ·
217189971	2000-11-18, 18:33	50110-01-19-00G	+ · + + ·
217757523	2000-11-25, 08:13	40100-01-23-00	+ + + + +
217764835	2000-11-25, 10:14	40100-01-23-01	+ · + + ·
218285875	2000-12-01, 10:58	50110-01-20-00	+ · + + ·
218290659	2000-12-01, 12:18	50110-01-20-00	+ + + + +
218296675	2000-12-01, 13:58	50110-01-20-01	+ · + + ·
218298771	2000-12-01, 14:33	50110-01-20-01	+ · + · ·
218302339	2000-12-01, 15:33	50110-01-20-02	+ · + + +
218308131	2000-12-01, 17:09	50110-01-20-03	+ · + + +
218313571	2000-12-01, 18:40	50110-01-20-04	+ · + + +
218423203	2000-12-03, 01:07	40100-01-24-00	+ · + + ·
218428227	2000-12-03, 02:31	40100-01-24-00	+ · + + +
218434851	2000-12-03, 04:21	40100-01-24-01	+ + + + ·
218439699	2000-12-03, 05:42	40100-01-24-01	+ · + + +
219668659	2000-12-17, 11:05	50110-01-21-00	+ · + + +
219674499	2000-12-17, 12:42	50110-01-21-01	+ + + + ·
219680659	2000-12-17, 14:25	50110-01-21-02	+ · + + +
219686563	2000-12-17, 16:03	50110-01-21-03	+ + + + ·
219690115	2000-12-17, 17:02	50110-01-21-04	+ + + + +
219692499	2000-12-17, 17:42	50110-01-21-04	+ · + + +
219804803	2000-12-19, 00:54	50119-01-04-00	+ + + + +
219811235	2000-12-19, 02:41	50119-01-04-01	+ · + + +
219994243	2000-12-21, 05:31	50119-01-05-00	+ · + + +
220000307	2000-12-21, 07:12	50119-01-05-00	+ · + + +
220006419	2000-12-21, 08:54	50119-01-05-01	+ · + + +
220012323	2000-12-21, 10:33	50119-01-05-02	+ · + + +
220098275	2000-12-22, 10:25	50109-01-01-00	+ · + + ·
220133619	2000-12-22, 20:14	50109-01-01-01	+ · + + +
220184259	2000-12-23, 10:18	50109-01-01-02	+ + + + +
220230611	2000-12-23, 23:11	50109-01-01-03	+ · + + +
220270243	2000-12-24, 10:11	50109-01-02-00	+ · + + +
220332211	2000-12-25, 03:24	50109-01-02-01	+ · + · +
220389539	2000-12-25, 19:19	50109-01-02-02	+ · + + ·
220424067	2000-12-26, 04:55	50109-01-02-03	+ · + + ·
220475523	2000-12-26, 19:13	50109-01-03-00	+ · + + ·
220522051	2000-12-27, 08:08	50109-01-03-01	+ · + + ·
220586723	2000-12-28, 02:06	50109-01-03-02	+ · + + ·
220664659	2000-12-28, 23:45	50109-01-03-03	+ · + + ·
220744899	2000-12-29, 22:02	50109-01-04-00	+ · + + +
220939747	2001-01-01, 04:10	50109-01-04-01	+ · + + ·
221043699	2001-01-02, 09:02	50110-01-22-00	+ · + + ·
221049651	2001-01-02, 10:41	50110-01-22-01	+ · + + ·
221055347	2001-01-02, 12:16	50110-01-22-02	+ + + · +
221061219	2001-01-02, 13:54	50110-01-22-03	+ + + · +
221209635	2001-01-04, 07:08	50119-01-06-00	+ · + + ·

T_{RXTE} (s)	Date (Y-m-d, H:M)	ObsID	PCUs 0 1 2 3 4
221215411	2001-01-04, 08:44	50119-01-06-01	+ · + + ·
221221347	2001-01-04, 10:23	50119-01-06-02	+ · + + ·
221227139	2001-01-04, 11:59	50119-01-06-03	+ · + + ·
221232851	2001-01-04, 13:35	50119-01-06-04	+ · + + ·
221237827	2001-01-04, 14:58	50119-01-06-05	+ · + + ·
221707699	2001-01-10, 01:29	50109-03-12-00	+ + + + ·
221787923	2001-01-10, 23:46	50109-03-13-00	+ · + + +
222252083	2001-01-16, 08:42	50110-01-23-00	+ · + · +
222257811	2001-01-16, 10:17	50110-01-23-03	+ + + · ·
222263971	2001-01-16, 12:00	50110-01-23-01	+ · + · +
222269411	2001-01-16, 13:31	50110-01-23-02	+ + + · ·
222855811	2001-01-23, 08:24	50109-01-05-02	+ + + + +
222859491	2001-01-23, 09:25	50109-01-05-00	+ · + + ·
222997027	2001-01-24, 23:38	50109-01-05-01	+ · + + +
223083011	2001-01-25, 23:31	50109-01-05-03 50109-01-06-00	+ · + + + + · + + +
223163251	2001-01-26, 21:48	50109-01-06-01	+ + + + +
223244387	2001-01-27, 20:20	50109-01-06-02	+ + + + +
223249219	2001-01-27, 21:41	50109-01-06-03	+ + + + +
223329619	2001-01-28, 20:01	50109-01-07-00	+ + + + +
223371235	2001-01-29, 07:34	50110-01-24-00	+ · + + ·
223377635	2001-01-29, 09:21	50110-01-24-01	+ · + + ·
223383699	2001-01-29, 11:02	50110-01-24-02	+ · + + ·
223389795	2001-01-29, 12:44	50110-01-24-03	+ · + + ·
223395731	2001-01-29, 14:23	50110-01-24-05	+ · + · ·
223398355	2001-01-29, 15:06	50110-01-24-04	+ · + + ·
223463587	2001-01-30, 09:14	50109-01-07-01	+ · + + ·
223561491	2001-01-31, 12:25	50109-01-07-02	+ · + + ·
223656339	2001-02-01, 14:46	50109-01-07-04	+ · + · ·
223715331	2001-02-02, 07:09	50109-01-08-00	+ · + + +
223721379	2001-02-02, 08:50	50109-01-08-01	+ · + + +
223727523	2001-02-02, 10:33	50109-01-08-02	+ · + + +
223801251	2001-02-03, 07:01	50109-01-08-04	+ · + + +
223807379	2001-02-03, 08:43	50109-01-08-05	+ · + + +
223813395	2001-02-03, 10:24	50109-01-08-06	+ · + + +
223917363	2001-02-04, 15:17	50109-01-09-00	+ · + + +
223967043	2001-02-05, 05:05	50109-01-09-01	+ · + + ·
224059075	2001-02-06, 06:38	50109-01-09-02	+ · + + +
224144995	2001-02-07, 06:30	50109-01-09-03	+ · + + +
224231011	2001-02-08, 06:24	50109-01-09-04	+ · + + +
224236915	2001-02-08, 08:02	50109-01-09-05	+ + + + ·
224310787	2001-02-09, 04:34	50109-01-10-00	+ · + + +
224408771	2001-02-10, 07:47	50110-01-25-00	+ · + + ·
224414899	2001-02-10, 09:29	50110-01-25-01	+ · + + ·
224420787	2001-02-10, 11:07	50110-01-25-02	+ · + + ·
224426739	2001-02-10, 12:46	50110-01-25-03	+ · + + ·
224432691	2001-02-10, 14:25	50110-01-25-04	+ · + + ·
224558851	2001-02-12, 01:28	50109-01-10-01	+ · + · ·
224861955	2001-02-15, 13:40	50109-01-10-02G	+ · + · ·
224865907	2001-02-15, 14:46	50109-01-10-03	+ · + · ·
225525603	2001-02-23, 06:01	50110-01-26-01	+ · + + ·
225531555	2001-02-23, 07:40	50110-01-26-02	+ · + + ·
225537283	2001-02-23, 09:15	50110-01-26-00	+ · + + ·
225542995	2001-02-23, 10:50	50110-01-26-03	+ · + + ·
225548163	2001-02-23, 12:17	50110-01-26-04	+ · + + ·
226911235	2001-03-11, 06:54	50110-01-41-00	+ + + + ·
226916851	2001-03-11, 08:28	50110-01-41-00	+ · + + +
226928291	2001-03-11, 11:39	50110-01-41-01	+ + + + ·
226934451	2001-03-11, 13:21	50110-01-41-02	+ + + + ·
228368227	2001-03-28, 03:38	50110-01-29-00	+ · + + ·
228374275	2001-03-28, 05:18	50110-01-29-01	+ · + + ·
228380243	2001-03-28, 06:58	50110-01-29-02	+ · + + ·
228386259	2001-03-28, 08:38	50110-01-29-03	+ · + + ·
228392131	2001-03-28, 10:16	50110-01-29-04	+ · + + ·
229232947	2001-04-07, 03:50	50110-01-30-00	+ + + + +
229238883	2001-04-07, 05:29	50110-01-30-04	+ · + + ·
229244883	2001-04-07, 07:09	50110-01-30-01	+ · + + ·
229256595	2001-04-07, 10:24	50110-01-30-03	+ · + + ·
231642275	2001-05-05, 01:05	50110-01-32-00	+ · + + ·
231648003	2001-05-05, 02:41	50110-01-32-00	+ · + · +
231653731	2001-05-05, 04:16	50110-01-32-00	+ · + + ·
231659731	2001-05-05, 05:56	50110-01-32-01	+ · + + ·
232852611	2001-05-19, 01:17	50110-01-33-00	+ · + · +

Table B.2: Continuous segments from *RXTE* PCA observations of Cyg X-1 between 1996-02-12 and 2010-10-12 (continued)

T_{RXTE} (s)	Date (Y-m-d, H:M)	ObsID	PCUs 0 1 2 3 4
232858643	2001-05-19, 02:58	50110-01-33-01	+ + + · ·
232864579	2001-05-19, 04:37	50110-01-33-02	+ + + · ·
232870483	2001-05-19, 06:15	50110-01-33-03	+ · + + ·
234231763	2001-06-04, 00:23	50110-01-34-00	+ · + · +
234237731	2001-06-04, 02:03	50110-01-34-01	+ + + · ·
234243571	2001-06-04, 03:40	50110-01-34-02	+ · + · +
234249363	2001-06-04, 05:17	50110-01-34-03	+ · + + +
234253667	2001-06-04, 06:28	50110-01-34-03	+ + + + ·
235261331	2001-06-15, 22:23	50110-01-35-01	+ · + + +
235266819	2001-06-15, 23:54	50110-01-35-00	+ · + + ·
235272547	2001-06-16, 01:30	50110-01-35-00	+ · + + ·
235278275	2001-06-16, 03:05	50110-01-35-00	+ · + · +
235283987	2001-06-16, 04:40	50110-01-35-00	+ + + · ·
236319907	2001-06-28, 04:26	60136-03-01-00	+ · + · +
236640435	2001-07-01, 21:28	50110-01-36-00	+ · + + +
236648707	2001-07-01, 23:46	50110-01-36-01	+ + + + ·
236654835	2001-07-02, 01:28	50110-01-36-02	+ · + + +
236663347	2001-07-02, 03:50	50110-01-36-03	+ · + + +
237010067	2001-07-06, 04:08	60136-03-02-00	+ · + + +
237101811	2001-07-07, 05:37	60136-03-02-01	+ + + · ·
237193587	2001-07-08, 07:07	60136-03-02-02	+ + + · ·
237273411	2001-07-09, 05:17	60136-03-02-03	+ + + · ·
237672643	2001-07-13, 20:11	50110-01-37-00	+ · + + +
237678595	2001-07-13, 21:50	50110-01-37-01	+ · + + ·
237684579	2001-07-13, 23:30	50110-01-37-02	+ · + + +
237690531	2001-07-14, 01:09	50110-01-37-03	+ · + + ·
237696451	2001-07-14, 02:48	50110-01-37-04	+ · + + +
238514387	2001-07-23, 14:00	40100-01-25-00	+ · + + ·
238518707	2001-07-23, 15:12	40100-01-25-00	+ + + · ·
238530675	2001-07-23, 18:32	40100-01-25-01	+ · + · +
238536595	2001-07-23, 20:10	40100-01-25-02	+ · + + ·
238977395	2001-07-28, 22:37	50110-01-38-01	+ · + + ·
238983155	2001-07-29, 00:13	50110-01-38-00	+ · + + +
238988083	2001-07-29, 01:35	50110-01-38-02	+ + + + ·
240344659	2001-08-13, 18:25	50110-01-39-00	+ · + · +
240349651	2001-08-13, 19:48	50110-01-39-00	+ + + · ·
240355379	2001-08-13, 21:23	50110-01-39-00	+ · + + ·
240361091	2001-08-13, 22:59	50110-01-39-00	+ · + · +
240366819	2001-08-14, 00:34	50110-01-39-00	+ · + · ·
240825139	2001-08-19, 07:53	60089-01-01-00	+ · + + ·
240832915	2001-08-19, 10:02	60089-01-01-01	+ · + + ·
240876083	2001-08-19, 22:02	60089-01-01-02	+ · + + ·
240910403	2001-08-20, 07:34	60089-01-02-00	+ · + + +
240916131	2001-08-20, 09:09	60089-01-02-00	+ · + + ·
240916787	2001-08-20, 09:20	60089-01-02-00	+ · + + ·
240990531	2001-08-21, 05:49	60089-01-03-00	+ · + · +
240996259	2001-08-21, 07:25	60089-01-03-01	+ · + + ·
241001987	2001-08-21, 09:00	60089-01-03-02	+ · + · ·
241025059	2001-08-21, 15:25	60089-01-04-00	+ · + + ·
241030595	2001-08-21, 16:57	60089-01-04-00	+ · + · ·
241076371	2001-08-22, 05:40	60089-01-05-00	+ · + + ·
241082099	2001-08-22, 07:15	60089-01-05-01	+ · + · ·
241087827	2001-08-22, 08:51	60089-01-05-02	+ · + · +
241116435	2001-08-22, 16:48	60089-01-06-00	+ · + + ·
241122163	2001-08-22, 18:23	60089-01-06-00	+ + + · ·
241190851	2001-08-23, 13:28	60089-01-07-00	+ · + + +
241196579	2001-08-23, 15:03	60089-01-07-00	+ + + + ·
241236627	2001-08-24, 02:11	60089-01-08-00	+ · + + ·
241328227	2001-08-25, 03:38	60089-01-08-01	+ · + + ·
241381747	2001-08-25, 18:30	50110-01-40-00	+ · + + +
241391203	2001-08-25, 21:07	50110-01-40-01	+ + + + ·
241394003	2001-08-25, 21:54	50110-01-40-01	+ + + + ·
241396931	2001-08-25, 22:43	50110-01-40-02	+ · + + ·
241402675	2001-08-26, 00:18	50110-01-40-03	+ · + + +
241485747	2001-08-26, 23:23	60089-01-08-02	+ · + + +
241488547	2001-08-27, 00:10	60089-01-08-03	+ · + + +
241645411	2001-08-28, 19:44	60089-01-09-00	+ · + + +
241657411	2001-08-28, 23:04	60089-01-09-01	+ · + + ·
241725187	2001-08-29, 17:54	60089-01-09-02	+ · + + +
241726067	2001-08-29, 18:08	60089-01-09-02	+ · + + +
241737155	2001-08-29, 21:13	60089-01-09-03	+ + + + ·
241763427	2001-08-30, 04:31	60089-01-09-04	+ + + + ·
242674867	2001-09-09, 17:42	50110-01-42-00	+ · + + ·
242680803	2001-09-09, 19:21	50110-01-42-01	+ · + · +
242686659	2001-09-09, 20:58	50110-01-42-02	+ + + · ·
242692627	2001-09-09, 22:38	50110-01-42-03	+ · + + ·
243881427	2001-09-23, 16:51	60089-02-01-00	+ · + + ·
243887219	2001-09-23, 18:27	60089-02-01-01	+ · + + ·
243892211	2001-09-23, 19:51	60089-02-01-01	+ · + + ·
243898611	2001-09-23, 21:37	60089-02-01-02	+ · + + ·
243903651	2001-09-23, 23:01	60089-02-01-02	+ · + + ·
245083859	2001-10-07, 14:51	60089-03-01-00	+ · + + ·
245087619	2001-10-07, 15:54	60089-03-01-00	+ · + + ·
245093331	2001-10-07, 17:29	60089-03-01-00	+ · + + ·
245099043	2001-10-07, 19:05	60089-03-01-01	+ · + · ·
245102019	2001-10-07, 19:54	60089-03-01-01	+ · + · ·
245110483	2001-10-07, 22:15	60089-03-01-02	+ · + · ·
245762531	2001-10-15, 11:23	60091-01-01-00	+ · + + +
245768243	2001-10-15, 12:58	60091-01-01-00	+ · + + ·
245773971	2001-10-15, 14:33	60091-01-01-00	+ + + + +
246204947	2001-10-20, 14:16	60091-01-02-00	+ · + + +
246211043	2001-10-20, 15:58	60091-01-02-01	+ · + + +
246217027	2001-10-20, 17:38	60091-01-02-02	+ + + + ·
246222963	2001-10-20, 19:17	60091-01-02-03	+ · + + ·
246226067	2001-10-20, 20:08	60091-01-02-03	+ · + + ·
246228883	2001-10-20, 20:55	60091-01-02-03	+ · + · ·
246231795	2001-10-20, 21:44	60091-01-02-03	+ · + · ·
246346259	2001-10-22, 05:31	60091-01-03-00	+ · + + +
246351987	2001-10-22, 07:07	60091-01-03-00	+ + + + ·
246357699	2001-10-22, 08:42	60091-01-03-00	+ · + + +
246902819	2001-10-28, 16:07	60089-02-02-00	+ + + + ·
246908723	2001-10-28, 17:46	60089-02-02-01	+ · + + +
246914643	2001-10-28, 19:25	60089-02-02-02	+ + + · ·
246918355	2001-10-28, 20:26	60089-02-02-03	+ · + · +
246920547	2001-10-28, 21:03	60089-02-02-03	+ · + · +
246924099	2001-10-28, 22:02	60089-02-02-04	+ · + + ·
246926323	2001-10-28, 22:39	60089-02-02-04	+ · + + ·
246929795	2001-10-28, 23:37	60089-02-02-05	+ + + + ·
246931651	2001-10-29, 00:08	60089-02-02-05	+ + + + ·
247411091	2001-11-03, 13:19	50110-01-31-00	+ · + + ·
247417011	2001-11-03, 14:57	50110-01-31-01	+ · + + ·
247422915	2001-11-03, 16:36	50110-01-31-02	+ · + + ·
247428835	2001-11-03, 18:14	50110-01-31-03	+ · + + ·
247434643	2001-11-03, 19:51	50110-01-31-04	+ + + + +
248256131	2001-11-13, 08:03	60089-03-02-00	+ · + + ·
248262035	2001-11-13, 09:41	60089-03-02-00	+ · + + ·
248890419	2001-11-20, 16:14	60089-03-03-00	+ + + + ·
248896147	2001-11-20, 17:50	60089-03-03-00	+ · + + +
248901859	2001-11-20, 19:25	60089-03-03-00	+ · + + ·
249027571	2001-11-22, 06:20	60089-03-03-01	+ · + + ·
251023971	2001-12-15, 08:53	50110-01-47-00	+ · + + ·
251029539	2001-12-15, 10:26	50110-01-47-00	+ · + + +
251035523	2001-12-15, 12:06	50110-01-47-04	+ + + · ·
251041491	2001-12-15, 13:45	50110-01-47-01	+ · + · ·
251047411	2001-12-15, 15:24	50110-01-47-02	+ · + · ·
251053347	2001-12-15, 17:03	50110-01-47-03	+ · + · ·
252497219	2002-01-01, 10:07	50110-01-49-00	+ · + + ·
252503139	2002-01-01, 11:46	50110-01-49-01	+ + + + ·
252508835	2002-01-01, 13:21	50110-01-49-01	+ · + + ·
252513523	2002-01-01, 14:39	50110-01-49-01	+ · + + +
252519235	2002-01-01, 16:14	50110-01-49-01	+ · + + ·
253786979	2002-01-16, 08:23	50110-01-50-00	+ + + + ·
253792691	2002-01-16, 09:59	50110-01-50-00	+ · + + ·
253798403	2002-01-16, 11:34	50110-01-50-00	+ + + + ·
253804115	2002-01-16, 13:09	50110-01-50-00	+ · + · ·
		50110-01-50-00	+ · + + ·
253809811	2002-01-16, 14:44	50110-01-50-01	+ · + · ·
254649155	2002-01-26, 07:53	50110-01-43-00	+ · + + ·
254657363	2002-01-26, 10:10	50110-01-43-01	+ · + + +
254663539	2002-01-26, 11:53	50110-01-43-02	+ · + + +
254669507	2002-01-26, 13:32	50110-01-43-03	+ · + + +
255855651	2002-02-09, 07:01	50110-01-44-00	+ + + · +
255861587	2002-02-09, 08:40	50110-01-44-01	+ · + · +
255867555	2002-02-09, 10:20	50110-01-44-02	+ + + · ·
255873459	2002-02-09, 11:58	50110-01-44-03	+ · + · +
255879379	2002-02-09, 13:37	50110-01-44-04	+ · + · +
256339619	2002-02-14, 21:27	60089-03-04-00	+ · + + ·
256345331	2002-02-14, 23:03	60089-03-04-00	+ · + + ·
256351107	2002-02-15, 00:39	60089-03-05-00	+ · + + ·
256380867	2002-02-15, 08:55	60089-03-05-01	+ · + + ·
256540131	2002-02-17, 05:09	60089-03-06-00	+ + + + ·
256546035	2002-02-17, 06:48	60089-03-06-01	+ · + + +
256551987	2002-02-17, 08:27	60089-03-06-02	+ · + + ·
256557843	2002-02-17, 10:05	60089-03-06-03	+ + + + ·
256699347	2002-02-19, 01:23	60089-03-07-00	+ · + + ·
256705251	2002-02-19, 03:01	60089-03-07-00	+ · + · +
256711187	2002-02-19, 04:40	60089-03-07-00	+ + + · ·
256717123	2002-02-19, 06:19	60089-03-08-00	+ · + + ·
256784883	2002-02-20, 01:09	60089-03-08-01	+ + + · ·
256790803	2002-02-20, 02:47	60089-03-08-01	+ · + + +
256888195	2002-02-21, 05:50	60089-03-08-02	+ · + · ·
257236275	2002-02-25, 06:32	50110-01-45-00	+ · + + ·
257241939	2002-02-25, 08:06	50110-01-45-01	+ · + + ·
257246947	2002-02-25, 09:30	50110-01-45-01	+ · + + ·
257252659	2002-02-25, 11:05	50110-01-45-01	+ · + + ·
257258355	2002-02-25, 12:40	50110-01-45-01	+ · + + ·
258182611	2002-03-08, 05:24	60090-01-01-00	+ · + + ·
258195891	2002-03-08, 09:05	50110-01-46-01	+ · + + ·
258201891	2002-03-08, 10:45	50110-01-46-00	+ + + · ·
258205443	2002-03-08, 11:45	50110-01-46-00	+ + + · ·
259644915	2002-03-25, 03:36	60090-01-02-00	+ · + + ·
259651043	2002-03-25, 05:18	50110-01-48-00	+ · + · +
259656995	2002-03-25, 06:57	50110-01-48-01	+ + + · ·
259662931	2002-03-25, 08:36	50110-01-48-02	+ · + + ·
259668819	2002-03-25, 10:14	50110-01-48-03	+ · + + ·
259671827	2002-03-25, 11:04	50110-01-48-03	+ · + + ·
260688803	2002-04-06, 05:34	60090-01-03-00	+ · + + ·
260694643	2002-04-06, 07:11	50110-01-51-01	+ · + + ·
260700579	2002-04-06, 08:50	50110-01-51-02	+ · + + ·
260706339	2002-04-06, 10:26	50110-01-51-00	+ · + + ·
261972355	2002-04-21, 02:06	60090-01-04-00	+ · + · ·
261976451	2002-04-21, 03:15	50110-01-52-00	+ · + · ·
261981699	2002-04-21, 04:42	50110-01-52-00	+ · + · ·
261987411	2002-04-21, 06:17	50110-01-52-00	+ · + · ·
261993107	2002-04-21, 07:52	50110-01-52-00	+ · + · ·
263264259	2002-05-06, 00:58	50110-01-53-00	+ · + + ·
263269955	2002-05-06, 02:33	60090-01-05-00	+ · + + ·
263275651	2002-05-06, 04:08	60090-01-05-00	+ · + + ·
263278467	2002-05-06, 04:55	60090-01-05-00	+ · + + ·
263870691	2002-05-13, 01:25	70104-01-01-00	+ · + + +
263950003	2002-05-13, 23:27	70104-01-01-01	+ · + · ·
263956115	2002-05-14, 01:09	70104-01-01-02	+ · + · +
264041603	2002-05-15, 00:54	70104-01-01-03	+ · + + ·
264560275	2002-05-21, 00:58	60090-01-06-00	+ + + + ·
264566211	2002-05-21, 02:37	60090-01-06-01	+ · + + ·
264572179	2002-05-21, 04:17	60090-01-06-02	+ · + + ·
265505875	2002-05-31, 23:38	60090-01-07-00	+ · + + ·
265511779	2002-06-01, 01:17	60090-01-07-01	+ · + + ·
265517715	2002-06-01, 02:56	60090-01-07-02	+ · + + ·
265528819	2002-06-01, 06:01	60090-01-07-03	+ · + + ·
266718659	2002-06-15, 00:31	60090-01-08-00	+ · + · ·
266730051	2002-06-15, 03:41	60090-01-08-01	+ · + + +
266735747	2002-06-15, 05:16	60090-01-08-01	+ + + + ·
268264979	2002-07-02, 22:03	60090-01-09-00	+ · + + ·
268270947	2002-07-02, 23:43	60090-01-09-03	+ · + + ·
268276979	2002-07-03, 01:23	60090-01-09-01	+ · + + ·
268285635	2002-07-03, 03:48	60090-01-09-02	+ · + · ·
269295875	2002-07-14, 20:25	60090-01-10-00	+ · + · ·
269301827	2002-07-14, 22:04	60090-01-10-01	+ · + · ·
269307731	2002-07-14, 23:43	60090-01-10-02	+ · + + ·
269313635	2002-07-15, 01:21	60090-01-10-03	+ · + + ·
269319523	2002-07-15, 02:59	60090-01-10-04	+ · + + ·
270332403	2002-07-26, 20:21	60090-01-11-02	+ · + · ·
270338355	2002-07-26, 22:00	60090-01-11-01	+ · + · ·
270344035	2002-07-26, 23:34	60090-01-11-00	+ · + + ·
270348723	2002-07-27, 00:53	60090-01-11-00	+ · + + ·
270354419	2002-07-27, 02:27	60090-01-11-00	+ · + + ·
270673987	2002-07-30, 19:14	70414-01-01-00	+ + + + ·
270679763	2002-07-30, 20:50	70414-01-01-01	+ + + + +
270687379	2002-07-30, 22:57	70414-01-01-02	+ + + + ·
270690499	2002-07-30, 23:49	70414-01-01-02	+ · + + +
270696195	2002-07-31, 01:24	70414-01-01-02	+ + + + ·
271710083	2002-08-11, 19:02	60090-01-12-00	+ · + · +
271715795	2002-08-11, 20:37	60090-01-12-01	+ · + · ·
271727171	2002-08-11, 23:47	60090-01-12-02	+ · + + ·
271732867	2002-08-12, 01:22	60090-01-12-03	+ · + + ·
272920019	2002-08-25, 19:07	60090-01-13-00	+ · + + ·
272925955	2002-08-25, 20:46	60090-01-13-03	+ · + + ·
272931907	2002-08-25, 22:26	60090-01-13-01	+ · + + ·
272937859	2002-08-26, 00:05	60090-01-13-02	+ · + + ·
274035683	2002-09-07, 17:02	60090-01-14-00	+ · + + ·
274041587	2002-09-07, 18:40	60090-01-14-01	+ · + + ·
274047571	2002-09-07, 20:20	60090-01-14-02	+ · + + ·
274053427	2002-09-07, 21:58	60090-01-14-03	+ + + · ·
274059267	2002-09-07, 23:35	60090-01-14-04	+ · + + ·
274741923	2002-09-15, 21:13	70015-04-01-00	+ · + + ·
274826755	2002-09-16, 20:46	70015-04-01-01	+ · + + +
274912035	2002-09-17, 20:28	70015-04-01-02	+ · + + +
275156963	2002-09-20, 16:30	60090-01-15-01	+ · + + ·
276118515	2002-10-01, 19:36	70104-01-02-00	+ · + + +
276289267	2002-10-03, 19:02	70104-01-03-00	+ · + + +
276374659	2002-10-04, 18:45	70104-01-04-00	+ + + + +
276377315	2002-10-04, 19:29	70104-01-04-00	+ + + + +
276456355	2002-10-05, 17:26	70104-01-04-01	+ + + + +
276460035	2002-10-05, 18:28	70104-01-04-01	+ + + + +
276534051	2002-10-06, 15:01	60090-01-16-00	+ · + · ·
276539747	2002-10-06, 16:36	60090-01-16-00	+ · + · ·
276545443	2002-10-06, 18:11	60090-01-16-00	+ · + · ·
276548211	2002-10-06, 18:57	60090-01-16-00	+ · + · ·
277572323	2002-10-18, 15:26	60090-01-17-00	+ · + · ·
277578291	2002-10-18, 17:05	60090-01-17-01	+ · + · ·
277584243	2002-10-18, 18:45	60090-01-17-02	+ · + · ·
277590195	2002-10-18, 20:24	60090-01-17-03	+ · + · ·
278863715	2002-11-02, 14:09	60090-01-18-01	+ · + + ·
278869667	2002-11-02, 15:48	60090-01-18-00	+ · + · ·
280069619	2002-11-16, 13:07	60090-01-19-02	+ · + · ·
280074915	2002-11-16, 14:36	60090-01-19-00	+ · + · ·
280080371	2002-11-16, 16:07	60090-01-19-03	+ · + · ·
280086051	2002-11-16, 17:41	60090-01-19-01	+ · + · ·
280785763	2002-11-24, 20:03	70414-01-02-01	+ + + + +
280927971	2002-11-26, 11:33	70414-01-02-00	+ · + + +
280933667	2002-11-26, 13:08	70414-01-02-00	+ + + + ·
281189667	2002-11-29, 12:15	60090-01-20-00	+ + + + ·
281198035	2002-11-29, 14:34	60090-01-20-03	+ · + + ·
281206755	2002-11-29, 17:00	60090-01-20-01	+ · + + ·
281212435	2002-11-29, 18:34	60090-01-20-02	+ · + + ·
281453939	2002-12-02, 13:39	70414-01-03-00	+ · + + +
281459939	2002-12-02, 15:19	70414-01-03-01	+ · + + +
281468499	2002-12-02, 17:42	70414-01-03-03	+ · + + +
281474195	2002-12-02, 19:17	70414-01-03-02	+ · + + +
281795043	2002-12-06, 12:25	70414-01-04-00	+ + + + ·
281801059	2002-12-06, 14:05	70414-01-04-01	+ + + + +
281880307	2002-12-07, 12:06	70414-01-04-02	+ + + + ·
281886307	2002-12-07, 13:46	70414-01-04-03	+ · + + ·
281965571	2002-12-08, 11:47	70414-01-04-04	+ · + + ·
282391923	2002-12-13, 10:13	60090-01-21-00	+ · + + ·
282397875	2002-12-13, 11:52	60090-01-21-01	+ · + + ·
282403747	2002-12-13, 13:30	60090-01-21-02	+ · + + ·
282409651	2002-12-13, 15:08	60090-01-21-03	+ · + + ·
282415571	2002-12-13, 16:47	60090-01-21-04	+ · + + ·
283744355	2002-12-29, 01:53	70414-01-05-00	+ · + + ·
283750035	2002-12-29, 03:28	70414-01-05-00	+ · + + +
283755811	2002-12-29, 05:04	70414-01-05-00	+ · + + ·
283773523	2002-12-29, 09:59	60090-01-22-00	+ · + · ·
283779347	2002-12-29, 11:36	60090-01-22-00	+ · + + ·
283785075	2002-12-29, 13:12	60090-01-22-00	+ · + · ·
283789843	2002-12-29, 14:31	60090-01-22-00	+ · + + ·
283795523	2002-12-29, 16:06	60090-01-22-00	+ · + + ·
283801219	2002-12-29, 17:41	70414-01-05-01	+ · + + ·
283806899	2002-12-29, 19:15	70414-01-05-01	+ · + + ·
283812595	2002-12-29, 20:50	70414-01-05-01	+ · + + ·
284807651	2003-01-10, 09:15	60090-01-23-02	+ · + + ·

Table B.2: Continuous segments from *RXTE* PCA observations of Cyg X-1 between 1996-02-12 and 2010-10-12 (continued)

T_{RXTE} (s)	Date (Y-m-d, H:M)	ObsID	PCUs 0 1 2 3 4
284813827	2003-01-10, 10:58	60090-01-23-01	+ · + + ·
284819043	2003-01-10, 12:25	60090-01-23-00	+ · + + ·
284824723	2003-01-10, 13:59	60090-01-23-00	+ + + + +
284830419	2003-01-10, 15:34	60090-01-23-00	+ · + + ·
286015203	2003-01-24, 08:41	60090-01-24-00	+ · + + ·
286021299	2003-01-24, 10:22	60090-01-24-00	+ · + + ·
286027331	2003-01-24, 12:03	60090-01-24-01	+ · + + ·
286035923	2003-01-24, 14:26	60090-01-24-03	+ · + + ·
287220275	2003-02-07, 07:25	60090-01-25-00	+ · + + ·
287226163	2003-02-07, 09:03	60090-01-25-01	+ · + + ·
287232131	2003-02-07, 10:43	60090-01-25-02	+ + + · ·
287238035	2003-02-07, 12:21	60090-01-25-03	+ · + + ·
287243891	2003-02-07, 13:59	60090-01-25-04	+ · + + ·
288606179	2003-02-23, 08:23	60090-01-26-00	+ + + + ·
288611859	2003-02-23, 09:58	60090-01-26-00	+ · + + +
288617555	2003-02-23, 11:33	60090-01-26-00	+ + + + ·
288623219	2003-02-23, 13:07	60090-01-26-01	+ · + + ·
289432691	2003-03-04, 21:59	80402-01-01-00	+ · + · ·
290061171	2003-03-12, 04:33	60090-01-27-00	+ · + + ·
290066851	2003-03-12, 06:08	60090-01-27-00	+ · + + ·
290075395	2003-03-12, 08:30	60090-01-27-01	+ · + + ·
290927315	2003-03-22, 05:09	60090-01-28-00	+ · + + ·
290933299	2003-03-22, 06:49	60090-01-28-02	+ · + + ·
290939203	2003-03-22, 08:27	60090-01-28-01	+ · + + ·
290945075	2003-03-22, 10:05	60090-01-28-03	+ · + + ·
292216707	2003-04-06, 03:19	60090-01-29-00	+ · + · +
292222643	2003-04-06, 04:58	60090-01-29-03	+ + + · ·
292228483	2003-04-06, 06:35	60090-01-29-04	+ · + · +
292234243	2003-04-06, 08:11	60090-01-29-01	+ · + · ·
292239747	2003-04-06, 09:43	60090-01-29-02	+ · + + ·
293335363	2003-04-19, 02:03	60090-01-30-00	+ · + + ·
293340883	2003-04-19, 03:35	60090-01-30-00	+ + + + +
293346563	2003-04-19, 05:10	60090-01-30-00	+ · + + ·
293352435	2003-04-19, 06:48	60090-01-30-01G	+ · + + ·
293357923	2003-04-19, 08:19	80111-01-01-01G	+ + + + +
293363603	2003-04-19, 09:54	80111-01-01-01G	+ · + · ·
293369315	2003-04-19, 11:29	80111-01-01-02	+ · + · +
293374979	2003-04-19, 13:03	80111-01-01-000	+ + + + ·
293380659	2003-04-19, 14:38	80111-01-01-000	+ · + + ·
293386339	2003-04-19, 16:13	80111-01-01-000	+ · + + ·
293392019	2003-04-19, 17:47	80111-01-01-000	+ · + + ·
293397699	2003-04-19, 19:22	80111-01-01-000 80111-01-01-000	+ · + + · + + + + ·
293403363	2003-04-19, 20:57	80111-01-01-001	+ · + + ·
293409043	2003-04-19, 22:31	80111-01-01-001	+ · + + +
293414787	2003-04-20, 00:07	80111-01-01-001	+ · + + ·
293420515	2003-04-20, 01:42	80111-01-01-001	+ · + + ·
293426099	2003-04-20, 03:15	80111-01-01-001	+ · + + +
293431779	2003-04-20, 04:50	80111-01-01-00 80111-01-01-00	+ · + + · + + + + ·
293437459	2003-04-20, 06:25	80111-01-01-00	+ · + + +
293443155	2003-04-20, 08:00	80111-01-01-03	+ · + + ·
294545331	2003-05-03, 02:09	60090-01-31-00	+ · + + +
294553763	2003-05-03, 04:30	60090-01-31-01	+ · + + ·
294562371	2003-05-03, 06:53	60090-01-31-02	+ · + + ·
295751891	2003-05-17, 01:19	60090-01-32-00	+ · + + ·
295757747	2003-05-17, 02:56	60090-01-32-01	+ · + + ·
295763683	2003-05-17, 04:35	60090-01-32-02	+ · + + ·
295769571	2003-05-17, 06:13	60090-01-32-03	+ · + · ·
297040755	2003-05-31, 23:20	60090-01-31-03	+ · + · ·
297046595	2003-06-01, 00:57	60090-01-31-03	+ · + · ·
297052259	2003-06-01, 02:31	60090-01-33-00	+ · + + ·
297057107	2003-06-01, 03:52	60090-01-33-00	+ + + + ·
297062787	2003-06-01, 05:27	60090-01-33-00	+ · + + +
298335219	2003-06-15, 22:54	60090-01-34-00	+ · + · ·
298340787	2003-06-16, 00:27	60090-01-34-03	+ · + · +
298346899	2003-06-16, 02:09	60090-01-34-01	+ · + + ·
298352147	2003-06-16, 03:36	60090-01-34-01	+ · + · ·
298357811	2003-06-16, 05:11	60090-01-34-02	+ · + · ·
299541411	2003-06-29, 21:57	60090-01-35-00	+ · + + +
299547411	2003-06-29, 23:37	60090-01-35-04	+ · + + ·
299553379	2003-06-30, 01:17	60090-01-35-03	+ · + · ·
299565219	2003-06-30, 04:34	60090-01-35-02	+ · + · ·

T_{RXTE} (s)	Date (Y-m-d, H:M)	ObsID	PCUs 0 1 2 3 4
300659923	2003-07-12, 20:39	60090-01-36-00	+ · + + ·
300665891	2003-07-12, 22:19	60090-01-36-01	+ · + + ·
300671747	2003-07-12, 23:56	60090-01-36-02	+ · + + ·
300677619	2003-07-13, 01:34	60090-01-36-03	+ · + + ·
300683475	2003-07-13, 03:12	60090-01-36-04	+ · + + ·
301869059	2003-07-26, 20:31	60090-01-37-01	+ · + · ·
301874707	2003-07-26, 22:06	60090-01-37-00	+ · + · ·
301879971	2003-07-26, 23:33	60090-01-37-00	+ · + · ·
301885651	2003-07-27, 01:08	60090-01-37-00	+ · + · ·
301892467	2003-07-27, 03:02	60090-01-37-02	+ · + · ·
303418883	2003-08-13, 19:02	60090-01-38-00	+ · + + ·
303430227	2003-08-13, 22:11	60090-01-38-03	+ · + + ·
303435907	2003-08-13, 23:46	60090-01-38-01	+ · + + ·
303441603	2003-08-14, 01:21	60090-01-38-02	+ · + + ·
304278371	2003-08-23, 17:47	60090-01-39-00	+ · + + ·
304284355	2003-08-23, 19:26	60090-01-39-04	+ · + + ·
304290259	2003-08-23, 21:05	60090-01-39-03	+ · + · +
304296195	2003-08-23, 22:44	60090-01-39-02	+ · + + ·
304302067	2003-08-24, 00:22	60090-01-39-01	+ · + + ·
305572595	2003-09-07, 17:17	60090-01-40-00	+ · + + ·
305578515	2003-09-07, 18:56	60090-01-40-01	+ · + + ·
305584387	2003-09-07, 20:34	60090-01-40-02	+ · + + ·
305590051	2003-09-07, 22:08	60090-01-40-03	+ · + + ·
305594515	2003-09-07, 23:22	60090-01-40-03	+ · + + ·
306866243	2003-09-22, 16:38	60090-01-41-01	+ · + + ·
306871939	2003-09-22, 18:13	60090-01-41-00	+ · + + ·
306877619	2003-09-22, 19:47	60090-01-41-00	+ · + · +
306883283	2003-09-22, 21:22	60090-01-41-00	+ · + · ·
306888963	2003-09-22, 22:57	60090-01-41-00	+ · + + ·
307303379	2003-09-27, 18:03	60090-01-53-00	+ · + · +
307309059	2003-09-27, 19:38	60090-01-53-08	+ + + · ·
307388547	2003-09-28, 17:43	60090-01-53-01	+ + + + ·
307399875	2003-09-28, 20:52	60090-01-53-09	+ · + + ·
307473683	2003-09-29, 17:22	60090-01-53-02	+ · + · ·
307485043	2003-09-29, 20:31	60090-01-53-10	+ + + · ·
307558851	2003-09-30, 17:01	60090-01-53-03	+ · + + ·
307570195	2003-09-30, 20:10	60090-01-53-11	+ · + + ·
307649683	2003-10-01, 18:15	60090-01-53-04	+ · + + ·
307655363	2003-10-01, 19:50	60090-01-53-06	+ · + · ·
307658563	2003-10-01, 20:43	60090-01-53-06	+ · + · ·
307734851	2003-10-02, 17:55	60090-01-53-05	+ · + · ·
307740531	2003-10-02, 19:29	60090-01-53-07	+ · + · ·
307822723	2003-10-03, 18:19	60090-01-42-00	+ · + · ·
307825699	2003-10-03, 19:09	60090-01-42-01	+ · + · ·
308156867	2003-10-07, 15:08	60090-01-42-02	+ · + + ·
308163139	2003-10-07, 16:53	60090-01-42-03	+ + + · ·
308169139	2003-10-07, 18:33	60090-01-42-04	+ · + + ·
308175091	2003-10-07, 20:12	60090-01-42-05	+ · + + ·
308183539	2003-10-07, 22:33	60090-01-42-06	+ · + + ·
309019939	2003-10-17, 14:53	60090-01-43-00	+ · + + ·
309025843	2003-10-17, 16:31	60090-01-43-02	+ · + + ·
309031763	2003-10-17, 18:10	60090-01-43-03	+ · + + ·
309037635	2003-10-17, 19:48	60090-01-43-04	+ · + + ·
309043507	2003-10-17, 21:26	60090-01-43-01	+ · + + ·
310999795	2003-11-09, 12:50	60090-01-44-00	+ · + + ·
311005267	2003-11-09, 14:22	60090-01-44-00	+ · + + ·
311010947	2003-11-09, 15:56	60090-01-44-00	+ · + + ·
311016627	2003-11-09, 17:31	60090-01-44-00	+ · + + ·
311022291	2003-11-09, 19:05	60090-01-44-00	+ + + · ·
311947283	2003-11-20, 12:02	60090-01-45-00	+ + + + ·
311952963	2003-11-20, 13:37	60090-01-45-00	+ · + + ·
311958627	2003-11-20, 15:11	60090-01-45-01	+ · + + ·
311969971	2003-11-20, 18:20	60090-01-45-02	+ · + + ·
312812115	2003-11-30, 12:16	60090-01-46-04	+ · + + ·
312818083	2003-11-30, 13:55	60090-01-46-00	+ · + + ·
312824051	2003-11-30, 15:35	60090-01-46-01	+ · + + ·
312829907	2003-11-30, 17:12	60090-01-46-02	+ · + + ·
312835779	2003-11-30, 18:50	60090-01-46-03	+ · + + ·
313850371	2003-12-12, 12:40	60090-01-47-00	+ · + · ·
313856211	2003-12-12, 14:17	60090-01-47-01	+ · + · ·
313862067	2003-12-12, 15:55	60090-01-47-02	+ · + · ·
313867907	2003-12-12, 17:32	60090-01-47-03	+ · + · ·
315307395	2003-12-29, 09:24	60090-01-35-01	+ · + + ·

T_{RXTE} (s)	Date (Y-m-d, H:M)	ObsID	PCUs 0 1 2 3 4
315314291	2003-12-29, 11:19	60090-01-44-01	+ · + + ·
315318563	2003-12-29, 12:30	60090-01-48-00	+ · + + ·
315324227	2003-12-29, 14:04	60090-01-48-00	+ · + + ·
315329907	2003-12-29, 15:39	60090-01-48-00	+ · + + ·
316600691	2004-01-13, 08:39	60090-01-49-00	+ · + + ·
316606355	2004-01-13, 10:13	60090-01-49-00	+ · + + ·
316612035	2004-01-13, 11:48	60090-01-49-01	+ · + + ·
316617715	2004-01-13, 13:22	60090-01-49-03	+ · + + ·
316623587	2004-01-13, 15:00	60090-01-49-02	+ · + + ·
317465235	2004-01-23, 08:48	60090-01-50-00	+ + + + ·
317471171	2004-01-23, 10:27	60090-01-50-02	+ · + · +
317477059	2004-01-23, 12:05	60090-01-50-01	+ · + + ·
317482931	2004-01-23, 13:43	60090-01-50-03	+ + + + ·
317488819	2004-01-23, 15:21	60090-01-50-04	+ · + + ·
318843187	2004-02-08, 07:34	60090-01-51-00	+ · + + ·
318849091	2004-02-08, 09:12	60090-01-51-01	+ · + + +
318854819	2004-02-08, 10:47	60090-01-51-02	+ · + + ·
318860227	2004-02-08, 12:18	60090-01-51-03	+ · + + ·
318865395	2004-02-08, 13:44	60090-01-51-04	+ · + + ·
319880291	2004-02-20, 07:39	60090-01-52-00	+ · + + ·
319885971	2004-02-20, 09:13	60090-01-52-00	+ · + + ·
319891635	2004-02-20, 10:48	60090-01-52-00	+ · + + ·
319897315	2004-02-20, 12:22	60090-01-52-00 60090-01-52-00	+ · + · · + · + + ·
319902979	2004-02-20, 13:57	60090-01-52-00	+ · + · ·
321424803	2004-03-09, 04:41	80110-01-01-00	+ · + + ·
321431075	2004-03-09, 06:25	80110-01-01-01	+ · + + ·
321437091	2004-03-09, 08:05	80110-01-01-02	+ · + + ·
321443027	2004-03-09, 09:44	80110-01-01-03	+ · + + ·
321451603	2004-03-09, 12:07	80110-01-01-04	+ + + · ·
322287123	2004-03-19, 04:13	80110-01-02-01	+ · + · ·
322292979	2004-03-19, 05:50	80110-01-02-00	+ · + · ·
322298883	2004-03-19, 07:29	80110-01-02-02	+ · + + ·
322304739	2004-03-19, 09:06	80110-01-02-03	+ · + + ·
322310611	2004-03-19, 10:44	80110-01-02-04	+ · + + ·
323579651	2004-04-03, 03:15	60090-01-54-02	+ · + + ·
323585427	2004-04-03, 04:51	60090-01-54-01	+ · + + ·
323591171	2004-04-03, 06:27	60090-01-54-00	+ · + + ·
323596019	2004-04-03, 07:47	60090-01-54-00	+ · + + ·
323601699	2004-04-03, 09:22	60090-01-54-00	+ · + + ·
323965203	2004-04-07, 14:21	90126-01-01-01	+ + + · ·
324140387	2004-04-09, 15:00	90126-01-02-00G	+ · + · ·
324147251	2004-04-09, 16:55	90126-01-02-01	+ · + · ·
324310819	2004-04-11, 14:21	90126-01-03-00	+ + + · ·
324316883	2004-04-11, 16:02	90126-01-03-01	+ · + · +
324871843	2004-04-18, 02:11	80110-01-03-00	+ · + + ·
324894899	2004-04-18, 08:35	80110-01-03-01	+ · + · ·
326093811	2004-05-02, 05:37	80110-01-04-02	+ · + + ·
326099699	2004-05-02, 07:15	80110-01-04-03	+ · + + ·
326105571	2004-05-02, 08:53	80110-01-04-01	+ · + + ·
327289315	2004-05-16, 01:42	80110-01-05-00	+ · + · ·
327295171	2004-05-16, 03:20	80110-01-05-01	+ · + · ·
327301059	2004-05-16, 04:58	80110-01-05-02	+ · + · ·
327306803	2004-05-16, 06:34	80110-01-05-03	+ · + · ·
327412995	2004-05-17, 12:04	80113-01-01-00	+ · + · ·
327418675	2004-05-17, 13:38	80113-01-01-00	+ + + · ·
327424339	2004-05-17, 15:13	80113-01-01-00	+ · + · ·
327758851	2004-05-21, 12:08	80113-01-02-01	+ + + + ·
327765251	2004-05-21, 13:55	80113-01-02-00	+ · + + +
327770195	2004-05-21, 15:17	80113-01-02-00	+ · + + ·
327920083	2004-05-23, 08:55	90414-03-01-01	+ · + + ·
328090483	2004-05-25, 08:15	90414-03-01-03	+ · + + ·
328405539	2004-05-28, 23:46	80110-01-06-00	+ · + · ·
328410867	2004-05-29, 01:15	80110-01-06-01	+ · + · ·
328416547	2004-05-29, 02:50	80110-01-06-01	+ · + · +
328422211	2004-05-29, 04:24	80110-01-06-01	+ + + · ·
328427875	2004-05-29, 05:58	80110-01-06-01	+ · + + ·
328701523	2004-06-01, 09:59	90414-03-02-00	+ · + · ·
329612755	2004-06-11, 23:06	80110-01-07-00	+ · + + ·
329618419	2004-06-12, 00:41	80110-01-07-00	+ · + + +
329624083	2004-06-12, 02:15	80110-01-07-00	+ · + + ·
329629763	2004-06-12, 03:50	80110-01-07-01	+ · + · ·
330810707	2004-06-25, 19:52	80110-01-08-00	+ · + + ·

T_{RXTE} (s)	Date (Y-m-d, H:M)	ObsID	PCUs 0 1 2 3 4
330816707	2004-06-25, 21:32	80110-01-07-02	+ · + + ·
330822675	2004-06-25, 23:12	80110-01-07-03	+ · + + ·
330828611	2004-06-26, 00:51	80110-01-08-01	+ · + + ·
330834483	2004-06-26, 02:29	80110-01-08-02	+ · + + ·
332029779	2004-07-09, 22:30	80110-01-09-01	+ · + · ·
332035635	2004-07-10, 00:08	80110-01-09-00	+ · + · ·
332890483	2004-07-19, 21:35	90026-01-01-00	+ + + + +
332975507	2004-07-20, 21:12	90026-01-01-01	+ + + + +
333066195	2004-07-21, 22:24	90026-01-02-00	+ + + + +
333151235	2004-07-22, 22:01	90026-01-02-01	+ + + + +
333236259	2004-07-23, 21:38	90026-01-03-00	+ · + + ·
333241923	2004-07-23, 23:13	90026-01-03-02	+ · + + ·
333321619	2004-07-24, 21:21	90026-01-03-01	+ · + · ·
333326963	2004-07-24, 22:50	90026-01-03-03	+ · + · ·
333576371	2004-07-27, 20:07	80110-01-10-00	+ · + + ·
333582035	2004-07-27, 21:41	80110-01-10-00	+ · + + ·
333587715	2004-07-27, 23:16	80110-01-10-03	+ · + · ·
333593379	2004-07-28, 00:50	80110-01-10-01	+ · + · ·
333599027	2004-07-28, 02:24	80110-01-10-02G	+ · + · ·
334625459	2004-08-08, 23:31	80110-01-11-02	+ + + + ·
334628131	2004-08-09, 00:16	80110-01-11-02	+ + + + ·
334630963	2004-08-09, 01:03	80110-01-11-01	+ · + + ·
334634003	2004-08-09, 01:54	80110-01-11-01	+ · + + ·
334636659	2004-08-09, 02:38	80110-01-11-00	+ · + + ·
335987331	2004-08-24, 17:49	80110-01-12-00	+ · + + ·
335993203	2004-08-24, 19:27	80110-01-12-01	+ · + + ·
335999107	2004-08-24, 21:06	80110-01-12-02	+ · + + ·
336004947	2004-08-24, 22:43	80110-01-12-03	+ · + + ·
336848563	2004-09-03, 17:03	80110-01-13-00	+ · + + ·
336854323	2004-09-03, 18:39	80110-01-13-01	+ · + + ·
336860115	2004-09-03, 20:16	80110-01-13-02	+ · + + ·
336864979	2004-09-03, 21:37	80110-01-13-02	+ · + + ·
338230883	2004-09-19, 17:02	80110-01-14-00	+ · + · ·
338236547	2004-09-19, 18:36	80110-01-14-01	+ · + · ·
338248115	2004-09-19, 21:49	80110-01-14-03	+ · + · ·
338253827	2004-09-19, 23:24	80110-01-14-02	+ · + · ·
339264707	2004-10-01, 16:12	80110-01-15-00	+ · + + +
339270675	2004-10-01, 17:52	80110-01-15-01	+ · + + ·
339276595	2004-10-01, 19:30	80110-01-15-02	+ · + + ·
339282467	2004-10-01, 21:08	80110-01-15-03	+ · + + ·
339288323	2004-10-01, 22:46	80110-01-15-04	+ + + + ·
340471555	2004-10-15, 15:26	80110-01-16-00	+ · + + ·
340477459	2004-10-15, 17:05	80110-01-16-01	+ · + + ·
340483347	2004-10-15, 18:43	80110-01-16-02	+ · + + ·
340489027	2004-10-15, 20:18	80110-01-16-03	+ · + + ·
340494467	2004-10-15, 21:48	80110-01-16-04	+ · + · ·
341847907	2004-10-31, 13:46	80110-01-17-02	+ · + + ·
341853235	2004-10-31, 15:14	80110-01-17-01	+ · + + +
341858899	2004-10-31, 16:49	80110-01-17-00	+ · + + ·
341864563	2004-10-31, 18:23	80110-01-17-00	+ · + + ·
341870227	2004-10-31, 19:58	80110-01-17-00	+ · + + ·
342885603	2004-11-12, 14:01	80110-01-18-00	+ + + · ·
342890339	2004-11-12, 15:19	80110-01-18-04	+ · + + ·
342892899	2004-11-12, 16:02	80110-01-18-04	+ · + + ·
342895971	2004-11-12, 16:53	80110-01-18-01	+ · + + ·
342901667	2004-11-12, 18:28	80110-01-18-02	+ · + + ·
342907187	2004-11-12, 20:00	80110-01-18-03	+ · + + ·
343048867	2004-11-14, 11:22	90104-01-01-01	+ + + · ·
343054531	2004-11-14, 12:56	90104-01-01-03	+ · + · +
343089299	2004-11-14, 22:35	90104-01-01-02	+ · + + +
343094211	2004-11-14, 23:57	90104-01-01-00	+ · + + ·
343099875	2004-11-15, 01:32	90104-01-01-00	+ · + + ·
343105539	2004-11-15, 03:06	90104-01-01-00	+ · + + ·
343111203	2004-11-15, 04:41	90104-01-01-00	+ · + + ·
343604515	2004-11-20, 21:42	90104-01-02-02	+ + + + ·
343610195	2004-11-20, 23:17	90104-01-02-01	+ · + + ·
343615859	2004-11-21, 00:51	90104-01-02-03	+ · + + ·
343621539	2004-11-21, 02:26	90104-01-02-00	+ · + + ·
343627203	2004-11-21, 04:01	90104-01-02-00	+ · + + ·
343632883	2004-11-21, 05:35	90104-01-02-00	+ · + + ·
343638547	2004-11-21, 07:10	90104-01-02-00	+ · + · ·
344120611	2004-11-26, 21:04	90104-01-03-00	+ · + + ·
344123011	2004-11-26, 21:44	90104-01-03-00	+ · + + ·

Table B.2: Continuous segments from *RXTE* PCA observations of Cyg X-1 between 1996-02-12 and 2010-10-12 (continued)

T_{RXTE} (s)	Date (Y-m-d, H:M)	ObsID	PCUs 0 1 2 3 4
344126179	2004-11-26, 22:37	90104-01-03-01	+ · + · ·
		90104-01-03-01	+ · ++ ·
344128291	2004-11-26, 23:12	90104-01-03-01	+ · + · ·
344131843	2004-11-27, 00:11	90104-01-03-01	+ · + · ·
344137523	2004-11-27, 01:46	90104-01-03-01	+ · + · ·
344143187	2004-11-27, 03:20	90104-01-03-01	+ · + · ·
344149731	2004-11-27, 05:09	90104-01-03-02	+ · ++ ·
344433411	2004-11-30, 11:57	80110-01-19-00	+ · ++ ·
344439283	2004-11-30, 13:35	80110-01-19-01	+ · ++ ·
344445171	2004-11-30, 15:13	80110-01-19-02	+ · ++ ·
344451043	2004-11-30, 16:51	80110-01-19-03	+ · ++ ·
344456931	2004-11-30, 18:29	80110-01-19-04	+ · ++ ·
344637619	2004-12-02, 20:41	90104-01-04-01	+ · ++ ·
344641907	2004-12-02, 21:52	90104-01-04-01	+ · ++ ·
344647571	2004-12-02, 23:27	90104-01-04-00	+ · ++ ·
		90104-01-04-01	+ · ++ ·
344653235	2004-12-03, 01:01	90104-01-04-00	+ · ++ ·
344658899	2004-12-03, 02:35	90104-01-04-00	+ · ++ ·
344664579	2004-12-03, 04:10	90104-01-04-00	+ · ++ ·
344670291	2004-12-03, 05:45	90104-01-04-02	+ · ++ ·
345554803	2004-12-13, 11:27	80110-01-20-02	+ · + · ·
345560563	2004-12-13, 13:03	80110-01-20-01	+ · + · ·
345565731	2004-12-13, 14:29	80110-01-20-03	+ · + · ·
345571075	2004-12-13, 15:58	80110-01-20-00	+ · + · ·
345576739	2004-12-13, 17:33	80110-01-20-04	+ · + · ·
345973507	2004-12-18, 07:46	90414-03-03-00	+ · ++ ·
346760755	2004-12-27, 10:26	80110-01-21-00	++++ ·
346766419	2004-12-27, 12:01	80110-01-21-00	+ · ++ ·
346772083	2004-12-27, 13:35	80110-01-21-00	+ · +++
346777747	2004-12-27, 15:10	80110-01-21-00	+ · ++ ·
347793939	2005-01-08, 09:26	80110-01-22-01	+ · + · ·
347800067	2005-01-08, 11:08	80110-01-22-02	+ · + · ·
347805987	2005-01-08, 12:47	80110-01-22-00	+ · + · ·
347814707	2005-01-08, 15:12	80110-01-22-03	+ · + · ·
347817747	2005-01-08, 16:03	80110-01-22-03	+ · + · ·
348915587	2005-01-21, 09:00	80110-01-23-00	+ · ++ ·
348921427	2005-01-21, 10:38	80110-01-23-01	+ · ++ ·
348927315	2005-01-21, 12:16	80110-01-23-02	+ · ++ ·
348933171	2005-01-21, 13:53	80110-01-23-03	+ · ++ ·
348939011	2005-01-21, 15:31	80110-01-23-04	+ · ++ ·
349861075	2005-02-01, 07:38	90127-01-01-04	+ · ++ ·
349866947	2005-02-01, 09:16	90127-01-01-05	+ · ++ ·
349872611	2005-02-01, 10:51	90127-01-01-00	+ · +++
349877363	2005-02-01, 12:10	90127-01-01-00	++++ ·
349883027	2005-02-01, 13:44	90127-01-01-00	+ · ++ ·
349888691	2005-02-01, 15:19	90127-01-01-00	+ · +++
349894355	2005-02-01, 16:53	90127-01-01-00	+ · ++ ·
349917027	2005-02-01, 23:11	90127-01-01-06	+ · ++ ·
349922691	2005-02-02, 00:45	90127-01-01-06	+ · ++ ·
349928355	2005-02-02, 02:20	90127-01-01-06	+ · ++ ·
349934195	2005-02-02, 03:57	90127-01-01-06	+ · ++ ·
349940083	2005-02-02, 05:35	90127-01-01-06	+ · ++ ·
349945971	2005-02-02, 07:13	90127-01-01-08	+ · ++ ·
349951795	2005-02-02, 08:50	90127-01-01-09	+ · ++ ·
349957491	2005-02-02, 10:25	90127-01-01-10	+ · ++ ·
349962323	2005-02-02, 11:46	90127-01-01-10	+ · ++ ·
349967987	2005-02-02, 13:20	90127-01-01-10	++ · · ·
349973651	2005-02-02, 14:55	90127-01-01-10	+ · + · +
349984979	2005-02-02, 18:03	90127-01-01-11	+ · ++ ·
349996323	2005-02-02, 21:13	90127-01-01-01	+ · ++ ·
350001987	2005-02-02, 22:47	90127-01-01-01	+ · ++ ·
350007651	2005-02-03, 00:21	90127-01-01-01	+ · ++ ·
350013315	2005-02-03, 01:56	90127-01-01-01	+ · ++ ·
350019107	2005-02-03, 03:32	90127-01-01-01	++ · · ·
350030883	2005-02-03, 06:49	90127-01-01-07	+ · + · +
350036691	2005-02-03, 08:25	90127-01-01-12	+ · ++ ·
350042387	2005-02-03, 10:00	90127-01-01-02	+ · ++ ·
350047299	2005-02-03, 11:22	90127-01-01-02	+ · ++ ·
350052963	2005-02-03, 12:57	90127-01-01-02	+ · ++ ·
350064291	2005-02-03, 16:05	90127-01-01-13	+ · +++
350069955	2005-02-03, 17:40	90127-01-01-14	+ · ++ ·
350075619	2005-02-03, 19:14	90127-01-01-03	+ · + · ·
350081283	2005-02-03, 20:49	90127-01-01-03	+ · + · ·
350086947	2005-02-03, 22:23	90127-01-01-03	+ · + · ·
350092611	2005-02-03, 23:57	90127-01-01-03	+ · + · ·
		90127-01-01-15	+ · + · ·
		90127-01-01-15	+ · ++ ·
350098275	2005-02-04, 01:32	90127-01-01-15	+ · ++ ·
350104003	2005-02-04, 03:07	90127-01-01-15	+ · ++ ·
350109891	2005-02-04, 04:45	90127-01-01-15	+ · ++ ·
350115779	2005-02-04, 06:23	90127-01-01-16	+ · ++ ·
350353187	2005-02-07, 00:20	90127-01-02-09	+ · ++ ·
350358851	2005-02-07, 01:55	90127-01-02-09	+ · ++ ·
350364531	2005-02-07, 03:29	90127-01-02-09	+ · ++ ·
350381491	2005-02-07, 08:12	90127-01-02-000	+ · ++ ·
350387155	2005-02-07, 09:46	90127-01-02-000	+ · ++ ·
350392819	2005-02-07, 11:21	90127-01-02-000	+ · ++ ·
350398483	2005-02-07, 12:55	90127-01-02-000	+ · ++ ·
350404147	2005-02-07, 14:30	90127-01-02-000	+ · ++ ·
350409811	2005-02-07, 16:04	90127-01-02-00	+ · ++ ·
		90127-01-02-000	+ · ++ ·
350421171	2005-02-07, 19:13	90127-01-02-010	+ · +++
350426819	2005-02-07, 20:47	90127-01-02-010	+ · ++ ·
350432483	2005-02-07, 22:22	90127-01-02-010	+ · ++ ·
350438147	2005-02-07, 23:56	90127-01-02-010	+ · ++ ·
350443811	2005-02-08, 01:31	90127-01-02-010	+ · ++ ·
350449459	2005-02-08, 03:05	90127-01-02-01	+ · ++ ·
350455283	2005-02-08, 04:42	90127-01-02-01	+ · ++ ·
350466467	2005-02-08, 07:48	90127-01-02-02	+ · + · +
350472131	2005-02-08, 09:23	90127-01-02-12	+ · ++ ·
350477795	2005-02-08, 10:57	90127-01-02-12	+ · ++ ·
350489123	2005-02-08, 14:06	90127-01-02-03	+ · ++ ·
350500435	2005-02-08, 17:14	90127-01-02-14	+ · + · ·
350506099	2005-02-08, 18:49	90127-01-02-15	+ · + · ·
350545907	2005-02-09, 05:52	90127-01-02-04	+ · + · +
350551411	2005-02-09, 07:24	90127-01-02-11	+ · + · ·
350557091	2005-02-09, 08:59	90127-01-02-05	+ · + · ·
350562755	2005-02-09, 10:33	90127-01-02-05	+ · ++ ·
350568419	2005-02-09, 12:07	90127-01-02-05	+ · ++ ·
350574083	2005-02-09, 13:42	90127-01-02-05	+ · ++ ·
350591219	2005-02-09, 18:27	90127-01-02-07	+ · ++ ·
350596851	2005-02-09, 20:01	90127-01-02-10	+ · + · ·
350602403	2005-02-09, 21:34	90127-01-02-10	+ · ++ ·
350608067	2005-02-09, 23:08	90127-01-02-10	+ · ++ ·
350613731	2005-02-10, 00:43	90127-01-02-10	+ · ++ ·
350619395	2005-02-10, 02:17	90127-01-02-10	+ · ++ ·
350630787	2005-02-10, 05:27	90127-01-02-06	+ · ++ ·
350636371	2005-02-10, 07:00	90127-01-02-13	+ · ++ ·
350642035	2005-02-10, 08:34	90127-01-02-13	+ · ++ ·
350647699	2005-02-10, 10:09	90127-01-02-13	+ · ++ ·
350653363	2005-02-10, 11:43	90127-01-02-13	+ · ++ ·
350659043	2005-02-10, 13:18	90127-01-02-08	+ · ++ ·
351412339	2005-02-19, 06:33	80110-01-25-00	+ · ++ ·
351418003	2005-02-19, 08:07	80110-01-25-00	+ · + · ·
		80110-01-25-00	+ · ++ ·
351423875	2005-02-19, 09:45	80110-01-25-03	+ · + · ·
351429331	2005-02-19, 11:16	80110-01-25-02	+ · + · ·
351435011	2005-02-19, 12:51	80110-01-25-01	+ · ++ ·
352705971	2005-03-06, 05:53	91096-01-01-00	+ · + · ·
352711907	2005-03-06, 07:32	91096-01-01-01	+ · + · ·
352717763	2005-03-06, 09:10	91096-01-01-02	+ · + · ·
352723683	2005-03-06, 10:49	91096-01-01-03	+ · + · ·
352729571	2005-03-06, 12:27	91096-01-01-04	+ · + · ·
353736403	2005-03-18, 04:07	91096-01-02-01	+ · ++ ·
353742227	2005-03-18, 05:44	91096-01-02-00	+ · + · ·
353748083	2005-03-18, 07:22	91096-01-02-02	+ · ++ ·
353753955	2005-03-18, 09:00	91096-01-02-03	+ · + · ·
353759587	2005-03-18, 10:34	91096-01-02-04	+ · + · ·
354943811	2005-04-01, 03:31	91096-01-03-00	+ · ++ ·
354947459	2005-04-01, 04:31	91096-01-03-00	+ · ++ ·
354953123	2005-04-01, 06:06	91096-01-03-00	+ · ++ ·
354958787	2005-04-01, 07:40	91096-01-03-00	+ · + · ·
354964451	2005-04-01, 09:15	91096-01-03-01	+ · + · ·
355582755	2005-04-08, 13:00	91407-01-01-00	+ · ++ ·
356238691	2005-04-16, 03:12	91096-01-04-00	+ · ++ ·
356244355	2005-04-16, 04:46	91096-01-04-00	+ · ++ ·
356247027	2005-04-16, 05:31	91096-01-04-00	+ · ++ ·
356255699	2005-04-16, 07:55	91096-01-04-01	+ · + · ·
356261347	2005-04-16, 09:30	91096-01-04-02	+ · + · ·
357356339	2005-04-29, 01:39	91096-01-05-00	+ · + · ·
357362259	2005-04-29, 03:18	91096-01-05-02	+ · + · ·
357368147	2005-04-29, 04:56	91096-01-05-01	+ · ++ ·
357374003	2005-04-29, 06:34	91096-01-05-03	+ · ++ ·
357379827	2005-04-29, 08:11	91096-01-05-04	+ · ++ ·
359427731	2005-05-23, 01:03	91096-01-06-00	+ · + · ·
359433395	2005-05-23, 02:37	91096-01-06-01	+ · + · ·
359439059	2005-05-23, 04:11	91096-01-06-01	+ · + · ·
360803763	2005-06-07, 23:17	91096-01-07-00	+ · + · ·
360811955	2005-06-08, 01:33	91096-01-07-01	+ · + · ·
360817939	2005-06-08, 03:13	91096-01-07-02	+ · + · ·
360826435	2005-06-08, 05:34	91096-01-07-03	+ · + · ·
361751347	2005-06-18, 22:30	91096-01-08-00	+ · + · ·
361757203	2005-06-19, 00:07	91096-01-08-01	+ · + · ·
361763075	2005-06-19, 01:45	91096-01-08-02	+ · + · ·
361768947	2005-06-19, 03:23	91096-01-08-03	+ · + · ·
361775043	2005-06-19, 05:05	91096-01-08-04	+ · + · ·
362871987	2005-07-01, 21:47	91096-01-09-01	+ · + · ·
362877891	2005-07-01, 23:25	91096-01-09-02	+ · ++ ·
362888883	2005-07-02, 02:29	91096-01-09-00	+ · ++ ·
362893891	2005-07-02, 03:52	91096-01-09-00	++ · · ·
363986691	2005-07-14, 19:25	91096-01-10-00	+ · ++ ·
363992275	2005-07-14, 20:58	91096-01-10-00	+ · ++ ·
363997939	2005-07-14, 22:33	91096-01-10-00	+ · ++ ·
364003603	2005-07-15, 00:07	91096-01-10-01	+ · + · ·
364009251	2005-07-15, 01:41	80110-01-24-01	+++ · ·
365545907	2005-08-01, 20:32	80110-01-24-02	+ · + · ·
365551843	2005-08-01, 22:11	80110-01-24-03	+ · + · ·
365557715	2005-08-01, 23:49	80110-01-24-04	+ · + · ·
365566611	2005-08-02, 02:17	80110-01-24-00	+ · + · ·
365569491	2005-08-02, 03:05	80110-01-24-00	+ · + · ·
366236515	2005-08-09, 20:22	80110-01-26-00	+ · + · ·
366248307	2005-08-09, 23:39	80110-01-26-03	+ · + · ·
366254115	2005-08-10, 01:16	80110-01-26-04	+ · + · ·
367436019	2005-08-23, 17:34	80110-01-27-01	+ · + · ·
367441843	2005-08-23, 19:11	80110-01-27-01	+ · + · ·
367447571	2005-08-23, 20:47	80110-01-27-00	+ · + · ·
367452803	2005-08-23, 22:14	80110-01-27-02	+ · + · ·
367458019	2005-08-23, 23:41	80110-01-27-03G	+ · + · ·
368901571	2005-09-09, 16:40	80110-01-28-00	+ · + · ·
		80110-01-28-00	+ · ++ ·
368907235	2005-09-09, 18:14	80110-01-28-00	+++ · ·
368912899	2005-09-09, 19:49	80110-01-28-00	+ · + · +
368918547	2005-09-09, 21:23	80110-01-28-00	+ · + · ·
368924211	2005-09-09, 22:57	80110-01-28-01	+ · ++ ·
370024659	2005-09-22, 16:38	80110-01-29-00	+ · + · ·
370030595	2005-09-22, 18:17	80110-01-29-01	+ · + · ·
370036579	2005-09-22, 19:57	80110-01-29-02	+ · + · ·
370042451	2005-09-22, 21:35	80110-01-29-03	+ · + · ·
370715203	2005-09-30, 16:27	80110-01-30-00	+ · ++ ·
370721011	2005-09-30, 18:04	80110-01-30-01	+ · + · +
370726931	2005-09-30, 19:43	80110-01-30-02	+++ · ·
370732819	2005-09-30, 21:21	80110-01-30-03	+ · ++ ·
370738659	2005-09-30, 22:58	80110-01-30-04	+ · ++ ·
371110211	2005-10-05, 06:11	91429-01-01-00	+ · ++ ·
371115875	2005-10-05, 07:45	91429-01-01-00	+ · + · ·
372010899	2005-10-15, 16:22	80110-01-31-00	+++ · ·
372015875	2005-10-15, 17:45	80110-01-31-00	+ · + · +
372021539	2005-10-15, 19:19	80110-01-31-00	+++ · ·
372027203	2005-10-15, 20:54	80110-01-31-00	+ · ++ ·
373296355	2005-10-30, 13:26	80110-01-32-00	+ · + · +
373300723	2005-10-30, 14:39	80110-01-32-00	+++ · ·
373306371	2005-10-30, 16:13	80110-01-32-00	+ · ++ ·
373312051	2005-10-30, 17:48	80110-01-32-03	+ · + · ·
373317715	2005-10-30, 19:22	80110-01-32-01	+ · ++ ·
373323363	2005-10-30, 20:57	80110-01-32-02	+ · ++ ·
374333139	2005-11-11, 13:26	80110-01-33-00	+ · + · ·
374339123	2005-11-11, 15:06	80110-01-33-01	+ · + · ·
374345027	2005-11-11, 16:44	80110-01-33-03	+ · ++ ·
374350915	2005-11-11, 18:22	80110-01-33-02	+ · ++ ·
374356787	2005-11-11, 20:00	80110-01-33-04	+ · ++ ·
375538355	2005-11-25, 12:13	80110-01-34-02	+ · ++ ·
375544243	2005-11-25, 13:51	80110-01-34-00	+ · ++ ·
375550131	2005-11-25, 15:29	80110-01-34-01	+ · ++ ·
375555955	2005-11-25, 17:06	80110-01-34-03	+ · ++ ·
375561603	2005-11-25, 18:41	80110-01-34-04	+ · ++ ·
376914995	2005-12-11, 10:37	80110-01-35-01	+ · ++ ·
376918659	2005-12-11, 11:38	80110-01-35-00	+ · +++
376924659	2005-12-11, 13:18	80110-01-35-03	+ ++ + ·
376930179	2005-12-11, 14:50	80110-01-35-02	+ · ++ ·
376935347	2005-12-11, 16:16	80110-01-35-04	+ · +++
376940995	2005-12-11, 17:50	80110-01-35-04	++ · · ·
		80110-01-35-04	++++ ·
377949123	2005-12-23, 09:53	80110-01-36-00	+ · + · ·
377954035	2005-12-23, 11:14	80110-01-36-04	+ · + · ·
377965347	2005-12-23, 14:23	80110-01-36-01	+ · + · ·
377971011	2005-12-23, 15:57	80110-01-36-02	++ · · ·
377976675	2005-12-23, 17:32	80110-01-36-03	+ · ++ ·
379676611	2006-01-12, 09:44	80110-01-37-00	+ · + · ·
379682451	2006-01-12, 11:21	80110-01-37-01	+ · + · ·
379688355	2006-01-12, 13:00	80110-01-37-04	+ · + · ·
379694163	2006-01-12, 14:37	80110-01-37-02	+ · + · ·
379699907	2006-01-12, 16:12	80110-01-37-03	+ · + · ·
380621203	2006-01-23, 08:07	80110-01-38-00	+ · ++ ·
380627011	2006-01-23, 09:44	80110-01-38-01	+ · ++ ·
380632691	2006-01-23, 11:19	80110-01-38-02	+ · ++ ·
381916387	2006-02-07, 07:54	80110-01-39-00	+ · ++ ·
381922131	2006-02-07, 09:29	80110-01-39-02	+ · ++ ·
381927715	2006-02-07, 11:02	80110-01-39-04	+ · + · +
381933603	2006-02-07, 12:41	80110-01-39-01	+ ++ · ·
381939027	2006-02-07, 14:11	80110-01-39-03	++ · · ·
382948515	2006-02-19, 06:36	80110-01-40-00	+ · + · ·
382954531	2006-02-19, 08:16	80110-01-40-01	+ · + · ·
382960515	2006-02-19, 09:56	80110-01-40-02	+ · + · ·
382966371	2006-02-19, 11:33	80110-01-40-03	+ · + · ·
382974931	2006-02-19, 13:56	80110-01-40-04	+ · + · ·
384153587	2006-03-05, 05:20	92090-01-01-00	+ · + · ·
384159459	2006-03-05, 06:58	92090-01-01-01	+ · + · ·
384165331	2006-03-05, 08:36	92090-01-01-02	+ · + · ·
384171155	2006-03-05, 10:13	92090-01-01-03	+ · + · ·
384177011	2006-03-05, 11:51	92090-01-01-04	+ · + · ·
385188755	2006-03-17, 04:53	92090-01-02-00	+ · + · ·
385194403	2006-03-17, 06:27	92090-01-02-01	+ · + · ·
385199667	2006-03-17, 07:55	92090-01-02-02	+ · + · +
385205667	2006-03-17, 09:35	92090-01-02-04	++ · · ·
385210771	2006-03-17, 11:00	92090-01-02-03	+ · + · ·
386653667	2006-04-03, 03:48	92090-01-03-00	+ · + · +
386659331	2006-04-03, 05:23	92090-01-03-04	+ · + · ·
386664979	2006-04-03, 06:57	92090-01-03-03	+ · + · ·
386670659	2006-04-03, 08:31	92090-01-03-01	+ · + · ·
386676323	2006-04-03, 10:06	92090-01-03-02	+ · + · ·
387776339	2006-04-16, 03:39	92090-01-04-00	+ ++++
387782259	2006-04-16, 05:18	92090-01-04-01	+ · + · ·
387788131	2006-04-16, 06:56	92090-01-04-02	+ · + · ·
387793955	2006-04-16, 08:33	92090-01-04-03	+ · + · ·
389150659	2006-05-02, 01:25	92090-01-05-00	+ · + · ·
389156515	2006-05-02, 03:02	92090-01-05-01	+ · ++ ·
389162307	2006-05-02, 04:39	92090-01-05-02	+ · + · ·
389168035	2006-05-02, 06:14	92090-01-05-03	+ · + · ·
389172899	2006-05-02, 07:35	92090-01-05-04	+ · + · ·
390338067	2006-05-15, 19:15	92090-01-06-01	+ · + · ·
390360691	2006-05-16, 01:32	92090-01-06-00	+ · + · +
390366339	2006-05-16, 03:06	92090-01-06-00	· ++ · ·
		92090-01-06-00	++ · · ·
390372003	2006-05-16, 04:41	92090-01-06-00	· · ++ ·
390377651	2006-05-16, 06:15	92090-01-06-00	· · + · ·
391305587	2006-05-27, 00:00	92090-01-07-00	+ · ++ ·
391311251	2006-05-27, 01:35	92090-01-07-03	+ · ++ ·
391313731	2006-05-27, 02:16	92090-01-07-03	+ · ++ ·
391322563	2006-05-27, 04:43	92090-01-07-01	+ · + · ·
391328227	2006-05-27, 06:18	92090-01-07-02	+ · + · ·
392597555	2006-06-10, 22:53	92090-01-08-00	+ · ++ ·
392603395	2006-06-11, 00:30	92090-01-08-01	+ · ++ ·

Table B.2: Continuous segments from *RXTE* PCA observations of Cyg X-1 between 1996-02-12 and 2010-10-12 (continued)

T_{RXTE} (s)	Date (Y-m-d, H:M)	ObsID	PCUs 0 1 2 3 4
392609251	2006-06-11, 02:08	92090-01-08-02	+ + + · ·
392615171	2006-06-11, 03:47	92090-01-08-03	+ · + + ·
392621011	2006-06-11, 05:24	92090-01-08-04	+ · + · +
393977507	2006-06-26, 22:12	92090-01-09-01	+ · + · ·
393983155	2006-06-26, 23:46	92090-01-09-00	· · + · ·
		92090-01-09-00	+ · + · ·
393988211	2006-06-27, 01:11	92090-01-09-00	· · + · ·
393993875	2006-06-27, 02:45	92090-01-09-00	· · + · ·
393999539	2006-06-27, 04:19	92090-01-09-00	· · + · +
395181907	2006-07-10, 20:46	92090-01-10-00	+ · + · ·
395187571	2006-07-10, 22:20	92090-01-10-00	+ · + · ·
395193219	2006-07-10, 23:54	92090-01-10-00	+ · + · ·
395198963	2006-07-11, 01:30	92090-01-10-01	+ · + · ·
395204531	2006-07-11, 03:03	92090-01-10-02	+ · + · ·
396128643	2006-07-21, 19:45	92090-01-11-00	+ + + · ·
396134739	2006-07-21, 21:26	92090-01-11-01	+ · + · ·
396140691	2006-07-21, 23:05	92090-01-11-02	+ · + · ·
396149683	2006-07-22, 01:35	92090-01-11-03	+ + + · ·
396152483	2006-07-22, 02:22	92090-01-11-03	+ + + · ·
396155347	2006-07-22, 03:10	92090-01-11-04	+ + + · ·
397508947	2006-08-06, 19:10	92090-01-12-00	· · + · ·
397515059	2006-08-06, 20:51	92090-01-12-01	· · + + ·
397520691	2006-08-06, 22:25	92090-01-12-02	· · + · ·
397526547	2006-08-07, 00:03	92090-01-12-03	· · + + ·
397532163	2006-08-07, 01:37	92090-01-12-04	+ · + · ·
398718691	2006-08-20, 19:12	92090-01-13-00	+ · + · ·
398724355	2006-08-20, 20:46	92090-01-13-00	+ · + · +
398730003	2006-08-20, 22:21	92090-01-13-00	+ · + + ·
398735667	2006-08-20, 23:55	92090-01-13-00	+ · + · ·
399838771	2006-09-02, 18:20	92090-01-14-00	+ · + + ·
399844419	2006-09-02, 19:54	92090-01-14-00	+ · + · +
399847107	2006-09-02, 20:39	92090-01-14-00	+ · + · +
399850083	2006-09-02, 21:29	92090-01-14-01	+ · + + ·
399855747	2006-09-02, 23:03	92090-01-14-02	+ + + · ·
399861411	2006-09-03, 00:37	92090-01-14-03	+ · + · ·
401215539	2006-09-18, 16:46	92090-01-15-00	· + + · ·
401221411	2006-09-18, 18:24	92090-01-15-01	· · + + ·
401227347	2006-09-18, 20:03	92090-01-15-02	+ · + · ·
401233203	2006-09-18, 21:41	92090-01-15-03	+ · + · +
401239091	2006-09-18, 23:19	92090-01-15-04	+ · + + ·
402335235	2006-10-01, 15:48	80110-01-41-02	+ · + · ·
402341123	2006-10-01, 17:26	80110-01-41-01	+ · + · +
402346771	2006-10-01, 19:00	80110-01-41-03	+ · + · +
402351411	2006-10-01, 20:17	80110-01-41-00G	+ · + · ·
402357059	2006-10-01, 21:51	80110-01-41-00G	+ · + · ·
402359203	2006-10-01, 22:27	80110-01-41-00G	+ · + · ·
403625795	2006-10-16, 14:17	80110-01-42-00	+ · + · +
403629811	2006-10-16, 15:24	80110-01-42-00	+ · + + ·
403635459	2006-10-16, 16:58	80110-01-42-00	+ · + · ·
403641123	2006-10-16, 18:33	80110-01-42-00	+ · + · ·
403646771	2006-10-16, 20:07	80110-01-42-00	+ · + · ·
404823619	2006-10-30, 11:01	80110-01-43-00	+ · + + ·
404830787	2006-10-30, 13:00	80110-01-43-01	+ · + · ·
404837059	2006-10-30, 14:45	80110-01-43-02	+ · + · +
404848947	2006-10-30, 18:03	80110-01-43-03	+ + + · ·
404857587	2006-10-30, 20:27	80110-01-43-04	+ · + + ·
406126291	2006-11-14, 12:52	80110-01-44-00	· · + + ·
406132131	2006-11-14, 14:29	80110-01-44-01	· · + · +
406138051	2006-11-14, 16:08	80110-01-44-02	+ + + · ·
406143827	2006-11-14, 17:44	80110-01-44-03	+ · + · ·
406149507	2006-11-14, 19:19	80110-01-44-04	+ · + · ·
407160867	2006-11-26, 12:15	80110-01-45-00	+ · + + ·
407166643	2006-11-26, 13:51	80110-01-45-00	+ + + · ·
407171683	2006-11-26, 15:15	80110-01-45-00	+ · + + ·
407183011	2006-11-26, 18:24	80110-01-45-01	+ · + · +
408365747	2006-12-10, 10:56	80110-01-46-00	+ · + + ·
408371155	2006-12-10, 12:26	80110-01-46-01	+ · + + ·
408376403	2006-12-10, 13:54	80110-01-46-01	+ · + + ·
408387715	2006-12-10, 17:02	80110-01-46-02	+ · + + ·
409487187	2006-12-23, 10:27	80110-01-47-00	+ · + · ·
409493187	2006-12-23, 12:07	80110-01-47-02	+ · + · +
409499027	2006-12-23, 13:44	80110-01-47-01	+ · + · +
409508371	2006-12-23, 16:20	80110-01-47-03	+ · + · ·
409510771	2006-12-23, 17:00	80110-01-47-03	+ · + · ·
410606739	2007-01-05, 09:26	80110-01-48-00	+ · + · +
410612547	2007-01-05, 11:03	80110-01-48-02	+ · + + ·
410618435	2007-01-05, 12:41	80110-01-48-03	+ + + · ·
410624259	2007-01-05, 14:18	80110-01-48-04	+ · + + ·
410629939	2007-01-05, 15:53	80110-01-48-01	+ · + · +
411986867	2007-01-21, 08:48	80110-01-49-00	+ · + · ·
411991395	2007-01-21, 10:04	80110-01-49-00	+ · + · ·
411997059	2007-01-21, 11:38	80110-01-49-00	+ · + · ·
412002707	2007-01-21, 13:12	80110-01-49-00	+ · + · ·
412008371	2007-01-21, 14:47	80110-01-49-00	+ · + · ·
413190419	2007-02-04, 07:07	80110-01-50-00	· + + · ·
413196051	2007-02-04, 08:41	80110-01-50-01	· · + · ·
413198483	2007-02-04, 09:22	80110-01-50-01	· · + · ·
413201715	2007-02-04, 10:16	80110-01-50-01	· · + · ·
413207379	2007-02-04, 11:50	80110-01-50-02	+ · + · ·
413213027	2007-02-04, 13:24	80110-01-50-03	+ · + · ·
414396995	2007-02-18, 06:17	80110-01-51-00	+ · + + ·
414402883	2007-02-18, 07:55	80110-01-51-01	+ · + + ·
414408787	2007-02-18, 09:34	80110-01-51-02	+ · + · +
414414675	2007-02-18, 11:12	80110-01-51-03	+ + + · ·
414420451	2007-02-18, 12:48	80110-01-51-04	+ · + + ·
415516387	2007-03-03, 05:14	80110-01-52-01	+ · + · ·
415522211	2007-03-03, 06:51	80110-01-52-02	· · + · ·
415527939	2007-03-03, 08:26	80110-01-52-03	+ · + · ·
415533187	2007-03-03, 09:54	80110-01-52-00	+ · + · +
415538291	2007-03-03, 11:19	80110-01-52-00	+ · + · ·
416273475	2007-03-11, 23:32	92130-01-01-00	+ · + · ·
416279123	2007-03-12, 01:06	92130-01-01-00	+ · + · ·
416725859	2007-03-17, 05:11	80110-01-53-02	+ · + · ·
416732563	2007-03-17, 07:03	80110-01-53-00	+ · + · +
416737171	2007-03-17, 08:20	80110-01-53-00	+ · + · ·
		80110-01-53-00	+ · + + ·
416742819	2007-03-17, 09:54	80110-01-53-00	+ · + · +
416748467	2007-03-17, 11:28	80110-01-53-01	+ + + · ·
418017411	2007-04-01, 03:57	80110-01-54-00	+ · + · +
418023443	2007-04-01, 05:38	80110-01-54-01	+ · + + ·
418029379	2007-04-01, 07:17	80110-01-54-02	· + + · ·
418035219	2007-04-01, 08:54	80110-01-54-03	+ · + + ·
418041091	2007-04-01, 10:32	80110-01-54-04	+ · + · +
419221619	2007-04-15, 02:27	80110-01-55-00	+ · + · +
419227427	2007-04-15, 04:04	80110-01-55-01	+ · + + ·
419233347	2007-04-15, 05:43	80110-01-55-02	· · + + ·
419239171	2007-04-15, 07:20	80110-01-55-03	+ · + · ·
419244947	2007-04-15, 08:56	80110-01-55-04	+ · + + ·
420601923	2007-05-01, 01:53	92090-01-16-01	+ · + + ·
420606083	2007-05-01, 03:02	92090-01-16-00	+ · + · +
420611747	2007-05-01, 04:36	92090-01-16-00	+ · + + ·
420617395	2007-05-01, 06:10	92090-01-16-00	+ · + · ·
420623043	2007-05-01, 07:45	92090-01-16-00	+ · + + ·
421635203	2007-05-13, 00:54	92090-01-17-00	+ + + · ·
421640867	2007-05-13, 02:28	92090-01-17-00	+ · + + ·
421646515	2007-05-13, 04:02	92090-01-17-00	+ · + · +
421652179	2007-05-13, 05:37	92090-01-17-01	+ · + · +
421657827	2007-05-13, 07:11	92090-01-17-02	+ · + · +
422073139	2007-05-18, 02:33	92090-01-17-10	· + + · ·
422079155	2007-05-18, 04:13	92090-01-17-12	· + + · ·
422082051	2007-05-18, 05:01	92090-01-17-13	· · + + ·
422093363	2007-05-18, 08:10	92090-01-17-11	· · + + ·
422757043	2007-05-26, 00:31	92090-01-18-00	+ · + + ·
422763027	2007-05-26, 02:11	92090-01-18-01	+ + + · ·
422768867	2007-05-26, 03:48	92090-01-18-02	+ · + · +
422774691	2007-05-26, 05:25	92090-01-18-03	+ · + + ·
422780595	2007-05-26, 07:04	92090-01-18-04	+ + + · ·
424136323	2007-06-10, 23:39	92090-01-19-03	+ · + · ·
424142243	2007-06-11, 01:18	92090-01-19-02	+ + + · ·
424147843	2007-06-11, 02:51	92090-01-19-01	+ · + · ·
424152435	2007-06-11, 04:08	92090-01-19-00	+ · + · ·
424158099	2007-06-11, 05:42	92090-01-19-00	+ · + · ·
425339891	2007-06-24, 21:59	92090-01-20-01	+ · + · ·
425345507	2007-06-24, 23:32	92090-01-20-00G	+ · + · ·
425351155	2007-06-25, 01:06	92090-01-20-00G	+ · + · ·
425356803	2007-06-25, 02:41	92090-01-20-00G	+ · + · ·
426374755	2007-07-06, 21:26	93121-01-01-00	+ · + · ·
426382851	2007-07-06, 23:41	93121-01-01-01	+ · + · ·
426385971	2007-07-07, 00:33	93121-01-01-04	+ · + · ·
426391635	2007-07-07, 02:08	93121-01-01-02	+ · + · ·
426397283	2007-07-07, 03:42	93121-01-01-03	+ · + · ·
427581027	2007-07-20, 20:31	93121-01-02-00	· · + + ·
427586915	2007-07-20, 22:09	93121-01-02-01	· + + · ·
427592755	2007-07-20, 23:46	93121-01-02-02	· · + · ·
427598675	2007-07-21, 01:25	93121-01-02-03	+ · + · ·
427604531	2007-07-21, 03:03	93121-01-02-04	+ · + · ·
428960131	2007-08-05, 19:36	93121-01-03-01	+ · + + ·
428965795	2007-08-05, 21:10	93121-01-03-00	+ + + · ·
428970851	2007-08-05, 22:35	93121-01-03-00	+ · + · ·
428976499	2007-08-06, 00:09	93121-01-03-00	+ · + · ·
428982147	2007-08-06, 01:43	93121-01-03-00	+ · + · ·
430164211	2007-08-19, 18:04	93121-01-04-00	+ + + · ·
430169491	2007-08-19, 19:32	93121-01-04-00	+ · + · ·
430175139	2007-08-19, 21:06	93121-01-04-00	+ · + · +
430180803	2007-08-19, 22:41	93121-01-04-00	+ · + · ·
430186451	2007-08-20, 00:15	93121-01-04-01	+ + + · ·
431200771	2007-08-31, 18:00	93121-01-05-00	· · + · ·
431206707	2007-08-31, 19:39	93121-01-05-01	+ · + · ·
431212691	2007-08-31, 21:19	93121-01-05-03	+ · + · ·
431218531	2007-08-31, 22:56	93121-01-05-02	+ · + · ·
431224435	2007-09-01, 00:34	93121-01-05-04	+ · + · ·
432404691	2007-09-14, 16:25	93121-01-06-00	+ · + · ·
432410563	2007-09-14, 18:03	93121-01-06-01	+ · + · +
432416435	2007-09-14, 19:41	93121-01-06-02	+ · + · ·
432422291	2007-09-14, 21:19	93121-01-06-03	+ · + · ·
432428019	2007-09-14, 22:54	93121-01-06-04	+ · + · ·
433698819	2007-09-29, 15:54	93121-01-07-00	+ · + · ·
434817987	2007-10-12, 14:47	93121-01-08-00	+ · + + ·
434823635	2007-10-12, 16:21	93121-01-08-00	+ + + · ·
434829283	2007-10-12, 17:55	93121-01-08-00	+ · + · +
434834947	2007-10-12, 19:30	93121-01-08-01	+ · + · +
434840611	2007-10-12, 21:04	93121-01-08-02	+ · + + ·
436018403	2007-10-26, 12:14	93121-01-09-00	· · + + ·
436024371	2007-10-26, 13:53	93121-01-09-01	· · + · +
436030275	2007-10-26, 15:32	93121-01-09-02	· · + · ·
436036131	2007-10-26, 17:09	93121-01-09-03	+ + + · ·
436041987	2007-10-26, 18:47	93121-01-09-04	+ + + · ·
437318723	2007-11-10, 13:26	93121-01-10-01	· · + + ·
437324515	2007-11-10, 15:02	93121-01-10-02	· + + · ·
437330195	2007-11-10, 16:37	93121-01-10-00	+ · + · ·
437334851	2007-11-10, 17:55	93121-01-10-00	+ · + + ·
437340499	2007-11-10, 19:29	93121-01-10-00	+ · + + ·
438606867	2007-11-25, 11:15	93121-01-11-00	+ + + · ·
438612531	2007-11-25, 12:49	93121-01-11-00	· · + · ·
		93121-01-11-00	+ · + · ·
438618179	2007-11-25, 14:23	93121-01-11-00	· · + · +
438623827	2007-11-25, 15:58	93121-01-11-00	· · + · ·
438629491	2007-11-25, 17:32	93121-01-11-00	· + + · ·
439988531	2007-12-11, 11:03	93121-01-12-00	· · + + ·
439994451	2007-12-11, 12:41	93121-01-12-01	· · + + ·
440000419	2007-12-11, 14:21	93121-01-12-02	· + + · ·
440006259	2007-12-11, 15:58	93121-01-12-03	· · + · ·
440012067	2007-12-11, 17:35	93121-01-12-04	+ · + · ·
441022835	2007-12-23, 10:21	93121-01-13-00	+ · + · +
441028707	2007-12-23, 11:59	93121-01-13-01	+ · + · ·
441034579	2007-12-23, 13:37	93121-01-13-02	+ · + + ·
441040419	2007-12-23, 15:14	93121-01-13-03	+ · + · ·
441046179	2007-12-23, 16:50	93121-01-13-04	+ + + · ·
442141747	2008-01-05, 09:10	93121-01-14-01	+ + + · ·
442147363	2008-01-05, 10:43	93121-01-14-00	+ · + · ·
442152499	2008-01-05, 12:09	93121-01-14-00	+ · + · ·
442158147	2008-01-05, 13:43	93121-01-14-00	· + + · ·
		93121-01-14-00	+ + + · ·
442163811	2008-01-05, 15:17	93121-01-14-00	· · + · ·
443436083	2008-01-20, 08:42	93121-01-15-00	· + + · ·
443441379	2008-01-20, 10:10	93121-01-15-00	· · + · ·
443447027	2008-01-20, 11:44	93121-01-15-03	· · + · ·
443452675	2008-01-20, 13:18	93121-01-15-01	· + + · ·
443458339	2008-01-20, 14:53	93121-01-15-02	· · + · +
444472643	2008-02-01, 08:38	93121-01-16-00	+ + + · ·
444478531	2008-02-01, 10:16	93121-01-16-01	+ · + · ·
444484435	2008-02-01, 11:54	93121-01-16-02	+ · + · ·
444490227	2008-02-01, 13:31	93121-01-16-03	+ · + · +
445676275	2008-02-15, 06:58	93121-01-17-00	+ · + + ·
445682083	2008-02-15, 08:35	93121-01-17-01	+ · + · ·
445687971	2008-02-15, 10:13	93121-01-17-02	+ · + · ·
		93121-01-17-02	+ · + + ·
445693699	2008-02-15, 11:49	93121-01-17-03	+ + + · ·
445699379	2008-02-15, 13:23	93121-01-17-04	+ + + · ·
447139395	2008-03-03, 05:24	93121-01-18-01	· · + · ·
447145059	2008-03-03, 06:58	93121-01-18-00	· · + · ·
447150707	2008-03-03, 08:32	93121-01-18-03	· · + · ·
447156403	2008-03-03, 10:07	93121-01-18-04	· + + · ·
448258723	2008-03-16, 04:19	93121-01-19-00	· + + · ·
448266803	2008-03-16, 06:34	93121-01-19-01	· · + · ·
448272851	2008-03-16, 08:15	93121-01-19-02	· + + · ·
448281347	2008-03-16, 10:36	93121-01-19-03	+ + + · ·
449470531	2008-03-30, 04:56	93121-01-20-00	· · + · ·
449476419	2008-03-30, 06:34	93121-01-20-01	· + + · ·
449482291	2008-03-30, 08:12	93121-01-20-02	· · + · ·
449488163	2008-03-30, 09:50	93121-01-20-03	· + + · ·
450589283	2008-04-12, 03:42	93121-01-21-02	· · + · ·
450595059	2008-04-12, 05:18	93121-01-21-01	· · + · ·
450600371	2008-04-12, 06:47	93121-01-21-00	· · + · ·
450605443	2008-04-12, 08:11	93121-01-21-00	· · + · ·
450611107	2008-04-12, 09:46	93121-01-21-03	· · + · ·
451142435	2008-04-18, 13:21	93120-01-01-000	· · + · +
451148083	2008-04-18, 14:55	93120-01-01-000	· · + · ·
451153747	2008-04-18, 16:30	93120-01-01-000	· + + · ·
451159395	2008-04-18, 18:04	93120-01-01-000	+ · + · ·
451165043	2008-04-18, 19:38	93120-01-01-000	· + + · ·
451170691	2008-04-18, 21:12	93120-01-01-00	· · + · ·
451176355	2008-04-18, 22:46	93120-01-01-00	· · + · +
451182147	2008-04-19, 00:23	93120-01-01-00	· · + · ·
451187811	2008-04-19, 01:57	93120-01-01-01	· + + · ·
451193315	2008-04-19, 03:29	93120-01-01-01	+ · + · ·
451244179	2008-04-19, 17:37	93120-01-01-02	+ · + · ·
451249827	2008-04-19, 19:11	93120-01-01-02	· + + · ·
451793667	2008-04-26, 02:15	93121-01-22-00	· · + · ·
451798099	2008-04-26, 03:29	93121-01-22-00	· · + · ·
451803747	2008-04-26, 05:03	93121-01-22-02	· · + · ·
451809395	2008-04-26, 06:37	93121-01-22-02	· · + · ·
451812403	2008-04-26, 07:27	93121-01-22-02	· · + · ·
451815059	2008-04-26, 08:11	93121-01-22-01	· · + · ·
453264563	2008-05-13, 02:50	93121-01-23-00	· · + · ·
453270467	2008-05-13, 04:28	93121-01-23-01	· + + · ·
453276291	2008-05-13, 06:05	93121-01-23-02	· · + · +
453282179	2008-05-13, 07:43	93121-01-23-03	· · + · ·
453288083	2008-05-13, 09:22	93121-01-23-04	· · + · ·
454292707	2008-05-25, 00:26	93121-01-24-00	· · + · ·
454298563	2008-05-25, 02:03	93121-01-24-01	+ · + · ·
454304483	2008-05-25, 03:42	93121-01-24-02	· · + · ·
454310211	2008-05-25, 05:17	93121-01-24-03	· + + · ·
454315923	2008-05-25, 06:53	93121-01-24-04	· · + · ·
455586147	2008-06-08, 23:43	93121-01-25-01	· · + · +
455591747	2008-06-09, 01:16	93121-01-25-00	· · + + ·
455597395	2008-06-09, 02:50	93121-01-25-00	· + + · ·
455603043	2008-06-09, 04:25	93121-01-25-00	· · + · ·
		93121-01-25-00	+ · + · ·
456705203	2008-06-21, 22:34	93121-01-26-00	· · + · ·
456710851	2008-06-22, 00:08	93121-01-26-00	· · + · ·
456713315	2008-06-22, 00:49	93121-01-26-00	· · + · ·
456722163	2008-06-22, 03:17	93121-01-26-02	· + + · ·
456727811	2008-06-22, 04:51	93121-01-26-03	· · + · ·
457911315	2008-07-05, 21:36	93121-01-27-00	· + + · ·
457917171	2008-07-05, 23:13	93121-01-27-01	+ · + · ·
457923043	2008-07-06, 00:51	93121-01-27-02	· + + · ·
457928883	2008-07-06, 02:29	93121-01-27-03	+ · + · ·
457934739	2008-07-06, 04:06	93121-01-27-04	· + + · ·
459029955	2008-07-18, 20:20	93121-01-28-00	· · + · ·
459035811	2008-07-18, 21:57	93121-01-28-01	· + + · ·
459041619	2008-07-18, 23:34	93121-01-28-02	+ · + · ·

Table B.2: Continuous segments from *RXTE* PCA observations of Cyg X-1 between 1996-02-12 and 2010-10-12 (continued)

T_{RXTE} (s)	Date (Y-m-d, H:M)	ObsID	PCUs 0 1 2 3 4
459047299	2008-07-19, 01:09	93121-01-28-03	· + + · ·
459051779	2008-07-19, 02:23	93121-01-28-03	· · + · ·
460238691	2008-08-01, 20:05	93121-01-29-00	+ · + · ·
460244355	2008-08-01, 21:40	93121-01-29-00	· · + · ·
460250003	2008-08-01, 23:14	93121-01-29-00	· + + · ·
460255651	2008-08-02, 00:48	93121-01-29-00	· · + · ·
460261299	2008-08-02, 02:22	93121-01-29-01	· · + · ·
461704883	2008-08-18, 19:22	93121-01-30-00	· · + · ·
461710867	2008-08-18, 21:02	93121-01-30-01	· · + · ·
461716739	2008-08-18, 22:39	93121-01-30-02	· · + · ·
461722627	2008-08-19, 00:18	93121-01-30-03	· · + · ·
463168307	2008-09-04, 17:52	93121-01-31-00	· · + + · +
463174131	2008-09-04, 19:29	93121-01-31-01	+ · + · +
463942275	2008-09-13, 16:52	93121-01-32-01	+ · + · ·
463947891	2008-09-13, 18:25	93121-01-32-00	· · + + ·
463952963	2008-09-13, 19:50	93121-01-32-00	· + + · ·
463958611	2008-09-13, 21:24	93121-01-32-00	· · + · ·
463964275	2008-09-13, 22:58	93121-01-32-00	· · + · ·
465405459	2008-09-30, 15:18	93121-01-33-00	· · + · ·
465411107	2008-09-30, 16:52	93121-01-33-02	· · + · ·
465416755	2008-09-30, 18:26	93121-01-33-01	· · + · ·
465422419	2008-09-30, 20:01	93121-01-33-04	· · + · ·
465428067	2008-09-30, 21:35	93121-01-33-03	· · + · ·
466442019	2008-10-12, 15:14	93121-01-34-00	· · + · ·
466447843	2008-10-12, 16:51	93121-01-34-01	+ · + · ·
466453731	2008-10-12, 18:29	93121-01-34-02	· + + · ·
466459587	2008-10-12, 20:07	93121-01-34-03	· + + · ·
466465571	2008-10-12, 21:47	93121-01-34-04	· + + · ·
467475923	2008-10-24, 14:26	93121-01-35-00	+ · + · ·
467481763	2008-10-24, 16:03	93121-01-35-01	· + + · ·
467487635	2008-10-24, 17:41	93121-01-35-02	· · + · ·
467493347	2008-10-24, 19:16	93121-01-35-03	+ · + · ·
467498659	2008-10-24, 20:45	93121-01-35-04	· · + · ·
468853923	2008-11-09, 13:13	93121-01-36-00	· · + · ·
468859571	2008-11-09, 14:47	93121-01-36-01 93121-01-36-01	· · + · · + · + · ·
468865235	2008-11-09, 16:21	93121-01-36-01	· + + · ·
468870867	2008-11-09, 17:55	93121-01-36-03	· · + · ·
468876531	2008-11-09, 19:29	93121-01-36-02	· + + · ·
469972931	2008-11-22, 12:03	93121-01-37-00	· + + · ·
469978579	2008-11-22, 13:37	93121-01-37-00	· · + · ·
469980995	2008-11-22, 14:17	93121-01-37-00	· · + · ·
469989907	2008-11-22, 16:46	93121-01-37-03	+ · + · ·
469995555	2008-11-22, 18:20	93121-01-37-02	+ · + · ·
471269299	2008-12-07, 12:09	93121-01-38-00	· · + · ·
471275139	2008-12-07, 13:46	93121-01-38-01	· + + · ·
471280963	2008-12-07, 15:23	93121-01-38-02	· · + · ·
471286851	2008-12-07, 17:01	93121-01-38-03	· · + · +
471292723	2008-12-07, 18:39	93121-01-38-04	· · + · +
472472435	2008-12-21, 10:21	93121-01-39-01	· + + · ·
472478227	2008-12-21, 11:58	93121-01-39-02	· · + + ·
472483955	2008-12-21, 13:33	93121-01-39-00	· · + + ·
472488723	2008-12-21, 14:53	93121-01-39-00	+ · + · ·
472494371	2008-12-21, 16:27	93121-01-39-03	· · + · +
473505939	2009-01-02, 09:26	94121-01-01-00 94121-01-01-00	· · + · · + · + · ·
473511587	2009-01-02, 11:00	94121-01-01-00	· + + · ·
473517235	2009-01-02, 12:34	94121-01-01-00	· · + + ·
473522899	2009-01-02, 14:09	94121-01-01-00	· · + · ·
473528547	2009-01-02, 15:43	94121-01-01-01	· · + · +
474887123	2009-01-18, 09:06	94121-01-02-00	+ · + · ·
474893123	2009-01-18, 10:46	94121-01-02-01	· + + · ·
474898947	2009-01-18, 12:23	94121-01-02-02	· · + + ·
474904899	2009-01-18, 14:02	94121-01-02-03	+ · + · ·
474910755	2009-01-18, 15:40	94121-01-02-04	· · + · ·
476090419	2009-02-01, 07:21	94121-01-03-00	+ · + · ·
476096307	2009-02-01, 08:59	94121-01-03-01	· · + + ·
476102083	2009-02-01, 10:35	94121-01-03-02	· · + · ·
476108003	2009-02-01, 12:14	94121-01-03-03	· · + · +
476113715	2009-02-01, 13:49	94121-01-03-04	+ · + · ·
477124131	2009-02-13, 06:29	94121-01-04-01	+ · + · ·
477129779	2009-02-13, 08:03	94121-01-04-00	· · + + ·
477134931	2009-02-13, 09:29	94121-01-04-00	· · + · ·

T_{RXTE} (s)	Date (Y-m-d, H:M)	ObsID	PCUs 0 1 2 3 4
477140579	2009-02-13, 11:03	94121-01-04-00	· · + · ·
477146211	2009-02-13, 12:37	94121-01-04-02	· · + · ·
478287683	2009-02-26, 17:42	94121-01-05-00	· · + · ·
478293347	2009-02-26, 19:16	94121-01-05-00	· · + · ·
478298995	2009-02-26, 20:50	94121-01-05-00	· · + · ·
479538787	2009-03-13, 05:14	94121-01-06-00	+ · + · ·
479544707	2009-03-13, 06:52	94121-01-06-01	· + + · ·
479550611	2009-03-13, 08:31	94121-01-06-02	+ · + · ·
479556435	2009-03-13, 10:08	94121-01-06-03	· + + · ·
479562307	2009-03-13, 11:46	94121-01-06-04	· + + · ·
480917187	2009-03-29, 04:07	94121-01-07-01	· + + · ·
480922995	2009-03-29, 05:44	94121-01-07-02	+ · + · ·
480928707	2009-03-29, 07:19	94121-01-07-03	· · + + ·
480934035	2009-03-29, 08:48	94121-01-07-04	· · + · +
480938931	2009-03-29, 10:09	94121-01-07-00	+ · + · ·
482116483	2009-04-12, 01:15	94121-01-08-01	+ · + · ·
482119923	2009-04-12, 02:13	94121-01-08-00	· · + · ·
482125571	2009-04-12, 03:47	94121-01-08-00 94121-01-08-00	· · + · · · · + + ·
482131219	2009-04-12, 05:21	94121-01-08-00	· · + · +
482137059	2009-04-12, 06:58	94121-01-08-02	· · + · ·
483150323	2009-04-24, 00:26	94121-01-09-00	· + + · ·
483154067	2009-04-24, 01:28	94121-01-09-00	· + + · +
483161987	2009-04-24, 03:40	94121-01-09-01	+ · + · ·
483171027	2009-04-24, 06:11	94121-01-09-02	+ · + · ·
483176691	2009-04-24, 07:45	94121-01-09-03	+ · + · ·
484268963	2009-05-06, 23:10	94121-01-27-00	· · + · ·
484274787	2009-05-07, 00:47	94121-01-27-00	· · + · ·
484280723	2009-05-07, 02:26	94121-01-27-00	· · + · ·
484879331	2009-05-14, 00:43	94121-01-10-00	· + + · ·
484885187	2009-05-14, 02:20	94121-01-10-01	· · + · +
484891043	2009-05-14, 03:58	94121-01-10-02	· · + + ·
484896883	2009-05-14, 05:35	94121-01-10-03	· · + · +
485399043	2009-05-20, 01:05	94121-01-11-02	+ · + · ·
485404835	2009-05-20, 02:41	94121-01-11-01	· + + · ·
485410547	2009-05-20, 04:16	94121-01-11-00	· · + + ·
485415203	2009-05-20, 05:34	94121-01-11-00	· · + · +
486767683	2009-06-04, 21:15	94121-01-12-01	· · + · +
486771283	2009-06-04, 22:15	94121-01-12-01	+ · + · ·
486776947	2009-06-04, 23:50	94121-01-12-01 94121-01-12-02 94121-01-12-02	+ + + · · · · + · · + · + · ·
486782595	2009-06-05, 01:24	94121-01-12-00	· + + · ·
486788243	2009-06-05, 02:58	94121-01-12-00	· · + · ·
488158035	2009-06-20, 23:28	94121-01-13-00	+ · + · ·
488163971	2009-06-21, 01:07	94121-01-13-01	· + + · ·
488169811	2009-06-21, 02:44	94121-01-13-02	· · + + ·
488175651	2009-06-21, 04:21	94121-01-13-03	· · + · +
489361091	2009-07-04, 21:39	94121-01-14-00	· · + + ·
489366883	2009-07-04, 23:15	94121-01-14-01	· · + + ·
489372771	2009-07-05, 00:53	94121-01-14-02	· · + · ·
489378467	2009-07-05, 02:28	94121-01-14-03	· · + · +
489383923	2009-07-05, 03:59	94121-01-14-04	· + + · ·
491688403	2009-07-31, 20:07	94121-01-16-00	+ · + · ·
491693715	2009-07-31, 21:36	94121-01-16-00	· · + + ·
491696259	2009-07-31, 22:18	94121-01-16-00	· · + + ·
491699555	2009-07-31, 23:13	94121-01-16-03	· · + · ·
491705027	2009-08-01, 00:44	94121-01-16-01	· · + · ·
491710675	2009-08-01, 02:18	94121-01-16-02	· · + · +
492978339	2009-08-15, 18:26	94121-01-17-00	· · + · ·
492984227	2009-08-15, 20:04	94121-01-17-01	+ · + · ·
492990131	2009-08-15, 21:43	94121-01-17-02	· + + · ·
492996019	2009-08-15, 23:21	94121-01-17-03	· · + + ·
493001811	2009-08-16, 00:57	94121-01-17-04	· · + · +
494187203	2009-08-29, 18:14	94121-01-18-02	· + + · ·
494192979	2009-08-29, 19:50	94121-01-18-01	· · + · ·
494198659	2009-08-29, 21:25	94121-01-18-03	+ · + · ·
494203363	2009-08-29, 22:43	94121-01-18-00	· · + · +
494209011	2009-08-30, 00:17	94121-01-18-00	· + + · ·
495395523	2009-09-12, 17:53	94121-01-19-01 94121-01-19-01	· · + · · · · + + ·
497719747	2009-10-09, 15:30	94121-01-21-00	· · + + ·
497725539	2009-10-09, 17:06	94121-01-21-01	· · + + ·

T_{RXTE} (s)	Date (Y-m-d, H:M)	ObsID	PCUs 0 1 2 3 4
497731507	2009-10-09, 18:46	94121-01-21-02	· · + + ·
497737283	2009-10-09, 20:22	94121-01-21-03	· · + · +
497743011	2009-10-09, 21:57	94121-01-21-04	+ · + · ·
500306243	2009-11-08, 13:58	94121-01-23-00	· + + · ·
500311891	2009-11-08, 15:32	94121-01-23-04	+ · + · ·
500317539	2009-11-08, 17:06	94121-01-23-01	+ · + · ·
500323187	2009-11-08, 18:40	94121-01-23-02	· · + + ·
500328835	2009-11-08, 20:14	94121-01-23-03	· · + · +
501094467	2009-11-17, 16:55	94121-01-15-00	· · + · ·
501100291	2009-11-17, 18:32	94121-01-15-01	· · + + ·
501687107	2009-11-24, 13:32	94121-01-24-00	· · + · ·
501692963	2009-11-24, 15:10	94121-01-24-01	· · + · ·
501698803	2009-11-24, 16:47	94121-01-24-02	· · + + ·
501704627	2009-11-24, 18:24	94121-01-24-03	· · + · ·
501710499	2009-11-24, 20:02	94121-01-24-04	· + + · ·
502291363	2009-12-01, 13:23	94121-01-28-04	+ · + · ·
502297251	2009-12-01, 15:01	94121-01-28-02	· + + · ·
502303075	2009-12-01, 16:38	94121-01-28-01	· · + + ·
502308707	2009-12-01, 18:12	94121-01-28-00	· · + · +
502312819	2009-12-01, 19:21	94121-01-28-00 94121-01-28-00	· · + · · + · + · ·
502348883	2009-12-02, 05:22	94108-01-01-00	+ · + · ·
502352563	2009-12-02, 06:23	94108-01-01-00	+ · + · ·
502358451	2009-12-02, 08:01	94108-01-01-00	· + + · ·
502364323	2009-12-02, 09:39	94108-01-01-00	· · + + ·
502906739	2009-12-08, 16:19	94121-01-25-00	· + + · ·
502911667	2009-12-08, 17:42	94121-01-25-00 94121-01-25-00	· · + · · · · + + ·
502917315	2009-12-08, 19:16	94121-01-25-00	+ · + · ·
503634883	2009-12-17, 02:35	94121-01-26-00	· + + · ·
503640451	2009-12-17, 04:08	94121-01-26-00	· · + + ·
503646099	2009-12-17, 05:42	94121-01-26-00	+ · + · ·
506054819	2010-01-14, 02:47	95338-07-01-00	· + + · ·
506059427	2010-01-14, 04:04	95338-07-01-00	· · + · ·
506065539	2010-01-14, 05:46	95338-07-01-00	· · + · ·
506071539	2010-01-14, 07:26	95338-07-01-00	+ · + · ·
506077427	2010-01-14, 09:04	95338-07-01-00	· · + · ·
506162099	2010-01-15, 08:35	95121-01-02-00	· · + · +
506167971	2010-01-15, 10:13	95121-01-02-01	· · + · ·
506173827	2010-01-15, 11:51	95121-01-02-02	· + + · ·
506179667	2010-01-15, 13:28	95121-01-02-03	· · + · ·
506185539	2010-01-15, 15:06	95121-01-02-04	· · + · +
507539987	2010-01-31, 07:20	95121-01-03-02	· · + · +
507545715	2010-01-31, 08:56	95121-01-03-01	+ · + · ·
507550835	2010-01-31, 10:21	95121-01-03-03	· · + · ·
507556339	2010-01-31, 11:53	95121-01-03-00	· + + · ·
507562003	2010-01-31, 13:27	95121-01-03-04 95121-01-03-04	· · + · · + · + · ·
508748259	2010-02-14, 06:58	95121-01-04-00	· · + · ·
508753923	2010-02-14, 08:33	95121-01-04-02	· + + · ·
508770851	2010-02-14, 13:15	95121-01-04-01	+ · + · ·
509784355	2010-02-26, 06:46	95121-01-05-00	· + + · ·
509790323	2010-02-26, 08:26	95121-01-05-01	· · + + ·
509796147	2010-02-26, 10:03	95121-01-05-02	· · + + ·
509802067	2010-02-26, 11:42	95121-01-05-03	· · + · ·
510987091	2010-03-12, 04:52	95121-01-06-00 95121-01-06-00	· · + · · + · + · ·
510992931	2010-03-12, 06:29	95121-01-06-01 95121-01-06-01	· · + · · · + + · ·
510998835	2010-03-12, 08:08	95121-01-06-02	· · + · +
511004627	2010-03-12, 09:44	95121-01-06-03	· · + + ·
511010339	2010-03-12, 11:19	95121-01-06-04	· · + · ·
512539459	2010-03-30, 04:05	95121-01-07-00	· · + · ·
512545107	2010-03-30, 05:39	95121-01-07-00 95121-01-07-00	· · + · · + · + · ·
512550755	2010-03-30, 07:13	95121-01-07-00	· + + · ·
513573315	2010-04-11, 03:16	95121-01-08-00	· · + + +
513578739	2010-04-11, 04:46	95121-01-08-01	+ · + + ·
513581251	2010-04-11, 05:28	95121-01-08-01	· · + · ·
513590051	2010-04-11, 07:55	95121-01-08-02	· + + · +
513596307	2010-04-11, 09:39	95121-01-08-03	· · + + ·
514778147	2010-04-25, 01:56	95121-01-09-00	+ · + · ·
514784035	2010-04-25, 03:34	95121-01-09-01	· + + · ·

T_{RXTE} (s)	Date (Y-m-d, H:M)	ObsID	PCUs 0 1 2 3 4
514789955	2010-04-25, 05:13	95121-01-09-02	· · + + ·
514795779	2010-04-25, 06:50	95121-01-09-03	· · + · +
514801603	2010-04-25, 08:27	95121-01-09-04	+ · + · ·
515895971	2010-05-08, 00:27	95121-01-10-00	+ · + · ·
517105891	2010-05-22, 00:32	95121-01-11-00	· · + · +
517109555	2010-05-22, 01:33	95121-01-11-00	+ · + · ·
517115187	2010-05-22, 03:07	95121-01-11-00	· + + · ·
517120835	2010-05-22, 04:41	95121-01-11-00	· · + · ·
517126499	2010-05-22, 06:15	95121-01-11-01	· · + · ·
518399443	2010-06-05, 23:51	95121-01-12-00	+ · + · ·
518405475	2010-06-06, 01:32	95121-01-12-01	· + + · ·
518411331	2010-06-06, 03:09	95121-01-12-02	· · + · +
518420099	2010-06-06, 05:35	95121-01-12-03	· · + · ·
519601987	2010-06-19, 21:54	95121-01-13-00	· · + · +
519607843	2010-06-19, 23:31	95121-01-13-01	+ · + · ·
519613667	2010-06-20, 01:08	95121-01-13-02	· + + · ·
520820883	2010-07-04, 00:29	95121-01-14-02 95121-01-14-02	· · + · · · · + + ·
520826707	2010-07-04, 02:06	95121-01-14-01	· + + · ·
520832195	2010-07-04, 03:37	95121-01-14-00	· + + · ·
521425123	2010-07-11, 00:19	95429-01-01-02	· · + · +
521430771	2010-07-11, 01:53	95429-01-01-02	· · + + ·
521436419	2010-07-11, 03:27	95429-01-01-02	· · + · +
522142323	2010-07-19, 07:33	95429-01-02-01	+ · + · ·
522187507	2010-07-19, 20:06	95121-01-15-00	· · + + ·
522193155	2010-07-19, 21:40	95121-01-15-00	+ · + · ·
522198787	2010-07-19, 23:14	95121-01-15-02	· · + · +
522201571	2010-07-20, 00:00	95121-01-15-02	· · + · +
522210083	2010-07-20, 02:22	95121-01-15-01	· · + + ·
522402147	2010-07-22, 07:43	95429-01-02-02	· + + · ·
522430387	2010-07-22, 15:34	95429-01-02-00	· + + · ·
522436035	2010-07-22, 17:08	95429-01-02-00	· · + · +
522441683	2010-07-22, 18:42	95429-01-02-00	· · + + ·
522611203	2010-07-24, 17:47	95429-01-03-00	· · + · ·
522616851	2010-07-24, 19:21	95429-01-03-00	· · + + ·
523223091	2010-07-31, 19:45	95121-01-16-00	+ · + · ·
523228979	2010-07-31, 21:23	95121-01-16-01	· · + · +
523234851	2010-07-31, 23:01	95121-01-16-02	· · + + ·
523240771	2010-08-01, 00:40	95121-01-16-03	· + + · ·
523246595	2010-08-01, 02:17	95121-01-16-04	· + + · ·
524431267	2010-08-14, 19:22	95121-01-17-01	· · + · +
524437075	2010-08-14, 20:58	95121-01-17-03	· · + · ·
524442851	2010-08-14, 22:35	95121-01-17-02	+ · + · ·
524448579	2010-08-15, 00:10	95121-01-17-00	· + + · ·
524452931	2010-08-15, 01:23	95121-01-17-00	· · + + ·
525638739	2010-08-28, 18:46	95121-01-18-00 95121-01-18-00	· · + · · + · + · ·
525644387	2010-08-28, 20:20	95121-01-18-00	· · + · ·
525650035	2010-08-28, 21:54	95121-01-18-00	· + + · ·
525655683	2010-08-28, 23:29	95121-01-18-00	· · + · +
526841571	2010-09-11, 16:53	95121-01-19-00	· · + · ·
526843235	2010-09-11, 17:21	95121-01-19-00	· · + · ·
526847235	2010-09-11, 18:28	95121-01-19-01	· · + · ·
526849731	2010-09-11, 19:09	95121-01-19-01	· · + · ·
526858531	2010-09-11, 21:36	95121-01-19-02	· · + · ·
526861587	2010-09-11, 22:27	95121-01-19-02	· · + · ·
527961555	2010-09-24, 16:00	95121-01-20-00	· · + · ·
527967395	2010-09-24, 17:37	95121-01-20-00	· · + · ·
527973283	2010-09-24, 19:15	95121-01-20-01	· · + · ·
527979139	2010-09-24, 20:53	95121-01-20-02	· · + · ·
527985011	2010-09-24, 22:31	95121-01-20-03	· · + · ·
529254035	2010-10-09, 15:01	95121-01-21-00	· + + · ·
529259795	2010-10-09, 16:37	95121-01-21-00	· · + · ·
529265395	2010-10-09, 18:10	95121-01-21-01	· · + + ·
529270387	2010-10-09, 19:34	95121-01-21-01	· · + + ·
529276035	2010-10-09, 21:08	95121-01-21-01	+ · + · ·

C *Chandra* HETGS observations of Cyg X-1

An overview of all *Chandra* HETGS observations of Cyg X-1 is given in Sect. 2.4.1. This appendix displays the supplemental images and (nearly) simultaneous *RXTE* PCA light curves.

C.1 Images from the TE mode data

Figures C.1–C.10 show the images from the *Chandra* observations of Cyg X-1 in TE mode, namely ObsIDs 107, 2741–2743, 3814, 8525, 9847, 11044, 12313, and 13219. Some observations employ "filter windows", which are no physical filters, but software-defined regions from where the onboard processor only inserts a given fraction of events into the telemetry stream.

C.2 Simultaneous *RXTE* light curves

Figures C.11–C.22 show PCA `standard2f` light curves at 16 s time resolution from the *RXTE* observations that were performed (nearly) simultaneous to the *Chandra* HETGS observations.

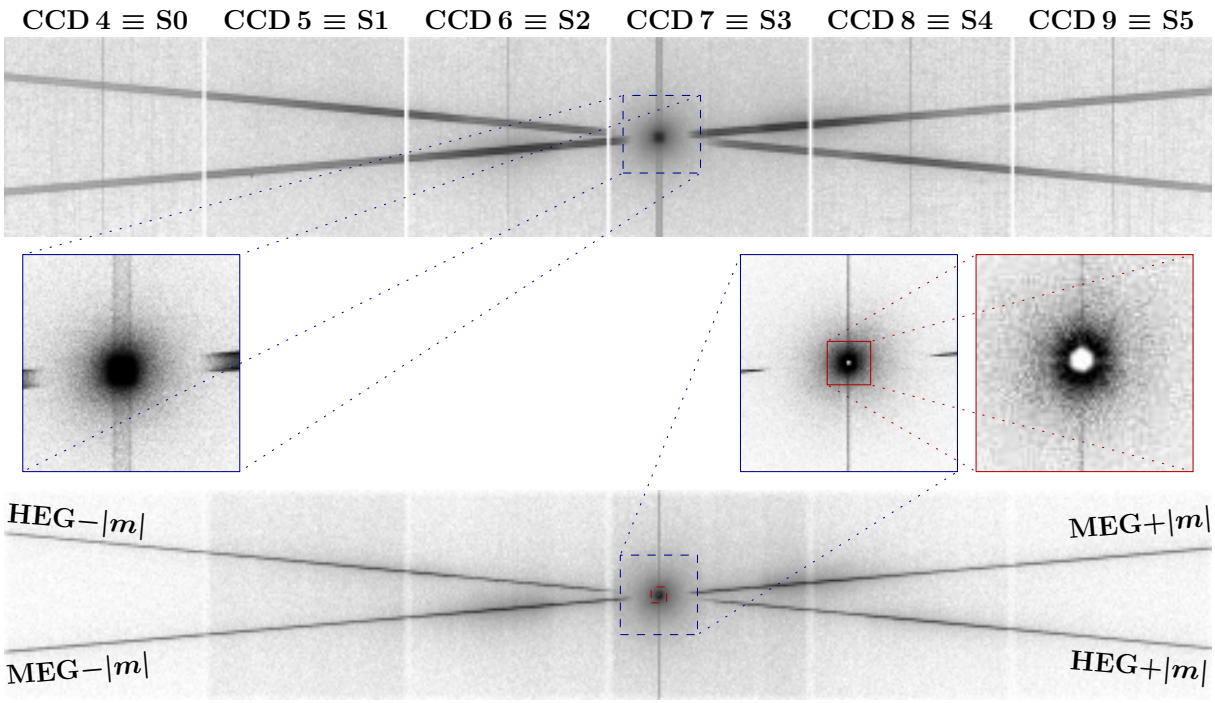

Figure C.1: Images of the *Chandra* HETGS observation 107. Top: Detector image from the unfiltered (level 1) event file. The CCD identification is shown above of it. Chips 5 and 7 are the back illuminated ones. Bottom: Dither-corrected sky image from the processed (level 2) event file. Middle: The three square boxes in between highlight the corresponding regions around the undispersed source image, whose center contains no valid events due to pileup. The ACIS alternating exposure mode was employed for ObsID 107, and this figure shows only long-frame data from the 3.3 s exposures. The short 0.3 s exposures are significantly less affected by pileup. The HEG spectrum extends from the top left ("negative" orders) to the bottom right ("positive" orders), and the MEG spectrum, vice versa, from the bottom left ($m<0$) to the top right ($m>0$). The vertical line through the zeroth order is the readout streak formed by out-of-time events occuring during the 41 ms when the charges are transferred to the frame store. The source is surrounded by a scattering halo seen in zeroth and first orders.

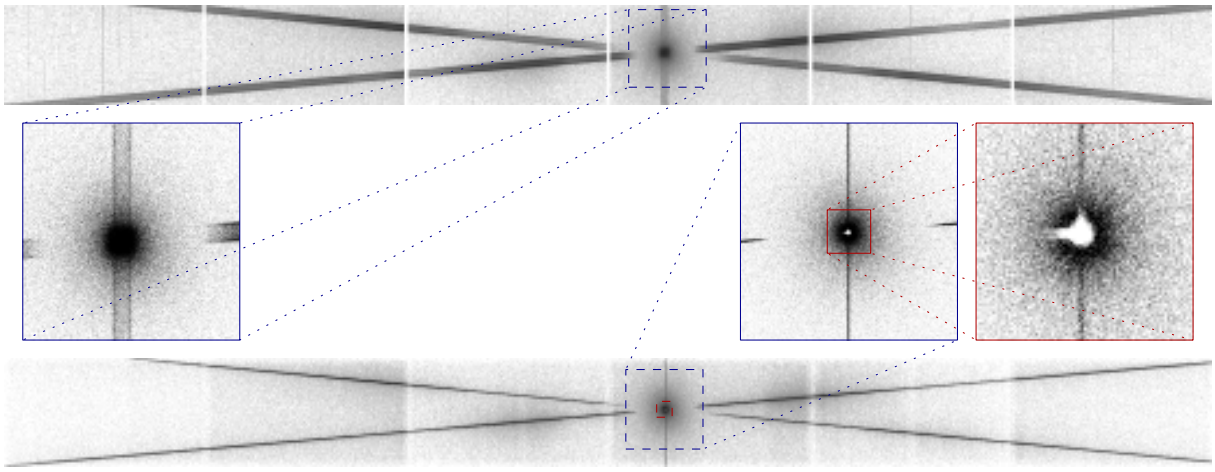

Figure C.2: Same as Fig. C.1, but for ObsID 2741, using a half subarray of the six CCDs.

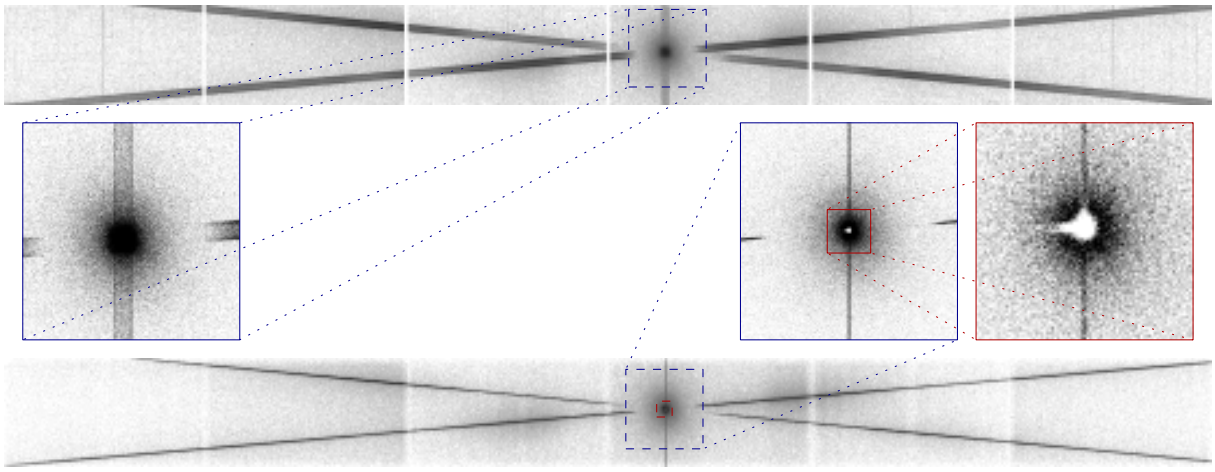

Figure C.3: Same as Fig. C.1, but for ObsID 2742, using a half subarray of the six CCDs.

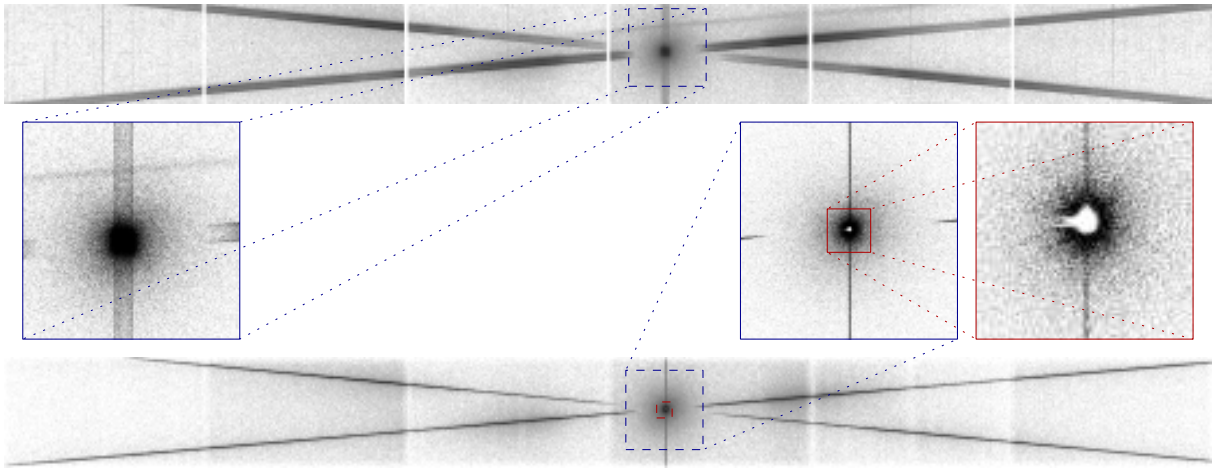

Figure C.4: Same as Fig. C.1, but for ObsID 2743, using a half subarray of the six CCDs.

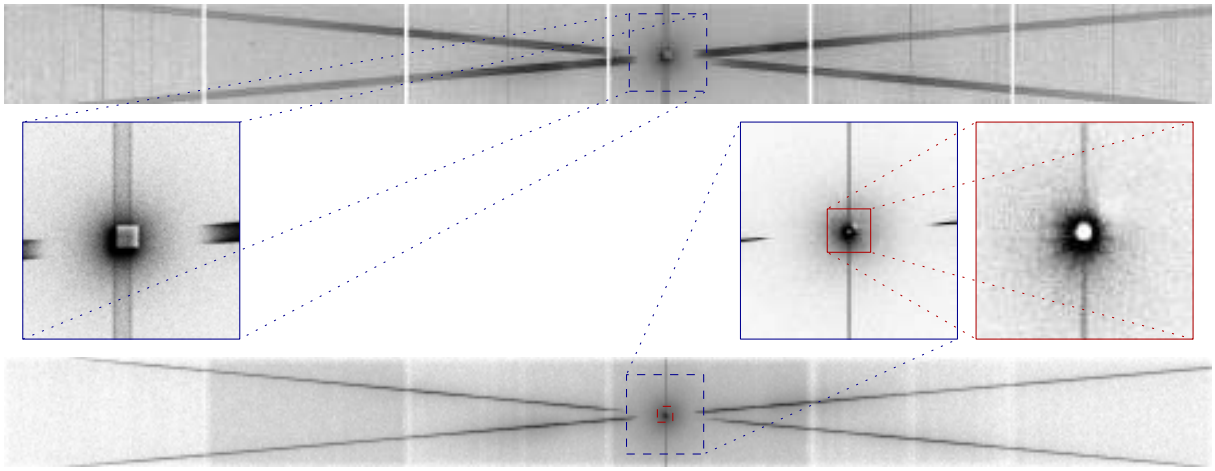

Figure C.5: Same as Fig. C.1, but for ObsID 3814, using a half subarray of the six CCDs and a 40×38 pixel window with 10 % duty cycle to block the zeroth order image.

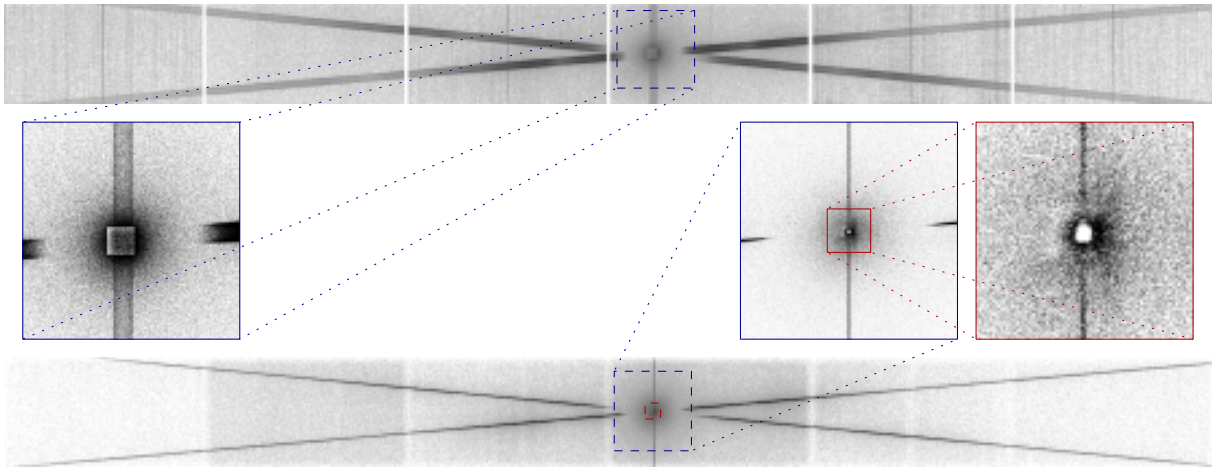

Figure C.6: Same as Fig. C.1, but for ObsID 8525, using a half subarray of the six CCDs and a 50×48 pixel window with 10 % duty cycle to block the zeroth order image.

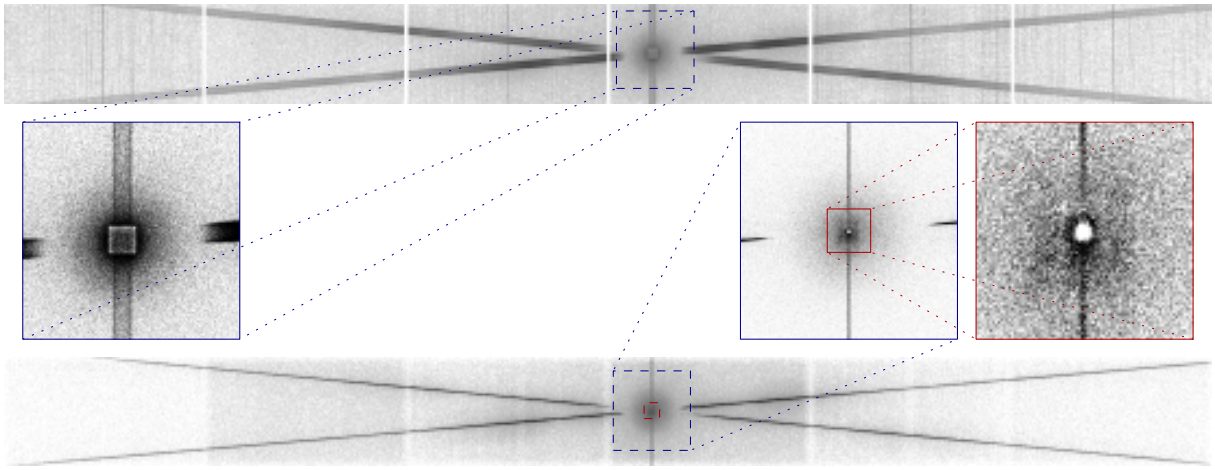

Figure C.7: Same as Fig. C.1, but for ObsID 9847, using a half subarray of the six CCDs and a 50×48 pixel window with 10 % duty cycle to block the zeroth order image.

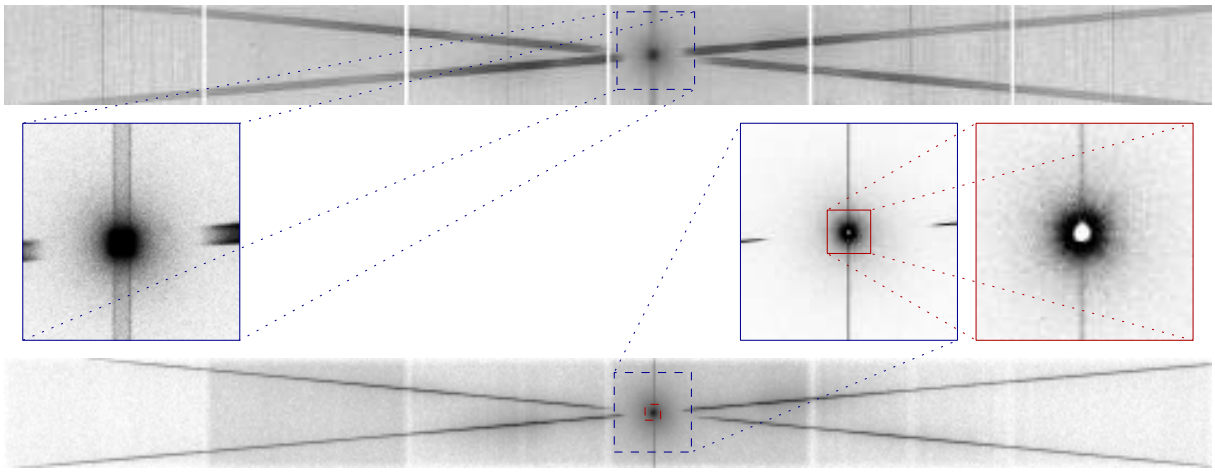

Figure C.8: Same as Fig. C.1, but for ObsID 11044, using a half subarray of the six CCDs.

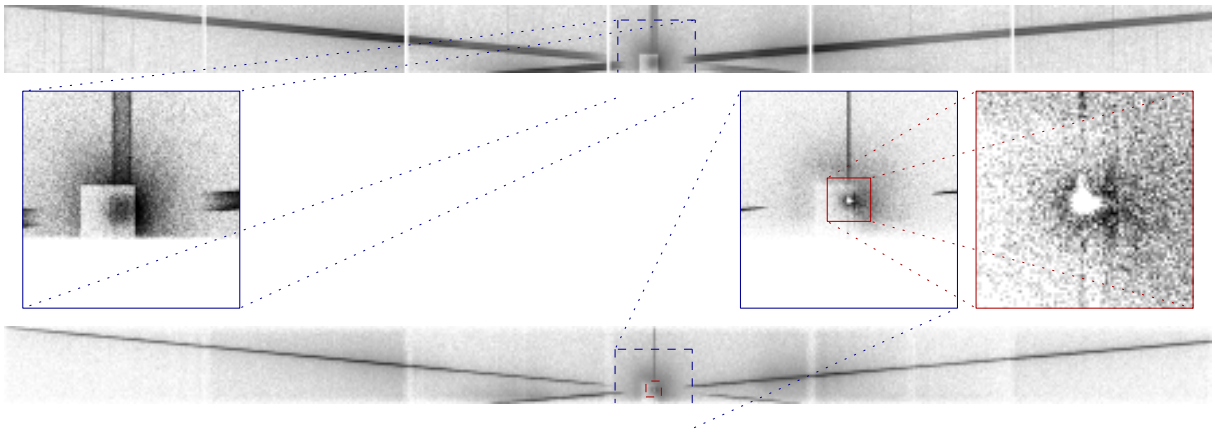

Figure C.9: Same as Fig. C.1, but for ObsID 12313, using a third subarray (348 rows) of the six CCDs and a 100×100 pixel window with 10 % duty cycle to block the zeroth order image. The MEG$-|m|$ and HEG$+|m|$ spectra were largely placed off the ACIS detector.

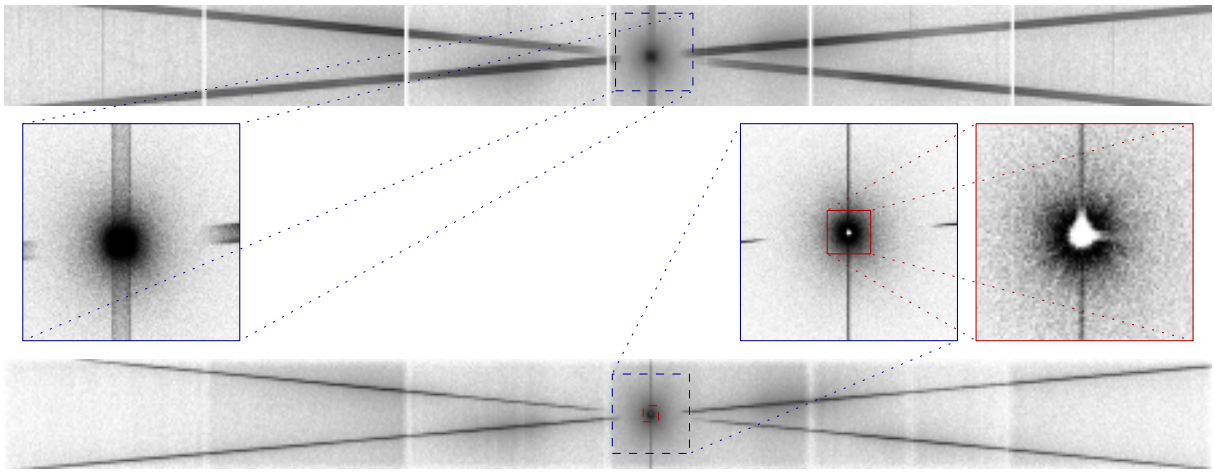

Figure C.10: Same as Fig. C.1, but for ObsID 13219, using a half subarray of the six CCDs. The apparent blooming along and perpendicular to the readout direction is only present in the filtered (level 2) events (compare with Fig. 2.51 on page 98, which shows unfiltered events). The vertical feature is probably due to pattern pileup from trailing charges, since electron clouds are shifted toward the bottom during the readout of the CCDs. It is present in all observations of Cyg X-1 in the soft state, see also Figs. C.2–C.4 and C.9. The asymmetric horizontal feature (perpendicular to the readout direction), which points here and in Fig. C.9 to the right, but in Figs. C.2–C.4 to the left, requires another explanation.

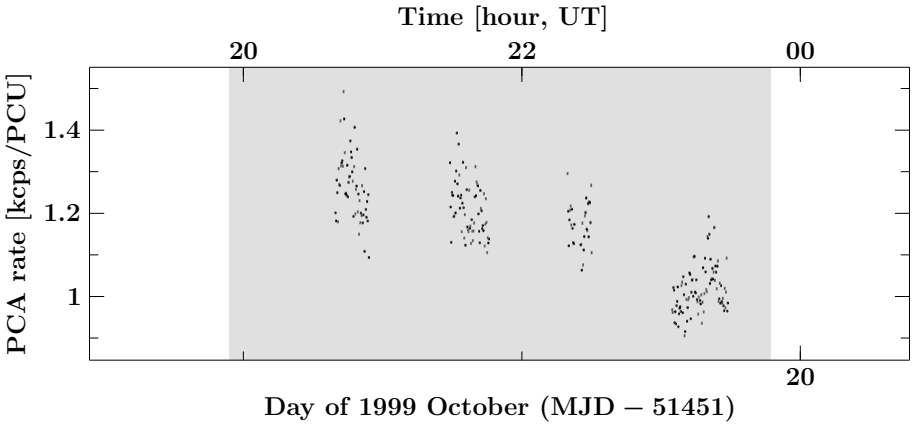

Figure C.11: PCA full layer light curve of *RXTE* ObsID 40100-01-08. The gray shaded region marks the time of the *Chandra* observation 107.

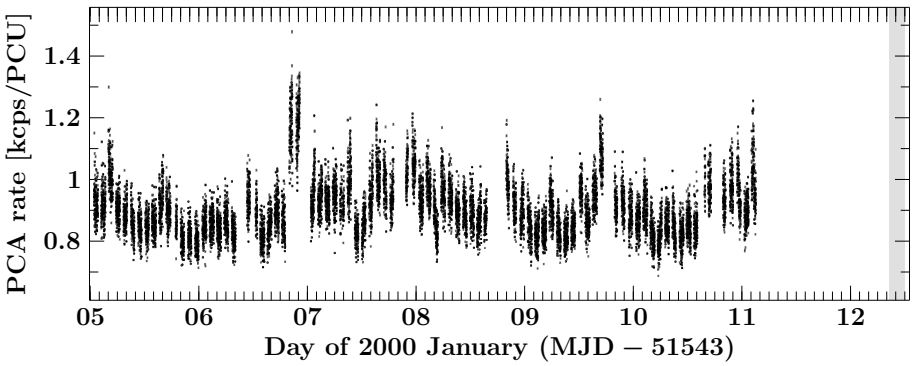

Figure C.12: PCA full layer light curve of *RXTE* ObsID 40102-01-01. The gray shaded region marks the time of the *Chandra* observation 1511.

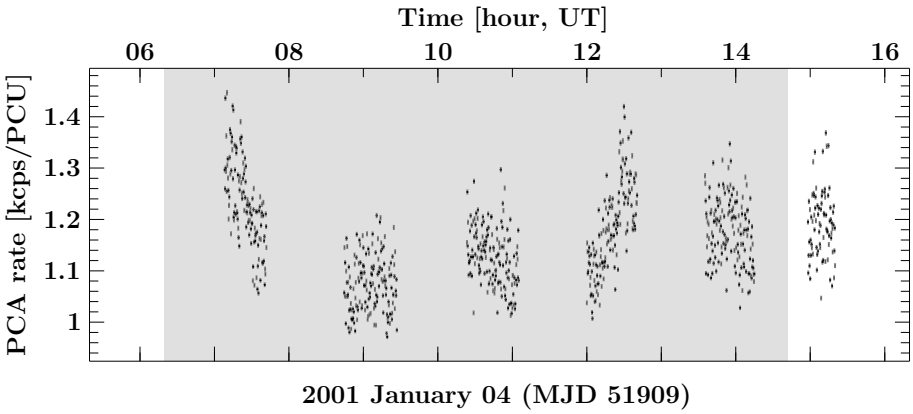

Figure C.13: PCA full layer light curve of *RXTE* ObsID 50119-01-06. The gray shaded region marks the time of the *Chandra* observation 2415.

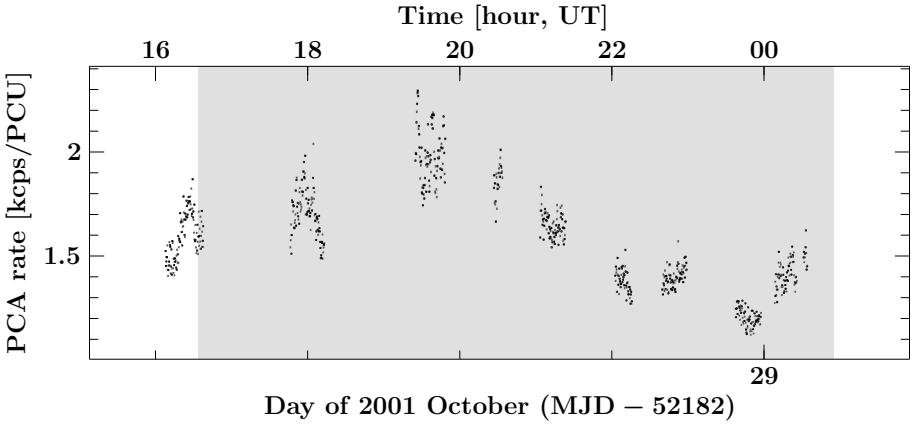

Figure C.14: PCA full layer light curve of *RXTE* ObsID 60089-02-02. The gray shaded region marks the time of the *Chandra* observation 3407.

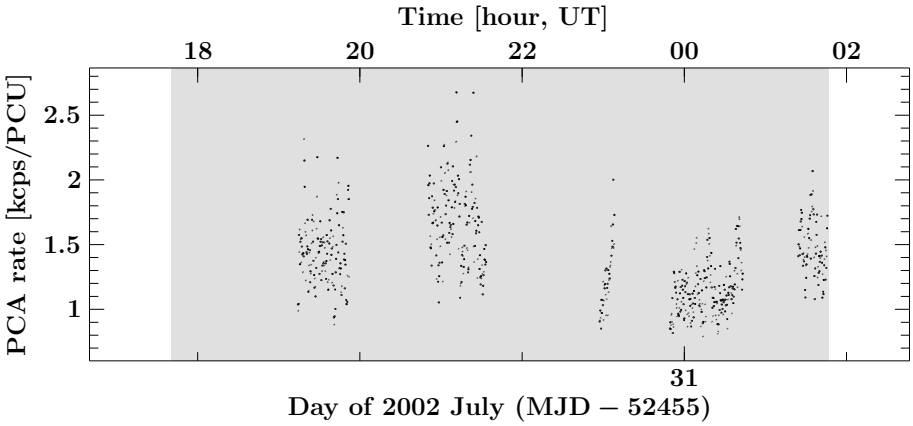

Figure C.15: PCA full layer light curve of *RXTE* ObsID 70414-01-01. The gray shaded region marks the time of the *Chandra* observation 3724.

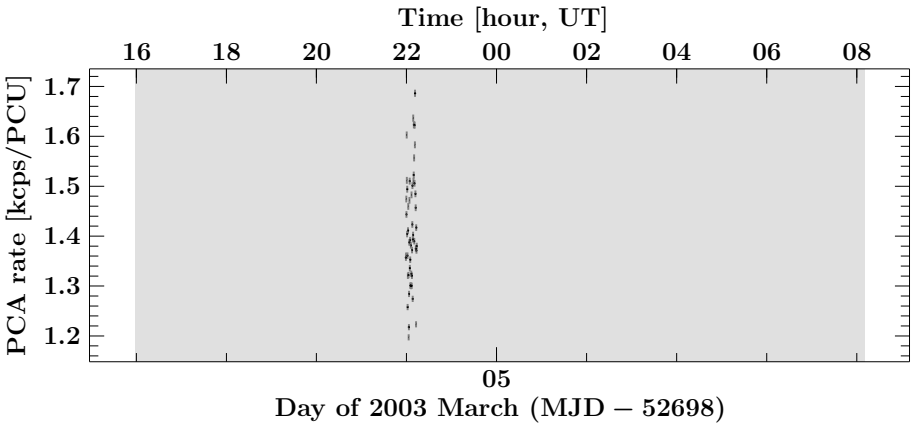

Figure C.16: PCA full layer light curve of *RXTE* ObsID 80402-01-01. The gray shaded region marks the time of the *Chandra* observation 3815.

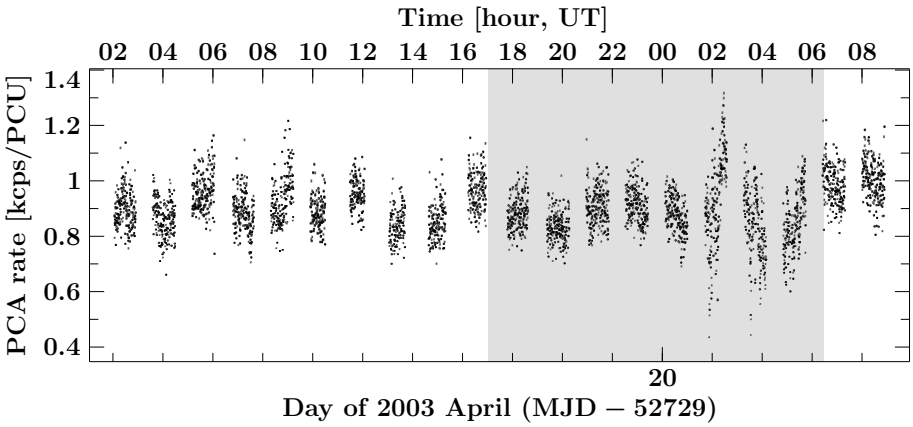

Figure C.17: PCA full layer light curve of *RXTE* ObsIDs 60090-01-30 and 80111-01-01. The gray shaded region marks the time of the *Chandra* observation 3814.

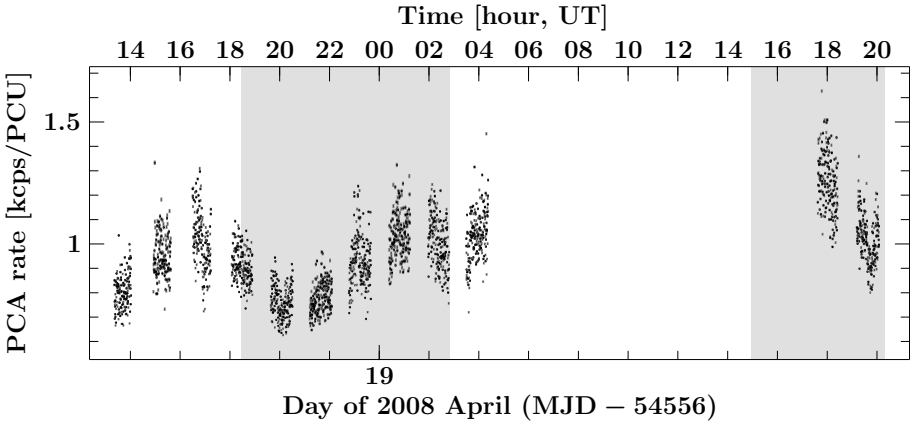

Figure C.18: PCA full layer light curve of *RXTE* ObsID 93120-01-01. The gray shaded regions mark the time of the *Chandra* observations 8525 and 9847.

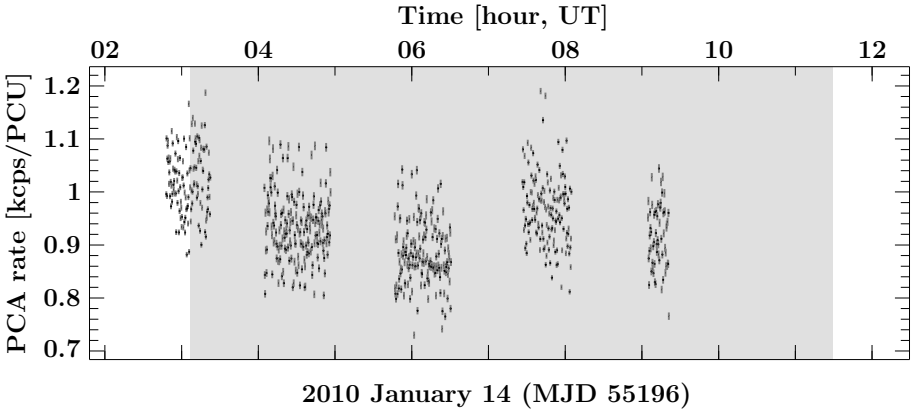

Figure C.19: PCA full layer light curve of *RXTE* ObsID 95338-07-01. The gray shaded region marks the time of the *Chandra* observation 11044.

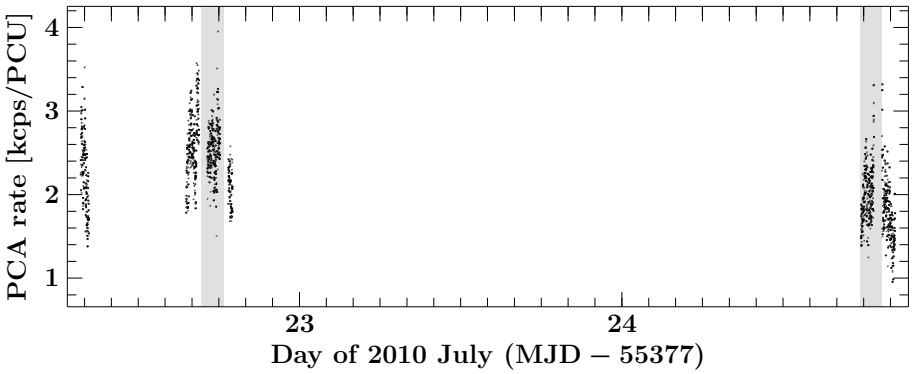

Figure C.20: PCA full layer light curve of *RXTE* ObsIDs 95429-01-02 and 95429-01-03. The gray shaded regions mark the time of the *Chandra* observations 12313 and 12314.

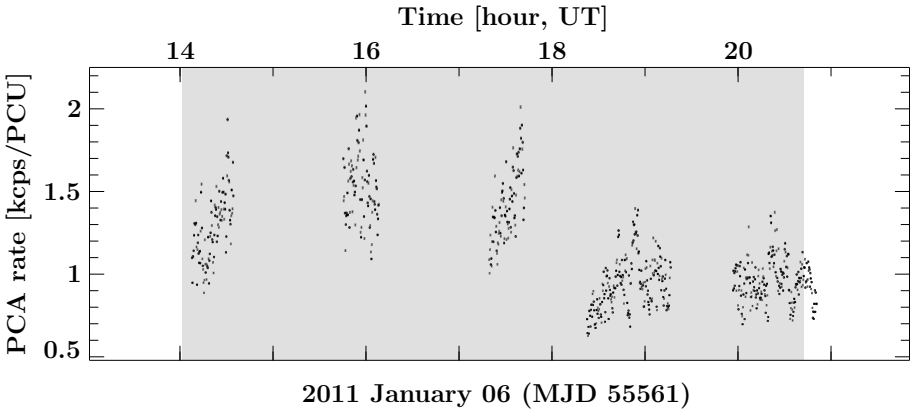

Figure C.21: PCA full layer light curve of *RXTE* ObsID 96378-03-01. The gray shaded regions mark the time of the *Chandra* observation 12472.

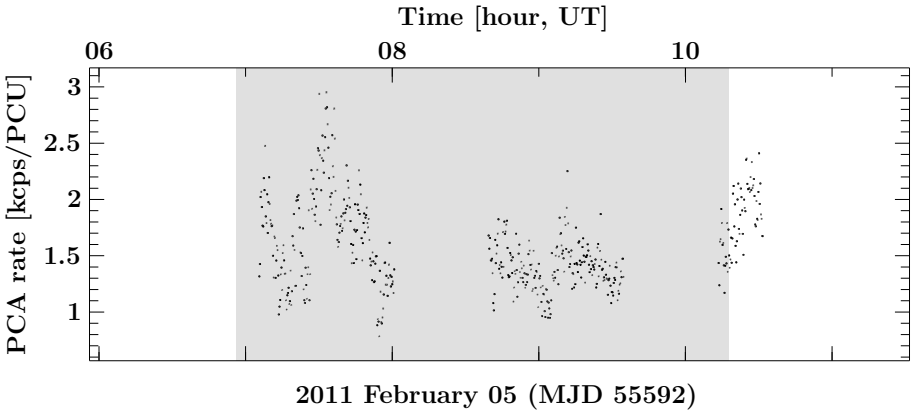

Figure C.22: PCA full layer light curve of *RXTE* ObsID 96121-01-03. The gray shaded regions mark the time of the *Chandra* observation 13219.

D Dynamically known high-mass X-ray binaries

Table D.1: Orbital periods of high-mass X-ray binaries from Liu et al. (2005, 2006), for the Magellanic Clouds (M) and our Galaxy (G), respectively

Source name		*RXTE*-ASM name	*Swift*-BAT name	Companion type	$P_{\rm orb}$ (days)
4U 2030+40	G	cygx3	Cyg X-3	WR star	0.2
2A 0532-664	M	lmcx4		O8 III	1.4
RX J0050.7-7316	M			B0III-Ve	1.416
1H 0538-641	M	lmcx3		B2.5 Ve	1.7
4U 1119-603	G	cenx3	Cen X-3	O6.5 II-III	2.09
SAX J1819.3-2525	G	v4641sgr	SAX J1819.3-2525	B9III	2.8
4U 1700-37	G	x1700-377	4U 1700-377	O6.5Iaf$^+$	3.41
4U 1538-52	G	x1538-522	H 1538-522	B0 Iab	3.73
2U 0115-737	M	smcx1		B0 Ib	3.89
RX J1826.2-1450	G	rxj1826.2-1450	RX J1826.2-1450	ON6.5V((f))	3.9
3A 0540-697	M	lmcx1		O8 III	4.22
4U 1909+07	G	x1908+075	4U 1909+07		4.4
SAX J1802.7-2017	G	igrj18027-2017	IGR J18027-2016		4.6
4U 1956+35	G	cygx1	Cyg X-1	O9.7 Iab	5 [†]
XTE J1855-026	G	xtej1855-026	XTE J1855-026		6.067
4U 1907+09	G	x1907+097	H 1907+097	O8-9 Ia	8.38
4U 0900-40	G	velax1	Vela X-1	B0.5 Ib	8.96
IGR J16320-4751	G	igrj16320-4751	AX J1631.9-4752		8.96
4U 2206+543	G	x2206+543	4U 2206+54	O9.5Ve	9.57
EXO 1722-363	G	exo1722-363	IGR J17252-3616		9.74
OAO 1657-415	G	x1657-415	EXO 1657-419	B SG	10.4
AX J0105-722	M			Be	11.09
SAX J0635.2+0533	G	saxj0635+0533		B2V-B1IIIe	11.2
2S 0114+650	G	x0114+650	3A 0114+650	B0.5 Ib	11.6
SAX J2103.5+4545	G	saxj2103.5+4545	SAX J2103.5+4545	B0Ve	12.68
3A 1909+048	G	ss433	SS 433	pec	13.1
IGR J19140+0951	G	igrj1914+0951	IGR J19140+0951		13.558
1E 1145.1-6141	G	x1145-616		B2Iae	14.4
IGR J00370+6122	G	rxj0037.2+6121	IGR J00370+6122	B0.5II-III	15.665
1A 0535-668	M			B0.5 IIIe	16.7
XTE J0421+560	G	xtej0421+560		sgB[e]	19.41
4U 1901+03	G	x1901+031	4U 1901+03		22.58
4U 0115+634	G	x0115+634	4U 0115+634	B0.2Ve	24.3
RX J0520.5-6932	M			O9Ve	24.4
RX J0531.2-6607	M			B0.7Ve	25.4
1E 0236.6+6100	G	lsi+61303	2CG 135+01	B0Ve	26.496
RX J0051.8-7231	M			Be	28
GRO J1750-27	G	groj1750-27	AX J1749.1-2639		29.8
2S 1553-542	G	x1553-542	H 1553-542		30.6
V 0332+53	G	v0332+53	V0332+53	O8.5Ve	34.25
3A 0726-260	G	x0726-260	4U 0728-25	O8-9Ve	34.5

[†] A *more precise* value of the orbital period of Cyg X-1 is given by Eq. (2.1).

Table D.1: Orbital periods of high-mass X-ray binaries (continued)

Source name		*RXTE*-ASM name	*Swift*-BAT name	Companion type	P_{orb} (days)
XTE J0055-727	M				34.8
KS 1947+300	G	ks1947+300		B0Ve	40.4
4U 1223-624	G	gx301-2	GX 301-2	B1-1.5 Ia	41.59
2S 1417-624	G	x1417-624	H 1417-624	B1Ve	42.12
2S 0050-727	M	smcx3		O9 III-Ve	45.1
EXO 2030+375	G	exo2030+375	EXO 2030+375	B0Ve	46.02
RX J0047.3-7312	M			B2e	48.8
IGR J11435-6109	G	igrj11435-6109	IGR J11435-6109	B3e	52.46
GRO J2058+42	G	groj2058+42	GRO J2058+42	O9.5-B0IV-Ve	55.03
RX J0058.2-7231	M			B2-3Ve	59.72
XTE SMC144s	M				61.2
RX J0051.9-7311	M			B[e]	67
RX J0101.3-7211	M			Be	74.7
XTE J1543-568	G	xtej1543-568			75.56
RX J0812.4-3114	G	rxj0812.4-3115		B0.2IVe	81.3
RX J0051.3-7216	M			Be	88.4
RX J0049.5-7310	M			Be	91.5
CXOU J005736.2-721934	M			Be	95.3
GS 0834-430	G	gs0834-430		B0-2 III-Ve	105.8
1A 0535+262	G	x0535+262	1A 0535+262	O9.7IIIe	111
XTE J0055-724	M			B0-B1III-V	123
CXOU J005323.8-722715	M			Be	125
4U 1258-61	G	gx304-1	GX 304-1	B0.7Ve	133
GRO J1008-57	G	groj1008-57	GRO J1008-57	B0e	135
1WGA J0053.8-7226	M			B1-B2III-Ve	139
XTE J1946+274	G	x1942+274		B0-1 IV-Ve	169.2
2S 1145-619	G	x1145-619	H 1145-619	B0.2IIIe	187.5
XTE J0050-732#1	M				189
RX J0052.9-7158	M			Be	200
2S 0053+604	G	gammacas	Gam Cas	B0.5 Ve	203.59
2S 1845-024	G	x1845-024		GS 1843-02	241
RX J0535.0-6700	M			B0Ve	241
4U 0352+309	G	xper	X Per	B0Ve	250.3
AX J0054.8-7244	M			O9Ve	261
SAX J2239.3+6116	G	saxj2239.3+6116		B0V-B2IIIe	262
XTE SMC95	M				280
1SAX J0544.1-7100	M			B0Ve	286
RX J0049.7-7323	M			B1-3Ve	394
AX J0049-729	M			Be	642

References: Liu et al. (2005) for sources in the Magellanic Clouds (M),
Liu et al. (2006) for galactic sources (G),
http://xte.mit.edu/ASM_lc.html, and
http://swift.gsfc.nasa.gov/docs/swift/results/transients/.

Bibliography

Aab O.E., 1983, SvA Letters 9, 315

Abbott D.C., 1982, ApJ 259, 282

Abubekerov M.K., Antokhina E.A., Cherepashchuk A.M., 2004, Astron. Rep. 48, 550

Anders E., Ebihara M., 1982, Geochim. Cosmochim. Acta 46, 2363

Anders E., Grevesse N., 1989, Geochim. Cosmochim. Acta 53, 197

Antonucci R., 1993, ARA&A 31, 473

Arnaud K.A., 1996, In: ASP Conf. Ser. 101, Jacoby G.H., Barnes J. (eds.) Astronomical Data Analysis Software and Systems V, ASP, San Francisco, CA, p.17

Asplund M., Grevesse N., Sauval A.J., Scott P., 2009, ARA&A 47, 481

Avni Y., Bahcall J.N., 1975, ApJ 197, 675

Baade W., Zwicky F., 1934, Phys. Rev. 46, 76

Bahcall J.N., Dyson F.J., Katz J.I., Paczynski B., 1974, ApJ 189, L17

Bahcall J.N., Rosenbluth M.N., Kulsrud R.M., 1973, Nat 243, 27

Bajaja E., Arnal E.M., Larrarte J.J., et al., 2005, A&A 440, 767

Balbus S.A., 2003, ARA&A 41, 555

Balbus S.A., Hawley J.F., 1991, ApJ 376, 214

Balbus S.A., Hawley J.F., 1998, Rev. Mod. Phys. 70, 1

Bałucińska M., Hasinger G., 1991, A&A 241, 439

Bałucińska-Church M., Church M.J., Charles P.A., et al., 2000, MNRAS 311, 861

Bałucińska-Church M., Gibiec A., Jackson N.K., Church M.J., 2010, A&A 512, A9

Bałucińska-Church M., Takahashi T., Ueda Y., et al., 1997, ApJ 480, L115

Bardeen J.M., Press W.H., Teukolsky S.A., 1972, ApJ 178, 347

Barthelmy S.D., Barbier L.M., Cummings J.R., et al., 2005, Space Sci. Rev. 120, 143

Behar E., Sako M., Kahn S.M., 2001, ApJ 563, 497

Belloni T., Homan J., Casella P., et al., 2005, A&A 440, 207

Belloni T.M., 2010, In: Belloni T.M. (ed.) The jet paradigm, Vol. 794. Lecture Notes in Physics, Springer Verlag, Berlin, p.53

Beuermann K.P., Braeuninger H., Truemper J., 1978, Appl. Opt. 17, 2304

Bevington P.R., Robinson D.K., 1992, Data reduction and error analysis for the physical sciences, McGraw-Hill, New York, 2nd edition

Bisiacchi G.F., Dultzin D., Firmani C., Hacyan S., 1974, ApJ 190, L59

Blaauw A., 1961, BAN 15, 265

Blondin J.M., 1994, ApJ 435, 756

Blondin J.M., Kallman T.R., Fryxell B.A., Taam R.E., 1990, ApJ 356, 591

Blondin J.M., Stevens I.R., Kallman T.R., 1991, ApJ 371, 684

Böck M., 2008, *Diploma thesis*, University of Regensburg

Böck M., Hanke M., Wilms J., et al., 2008, In: Kalemci E. (ed.) Microquasars and Beyond, Proceedings of Science, Trieste, p. 89

Böck M., Wilms J., Grinberg V., et al., 2010, In: AIP Conf. Ser. 1248, Comastri A., Angelini L., Cappi M. (eds.) X-ray Astronomy 2009: Present Status, Multi-Wavelength Approach and Future Perspectives, AIP, Melville, NY, p.143

Bolton C.T., 1972a, Nat 235, 271

Bolton C.T., 1972b, Nat 240, 124

Bolton C.T., 1975, ApJ 200, 269

Boltzmann L., 1884, Ann. Phys. 258, 291

Bondi H., 1952, MNRAS 112, 195

Bondi H., Hoyle F., 1944, MNRAS 104, 273

Boroson B., Vrtilek S.D., 2010, ApJ 710, 197

Bowyer S., Byram E.T., Chubb T.A., Friedman H., 1965, Sci 147, 394

Boyer R.H., Lindquist R.W., 1967, J. Math. Phys. 8, 265

Bradt H., Levine A.M., Morgan E.H., Remillard R., 2007, In: AIP Conf. Ser. 924, di Salvo T., Israel G.L., Piersant L., Burderi L., Matt G., Tornambe A., Menna M.T. (eds.) The Multicolored Landscape of Compact Objects and Their Explosive Origins, AIP, p.481

Bradt H.V.D., McClintock J.E., 1983, ARA&A 21, 13

Braes L.L.E., Miley G.K., 1971, Nat 232, 246

Brinkman A.C., Gunsing C.J., Kaastra J.S., et al., 1997, In: Proc. SPIE 3113, R. B. Hoover & A. B. Walker (ed.) Grazing Incidence and Multilayer X-Ray Optical Systems, SPIE, Bellingham, WA, p.181

Brocksopp C., Tarasov A.E., Lyuty V.M., Roche P., 1999, A&A 343, 861

Brucato R.J., Kristian J., 1972, IAU Circ. 2421, 1

Brucato R.J., Zappala R.R., 1974, ApJ 189, L71

Burbidge G.R., Burbidge E.M., Sandage A.R., 1963, Rev. Mod. Phys. 35, 947

Burrows D.N., Hill J.E., Nousek J.A., et al., 2005, Space Sci. Rev. 120, 165

Byram E.T., Chubb T.A., Friedman H., 1966, Sci

152, 66
Caballero-Nieves S.M., Gies D.R., Bolton C.T., et al., 2009, ApJ 701, 1895
Canalizo G., Koenigsberger G., Peña D., Ruiz E., 1995, Rev. Mex. Astron. Astrophys. 31, 63
Canizares C.R., Davis J.E., Dewey D., et al., 2005, PASP 117, 1144
Cantiello M., Langer N., Brott I., et al., 2009, A&A 499, 279
Carter B., 1971, Phys. Rev. Lett. 26, 331
Cassinelli J.P., 1979, ARA&A 17, 275
Castor J.I., Abbott D.C., Klein R.I., 1975, ApJ 195, 157
Chadwick J., 1932, Nat 129, 312
Chakrabarti S., Titarchuk L.G., 1995, ApJ 455, 623
Chandrasekhar S., 1931, ApJ 74, 81
Chang C., Cui W., 2007, ApJ 663, 1207
Clayton D.D., 1983, Principles of stellar evolution and nucleosynthesis, University of Chicago Press, Chicago and London
Compton A.H., 1923, Phys. Rev. 21, 483
Coppi P.S., 1999, In: ASP Conf. Ser. 161, Poutanen J., Svensson R. (eds.) High Energy Processes in Accreting Black Holes, ASP, San Francisco, CA, p.375
Coppi P.S., 2000, In: HEAD Meeting, Vol. 32. BAAS, p. 1217
Coppi P.S., 2004, In: AIP Conf. Ser. 714, Kaaret P., Lamb F.K., Swank J.H. (eds.) X-ray Timing 2003: Rossi and Beyond, AIP, Melville, NY, p.79
Cowley A.P., 1992, ARA&A 30, 287
Cowley A.P., Hutchings J.B., Crampton D., 1978, AJ 83, 1619
Cowley A.P., Schmidtke P.C., Anderson A.L., McGrath T.K., 1995, PASP 107, 145
Cui W., Feng Y.X., Zhang S.N., et al., 2002, ApJ 576, 357
Cui W., Heindl W.A., Rothschild R.E., et al., 1997, ApJ 474, L57
CXC 2005, The Chandra ABC Guide to Pileup, `http://cxc.harvard.edu/ciao/download/doc/pileup_abc.ps`
CXC 2010a, The Chandra ABC Guide to Pileup, `http://cxc.harvard.edu/ciao/download/doc/pileup_abc.pdf`
CXC 2010b, The Chandra Proposers' Observatory Guide, Version 13, `http://cxc.harvard.edu/proposer/POG/`
Dauser T., Wilms J., Reynolds C.S., Brenneman L.W., 2010, MNRAS 1460
Davidson K., 1972, ApJ 171, 213
Davis J.E., 2002, In: Branduardi-Raymont G. (ed.) High Resolution X-ray Spectroscopy with XMM-Newton and Chandra, MSSL, London
Davis J.E., 2003, In: Proc. SPIE 4851, Trümper J.E., Tananbaum H.D. (eds.) X-Ray and Gamma-Ray Telescopes and Instruments for Astronomy, SPIE, Bellingham, WA, p.101
Davis R., Hartmann L., 1983, ApJ 270, 671
de Zeeuw P., Molster F., (eds.) 2007, A Science Vision for European Astronomy, ASTRONET, available online at `http://www.astronet-eu.org/spip.php?article86`
den Herder J.W., Brinkman A.C., Kahn S.M., et al., 2001, A&A 365, L7
Dessart L., Owocki S.P., 2003, A&A 406, L1
Dhawan V., Mirabel I.F., Rodríguez L.F., 2000, ApJ 543, 373
Di Cocco G., Bianchin V., Foschini L., et al., 2007, In: Grebenev S., Sunyaev R., Winkler C. (eds.) The Obscured Universe, Vol. 622. ESA Special Publication, Noordwijk, p.619
Dickey J.M., Lockman F.J., 1990, ARA&A 28, 215
Dolan J.F., 1992, ApJ 384, 249
Dolan J.F., Tapia S., 1989, ApJ 344, 830
Done C., Mulchaey J.S., Mushotzky R.F., Arnaud K.A., 1992, ApJ 395, 275
Done C., Życki P.T., Smith D.A., 2002, MNRAS 331, 453
Dong A., Wang J., Xue L., 2007, Chin. Astron. Astrophys. 31, 21
Ducci L., Sidoli L., Mereghetti S., et al., 2009, MNRAS 398, 2152
Dufour R.J., 1984, In: IAU Symp. 108, van den Bergh S., Boer K.S.D. (eds.) Structure and Evolution of the Magellanic Clouds, D. Reidel, Dordrecht, p.353
Eardley D.M., Lightman A.P., Shapiro S.L., 1975, ApJ 199, L153
Ebisawa K., Mitsuda K., Inoue H., 1989, PASJ 41, 519
Edgar R., 2004, New Astronomy Reviews 48, 843
Eggleton P.P., 1983, ApJ 268, 368
Einstein A., 1916, Ann. Phys. 354, 769
Esin A.A., McClintock J.E., Narayan R., 1997, ApJ 489, 865
Eversberg T., Lepine S., Moffat A.F.J., 1998, ApJ 494, 799
Fabian A.C., Pringle J.E., Whelan J.A.J., 1974, Nat 247, 351
Fasano G., Vio R., 1988, Bulletin d'Information du Centre de Donnees Stellaires 35, 191
Feldman U., 1992, Phys. Scr. 46, 202
Feldmeier A., Puls J., Pauldrach A.W.A., 1997, A&A 322, 878
Fender R., 2002, In: Guthmann A.W., Georganopoulos M., Marcowith A., Manolakou K. (eds.) Relativistic Flows in Astrophysics, Vol. 589. Lecture Notes in

Physics, Springer Verlag, Berlin, p. 101
Fender R.P., Belloni T.M., Gallo E., 2004, MNRAS 355, 1105
Fender R.P., Homan J., Belloni T.M., 2009, MNRAS 396, 1370
Fender R.P., Stirling A.M., Spencer R.E., et al., 2006, MNRAS 369, 603
Feng Y.X., Cui W., 2002, ApJ 564, 953
Feng Y.X., Tennant A.F., Zhang S.N., 2003, ApJ 597, 1017
Fewell M.P., 1995, Am. J. Phys. 63, 653
Fisher P.C., Johnson H.M., Jordan W.C., et al., 1966, ApJ 143, 203
Friend D.B., Abbott D.C., 1986, ApJ 311, 701
Friend D.B., Castor J.I., 1982, ApJ 261, 293
Friend D.B., Castor J.I., 1983, ApJ 272, 259
Fritz S., 2008, Ph.D. thesis, Universität Tübingen
Fruscione A., McDowell J.C., Allen G.E., et al., 2006, In: Proc. SPIE 6270, Observatory Operations: Strategies, Processes, and Systems, SPIE, Bellingham, WA, p. 62701V
Fryer C.L., 1999, ApJ 522, 413
Fuchs Y., Rodríguez J., Mirabel I.F., et al., 2003, A&A 409, L35
Fürst F., Kreykenbohm I., Pottschmidt K., et al., 2010, A&A 519, A37
Fürst F., Wilms J., Rothschild R.E., et al., 2009, Earth and Planet. Sci. Lett. 281, 125
Gabriel A.H., Jordan C., 1969, MNRAS 145, 241
Garmire G.P., Bautz M.W., Ford P.G., et al., 2003, In: Proc. SPIE 4851, Truemper J.E., Tananbaum H.D. (eds.) X-Ray and Gamma-Ray Telescopes and Instruments for Astronomy, SPIE, Bellingham, WA, p.28
Garnett D.R., 1999, In: Chu Y.H., Suntzeff N., Hesser J., Bohlender D. (eds.) New Views of the Magellanic Clouds, Vol. 190. IAU Symposium, ASP, San Francisco, CA, p. 266
Giacconi R., Gorenstein P., Gursky H., Waters J.R., 1967, ApJ 148, L119
Giacconi R., Gursky H., Paolini F.R., Rossi B.B., 1962, Phys. Rev. Lett. 9, 439
Gierliński M., Maciołek-Niedźwiecki A., Ebisawa K., 2001, MNRAS 325, 1253
Gierliński M., Zdziarski A.A., Poutanen J., et al., 1999, MNRAS 309, 496
Gies D.R., Bolton C.T., 1982, ApJ 260, 240
Gies D.R., Bolton C.T., 1986a, ApJ 304, 371
Gies D.R., Bolton C.T., 1986b, ApJ 304, 389
Gies D.R., Bolton C.T., Blake R.M., et al., 2008, ApJ 678, 1237
Gies D.R., Bolton C.T., Thomson J.R., et al., 2003, ApJ 583, 424
Gleissner T., Wilms J., Pooley G.G., et al., 2004a, A&A 425, 1061
Gleissner T., Wilms J., Pottschmidt K., et al., 2004b, A&A 414, 1091
Gou L., McClintock J.E., Liu J., et al., 2009, ApJ 701, 1076
Grevesse N., Sauval A.J., 1998, Space Sci. Rev. 85, 161
Grinberg V., Boeck M., Pottschmidt K., et al., 2010, The Astronomer's Telegram 2751
Grinberg V., Marcu D.M., Pottschmidt K., et al., 2011, In: Proceedings of the 8th INTEGRAL Workshop, submitted
Groenewegen M.A.T., Lamers H.J.G.L.M., 1989, A&AS 79, 359
Gruber D.E., Blanco P.R., Heindl W.A., et al., 1996, A&AS 120, C641
Guinan E.F., Dorren J.D., Siah M.J., Koch R.H., 1979, ApJ 229, 296
Gursky H., Giacconi R., Paolini F.R., Rossi B.B., 1963, Phys. Rev. Lett. 11, 530
Haardt F., Galli M.R., Treves A., et al., 2001, ApJS 133, 187
Hadrava P., 2007, In: Hledík S., Stuchlík Z. (eds.) Proceedings of RAGtime 8/9: Workshops on Black Holes and Neutron Stars., Silesian Univ., Opava, Czech Republic, p.71
Hamann W., Feldmeier A., Oskinova L.M., (eds.) 2008, Clumping in Hot-Star Winds, Universitätsverlag Potsdam, Potsdam, `http://opus.kobv.de/ubp/volltexte/2008/1398/`
Hanke M., 2007, *Diploma thesis*, University of Regensburg
Hanke M., Wilms J., Nowak M.A., et al., 2010a, In: The Energetic Cosmos: from Suzaku to ASTRO-H. JAXA Special Publication JAXA-SP-09-008E ISSN 1349-113X, p.294
Hanke M., Wilms J., Nowak M.A., et al., 2010b, A&A 509, L8
Hanke M., Wilms J., Nowak M.A., et al., 2009, ApJ 690, 330
Hanke M., Wilms J., Nowak M.A., et al., 2008, In: E. Kalemci (ed.) Microquasars and Beyond, Proceedings of Science, Trieste, p. 29
Harmon B.A., Fishman G.J., Wilson C.A., et al., 2002, ApJS 138, 149
Hatchett S., McCray R., 1977, ApJ 211, 552
Hawking S.W., 1974, Nat 248, 30
Herrero A., Kudritzki R.P., Gabler R., et al., 1995, A&A 297, 556
Hirschi R., Meynet G., Maeder A., et al., 2010, In: ASP Conf. Ser. 425, Leitherer C., Bennett P., Morris P., van Loon J. (eds.) Hot and Cool: Bridging Gaps in Massive Star Evolution, ASP, San Francisco, CA, p.13
Hjellming R.M., Wade C.M., 1971, ApJ 168, L21
Holt S.S., Boldt E.A., Serlemitsos P.J., Kaluzienski L.J., 1976, ApJ 203, L63

Homan J., Belloni T., 2005, Ap&SS 300, 107
Houck J.C., 2002, In: Branduardi-Raymont G. (ed.) High Resolution X-ray Spectroscopy with XMM-Newton and Chandra, MSSL, London
Houck J.C., Denicola L.A., 2000, In: ASP Conf. Ser. 216, Manset N., Veillet C., Crabtree D. (eds.) Astronomical Data Analysis Software and Systems IX, ASP, San Francisco, CA, p. 591
House L.L., 1969, ApJS 18, 21
Hoyle F., Lyttleton R.A., 1939, Proc. Cam. Phil. Soc., p. 405
Hua X., Titarchuk L., 1995, ApJ 449, 188
Huenemoerder D.P., Mitschang A., Dewey D., et al., 2011, AJ 141, 129
Hutchings J.B., 1978, ApJ 226, 264
Hutchings J.B., Cowley A.P., Crampton D., et al., 1974, ApJ 191, 743
Hutchings J.B., Crampton D., Bolton C.T., 1979, PASP 91, 796
Hutchings J.B., Crampton D., Cowley A.P., 1983, ApJ 275, L43
Hutchings J.B., Crampton D., Cowley A.P., et al., 1987, AJ 94, 340
Hutchings J.B., Crampton D., Glaspey J., Walker G.A.H., 1973, ApJ 182, 549
Iben, Jr. I., 1991, ApJS 76, 55
Jahoda K., Markwardt C.B., Radeva Y., et al., 2006, ApJS 163, 401
Jahoda K., Swank J.H., Giles A.B., et al., 1996, In: Proc. SPIE 2808, Siegmund O.H., Gummin M.A. (eds.) EUV, X-Ray, and Gamma-Ray Instrumentation for Astronomy VII, SPIE, Bellingham, WA, p.59
Janka H., Langanke K., Marek A., et al., 2007, Phys. Rep. 442, 38
Jansen F., Lumb D., Altieri B., et al., 2001, A&A 365, L1
Juett A.M., Schulz N.S., Chakrabarty D., 2004, ApJ 612, 308
Juett A.M., Schulz N.S., Chakrabarty D., Gorczyca T.W., 2006, ApJ 648, 1066
Kalberla P.M.W., Burton W.B., Hartmann D., et al., 2005, A&A 440, 775
Kallman T., Bautista M., 2001, ApJS 133, 221
Kallman T.R., 2010, Space Sci. Rev. 136
Karitskaya E.A., Agafonov M.I., Bochkarev N.G., et al., 2005, Astronomical and Astrophysical Transactions 24, 383
Karitskaya E.A., Bochkarev N.G., Bondar' A.V., et al., 2008, Astron. Rep. 52, 362
Karttunen H., Krüger P., Oja H., et al., (eds.) 2007, Fundamental Astronomy, Springer, Berlin
Kendziorra E., Wilms J., Haberl F., et al., 2004, In: Proc. SPIE 5488, Hasinger G., Turner M.J.L. (eds.) UV and Gamma-Ray Space Telescope Systems, SPIE, Bellingham, WA, p.613
Kepler J., 1619, Harmonices Mundi V., Linz
Kerr R.P., 1963, Phys. Rev. Lett. 11, 237
Kirsch M.G.F., Schönherr G., Kendziorra E., et al., 2006, A&A 453, 173
Kitamoto S., Egoshi W., Miyamoto S., et al., 2000, ApJ 531, 546
Kitamoto S., Miyamoto S., Tanaka Y., et al., 1984, PASJ 36, 731
Klein O., Nishina T., 1929, Z. Physik 52, 853
Kompaneets A.S., 1956, Zh.E.F.T. 31, 876 (English translation: 1957, Sov. Phys. JETP, 4, 730)
Korn A.J., Keller S.C., Kaufer A., et al., 2002, A&A 385, 143
Korn A.J., Nieva M.F., Daflon S., Cunha K., 2005, ApJ 633, 899
Krolik J.H., McKee C.F., Tarter C.B., 1981, ApJ 249, 422
Kruskal M.D., 1960, Phys. Rev. 119, 1743
Kubota A., Tanaka Y., Makishima K., et al., 1998, PASJ 50, 667
Kwan J., Krolik J.H., 1981, ApJ 250, 478
Lachowicz P., Zdziarski A.A., Schwarzenberg-Czerny A., et al., 2006, MNRAS 368, 1025
Lamers H.J.G.L.M., 1998, Ap&SS 260, 81
Lamers H.J.G.L.M., Cassinelli J.P., 1999, Introduction to Stellar Winds, Cambridge University Press, Cambridge
Larmor J., 1897, Royal Society of London Philosophical Transactions Series A 190, 205
LaSala J., Charles P.A., Smith R.A.D., et al., 1998, MNRAS 301, 285
Leahy D.A., Ananth A.G., 1992, MNRAS 256, 39
Lépine S., Moffat A.F.J., 2008, AJ 136, 548
Levine A.M., Bradt H., Cui W., et al., 1996, ApJ 469, L33
Levine A.M., Corbet R., 2006, The Astronomer's Telegram 940
Li K.F., Clark G.W., 1974, ApJ 191, L27
Li L.X., Zimmerman E.R., Narayan R., McClintock J.E., 2005, ApJS 157, 335
Lightman A.P., Eardley D.M., 1974, ApJ 187, L1
Lightman A.P., White T.R., 1988, ApJ 335, 57
Lightman A.P., Zdziarski A.A., 1987, ApJ 319, 643
Ling C.J., Mahoney A.W., Wheaton A.W., Lamb C.R., 1990, In: Proceedings of the 21st International Cosmic Ray Conference, Vol. 1., Univ. of Adelaide, Adelaide, p. 197
Ling Z., Zhang S.N., Xiang J., Tang S., 2009, ApJ 690, 224
Liu Q.Z., van Paradijs J., van den Heuvel E.P.J.,

2000, A&AS 147, 25
Liu Q.Z., van Paradijs J., van den Heuvel E.P.J., 2005, A&A 442, 1135
Liu Q.Z., van Paradijs J., van den Heuvel E.P.J., 2006, A&A 455, 1165
Lodders K., 2003, ApJ 591, 1220
Lucy L.B., Solomon P.M., 1970, ApJ 159, 879
Lynden-Bell D., 1969, Nat 223, 690
Lyutyi V.M., Syunyaev R.A., Cherepashchuk A.M., 1973, SvA 17, 1
Magdziarz P., Zdziarski A.A., 1995, MNRAS 273, 837
Maitra D., Markoff S., Brocksopp C., et al., 2009, MNRAS 398, 1638
Makishima K., Maejima Y., Mitsuda K., et al., 1986, ApJ 308, 635
Mark H., Price R., Rodrigues R., et al., 1969, ApJ 155, L143
Markoff S., Nowak M.A., Wilms J., 2005, ApJ 635, 1203
Markova N., Puls J., Scuderi S., Markov H., 2005, A&A 440, 1133
Marshall H.L., Schulz N.S., Fang T., et al., 2001, In: Yaqoob T., Krolik J.H. (eds.) X-ray Emission from Accretion onto Black Holes., Johns Hopkins Univ., Baltimore, MD
Mason K.O., Hawkins F.J., Sanford P.W., et al., 1974, ApJ 192, L65
Matsuoka M., Kawasaki K., Ueno S., et al., 2009, PASJ 61, 999
McConnell M.L., Zdziarski A.A., Bennett K., et al., 2002, ApJ 572, 984
Merloni A., Fabian A.C., Ross R.R., 2000, MNRAS 313, 193
Mihalas D., 1978, Stellar atmospheres, W. H. Freeman, San Francisco
Miller J.M., 2007, ARA&A 45, 441
Miller J.M., Cackett E.M., Reis R.C., 2009a, ApJ 707, L77
Miller J.M., Fabian A.C., Wijnands R., et al., 2002, ApJ 578, 348
Miller J.M., Reynolds C.S., Fabian A.C., et al., 2009b, ApJ 697, 900
Miller J.M., Wojdowski P., Schulz N.S., et al., 2005, ApJ 620, 398
Mitsuda K., Inoue H., Koyama K., et al., 1984, PASJ 36, 741
Miškovičová I., Hanke M., Wilms J., et al., 2011, In: Polackova I. (ed.) Acta Polytechnica, submitted (arXiv: 1103.2711)
Miyamoto S., Kimura K., Kitamoto S., et al., 1991, ApJ 383, 784
Morris S.L., 1985, ApJ 295, 143
Müller A., 2004, Ph.D. thesis, University of Heidelberg
Murdin P., Webster B.L., 1971, Nat 233, 110
Murray S.S., Austin G.K., Chappell J.H., et al., 2000, In: Proc. SPIE 4012, J. E. Truemper & B. Aschenbach (ed.) X-Ray Optics, Instruments, and Missions III, SPIE, Bellingham, WA, p.68
Nagae O., Kawabata K.S., Fukazawa Y., et al., 2009, AJ 137, 3509
Negueruela I., Coe M.J., 2002, A&A 385, 517
Netzer H., 2004, ApJ 604, 551
Newman E.T., Couch E., Chinnapared K., et al., 1965, J. Math. Phys. 6, 918
Newton I., 1687, Philosophiæ Naturalis Principia Mathematica, London
Ninkov Z., Walker G.A.H., Yang S., 1987a, ApJ 321, 438
Ninkov Z., Walker G.A.H., Yang S., 1987b, ApJ 321, 425
Noble M.S., Houck J.C., Davis J.E., et al., 2006, In: ASP Conf. Ser. 351, Gabriel C., Arviset C., Ponz D., Enrique S. (eds.) Astronomical Data Analysis Software and Systems XV, ASP, San Francisco, CA, p. 481
Noble M.S., Nowak M.A., 2008, PASP 120, 821
Nowak M.A., Hanke M., Trowbridge S.N., et al., 2011, ApJ 728, 13
Nowak M.A., Juett A., Homan J., et al., 2008, ApJ 689, 1199
Nowak M.A., Wilms J., Heindl W.A., et al., 2001, MNRAS 320, 316
Oda M., 1977, Space Sci. Rev. 20, 757
Oppenheimer J.R., Volkoff G.M., 1939, Phys. Rev. 55, 374
Orosz J.A., Steeghs D., McClintock J.E., et al., 2009, ApJ 697, 573
Oskinova L.M., Feldmeier A., Hamann W., 2006, MNRAS 372, 313
Oskinova L.M., Hamann W.R., Feldmeier A., 2007, A&A 476, 1331
Overbeck J.W., Tananbaum H.D., 1968, Phys. Rev. Lett. 20, 24
Overbeck J.W., Womack E.A., Tananbaum H.D., 1967, ApJ 150, 47
Owocki S., 2004, In: Heydari-Malayeri M., Stee P., Zahn J.P. (eds.) Evolution of Massive Stars, Mass Loss and Winds, Vol. 13. EAS Publ. Ser., EDP Sciences, Les Ulis, p.163
Owocki S., van Marle A.J., 2008, In: IAU Symp. 250, Bresolin F., Crowther P.A., Puls J. (eds.) Massive Stars as Cosmic Engines, p.71
Owocki S.P., Castor J.I., Rybicki G.B., 1988, ApJ 335, 914
Owocki S.P., Rybicki G.B., 1984, ApJ 284, 337
Paciesas W.S., Robinson C.R., McCollough M.L., et al., 1997, In: AIP Conf. Ser. 410, Dermer C.D., Strickman M.S., Kurfess J.D.

(eds.) Proceedings of the Fourth Compton Symposium, AIP, New York, p. 834
Pakull M., 1980, IAU Circ. 3472, 1
Palmeri P., Quinet P., Mendoza C., et al., 2008, ApJS 177, 408
Parker E.N., 1958, ApJ 128, 664
Parker E.N., 1960, ApJ 132, 821
Parmar A.N., Heger D., Metcalfe L., et al., 2008, Astron. Nachr. 329, 114
Parsignault D.R., Epstein A., Grindlay J., et al., 1976, Ap&SS 42, 175
Pauldrach A., Puls J., Kudritzki R.P., 1986, A&A 164, 86
Persi P., Ferrari-Toniolo M., Grasdalen G.L., Spada G., 1980, A&A 92, 238
Planck M., 1901, Ann. Phys. 309, 553
Pooley G., 2001, IAU Circ. 7729, 3
Pooley G.G., Fender R.P., Brocksopp C., 1999, MNRAS 302, L1
Porter J.M., Rivinius T., 2003, PASP 115, 1153
Pottschmidt K., Wilms J., Nowak M.A., et al., 2000, A&A 357, L17
Pottschmidt K., Wilms J., Nowak M.A., et al., 2003, A&A 407, 1039
Poutanen J., Zdziarski A.A., Ibragimov A., 2008, MNRAS 389, 1427
Pozdnyakov L.A., Sobol I.M., Syunyaev R.A., 1983, Astrophysics and Space Physics Reviews 2, 189
Pravdo S.H., White N.E., Becker R.H., et al., 1980, ApJ 237, L71
Predehl P., Braeuninger H.W., Brinkman A.C., et al., 1997, In: Proc. SPIE 3113, R. B. Hoover & A. B. Walker (ed.) Grazing Incidence and Multilayer X-Ray Optical Systems, SPIE, Bellingham, WA, p.172
Predehl P., Schmitt J.H.M.M., 1995, A&A 293, 889
Price R.E., Groves D.J., Rodrigues R.M., et al., 1971, ApJ 168, L7
Pringle J.E., 1981, ARA&A 19, 137
Przybilla N., Nieva M.F., Heber U., et al., 2008, A&A 480, L37
Puls J., Kudritzki R.P., Herrero A., et al., 1996, A&A 305, 171
Puls J., Markova N., Scuderi S., et al., 2006, A&A 454, 625
Puls J., Vink J.S., Najarro F., 2008, Astron. Astrophys. Rev. 16, 209
Rappaport S., Zaumen W., Doxsey R., 1971, ApJ 168, L17
Remillard R.A., Canizares C.R., 1984, ApJ 278, 761
Remillard R.A., McClintock J.E., 2006, ARA&A 44, 49
Richter O.G., Tammann G.A., Huchtmeier W.K., 1987, A&A 171, 33
Rothschild R.E., Blanco P.R., Gruber D.E., et al., 1998, ApJ 496, 538
Rowland H.A., 1882, The Observatory 5, 224
Rushton A., Miller-Jones J., Paragi Z., et al., 2011, arXiv 1101.3322
Rybicki G.B., Lightman A.P., 1979, Radiative processes in astrophysics, Wiley-Interscience, New York
Schlegel E.M., Marshall F.E., Mushotzky R.F., et al., 1994, ApJ 422, 243
Schmid C., Martin M., Wilms J., et al., 2010, In: AIP Conf. Ser. 1248, Comastri A., Angelini L., Cappi M. (eds.) X-ray Astronomy 2009: Present Status, Multi-Wavelength Approach and Future Perspectives, AIP, Melville, NY, p.591
Schramkowski G.P., Torkelsson U., 1996, Astron. Astrophys. Rev. 7, 55
Schulz N.S., Cui W., Canizares C.R., et al., 2002, ApJ 565, 1141
Schulz N.S., Huenemoerder D.P., Ji L., et al., 2009, ApJ 692, L80
Schwarzschild K., 1916, Pr.Akad.Wiss. 189
Sedlmayr E., Dominik C., 1995, Space Sci. Rev. 73, 211
Shafter A.W., Harms R.J., Margon B., Katz J.I., 1980, ApJ 240, 612
Shakura N.I., Sunyaev R.A., 1973, A&A 24, 337
Shapiro S.L., Lightman A.P., Eardley D.M., 1976, ApJ 204, 187
Shaposhnikov N., Titarchuk L., 2007, ApJ 663, 445
Shimura T., Takahara F., 1995, ApJ 445, 780
Shrader C., Titarchuk L., 1998, ApJ 499, L31
Smale A., Appendix F: The XTE Technical Appendix, `http://heasarc.gsfc.nasa.gov/docs/xte/RXTE_tech_append.pdf`
Smith D.M., Dawson D.M., Swank J.H., 2007, ApJ 669, 1138
Smith D.M., Heindl W.A., Swank J.H., 2002, ApJ 569, 362
Smith R.K., Brickhouse N.S., Liedahl D.A., Raymond J.C., 2001, In: ASP Conf. Ser. 247, G. Ferland & D. W. Savin (ed.) Spectroscopic Challenges of Photoionized Plasmas, ASP, San Francisco, CA, p.161
Sowers J.W., Gies D.R., Bagnuolo W.G., et al., 1998, ApJ 506, 424
Spitzer L., 1978, Physical processes in the interstellar medium, Wiley-Interscience, 1978., New York
Steiner J.F., Narayan R., McClintock J.E., Ebisawa K., 2009, PASP 121, 1279
Stelzer B., Wilms J., Staubert R., et al., 1999,

A&A 342, 736
Stevens I.R., 1991, ApJ 379, 310
Stirling A.M., Spencer R.E., de la Force C.J., et al., 2001, MNRAS 327, 1273
Strobel E., 2010, *Master's thesis*, University of Erlangen-Nuremberg
Strüder L., Briel U., Dennerl K., et al., 2001, A&A 365, L18
Sturner S.J., Shrader C.R., Weidenspointner G., et al., 2003, A&A 411, L81
Suchy S., Pottschmidt K., Wilms J., et al., 2008, ApJ 675, 1487
Sunyaev R.A., Titarchuk L.G., 1980, A&A 86, 121
Svensson R., 1987, MNRAS 227, 403
Szostek A., Zdziarski A.A., 2007, MNRAS 375, 793
Tananbaum H., Gursky H., Kellogg E., et al., 1972, ApJ 177, L5
Tananbaum H., Kellogg E., Gursky H., et al., 1971, ApJ 165, L37
Tarasov A.E., Brocksopp C., Lyuty V.M., 2003, A&A 402, 237
Tarter C.B., Tucker W.H., Salpeter E.E., 1969, ApJ 156, 943
Thorne K.S., Price R.H., 1975, ApJ 195, L101
Titarchuk L., 1994, ApJ 434, 570
Titarchuk L., Hua X., 1995, ApJ 452, 226
Titarchuk L., Lyubarskij Y., 1995, ApJ 450, 876
Tolman R.C., 1939, Phys. Rev. 55, 364
Treves A., Chiappetti L., Tanzi E.G., et al., 1980, ApJ 242, 1114
Turner M.J.L., Abbey A., Arnaud M., et al., 2001, A&A 365, L27
Unsöld A., Baschek B., 2001, The new cosmos: an introduction to astronomy and astrophysics, Springer, Berlin, 5th edition
Urry C.M., Padovani P., 1995, PASP 107, 803
Uttley P., McHardy I.M., Vaughan S., 2005, MNRAS 359, 345
van Paradijs J., 1995, In: Lewin W.H.G., van Paradijs J., van den Heuvel E.P.J. (eds.) X-ray Binaries., Cambridge Univ. Press, Cambridge, p.536
Verbunt F., 1993, ARA&A 31, 93
Verner D.A., Yakovlev D.G., 1995, A&AS 109, 125
Voloshina I.B., Lyutyi V.M., Tarasov A.E., 1997, Astron. Let. 23, 293
Vrtilek S.D., Boroson B., Hunacek A., et al., 2008, ApJ 678, 1248
Wade C.M., Hjellming R.M., 1972, Nat 235, 271
Walborn N.R., 1973, ApJ 179, L123
Walker E.N., 1972, MNRAS 160, 9P
Webster B.L., Murdin P., 1972, Nat 235, 37
Wen L., Cui W., Levine A.M., Bradt H.V., 1999, ApJ 525, 968
Weymann R., 1965, Physics of Fluids 8, 2112
White N.E., 1989, A&A 1, 85
Wilkinson T., Uttley P., 2009, MNRAS 397, 666
Wilms J., 2006, Nat 444, 699
Wilms J., Allen A., McCray R., 2000, ApJ 542, 914
Wilms J., Nowak M.A., Pottschmidt K., et al., 2001, MNRAS 320, 327
Wilms J., Nowak M.A., Pottschmidt K., et al., 2006, A&A 447, 245
Wilms J., Nowak M.A., Pottschmidt K., et al., 2003, In: Durouchoux P., Fuchs Y., Rodriguez J. (eds.) New Views on Microquasars., Center for Space Physics, Kolkata (India), p. 49
Woitke P., 2006, A&A 452, 537
Wolter H., 1952a, Ann. Phys. 445, 94
Wolter H., 1952b, Ann. Phys. 445, 286
Woosley S., Janka T., 2005, Nature Physics 1, 147
XMM SOC 2010, XMM-Newton Users Handbook, Issue 2.8.1, `http://xmm.esac.esa.int/external/xmm_user_support/documentation/uhb/index.html`
Yan J., Liu Q., Hadrava P., 2008, AJ 136, 631
Yao Y., Wang Q.D., Nan Zhang S., 2005, MNRAS 362, 229
Yu W., Yan Z., 2009, ApJ 701, 1940
Zdziarski A.A., 1985, ApJ 289, 514
Zhang S.N., Cui W., Harmon B.A., et al., 1997, ApJ 477, L95
Zhang S.N., Ling Z., Xiang J., Tang S., 2009, In: ASP Conf. Ser. 404, Murphy S.J., Bessell M.S. (eds.) The Eighth Pacific Rim Conference on Stellar Astrophysics: A Tribute to Kam-Ching Leung, ASP, San Francisco, CA, p.144
Ziółkowski J., 2005, MNRAS 358, 851

Acknowledgments

I'd like to thank Jörn Wilms, who introduced me to the exciting field of X-ray astronomy and who never stops coming up with new ideas, for giving me the opportunity to conduct this research, for the trust in myself, and for allowing me to follow my own ideas. He made a lot of effort to organize external funds enabling me, e.g., to spend several research periods with our colleagues and to attend international conferences.

I want to thank all my colleagues from Dr. Karl Remeis observatory who maintain a collaborative atmosphere as it used to be when the group was still smaller. I'm particularly grateful for the strong support from my office mates, who also proof read parts of this thesis and gave helpful comments. Moritz Böck has always been the first with whom I could discuss ideas, news, or problems. His insight in astrophysical processes, his ($\geq$3-dimensional) imagination, and his critical view have contributed a lot to the interpretation of my results. Likewise, Thomas Dauser has always had a sympathetic ear – not only for questions of General Relativity and perl programming. Thanks to both for the jolly good time – and also to our next-door fellows! In particular, I'd like to thank Felix Fürst for thousand open-minded discussions; Christian Schmid for his help with CFITSIO, C programming, and CCD detectors; and Laura Barragán for her help in Madrid and for her support with *Suzaku* and *Swift* data reduction. Thanks to Victoria Grinberg for her work on *INTEGRAL* light curves. Thanks to Eckhard Strobel for the nice project on absorption dips, and to Ivica Miškovičová for discussions about Cyg X-1. I'm grateful to Ingo Kreykenbohm for taking over with the computer adminstration, and to Fritz Schwarm for his efforts on parallel computing and the new batch system on our cluster. I thank all members of the institute for the fun and all the events at the observatory. I'm finally grateful to Uli Heber for providing a review of this thesis.

It's a pleasure to thank my colleagues from MIT Kavli Institute / CXC – not only for their hospitality during five visits and for their cooperativeness. Michael A. Nowak was always a reliable contact person whenever an unbiased opinion on any kind of issue or result was needed. I admire his deep insights and ability to pinpoint the truth behind the scenes. Doing creative interpretational research requires flexible tools that allow to get familiar with the data and to test one's ideas. I'm therefore thankful to John C. Houck, John E. Davis, and Michael S. Noble for their work on ISIS and S-Lang, and for all their open source projects that have simplified data analysis so much. All four abovementioned scientists have taught me a lot, both in person, and by their codes. John E. Davis deserves special thanks – not only for software like the `jed` editor and the S-Lang xfig module that was used to express my ideas and results – but also for the kind invitation to 2010's Easter Sunday barbeque with his family. I acknowledge helpful discussions with Norbert S. Schulz, David P. Huenemoerder – and Julia C. Lee from Harvard / CfA, who kindly agreed to provide an assessment of this thesis.

I want to thank the group at Goddard Space Flight Center, in particular Katja Pottschmidt for her hospitality and help, and Tim Kallman for his help on `xstar` and the `warmabs` model.

This research has made frequent use of NASA's Astrophysics Data System Service[3], of the High Energy Astrophysics Science Archive Research Center, in particular the data archive browser[4] provided by NASA's Goddard Space Flight Center, as well as the monitoring light curves provided by the *Swift* BAT team at GSFC[5] and the *RXTE* ASM team at MIT[6].

[3] See `http://adsabs.harvard.edu/abstract_service.html`.
[4] See `http://heasarc.gsfc.nasa.gov/db-perl/W3Browse/w3browse.pl`.
[5] See `http://swift.gsfc.nasa.gov/docs/swift/results/transients`.
[6] See `http://xte.mit.edu/ASM_lc.html`.

Financially, I acknowledge • the funding of my university studies for four years from the Bavarian Gifted Students Scholarship, • the allowance during my student traineeship at the European Space Astronomy Center for three months from the Internship programme of the European Space Agency, • the funding as a research associate for 3¼ years from the *Bundesministerium für Wirtschaft und Technologie* through the *Deutsches Zentrum für Luft- und Raumfahrt* under contract 50 OR 0701, • the accomodation and per diem during three visits at the International Space Science Institute (Berne) from the ISSI, • the nomination for and funding of my participation in the 60th Meeting of Nobel Laureates in Lindau by – the Chair of Applied Physics of the University of Erlangen-Nuremberg, – the *Verein der Bayerischen Chemischen Industrie*, and – the Wilhelm and Else Heraeus Foundation, • additional travel support from – the Black Hole Universe Consortium funded by the European Commission through grant PITN-GA-2008-215212, and – the Elite Network of Bavaria through the Elite Graduate Program 'Physics with Integrated Doctorate Program', as well as • the *Bundesagentur für Arbeit* helping me to bridge four months to finish my PhD.

I'm grateful to my family, who has let me follow my own ways, for the confidence and understanding they had to show – in particular during the final phase of this work.

Ich danke meiner Familie, die mich meine eigenen Wege gehen ließ, für das Vertrauen und Verständnis, das sie mir – besonders in der Endphase dieser Arbeit – entgegenbringen mußte.

Even more, I have to thank Alexandra Hundschell for her patience while standing by me! After a long time of deprivation, this thesis is now finished, but our new life has just begun.

This thesis has been typeset from a TEX/LATEX file prepared by the author.